Satoru Kaneko · Masami Aono ·
Alina Pruna · Musa Can · Paolo Mele ·
Mehmet Ertugrul · Tamio Endo *Editors*

Carbon Related Materials

Commemoration for Nobel Laureate Professor Suzuki Special Symposium at IUMRS-ICAM2017

Springer

Carbon Related Materials

Nobel Prize Laureate Prof. Suzuki IUMRS-ICAM2017

Special Symposium: Carbon Related Materials

The 15th International Conference on Advanced Materials

VENUE: KYOTO UNIVERSITY, JAPAN
DATE: AUG. 27 (SUN.) - SEP. 1 (FRI.), 2017
URL: HTTP://WWW.IUMRS-ICAM2017.ORG

Call for papers

Dr. Satoru Kaneko
(Kanagawa Inst. of Ind. Sci. Tech., KISTEC)
satoru@kanagawa-iri.jp

Dr. Masami Aono
(National Defence Academy)

Dr. Tetsuo Tsuchiya (AIST)

Prof. Tamio Endo (Mie University)

Prof. Masahiro Yoshimura
(Nat. Cheng Kung Univ. Taiwan)

Prof. Nobuyuki Iwata (Nihon Univ.)

Prof. Paolo Mele (Muroran Inst. Tch.)

Prof. Hiroaki Nishikawa (Kinki Univ.)

Prof. Tomoaki Terasako (Ehime Univ.)

Prof. Sarawut Rimdusit (Chulalongkorn University)

Prof. Yasuteru Mawatari (Muroran Inst. Tech.)

Prof. Yudi Darma (Inst. tech. Bandung)

Prof. Kung-Sen Sung
(Nat. Cheng Kung Univ. Taiwan)

Dr. Alina Pruna (Polytec. Univ. Bucharest)

Prof. Mariana Ionita (Polytec. Univ. Bucharest)

Prof. Rodringo Martins (Universidade Nova)

Team Harmonized Oxides

URL:http://www.nims.go.jp/nqe/sa/tho/

CARBON Symposium
in Honor of Prof. SUZUKI

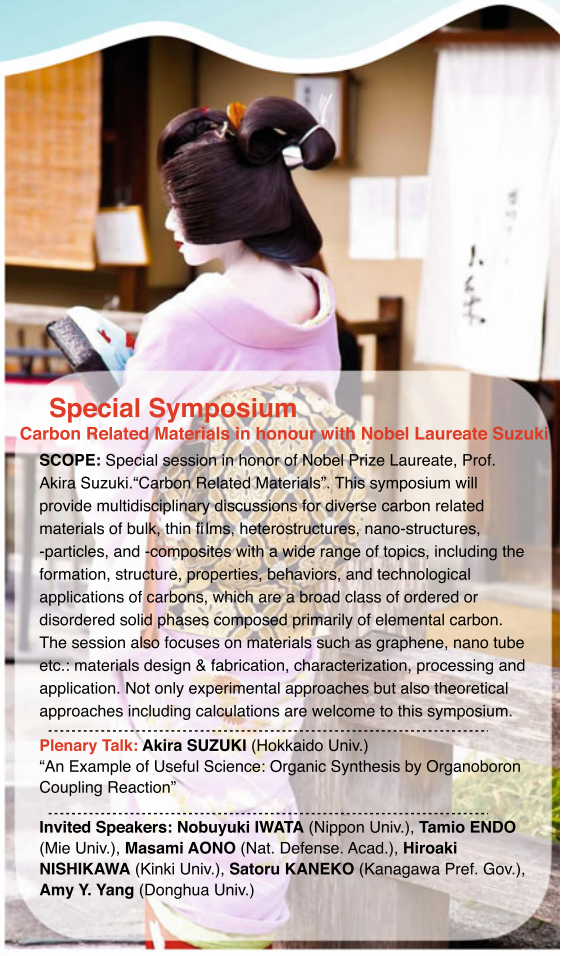

Special Symposium

Carbon Related Materials in honour with Nobel Laureate Suzuki

SCOPE: Special session in honor of Nobel Prize Laureate, Prof. Akira Suzuki."Carbon Related Materials". This symposium will provide multidisciplinary discussions for diverse carbon related materials of bulk, thin films, heterostructures, nano-structures, -particles, and -composites with a wide range of topics, including the formation, structure, properties, behaviors, and technological applications of carbons, which are a broad class of ordered or disordered solid phases composed primarily of elemental carbon. The session also focuses on materials such as graphene, nano tube etc.: materials design & fabrication, characterization, processing and application. Not only experimental approaches but also theoretical approaches including calculations are welcome to this symposium.

Plenary Talk: Akira SUZUKI (Hokkaido Univ.)
"An Example of Useful Science: Organic Synthesis by Organoboron Coupling Reaction"

Invited Speakers: Nobuyuki IWATA (Nippon Univ.), **Tamio ENDO** (Mie Univ.), **Masami AONO** (Nat. Defense. Acad.), **Hiroaki NISHIKAWA** (Kinki Univ.), **Satoru KANEKO** (Kanagawa Pref. Gov.), **Amy Y. Yang** (Donghua Univ.)

designed by Satoru Kaneko

Satoru Kaneko · Masami Aono · Alina Pruna ·
Musa Can · Paolo Mele · Mehmet Ertugrul ·
Tamio Endo
Editors

Carbon Related Materials

Commemoration for Nobel Laureate Professor Suzuki Special Symposium at IUMRS-ICAM2017

Springer

Editors
Satoru Kaneko
Kanagawa Institute of Industrial Science and Technology
Ebina, Kanagawa, Japan

Alina Pruna
Center for Surface Science and Nanotechnology
University Politehnica of Bucharest
Bucureşti, Romania

Paolo Mele
Shibaura Institute of Technology
Tokyo, Japan

Tamio Endo
Japan Advanced Chemicals
Atsugi, Kanagawa, Japan

Masami Aono
Department of Electrical and Electronics Engineering
Kagoshima University
Kagoshima, Japan

Musa Can
Department of Physics
Faculty of Science
Istanbul University
Istanbul, Turkey

Mehmet Ertugrul
Faculty of Engineering
Ataturk University
Erzurum, Turkey

ISBN 978-981-15-7609-6 ISBN 978-981-15-7610-2 (eBook)
https://doi.org/10.1007/978-981-15-7610-2

This Springer imprint is published by the registered company Springer Nature Singapore Pte Ltd.
The registered company address is: 152 Beach Road, #21-01/04 Gateway East, Singapore 189721, Singapore

Foreword

I am not a specialist in studies on carbon-related materials. I attended the International Conference of IUMRS-ICAM-2017 (International Union of Materials Research Societies—International Conference on Advanced Materials, August 27–September 1, 2017, Kyoto), by the invitation of Prof. Tamio Endo (Japan Advanced Chemicals, Professor Emeritus Mie University) and conference committee. I delivered Nobel Lecture on "An Example of Useful Science: Organic Synthesis by Organoboron Coupling Reaction". There I made many friends including Dr. Satoru Kaneko (KISTEC) and Prof. Paolo Mele (Shibaura Institute of Technology). This time, they requested me to write the Foreword for this book.

In 1963, I joined Prof. Herbert C. Brown's research group, who received Nobel Prize in Chemistry 1997, in Purdue University, the USA, as a postdoctoral associate, fascinated with the interesting new reaction, hydroboration. After two years stay in Purdue, I returned to Hokkaido University where I started to study for organic synthesis using organoboron compounds. We recognized the potential of organoboranes as intermediates in organic synthesis. Our discoveries of haloboration and cross-coupling reactions are a fundamental contribution to the organic chemistry of boron and synthetic methodology.

The cross-coupling reaction is widely used for the stereodefined construction of carbon–carbon bonding in multifunctional systems. I retired from the university. However, I am very happy to have a chance to meet many young researchers at international meetings to discuss the chemistry. I hope this book is useful for such young chemists.

Prof. Akira Suzuki
Hokkaido University Professor

Nobel Laureate in Chemistry, 2010

Hokkaido University
Sapporo, Japan

Preface

We, (Team Harmonized Oxides: THO), organized five Symposia in IUMRS-ICAM-17 in Kyoto University (International Union of Materials Research Societies—International Conference on Advanced Materials, August 27–September 1, 2017, Kyoto). THO is a unique scientist group which was established by Tamio Endo (Mie University) and Kazuhiro Endo (AIST) to develop materials sciences and to promote International Comprehensions and World Peace. Under such policies, the five Symposia were conducted; (1) Magnetic Oxide Thin Films and Hetero-structures, (2) **Nobel Laureate Prof. Suzuki Special Symposium—Carbon-Related Materials**, (3) Superconducting Materials and Applications, (4) Thermoelectric Materials for Sustainable Development—ACT2017 and (5) Synthesis of Functional Materials for Next Generation Innovative Devices Applications. These were arranged as (3rd Bilateral MRS-J/E-MRS Symposium), then many of European Scientists were invited such as Ulrich Habermeier (Germany), Josep Nogues (Spain), Rodrigo Martins (Portugal), Oleksandr Tovstolytkin (Ukraine) and Jacobo Santamaria (Spain). We invited Axel Hoffmann (Argonne Nat. Lab., one of THO international members) from the USA to deliver Plenary Lecture.

The Symposium of Carbon-Related Materials (2) was held in recognition of Nobel Plenary Lecture by **Prof. Akira Suzuki** (Professor Emeritus Hokkaido University, Nobel Prize, Chemistry, 2010).

Organizers of Symposium

Satoru Kaneko (Kanagawa Industrial Technology Center)
Masami Aono (National Defense Academy of Japan)
Tetsuo Tsuchiya (National Institute of AIST)
Tamio Endo (Sagamihara Surface Laboratory)
Masahiro Yoshimura (National Cheng Kung University)
Nobuyuki Iwata (Nihon University)
Paolo Mele (Muroran Institute of Technology)

Hiroaki Nishikawa (Kinki University)
Tomoaki Terasako (Ehime University)
Yasuteru Mawatari (Muroran Institute of Technology)
Sarawut Rimdusit (Chulalongkorn University)
Yudi Darma (Institute Technology Bandung)
Kuang-Sen Sung (National Cheng Kung University)
Alina Pruna (Polytechnic University of Bucharest)
Mariana Ionita (Polytechnic University of Bucharest)
Rodrigo Martins (Universidade Nova)

Invited Keynote Speakers of Symposium

Yoshitake Nishi, Masataka Hasegawa, Hiroki Ago, Kazuhiko Matsumoto, Masahiro Yoshimura, Thomas Lippert, Yoku Inoue, Naum Naveh, Mehmet Ali Gulgun

Scope of Symposium

This is Special Symposium in honor of Nobel Prize Laureate, Prof. Akira Suzuki. Recently, "Carbon-Related Materials" have been becoming very popular and important. We promote researches on these materials, including categories of formations, structures, electrical/magnetic/optical properties, mechanical behaviors, in view of their technological applications. We discuss a broad class of ordered and disordered solid phases composed primarily of elemental carbon. Organic materials are included as well as inorganic materials. The Symposium focuses on materials such as diamonds, graphites, graphenes, C-nanotubes, carbon fibers and composites; and we discuss them together. One special session touches upon CNT composites with respect to Prof. Sumio Iijima. It is welcomed to discuss chemical bonds of C–C and others such as C–O.

All the participants presented their excellent papers, and we had very active and excited discussions in this Symposium. Then we, organizers, determined to publish a memorial book of this Symposium. We requested the participants and their affiliated scientists to contribute on one chapter in consonance with the Symposium Scope in the book. We are convinced, these authors are submitting exquisite papers, then readers can get profitable knowledge from this book. We would like to express our special thanks to all the authors of chapters, reviewers and editors of this book.

Supplementary we would like to note, these five Symposia by THO were held in conjunction with the meeting of MRS Japan: Nano Oxides Materials Research Society.

Lastly, we would like to mention, Prof. Hanns-Ulrich Habermeier (Max-Planck, Stuttgart) has passed away on July 20, 2019, in Stuttgart, Germany. He acted as President of IUMRS (2015–2016) and President of E-MRS (2000–2003). He was a

nice guy, an international member of THO and our close friend. He kindly delivered his fruitful keynote talk in Symposium (1), greatly appreciated! “Our sympathies are with him!”

Nobel Plenary Lecture by Prof. Akira Suzuki

Satoru Kaneko, Head Organizer

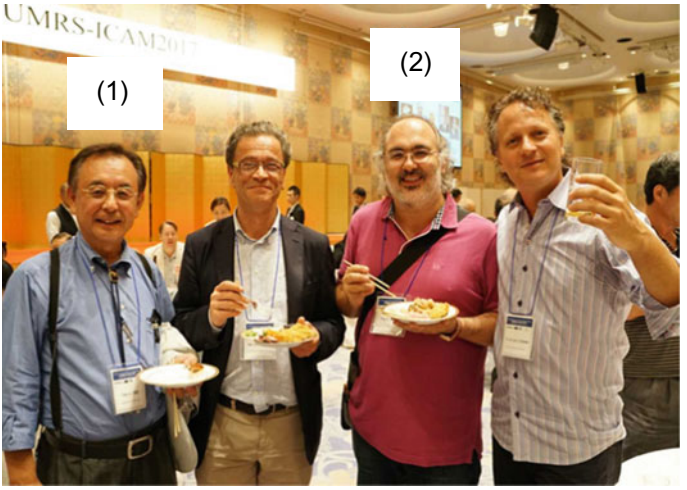

(1)Tamio Endo, (2) Paolo Mele, Organizers

(1) Axel Hoffmann, Plenary Speaker, Kyoto University Campus

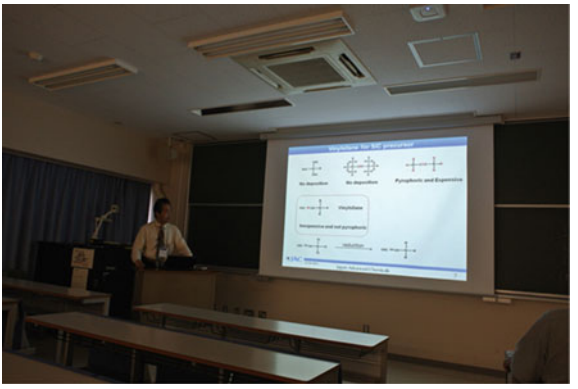

One scene of Carbon Related Materials Symposium, Shigeo Yasuhara

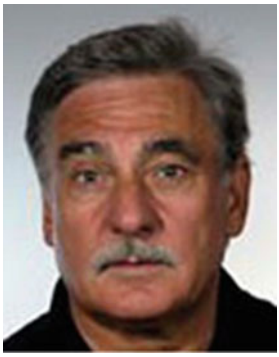

Prof. Hanns-Ulrich
Habermeier (Departed)

Tsu, Japan
November 2019

Tamio Endo
Japan Advanced Chemicals
Atsugi, Japan

Professor Emeritus Mie University

Honorary Professor
South West Jiaotong University
Chengdu, China

Satoru Kaneko
Kanagawa Institute of Industrial Science
and Technology (KISTEC)
Ebina, Japan

Paolo Mele
Shibaura Institute of Technology
Saitama, Japan

Contents

Chapter 1
From Unidimensional Carbonaceous Materials to Multidimensional Structures Through Molecular Modeling

Elena Alina Chiticaru, Sebastian Muraru, and Mariana Ioniţă

1.1 Introduction

Carbon, the sixth element on the periodic table, it is among the most abundant elements in the universe, on Earth, and in the human body, being the foundation of all life forms. The versatility of this element, capable of binding itself as well as many other elements and molecules, has attracted great interest from the scientific community. Carbon's existence in many forms is called allotropy, an advantageous quality exploited by industrial and academic fields for a wide range of applications [1]. Two natural carbon allotropes, diamond and graphite, are long-known, yet still the subject of intensive research even though they are already the basis of many commercial applications. For example, crystalline diamond, known for its hardness, is used in various experiments as hard tips or in the jewelry industry, while amorphous graphite has semi-conductive properties and is employed in lithium-ion batteries [2].

A carbon allotrope revolution began with the discovery of synthetic allotropes, specifically zero-dimensional fullerenes [3], rewarded with a Nobel Prize highlighting the importance of the event. Six years later, the accidental discovery of carbon nanotubes (CNTs) marked another turning point in the scientific field followed by the Nobel awarded graphene, the first two-dimensional material, experimentally obtained and characterized by a team from University of Manchester [4]. However, the search for new allotropes has not ended. By altering the carbon bonds in graphene or diamond, for example, an abundance of novel structures have been proposed in

Elena Alina Chiticaru and Sebastian Muraru: These authors have contributed equally to this work.

E. A. Chiticaru · S. Muraru · M. Ioniţă (✉)
Faculty of Medical Engineering, University Politehnica of Bucharest, Gh. Polizu 1-7, 011061 Bucharest, Romania
e-mail: mariana.ionita@polimi.it

M. Ioniţă
Advanced Polymer Materials Group, University Politehnica of Bucharest, Gh. Polizu 1-7, 011061 Bucharest, Romania

S. Kaneko et al. (eds.), *Carbon Related Materials*,
https://doi.org/10.1007/978-981-15-7610-2_1

the last years. These novel materials, including graphyne and penta-graphene, are investigated by means of computational methods, and some, e.g., graphydyine and T-carbone, are already synthesized in the laboratory [2].

1.2 Classification and Fabrication of Carbon Allotropes

1.2.1 Classification

The ability of carbon atoms to form three types of hybridization bonds allows carbon allotrope classification according to three main categories. The first one refers to sp^3 hybridization, characteristic for diamond structure. The second group is represented by graphite (and graphenic structures, such as carbon nanotubes, nanohorns, graphene quantum dots) containing only sp^2 carbon atoms. The *sp* hybridization corresponds to carbyne, a compound of molecular structure including an electrically neutral carbon atom with three non-bonded electrons. Further, carbon allotropes that have a mixed hybrid state are called transitional forms [5].

Another classification that includes all carbon structures is based on the dimensionality of the configuration (Fig. 1.1). The interesting property of elemental carbon is its capacity to exist in all dimensions, starting with zero-dimension nanostructures (e.g., fullerenes, carbon dots, graphene quantum dots, nanodiamond, diamondoids, onion-like carbon), one-dimensional allotropes (e.g., CNTs, nanohorns, nanofibers), two-dimensional materials (graphene and its derivatives),

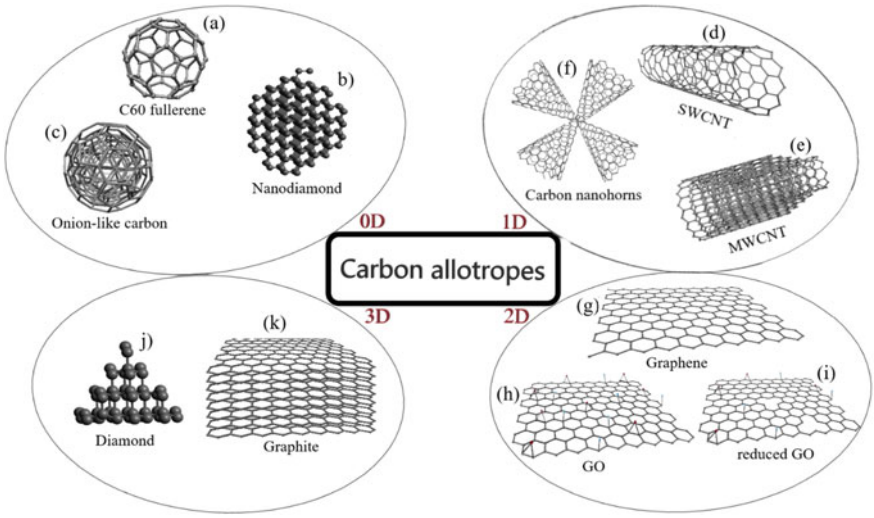

Fig. 1.1 Carbon allotropes arranged based on their dimensionality

ending up with three-dimensional structures (e.g., diamond, graphite, lonsdaleite, and synthetic nanostructures). We discuss each class of carbon allotropes based on this classification.

1.2.2 Synthesis of Carbonaceous Materials

Carbon allotropes can form naturally, like diamond and graphite, or can be synthesized by physical and chemical methods, with specific size, shape, and properties. Nanostructured allotropes are developed by the top-down or bottom-up approach. Briefly, the top-down method implies the use of a bulk or macroscopic material as a precursor that is controllable reorganized so as to obtain a nanosized material with precise properties [6]. For example, zero-dimensional allotropes can be synthesized from various precursors, such as carbon nanotubes, graphene, graphene oxide, graphite, carbon black, or coal, to obtain fullerenes, carbon dots, and graphene quantum dots, using laser ablation, arc discharge, or carbon vapor deposition (CVD) [1]. By the same principle, CNTs are produced from graphene or graphite by arc discharge or CVD, while graphene can be fabricated by exfoliation of graphite or reduction of graphite oxide [6].

By contrast, in the bottom-up approach, elemental precursors (e.g., atoms, molecules) are used to synthesize nanostructures, permitting a higher degree of precision controlling the shape and size of the desired material [7]. However, this route of synthesis is not used in practice as often as the top-down approach. Nevertheless, fullerenes have been obtained experimentally starting from graphite molecules or corannulene ($C_{20}H_{10}$), the smallest subunit of C_{60}. Also, graphene quantum dots can be fabricated from aromatic molecules, while graphene can be prepared using biphenyl molecules that are cross-linked and annealed [6].

1.3 Carbon Allotropes by Dimensionality

1.3.1 Zero-Dimensional Carbon Materials

1.3.1.1 Fullerenes

The fullerenes are closed hollow carbon cages arranged into 12 pentagonal rings and a number of hexagons that can be calculated according to the total number of carbon atoms [6]. The first type of this nanometric structure to be isolated was the C_{60} molecule, also called buckminsterfullerene, reported by Kroto et al. in 1985 [3]. C_{60}, the most abundant experimentally obtained fullerene, represents a simple and highly symmetrical spherical network consisting of sixty carbon atoms [3]. Initially, it was believed that fullerenes had sp^2 hybridized atoms, but it was subsequently

shown that they actually have a very interesting intermediate hybridization between sp^2 and sp^3. In particular, C_{60} has $sp^{2.28}$ hybridization [8]. Also, this molecule has an external diameter of 7.1 Å and the structure of a truncated icosahedron (football-like shape) with 12 pentagonal and 20 hexagonal faces (Fig. 1.1a) that provide excellent stability [3, 6]. Carbon atoms from two adjacent hexagons are connected by double bonds with the length of 1.38 Å, while the length of the single bond between carbons pairing hexagon–pentagon faces is 1.45 Å [9]. At room temperature, C_{60} can exist in solid form having a crystalline, face-centered cubic (fcc) structure that can aggregate and self-assemble into a two-dimensional monolayer [10] or into nanoparticles [11].

Since their discovery, fullerenes have been intensively studied due to the interesting properties they possess, with wide applicability in technology and medicine. Like other fullerenes, C_{60} is insoluble in polar solvents and aqueous solutions but highly soluble in various organic solvents, e.g., toluene, carbon disulfide, and xylenes [12]. The hydrophobicity of these carbon allotropes can be overcome by surface functionalization that enables the design of new materials. The structural morphology of C_{60} facilitates the reaction with free radicals, so it can be used as an antioxidant in biological systems and cosmetics [6]. Notably, hydrophilic fullerenes have the capacity to inhibit human immunodeficiency virus (HIV) activity [13].

The most important property of fullerenes is an efficient electron accepting ability, which is exploited in energy conversion systems as components of organic photovoltaic cells. For instance, by combining an acceptor fullerene derivative ([6, 6]-phenyl-C_{61}-butyric acid methyl ester—PCBM) with a donor polymer (poly(3-hexylthiophene)—P3HT), it is possible to obtain compounds that simulate photosynthesis, used in efficient, low cost, organic solar cells [14]. Another fundamental property of fullerenes concerns the relative inertness of the hollow cages that permits doping with various molecular species. In particular, the capture of alkali metals transforms fullerenes into superconductive crystals [6]. Moreover, the optical limiting properties of these materials make them suitable for the fabrication of protective eyewear [15] and sensors.

Fullerenes include a high number of representatives, from small molecules (C_{20}, C_{24}, C_{26}, C_{28}, C_{30}, C_{32}, C_{36}, C_{50}) to big (C_{70}, C_{76}, C_{78}, C_{80}, C_{82}, C_{84}, C_{90}) and even relatively huge compounds (C_{140}, C_{180}, C_{240}, C_{320}, C_{540}). Some of these have already been experimentally isolated, while others are currently studied by computational methods.

1.3.1.2 Carbon Dots and Graphene Quantum Dots

Carbon dots (CDs), also referred to as carbon quantum dots (CQDs), represent a class of fluorescent materials, with quasi-spherical shape and diameters below 10 nm [7]. These nanoparticles were accidentally discovered by Xu et al. [16] in 2004 during electrophoretic purification of single-walled carbon nanotubes. Graphene quantum dots (GQDs), on the other hand, are small photoluminescent particles that consist of graphene nanosheets with the lateral dimension below 100 nm (usually 3–20 nm), fabricated for the first time in 2008 by the same group that discovered graphene [17].

These two materials have different structure; CDs contain a combination of sp^2 and sp^3 hybridized carbon atoms with an amorphous phase, while GQDs are composed of mainly sp^2 carbons [6], reflecting a higher crystallinity. X-ray diffraction (XRD) measurements reveal a lattice spacing of 4.5 Å for CDs [18] that is higher than the value measured for GQDs (2.1 Å) [19], confirming the partial amorphous nature of the CD particles. However, X-ray photoelectron spectroscopy (XPS) indicated the presence of oxygenated functional groups on the surface of both these nanodots, and depending on their density plus other parameters, the lattice spacing can vary altering properties [7, 18].

The most important property common to these two materials is the strong photoluminescence (PL) that can be tuned by changing their shape, size, or geometry. Alongside photochemical stability and chemical inertness, the fluorescence properties avail carbonaceous nanodots to be used in bioimaging and biosensing [20]. Moreover, the richly oxygenated functional groups on the surface of the nanoparticles grant them high water dispersibility and facilitate further functionalization with biomolecules. Due to low toxicity and high biocompatibility, CDs and GQDs are more suitable than metallic quantum dots in nanomedicine and in vivo applications [21]. All these advantageous properties encouraged scientists to study their efficiency in drug delivery systems (with simultaneous particle tracking), gene delivery applications, and also as therapeutic agents [18]. Since Tour et al. [22] found a cheap way to produce PL carbon dots from coal at an industrial scale, one can expect these fascinating materials to be used in many practical applications, like road and safety signs, bicycle reflectors, and luminous clothing.

1.3.1.3 Nanodiamonds and Diamondoids

Another important zero-dimensional carbon allotrope is represented by nanodiamonds. These nanoparticles were first observed in 1963, during the detonation of military explosives in USSR, and hidden from the rest of the scientific community until 1990 [23]. In 2005, progress was made regarding the research of these nanomaterials, and at present, it is known that nanodiamonds have a spherical shape, consisting of mostly sp^3 hybridized carbon atoms, with a crystalline structure (Fig. 1.1b) and particle diameters of 4–5 nm [6]. Also, diamondoids are described in the literature as diamond nanostructures, with small particle size of 1–2 nm, that are abundant in fossil fuels [24].

Carbon nanodiamonds combine many important properties, like chemical stability, high surface area, biocompatibility, non-toxicity, and easy surface functionalization, making them suitable for biomedical applications; maybe the most important one is the use as a drug delivery agent, when combined with a chemotherapeutic drug (doxorubicin) for cancer treatment [23]. In addition, this nanomaterial has a high Young's modulus, so it is very hard and strong, resistant to degradation, with high thermal conductivity, electrical resistivity, and a large optical band gap [6]. One unique feature of nanodiamonds is the optical transparency and the ability to introduce nitrogen-vacancy (N-V) defects as color centers that under visible light

excitation can emit strong fluorescence with high photostability [23, 25]. This important property allows nanodiamonds to be employed in biolabeling and bioimaging applications and in the design of stable and sensitive sensors [26]. Another expected application of nanodiamonds is in skin care cosmetics and makeup products, due to their high adsorption capacity [26]. There are many potential applications outside the medical field as well, including faster optical transistors that operate at room temperature, plus quantum computing, solar energy conversion, abrasives, and lubricants [27].

1.3.1.4 Onion-like Carbon

A less known carbon derivative is the onion-like carbon (OLC), consisting of a fullerene core enclosed by concentric graphitic layers, having a quasi-spherical shape (Fig. 1.1c) [26, 28]. These nanoparticles were discovered in 1992 by Ugarte [29] via strong irradiation of carbon nanotubes with electron beams. The particle size of OLC can vary between 3 and 30 nm, depending on the synthesis method with the distance between the graphite sheets ≈0.35 nm [6]. The main properties of these allotropes remain similar to any carbon nanoparticles: high surface-to-volume ratio, low toxicity, high cellular uptake, and low density. Due to the relatively modest specific surface area (500–600 m^2/g), in comparison with other carbon structures, OLC was not found very fitting for sensing applications [26]. However, current research indicates that it shows a very strong optical limiting action with prospective photonic applications [30]. Moreover, these nanoparticles reveal a high ion adsorption capacity, good electrical conductivity, high capacity for energy storage but low volumetric capacitance [31]. These key features have attracted use of OLC in the design of electrochemical capacitors [28, 31].

1.3.2 One-Dimensional Carbon Allotropes

1.3.2.1 Carbon Nanotubes

Carbon nanotubes (CNTs) are tubular structures consisting of rolled-up graphene sheets, discovered in June 1991 by Iijima [32] while examining graphite cathode surfaces used in electric-arc evaporation, under an electron microscope. Depending on the number and arrangement of cylinders, these materials can be classified in two categories: single-walled carbon nanotubes (SWCNTs), a single cylinder (Fig. 1.1d) with a diameter of 1–2 nm [33], and multi-walled carbon nanotubes (MWCNTs) that are formed of several concentric tubular graphene structures (Fig. 1.1e) with 0.34 nm between adjacent shells [34]. The structure of the carbon nanotubes renders their unicity and extraordinary properties. The strong covalent bonds of sp^2 carbon atoms increase the stiffness and the mechanical properties in general. Carbon atoms are arranged in a helical lattice that can form three types of structures: armchair,

zigzag, and chiral configurations [33, 34]. Also, the smaller diameter of SWCNTs and the free chirality of the tubes bring a smaller Young's modulus compared to MWCNTs [35].

Properties of CNTs are strongly dependent on the combination of size, topology, and structure. For instance, the armchair configuration has metallic character, while the other two structures can be either metallic or semi-metallic (semi-conductive) [35]. These two properties make carbon nanotubes very attractive for the construction of various sensors and biosensors [26], in molecular electronics, and as refined materials for antistatic paints and shielding [36]. The versatility of these carbon allotropes is matched only by graphene. Carbon nanotubes have superior mechanical properties, among them high tensile strength (50–500 GPa for SWCNTs; 10–60 GPa for MWCNTs) and high elasticity (Young modulus up to 1 TPa), that make them very strong and flexible materials, being able to resist to external damage and return to the original form [37]. Moreover, carbon nanotubes exhibit outstanding electrical properties: The electrical conductivity of CNT fibers at 27 °C is 595 S cm^{-1}, but by chemical modification, it can reach 1152 S cm^{-1} [38]. Thermal properties are also excellent, with a conductivity measuring 3000 W m^{-1} K^{-1} and stability preserved at more than 700 °C in air and up to 2800 °C in vacuum [39]. Due to these exceptional characteristics, CNTs have been employed in a wide range of applications, such as electronic devices (single-electron transistors, field-effect transistors, logic circuits, rectifying diodes) [40], plus energy storage and generation (Li-ion batteries, solar and fuel cells, high-capacity energy storage systems) [41]. Considering also the optical properties (photoluminescence, photostability), nanotubes have utility in biological fields, such as bioimaging [41], tissue regeneration, and delivery systems [42]. However, the most interesting applications include carbon nanotube inks for 3D printing flexible electronics [43], the attachment of CNTs to the atomic force microscope (AFM) tip to be used as nanoprobe (already on the market) [33], the production of selective membrane filters [44], the use as actuators in artificial muscles [33], and the development of invisible electronic circuits based on transparent and flexible transistors [41].

1.3.2.2 Carbon Nanohorns

Similar to carbon nanotubes, they are single-walled carbon nanohorns (SWCNHs), discovered by Harris et al. in 1994 [45]. Five years later, Iijima et al. [46] managed to prepare them in large quantities allowing commercial production and the ensuing research of these interesting materials. SWCNHs are conical nanostructures (Fig. 1.1f) with a typical diameter of 2–3, 30–50 nm length and unique opening angle of 20° that tends to aggregate in a spherical shape of 80–100 nm diameter, resembling a dahlia flower [46–48].

Pristine carbon nanohorns have intriguing properties, the most attractive being the high microporosity (pore volume of 0.11 mL/g) and the extensive surface area (308 m^2/g) [49], that favor the adsorption of small molecules onto them. These are promising features for energy storage systems, and SWCNHs were demonstrably

superior in fuel cells for mobile devices, when compared to single-walled carbon nanotubes [50]. Advantageously, non-cytotoxic, these materials have applicability in medicine, mostly in cancer therapy. The size of the aggregates is ideal for penetrating tumor tissue, attaining an enhanced permeability and retention effect [51].

1.3.2.3 Carbon Nanofibers

Carbon nanofibers (CNFs) have a long history, reported since 1889 as carbon filaments. Variable dimensions are observed for these carbonaceous materials, with diameters ranging from 3 to 100 nm and lengths between 0.1 and 1000 μm [52]. Similar to carbon nanotubes, they consist of sp^2 carbon atoms that form a hexagonal network known as graphene. However, the closed cage structure of nanofibers is not hollow because the graphene sheets are short and connected in different assemblies [53]. Even though the mechanical properties are not as good as CNTs, they are still outstanding, having a Young's modulus and tensile strength higher than steel. For this important aspect, carbon nanofibers are used as additives in a polymer matrix to obtain composite materials and for the moment are unlikely to be replaced by more costly CNTs [52, 53]. Besides the typical applications of carbon nanostructures, CNFs can be employed in the fabrication of point X-ray sources, generating high-resolution radiographies [54].

1.3.3 Two-Dimensional Carbon Structures: Graphene

In 2004, Novoselov et al. [4] isolated for the first time a two-dimensional material called graphene, which proved to be highly versatile, with extraordinary properties that might revolutionize the industry. Graphene represents a monoatomic layer of sp^2 conjugated carbons packed in a hexagonal crystal lattice (Fig. 1.1g) [55]. Each carbon atoms are connected with three other atoms by strong σ bonds (C–C) with a length of 1.42 Å, with an ability to form another weaker bond through the π orbitals perpendicular to the plane, allowing an interaction between layers [55, 56].

The great interest for this thinnest material reflected a unique combination of mechanical, electronic, electrical, and thermal properties. The extensive surface area (2630 cm^2/g) and the high Young's modulus (1 TPa) are combined with the low density of graphene dethroned CNTs as the strongest, lightest material [57]. In addition, graphene acts as a semiconductor, is chemically inert, and has the capacity to absorb light at all wavelengths, although the absorption rate of white light is very low. Truly remarkable about graphene is the optical transparency, the high thermal (5000 $W\ m^{-1}\ K^{-1}$) and electrical conductivity at room temperature (electron mobility more than 200,000 $cm^2\ V^{-1}\ s^{-1}$), and the low Johnson noise (electronic noise) [56] that encouraged numerous applications, especially in domains like electronics, photonics and optoelectronics, spintronics, energy storage and conversion, sensors and biomedicine [55].

Graphene is also super hydrophobic, though this need not be desirable for every application. Depending on requirements, a preferred graphene derivative is graphene oxide (GO) or reduced graphene oxide (rGO). GO is rich in oxygen containing functionalities, like carboxyl, carbonyl, ester, epoxy, and hydroxyl groups (Fig. 1.1h) [58], that make it easy to disperse in various solvents, but this affects its conductivity. In order to recover this important property, GO can be reduced usually by chemical, electrochemical, thermal, or photocatalytic deoxygenation. The resulting material, rGO, has fewer oxidized groups mainly restricted to the edges that do not interfere with the conductivity, and lattice defects are introduced within the plane (Fig. 1.1i) [55, 58]. Both GO and rGO are hydrophilic derivatives that preserve most of the great properties of graphene, and additionally, they are highly biocompatible and easy to functionalize.

Novel allotropes based on graphene (Fig. 1.2) were predicted in the last few years that can be obtained by tampering with the C–C bonds. Theoretical studies already facilitated the synthesis of some graphene allotropes, such as graphenylene, biphenylene, and graphdyine, while penta-graphene, twin-graphene, graphyne, phagraphene, and T-graphene are still investigated by computational chemistry methods [2, 59]. Graphyne and twin-graphene have a semi-conductive character and are obtained through bond extension. By reducing some C–C bonds, penta-graphene is obtained, characterized by a negative Poisson's ratio and the highest relative energy in comparison with the other allotropes. Finally, graphenylene, biphenylene, and phagraphene

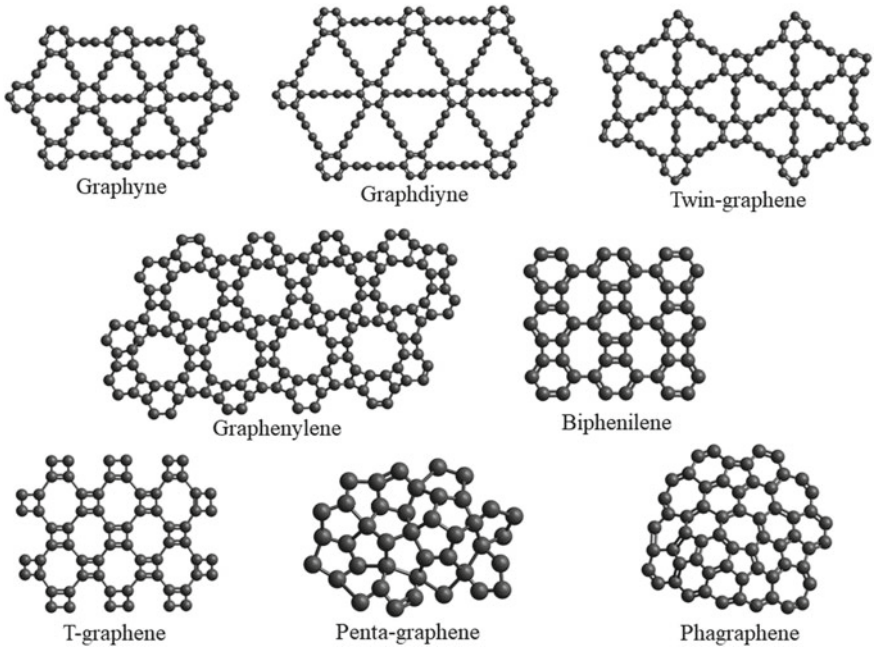

Fig. 1.2 Derivatives of graphene structure

can be obtained by rotating the C–C bonds, and compared to graphene, they have the lowest relative energy [2].

There is extensive ongoing research and massive interest from multinational companies regarding graphene as a key material for future innovative devices. Conceptually, batteries will charge faster (within minutes or even seconds) and last longer, so electric cars will be more accessible. Also, flexible touch screen devices and smart-windows will soon be commercially available [57]. Feasible innovations include ultrafast, super small, flexible computers, clothing with pockets incorporating supercapacitors and photovoltaic cells for charging electronic devices, and even invisibility cloaks [57, 60].

1.3.4 Three-Dimensional Carbon Materials

1.3.4.1 Natural Allotropes

The most common carbon allotropes are diamond and graphite, both natural and crystalline allotropes, but with different structure and properties. Diamond consists of tetrahedral sp^3 hybridized carbon atoms that form a cubic structure (Fig. 1.1j), while graphite contains only sp^2 bonds, and it has a layered structure (stacked graphene sheets) [6]. In terms of properties, diamond is transparent, acts as an insulator, and it has a very high stiffness [35]. In contrast, graphite is a black material, good conductor of electricity but with low tensile strength [53]. The hexagonal structure of diamond is called lonsdaleite, which is a very rare mineral that forms when meteorites hit the Earth. Although it is very hard to synthesize this material, theoretical studies suggest that it may have superior properties to diamond, including twice the compressive strength [61].

1.3.4.2 Synthetic Allotropes

Derived from diamond and graphite, other carbon-based structures have been proposed. On one hand, three-dimensional metallic carbon materials have been intensively investigated in the last decade. To date, various promising structures were proposed by computational chemistry. It was found that H_{18} carbon [62] and Hex-C_{18} [63], both derivatives of graphene obtained by bond rotation, have a shear modulus over 250 GPa. Moreover, Tri-C_9 [64] may be produced by compressing graphite at high pressure, and its shear modulus is calculated to be around 270 GPa. Derivatives of diamond, O-type and T-type carbon [65] with orthorhombic and tetragonal symmetry, respectively, are both thermally and mechanically stable, while having high cohesive energy [2].

On the other hand, superhard carbon is also thoroughly researched. Theoretical designs of a semiconductor tetragonal C_{64} [66] and an insulator C_{20} T-carbon [67] were proposed as well as a derivative of carbon nanotubes, called P-carbon [68],

that has a semi-conductive character. C_{64} is mechanically stable and has lower electronic band gap (1.32 eV) and shear modulus (217 GPa) compared to C_{20} T-carbon (5.44 eV and 427 GPa, respectively). These allotropes are in the category of superhard materials due to the hardness values predicted: 60.2 GPa for tetragonal C_{64} and 72.76 GPa for C_{20} T-carbon [2]. P-carbon also has tetragonal symmetry, but with porous structure, which is stable at high pressure. Its electronic band gap and shear modulus are between C_{64} and C_{20} T-carbon, 3.52 eV and 360 GPa, respectively, but the hardness has the highest value around 86 GPa. In addition, two more allotropes were predicted, started from the diamond structure, C_{14}-diamond and T-carbon. C_{14} [69] has similar density and cohesive energy to diamond and a hardness of 55.8 GPa. T-carbon was proposed theoretically in 2011 [70] and 6 years later was experimentally obtained and characterized [71]. It has a band gap of 2.25 eV, a shear modulus of 70 GPa, and a high hardness around 61 GPa [2, 70].

1.4 Carbon Nanomaterials by Computational Chemistry

In this subchapter, we provide a brief introduction to computational chemistry for a basic understanding of the field within a multidisciplinary background. Saliently, carbon allotropes may now be studied based on computational techniques, both before and after being synthesized in the laboratory.

> The underlying physical laws necessary for the mathematical theory of a large part of physics and the whole of chemistry are thus completely known, and the difficulty is only that the exact application of these laws leads to equations much too complicated to be soluble. It therefore becomes desirable that approximate practical methods of applying quantum mechanics should be developed, which can lead to an explanation of the main features of complex atomic systems without too much computation. [72]

1.4.1 Computational Chemistry

Computational chemistry is principally concerned with the numerical computation of molecular electronic structures and molecular interactions. Today, we mostly find computational chemistry divided into two main branches: molecular modeling concerned with structure phenomena and molecular simulations concerned with interaction phenomena [73].

The origins of this field span back to the late 1920s, early 1930s when theoretical physicists were attempting to solve the Schrödinger equation using mechanical calculating machines. At the time, it was only possible to generate exact solutions for very small systems such as the helium and hydrogen atoms. For anything larger, solutions were reached by making use of certain approximations. Nevertheless, these calculations made it possible for scientists involved with physics and chemistry to answer questions regarding the different properties of matter [74].

Later on, computers became available and used in research. However, by this time, most physicists had shifted their main focus to nuclear structures, leaving chemists to work on extracting quantitative information regarding the behavior of different molecules [74]. This area of work slowly developed into what we today call computational chemistry. As with many other numerical fields, the recent success and massive growth are predominantly related to the tremendous increase in computer affordability and processing power [74].

There are many incentives for integrating computational chemistry in one's research. Firstly, performing an experiment in silico may aid in having a better understanding about a certain interaction or phenomena before actually performing the experiment in the laboratory. Secondly, the in silico experiment can be performed in an affordable and risk-averse manner, saving the laboratory both financial costs and time. Thirdly, it grants the researcher an additional degree of control in the sense that one is able to isolate phenomena by controlling the variables involved. A suitable example would be testing the behavior of a new material both in very high and very low temperatures or in high versus low-pressure environments. These kinds of adjustments are easily made computationally by changing the value of a variable, such as temperature or pressure, whereas equivalent laboratory experiments may be difficult to setup. There are indeed some disadvantages that one must be well informed of before attempting to perform in silico experiments. It is important to realize that many calculations may not always lead to numerically relevant results often due to need for mathematical approximations; therefore, there is a slight chance for molecules to behave differently in the laboratory-based experiments. The accuracy of all calculations is dependent upon how well one builds and defines their initial model. The better one can do so, the more accurate and applicable the results are. And finally, learning to implement in silico experiments may involve a steep learning curve, depending on the complexity of the experiment and clarity of software documentation.

When aiming to do in silico experiments, for example designing a new drug carrier or assessing the performance of a biosensor, one needs to carefully choose the best experiments to perform. Computational chemistry is split into three main branches, known as ab initio, semi-empirical, and empirical methods. For the purpose of this chapter, we will provide a short introduction into ab initio methods, more precisely the density functional theory technique, as we find it to be the most relevant for revealing new carbon allotropes and also a very helpful tool for researching innovative carbon-based materials.

1.4.2 Ab Initio Methods

The Latin term ab initio means "from the beginning," although the described methods may also be called *Quantum Mechanical* or *First Principles* techniques.

Ab initio methods allow us to perform calculations based purely on theoretical principles. This implies no need to include any data obtained experimentally when setting up our initial model. Once the initial system has been setup, the

computer performs mathematical calculations according to the chosen method (*N.B.,* the formulae may be based on previous empirical data obtained independently). Once the calculations successfully reach a solution, one can extract numerous characteristics specific to the defined system such as the structural, vibrational, electromagnetic, and optical according to interest. This makes ab initio methods special to all other types of experiments. However, despite the enthusiasm, one may experience because of not having to use any empirical data, the main drawback of an ab initio method is that it consumes an incredible amount of processing power. What should be well understood is that ab initio experiments are normally performed for very small systems. The maximum amount of atoms that can be present in a system depends upon the approximations and techniques being used. The two best known ab initio methods are known as Hartree–Fock (HF) and density functional theory (DFT). Given the purpose of this chapter, we will only provide a brief introduction into the calculations behind the DFT method.

For a better understanding of ab initio methods from a theoretical point of view, consider we are looking at a system defined as a cluster of atoms. Zoom in further and one looks at nuclei and their corresponding electrons. In order to be able to extract the desired properties, including electronic, structural, and optical qualities, one must first solve the energy equation. Given focus on nuclei and electrons, the calculations must conform to the quantum world. Therefore, one will have to solve Schrödinger's equation for the whole system:

$$H\Psi(\{r_i\},\{R_I\}) = E\Psi(\{r_i\},\{R_I\}) \tag{1.1}$$

where $\hat{H}$ represents the Hamiltonian of the system, Ψ represents the corresponding wave functions, r_i and R_I represent the position vectors of each electron and nucleus, respectively. This formula is also known as the many-body Schrödinger's equation.

As this equation may look unfamiliar to many readers, we hereby provide help in understanding what each term means. Firstly, consider a quantum system defined by only one quantum particle, for example an electron. The corresponding time-independent form of Schrödinger's equation is the following:

$$E\Psi(x) = \frac{-\hbar^2}{2m}\frac{\mathrm{d}^2\psi(x)}{\mathrm{d}x^2} + V\Psi(x) \tag{1.2}$$

where E refers to the energy levels the electron is allowed to have, Ψ, as previously, is defined as the wave function, $\hbar$ is the reduced Planck's constant 6.626×10^{-34} Js, the smallest dimension of physical action, m is the mass of the object, and V represents the electronic potential. To explain the key elements of this equation, we first discuss its terms on the left-hand side, then the terms on the right-hand side of the equation. From classical mechanics, for an object of mass m, we have Newton's equation $F = ma$ when a force F is acting on the object with mass m and acceleration a. Should we know the numerical values of all variables involved in this equation and given a certain time t, we can extract the position of the object knowing that $\frac{\mathrm{d}x^2}{\mathrm{d}^2t} = a$. We can also extract its velocity $v = \frac{\mathrm{d}x}{\mathrm{d}t}$, momentum $p = m\frac{\mathrm{d}x}{\mathrm{d}t}$, kinetic

energy $KE = \frac{mv^2}{2}$, and so on. Therefore, we can say that the equation $F = ma$ is essential to deriving all other properties of interest belonging to the object.

Schrödinger's equation is of a similar status in the quantum mechanics world as the $\boldsymbol{F} = m\boldsymbol{a}$ equation is for classical mechanics. We should be able to find all properties of interest if the values required to solve Schrödinger's equation are known. The main difference is that for a quantum particle one cannot know the exact position and momentum at the same time. This is known as Heisenberg's uncertainty principle that can be expressed by the relationship: $\Delta x \Delta p \geq \hbar$, where Δx represents the uncertainty in position, Δp represents the uncertainty in momentum, and $\hbar$ is the reduced Planck's constant. However, the quantum particle properties that can be known are its energy levels and its wave function denoted by E and the Greek letter Psi, Ψ in Eq. (1.2). This represents the left-hand side of the equation, the value one is aiming to find.

The wave function basically lets us know where the electron can be found. The square of the wave function returns a probability distribution showing where the electron is likely to be, but without knowing where it actually is. In order to know exactly where an electron is, the particle would have to be observed, which would force it to choose a state. Should it not be observed, the electron will find itself in a superposition situation, where it can be considered present in all its possible positions.

Regarding the energy values denoted by E, Einstein's relation states that $E = hf$, where h is Planck's constant, and f is the frequency. However, given that the space in which the electron may be found is defined and finite, only the frequency values that do not place the particle outside of this defined space can be considered valid. Therefore, this observation leads to the understanding that the electron can only take certain energy levels pointing to the fact that everything is quantized in the quantum world.

Regarding the right-hand side of the equation, the total energy of the particle is equal to the sum of the kinetic energy and the potential energy. Thus, the kinetic energy $\frac{-\hbar^2}{2m}\frac{\mathrm{d}^2\psi(x)}{\mathrm{d}x^2}$ is summed up with the potential energy $V\Psi(x)$. This is what we must solve in order to find the energy levels that our particle is allowed to have and its corresponding wave function, out of which all other properties can be extracted. Having clarified the terms of Schrödinger's equation, return to ab initio methods and Eq. (1.1). In order to be able to extract the desired properties out of a system, the ground state of the many-body equation needs to be found. Again this means calculating the sum of the kinetic energy and the potential energy, in this case the Coulomb potential, bearing the following formula for a pair of charged particles: $\frac{q_1 q_2}{|r_i - r_j|}$. Solving Eq. (1.1) given a system considered to be composed of quite a few nuclei and many electrons may prove difficult at this stage. Therefore, we rely on a number of approximations to simplify the process without significantly compromising the accuracy of the calculations.

The first approximation made in ab initio methods is called the Born–Oppenheimer approximation, which basically states that given the difference in size and speed between electrons and nuclei, the nuclei can be considered as very heavy and

stationary and the electrons as light and fast moving. This means that the terms related to the two types of particles can be considered separately, meaning $\Psi(\{r_i\}, \{R_I\})$ can be written as $\Psi_N(\{r_i\}) * \Psi_e(\{R_I\})$. The Born–Oppenheimer approximation also points toward the observation that the fast moving electrons experience an external potential associated to the static nuclei. In essence, the electronic wave function of the electrons is considered to be dependent only on the positions of the nuclei and not on their velocities. This observation is helpful in that, for one set of atomic positions, one can now focus on determining the ground state of the electrons. The system's Hamiltonian for is thus:

$$H = \frac{-h^2}{2m_e} \sum_i^{N_e} \nabla_i^2 + \sum_i^{N_e} V_{ext}(r_i) + \sum_{i=1}^{N_e} \sum_{j>i}^{N_e} U\left(r_i, r_j\right) \tag{1.3}$$

where $\frac{-h^2}{2m_e} \sum_i^{N_e} \nabla_i^2$ represents the kinetic energy of the electrons, $\sum_i^{N_e} V_{ext}(r_i)$ represents the potential energies between electrons and nuclei, and $\sum_{i=1}^{N_e} \sum_{j>i}^{N_e} U\left(r_i, r_j\right)$ represents the potential electron–electron energies.

Looking at Eq. (1.3), one can see that for a number N_e of electrons we end up with a $3N_e$ dimensional situation (without considering the spin of the electrons). This may prove impractical for most systems. However, there are more efficient ways of conducting this kind of calculations, including the density functional theory (DFT), method that reduces the dimensions of the problem from $3N_e$ to 3 by using a number of mathematical approximations while introducing the concept of electron density. The electron density is in fact the square of the wave function showing the probability that an electron will be found at a certain location, and it is written in the following manner:

$$n(r) = \Psi * (r_1, r_2, \ldots, r_N)\Psi\left(r_{1,} r_2, \ldots, r_N\right) \tag{1.4}$$

where $\Psi*$ represents the complex conjugate of the wave function. Another approximation being used when applying DFT is known as the Hartree product. This mathematical approximation simplifies the problem of having numerous electrons by having many single electrons and considering the electrons to be non-interacting with each other yet keeping the electron density the same as if they were:

$$\Psi\left(r_{1,} r_2, \ldots, r_N\right) = \Psi_1(r_1) * \Psi_2(r_2) * \cdots * \Psi_N(r_N) \tag{1.5}$$

The density functional theory is based on the following two theorems known as the Hohenberg–Kohn theorems:

1. *The ground-state density of a many-body quantum system in some external potential* $v_{ext}(r)$ *determines this potential uniquely* [75]. This theorem basically states that the electron density is all that is required to find the ground-state energy of the system.

2. *For any trial density $n(r)$, it holds $E_0 \leq E[n(r)]$, where E_0 is the ground-state energy for the system* [75]. In other words, in order to find E_0 one would have to minimize along the energy functional $E[n(r)]$.

The issue at this DFT step is finding a way to calculate the energy functional $E[n(r)]$, which is usually split into both known and unknown terms. The known term includes the kinetic energy of the electron, nuclei–electron potential energy, electron–electron potential energy, and the energy of the interactions of the nuclei:

$$E_{\text{known}}[\{\Psi_i\}] = \frac{h^2}{m}\sum_i \int \Psi_i * \nabla^2 \Psi_i \mathrm{d}^3 r + \int V(r) n(r) \mathrm{d}^3 r + \frac{\mathrm{e}^2}{2} \iint \frac{n(r) n(r')}{|r - r'|} \mathrm{d}^3 r \mathrm{d}^3 r' + E_{\text{nuclei}} \tag{1.6}$$

The unknown is called the exchange–correlation functional and includes all quantum mechanical effects. To understand more about this unknown exchange–correlation term, you could start by looking into local density approximation (LDA), generalized gradient approximation (GGA), and vDW-DF [76, 77].

An approach to obtain the correct electron density comes from an algorithm developed by Kohn and Sham in 1965 known as the Kohn–Sham Scheme. Essentially, one has to solve a set of single-electron equations having the following form:

$$\frac{h^2}{2m}\nabla^2 \Psi_i(r) + V(r)\Psi_i(r) + V_{XC}(r)\Psi_i(r) = \varepsilon_i \Psi_i(r). \tag{1.7}$$

The algorithm is beautifully summarized in four steps by Sholl and Steckel in their book titled *Density Functional Theory: A Practical Introduction* [78], whereby initially one has to guess a trial density $n(r)$. Following that, the wave functions of each electron would have to be determined by solving all equations of the form presented above (1.7). The values obtained for the wave functions are then used to calculate the electron density using the following formula: $n_{\text{KS}}(r) = 2\sum_i \Psi_i * (r)\Psi_i(r)$. Should the value calculated for $n_{\text{KS}}(\mathbf{r})$ be the same with the previously guessed $n(\mathbf{r})$ value, it follows that one has found the ground-state electron density and may proceed in computing the total energy. Otherwise, the process would have to be restarted with a revised $n(\mathbf{r})$.

1.4.3 Examples of the Use of DFT in Carbon Allotropes Research

Currently, given the increase in processing power and affordability of computers, plus the latest optimizations and enhanced development of the field, computational chemistry incorporating methods such as the DFT can be used to both design new carbon allotropes and analyze those found experimentally. One highly informative example

that was initially discovered experimentally and further studied by performing in silico experiments is the C_{60} buckyball [2]. The C_{60} buckyball has been studied as a drug delivery system for a wide spectra of molecules, using DFT, years after its chemical structure was proposed in 1985 [3]. Some of these drugs include penicillamine [79] used in the treatment of Wilson's disease and 5-fluorouracil [79] used in cancer treatment. In the study of Ghasemi et al. [79], the process of physiosorption of penicillamine on the outside surface of the C_{60} fullerene was confirmed. Further on, a more energetically favorable configuration was found by investigating an Al-doped C_{60} structure, which would interact with penicillamine through chemisorption [79]. In the case of 5-fluorouracil, the Al-doped C_{60} was again investigated in the study of Hazratiet al. [80] and found to have the most stable configuration when compared to a number of alternative configurations, such as pristine, B-doped, and Si-doped C_{60} [80]. All these results were purely based on DFT calculations and led to a better understanding of potential applications of the newly discovered allotrope.

A predicted carbon allotrope, T-carbon, was found initially by performing in silico experiments using DFT [70] and experimentally validated in 2017, six years after its theoretical discovery [71]. Most of the DFT calculations involved the projector augmented wave (PAW) method [70]. Although the PAW method has not been described in this short chapter, a good overview can be found in the text by Rostgaard in 2009 [81]. A key aspect of the PAW method is that it involves transforming the wave function Ψ using an operator, with the goal of smoothening it out. Further on, both LDA and GGA were used for the exchange–correlation potential [70]. The lattice constant was located at 4.495 Å, while the C–C bonds may take four different values: 1.541, 1.548, 1.550, and 1.541 Å [2]. It was also found to display high hardness calculated at 72.76 GPa, with a bulk and shear modulus of 395 and 427 GPa [2]. T-carbon was predicted to have potential uses in hydrogen storage and aerospace materials [70].

Diamond has been traditionally regarded as the material with the highest number density (atoms per unit volume), while also displaying a high valence electron density [82]. Finding structures displaying an even higher number density has been considered impractical if attempting to do so in the experimental laboratory. However, Zhu et al. conducted in silico experiments, searching computationally for carbon allotropes denser than diamond and uncovered three new super dense carbon structures called hP3, tP12, and tI12 [82] that should have a 3% higher density. Using DFT with PAW and GGA, Zhu was able to define properties such as density, chemical structure, energies, dynamical stability, compressibility, intrinsic hardness of the new materials and propose ways to obtain them experimentally such as by rapid dynamic compression of low-density forms of carbon. Together with a few other computational chemistry techniques, the band gap was estimated and ranged between 3.0 and 7.3 eV between the three carbon forms. Band gap refers to the minimal energy separation between occupied and unoccupied electronic orbitals, representing a most important characteristic of the electronic structure of materials, advantageously, a

wide range implied prospects for tuning the electronic properties. Also, the dielectric and optical properties of the new carbon allotropes were examined, and thus, the materials were found to display a greater dispersion of light and stronger color effects compared to diamond [82].

This brief overview illustrated a few situations in which DFT and computational chemistry techniques have proved useful in designing and studying leading edge carbon-based materials. We consider that, given the current pace of development of computational chemistry and the yearly increases in computational power, computational chemistry will become even more central to how new and old materials are being researched.

1.5 Conclusions

This chapter has focused on the importance of carbon materials, having applications in a wide range of fields in both academia and industry. Besides the well-known natural allotropes—diamond and graphite, synthetic carbon structures represented by fullerenes, carbon nanotubes, and graphene, have been intensively researched since their discovery for their outstanding and unique properties. The ability of the carbon atom to catenate makes possible the existence of its allotropes in all dimensions and encourages scientists around the world to keep searching and studying novel structures with fascinating architectures. Thus, carbon represents the key player in the nanoworld with active research being invested both experimentally and theoretically (computationally) for the development of novel materials and novel applications to existing materials. Its serious versatility allows for exploring unidimensional to multidimensional structures, providing researchers freedom to explore creatively. We have shown that computational studies complement experimental research in this pursuit, by providing a means to test otherwise almost unreachable perspectives, focused entirely on the nano-dimensions. We have provided an introduction into the DFT technique in order to get the reader acquainted with the kind of calculations involved and mentioned examples of the useful outcomes obtained through computational studies, showcasing that current research has shifted from previously being entirely experimental to a hybrid between experimental and computational studies.

Acknowledgements This work was supported by a grant of the Ministry of Research and Innovation, Operational Program Competitiveness Axis 1-Section E, Program co-financed from European Regional Development Fund “Investments for your future” under the project number 154/25.11.2016, P_37_221/2015, “A novel graphene biosensor testing osteogenic potency; capturing best stem cell performance for regenerative medicine” (GRABTOP).

References

1. A. Hirsch, The era of carbon allotropes. Nat. Mater. **9**(11), 868 (2010)
2. R.-S. Zhang, J.-W. Jiang, The art of designing carbon allotropes. Front. Phys. **14**(1), 13401 (2019)
3. H.W. Kroto et al., C_{60}: Buckminsterfullerene. Nature **318**, 162 (1985)
4. K.S. Novoselov et al., Electric field effect in atomically thin carbon films. Science **306**(5696), 666–669 (2004)
5. E.A. Belenkov, V.A. Greshnyakov, Classification of structural modifications of carbon. Phys. Solid State **55**(8), 1754–1764 (2013)
6. V. Georgakilas et al., Broad family of carbon nanoallotropes: classification, chemistry, and applications of fullerenes, carbon dots, nanotubes, graphene, nanodiamonds, and combined superstructures. Chem. Rev. **115**(11), 4744–4822 (2015)
7. Y. Dong et al., Graphene quantum dots, graphene oxide, carbon quantum dots and graphite nanocrystals in coals. Nanoscale **6**(13), 7410–7415 (2014)
8. R. Haddon, The fullerenes: powerful carbon-based electron acceptors. Phil. Trans. R. Soc. Lond. A **343**(1667), 53–62 (1993)
9. P.P. Shanbogh, N.G. Sundaram, Fullerenes revisited. Resonance **20**(2), 123–135 (2015)
10. C.D. Reddy, Z. Gen Yu, Y.-W. Zhang, Two-dimensional van der Waals C_{60} molecular crystal. Sci. Rep. **5**, 12221 (2015)
11. K.L. Chen, M. Elimelech, Aggregation and deposition kinetics of fullerene (C_{60}) nanoparticles. Langmuir **22**(26), 10994–11001 (2006)
12. R. Ruoff et al., Solubility of fullerene (C_{60}) in a variety of solvents. J. Phys. Chem. **97**(13), 3379–3383 (1993)
13. S.H. Friedman et al., Inhibition of the HIV-1 protease by fullerene derivatives: model building studies and experimental verification. J. Am. Chem. Soc. **115**(15), 6506–6509 (1993)
14. Y. Kim et al., A strong regioregularity effect in self-organizing conjugated polymer films and high-efficiency polythiophene: fullerene solar cells. Nat. Mater. **5**, 197 (2006)
15. S.M. Hartley, R.A. Sallavanti, B. Sutter, Eyewear for ballistic and light protection. Google Patents (2003)
16. X. Xu et al., Electrophoretic analysis and purification of fluorescent single-walled carbon nanotube fragments. J. Am. Chem. Soc. **126**(40), 12736–12737 (2004)
17. L.A. Ponomarenko et al., Chaotic dirac billiard in graphene quantum dots. Science **320**(5874), 356–358 (2008)
18. R. Jelinek, *Carbon Quantum Dots: Synthesis, Properties and Applications* (Springer International Publishing, 2016)
19. J. Lee et al., Uniform graphene quantum dots patterned from self-assembled silica nanodots. Nano Lett. **12**(12), 6078–6083 (2012)
20. R. Das, R. Bandyopadhyay, P. Pramanik, Carbon quantum dots from natural resource: a review. Mater. Today Chem. **8**, 96–109 (2018)
21. H. Li et al., Carbon nanodots: synthesis, properties and applications. J. Mater. Chem. **22**(46), 24230–24253 (2012)
22. R. Ye et al., Coal as an abundant source of graphene quantum dots. Nat. Commun. **4**, 2943 (2013)
23. D.N. Ho, *Applications in Biology and Nanoscale Medicine*, vol. 10 (Springer, US, 2010), p. 978-1
24. S. Legoas et al., Ordered phases of encapsulated diamondoids into carbon nanotubes. Nanotechnology **22**(31), 315708 (2011)
25. S.-J. Yu et al., Bright fluorescent nanodiamonds: no photobleaching and low cytotoxicity. J. Am. Chem. Soc. **127**(50), 17604–17605 (2005)
26. F.R. Baptista et al., Recent developments in carbon nanomaterial sensors. Chem. Soc. Rev. **44**(13), 4433–4453 (2015)
27. V.N. Mochalin et al., The properties and applications of nanodiamonds. Nat. Nanotechnol. **7**(1), 11 (2012)

28. D. Pech et al., Ultrahigh-power micrometre-sized supercapacitors based on onion-like carbon. Nat. Nanotechnol. **5**(9), 651 (2010)
29. D. Ugarte, Curling and closure of graphitic networks under electron-beam irradiation. Nature **359**, 707 (1992)
30. E. Koudoumas et al., Onion-like carbon and diamond nanoparticles for optical limiting. Chem. Phys. Lett. **357**(5–6), 336–340 (2002)
31. P. Simon, Y. Gogotsi, Capacitive energy storage in nanostructured carbon–electrolyte systems. Acc. Chem. Res. **46**(5), 1094–1103 (2012)
32. S. Iijima, Nature (London) **354**, 56 (1991)
33. P.M. Ajayan, O.Z. Zhou, Applications of carbon nanotubes, in *Carbon Nanotubes* (Springer, 2001), pp. 391–425
34. G. Mittal et al., A review on carbon nanotubes and graphene as fillers in reinforced polymer nanocomposites. J. Ind. Eng. Chem. **21**, 11–25 (2015)
35. H. Hanaei, M.K. Assadi, R. Saidur, Highly efficient antireflective and self-cleaning coatings that incorporate carbon nanotubes (CNTs) into solar cells: a review. Renew. Sustain. Energy Rev. **59**, 620–635 (2016)
36. G.-L. Zhao, E. Khosravi, S. Yang, Dioxygen adsorption and dissociation on nitrogen doped carbon nanotubes from first principles simulation, in *Carbon Nanotubes-From Research to Applications* (InTech, 2011)
37. Y.T. Ong et al., A review on carbon nanotubes in an environmental protection and green engineering perspective. Braz. J. Chem. Eng. **27**, 227–242 (2010)
38. Q. Li et al., Structure-dependent electrical properties of carbon nanotube fibers. Adv. Mater. **19**(20), 3358–3363 (2007)
39. X.-L. Xie, Y.-W. Mai, X.-P. Zhou, Dispersion and alignment of carbon nanotubes in polymer matrix: a review. Mater. Sci. Eng. R Rep. **49**(4), 89–112 (2005)
40. V.N. Popov, Carbon nanotubes: properties and application. Mater. Sci. Eng. R Rep. **43**(3), 61–102 (2004)
41. M. Endo, M.S. Strano, P.M. Ajayan, Potential applications of carbon nanotubes, in *Carbon Nanotubes* (Springer, 2007), pp. 13–62
42. W. Yang et al., Carbon nanotubes for biological and biomedical applications. Nanotechnology **18**(41), 412001 (2007)
43. K. Kordás et al., Inkjet printing of electrically conductive patterns of carbon nanotubes. Small **2**(8–9), 1021–1025 (2006)
44. B.J. Hinds et al., Aligned multiwalled carbon nanotube membranes. Science **303**(5654), 62–65 (2004)
45. P.J. Harris et al., High-resolution electron microscopy studies of a microporous carbon produced by arc-evaporation. J. Chem. Soc. Faraday Trans. **90**(18), 2799–2802 (1994)
46. S. Iijima et al., Nano-aggregates of single-walled graphitic carbon nano-horns. Chem. Phys. Lett. **309**(3–4), 165–170 (1999)
47. T. Murakami et al., Drug-loaded carbon nanohorns: adsorption and release of dexamethasone in vitro. Mol. Pharm. **1**(6), 399–405 (2004)
48. M. Yudasaka, S. Iijima, V.H. Crespi, Single-wall carbon nanohorns and nanocones, in *Carbon Nanotubes* (Springer, 2007), pp. 605–629
49. N. Karousis et al., Structure, properties, functionalization, and applications of carbon nanohorns. Chem. Rev. **116**(8), 4850–4883 (2016)
50. H. Wang et al., Large-scale synthesis of single-walled carbon nanohorns by submerged arc. Nanotechnology **15**(5), 546 (2004)
51. K. Ajima et al., Carbon nanohorns as anticancer drug carriers. Mol. Pharm. **2**(6), 475–480 (2005)
52. K.P. De Jong, J.W. Geus, Carbon nanofibers: catalytic synthesis and applications. Catal. Rev. **42**(4), 481–510 (2000)
53. A.V. Melechko et al., Vertically aligned carbon nanofibers and related structures: controlled synthesis and directed assembly. J. Appl. Phys. **97**(4), 041301 (2005)

54. T. Tan et al., X-ray generation using carbon-nanofiber-based flexible field emitters. Appl. Phys. Lett. **88**(10), 103105 (2006)
55. S. Ray, *Applications of Graphene and Graphene-Oxide Based Nanomaterials* (William Andrew, 2015)
56. W. Choi et al., Synthesis of graphene and its applications: a review. Crit. Rev. Solid State Mater. Sci. **35**(1), 52–71 (2010)
57. E.P. Randviir, D.A.C. Brownson, C.E. Banks, A decade of graphene research: production, applications and outlook. Mater. Today **17**(9), 426–432 (2014)
58. S. Pei, H.-M. Cheng, The reduction of graphene oxide. Carbon **50**(9), 3210–3228 (2012)
59. Y. Liu et al., Structural and electronic properties of T graphene: a two-dimensional carbon allotrope with tetrarings. Phys. Rev. Lett. **108**(22), 225505 (2012)
60. O. Salihoglu et al., Graphene-based adaptive thermal camouflage. Nano Lett. **18**(7), 4541–4548 (2018)
61. P. Németh et al., Lonsdaleite is faulted and twinned cubic diamond and does not exist as a discrete material. Nat. Commun. **5**, 5447 (2014)
62. C.-X. Zhao et al., H_{18} carbon: a new metallic phase with sp^2–sp^3 hybridized bonding network. Sci. Rep. **6**, 21879 (2016)
63. J. Liu et al., A new metallic carbon allotrope with high stability and potential for lithium ion battery anode material. Nano Energy **38**, 263–270 (2017)
64. Y. Cheng et al., Three dimensional metallic carbon from distorting sp^3-bond. Cryst. Growth Des. **16**(3), 1360–1365 (2016)
65. Y. Liu et al., New metallic carbon: three dimensionally carbon allotropes comprising ultrathin diamond nanostripes. Carbon **126**, 601–610 (2018)
66. Q. Wei et al., A new superhard carbon allotrope: tetragonal C_{64}. J. Mater. Sci. **52**(5), 2385–2391 (2017)
67. W. Jia-Qi et al., C_{20}—T carbon: a novel superhard sp^3 carbon allotrope with large cavities. J. Phys. Condens. Matter **28**(47), 475402 (2016)
68. Y. Pan et al., A superhard sp^3 microporous carbon with direct bandgap. Chem. Phys. Lett. **689**, 68–73 (2017)
69. X. Wu et al., Superhard three-dimensional carbon with metallic conductivity. Carbon **123**, 311–317 (2017)
70. X.-L. Sheng et al., T-carbon: a novel carbon allotrope. Phys. Rev. Lett. **106**(15), 155703 (2011)
71. J. Zhang et al., Pseudo-topotactic conversion of carbon nanotubes to T-carbon nanowires under picosecond laser irradiation in methanol. Nat. Commun. **8**(1), 683 (2017)
72. P.A.M. Dirac, Quantum mechanics of many-electron systems. Proc. R. Soc. Lond. Ser. A **123**(792), 714–733 (1929)
73. K. Ramachandran, G. Deepa, K. Namboori, *Computational Chemistry and Molecular Modeling: Principles and Applications* (Springer Science & Business Media, 2008)
74. N.R. Council, *Mathematical Challenges from Theoretical/Computational Chemistry*, vol. 144 (The National Academies Press, Washington, DC, 1995)
75. P. Hohenberg, W. Kohn, Inhomogeneous electron gas. Phys. Rev. **136**(3B), B864–B871 (1964)
76. M. Dion et al., Van der Waals density functional for general geometries. Phys. Rev. Lett. **92**(24), 246401 (2004)
77. M. Dion, et al., Erratum: Van der Waals density functional for general geometries [Phys. Rev. Lett. 92, 246401 (2004)]. Phys. Rev. Lett. **95**(10), 109902 (2005)
78. D. Sholl, J.A. Steckel, *Density Functional Theory: A Practical Introduction* (Wiley, 2011)
79. A.S. Ghasemi, F. Mashhadban, F. Ravari, A DFT study of penicillamine adsorption over pure and Al-doped C_{60} fullerene. Adsorption **24**(5), 471–480 (2018)
80. M.K. Hazrati, N.L. Hadipour, Adsorption behavior of 5-fluorouracil on pristine, B-, Si-, and Al-doped C_{60} fullerenes: a first-principles study. Phys. Lett. A **380**(7), 937–941 (2016)
81. C. Rostgaard, The projector augmented-wave method. arXiv preprint arXiv:0910.1921 (2009)
82. Q. Zhu et al., Denser than diamond: ab initio search for superdense carbon allotropes. Phys. Rev. B **83**(19), 193410 (2011)

Chapter 2
Synergetic Effect of Graphene Oxide and Metal Organic Framework Nanocomposites as Electrocatalysts for Hydrogen Evolution Reaction

Mogwasha D. Makhafola, Mpitloane J. Hato, Kabelo E. Ramohlola, Phuti S. Ramaripa, Thabiso C. Maponya, Gobeng R. Monama, Kerileng M. Molapo, Emmanuel I. Iwuoha, Lebogang M. Katata-Seru, Katlego Makgopa, and Kwena D. Modibane

2.1 Introduction

2.1.1 Background on Hydrogen Energy

The global energy crisis and environmental pollution are becoming more serious due to the utilisation of non-renewable energy resources (i.e. fossil fuels) [9]. Developing a new, efficient and sustainable clean energy source based on renewable energy is extremely urgent [58]. Conversion of hydrogen gas into energy is the most promising strategy to resolve these crises. Hydrogen is a colourless and tasteless element which is abundant on the universe [85], but may be found in chemical compound such

M. D. Makhafola · M. J. Hato (✉) · K. E. Ramohlola · P. S. Ramaripa · T. C. Maponya · G. R. Monama · K. D. Modibane (✉)
Nanotechnology Research Lab, Department of Chemistry, School of Physical and Mineral Sciences, University of Limpopo (Turfloop), Polokwane, Sovenga 0727, South Africa
e-mail: mpitloane.hato@ul.ac.za

K. D. Modibane
e-mail: kwena.modibane@ul.ac.za

K. M. Molapo · E. I. Iwuoha
SensorLab, Chemistry Department, University of the Western Cape, Cape Town, South Africa

L. M. Katata-Seru
Department of Chemistry, School of Physical and Chemical Sciences, North-West University (Mafikeng Campus), Mmabatho 2735, South Africa

K. Makgopa
Department of Chemistry, Faculty of Science, Tshwane University of Technology (Acardia Campus), Pretoria 2735, South Africa

S. Kaneko et al. (eds.), *Carbon Related Materials*,
https://doi.org/10.1007/978-981-15-7610-2_2

as water and hydrocarbons [30]. Unlike conventional petroleum-based fuels and natural gas derivatives, hydrogen gas has high energy density and light molecular structure. In this regard, hydrogen is expected to play an important role in the future energy economy. This is because hydrogen is carbon-free, non-toxic, and its thermal or electrochemical combustion with oxygen yields energy and water although its combustion in air might generate nitric oxide air pollutants in controllable amounts [32].

As it can be produced from a range of renewable and non-renewable sources, hydrogen has the potential to form the basis of a clean and virtually limitless energy system [52]. Another advantage is that the main source of hydrogen is water, which is essentially an unlimited resource. To utilise hydrogen gas as an energy source, there must be a technology that converts the chemical form of hydrogen to electrical energy. The convenient form of electrical energy conversion is through hydrogen fuel cell (HFC) technology. The HFC technology generates electrical energy from an electrochemical process and gives water as a by-product [107, 142]. The hydrogen fuel cells are not only environmentally friendly, but their energy efficiency is two times more than the traditional combustion technologies [89]. A basic fuel cell set-up comprising two electrodes (anode and cathode) separated by an electrolyte and a membrane that conducts ions is shown in Fig. 2.1. The HFC principle involves the hydrogen gas flowing through the channel of anode where oxidation process occurs [124].

The oxidation process takes places when an electrocatalyst (e.g. platinum) causes hydrogen molecule to separate into protons and electrons. The membrane which differs from fuel cell to fuel cell allows protons to pass through. The protons will combine with oxidised air to form water. The electrons flow to the cathode to generate electricity or power [9, 43, 124]. Commercialisation of HFC is hampered by demand and supply of pure hydrogen gas. The demand and supply of pure hydrogen gas can be addressed by tackling two major concepts of hydrogen technology, thus production and storage. Several technologies or processes are currently employed to address this, and they are briefly discussed in the next sections.

2.1.2 Hydrogen Storage

When hydrogen is produced, it needs to be stored in order to overcome daily and seasonal discrepancies between energy source availability and demand. Depending on storage size and application, several types of hydrogen storage systems are available.

2.1.2.1 Compressed Gas Storage

The most common method which is employed to store hydrogen is through compression of gas [42]. This method brings several advantages such as high H_2 fraction,

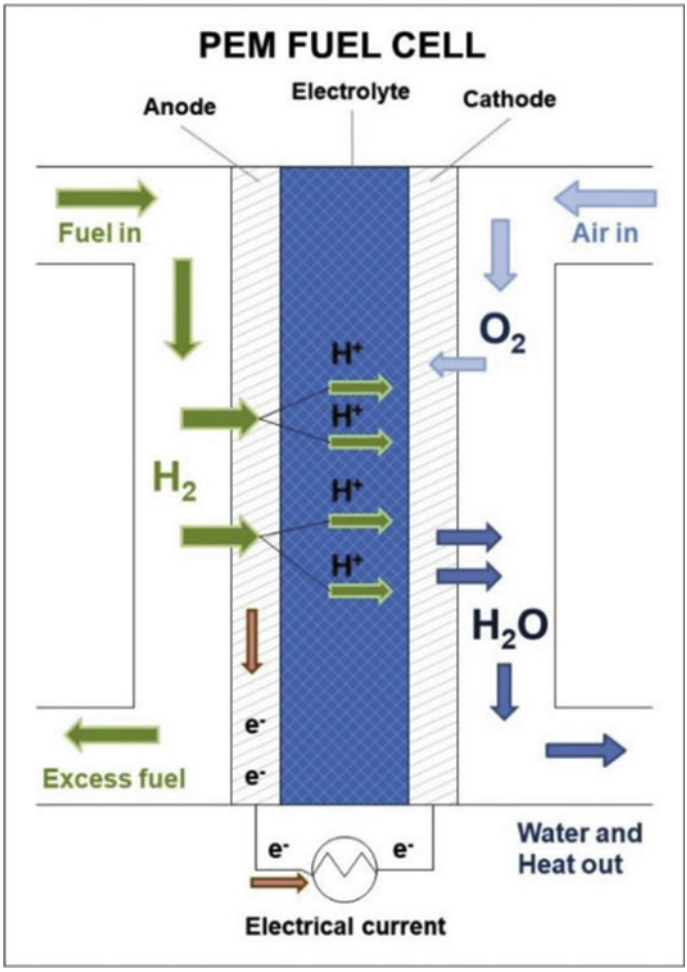

Fig. 2.1 Schematic representation of proton-exchange membrane (PEM) fuel cell [124]

rapid refuelling capability and excellent dormancy characteristics [111]. Its major challenge is the volume of the system which does not reach the target and its cylindrical shape which makes it difficult to conform storage to available space and the weight/energy penalties. Another drawback includes a rapid loss of H_2 in an accident which can cause an explosion [13]. In addition, a hydrogen gas can be stored using glass microspheres which are more advantageous than the compression gaseous method. The process of storage occurs in three stages: charging, filling and discharging. In principle, hollow glass spheres are filled with hydrogen gas at high pressures and temperatures by permeation in high-pressure vessels. After that process, the sphere is cooled to ambient temperatures and stored in vehicle tanks. Finally, the microspheres are heated to release hydrogen gas. The major setback in

utilising this method are low volumetric density, high pressure needed for filling and high temperatures for releasing hydrogen [1].

2.1.2.2 Liquid Hydrogen Storage

Unlike compressed hydrogen storage, liquid hydrogen has high density at low pressure, which enables light and compact vehicular storage and efficient delivery by truck [11]. Liquefying hydrogen is a way of increasing volumetric energy density by cooling hydrogen gas below its boiling temperature of −253 °C. A major problem associated with this process is the transformation of hydrogen from the ortho- to para-state during cooling [66]. Hydrogen in liquid form has a considerably higher energy density than in its gaseous form, making it an attractive storage medium [66, 73]. Although this process is costly in energy, it increases H_2 volumetric energy density from 5 MJ L^{-1} for compressed H_2 at 345 atm to 8 MJ L^{-1} for liquid hydrogen [73]. This clearly means that liquid hydrogen has a much better energy density than the compressed gas since it can store high energy at low pressures. The main limitation with liquid hydrogen process is the efficiency of the liquefaction process and the boil-off of the liquid [108]. Because of the low critical temperature of hydrogen (33 K), the liquid form can only be stored in open systems, as there is no liquid phase existent above the critical temperature [11].

2.1.2.3 Hydrogen Storage in Solid Materials

The development of efficient methods for hydrogen storage is a major hurdle that must be overcome to enable the use of hydrogen as an alternative energy carrier [116]. The development of high-capacity, hydrogen storage materials that can be recharged under moderate conditions is a key barrier to the realisation of a hydrogen economy [109, 139]. In solid storage materials, hydrogen can bind/interact with the adsorbent in two ways, i.e. physisorption or chemisorption. In physisorption, hydrogen can adsorb on the surface of the materials (adsorbent) and stored in a much convenient and safer way. The main advantage of adsorption over other physical storage systems (compressed gas and liquid hydrogen) is that it stores large quantity of hydrogen [59]. The adsorbed hydrogen does not chemically react with the adsorbent since hydrogen binds via weak van der Waals forces and therefore does not accumulate impurities which can poison operations of fuel cell [59, 135]. In chemisorption, hydrogen predominately binds stronger in an adsorbent than in physisorption.

Nonetheless, physisorption has a great advantage as compared to chemisorption due to its fast kinetics (during release of hydrogen) and its complete reversibility [27]. The problem with physisorption-based hydrogen storage is due to weak interaction between hydrogen and adsorbent causing a reduction in hydrogen density at ambient temperature [27]. In relation to this, several studies report the development of hydrogen storage materials such as metal hydrides [109], carbon-based materials, boron compounds [6], metal organic frameworks [59]. An optimum hydrogen storage material must possess the characteristics such as high volumetric/gravimetric hydrogen storage capacity, fast absorption kinetics, near room temperature and ambient pressure operation, lightweight materials and be affordable. However, some of these storage materials do not meet these requirements.

2.1.3 Production of Hydrogen

A wide range of methods are being used to generate hydrogen from different resources, and they are discussed as follows:

2.1.3.1 Fossil Fuels

1. Steam Methane Reforming (SMR)

A steam reforming (SMR) of natural gas is the most widely used process for industrial hydrogen generation. In this method, hydrogen production is through extraction by breaking the bonds between hydrogen and carbon content [85]. Basically, the SMR process consists of two main steps given in (2.1) and (2.2). The first step is an endothermic process (1) occurring at a high temperature ranges between ~800 and 1000 °C and varying pressures of 20–35 atm. An exothermic water gas shift (WGS) reaction running at a lower t ~200–400 °C and 10–15 atm is presented in (2.2).

$$H_2O(g) + CH_4(g) \rightarrow CO(g) + 3H_2(g) \text{(endothermic SMR)} \tag{2.1}$$

$$H_2O(g) + CO(g) \rightarrow CO_2(g) + H_2(g) \text{ (exothermic SMR)} \tag{2.2}$$

The overall reaction is provided in (2.3) as

$$CH_4(g) + 2H_2O(g) \rightarrow 4CO_2(g) + 4H_2(g) \tag{2.3}$$

A reasonable production price and possibility of mass production are the main advantages of fossil fuel-based hydrogen production [85, 112]. However, this approach of hydrogen production suffers from pollution ratings (i.e. emission of CO or CO_2) and limited resources [56, 85].

2. Partial Oxidation

In the partial oxidation process which is also known as a gasification, hydrogen is produced from a range of hydrocarbon fuels including coal and oils. In this process, the coal is first reacted with oxygen and steam under high pressures and temperatures to form a gas mixture CO and hydrogen [115]. The impurities are removed from the mixture, and the CO in the gas mixture is reacted with steam through the WGS reaction to produce additional hydrogen and CO_2. Hydrogen is removed by a separation system and the highly concentrated CO_2 stream can subsequently be captured and sequestered. The hydrogen can be used in a combustion turbine or solid oxide fuel cell to produce power, or utilised as a fuel or chemical feedstock [14, 109]. The fact that fossil fuel-based production of hydrogen is associated with the emission of such enormous quantities of CO_2, and other greenhouse gases may diminish the environmental appeal of hydrogen as an ecologically clean fuel.

2.1.3.2 Biomass

Hydrogen can be obtained from biomass by a pyrolysis/gasification process [28]. The biomass preparation step involves heating of the biomass/water slurry to high temperatures under pressure in a reactor. This process decomposes and partially oxidises the biomass producing a gas product consisting of hydrogen, methane, CO_2, CO and nitrogen. Mineral matter is removed from the bottom of the reactor. The gas stream goes to a high-temperature shift reactor where the hydrogen content is increased [99]. Nevertheless, biomass utilisation possesses some challenges such as high cost and the large area required for its production [76, 77]. The reason for the high cost for biomass production is attributed to labour cost and also an effective production of biomass requires fuels for machines and fertilisers produced by petroleum chemistry [136]. The utilisation of agricultural residue and environmental sewage sludge are expected to reduce the high cost to a large extent [4, 31]. The use of land for biomass cropping rather than food production could also cause problems owing to an increase in world population resulting in an increased food production demand [76, 77, 88]. Thus, fertile land in the world will be required for food production, and it is therefore questionable if sufficient land area will be left for biomass production.

2.1.3.3 Photolysis

Photolysis (or direct extraction of hydrogen from water using only sunlight as an energy source) can be accomplished by employing photobiological systems, photochemical assemblies or photoelectron–chemical cells. Intensive research activities are opening new perspectives for photo-conversion where new redox catalysts, colloidal semiconductors, immobilised enzymes and selected microorganisms could provide means of large-scale solar energy harvesting and conversion into hydrogen

[14]. However, the enzyme hydrogenase is very sensitive to oxygen, which inhibits hydrogenase activity and stops it from producing hydrogen [14].

2.1.3.4 Electrolysis

Electrochemical/photochemical water splitting has been regarded as a promising approach for energy storage and conversion to in order to circumvent the energy crisis and environmental issues [22]. In this method, water is subjected to an electric current to force its molecules to decompose into hydrogen and oxygen [22, 143]. The occurring half-reactions at the electrodes are given in (2.4) and (2.5);

$$H_2O \rightarrow 2H^+ + O_2 + 2e^- (\text{anode}) \tag{2.4}$$

$$2H^+ + 2e^- \rightarrow H_2 (\text{cathode}) \tag{2.5}$$

The overall chemical reaction of a water electrolysis process is given by (2.6)

$$H_2O \rightarrow H_2 + \left(\frac{1}{2}\right)O_2 \tag{2.6}$$

Electrochemical water splitting, however, has several barriers to the commercialisation of water electrolysis such as water electrolysis (expensive as compared to hydrocarbon reforming), which is the most widely used technology for hydrogen production. HER can be started at large overpotential, and the water electrolysis system is unstable over long-term and shut down operations [93].

Photo-Electrocatalytic Water Splitting

Development of efficient processes to utilise naturally available solar energy directly to generate hydrogen by water splitting has emerged as a strong contender. Therefore, water electrolysis has always had a central role in the realm of electrochemistry owing to its industrial importance. This process can be employed for the energy storage if the required energy is supplied from a renewable resource [136]. In a simple cell design, a photovoltaic (PV) cell generating appropriate voltage can be coupled with an electrolysis cell to produce hydrogen and oxygen by the solar energy conversion [88]. A variety of criteria have been employed to evaluate the performance of a photocatalyst especially for photo-electrochemical (PEC) water splitting [88] and HER [62, 71]. A photocatalytic water splitting involves an extremely complex series of photophysical and electrocatalytic steps. During a water splitting hydrogen generation, an incident light is irradiated on the catalyst generating electrons and holes in the conduction and valence bands as shown in Fig. 2.2 [63]. The generated electrons and holes cause redox reactions similar to electrolysis. Water molecules are

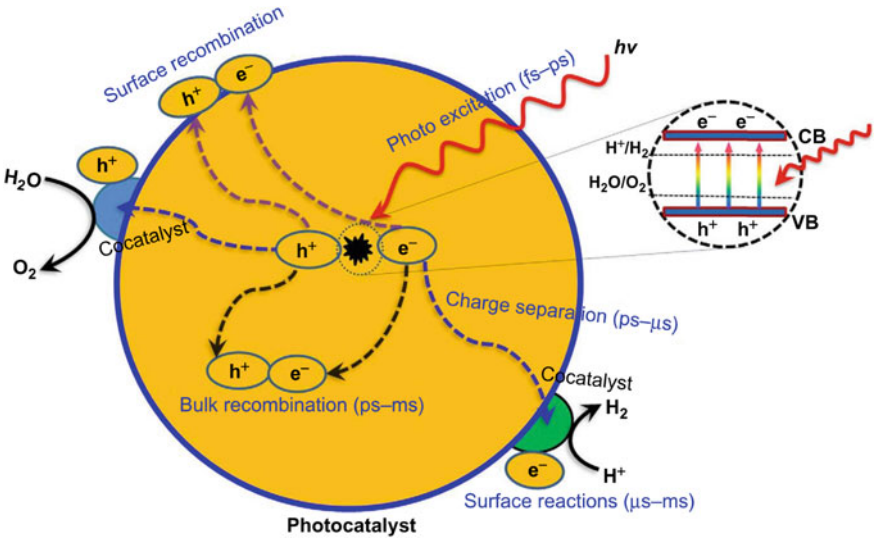

Fig. 2.2 Mechanism of photocatalytic water splitting using a semiconductor-based photocatalyst [63]

adsorbed at the electron holes and oxidised to form protons and O_2. The generated protons are further reduced to H_2 leading to overall water splitting [62, 71, 88, 136].

The primary challenge is of course, finding the most appropriate materials with highest efficiencies for photon absorption and electrocatalysis. The choice of photo/electrocatalyst to exploit the visible light regime and near-infrared region, thus, becomes crucial. Since this technology is deemed the future hydrogen production method, there is a need for its intense study to find the best semiconductor/catalysts that can overcome the challenges imposed by this technology.

Hydrogen Evolution Reaction

A hydrogen evolution reaction (HER) is the production of hydrogen through the process of water electrolysis. The evolution of hydrogen is possibly limited and based on the desorbing of molecules coming from the cathode surface [50]. This process is a crucial step in electrochemical water splitting and demands an efficient, durable and cheap catalyst if it is to succeed in real applications [50, 92]. For an energy-efficient HER, a catalyst must be able to trigger proton reduction with minimal overpotential and have fast kinetics [8]. However, catalyst surface having too weak bonding strength with hydrogen atoms cannot efficiently adsorb the reactant to initiate the HER and a catalyst surface having too strong bonding strength would have a difficulty in releasing the product towards completion of the HER [12, 106].

The mechanism of the HER in aqueous acid or alkaline solutions proceeds in a series of three elementary reaction steps which comprise two electrochemical steps

and one chemical step [8, 12, 105, 106]. In an acidic medium, the HER could proceed via three main steps shown in (2.7)–(2.9);

$$H^+ + e^- \rightarrow H_{ad} \text{Volmer reaction (electrochemical discharge reaction)} \quad (2.7)$$

$$H_{ad} + H^+ + e^- \rightarrow H_2 \text{Heyrovsky reaction (electrochemical desorption)} \quad (2.8)$$

$$H_{ad} + H_{ad} \rightarrow H_2 \text{Tafel reaction (catalytic desorption)} \quad (2.9)$$

while in alkaline solution, HER takes place according to (2.10)–(2.12);

$$H_2O + e^- \rightarrow OH^- + H_{ad} \text{Volmer reaction (electrochemical discharge)} \quad (2.10)$$

$$H_{ad} + H_2O + e^- \rightarrow OH^- + H_2 \text{Heyrovsky reaction (electrochemical desorption)} \quad (2.11)$$

$$H_{ad} + H_{ad} \rightarrow H_2 \text{Tafel reaction(catalytic desorption)} \quad (2.12)$$

In an acidic solution, the first step, (2.7) is the Volmer reaction in which a proton receives an electron and generates an adsorbed hydrogen atom (H_{ad}) at the active site as an intermediate [50]. Then, the second step can be Heyrovsky or Tafel reaction. In Heyrovsky mechanism, a proton reacts with one adsorbed hydrogen to form H_2 as illustrated in (2.8). In the Tafel mechanism, two adsorbed surface hydrogens next to each other react to form H_2 molecule as shown in (2.9) [12, 50, 106]. Since HER involves the adsorption and desorption of the hydrogen atoms on the surface of the catalyst, a suitable catalyst for HER should have a good balance between the two steps [12, 106].

The efficiency and commercialisation of HER depend mostly on the electrocatalyst; hence, most studies have been conducted in electrocatalysis with the great hope of finding a best suitable electrocatalyst for HER [53, 65, 105, 110, 113]. The advanced and ideally electrocatalyst should reduce the overpotential and increase the hydrogen production efficiency [110]. In addition, the efficient electrocatalyst must encounter different characteristics such as high thermal and mechanical stability as well as low cost [55, 141]. The HER activities of various catalysts can be summarised in the "Volcano plot" depicted in Fig. 2.3, where the exchange current density (i_0) for different catalysts in acid is plotted as a function of the Gibbs free energy (E_H) of adsorbed atomic hydrogen on the catalyst [110]. Platinum group metals (PGMs) such as Pt, Pd, Ir and Rh can be found on the apex of the Volcano plot and are the frequently used electrocatalysts for HER [65, 104, 141, 140]. PGMs, especially Pt-based electrocatalysts, meet various requirements for HER electrocatalyst application due their lower overpotential, high catalytic activity, fast kinetics and are most stable. However, their extremely high cost and limited abundance or scarcity hampers

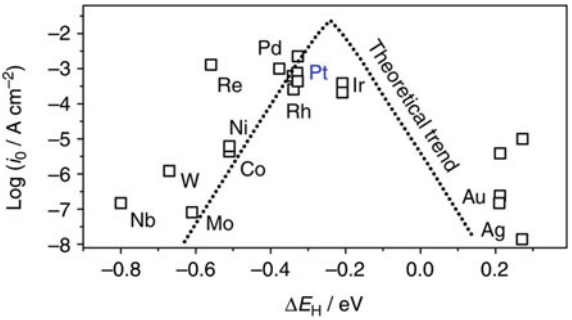

Fig. 2.3 Trends in hydrogen evolution reaction activity. Experimental HER activity expressed as the exchange current density, $\log(i_0)$, for different metal surfaces as a function of the calculated $^*H_{ad}$ chemisorption energy, ΔEH. The result of a simple theoretical kinetic model is also shown as a dotted line [126]

their industrial applications [104, 140]. Thus, the important goal of the modern electrocatalysis is to develop electrocatalysts that could perform better than PGM-based materials with low cost and catalytic activity [3, 123]. Although non-platinum active metals such as Fe, Ni, Mo or Co are considerably cheaper, they suffer from corrosion and passivation under reaction conditions [36, 62, 106]. Electrocatalyst-based carbons (graphene oxide) and/or metal organic frameworks have been rarely investigated for HER. These materials have shown to possess great catalytic activity, low cost and have a wide range potential window [17, 20, 70, 89].

2.2 Graphene Oxide (GO)

2.2.1 Background on GO

Graphene oxide (GO), also called graphitic acid, has attracted a mammoth attention of many researchers [29, 33, 64, 96]. GO is a component in composite materials with photochemical, electric or adsorptive properties [64, 96], and it is a layered material formed by the oxidation of graphite [96]. In comparison to pristine graphite, the graphene-derived sheets in graphite oxide (GO sheets) are heavily oxygenated [16, 96]. Oxidation of graphite enables the incorporation of oxygen atoms on the basal planes and edges of graphene layers. These oxygen functional groups identified so far on the surface of GO are epoxide, keto and hydroxylic groups on the basal planes, and carboxylic groups on the edges [29]. Direct incorporation of oxygen atoms into the graphene layers was also observed in other studies [24, 100, 118, 33]. Owing to its abundant oxygen functional groups, GO has a hydrophilic character and molecules of water can easily be intercalated between the graphene layers [87, 118]. The hydrophilic character is also responsible for homogeneous dispersion

of GO in water, alkaline solutions or alcoholic media [60, 130]. Not only does the oxidation of graphite enable the incorporation of oxygen groups, but it also leads to the formation of defects [45, 83]. These defects usually correspond to vacancies or adatoms in the graphene layers [45, 83]. Considering this, GO is commonly represented as distorted/corrugated graphene layers stacked in a more or less ordered fashion [24, 100, 33].

2.2.1.1 GO Structure

GO is obtained from chemical exfoliation of graphite in which graphite powder is oxidised with strong oxidising agents such as $KMnO_4$ in the presence of concentrated H_2SO_4 [114]. The oxidation of graphite breaks up the extended two-dimensional pie-conjugation of the stacked graphene sheets into nanoscale graphitic sp^2 domains surrounded by disordered, highly oxidised sp^3 domains as well as defects of carbon vacancies [19]. The resulting GO sheets are derivatised by carboxylic acid at the edges, and phenol, hydroxyl and epoxide groups mainly at the basal plane as shown in Fig. 2.4 [82]. After centrifugation, the graphene oxide can be reduced to regular graphene [57] by thermal or chemical methods [37, 87]. It is hardly possible remove all the oxygen containing groups, depending on the reducing agent used. Therefore, a wide range of reducing agents are available and each with its own different reducing ability/capacity.

2.2.2 Synthesis of GO

The most important and widely applied method for the synthesis of GO is the one developed by Hummers and Offeman [18, 95, 100]. This method, at least, has three important advantages over previously used techniques. Firstly, the reaction can be completed within a few hours. Secondly, $KClO_3$ was replaced by $KMnO_4$ to improve the reaction safety, avoiding the evolution of explosive ClO_2. And lastly, the use of

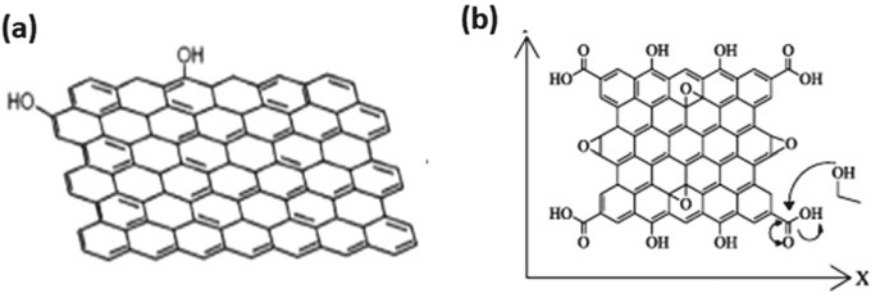

Fig. 2.4 Structural arrangements of **a** graphene [57] and **b** graphene oxide [82]

$NaNO_3$ instead of fuming HNO_3 eliminates the formation of acid fog. In brief, the method involves the oxidation of graphite powder with a mixture of $KMnO_4$ and concentrated H_2SO_4, wherein potassium permanganate serves as an oxidant [78] depicted in Fig. 2.5. The oxidative treatment of graphite helps to increase the interlayer distance between graphene sheets in graphite for an easy exfoliation, since the sheets are usually held by strong van der Waals forces [72, 100]. The produced graphite oxide can be exfoliated directly in several polar solvents such as water,

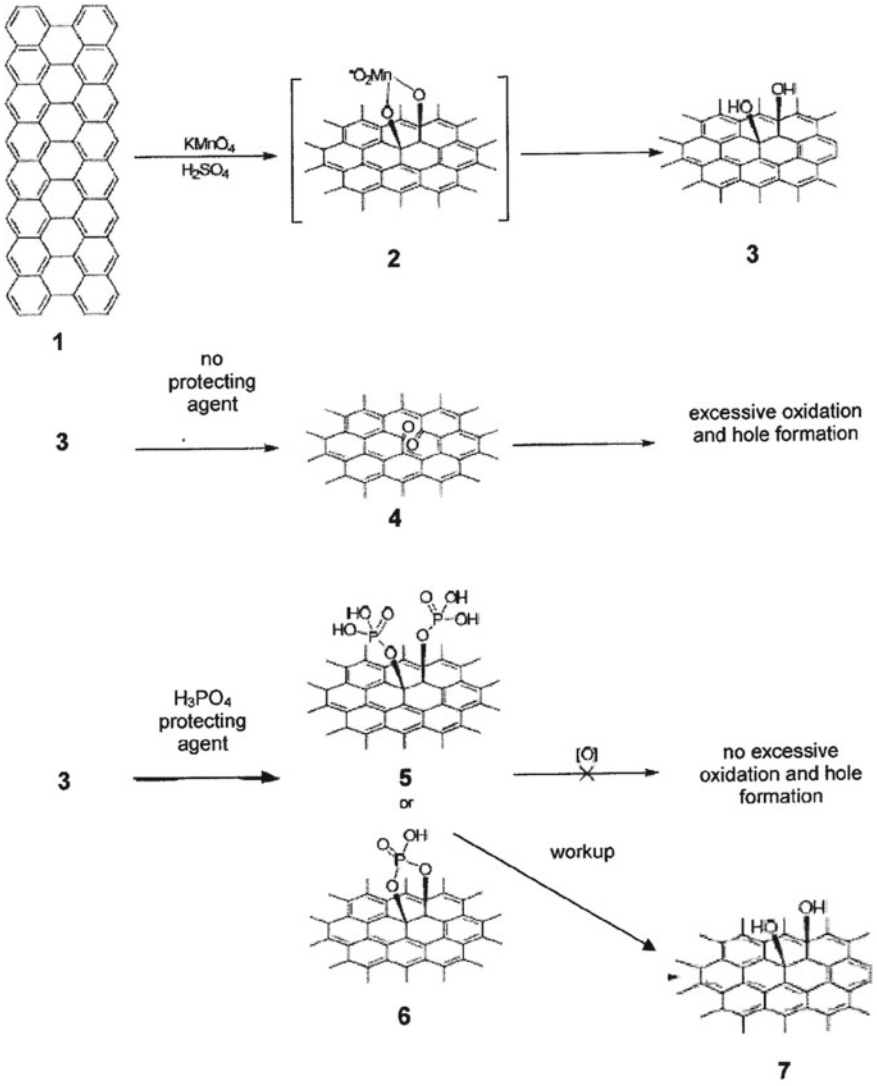

Fig. 2.5 Schematic diagram for the synthesis of graphene oxide by Hummers method [78]

ethylene glycol, *N*,*N*-dimethylformamide (DMF), *N*-methylpyrrolidone (NMP) and tetrahydrofuran (THF) [72]. This process results in the formation of various oxide-containing species including carboxyls, lactones, and ketones [40]. The resulting GO has a non-stoichiometric and amorphous structure [118]. Due to these functional groups, graphene oxide is hydrophilic and can be dissolved in water by sonication or stirring [35, 114, 121]. Thereby the layers become negatively charged and thus a recombination is inhibited by the electrical repulsion. This material has been applied in several fields such as in composite materials, as the electrode materials for electrochemical sensors, as absorbers for both gases and liquids, and as electrode materials for devices involved in electrochemical energy storage and conversion.

2.2.3 GO-Based Materials for HER

The nanostructured and carbonaceous materials are the most fruitful nominees for enhanced electrochemical performance. Recently, HER on GO-based materials as electrocatalysts have been widely studied in both acidic and alkaline conditions [15, 60, 90, 91, 144]. For example, the Tafel slope (b) values for Ni metal and GO denoted (GN) (Table 2.1 and Fig. 2.6) were found to be 85, 64, and 68 mV dec^{-1} for Ni to GO ratios of 2.0 (GN2), 6.0 (GN6) and 8.0 wt% (GN8), respectively, which did not correspond to any simple kinetic model (Volmer, Heyrovsky or Tafel reaction), indicating complex mechanisms for hydrogen evolution on the GN hybrids [144]. Furthermore, the b value for GN2 was higher, while the Tafel slope for GN6 was close to that for GN8, probably due to the difference in the interaction between the carbon-vacancy defects and Ni nanoparticles (NPs), and the difference in their sandwich structures [144]. Moreover, Sun et al. [123] showed GGNR@MoS_2 hybrid exhibiting good HER performance, with a low onset potential of −105 mV, a small Tafel slope of 49 mV per decade and a large exchange current density (i_0) (10.0 mA cm^{-2} at $\eta = 183$ mV), making this composite promising and highly efficient electrocatalyst for HER. The NFO/rGO catalyst exhibited HER activity than bare NFO and other

Table 2.1 Comparison between the ability of various GO- and rGO electrocatalysts towards Tafel slope (b) and exchange current density (i_0) parameters for HER

Material	H_2 source in electrolyte (0.5M)	b (mV dec^{-1})	i_o (mA cm^{-2})	References
PdNPs-GO	H_2SO_4	–	5.2	Chen et al. [18]
NFO/rGO	H_2SO_4	58	25.2×10^{-2}	Mukherjee et al. [90]
rGO-Au48Pd52	H_2SO_4	149	–	Cardoso et al. [15]
CFG	H_2SO_4	116.6	47.9	Nivetha et al. [91]
NFG	H_2SO_4	121.4	41.2	Nivetha et al. [91]
$CoMoS_2$/NGO	H_2SO_4	34.13	30.0	Hou et al. [46]
CoP/rGO-400	H_2SO_4	50.0	10.0	Jiao et al. [51]

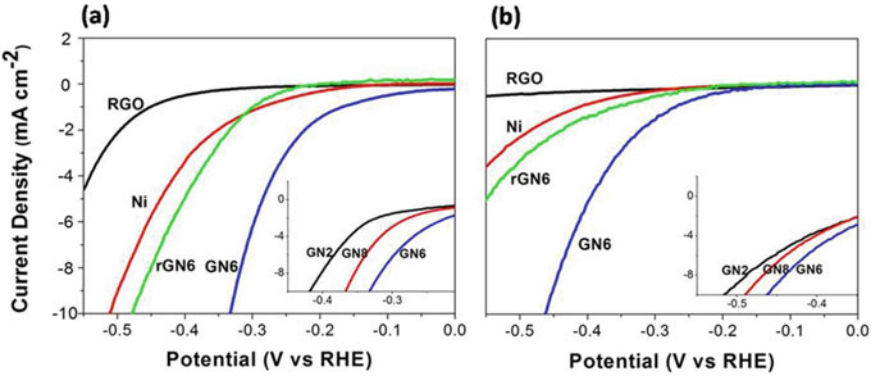

Fig. 2.6 Linear sweep voltammetry (LSV) curves of rGO, Ni, rGN6 and GN6 in 0.50M H_2SO_4 solution (**a**) and in 0.50M Na_2SO_4 solution of pH 10 (**b**). The insets are LSV curves of GN2, GN6 and GN8 composites with reference to Ni [144]

reported catalysts such as sulphides, carbides, phosphides, bimetals of molybdenum and iron–cobalt. With a low onset overpotential of 5 mV (vs. reference hydrogen electrode (RHE)), high cathodic current density, low Tafel slope of 58 mV dec^{-1}, low charge transfer resistance and turnover frequency of 0.48 s^{-1} [90]. Nivetha et al. [91] showed HER activity of nanocomposites (CFG and NFG) which were tested for hydrogen production at an applied potential window of −1.2 to 0.8 V in acidic electrolyte. The nanocomposites revealed good i_0 values of 47.9 and 41.2 mA cm^{-2} at over potential of 248.3 and 259 mV and Tafel slopes of 116.6 and 121.4 mV dec^{-1} for CFG and NFG nanocomposite, respectively [91].

In another study, Hou et al. [46] investigated the cobalt–molybdenum bimetallic sulphide catalysts supported on nitrogen-doped graphene ($CoMoS_2$/NGO) for HER application as depicted in Fig. 2.7a–e. In this study, they used hydrogen peroxide (H_2O_2) as an additive during hydrothermal process. Their composite exhibited more efficiency towards HER, depicting as low onset potential −54 mV in 0.5 M H_2SO_4. Typical H_2O_2-assisted composite realised a remarkable cathodic current density of 30 mA cm^{-2} at an overpotential = −137 mV and Tafel slope of 34.13 mV dec^{-1}. The composite also exhibited an excellent cycling stability and superior electronic exchange rate. Jiao et al. [51] evaluated the HER activity using cobalt phosphate/reduced graphene oxide (CoP/rGO-400) by using 0.5M H_2SO_4 and alkaline (1M KOH) media. The composite exhibited very high activity, possibly due to the synergistic character between the porous CoP and conductive rGO.

As observed in Table 2.1, a few electrochemists paid more consideration to GO or rGO because of their admirable conductivity, less weight, strong mechanical properties, high surface area and good chemical stability [29, 60, 114]. However, the electrochemical applications of these materials have some barriers due to their insulation properties which are interrelated to the manifestation of oxygen functionalities. To overcome this issue, a number of studies using GO incorporated with metal particles, metal oxide, conductive polymers and biopolymers to fabricate composites with

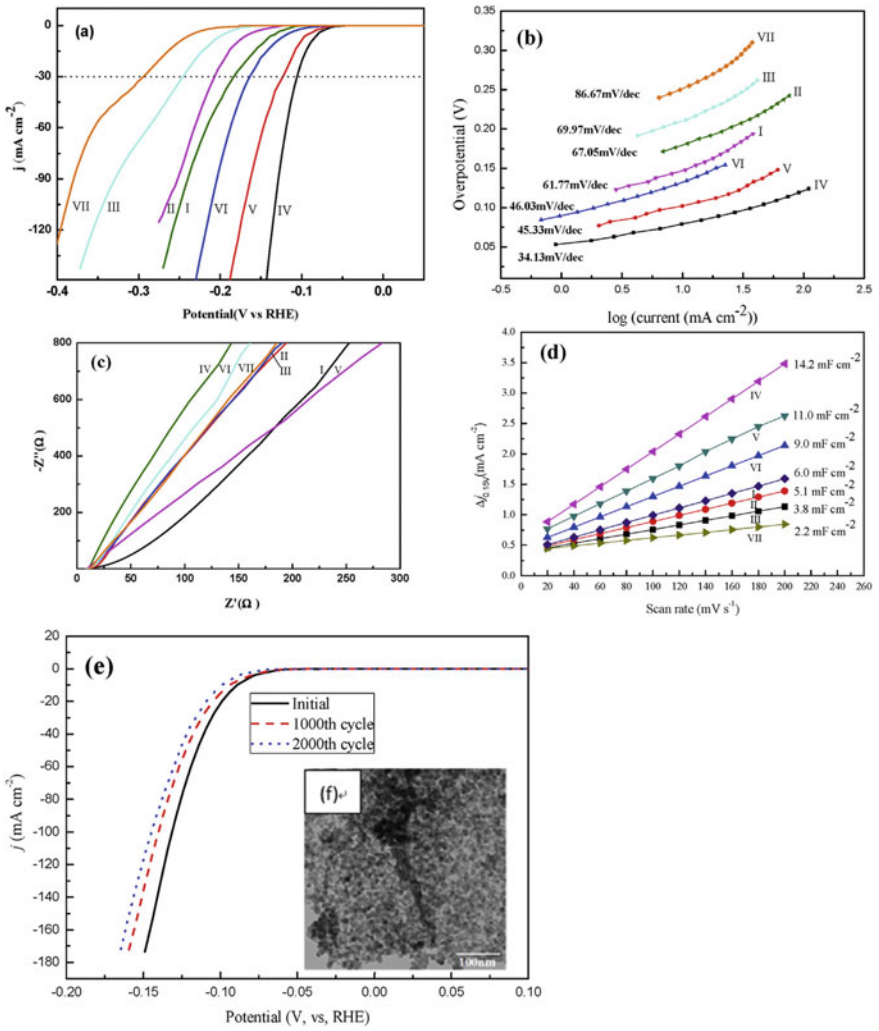

Fig. 2.7 LSV showing **a** the overall electrocatalytic activity, **b** corresponding Tafel plots of different catalysts, **c** EIS spectra of all $CoMoS_2$/NGO composites, **d** calculation of C_{dl} by plotting charging current density differences ($\Delta\ j = ja - jc$)/2 versus scanning rate in (I) $CoMoS_2$/NGO-I, (II) $CoMoS_2$/NGO-II, (III) $CoMoS_2$/NGO-III, (IV) $CoMoS_2$/NGO-IV, (V) $CoMoS_2$/NGO-V, (VI) $CoMoS_2$/NGO-VI, (VII) $CoMoS_2$/NGO-VII, **e** a comparison between initial activity and that after 1000 and 2000 cycles in 0.5M H_2SO_4 medium for $CoMoS_2$/NGO-VI and **f** TEM image after 2000 cycles for $CoMoS_2$/NGO-IV [46]

better performance were reported [10, 38, 120, 134]. As mentioned above, small-sized metal particles have been acknowledged as good mediators on the fabrication of materials for electrochemical applications due to their biocompatibility, fast electron transfer rate and excellent conductivity. Therefore, decoration of small-sized metal nanoparticles and/or organometallic compounds on the surface of GO sheets is proposed to not only further resolve the insulation properties problem of GO but also significantly increase the electrochemical activity.

2.3 Metal Organic Frameworks (MOFs)

2.3.1 Background

Metal organic frameworks (MOFs) are class of adsorbent materials, consisting of metal ions and organic ligands that involve O and N [128]. As there was no accepted standard nomenclature during the development of this new class of hybrid solids, several names have been proposed and are in use [17, 20, 128]. Examples include porous coordination polymers [67] and networks [69], microporous coordination polymers [59], zeolite-like MOFs [122], and isoreticular MOFs [59, 67, 131]. In MOFs, the inorganic and organic building units are linked via coordination bonds. Generally, the inorganic units are metal ions or metal cluster, and the organic units (known as linkers or bridging ligands) are di-, tri- or tetradentate organic ligands [44, 94, 122] such as carboxylates or other organic anions (phosphonate, sulphonate and heterocyclic compounds). A lot of features of these types of crystalline materials caught the eyes of many researchers in various fields owing to their adjustable pore size and high surface area [150].

2.3.2 Structure of MOFs

MOF materials are formed by assembling metal nodes and organic ligands [17, 20, 71]. The metal node precursors mainly come from metal nitrates or chlorides, while the organic ligands mainly include benzimidazolate [84], dicarboxylic acid.

2.3.2.1 Organic Ligands

Organic ligands are known for their complex nature and ability to form coordination bonds [17, 20, 59, 128] as depicted in Fig. 2.8 [48]. The preferred organic linker is the one that will bring much stability to the MOF structure due to the rigidity of the backbone of the linker or ligand. The rigidity on the backbone of the linker makes it easier to predict the network geometry and helps to sustain the open-pore structure

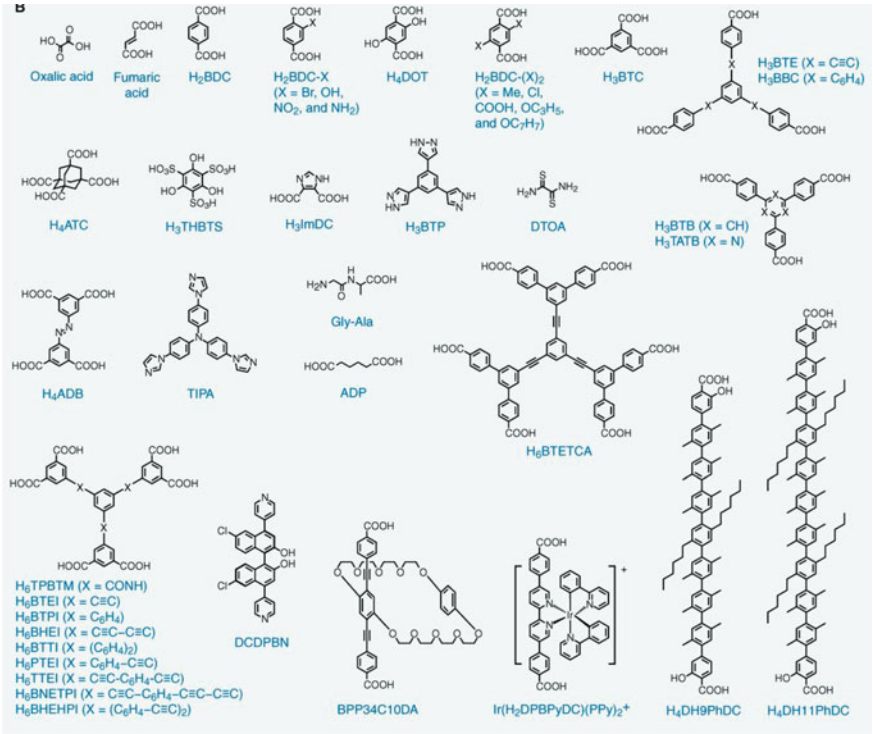

Fig. 2.8 Examples of some organic ligands used for the synthesis of metal organic frameworks [48]

after the removal of the included solvent. The organic linkers can be electrically neutral, anionic or cationic [48].

2.3.2.2 Metal Sites

Metal sites have tremendous influences on the adsorption and catalytic properties of MOFs [148]. The metal sites can act as Lewis acids and activate the coordinated organic substrate for subsequent organic transformation [47]. Furthermore, the metal sites have been reported to enhance H_2 adsorption in MOFs [47, 148]. These commonly used transition metals give different geometries depending on their number of oxidation states such as copper–electron configuration of zero-valent $[Ar]3d^{10}4s^1$. Copper nodes are often in distorted octahedral and square-planar geometries which assist in rapid electron transfer to facilitate electron mobility in HER process [89]. The distortion occurs mainly due to Jahn–Teller distortion commonly resulting in octahedral geometries having four short bonds and two longer bonds as the d_z^2 orbital is filled while the $d_{x^2-y^2}$ orbital is only partially filled.

2.3.2.3 Secondary Building Units

Secondary building units (SBUs) play important role as it dictates the final topology of MOFs. The geometry and chemical attributes of the SBUs and organic linkers lead to the prediction of the design and the synthesis of MOFs [47, 135, 148]. It was reported that under careful selected conditions, multidentate linkers could aggregate and lock metal ions at certain positions, forming SBUs [47, 132]. These SBUs will subsequently be joined by rigid organic links to produce MOFs that exhibit high structural stability [54]. Studies have proved that the geometry of the SBU depends on metal-to-ligand ration, the solvent and the source of anions to balance the charges of the metal ions [80, 148].

2.3.2.4 Pores in MOFs

Pores are empty space formed within MOFs upon the removal of guest molecules. The wide open MOF structures with pores of internal diameter of up to 4.8 nm provide extra-large free space that can be used for H_2 storage [79]. The ideal pore size for porous adsorbents should give an optimal interaction of the absorbate gas with the potential surface of all the surrounding walls. The pore size should be close to the kinetic diameter of H_2 molecule (0.289 nm) to promote stronger interaction between H_2 molecules and the framework. For example, NU-100 contains micropores (<2 nm) and have storage capacity of 8 wt% [7], while MOF-5 have micropores of (0.77 nm) and stores close to 7 wt% [132]. Generally, the larger the pore size the more likely that the structural collapse could occur, and is more difficult to achieve permanent porosity. Nevertheless, this kind of structures may lead to improved performance in some application such as H_2 storage [132].

2.3.3 Synthesis of MOFs

The most preparation methods for MOFs are liquid-phase synthesis, whereby metal salt and ligand solutions are mixed together in a reaction vial [98].

2.3.3.1 Microwave-Assisted Synthesis

Microwave-assisted synthesis relies on the interaction of electromagnetic waves with mobile electric charges. These can be polar solvent molecules/ions in a solution or electrons/ions in a solid. In the solid, an electric current is formed and heating is due to electric resistance of the solid [2, 61, 133]. In solution, polar molecules try to align themselves in an electromagnetic field and in an oscillating field so that the molecules change their orientations permanently [23, 75]. Thus, applying the appropriate frequency, collision between the molecules will take place, which leads

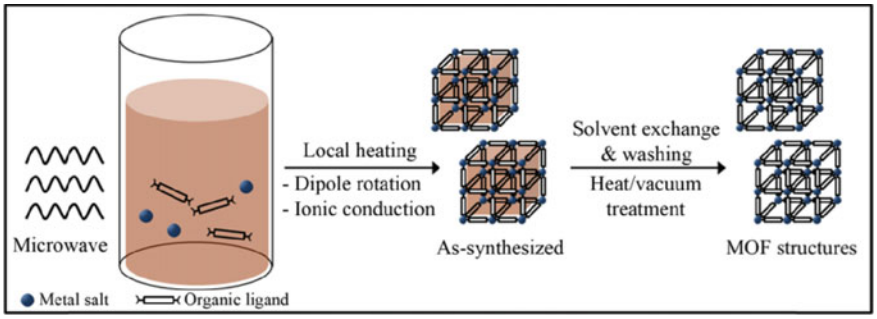

Fig. 2.9 A schematic representation of a microwave-assisted solvothermal synthesis of MOF structures [61]

to an increase in kinetic energy, i.e. temperature of the system. Furthermore, several metal (III) carboxylate-based MOFs (M = Fe, Al, Cr, V, Ce) have been prepared by MW-assisted synthesis route as shown in Fig. 2.9 [17, 20, 23, 75, 127]. During microwave synthesis, heat is generated internally within reaction media by dielectric heating as opposed to the conventional heating in which heat is conducted to the media from external sources, thus, facilitating the nucleation and crystal growth in the synthesis of MOFs [34, 61, 68].

2.3.3.2 Mechanochemical Synthesis

In mechanochemical synthesis, there is an occurrence of mechanical breakage of intramolecular bonds followed by a chemical transformation. This method has a long history in synthetic chemistry [21, 97, 117], and it has recently been employed in multicomponent (ternary and higher) reactions to form pharmaceutically active co-crystals and in inorganic solid-state chemistry, organic synthesis and polymer science [61, 98, 117]. Its use for the synthesis of porous MOFs was first reported in 2006 [23], and results of selected mechanochemical studies were summarised recently [98, 117]. A significant advantage of this approach is the possibility to fabricate MOFs with only water as a by-product, and no purification is required. Addendum to this, pure powders with the high yield (>90%) with the use of a solvent as well as microporous MOFs can be obtained as shown in Fig. 2.10a–c [97, 145]. This is accomplished by using hydroxides or oxides as the metal precursors, which then in combination with protons generated from the organic ligand forms water. With this strategy, a ZIF-8-type MOF with the BET surface area of 1480 m^2/g can be achieved.

2.3.3.3 MOFs Synthesis via Electrochemical Route

Electrochemical synthesis involves the use of electrochemical cell to prepare the MOF compounds, and this is presented in Fig. 2.11a. For this synthesis, galvanic

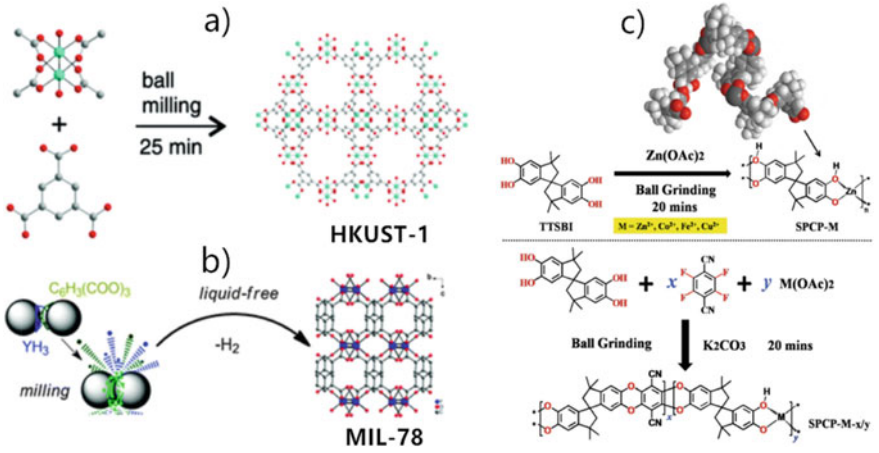

Fig. 2.10 Mechanochemical synthesis of different MOFs **a** synthesis of HKUST-1 from copper salt and trimesic acid, **b** synthesis of MIL-78, **c** fabrication of 1-D porous coordination polymers [21]

cell, potentiostat and two electrode set-up are required. Synthesis of MOFs using this route is still a new topic and was first reported by researchers in BASF in 2005 [41, 138]. Instead of adding a metal salt during the synthesis, the principle relies on supplying the metal ion by anodic dissolution to a mixture that containing the organic linker and the electrolyte [17, 20, 41, 138]. The metal deposition process on the cathode which can have a negative effect during synthesis can be avoided by employing a protic solvent; nonetheless, a hydrogen gas will be produced in the process [5]. Electrochemical methods have several advantages over other traditional methods such as hydro/solvothermal and microwave-assisted that requires high temperature and long reaction time conditions [25]. It also provides the possibility to influence the reaction directly in real-time offering both more control and the ability to perform the synthesis in a continuous fashion. Furthermore, the localised nature of electrochemical methods allows the formation of directed thin films without the need to pre-treat the surface as is usually the case. The mild temperatures used during synthesis also reduce the effects of thermally induced film cracking, which is often a problem with hydrothermal methods [26]. Nonetheless, this strategy has shown some drawbacks coming form an insulating character of MOFS. Thus, in order to circumvent this challenge, Wang et al. developed an effective electrochemical deposition strategy of MOFs by interweaving flexible ZIF-67 crystals/carbon cloth with conductive polyaniline (PANI), which could act as bridges for electron transportation between the external circuit and the internal surface of MOFs as shown in Fig. 2.11b.

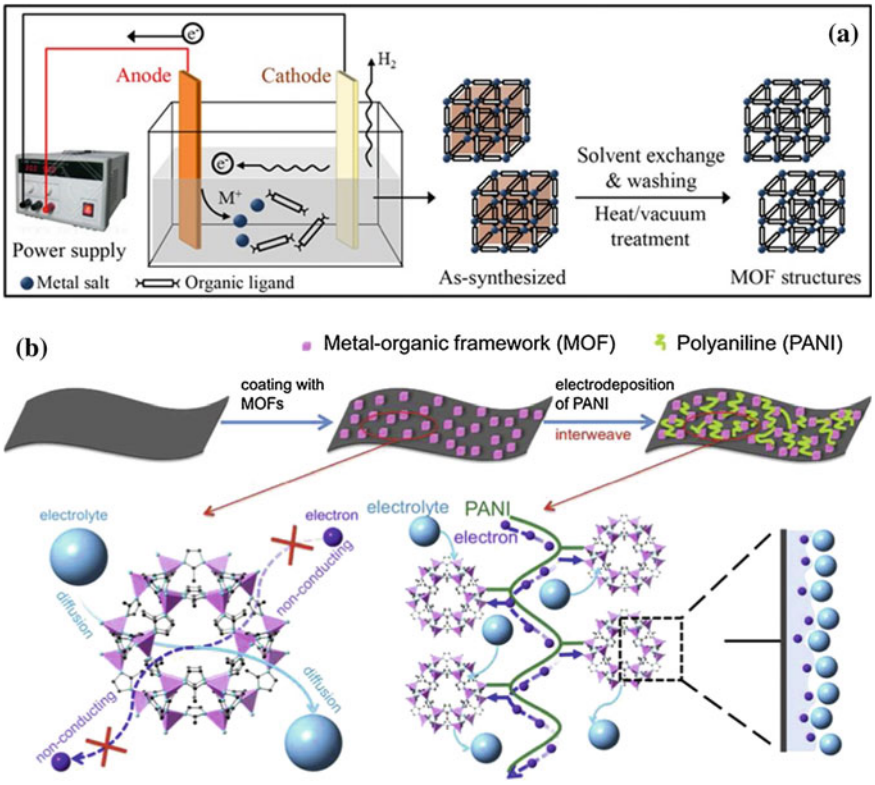

Fig. 2.11 **a** Electrochemical synthesis route of metal organic frameworks [61] and **b** schematic illustration of the preparation of PANI-ZIF-67-carbon cloth [129]

2.3.3.4 Solvo/Hydrothermal Synthesis

The solvo/hydrothermal method is a process of crystallisation in which the compounds are synthesised depending on the solubility of compound in water at autogenous pressure. The crystallisation process is done in a vessel called an autoclave [7, 119]. The autoclave is usually made of thick-walled steel cylinders, which can withstand high temperatures and pressures for prolonged periods of time [17, 20, 128, 39, 41, 138]. The autoclave is especially designed to withstand corrosiveness and also has protective seals. The inside of the autoclave is layered with Teflon or titanium or glass depending on the nature of the solvent used. The samples are first placed within the Teflon bags. The bags are sealed and kept in the Teflon cup. The Teflon cup is closed with a cap on the top, and then, this cup is placed into the autoclave. The autoclave is tightly closed and placed within the oven for high temperatures [75, 41, 138]. A schematic representation of solvothermal synthesis of various MOFs with high surface area, crystallinity, good conductivity as well as good stability is shown in Fig. 2.12.

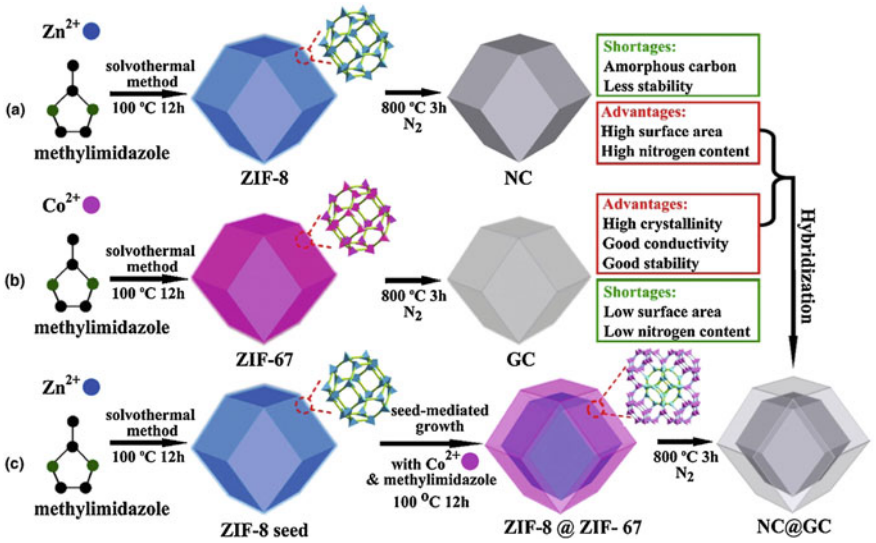

Fig. 2.12 Synthetic scheme for the preparation of **a** MOFs (ZIF-8), **b** ZIF-67 crystals and NC@GC, and core–shell ZIF-8@ZIF-67 crystals and NC@GC via a conventional solvothermal method [125]

2.3.4 MOF-Based Materials as HER Electrocatalysts

The electrochemical water-splitting process includes two half-reactions: HER and oxygen evolution reaction (OER). Given that the water splitting needs high activation energy and large overpotential, high-performance electrocatalysts with low cost are highly desired to enhance the performance of electrocatalytic water splitting. Complexes with precise structures are beneficial for mechanism studies by using various electrochemical measurements and other techniques [81, 109, 137, 143]. Such homogeneous catalysts can also fully utilise all catalytic sites, when they are used at low concentrations, giving particularly high activity in the term of turnover frequency (TOF). Such catalysts usually suffer from low stability [64, 67, 86, 146]. Combining the advantages of conventional heterogeneous and homogeneous catalysts, MOF-derived inorganic materials can solve many of the above-mentioned problems [38, 95, 149, 147]. In this regard, Sandra Loera-Serna et al. [74] showed the electrochemical behaviour Cu-MOF, confirming that this material has a high catalytic activity. Furthermore, Lin et al. [70] constructed metal–organic frameworks derived cobalt diselenide (MOF-$CoSe_2$) with $CoSe_2$ nanoparticles anchored into nitrogen-doped (N-doped) graphitic carbon through in situ selenisation of Co-based MOFs. It was detected that the MOF-$CoSe_2$ delivered excellent HER performance with an onset potential of approximately 150 mV and high current density of 80 mA cm^{-2} at about −0.33 V (vs. RHE), which behaved better than bare $CoSe_2$. The Tafel slope of the MOF-$CoSe_2$ was 42 mV dec^{-1}, which is much smaller than that of bare $CoSe_2$ of 72 mV dec^{-1}. Moreover, Ramohlola and co-workers [102, 103] showed the merits of

combining MOF material with conductive polymers to produce a highly active material with Tafel plots presented in Fig. 2.13 [102]. Table 2.2 presents the Tafel parameters of MOF-polyaniline (PANI), MOF-3wt% poly(3-aminobenzoic acid) (PABA), PABA-MOF and MOF-5 wt% PABA composite with high i_0 values of 7.943 A m^{-2} [103], 31.62 A m^{-2} [102], 35.48 A m^{-2} [101] and 50.12 A m^{-2} [102] and Tafel slopes of 199.3 [103], 166.7 A m^{-2} [102], 130.5 A m^{-2} [101] and 153.5 mV dec^{-1} [102], respectively.

The integration of Cu-MOF with graphene oxide (GO) can effectively enhance the electron transfer, which further significantly improve HER activity [49]. It was also found that the GO content affected the HER activity of the nanocomposite catalysts. The optimised GO content was about 8 wt%. The HER current density of the (GO 8wt%) Cu-MOF (Table 2.2) was high up to −30 mA cm^{-2} at an overpotential of −2.0 V in N_2 saturated 0.5M H_2SO_4, whereas the overpotential of 30 wt% Pt was -0.06 V at the current density of -30 mA.cm^{-2} [49]. The electrochemical hydrogen evolution reaction performance of the Pd@CuPc/MOF and Tafel analysis were evaluated by Monama et al. [89]. The Tafel slope of this composite was found to be 176.9 mV/dec and the transfer coefficient of 0.67, with the exchange current density of 8.9 A m^{-2} (Table 2.2). The HER results revealed that the Pd@CuPc/MOF composite has better catalytic characteristic such as high catalytic activity and lowest onset potential compared to MOF. More importantly, they reported the significant enhancement of HER performance at ambient temperature for the composite with Pd content to be ascribed to the hydrogen spillover mechanism in such a system.

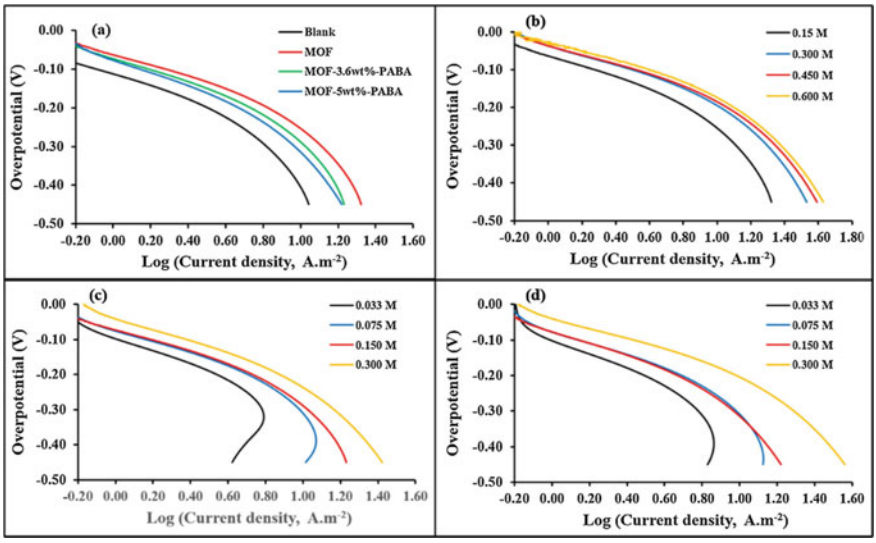

Fig. 2.13 **a** Tafel plots of blank, MOF and MOF-PABA; and **b** MOF, **c** MOF-3.6wt%-PABA and **d** MOF-5wt%-PABA at 0.10 V s^{-1} in the presence of different H_2SO_4 concentration on gold electrode in 0.1 mol L^{-1} dimethylsulphoxide/tetrabutylammonium percholate (DMSO/TBAP) electrolytic system [102]

Table 2.2 Comparison between the ability of various MOF electrocatalysts towards Tafel slope (b) and exchange current density (i_0) parameters for HER

Material	H_2 source in electrolyte	b (mV dec^{-1})	i_0 (A m^{-2})	References
MOF-$CoSe_2$	0.5M H_2SO_4	42	0.080	Monama et al. [89]
MOF-5wt%-PABA	0.3M H_2SO_4	153.5	50.12	Ramohlola et al. [102]
PABA/MOF	0.3M H_2SO_4	130.5	35.48	Ramohlola et al. [101]
Pd@CuPc/MOF	0.3M H_2SO_4	176.9	8.900	Monama et al. [89]
MOF-3wt%-PABA	0.3M H_2SO_4	166.7	31.62	Ramohlola et al. [102]
MOF/PANI	0.3M H_2SO_4	199.3	7.943	Ramohlola et al. [103]
Cu-MOF/8 wt% GO	0.5M H_2SO_4	–	−300	Jahan et al. [49]

2.4 Summary and Future Prospects

The upsurge in the necessity for clean and renewable energy for the next generation of sustainable society led to the development of new advanced electrocatalysts for hydrogen evolution reaction application. The HER is the heart of distinct energy storage and conversation systems in the future of renewable energy. The HER electrocatalysis can be well conducted by a Pt metal with a low overpotential near zero and a Tafel slope value around 30 mV dec^{-1}. Nevertheless, the practical developments to satisfy the growing demands require very cost-effective electrocatalysts. Noble metals are still the promising candidates, though further enhancement is needed to improve the performance of HER efficiency. Carbon nanomaterials, such as graphene and GO, have been able to secure a prominent position in order to meet the requirements for electrocatalysts in HER. This is because these electrocatalysts possess electron rich properties and functional groups enrichment character emanating from GO. Nonetheless, the electrochemical application of these materials possesses some drawbacks owing to their insulating character caused by oxygen functionalities on the surface of the GO. However, it was observed that decorating graphene sheets with metal nanoparticles, metal sulphides and different types of MOFs can enhance an electrochemical activity of composites for HER application. MOF-based materials can effectively convert water/H_2SO_4 to hydrogen energy. Unfortunately, most of these MOFs are insoluble in water, which hamper them to be widely utilised in water splitting application. In order to circumvent this, the introduction of hydrophobic substituents in the ligands has shown to be effective in that regard. It was found that MOFs and their composites maintain the original structures after modification with nanoparticles or other guest species. However, some new strategies and/or challenges still deserve further consideration to improve the catalytic efficiency of MOF-based electrocatalysts for water splitting system. It is therefore evident that a significant

amount of work has been made in HER, which has generated global attention in efficient electrocatalyst materials owing to the need to resolve high demands for clean and sustainable energy in order to resolve potential threat posed by fossil fuels to the environment and thereby deemed unreliable.

The reaction mechanisms of HER, the transfer and diffusion properties of reactants and products as well as the effects of electrolyte on the catalytic performance of MOF-based electrocatalysts were identified as an alternative route to study the hydrogen storage and production behaviour of these materials. However, the vast majority of the synthesised MOFs suffer from poor electronic conductivity leading to low electron transfer efficiency, thus, restricts catalytic performance of these materials. Therefore, strategies such as fabrication of core–shell, hollow-structured electrocatalysts, decoration of electrocatalysts with amines are the efficient approaches to enhance the activity, stability and durability for HER. Therefore, an integration of MOFs with GO can effectively enhance the electron transfer, which further significantly improves HER activity. Furthermore, the HER mechanisms, transfer and diffusion properties of GO-based MOF electrocatalysts need to be investigated as a future alternative route in hydrogen production and storage technologies to meet high energy demands.

Acknowledgements KDM and MJH would like to thank the National Research Foundation (NRF) under Thuthuka program (Grant Nos. 118113 and 117727), University of Limpopo and Sasol Foundation of South Africa for funding this project.

Conflict of interest We declare there are no conflicts of interest.

References

1. R.K. Ahluwalia, T.Q. Hua, J.K. Peng, S. Lasher, K. McKenney, J. Sinha, M. Gardiner, Technical assessment of cryo-compressed hydrogen storage tank systems for automotive applications. Int. J. Hydrogen Energy **35**, 4171–4184 (2010)
2. P. Amo-Ochoa, G. Givaja, P.J.S. Miguel, O. Castillo, F. Zamora, Microwave assisted hydrothermal synthesis of a novel CuI-sulfate-pyrazine MOF. Inorg. Chem. Commun. **10**, 921–924 (2007)
3. C.O. Ania, M. Seredych, E. Rodriguez-Castellon, T.J. Bandosz, New copper/GO based material as an efficient oxygen reduction catalyst in an alkaline medium: the role of unique Cu/rGO architecture. Appl. Catal. B Environ. **163**, 424–435 (2015)
4. M. Asif, T. Muneer, Energy supply, its demand and security issues for developed and emerging economies. Renew. Sustain. Energy Rev. **11**, 1388–1413 (2007)
5. T.R.C. Van Assche, N. Campagnol, T. Muselle, H. Terryn, J. Fransaer, J.F.M. Denayer, On controlling the anodic electrochemical film deposition of HKUST-1 metal-organic frameworks. Microporous Mesoporous Mater. **224**, 302–310 (2016)
6. T. Autrey, Boron-nitrogen-hydrogen (BNH) compounds: recent developments in hydrogen storage, applications in hydrogenation and catalysis, and new syntheses. Energy Enviro. Sci. **5**, 9257–9268 (2012)
7. F.N. Azad, M. Ghaedi, K. Dashtian, S. Hajati, V. Pezeshkpour, Ultrasonically assisted hydrothermal synthesis of activated carbon-HKUST-1-MOF hybrid for efficient simultaneous ultrasound-assisted removal of ternary organic dyes and antibacterial investigation: Taguchi optimization. Ultrason. Sonochem. **31**, 383–393 (2016)

8. O. Azizi, M. Jafarian, F. Gobal, H. Heli, M.G. Mahjani, The investigation of the kinetics and mechanism of hydrogen evolution reaction on tin. Int. J. Hydrogen Energy **32**, 1755–1761 (2007)
9. M. Balat, Potential importance of hydrogen as a future solution to environmental and transportation problems. Int. J. Hydrogen Energy **33**, 4013–4029 (2008)
10. P.C. Banerjee, D.E. Lobo, R. Middag, W.K. Ng, M.E. Shaibani, M. Majumder, Electrochemical capacitance of Ni-doped metal organic framework and reduced graphene oxide composites: more than the sum of its parts. ACS Appl. Mater. Interfaces **7**, 3655–3664 (2015)
11. H. Barthelemy, M. Weber, F. Barbier, Hydrogen storage: recent improvements and industrial perspectives. Int. J. Hydrogen Energy **42**, 7254–7262 (2017)
12. R. Bocutti, M.J. Saeki, A.O. Florentino, C.L.F. Oliveira, A.C.D. Ângelo, Hydrogen evolution reaction on codeposited Ni-hydrogen storage intermetallic particles in alkaline medium. Int. J. Hydrogen Energy **25**, 1051–1058 (2000)
13. R.K. Brow, M.L. Schmitt, A survey of energy and environmental applications of glass. J. Eur. Ceram. Soc. **29**, 1193–1201 (2009)
14. D.D. Burnette, G.G. Kremer, D.J. Bayless, The use of hydrogen-depleted coal syngas in solid oxide fuel cells. J. Power Sourc. **182**, 329–333 (2008)
15. J.A.S.B. Cardoso, L. Amaral, O. Metin, D.S.P. Cardoso, M. Sevim, T. Sener, C.A.C. Sequeira, D.M.F. Santos, Reduced graphene oxide assembled Pd-based nanoalloys for hydrogen evolution reaction. Int. J. Hydrogen Energy **42**, 3916–3925 (2017)
16. V. Chabot, D. Higgins, A. Yu, Z. Chen, J. Zhang, A review of graphene and graphene oxide sponge: material synthesis and applications to energy and the environment. Energy Environ. Sci. **7**, 1564–1596 (2014)
17. Y. Chen, D. Ni, X. Yang, C. Liu, J. Yin, K. Cai, Microwave-assisted synthesis of honeycomblike hierarchical spherical Zn-doped Ni-MOF as a high-performance battery-type supercapacitor electrode material. Electrochim. Acta **278**, 114–123 (2018)
18. X. Chen, G. Wu, J. Chen, X. Chen, Z. Xie, X. Wang, Synthesis of 'clean' and well-dispersive Pd nanoparticles with excellent electrocatalytic property on graphene oxide. J. Am. Chem. Soc. **133**, 3693–3695 (2011)
19. J. Chen, B. Yao, C. Li, G. Shi, An improved Hummers method for eco-friendly synthesis of graphene oxide. Carbon **64**, 225–229 (2013)
20. Y.Z. Chen, R. Zhang, L. Jiao, H.L. Jiang, Metal–organic framework-derived porous materials for catalysis. Coord. Chem. Rev. **362**, 1–23 (2018)
21. D. Chen, J. Zhao, P. Zhang, S. Dai, Mechanochemical synthesis of metal–organic frameworks. Polyhedron **162**, 59–64 (2019)
22. J. Chi, H. Yu, Water electrolysis based on renewable energy for hydrogen production. Chin. J. Catal. **39**, 390–394 (2018)
23. J.Y. Choi, J. Kim, S.H. Jhung, H. Kim, J. Chang, H.K. Chae, Microwave synthesis of a porous metal-organic framework, zinc terephthalate MOF-5. Bull. Korean Chem. Soc. **27**, 1523–1524 (2006)
24. C.K. Chua, M. Pumera, Chemical reduction of graphene oxide: a synthetic chemistry viewpoint. Chem. Soc. Rev. **43**, 291–312 (2014)
25. Y. Cui, B. Chen, G. Qian, Lanthanide metal-organic frameworks for luminiscent sensing and light-emitting applications. Coordination Chem. Rev. **273–274**, 76–86 (2014)
26. D. Braga, S.L. Giaffreda, F. Grepioni, A. Pettersen, L. Maini, M. Curzi, M. Polito, Dalton Trans. **37**, 1249 (2006)
27. D.P. Broom, C.J. Webb, K.E. Hurst, P.A. Parilla, T. Gennett, C.M. Brown, R. Zacharia, E. Tylianakis, E. Klontzas, G.E. GFroudakis, T.A. Steriotis, P.N. Trikalitis, D.L. Anton, B. Hardy, D. Tamburello, C. Corgnale, B.A. van Hassel, D. Cossement, R. Chahine, M. Hirscher, Outlook and challenges for hydrogen storage in nanoporous materials. Appl. Phys. A Mater. Sci. Process **122**, 1–21 (2016)
28. A. Demirbaş, Biomass resource facilities and biomass conversion processing for fuels and chemicals. Energy Convers. Manag. **42**, 1357–1378 (2001)

29. D.R. Dreyer, S. Park, W. Bielawski, R.S. Ruoff, The chemistry of graphene oxide. Chem. Soc. Revs. **39**, 228–240 (2010)
30. S. Dunn, Hydrogen futures: Toward a sustainable energy system. Int. J. Hydrogen Energy **27**, 235–264 (2002)
31. O. Ellabban, H. Abu-Rub, F. Blaabjerg, Renewable energy resources: Current status, future prospects and their enabling technology. Renew. Sustain. Energy Rev. **39**, 748–764 (2014)
32. H. Fayaz, R. Saidur, N. Razali, F.S. Anuar, A.R. Saleman, M.R. Islam, An overview of hydrogen as a vehicle fuel. Renew. Sustain. Energy Rev. **16**, 5511–5528 (2012)
33. G. Wang. Y. Ma, L. Zhang, J. Mu, Z. Zhang, X. Zhang, H. Che, Y. Bai, H.Y., Hou, Facile synthesis of manganese ferrite/graphene oxide nanocomposites for controlled targeted drug delivery. J. Magn. Magn. Mater. **401**, 647–650 (2016)
34. S.G.C. Gabriel, E.H. Grant, B.S.J. Halstead, D.M.P. Mingos, Chem. Soc. Rev. **27**, 213–223 (1998)
35. B.M. Ganesh, A.M. Isloor, A.F. Ismail, Enhanced hydrophilicity and salt rejection study of graphene oxide-polysulfone mixed matrix membrane. Desalination **313**, 199–207 (2013)
36. M.R. Gao, J.X. Liang, Y.R. Zheng, Y.F. Xu, J. Jiang, Q. Gao, J. Li, S.H. Yu, An efficient molybdenum disulfide/cobalt diselenide hybrid catalyst for electrochemical hydrogen generation. Nat. Commun. **6**, 1–7 (2015)
37. Y. Gao, D. Ma, C. Wang, J. Guan, X. Bao, Reduced graphene oxide as catalyst for hydrogenation of nitrobenzene. Structure **47**, 2432–2434 (2011)
38. V. Gargiulo, L. Lisi, R. Di, M. Alf, Synthesis and characterization of conductive copper-based metal-organic framework/graphene-like composites. Mater. Chem. Phys. **147**, 744–750 (2014)
39. J. Gascon, S. Aguado, F. Kapteijn, Manufacture of dense coatings of $Cu_3(BTC)_2$ (HKUST-1) on α-alumina. Microporous Mesoporous Mater. **113**, 132–138 (2008)
40. V. Gupta, N. Sharma, U. Singh, M. Arif, A. Singh, Higher oxidation level in graphene oxide. Optik (Stuttg). **143**, 115–124 (2017)
41. H. Yang, H. Du, L. Zhang, W. Liang Zli, Electrosynthesis and electrochemical mechanism of Zn-based metal-organic frameworks. Int. J. Electrochem. Sci. **10**, 1420–1433 (2015)
42. I. Hadjipaschalis, A. Poullikkas, V. Efthimiou, Overview of current and future energy storage technologies for electric power applications. Renew. Sustain. Energy Rev. **13**, 513–1522 (2009)
43. S.M. Haile, Fuel cell materials and components. Acta Mater. **51**, 5981–6000 (2003)
44. Z. Hasan, S.H. Jhung, Removal of hazardous organics from water using metal-organic frameworks (MOFs): Plausible mechanisms for selective adsorptions. J. Hazard. Mater. **283**, 329–339 (2015)
45. A.L. Higginbotham, D.V. Kosynkin, A. Sinitskii, Z. Sun, J.M. Tour, Lower-defect graphene oxide nanotubes. ACS Nano **4**, 2059–2069 (2010)
46. X. Hou, Y. Li, L. Cheng, X. Feng, H. Zhang, S. Han, Cobalt-molybednum disulfide supported on nitrogen-doped graphene towards an efficient hydrogen evolution reaction. Int. J. Hydrogen Energy **44**, 11664–11674 (2019)
47. R.J.T. Houk, B.W. Jacobs, F.E. Gabaly, N.N. Chang, A.A. Talin, D.D. Graham, S.D. House, I.M. Robertson, M.D. Allendorf, Silver cluster formation, dynamics, and chemistry in metal-organic frameworks. Nano Lett. **9**, 3413–3418 (2009)
48. J. Bedia, V. Muelas-Ramos, M. Peñas-Garzón, A. Gómez-Avilés, J.J. Rodríguez, C. Belver, A review on the synthesis and characterization of metal organic frameworks for photocatalytic water purification. Catalysis **9**, 1–43 (2019)
49. M. Jahan, Z. Liu, K.P. Loh, A graphene oxide and copper-centered metal organic framework composite as a tri-functional catalyst for HER, OER, and ORR. Adv. Funct. Mater. **23**, 5363–5372 (2013)
50. T. Jesionowski, Influence of aminosilane surface modification and dyes adsorption on zeta potential of spherical silica particles formed in emulsion system. Colloids Surf. Physicochem. Eng. Asp. **222**, 87–94 (2003)
51. L. Jiao, Y.-X. Zhou, H.-L. Jiang, Metla-organic framework-based CoP/reduced graphene oxide: high-performance bifunctional electrocatalyst for overall water splitting. Chem. Sci. **7**, 1690–1695 (2016)

52. K. O'Malley, G. Ordaz, J. Adams, K. Randolph, C.C. Ahn, N.T. Stetson, Applied hydrogen storage research and development: a perspective from the U.S. Department of Energy. J. Alloys Compd. **645**, S419–S422 (2015)
53. P.E. Karthik, K.A. Raja, S.S. Kumar, K.L.N. Phani, Y. Liu, S.X. Guo, J. Zhang, A.M. Bond, Electroless deposition of iridium oxide nanoparticles promoted by condensation of $[Ir(OH)_6]^{2-}$ on an anodized Au surface: application to electrocatalysis of the oxygen evolution reaction. RSC Adv. **5**, 3196–3199 (2015)
54. F. Ke, L.G. Qiu, Y.P. Yuan, F.M. Peng, X. Jiang, A.J. Xie, Y.H. Shen, J.F. Zhu, Thiol-functionalization of metal-organic framework by a facile coordination-based postsynthetic strategy and enhanced removal of Hg^{2+} from water. J. Hazard. Mater. **196**, 36–43 (2011)
55. S. Kempahanumakkagari, K. Vellingiri, A. Deep, E.E. Kwon, N. Bolan, K. Kim, Metal—organic framework composites as electrocatalysts for electrochemical sensing applications. Coord. Chem. Rev. **357**, 105–129 (2018)
56. A.M. Kler, E.A. Tyurina, Y.M. Potanina, A.S. Mednikov, Estimation of efficiency of using hydrogen and aluminum as environmentally-friendly energy carriers. Int. J. Hydrogen Energy **40**, 14775–14783 (2015)
57. V. Kumar, K.H. Kim, J.W. Park, J. Hong, S. Kumar, Graphene and its nanocomposites as a platform for environmental applications. Chem. Eng. J. **315**, 210–232 (2017)
58. P. Laha, B. Chakraborty, Energy model—a tool for preventing energy dysfunction. Renew. Sustain. Energy Rev. **73**, 95–114 (2017)
59. H.W. Langmi, J. Ren, B. North, M. Mathe, D. Bessarabov, Hydrogen storage in metal-organic frameworks: a review. Electrochim. Acta **128**, 368–392 (2014)
60. J. Lee, H.R. Chae, Y.J. Won, K. Lee, C.H. Lee, H.H. Lee, I.C. Kim, J.M. Lee, Graphene oxide nanoplatelets composite membrane with hydrophilic and antifouling properties for wastewater treatment. J. Memb. Sci. **448**, 223–230 (2013)
61. S. Lee, S. Hun, J. Suk, S. Hyun, Large-scale production of high-quality reduced graphene oxide. Chem. Eng. J. **233**, 297–304 (2013)
62. C.F. Leung, Y.Z. Chen, H.Q. Yu, S.M. Yiu, C.C. Ko, T.C. Lau, Electro- and photocatalytic hydrogen generation in acetonitrile and aqueous solutions by a cobalt macrocyclic Schiff-base complex. Int. J. Hydrogen Energy **36**, 11640–11645 (2011)
63. R. Li, Latest progress in hydrogen production from solar water splitting via photocatalysis, photoelectrochemical, and photovoltaic-photoelectrochemical solutions. Chin. J. Catal. **38**, 5–12 (2017)
64. F. Li, X. Jiang, J. Zhao, S. Zhang, Graphene oxide: a promising nanomaterial for energy and environmental applications. Nano Energy **16**, 488–515 (2015)
65. D.N. Li, A.J. Wang, J. Wei, Q.L. Zhang, J.J. Feng, Facile synthesis of flower-like Au@AuPd nanocrystals with highly electrocatalytic activity for formic acid oxidation and hydrogen evolution reactions. Int. J. Hydrogen Energy **42**, 19894–19902 (2017)
66. L. Li, M. Yang, Y. Dong, P. Mei, H. Cheng, Hydrogen storage and release from a new promising liquid organic hydrogen storage carrier (LOHC): 2-methylindole. Int. J. Hydrogen Energy **41**, 16129–16134 (2016)
67. P.Q. Liao, J.Q. Shen, J.P. Zhang, Metal-organic frameworks for electrocatalysis. Coord. Chem. Rev. **373**, 22–48 (2018)
68. J.T.P. Lidstroma, B. Watheyb, J. Westmana, Tetrahedron **57**, 9225–9283 (2001)
69. K.A. Lin, S. Chen, A.P. Jochems, Zirconium-based metal organic frameworks: Highly selective adsorbents for removal of phosphate from water and urine. Mater. Chem. Phys. **160**, 168–176 (2015)
70. J. Lin, J. He, F. Qi, B. Zheng, X. Wang, B. Yu, K. Zhou, W. Zhang, Y. Li, Y. Chen, In-situ selenization of Co-based metal-organic frameworks as a highly efficient electrocatalyst for hydrogen evolution reaction. Electrochim. Acta **247**, 258–264 (2017)
71. R. Lin, L. Shen, Z. Ren, W. Wu, Y. Tan, H. Fu, J. Zhang, L. Wu, Enhanced photocatalytic hydrogen production activity via dual modification of MOF and reduced graphene oxide on CdS. Chem. Commun. **50**, 8533–8535 (2014)

72. J. Liu, H. Jeong, J. Liu, K. Lee, J.Y. Park, Y.H. Ahn, S. Lee, Reduction of functionalized graphite oxides by trioctylphosphine in non-polar organic solvents. Carbon **48**, 2282–2289 (2010)
73. S.Y. Liu, P. Kundu, T.W. Huang, Y.J. Chuang, F.G. Tseng, Y. Lu, M.L. Sui, F.R. Chen, Quasi-2D liquid cell for high density hydrogen storage. Nano Energy **31**, 218–224 (2017)
74. S. Loera-serna, M.A. Oliver-Telentino, M.L. Lopez-Nunez, A. Santana-Cruz, A. Guzman-Vargas, R. Cabrera-Sierra, H.I. Beltran, J. Flores, Electrochemical behavior of $[Cu_3(BTC)_2]$ metal–organic framework: the effect of the method of synthesis. J. Alloys Compd. **540**, 113–120 (2012)
75. C.M. Lu, J. Liu, K. Xiao, A.T. Harris, Microwave enhanced synthesis of MOF-5 and its CO_2 capture ability at moderate temperatures across multiple capture and release cycles. Chem. Eng. J. **156**, p465–p470 (2010)
76. H. Lund, Renewable energy strategies for sustainable development. Energy **32**, 912–919 (2007)
77. H. Lund, B.V. Mathiesen, Energy system analysis of 100% renewable energy systems-the case of Denmark in years 2030 and 2050. Energy **34**, 524–531 (2009)
78. M. Sohail, M. Saleem, S. Ullah, N. Saeed., A. Afridi, M. Khan, M. Arif, Modified and improved Hummer's synthesis of graphene oxide for capacitors applications. Mod. Electron. Mater. **3**, 110–116 (2017)
79. M. Eddaoudi, J. Kim, N. Rosi, D. Vodak, J. Wachter, T.M. O'keeffe, O.M. Yaghi, Systematic design of pore size and functionality in isoreticular MOFs and their application in methane storage. Science 2**95**, 469–472 (2016)
80. M. Eddaoudi, D.B. Moler, H. Li, B. Chen, T.M. Reineke, T.M. O'keeffe, O.M. Yaghi, Modular chemistry: Secondary building units as a basis for the design of highly porous and robust metal-organic carboxylate frameworks. Acc. Chem. Res. **34**, 319–330 (2001)
81. M. Ma, L. Wang, Y. Wang, W. Xiang, P. Lyu, B. Tang, X. Tan, Effect of hydrogen content on hydrogen desorption kinetics of titanium hydride. J. Alloys Compd. **709**, 445–452 (2017)
82. S.S. Maktedar, S.S. Mehetre, M. Singh, R.K. Kale, Ultrasound irradiation: a robust approach for direct functionalization of graphene oxide with thermal and antimicrobial aspects. Ultrason. Sonochem. **21**, 1407–1416 (2014)
83. D.C. Marcano, D.V. Kosynkin, J.M. Berlin, A. Sinitskii, Z. Sun, A. Slesarev, L.B. Alemany, W. Lu, J.M. Tour, Improved synthesis of graphene oxide. ACS Nano **4**, 183–191 (2010)
84. G. Mashao, K.E. Ramohlola, S.B. Mdluli, G.R. Monama, M.J. Hato, K. Makgopa, M.M. Molapo, M.E. Ramoroka, E.I. Iwuoha, K.D. Modibane, Zinc-based zeolitic benzimidazolate framework/polyaniline nanocomposite for electrochemical sensing of hydrogen gas *Mat*. Chem. Phys. **230**, 287–298 (2019)
85. K. Mazloomi, C. Gomes, Hydrogen as an energy carrier: prospects and challenges. Renew. Sustain. Energy Rev. **16**, 3024–3033 (2012)
86. J.R. Mckone, S.C. Marinescu, B.S. Brunschwig, J.R. JWinkler, H.B. Gray, Earth-abundant hydrogen evolution electrocatalysts. Chem Sci **5**, 865–878 (2014)
87. F. Mindivan, The synthesis and characterization of graphene oxide (GO) and reduced graphene oxide (rGO). Mach. Technol. Mater. **6**, 32–35 (2017)
88. M. Momirlan, T. Veziroglu, Current status of hydrogen energy. Renew. Sustain. Energy Rev. **6**, 141–179 (2002)
89. G.R. Monama, S.B. Mdluli, G. Mashao, M.D. Makhafola, K.E. Ramohlola, K.M. Molapo, M.J. Hato, K. Makgopa, E.I. Iwuoha, K.D. Modibane, Palladium deposition on copper(II) phthalocyanine/metal organic framework composite and electrocatalytic activity of the modified electrode towards the hydrogen evolution reaction. Renew. Energy **119**, 62–72 (2018)
90. A. Mukherjee, S. Chakrabarty, W.N. Su, S. Basu, Nanostructured nickel ferrite embedded in reduced graphene oxide for electrocatalytic hydrogen evolution reaction. Mater. Today Energy **8**, 118–124 (2018)
91. R. Nivetha, S. Chella, P. Kollu, S.K. Jeong, A. Bhatnagar, N.G. Andrews, Cobalt and nickel ferrites based graphene nanocomposites for electrochemical hydrogen evolution. J. Magn. Magn. Mater. **448**, 165–171 (2018)

92. J.K. Nørskov, T. Bligaard, A. Logadottir, J.R. Kitchin, J.G. Chen, S. Pandelov, U. Stimming, Trends in the exchange current for hydrogen evolution. J. Electrochem. Soc. **152**, J23–J26 (2005)
93. C.R.P. Patel, P. Tripathi, A.K. Vishwakarma, M. Talat, P.K. Soni, T.P. Yadav, O.N. Srivastava, Enhanced hydrogen generation by water electrolysis employing carbon nano-structure composites. Int. J. Hydrogen Energy **43**, 3180–3189 (2018)
94. C. Petit, T.J. Bandosz, Engineering the surface of a new class of adsorbents: metal-organic framework/graphite oxide composites. J. Colloid Interface Sci. **447**, 139–151 (2015)
95. C. Petit, J. Burress, T.J. Bandosz, The synthesis and characterization of copper-based metal-organic framework/graphite oxide composites. Carbon **49**, 563–572 (2011)
96. C. Petit, M. Seredych, T.J. Bandosz, Revisiting the chemistry of graphite oxides and its effect on ammonia adsorption. J. Mater. Chem. **19**, 9176–9185 (2009)
97. A. Pichon, A. Lazuen-Garay, S.L. James, Solvent-free synthesis of microporous metal-organic framework. Cryst. Eng. Comm. **8**, 211–214 (2006)
98. M. Pilloni, F. Padella, G. Ennas, S. Lai, M. Bellusci, E. Rombi, F. Sini, M. Pentimalli, C. Delitala, A. Scano, V. Cabras, Liquid-assisted mechanochemical synthesis of an iron carboxylate metal organic framework and its evaluation in diesel fuel desulfurization. Microporous Mesoporous Mater. **213**, 14–21 (2015)
99. A.V. Puga, Photocatalytic production of hydrogen from biomass-derived feedstocks. Coord. Chem. Rev. **315**, 1–66 (2016)
100. R.M.N.M. Rathnayake, H.W.M.A.C. Wijayasinghe, H.M.T.G.A. Pitawala, M. Yoshimura, H.H. Huang, Synthesis of graphene oxide and reduced graphene oxide by needle platy natural vein graphite. Appl. Surf. Sci. **393**, 309–315 (2017)
101. K.E. Ramohlola, M. Masikini, S.B. Mdluli, G.R. Monama, M.J. Hato, K.M. Molapo, E.I. Iwuoha, K.D. Modibane, Electrocatalytic hydrogen production properties of poly(3-aminobenzoic acid) doped with metal organic frameworks. Int. J. Electrochem. Sci. **12**, 4392–4405 (2017)
102. K.E. Ramohlola, M. Masikini, S.B. Mdluli, G.R. Monama, M.J. Hato, K.M. Molapo, K.D. Modibane, E.I. Iwuoha, Electrocatalytic hydrogen evolution reaction of metal organic frameworks decorated with poly(3-aminobenzoic acid). Electrochim. Acta **246**, 1174–1182 (2017)
103. K.E. Ramohlola, G.R. Monama, M.J. Hato, K.D. Modibane, K.M. Molapo, M. Masikini, S.B. Mdluli, E.I. Iwuoha, Polyaniline-metal organic framework nanocomposite as an efficient electrocatalyst for hydrogen evolution reaction. Compos. Part B Eng. **137**, 129–139 (2018)
104. J.B. Raoof, R. Ojani, S.A. Esfeden, S.R. Nadimi, Fabrication of bimetallic Cu/Pt nanoparticles modified glassy carbon electrode and its catalytic activity toward hydrogen evolution reaction. Int. J. Hydrogen Energy **35**, 3937–3944 (2010)
105. F. Rosalbino, G. Borzone, E. Angelini, R. Raggio, Hydrogen evolution reaction on Ni-RE (RE = rare earth) crystalline alloys. Electrochim. Acta **48**, 3939–3944 (2003)
106. F. Rosalbino, S. Delsante, G. Borzone, E. Angelini, Electrocatalytic behaviour of Co-Ni-R (R = Rare earth metal) crystalline alloys as electrode materials for hydrogen evolution reaction in alkaline medium. Int. J. Hydrogen Energy **33**, 6696–6703 (2008)
107. D. Ross, Hydrogen storage: the major technological barrier to the development of hydrogen fuel cell cars. Vacuum **80**, 1084–1089 (2006)
108. J. Sakamoto, J. Nakayama, T. Nakarai, N. Kasai, T. Shibutani, A. Miyake, Effect of gasoline pool fire on liquid hydrogen storage tank in hybrid hydrogen-gasoline fueling station. Int. J. Hydrogen Energy **41**, 2096–2104 (2016)
109. B. Sakintuna, F. Lamari-Darkrim, M. Hirscher, Metal hydride materials for solid hydrogen storage: a review. Int. J. Hydrogen Energy **32**, 1121–1140 (2007)
110. M. Schalenbach, F.D. Speck, M. Ledendecker, O. Kasian, D. Goehl, A.M. Mingers, B. Breitbach, H. Springer, S. Cherevko, K.J.J. Mayrhofer, Nickel-Molybdenum alloy catalysts for the hydrogen evolution reaction: activity and stability revised. Electrochim. Acta **259**, 1154–1161 (2018)

111. L. Schlapbach, A. Züttel, Hydrogen storage materials for mobile applications. Nature **414**, 353–358 (2001)
112. K. Schoots, F. Ferioli, G.J. Kramer, B.C.C. van der Zwaan, Learning curves for hydrogen production technology: an assessment of observed cost reductions. Int. J. Hydrogen Energy **33**, 2630–2645 (2008)
113. M. Seredych, E. Rodriguez-Castellon, T.J. Bandosz, New CuxSy/nanoporous carbon composites as efficient oxygen reduction catalysts in alkaline medium. J. Mater. Chem. A **2**, 20164–20176 (2014)
114. L. Shahriary, A.A. Athawale, Graphene oxide synthesized by using modified Hummers approach. Int. J. Renew. Energy Environ. Eng. **2**, 58–63 (2014)
115. A. Sharma, S.K. Arya, Hydrogen from algal biomass: a review of production process. Biotechnol. Rep. **15**, 63–69 (2017)
116. S.A. Sherif, F. Barbir, T.N. Veziroglu, Towards a hydrogen economy. Electric. J. **18**, 62–76 (2005)
117. N.K. Singh, S. Gupta, V.K. Pecharsky, V.P. Balema, Solvent-free mechanochemical synthesis and magnetic properties of rare-earth based metal-organic frameworks. J. Alloys Compd. **696**, 118–122 (2017)
118. J. Song, X. Wang, C.T. Chang, Preparation and characterization of graphene oxide paper. J. Nanomater. **448**, 457–460 (2014)
119. Y.S. Song, B. Yan, Z.X. Chen, Hydrothermal synthesis, crystal structure and luminescence of four novel metal-organic frameworks". J. Solid State Chem. **179**, 4037–4046 (2006)
120. S. Stankovich, D.A. Dikin, G.H.B. Dommett, K.M. Kohlhaas, E.J. Zimney, E.A. Stach, R.D. Piner, S.T. Nguyen, R.S. Ruoff, Graphene-based composite materials. Letters **442**, 282–286 (2006)
121. S. Stankovich, D.A. Dikin, R.D. Piner, K.A. Kohlhaas, A. Kleinhammes, Y. Jia, Y. Wu, S.T. Nguyen, R.S. Ruof, Synthesis of graphene-based nanosheets via chemical reduction of exfoliated graphite oxide. Carbon **45**, 1558–1565 (2007)
122. N. Stock, S. Biswas, Synthesis of metal-organic frameworks (MOFs): routes to various MOF topologies, morphologies, and composites. Chem. Rev. **112**, 933–969 (2012)
123. Z. Sun, W. Fan, T. Liu, Graphene/graphene nanoribbon aerogels as tunable three-dimensional framework for efficient hydrogen evolution reaction. Electrochim. Acta **250**, 91–98 (2017)
124. T. Ozgur, A.C. Yakaryılmaz, A review: Exergy analysis of PEM and PEM fuel cell based CHP systems. Int. J. Hydrogen Energy doi: https://doi.org/10.1016/j.ijhydene.2018.01.106
125. J. Tang, R.R. Salunkhe, J. Liu, N.L. Torad, M. Imura, S. Furukawa, Y. Yamauchi, Thermal conversion of core-shell metal-organic frameworks: a new method for selectively functionalized nanoporous hybrid carbon. J. Am. Chem. Soc. **137**, 1572–1580 (2015)
126. J. Tymoczko, F. Calle-Vallejo, W. Schuhmann, A.S. Bandarenka, Making the hydrogen evolution reaction in polymer electrolyte membrane electrolysers even faster. Nat. Commun. **7**, 10990–10995 (2016)
127. R. Vakili, S. Xu, N. Al-Janabi, P. Gorgojo, S.M. Holmes, X. Fan, Microwave-assisted synthesis of zirconium-based metal organic frameworks (MOFs): optimization and gas adsorption. Microporous Mesoporous Mater. **260**, 45–53 (2018)
128. B. Valizadeh, T.N. Nguyen, K.C. Stylianou, Shape engineering of metal–organic frameworks. Polyhedron **145**, 1–15 (2018)
129. L. Wang, X. Feng, L. Ren, Q. Piao, J. Zhong, Y. Wang, H. Li, Y. Chen, B. Wang, Flexible solid-state supercapacitor based on a metal–organic framework interwoven by electrochemically-deposited PANI. J. Am. Chem. Soc. **137**, 4920–4923 (2015)
130. G. Wang, X. Shen, B. Wang, J. Yao, J. Park, Synthesis and characterisation of hydrophilic and organophilic graphene nanosheets. Carbon **47**, 1359–1364 (2009)
131. L. Wang, R.T. Yang, New sorbents for hydrogen storage by hydrogen spillover—a review. Energy Environ. Sci. **1**, 268–279 (2008)
132. A.G. Wong-Foy, A.J. Matzger, O.M. Yaghi, Exceptional H_2 saturation uptake in microporous metal-organic frameworks. J. Am. Chem. Soc. **128**, 3494–3495 (2006)

133. X. Wu, Z. Bao, B. Yuan, J. Wang, Y. Sun, H. Luo, S. Deng, Microwave synthesis and characterization of MOF-74 (M = Ni, Mg) for gas separation. Microporous Mesoporous Mater. **180**, 114–122 (2013)
134. Z.S. Wu, G. Zhou, L.C. Yin, W. Ren, F. Li, H.M. Cheng, Graphene/metal oxide composite electrode materials for energy storage. Nano Energy **1**, 107–131 (2012)
135. B. Xiao, Q. Yuan, Nanoporous metal organic framework materials for hydrogen storage. Particuology **7**, 129–140 (2009)
136. Y. Yan, Y. Xia, X. Wang, A review on noble-metal-free bifunctional heterogeneous catalysts for overall electrochemical water splitting. J. Mater. Chem. A Mater. Energy Sustain. **4**, 17587–17603 (2016)
137. J. Yang, F. Cheng, J. Liang, J. Chen, Hydrogen generation by hydrolysis of ammonia borane with a nanoporous cobalt-tungsten-boron-phosphorus catalyst supported on Ni foam. Int. J. Hydrogen Energy **36**, 1411–1417 (2011)
138. H.M. Yang, X. Liu, X.L. Song, T.L. Yang, Z.H. Liang, C.M. Fan, In-situ electrochemical synthesis of MOF-5 and its application in improving photocatalytic activity of BiOBr. Trans. Nonferrous Met. Soc. China **25**, 3987–3994 (2015)
139. F.H. Yang, R.T. Yang, Ab initio molecular orbital study of adsorption of atomic hydrogen on graphite: Insight into hydrogen storage in carbon nanotubes. Carbon **40**, 437–444 (2002)
140. Q. Ye, A. Chen, W. Huang, J. Zhang, X. Liu, G. Xu, Z. Zhou, Titanium-supported nanoporous bimetallic Pt-Ir electrocatalysts for formic acid oxidation. Electrochem. Commun. **9**, 1513–1518 (2007)
141. F. Ye, C. Xua, G. Liub, J. Lid, X. Wangd, X. Dua, J.K. Leeb, A novel PtRuIr nanoclusters synthesized by selectively electrodepositing Ir on PtRu as highly active bifunctional electrocatalysts for oxygen evolution and reduction. Energy Convers. Manag. **155**, 182–187 (2018)
142. A. Yilanci, I. Dincer, H.K. Ozturk, A review on solar-hydrogen/fuel cell hybrid energy systems for stationary applications. Prog. Energy Combust. Sci. **35**, 231–244 (2009)
143. K. Zeng, D. Zhang, Recent progress in alkaline water electrolysis for hydrogen production and applications. Prog. Energy Combust. Sci. **36**, 307–326 (2010)
144. P.F. Zhang, H. Li, G.M. Veith, S. Dai, Soluble porous coordination polymers by mechanochemistry: from metal-containing films/membranes to active catalysts for aerobic oxidation. Adv. Mater. **27**, 234–239 (2015)
145. W. Zhang, Y. Li, X. Zeng, S. Peng, Synergetic effect of metal nickel and graphene as a cocatalyst for enhanced photocatalytic hydrogen evolution via dye sensitization. Sci. Rep. **5**, 1–12 (2015)
146. Y. Zhang, J. Tan, F. Wen, Z. Zhou, M. Zhu, Platinum nanoparticles deposited nitrogen-doped carbon nanofiber derived from bacterial cellulose for hydrogen evolution reaction. Int. J. Hydrogen Energy **43**, 6167–6176 (2018)
147. W. Zhou, J. Jia, J. Lu, L. Yang, D. Hou, G. Li, S. Chen, Recent developments of carbon-based electrocatalysts for hydrogen evolution reaction. Nano Energy **28**, 29–43 (2016)
148. H.C.J. Zhou, S. Kitagawa, Metal–organic frameworks (MOFs). Chem. Soc. Rev. **43**, 5415–5418 (2014)
149. H. Zhou, J. Zhang, D. Ji, A. Yuan, X. Shen, Effect of catalyst loading on hydrogen storage capacity of ZIF-8/graphene oxide doped with Pt or Pd via spillover. Microporous Mesoporous Mater. **229**, 68–75 (2016)
150. H. Zhou, J. Zhang, J. Zhang, X. Yan, X. Shen, A. Yuan, Spillover enhanced hydrogen storage in Pt-doped MOF/graphene oxide composite produced via an impregnation method. INOCHE **54**, 54–56 (2015)

Chapter 3
Characterization of Hydrogen-Free and Hydrogenated DLC Films

Toru Harigai, Takahiro Imai, Hirofumi Takikawa, Satoru Kaneko, Shinsuke Kunitsugu, Masahito Niibe, Kazuhiro Kanda, and Masao Kamiya

3.1 Introduction

Diamond-like carbon (DLC) films are a hard amorphous carbon film. DLC films with excellent properties mechanically, electrically, optically, and chemically are widely used in industry. Basically, the DLC films contain only carbon or carbon and

T. Harigai (✉) · T. Imai · H. Takikawa
Toyohashi University of Technology, 1-1 Hibarigaoka, Tempaku, Toyohashi, Aichi 441-8580, Japan
e-mail: harigai@ee.tut.ac.jp

T. Imai
e-mail: imai.takahiro@pes.ee.tut.ac.jp

H. Takikawa
e-mail: Takikawa@ee.tut.ac.jp

S. Kaneko
Kanagawa Institute of Industrial Science and Technology, 705-1 Shimoimaizumi, Ebina, Kanagawa 243-0435, Japan
e-mail: satoru@kanagawa-iri.jp

S. Kunitsugu
Industrial Technology Center of Okayama Prefecture, 5301 Haga, Okayama, Okayama 701-1296, Japan
e-mail: shinsuke_kunitsugu@pref.okayama.lg.jp

M. Niibe · K. Kanda
University of Hyogo, 3-1-2 Koto, Kamigori-cho, Ako-gun, Hyogo 678-1205, Japan
e-mail: niibe@lasti.u-hyogo.ac.jp

K. Kanda
e-mail: kanda@lasti.u-hyogo.ac.jp

M. Kamiya
Itoh Optical Industrial Co., Ltd., 3-19 Miyanarityo, Gamagori, Aichi 443-0041, Japan
e-mail: m-kamiya@itohopt.co.jp

S. Kaneko et al. (eds.), *Carbon Related Materials*,
https://doi.org/10.1007/978-981-15-7610-2_3

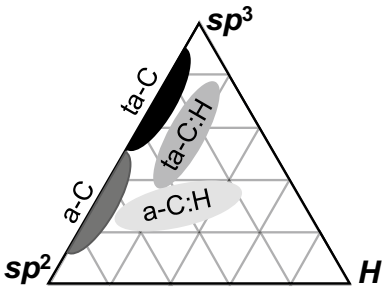

Fig. 3.1 DLC films on ternary phase diagram of bonding in amorphous carbon films [1, 2]

hydrogen as constituent elements. Carbons in the DLC films are thought to form sp^2 and sp^3 bonding structures in the amorphous structure [1]. The abundance ratio (sp^3 fraction) of sp^2 and sp^3 bonding structures and hydrogen content in the DLC films are important parameters determining the film properties of the DLC films. DLC films are divided into a hydrogen-free DLC film and a hydrogenated DLC film from the content of hydrogen in the film and is further often classified into four types from the difference in the sp^3 fraction. In the hydrogen-free DLC films, the films with high and low sp^3 fraction are called a tetrahedral amorphous carbon (ta-C) film and an amorphous carbon (a-C) film, respectively. Similarly, the hydrogenated DLC films are divided into a tetrahedral hydrogenated amorphous carbon (ta-C:H) film and a hydrogenated amorphous carbon (a-C:H) film. Figure 3.1 shows the positioning of four types of DLC films in carbon films composed of carbon and hydrogen. ta-C films have extremely high mechanical hardness comparable to diamond [3]. The ta-C films also having excellent mechanical properties such as high surface flatness and low friction coefficient [4, 5] are useful as a protective film for cutting tools and molds [5–7]. The a-C films, which is softer than the ta-C films, can be expected to improve electrical conductivity due to increased sp^2 bonding structures. It has been reported that hydrogenated DLC films have high biocompatibility [8, 9]. Not all DLC films have excellent mechanical, optical, electrical, and chemical properties, and it is necessary to selectively use each DLC film for the application.

In this chapter, hydrogen-free and hydrogenated DLC films are prepared by filtered vacuum arc deposition method, and the DLC films are characterized by various analytical methods. The classification methods of DLC films from the relationship of each property of DLC films are proposed.

3.2 Preparation of Hydrogen-Free and Hydrogenated DLC Films

A variety of DLC film deposition methods have been developed due to the difference in the fabricated DLC films and the applications. The plasma chemical vapor deposition (CVD) methods and the plasma ion implantation and deposition methods using

a hydrocarbon gas as a carbon source are obtained a-C:H films, and these methods facilitate the film deposition in a wide area [10, 11]. In the plasma sputtering methods and the vacuum cathodic arc deposition (VAD or CAD) methods classified as physical vapor deposition (PVD), a solid target such as graphite is used as a carbon source, and a-C films or ta-C films are obtained [12–23]. In particular, the VAD methods which can produce ta-C films with the nanoindentation hardness of 50 GPa or more are the most common fabrication process in the ta-C film fabrication methods.

In VAD methods, a material to be deposited as a thin film is used as a solid cathode target. An arc spot with a very active and high temperature is generated on the solid cathode by an arc discharge in vacuum, and the solid cathode material evaporates from its arc spot. The evaporated cathode material has high ion energy and ionization rate [20] and deposits on a substrate placed on the opposite side of the solid cathode.

In the VAD methods, the emission of fine particles (called droplets) from a cathode target accompanying evaporation of the cathode target becomes a problem. When the droplets are taken into a DLC film, various properties such as flatness and mechanical hardness of the DLC film are significantly deteriorated. Filtered vacuum arc deposition (FAD) methods have been developed [13–23] as a method to suppress the inclusion of droplets into a DLC film. In the FAD method, the distance from a solid cathode target to a substrate is increased as compared with the normal VAD method. Charged particles generated by evaporation of cathode material are transported from the cathode to the substrate by magnetic fields. As the distance from the cathode to the substrate increases, the number of droplets reaching the substrate decreases because most of the droplets are electrically neutral. Typical FAD systems are shown in Fig. 3.2. The linear-FAD as shown in Fig. 3.2a is a FAD system which is the simplest configuration, and the substrate is placed on a straight line with the cathode. In the torus-FAD of Fig. 3.2b and the T-FAD of Fig. 3.2c, the substrate is set in the out-of-sight position for the cathode. Figure 3.3 shows the difference in the number of droplets included in the DLC films fabricated using normal VAD and FAD systems. It is clear that the number of droplets in DLC films fabricated by using FAD systems decreased with respect to the normal VAD system. Furthermore, the number of included droplets decreased as the substrate setting angle relative to the cathode was larger. In the T-FAD system, the number of droplets in a DLC film decreased

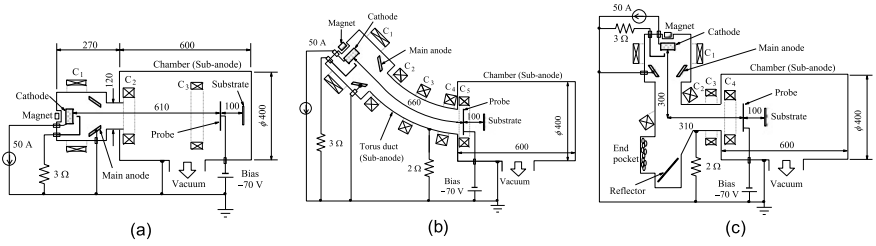

Fig. 3.2 Schematic diagrams of various FAD systems. **a** Straight-type FAD (liner-FAD). **b** 45° torus-FAD (torus-FAD). **c** T-shape FAD (T-FAD). Reprinted from [16], Copyright 2003, with permission from Elsevier

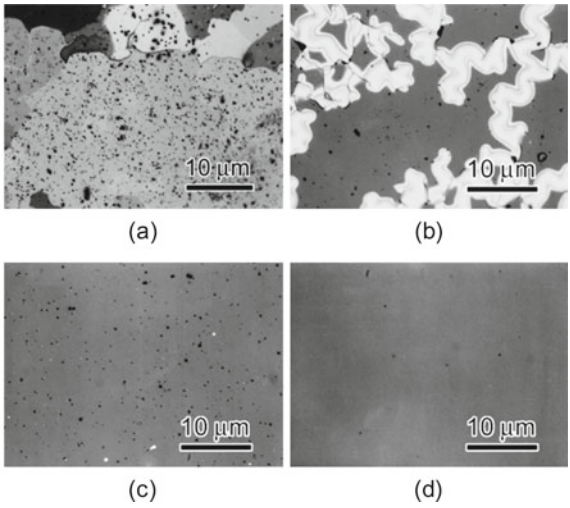

Fig. 3.3 Optical micrographs of a DLC film on a Si substrate [16]. **a** Normal VAD. **b** Liner-FAD. **c** Torus-FAD. **d** T-FAD], Copyright 2003, with permission from Elsevier

to 0.03 $(nm/min)^{-1}$ (deposition rate) in the region of 0.1 mm^2 by introducing an electrostatic trap and a plasma beam deflection mechanism [21, 22].

DLC films were prepared on tungsten carbide (WC) and silicon (Si) substrates using the T-FAD system. In the fabrication of hydrogen-free DLC films, the inside of a chamber was maintained under high vacuum condition in order to prevent hydrogen being mixed into the DLC films. The base pressure in the chamber was 8×10^{-4} Pa or less using the vacuum system combining a rotary pump and a turbo molecular pump. The cathode material was graphite. Prior to the DLC deposition process, a pretreatment process was conducted in order to improve the adhesion between the film and the substrate. In the pretreatment process, an arc discharge was generated in an argon (Ar) gas atmosphere chamber. An Ar-dominated carbon plasma beam occurred by the arc discharge was irradiated to the substrate [23]. Contamination and oxide layer on the substrate surface were removed by irradiating the Ar-dominated carbon plasma beam. DLC films were fabricated on the pretreated substrates. The arc current was 30 A, and the substrate-bias voltage was adjusted to pulsed DC − 100 V. Depending on the substrate-bias voltage, the energy of the ions reaching the substrate changes, and the film properties of the formed DLC film vary [3, 24–26]. In the fabrication of hydrogenated DLC films, hydrogen (H_2) gas or hydrocarbon gas such as acetylene (C_2H_2) or ethylene (C_2H_4) was introduced into the chamber during the DLC deposition in addition to the fabrication process of hydrogen-free DLC films using the T-FAD system. The gas flow rates were changed under a constant evacuation speed by fixing the vacuum valve.

The film thickness of the DLC films was measured with a stylus surface profiler (Veeco Dektak 3). The DLC deposition rates were calculated from the measured film thickness and the deposition duration. The deposition rate of the DLC films prepared using the T-FAD system was shown in Fig. 3.4. When the hydrocarbon gas was introduced, the deposition rate was significantly improved with respect to

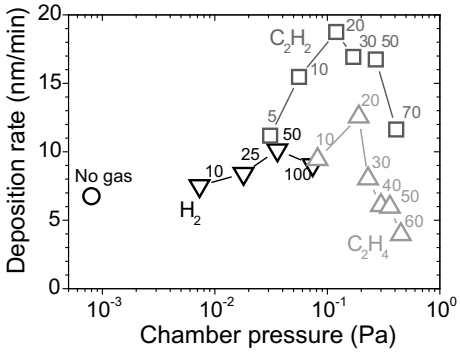

Fig. 3.4 Changes of DLC deposition rate for chamber pressure under the pulsed DC substrate-bias voltage of −100 V. Numbers in the figure indicate a gas flow rate in units of sccm

the deposition rate without introduction gas. In DLC film deposition with hydrocarbon gas, DLC deposition by decomposition of hydrocarbon gas, which is CVD, occurs in addition to DLC deposition by carbon plasma beam which is PVD [19]. It was considered that the DLC deposition rate improved by increasing the deposition amount of carbon by the hybrid deposition process of PVD and CVD. The film density of DLC films decreases by containing hydrogen in the film [3]. The reduction of film density is also a factor for increasing the deposition rate of DLC. When H_2 gas or a hydrocarbon gas was introduced in the T-FAD method, the DLC deposition rate was improved, whereas the deposition rate decreased under too high the chamber pressure. It was thought that the number of collisions between the carbon plasma beam and the atmospheric-gas molecule increased under high chamber pressure, and the carbon plasma beam did not sufficiently reach the substrate. Compared with the introduction of C_2H_4 gas, the use of C_2H_2 gas showed a tendency to have a higher deposition rate. The proportion of the number of hydrogen to the number of carbon constituting C_2H_2 molecule is smaller than that of C_2H_4 molecule. Since hydrogens play a role of etching carbons, the introduction of C_2H_2 gas with a small proportion of hydrogen to carbon was considered to have a higher deposition rate. In addition, C_2H_2 gas has a lower ionization potential than C_2H_4 gas, and the plasma CVD method using C_2H_2 gas as precursor gas showed the high deposition rate of DLC films in the plasma CVD methods [1].

Figure 3.5 shows the hydrogen content of the DLC films prepared by T-FAD system. The hydrogen content of the DLC films was analyzed by Rutherford backscattering spectrometry/elastic recoil detection analysis (RBS/ERDA) using 2.5 MeV $^4He^{2+}$ from tandetron ion accelerator. The hydrogen content of the hydrogen-free DLC films fabricated without gas introduction was 1 at.% or less. The amount of hydrogen contained in the DLC films increased owing to the introduction of the gas and the increase of the chamber pressure with increasing the flow rate. In the case of hydrocarbon gas introduction, the hydrogen content of the DLC films tended to increase in C_2H_4 gas rather than in C_2H_2 gas under similar chamber pressure. It was considered that the hydrogen content in the formed film increased because the composition ratio of hydrogen to carbon in the chamber atmosphere gas was larger in C_2H_4 gas compered in C_2H_2 gas. When DLC films were prepared with

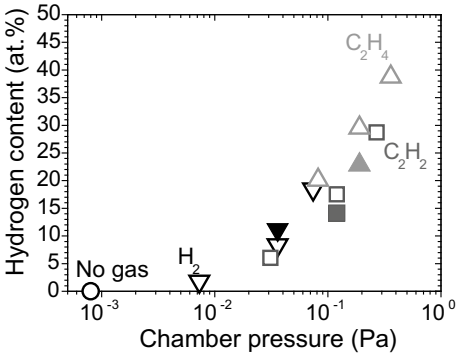

Fig. 3.5 Changes of hydrogen content in DLC film for chamber pressure and substrate -bias voltage. Open and solid marks indicate the pulsed DC substrate-bias voltage of −100 V and −1 kV, respectively

a hydrocarbon gas at a high substrate-bias voltage of −1 kV, the hydrogen content decreased compared with DLC films prepared at that of −100 V. On the other hand, when H_2 gas was introduced, the hydrogen content slightly increased at the high substrate-bias voltage. In hydrocarbon gas atmosphere, it was considered that ion bombardment accelerated by a high substrate-bias voltage destroyed C–H bonds in DLC films, and hydrogen was released from the film. In H_2 gas atmosphere, hydrogen ion bombardment may be increased the hydrogen content of DLC films due to the effect of ion implantation.

Figure 3.6 shows the sp^3 fraction of the DLC films prepared using T-FAD system. The sp^3 fraction of the DLC films was analyzed by near edge X-ray absorption fine structure (NEXAFS) spectroscopy using a synchrotron accelerator (NewSUBARU in Japan). The sp^3 fraction decreased with the increase of the chamber pressure. The ion energy region where the sp^3 bonding structure of the C–C bond is obtained

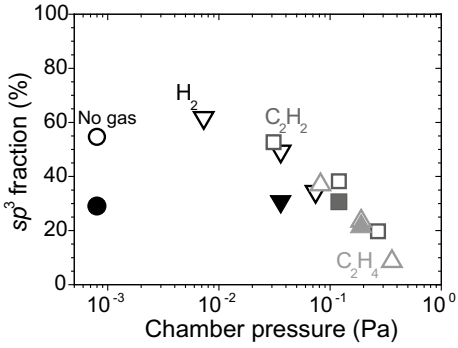

Fig. 3.6 Change of sp^3 fraction in DLC films for chamber pressure and substrate-bias voltage. Open and solid marks indicate the pulsed DC substrate-bias voltage of −100 V and −1 kV, respectively

by colliding carbon ions during DLC film formation is very narrow. It is guessed that the ion energy distribution to deposit a DLC film with the high sp^3 fraction is obtained when the substrate-bias voltage is about −100 V because DLC films with the high hardness were obtained at the substrate-bias voltage of −100 V [3]. It was considered that carbon ions collided with gas molecules in the atmosphere before reaching a substrate when the substrate-bias voltage was constant and the chamber pressure increased by gas introduction. Thus, the ions would lose the energy. In the DLC deposition at a high substrate-bias voltage of −1 kV, the sp^3 fractions were about 30% regardless of the gas introduction and the gas type. The collisions of ions accelerated by a too high substrate-bias voltage were considered to have inhibited the formation of the sp^3 bonding structure on the DLC films.

From Figs. 3.5 and 3.6, it was found that various DLC films with the hydrogen content from several at.% to 40 at.% and the sp^3 fraction from 10 to 60% were obtained by the T-FAD method combined the introduction of gas and the control of substrate-bias voltage during the deposition process.

3.3 Properties of DLC Films Prepared by Filtered Arc Deposition

The sp^3 fraction and the hydrogen content for characterizing DLC films are analyzed quantitatively by the NEXAFS spectroscopy and the RBS/ERDA method as shown in Sect. 3.2. However, the NEXAFS spectroscopy and the RBS/ERDA method which need to use an ion accelerator are limited the facilities that can be analyzed. In Sect. 3.3, the properties of DLC films are analyzed by common analytical techniques.

Raman spectroscopy is a technique that can easily obtain the bonding structure of DLC films. The characteristic broad spectrum of DLC films includes D-peak and G-peak band spectra appearance between 1000 and 1800 cm^{-1} in Raman shift [1, 27, 28]. The G-peak band spectrum which has a band-center at around 1580 cm^{-1} expresses actually the stretching vibration of any pair of sp^2 bonding structures, in C=C chains or in aromatic rings. The D-peak band spectrum with a peak of around 1360 cm^{-1} is attributable to the breathing mode of those sp^2 bonding structures only in rings having a dangling bond which appears as a defect in the graphite structure. Figure 3.7 shows the Raman spectra of the DLC films prepared by changing the gas species and chamber pressure on the deposition process using the T-FAD system. The Raman spectra were obtained by a laser microscopic Raman spectroscope (JASCO NRS-100) with a laser wavelength of 532 nm. A broad spectrum of a typical DLC film appeared in all Raman spectra. The Raman spectrum the DLC films with high hydrogen content had a large inclination. The inclination of the Raman spectra was considered to be the fluorescence component of hydrogen in the films. Thus, the hydrogen content in a DLC film may be able to be inferred from the inclination of the Raman spectrum; however, in DLC films with a small hydrogen content, the difference in the inclination of the spectrum did not appear markedly. The ratio of

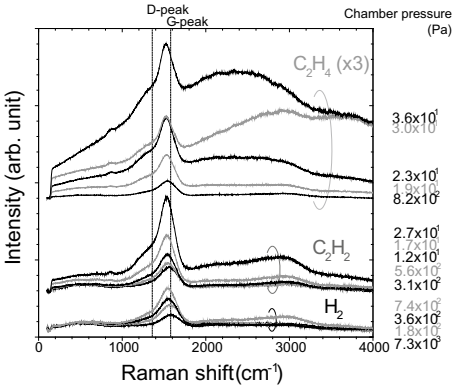

Fig. 3.7 Raman spectra of DLC films prepared under different chamber pressure. The pulsed DC substrate-bias voltage was −100 V. The intensity of Raman spectra on DLC films prepared using C_2H_4 gas is 1/3 times

D-peak and G-peak intensities (I_D/I_G ratio) and the G-peak position as shown in Fig. 3.8 were obtained by waveform separation analysis of the Raman spectrum in Fig. 3.7. As the chamber pressure increased, the I_D/I_G ratio increased, and the G-peak position shifted to the lower wave number. An increase in the I_D/I_G ratio with a low wave number shift of the G-peak position indicates the increase of the sp^2 bonding structure in a DLC film.

Figure 3.9 shows the Raman spectra of the DLC films prepared with different substrate-bias voltages on the deposition process using the T-FAD system. The intensity of the Raman spectrum on the DLC films fabricated under a high substrate-bias voltage was lower than that of a low substrate-bias voltage. DLC films become opaque in the visible light wavelength region when the sp^2 bonding structure in the DLC films increase, and then, the intensity of Raman scattered light becomes weaker. The I_D/I_G ratio and the G-peak position as shown in Fig. 3.10 were obtained from the

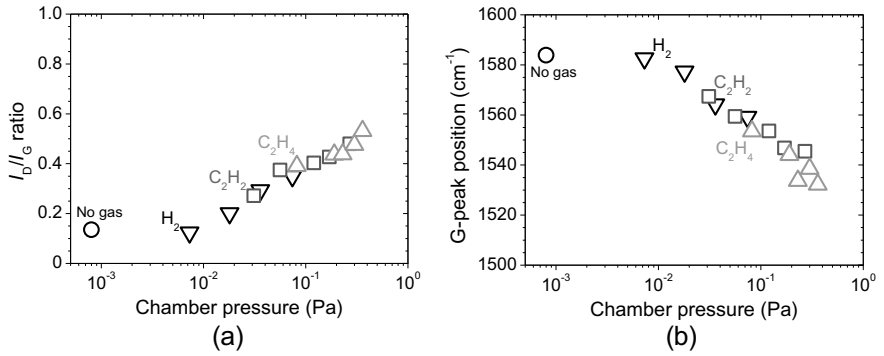

Fig. 3.8 **a** I_D/I_G ratio and **b** G-peak position obtained from Raman spectra in Fig. 3.7

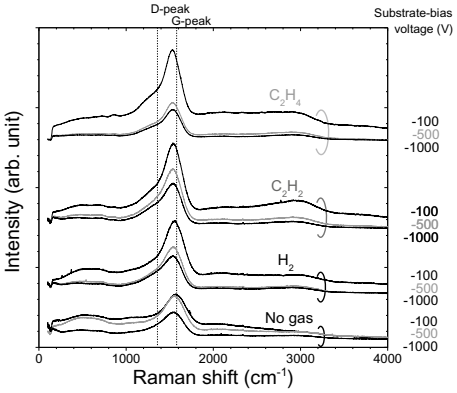

Fig. 3.9 Raman spectra of DLC films prepared under different substrate-bias voltage. The chamber pressure was 3.6×10^{-2} Pa using H_2 gas, 1.2×10^{-1} Pa using C_2H_2 gas, or 1.9×10^{-1} Pa using C_2H_4 gas. The intensity of Raman spectra on DLC films prepared using C_2H_4 gas is 1/3 times

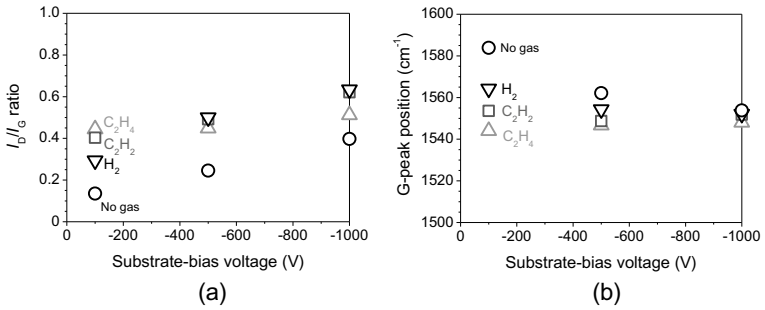

Fig. 3.10 **a** I_D/I_G ratio and **b** G-peak position obtained from Raman spectra in Fig. 3.9

Raman spectrum in Fig. 3.9. In the DLC films fabricated using H_2 or C_2H_2 gas, an increase in the I_D/I_G ratio and a shift to low wave number of the G-peak position were found with increasing substrate-bias voltage, while in C_2H_4 gas, the I_D/I_G ratio and the G-peak position did not vary even when the substrate-bias voltage was changed. As shown in Fig. 3.5, the DLC films prepared using C_2H_4 gas were considered to be close to a polymer-like DLC film having a lot of C–H bonds because of its high hydrogen content. Since the D-peak and the G-peak band spectra are attributable to the sp^2 bonding structure of the DLC film, it was considered that a large difference did not appear in the Raman spectrum in the DLC films with high hydrogen content.

The nanoindentation hardness of the DLC films measured with a nanoindenter (Hysitron Triboindenter TI 950) and the film density of the DLC films calculated from the X-ray reflectivity (XRR) analysis (Phillips X'Pert PRO MRD) are shown in Fig. 3.11. The nanoindentation hardness and the film density of the DLC films decreased with the increase of the chamber pressure associated with gas introduction.

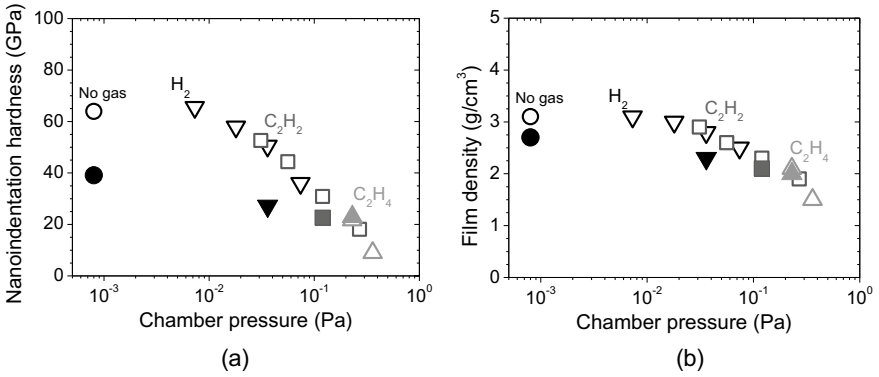

Fig. 3.11 **a** Nanoindentation hardness and **b** film density of DLC films prepared using T-FAD system. Open and solid marks indicate the pulsed DC substrate-bias voltage of −100 V and −1 kV, respectively

It was thought that the decrease of sp^3 ratio in DLC films caused the reduction of the hardness and the film density because the collision energy of ions to a substrate decreased owing to increasing the chamber pressure and the hydrogen mixed in the film owing to introducing the gas. The hardness and the film density decreased even in the deposition process with high substrate-bias voltage. The decrease of the hardness and the film density due to high substrate-bias voltage was considered to be caused by the increase of sp^2 bonding structure in the DLC films because of substrate temperature rise accompanying the collision of high-energy ions.

Figure 3.12 shows the optical constants of the DLC films for the film density with the data of Ref. [29]. The optical constants of graphite and diamond were referred

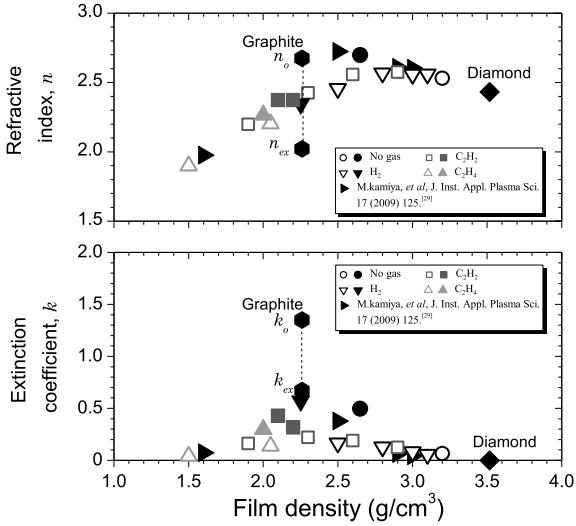

Fig. 3.12 Optical constants at e-line (546.1 nm) of DLC films for the film density. Open and solid marks indicate the pulsed DC substrate-bias voltage of −100 V and −1 kV, respectively

from Refs. [30, 31]. The optical constants were calculated based on the measured film reflectance using spectral reflectometry (Olympus USPM-RU II). The refractive index (n) and the extinction coefficient (k) of hydrogen-free DLC films increased with decrease of the film density, while the refractive index of hydrogenated DLC films decreased with decrease of the film density. In the relationship between the film density and the optical constants, the DLC films exhibited different trend of two types. It was thought that the two-type trends indicate the graphitization and the hydrocarbon polymerization of DLC films with decrease of the film density.

3.4 Classification of DLC Films

In order to selectively use DLC films as a function of the application, it is important to easily identify the properties of the DLC films properties. As shown in Fig. 3.1 in Sect. 3.1, DLC films can be distinguished by the relationship between the sp^3 fraction and the hydrogen content; however, a method capable of quantitatively and easily measuring sp^3 fraction and hydrogen content in DLC films has not yet been developed. From the relationship between the sp^3 fraction of DLC films shown in Sect. 3.2 and the nanoindentation hardness and the film density of the DLC film shown in Sect. 3.3, classification diagrams of DLC films instead of the ternary diagram shown in Fig. 3.1 are proposed.

In Fig. 3.13, the relationship between the sp^3 fraction and the nanoindentation hardness of the DLC films is shown. Most of the DLC films were on the straight line connecting the diamond from the origin. The DLC films prepared without gas introduction deviated from the straight line. The analysis range in the depth direction in the NEXAFS spectroscopy is several nm from the film surface. Thus, the NEXAFS spectroscopy is sensitive to the surface condition of the film. Carbons on the surface of DLC films fabricated without gas introduction can be considered to have more dangling bonds than that of DLC films fabricated with gas introduction. In the case of the DLC films fabricated with gas introduction, it was thought that the dangling bonds

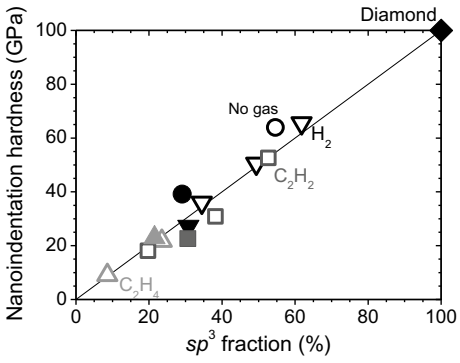

Fig. 3.13 Relationship between sp^3 fraction and nanoindentation hardiness on DLC films. Open and solid marks indicate the pulsed DC substrate-bias voltage of −100 V and −1 kV, respectively

on the surface of the DLC film were terminated with hydrogen. The dangling bonds on the surface of DLC films were thought to be terminated by the contamination such as organic compounds and water in the air when exposed to the atmosphere from the vacuum, and the surface condition of the films was changed. Thus, the sp^3 fraction measured by NEXAFS spectroscopy of the DLC films fabricated without gas introduction became slightly lower than the true sp^3 fraction in the films. When shifting the sp^3 fraction of DLC films fabricated without gas introduction to a value about 10% higher, the values of the sp^3 fraction were on the straight line connected between the origin and the diamond.

Figure 3.14 shows the relationship between the film density and the nanoindentation hardness of the DLC films. The approximate line to the value of DLC films through the diamond in Fig. 3.14 can be expressed by Eq. (3.1)

$$H_{\mathrm{IT}} = 2.3 \times \rho^3 \tag{3.1}$$

where H_{IT} and ρ are the nanoindentation hardness and the film density of a DLC film, respectively. It was clear that the film density and the nanoindentation hardness had a strong correlation.

From Figs. 3.13 and 3.14, there were clear correlation between the sp^3 fraction, the nanoindentation hardness, and the film density of the DLC films. Figure 3.15 is the classification diagrams of DLC films proposed by based on the relationship between the sp^3 fraction, the nanoindentation hardness, and the film density. In addition, the characteristics of the DLC films shown in Sects. 3.2 and 3.3 were plotted in Fig. 3.15. A classification index of DLC films based on the relationship between the sp^3 fraction and the hydrogen content was suggested by Otake et al. [32]. The classification index of DLC films in Fig. 3.15 was defined by based on our consideration in addition to that of Ref. [32]. Since the hydrogen content of the DLC films increases by several at.% by hydrogen adsorption to the surface in the atmosphere, the hydrogen content in the hydrogen-free DLC films (ta-C and

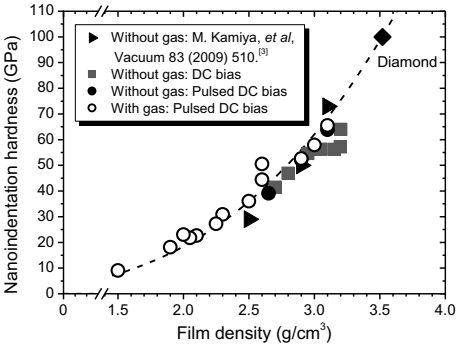

Fig. 3.14 Relationship between film density and nanoindentation hardiness on DLC films. Open and solid marks except the values from Ref. [3] indicate the pulsed DC substrate-bias voltage of −100 V and −1 kV, respectively

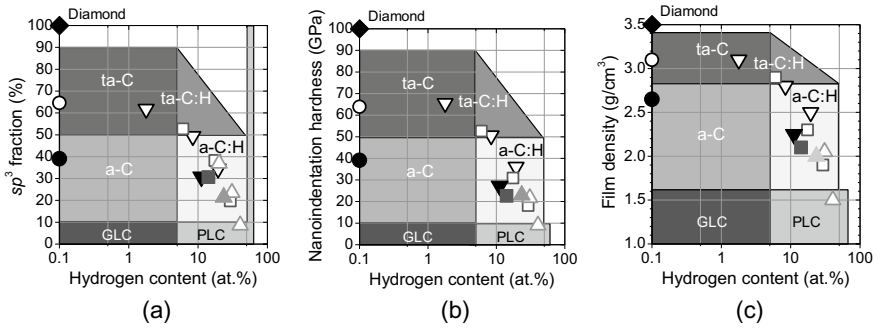

Fig. 3.15 Classification diagrams of DLC films based on hydrogen content and **a** sp^3 fraction, **b** nanoindentation hardness, or **c** film density

a-C films) was defined as 5 at.% or less in Fig. 3.15. The regions of graphite-like carbon (GLC) films and polymer-like carbon (PLC) films were also added to the classification diagrams. The boundary between DLC and GLC or PLC is not clear. In Fig. 3.15, the carbon film with the nanoindentation hardness up to 10 GPa was a DLC film because the carbon film of approximately 10 GPa has already been widely used in the industry, and it is known as a DLC film. The values of the sp^3 ratio and the film density were determined from the correlation with the nanoindentation hardness.

In any of the classification diagrams, the DLC films showed a tendency to shift from the ta-C film through the ta-C:H film to the a-C:H film as the hydrogen content increased. From the shift trend, it was inferred that the region of the ta-C:H film is very small as shown in Fig. 3.15. Figure 3.15 indicates that easily analysis techniques such as nanoindentation test and XRR analysis are effective the characterization and classification of various DLC films instead of quantitative measurement of sp^3 fraction using an accelerator. In the future, it is desirable to classify DLC films expected to be applied in widely applications based on the properties such as hardness and film density which can be measured by common analytical techniques.

3.5 Conclusion

In the FAD methods equipped with a filter for removing droplets, hydrogen-free and high-hardness DLC films can be obtained. In addition, various DLC films with the hydrogen content from several at.% to 40 at.% and the sp^3 fraction from 10 to 60% were obtained by the T-FAD process and introduction of hydrogen or hydrocarbon gas into the chamber. The introduction of H_2 gas was suitable for slightly adding hydrogen to DLC films. In the introduction of C_2H_2 gas, higher deposition rate of DLC films was obtained. The introduction of C_2H_4 gas was suitable for increasing the hydrogen content of DLC films.

Hydrogenated DLC films fabricated by the T-FAD method became soft and had a low film density with increasing pressure in the chamber. The change of the refractive index and the extinction coefficient with respect to the film density of DLC films showed a tendency to be different between the hydrogen-free DLC films and the hydrogenated DLC films. The classification diagrams of DLC films based on the relationships between the hydrogen content and the sp^3 fraction, the nanoindentation hardness, or the film density were proposed. It is expected that the classification of DLC films by using the nanoindentation hardness and the film density is useful for defining various DLC films because the analytical techniques such as nanoindentation test for measuring the nanoindentation hardness and XRR analysis for calculating the film density are easier than NEXSAFS spectroscopy for analyzing the sp^3 fraction.

Acknowledgements The authors would like to thank T. Toya for modifying the figures in this chapter. This work was supported by JSPS KAKENHI Grants-in-Aid for Science Research.

References

1. J. Robertson, Diamond-like amorphous carbon. Mater. Sci. Eng. R **37**, 129–281 (2002)
2. W. Jacob, W. Moller, On the structure of thin hydrocarbon films. Appl. Phys. Lett. **63**, 1771–1773 (1993)
3. M. Kamiya, H. Tanoue, H. Takikawa, M. Taki, Y. Hasegawa, M. Kumagai, Preparation of various DLC films by T-shaped filtered arc deposition and the effect of heat treatment of film properties. Vacuum **83**, 510–514 (2009)
4. M. Kano, Super low friction of DLC applied to engine cam follower lubricated with ester-containing oil. Tribol. Int. **39**, 1682–1685 (2006)
5. T. Yokota, T. Sawa, M. Yokouchi, K. Tozawa, M. Anzai, T. Aizawa, Frictional properties of diamond-like carbon coated tool in dry intermittent machining of aluminum alloy 5052. Precis. Eng. **38**, 365–370 (2014)
6. H. Fukui, J. Okida, N. Omori, H. Moriguchi, K. Tsuda, Cutting performance of DLC coated tools in dry machining aluminum alloys. Surf. Coat. Technol. **187**, 70–76 (2004)
7. Y. Fujii, T. Imai, Y. Miyamoto, N. Ueda, M. Hosoo, T. Harigai, Y. Suda, H. Takikawa, H. Tanoue, M. Kamiya, M. Taki, Y. Hasegawa, N. Tsuji, S. Kaneko, Dry machining of metal using an engraving cutter coated with a droplet-free ta-C film prepared via a T-shape filtered arc deposition. Surf. Coat. Technol. **307**, 1029–1033 (2016)
8. Y. Mine, T. Nakatani, K. Okamoto, S. Hara, K. Takagi, H. Nikawa, Impact of biomimetic diamond-like carbon coated titanium on osteoblast and osteoclast differentiation in vitro. J. Photopolym. Sci. Technol. **27**, 373–378 (2014)
9. T. Nakatani, K. Shiraishi, S. Kunitsugu, Development of new hydrogen-containing tetrahydral amorphous carbon thin films using cathodic arc plasma for dental implant. J. Photopolym. Sci. Technol. **28**, 471–474 (2015)
10. X.D. Yang, T. Saito, Y. Nakamura, Y. Kondo, N. Ohtake, Mechanical properties of DLC films prepared inside of micro-holes by pulse plasma CVD. Diam. Relat. Mater. **13**, 1984–1988 (2004)
11. S. Miyagawa, S. Nakao, M. Ikeyama, Y. Miyagawa, Deposition of diamond-like carbon films using plasma based ion implantation with bipolar pulses. Surf. Coat. Technol. **156**, 322–327 (2002)
12. V. Bellido-Gonzalez, J. Hampshire, A.H.S. Jones, T.J. Allen, J. Witts, D.G. Teer, B. Pierret, Advances in the analysis and characterization of DLC coatings. Surf. Coat. Technol. **98**, 1272–1279 (1998)

13. R.L. Boxman, V. Zhitomirsky, B. Alterkop, E. Gidalevich, I. Beilis, M. Keidar, S. Goldsmith, Recent progress in filtered vacuum arc deposition. Surf. Coat. Technol. **86**, 243–253 (1996)
14. M.C. Polo, J.L. Andujar, A. Hart, J. Robertson, W.I. Milne, Preparation of tetrahedral amorphous carbon films by filtered cathodic vacuum arc deposition. Diam. Relat. Mater. **9**, 663–667 (2000)
15. P.J. Martin, A. Bendavid, Review of the filtered vacuum arc process and materials deposition. Thin Solid Films **394**, 1–15 (2001)
16. H. Takikawa, K. Izumi, R. Miyano, T. Sakakibara, DLC thin film preparation by cathodic arc deposition with a super droplet-free system. Surf. Coat. Technol. **163–164**, 368–373 (2003)
17. B. Petereit, P. Siemroth, H.H. Schneider, H. Hilgers, High current filtered arc deposition for ultra thin carbon overcoats on magnetic hard disks and read-write heads. Surf. Coat. Technol. **174–175**, 648–650 (2003)
18. Y. Iwasaki, S. Minamisawa, H. Takikawa, T. Sakakibara, H. Hasegawa, Influence of duct bias on deposition rate of DLC film in T-shape filtered arc deposition. Vacuum **80**, 1266–1271 (2006)
19. N. Miyakawa, S. Minamisawa, H. Takikawa, T. Sakakibara, Physical-chemical hybrid deposition of DLC film on rubber by T-shape filtered-arc-deposition. Vacuum **73**, 611–617 (2004)
20. H. Takikawa, H. Tanoue, Review of cathodic arc deposition for preparing droplet-free thin films. IEEE Trans. Plasma Sci. **35**, 992–999 (2007)
21. M. Kamiya, T. Yanagita, H. Tanoue, S. Oke, Y. Suda, H. Takikawa, M. Taki, Y. Hasegawa, T. Ishikawa, H. Yasui, T-shape filtered arc deposition system with built-in electrostatic macroparticle trap for DLC film preparation. Thin Solid Films **518**, 1498–1502 (2009)
22. H. Okuda, M. Kamiya, H. Tanoue, Y. Suda, H. Takikawa, Preparation of droplet-free diamond-like carbon film by magnetically controlled filtered-arc-plasma beam. J. Inst. Appl. Plasma Sci. **18**, 159–164 (2010). (in Japanese)
23. H. Tanoue, M. Kamiya, S. Oke, Y. Suda, H. Takikawa, Y. Hasegawa, M. Taki, M. Kumagai, M. Kano, T. Ishikawa, H. Yasui, Argon-dominated plasma beam generated by filtered vacuum arc and its substrate etching. Appl. Surf. Sci. **255**, 7780–7785 (2009)
24. J.C. Sánchez-López, C. Donnet, J.L. Loubet, M. Belin, A. Grill, V. Patel, C. Jahnes, Tribological and mechanical properties of diamond-like carbon prepared by high-density plasma. Diam. Relat. Mater. **10**, 1063–1069 (2001)
25. J. Zhu, J. Han, S. Meng, J. Wang, W. Zheng, Correlations between substrate bias, microstructure and surface morphology of tetrahedral amorphous carbon films. Vacuum **72**, 285–290 (2004)
26. D. Sheeja, B.K. Tay, S.P. Lau, X. Shi, Tribological properties and adhesive strength of DLC coatings prepared under different substrate bias voltages. Wear **249**, 433–439 (2001)
27. A.C. Ferrari, Determination of bonding in diamond-like carbon by Raman spectroscopy. Diam. Relat. Mater. **11**, 1053–1061 (2002)
28. S. Prawer, K.W. Nugent, Y. Lifshitz, G.D. Lempert, E. Grossman, J. Kulik, I. Avigal, R. Kalish, Systematic variation of the Raman spectra of DLC films as a function of sp^2:sp^3 composition. Diam. Relat. Mater. **5**, 433–438 (1996)
29. M. Kamiya, Y. Kawaguchi, H. Tanoue, Y. Suda, H. Takikawa, Optical properties of various diamond-like carbon films fabricated by filtered arc deposition. J. Inst. Appl. Plasma Sci. **17**, 125–132 (2009). (in Japanese)
30. D.F. Edwards, H.R. Philipp, Cubic carbon (diamond), in *Handbook of Optical Constants of Solids*, ed. by E.D. Palik (Academic Press, 1985), pp. 665–673
31. A. Borghesi, G. Guizzetti, Graphite (C), in *Handbook of Optical Constants of Solids II*, ed. by E.D. Palik (Academic Press, 1991), pp. 449–460
32. N. Otake, M. Hiratsuka, H. Saitoh, DLC maku no bunrui to hyoujunka. New Diam. **28**, 12–18 (2012). (in Japanese)

Chapter 4
Energy Stored in a Slab Covered by Graphene Sheets

Mustafa Sarısaman, Musa Mutlu Can, Murat Tas, Mehmet Ertugrul, Satoru Kaneko, and Tamio Endo

4.1 Introduction

Recently, there has been novel and rapid advances on two different realms of physics, one is in non-Hermition quantum mechanics and its applications in various fields of physics, and the other one is the 2D materials including especially the graphene and their applications in many fields of science and technology. Studies in these distinctive areas are impressive and it would be intriguing to investigate applications of graphene in view of non-Hermition quantum mechanics.

M. Sarısaman
Department of Physics, Istanbul University, 34134 Vezneciler, Istanbul, Turkey
e-mail: mustafa.sarisaman@istanbul.edu.tr

M. Mutlu Can (✉)
Renewable Energy and Oxide Hybrid Systems Laboratory, Department of Physics, Faculty of Science, Istanbul University, Vezneciler, Istanbul, Turkey
e-mail: musa.can@istanbul.edu.tr

M. Tas
Department of Physics, Gebze Technical University, 41400 Kocaeli, Turkey
e-mail: murat.tas@gtu.edu.tr

M. Ertugrul
Department of Electrical and Electronic, Faculty of Engineering, Ataturk University, Erzurum, Turkey
e-mail: ertugrul@atauni.edu.tr

S. Kaneko
Kanagawa Industrial Technology Center, Kanagawa Prefectural Government, Ebina 236-0435, Japan
e-mail: satoru@kanagawa-iri.jp

T. Endo
Sagamihara Surface Treatment Laboratory, SIC, Sagamihara, Kanagawa, Japan
e-mail: endotamio@yahoo.co.jp

S. Kaneko et al. (eds.), *Carbon Related Materials*,
https://doi.org/10.1007/978-981-15-7610-2_4

Quantum mechanics, which has been celebrated since its first debut by the widely accepted essential fact that Hermitian operators give rise to real energies [1–3], suffered remarkable changes in last couple of decades. Understanding and clarifying its mystifying extensions in the realm of $\mathcal{PT}$-symmetric [4–6], pseudo-Hermitian [7–9] and non-Hermitian quantum mechanics [10–12] inspired numerous notable research activities in almost many fields of physics essentially including quantum field theories [8], lie algebras [13], optical, and condensed matter systems [14–24]. In particular, non-Hermitian quantum mechanics and its applications in optics, condensed matter physics, and material science caused unraveling new scientific phenomena and developments of many technological devices, including dynamic power oscillations of light propagation, coherent perfect absorber lasers [25–33], spectral singularities [34–39], and unidirectional invisibility [14, 19, 20, 40–56]. In this respect, non-Hermitian complex potentials within the framework of quantum scattering formalism pioneer a leading role in understanding these mysterious structures [57–68].

On the other hand, recent advances on the side of 2D materials have laid the groundwork for the development of a vast area of research, not only about their physical properties, but also applications in various fields of physics, especially in optics [69–80] and condensed matter physics. Among all the class of 2D materials, graphene has the leading role due to its well-documented physical properties and numerous applications [81–85]. As the family of 2D materials expands to include new members such as 2D Weyl semimetals, 2D semiconductors, boron nitride and more recently, transition metal dichalcogenides and Xenes, atomically thin forms of these materials offer endless possibilities for fundamental research, as well as the demonstration of improved or even entirely novel technologies [85–88]. New 2D material treatments could unleash new uses. These exciting properties of 2D materials reveal that they may interact with electromagnetic waves in anomalous and exotic ways, providing new phenomena and applications. Thus, the new distinctive studies with 2D materials have arisen.

Graphene is the single atom-layered, two-dimensional plane structure which is obtained from the source material known as graphite. Recent researches show that graphene displays strong potential to meet the energy demand in various ways [94]. Graphene and its different composites can be used in various places like supercapacitors [89, 90], solar cells [91, 92], and batteries [93, 94] to enhance power density, rate performance, and energy efficiency. In general, it is possible to classify the use of graphene into two vast categories as energy storage and energy conversion devices. It is obvious that graphene-based devices can provide clean energy with proposed zero waste emission. Especially, recent works on this field originate essential motivation of our work [62, 95–100]. In this chapter, we describe a way to use the graphene to enhance the energy storage within a gain slab which has a complex-valued potentials by means of its specially engineered structure. Using various synthesis techniques for obtaining graphene, it is possible to construct our design so that the effect of graphene for energy purposes can be distinguished quite easily. Application of the graphene proposed here will be aimed at providing an important scientific reference on energy applications for realizing large-scale energy conversion and storage in the near future [94]. Thus, in this study, we offer one of the potential applica-

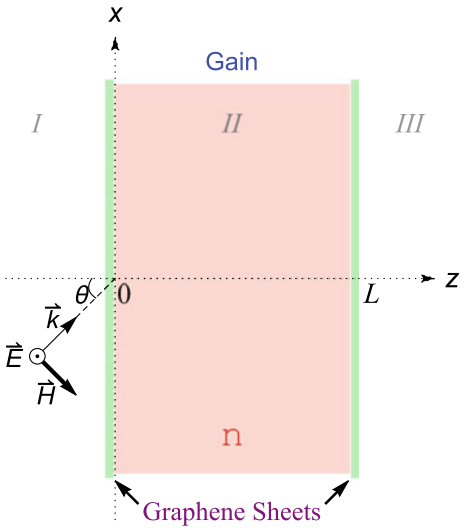

Fig. 4.1 Configuration of the s-polarized electromagnetic waves obliquely incident upon the complex optical slab which is covered by the graphene sheets. Incidence angle θ is measured from the normal to the surface

tions of graphene/graphene oxide in the field of energy enhancement and storage together with the fascinating non-Hermitian attributes in optical systems. Our system is depicted in Fig. 4.1.

It is of great interest to assemble graphene applications with non-Hermitian and even $\mathcal{PT}$-symmetric quantum optics and condensed matter physics under the same roof. In this respect, we look for the prospect of realization of energy enhancement in a gain-doped optical slab material covered by graphene sheets. Our purpose of incorporating graphene sheets would be to inquire for optimal control of system parameters so as to obtain efficient energy configurations inside the slab. This is expected to yield possible new applications of graphene studies in various related fields. We base our work on the fundamental principles extending to Maxwell's equations. We take advantage of transfer matrix formalism just because of its role in extracting information about interaction of matter with waves. In fact, transfer matrix leads to construct distinctive optical, electrical, and magnetic phenomena by means of the information it contains about reflection and transmission amplitudes. Thus, one can study spectral singularities, transparency, reflectionlessness, and invisibility phenomena in this direction. Therefore, in view of this motivation, we aim to employ graphene layers to settle up the problem of energy storage confined in a complex gain slab and achieve maximum energy configurations in an optically active slab system covered by graphene layers in the present work, see Fig. 4.1.

In our analysis, we present s-polarized (transverse electric mode) solutions that support the most general energy configurations, schematically demonstrate their behaviors, and show the effects of various parameter choices. In particular, we indicate that optimal control of parameters of the slab and graphene/graphene oxide, i.e., gain coefficient, incidence angle, slab thickness, and temperature T and chemical potential μ of graphene sheets, give rise to the desired energy expressions. We

present exact conditions and display the role of graphene in the gain adjustment and energy storage purposes. Our findings can be experimentally realized with ease. Our method and hence results are quite reliable for all realistic slab materials of practical concern.

4.2 S-Polarized Waves and Effect of Graphene for a Single Slab

Although graphene displays a very good electrical conductivity and is good in electron transport, conductivity of graphene oxide highly depends on the degree of oxidation. Therefore, without pointing out a special graphene oxide compound, we discuss only graphene throughout whole calculations. One may easily adapt our method developed below just by replacing the graphene conductivity expression by the conductivity of graphene oxide which is intended to be employed. We consider that graphene layers surround a linear homogeneous and optically active gain slab system which is aligned along the z-axis as depicted in Fig. 4.1. The slab geometry in which energy storage will be investigated is formed such that it has a thickness L and a complex refractive index $\mathfrak{n}$ which is uniform between the graphene sheets in the region $0 < z < L$. Interaction of this optical slab-graphene system with the electromagnetic waves is governed by the following Maxwell's equations

$$\boldsymbol{\nabla} \cdot \mathcal{D} = \rho(z), \qquad \boldsymbol{\nabla} \cdot \mathcal{B} = 0, \tag{4.1}$$

$$\boldsymbol{\nabla} \times \mathcal{H} - \partial_t \mathcal{D} = \mathcal{J}(z), \qquad \partial_t \mathcal{B} + \boldsymbol{\nabla} \times \mathcal{E} = \mathbf{0}. \tag{4.2}$$

Here, $\mathcal{E}$ and $\mathcal{B}$ denote the electric and magnetic fields, respectively, and are related to $\mathcal{D}$ and $\mathcal{H}$ fields by the following constitutive relations

$$\mathcal{D} := \varepsilon\, \mathcal{E}, \qquad \mathcal{B} := \mu \mathcal{H},$$

where ε and μ are, respectively, the permittivity and permeability of the slab medium in which electromagnetic waves propagate. Magnetic materials usually give rise to magneto-optical effects such that the Faraday and Kerr rotations could be observed inside and outside the slab material [101]. To ignore those effects, for simplicity, we consider a non-magnetic environment such that permeability is $\mu = \mu_0$ within the slab. Permittivity ε is given by $\varepsilon := \varepsilon_0 \mathfrak{z}(z)$, where

$$\mathfrak{z}(z) := \begin{cases} \mathfrak{n}^2 \text{ for } & z \in [0, L], \\ 1 \text{ for } & z \notin [0, L]. \end{cases} \tag{4.3}$$

Charge $\rho(z)$ and electric current density $\mathcal{J}(z)$ appearing in Maxwell's equations are specified on the boundaries due to the presence of graphene sheets. Notice that $\mathcal{J}(z)$

is given in terms of conductivities of graphene and $\mathcal{J}(z) := \sigma(z)\mathcal{E}$. Thus, free charge and conductivity effects in our optical setup are denoted, respectively, as follows

$$\rho(z) := \sum_{i=1}^{2} \rho_i\, \delta(z - z_i), \qquad \sigma(z) := \sum_{i=1}^{2} \sigma_i\, \delta(z - z_i),$$

where ρ_i and σ_i are, respectively, the free charge and conductivity on the i^{th} surface, and z_i denotes the positions of the boundaries along z-axis, and $z_1 = 0$ and $z_2 = L$ for our case. We emphasize that $\rho(z)$ and $\mathcal{J}(z)$ satisfy the continuity equation

$$\boldsymbol{\nabla} \cdot \mathcal{J}(z) + \partial_t \rho(z) = 0. \tag{4.4}$$

The conductivity of graphene sheets is attained by means of the random phase approximation in [102–104], consisting of the sum of intraband and interband contributions, i.e., $\sigma = \sigma_{\text{intra}} + \sigma_{\text{inter}}$, for each surface i as follows

$$\begin{aligned}
\sigma_{\text{intra}} &:= \frac{i\mathrm{e}^2 \chi}{\pi \hbar^2 (\omega + i\Gamma)} \ln\left[2\cosh\left(\frac{\mu}{\chi}\right)\right], \\
\sigma_{\text{inter}} &:= \frac{\mathrm{e}^2}{4\pi\hbar}\left[\frac{\pi}{2} + \arctan\left(\frac{\nu_-}{\chi}\right) - \frac{i}{2}\ln\frac{\nu_+^2}{\nu_-^2 + \chi^2}\right],
\end{aligned} \tag{4.5}$$

where we define $\nu_\pm := \hbar\omega \pm 2\mu$ and $\chi := 2k_B T$. Here, $-e$ is the charge of an electron, $\hbar$ is the reduced Planck's constant, k_B is Boltzmann's constant, T is the temperature of the graphene sheet, Γ is the scattering rate of charge carriers, μ is the chemical potential of the corresponding graphene sheet, and $\hbar\omega$ is the photon energy [80]. Notice that $\mathcal{E}(\mathbf{r}, t)$ and $\mathcal{H}(\mathbf{r}, t)$ fields in time harmonic forms are expressed by $\mathcal{E}(\mathbf{r}, t) = \mathrm{e}^{-i\omega t}\mathbf{E}(\mathbf{r})$ and $\mathcal{H}(\mathbf{r}, t) = \mathrm{e}^{-i\omega t}\mathbf{H}(\mathbf{r})$, respectively. Thus, Maxwell's equations yielding the s-polarized waves are reduced to the following Helmholtz equations in three dimensions:

$$\left[\nabla^2 + k^2 \mathfrak{z}(z)\right]\mathbf{E}(\mathbf{r}) = 0, \qquad \mathbf{H}(\mathbf{r}) = -\frac{i}{kZ_0}\boldsymbol{\nabla} \times \mathbf{E}(\mathbf{r}), \tag{4.6}$$

where $\mathbf{r} := (x, y, z)$ is the coordinate vector, $k := \omega/c$ is the wavenumber, $c := 1/\sqrt{\mu_0 \varepsilon_0}$ is the speed of light in vacuum, and $Z_0 := \sqrt{\mu_0/\varepsilon_0}$ is the impedance of the vacuum. Notice that Eq. 4.6 gives rise to the solutions of s-polarized waves for which electric field vector $\mathbf{E}(\mathbf{r})$ is aligned along the surface of the slab, which is in y-direction in our geometrical configuration. Once a plane wave is emitted from left-hand side of the slab obeying the condition of s-polarization with an incident angle θ, the wave vector $\mathbf{k}$ builds up, which has components

$$\mathbf{k} = k_x \hat{e}_x + k_z \hat{e}_z, \qquad k_x := k \sin\theta, \qquad k_z := k \cos\theta, \tag{4.7}$$

where $\hat{e}_x$, $\hat{e}_y$, and $\hat{e}_z$, are, respectively, the unit vectors along the x-, y-, and z-axes, and $\theta \in [-90°, 90°]$ is the incidence angle (See Fig. 4.1.) Then, the corresponding electric field is given by

$$\mathbf{E}(\mathbf{r}) = \mathscr{E}(z)\mathrm{e}^{ik_x x}\hat{e}_y, \tag{4.8}$$

where $\mathscr{E}$ is solution of the Schrödinger equation

$$-\psi''(z) + v(z)\psi(z) = k^2\psi(z), \qquad z \notin \{0, L\}, \tag{4.9}$$

for the potential $v(z) := k^2[1 + \sin^2\theta - \mathfrak{z}(z)]$. The fact that potential $v(z)$ is homogeneous and piece-wise constant in relevant spaces leads to a solution in corresponding regions

$$\psi(z) := \begin{cases} A_+\,\mathrm{e}^{ik_z z} + A_-\,\mathrm{e}^{-ik_z z} & \text{for } z \in I, \\ B_+\,\mathrm{e}^{ik_z \tilde{\mathfrak{n}} z} + B_-\,\mathrm{e}^{-ik_z \tilde{\mathfrak{n}} z} & \text{for } z \in II, \\ C_+\,\mathrm{e}^{ik_z z} + C_-\,\mathrm{e}^{-ik_z z} & \text{for } z \in III, \end{cases} \tag{4.10}$$

where $A_\pm$, $B_\pm$, and $C_\pm$ are k-dependent complex coefficients, and

$$\tilde{\mathfrak{n}} := \sec\theta\sqrt{\mathfrak{n}^2 - \sin^2\theta}. \tag{4.11}$$

To be more precise, $\mathscr{E}(z)$ is expressed by the right-hand side of (4.10) with generally different choices for the coefficients $A_\pm$, $B_\pm$ and $C_\pm$. These coefficients are expressed by employing the appropriate boundary conditions which are described by the fact that tangential components of $\mathbf{E}$ and $\mathbf{H}$ are continuous across the surface while the normal components of $\mathbf{H}$ have a step of unbounded surface currents across the interface of graphene sheets. Notice that all the field configurations inside and outside the slab are given by

$$\begin{aligned} E_y(\mathbf{r}) &= \mathrm{e}^{ik_x x}\mathcal{F}_+(z), \\ H_x(\mathbf{r}) &= -\frac{\sqrt{\mathfrak{z}(z) - \sin^2\theta}}{Z_0}\mathrm{e}^{ik_x x}\mathcal{F}_-(z), \\ H_z(\mathbf{r}) &= \frac{\sin\theta}{Z_0}\mathrm{e}^{ik_x x}\mathcal{F}_+(z), \end{aligned}$$

where $\mathcal{F}_\pm(z)$ are denoted as follows

$$\mathcal{F}_\pm(z) := \begin{cases} A_+\,\mathrm{e}^{ik_z z} \pm A_-\,\mathrm{e}^{-ik_z z} & \text{for } z \in I, \\ B_+\,\mathrm{e}^{ik_z \tilde{\mathfrak{n}} z} \pm B_-\,\mathrm{e}^{-ik_z \tilde{\mathfrak{n}} z} & \text{for } z \in II, \\ C_+\,\mathrm{e}^{ik_z z} \pm C_-\,\mathrm{e}^{-ik_z z} & \text{for } z \in III. \end{cases} \tag{4.12}$$

Thus, one can obtain the boundary conditions as in Table 4.1.

Table 4.1 Boundary conditions for s-polarized waves. Here, $\mathfrak{u}_{\pm}^{(1,2)}$ is defined by (4.13)

$z=0$	$B_+ + B_- = A_+ + A_-, \quad B_+ - B_- = \mathfrak{u}_-^{(1)} A_+ - \mathfrak{u}_+^{(1)} A_-$
$z=L$	$B_+ \mathrm{e}^{ik_z \tilde{\mathfrak{n}} L} + B_- \mathrm{e}^{-ik_z \tilde{\mathfrak{n}} L} = C_+ \mathrm{e}^{ik_z L} + C_- \mathrm{e}^{-ik_z L}$ $B_+ \mathrm{e}^{ik_z \tilde{\mathfrak{n}} L} - B_- \mathrm{e}^{-ik_z \tilde{\mathfrak{n}} L} = \mathfrak{u}_+^{(2)} C_+ \mathrm{e}^{ik_z L} - \mathfrak{u}_-^{(2)} C_- \mathrm{e}^{-ik_z L})$

Here, $\mathfrak{u}_{\pm}^{(1,2)}$ are specified as follows

$$\mathfrak{u}_{\pm}^{(j)} := \frac{1 \pm Z_0 \sigma_j \cos\theta^{-1}}{\tilde{\mathfrak{n}}}, \tag{4.13}$$

with $j = 1, 2$ represents the graphene ordering from left to right (i.e., j=1 corresponds to the graphene sheet at $z = 0$ and j=2 to the graphene sheet at $z = L$). Notice the crucial role of graphene sheets on boundary conditions such that once all graphene sheets are removed, the distinction between $\mathfrak{u}_+^{(1,2)}$ and $\mathfrak{u}_-^{(1,2)}$ disappears, and therefore, problem boils down to a regular slab problem. To understand the effect of graphene better, we elaborate our analysis further by constructing the transfer matrix which contains very valuable information about the system behavior in various cases to be studied by finding reflection and transmission amplitudes explicitly. It is rather illustrative to express the transfer matrix $\mathbf{M}$ as follows

$$\begin{bmatrix} C_+ \\ C_- \end{bmatrix} = \mathbf{M} \begin{bmatrix} A_+ \\ A_- \end{bmatrix},$$

where $\mathbf{M}$ is manifestly obtained by means of standard boundary conditions as

$$\mathbf{M} = \frac{1}{2\gamma} \begin{pmatrix} \zeta(\mathfrak{u}_+^{(1)}; \mathfrak{u}_-^{(2)})\, \mathrm{e}^{-ik_z L} & \zeta(\mathfrak{u}_-^{(1)}; \mathfrak{u}_-^{(2)})\, \mathrm{e}^{-ik_z L} \\ -\zeta(\mathfrak{u}_+^{(1)}; \mathfrak{u}_+^{(2)})\, \mathrm{e}^{ik_z L} & -\zeta(\mathfrak{u}_-^{(1)}; \mathfrak{u}_+^{(2)})\, \mathrm{e}^{ik_z L} \end{pmatrix}, \tag{4.14}$$

where γ and ζ are complex-valued functions and are defined as follows

$$\begin{aligned} \gamma &:= \mathfrak{u}_-^{(2)} + \mathfrak{u}_+^{(2)}, \\ \zeta(\alpha_{\mathfrak{a}}; \beta_{\mathfrak{b}}) &:= (1 + \mathfrak{a}\alpha_{-\mathfrak{a}})(1 - \mathfrak{b}\beta_{\mathfrak{b}})\, \mathrm{e}^{ik_z \tilde{\mathfrak{n}} L} - (1 - \mathfrak{a}\alpha_{-\mathfrak{a}})(1 + \mathfrak{b}\beta_{\mathfrak{b}})\, \mathrm{e}^{-ik_z \tilde{\mathfrak{n}} L}. \end{aligned}$$

Here, $\mathfrak{a}$ and $\mathfrak{b}$ take values of $+$ and $-$ while α and β are, respectively, taking values $\mathfrak{u}_{\pm}^{(1)}$ and $\mathfrak{u}_{\pm}^{(2)}$. Notice that the functions γ and ζ exhibit the presence of graphene sheets in our configurations. We make use of the information of transfer matrix about the reflection and transmission coefficients. Since we have the reciprocity principle, left and right transmission amplitudes are the same and we state the transfer matrix as follows

$$\mathbf{M} = \begin{pmatrix} \mathrm{T} - \frac{\mathrm{R}^l \mathrm{R}^r}{\mathrm{T}} & \frac{\mathrm{R}^r}{\mathrm{T}} \\ -\frac{\mathrm{R}^l}{\mathrm{T}} & \frac{1}{\mathrm{T}} \end{pmatrix}. \tag{4.15}$$

Therefore, with the help of (4.14) and (4.15), one obtains the reflection and transmission amplitudes

$$R^l = -\frac{\zeta(\mathfrak{u}_+^{(1)};\mathfrak{u}_+^{(2)})}{\zeta(\mathfrak{u}_-^{(1)};\mathfrak{u}_+^{(2)})}, \quad R^r = -\frac{\zeta(\mathfrak{u}_-^{(1)};\mathfrak{u}_-^{(2)})}{\zeta(\mathfrak{u}_-^{(1)};\mathfrak{u}_+^{(2)})}\,\mathrm{e}^{-2ik_zL}, \quad T = -\frac{2\gamma\,\mathrm{e}^{-ik_zL}}{\zeta(\mathfrak{u}_-^{(1)};\mathfrak{u}_+^{(2)})}. \tag{4.16}$$

Notice that our construction up to now distinguishes the graphene sheets surrounding the gain slab. Although this interpretation involves the most general situation, we confine our attention to some special cases where parity is preserved and reversed. In the former case, $\mathfrak{u}_\pm^{(1)} = \mathfrak{u}_\pm^{(2)} = \mathfrak{u}_\pm$ is satisfied and both graphene sheets contain the same amount of conductivity. This is fairly easy case and can be adjusted in a convenient way. This results in the current flow on the graphene sheets in the same direction. In the latter case, however, one has the condition $\mathfrak{u}_\pm^{(1)} = \mathfrak{u}_\mp^{(2)} = \mathfrak{u}_\pm$. In this case, currents on the surfaces of graphene sheets flow in opposite directions.

4.3 Energy Stored Inside the Slab Between Graphene Sheets: General Case

In this section, we provide energy densities inside and outside the slab covered by the graphene sheets. In general, energy density is given by

$$\langle \mathfrak{u} \rangle = \frac{1}{4}\mathrm{Re}\left(E\cdot D^\star + B\cdot H^\star\right). \tag{4.17}$$

Transfer matrix information in (4.14) gives rise to energy densities in different regions of space as follows

$$\begin{aligned}
\langle \mathfrak{u} \rangle_I &= \frac{1}{4\varepsilon_0}\left\{\left[1+\sin^2\theta\right]\left|A_+\mathrm{e}^{ik_zz}+A_-\mathrm{e}^{-ik_zz}\right|^2+\cos^2\theta\left|A_+\mathrm{e}^{ik_zz}-A_-\mathrm{e}^{-ik_zz}\right|^2\right\},\\
\langle \mathfrak{u} \rangle_{II} &= \frac{1}{64\varepsilon_0|\gamma|^2}\Big\{\left[\mathrm{Re}[\mathfrak{n}^{2\star}]+\sin^2\theta\right]\\
&\quad\Big|\left[(1+\mathfrak{u}_+^{(2)})\mathrm{e}^{ik_z\tilde{\mathfrak{n}}(z-L)}+(1-\mathfrak{u}_+^{(2)})\mathrm{e}^{-ik_z\tilde{\mathfrak{n}}(z-L)}\right]\left[A_+\zeta_{+-}+A_-\zeta_{--}\right]\\
&\quad-\left[(1-\mathfrak{u}_-^{(2)})\mathrm{e}^{ik_z\tilde{\mathfrak{n}}(z-L)}+(1+\mathfrak{u}_-^{(2)})\mathrm{e}^{-ik_z\tilde{\mathfrak{n}}(z-L)}\right]\left[A_+\zeta_{++}+A_-\zeta_{-+}\right]\Big|^2\\
&\quad+\left|\tilde{\mathfrak{n}}\right|^2\cos^2\theta\Big|\left[(1+\mathfrak{u}_+^{(2)})\mathrm{e}^{ik_z\tilde{\mathfrak{n}}(z-L)}-(1-\mathfrak{u}_+^{(2)})\mathrm{e}^{-ik_z\tilde{\mathfrak{n}}(z-L)}\right]\left[A_+\zeta_{+-}+A_-\zeta_{--}\right]\\
&\quad-\left[(1-\mathfrak{u}_-^{(2)})\mathrm{e}^{ik_z\tilde{\mathfrak{n}}(z-L)}-(1+\mathfrak{u}_-^{(2)})\mathrm{e}^{-ik_z\tilde{\mathfrak{n}}(z-L)}\right]\left[A_+\zeta_{++}+A_-\zeta_{-+}\right]\Big|^2,
\end{aligned}$$

$$\langle \mathrm{u} \rangle_{III} = \frac{1}{16\varepsilon_0 |\gamma|^2} \Big\{ \big[1 + \sin^2\theta\big] \Big| \big[A_+\zeta_{+-} + A_-\zeta_{--}\big] \mathrm{e}^{ik_z(z-L)} - \big[A_+\zeta_{++} + A_-\zeta_{-+}\big] \mathrm{e}^{-ik_z(z-L)} \Big|^2 + \cos^2\theta \Big| \big[A_+\zeta_{+-} + A_-\zeta_{--}\big] \mathrm{e}^{ik_z(z-L)} + \big[A_+\zeta_{++} + A_-\zeta_{-+}\big] \mathrm{e}^{-ik_z(z-L)} \Big|^2 \Big\},$$

where we define $\zeta_{ij} := \zeta(\mathrm{u}_i^{(1)}; \mathrm{u}_j^{(2)})$ for simplicity. In particular, these complicated expressions valid for the most general case could be specialized to more restricted forms once we impose certain conditions on the transfer matrix components. For instance, we may inquire the maximum energy consideration within the slab by the requirement of spectral singularity conditions. This case corresponds to the lasing threshold condition and is obtained by searching the real values of wavenumber k such that M_{22} component of transfer matrix is set to zero. Therefore, transmission and reflection amplitudes diverge and purely outgoing wave configuration arises. In this scenario, energy stored within the graphene sheets are maximized. Also, one can consider the cases of transparency which is obtained by the condition $T = 1$. Another interesting situation where the energy configurations are worth to study is the left and right reflectionlessness of the slab surrounded by the graphene sheets, which are obtained by setting $R^l = 0$ and $R^r = 0$, respectively.

4.4 Energy Configurations in Case of Spectral Singularities: A Toy Model

For the maximal energy implementations, one considers the case of spectral singularities, which confines energy within a slab so that reflection and transmission amplitudes are divergent [105, 106]. To be more precise, spectral singularities correspond to the real k-values such that $M_{22} = 0$. Notice that in our case they are given by

$$\zeta(\mathrm{u}_-^{(1)}; \mathrm{u}_+^{(2)}) = 0. \tag{4.18}$$

More precisely, it is stated as

$$\mathrm{e}^{2ik_z\tilde{\mathrm{n}}L} = \frac{(1 + \mathrm{u}_+^{(1)})(1 + \mathrm{u}_+^{(2)})}{(1 - \mathrm{u}_+^{(1)})(1 - \mathrm{u}_+^{(2)})}. \tag{4.19}$$

Once we impose the condition (4.19), we secure that purely outgoing waves are emergent out of the graphene surfaces. Therefore, we get $A_+ = C_- = 0$. Substituting all these requirements into the energy expressions in all regions of space found in previous section gives rise to the maximum energy configurations inside the slab, which correspond to lasing threshold condition energy expressions

$$\langle \mathrm{u} \rangle_I = \frac{|A_-|^2}{2\varepsilon_0}, \tag{4.20}$$

$$\langle \mathrm{u} \rangle_{II} = \frac{\mathcal{Y}\,|A_-|^2}{16\varepsilon_0 \mathcal{X}} \left\{ \left[\mathrm{Re}[\mathfrak{n}^{2\star}] + \sin^2\theta \right] \mathcal{U}_+ + \left|\tilde{\mathfrak{n}}\right|^2 \cos^2\theta\, \mathcal{U}_- \right\}, \tag{4.21}$$

$$\langle \mathrm{u} \rangle_{III} = \frac{\mathcal{Y}\,|A_-|^2}{2\varepsilon_0}, \tag{4.22}$$

where Re and Im represent the real and imaginary parts of the corresponding argument, respectively, and $\mathcal{X}$, $\mathcal{Y}$ and $\mathcal{U}_\pm$ are denoted as follows

$$\mathcal{X} = \left| \left(1 - \left[\mathrm{u}_+^{(1)}\right]^2\right) \left(1 - \left[\mathrm{u}_+^{(2)}\right]^2\right) \right|^{\frac{z}{L}-1},$$

$$\mathcal{Y} = \left| \frac{(1 + \mathrm{u}_+^{(1)})}{(1 - \mathrm{u}_+^{(2)})} \right|^2 \mathrm{e}^{2k_z L \mathrm{Im}[\tilde{\mathfrak{n}}]},$$

$$\mathcal{U}_\pm = \left| (1 + \mathrm{u}_+^{(1)})^{\frac{z}{L}-1} (1 + \mathrm{u}_+^{(2)})^{\frac{z}{L}} \pm (1 - \mathrm{u}_+^{(1)})^{\frac{z}{L}-1} (1 - \mathrm{u}_+^{(2)})^{\frac{z}{L}} \right|^2.$$

We notice from (4.20) and (4.22) that energies leaving the graphene sheets from both sides are different from each other by the amount of $\mathcal{Y}$ which occurs due to the presence of gain factor of the slab and distinction between graphene sheets. If the gain amount is incredibly reduced and both graphene sheets are allowed to flow weak enough currents (possibly in the same direction), energy leaving out of both graphene sheets gets closer to each other. To have a concrete idea about these energy statements, we elaborate our analysis so that refractive index of the slab material can be written as real and imaginary parts as follows

$$\mathfrak{n} = \eta + i\kappa. \tag{4.23}$$

For most materials of practical concern, one can safely show that $|\kappa| \ll \eta - 1 < \eta$ such that the factor κ is a rather small quantity. We next introduce another physically applicable parameter g, which is the gain coefficient of the slab material defined by

$$g := -2k\kappa = -\frac{4\pi\kappa}{\lambda}. \tag{4.24}$$

We then realize that substitution of (4.23) and (4.24) into the spectral singularity expression (4.19) gives rise to the extraction of spectral singularity points. Once we impose those points in the energy statements given by (4.20)–(4.22), we can compute energies inside and outside graphene sheets. Notice that amount of gain required for lasing threshold condition is figured out to have the form

$$g = \frac{\sqrt{\eta^2 - \sin^2\theta}}{\eta L} \ln \left| \frac{(1 + \mathrm{u}_+^{(1)})(1 + \mathrm{u}_+^{(2)})}{(1 - \mathrm{u}_+^{(1)})(1 - \mathrm{u}_+^{(2)})} \right|. \tag{4.25}$$

One can adjust the required gain value by means of (4.25) which guarantees the existence of spectral singularity points in a lasing system. As an illustration, we make use of Nd:YAG crystal for the slab environment covered by the graphene sheets with the following characteristics, respectively [107]

$$\eta = 1.8217, \quad L = 1 \text{ cm}, \quad \theta = 30^\circ, \tag{4.26}$$

$$T = 300 \text{ K}, \quad \Gamma = 0.1 \text{ meV}, \quad \mu = 0.05 \text{ eV}. \tag{4.27}$$

Figure 4.2 indicates the dependence of gain amount on the incidence angle θ for the cases corresponding to currents flowing in the same direction and opposite directions on the surfaces of graphene sheets (left and right panels, respectively). In case of current flows in the same direction, parity is conserved, and presence of graphene sheets reduces the gain amount considerably. This illustrates the significance of graphene sheets in producing the lasing threshold condition at very low gain amounts. However, when both currents on the graphene sheets flow in opposite directions, situation changes incredibly. In this case, lasing does not occur because of the violation of

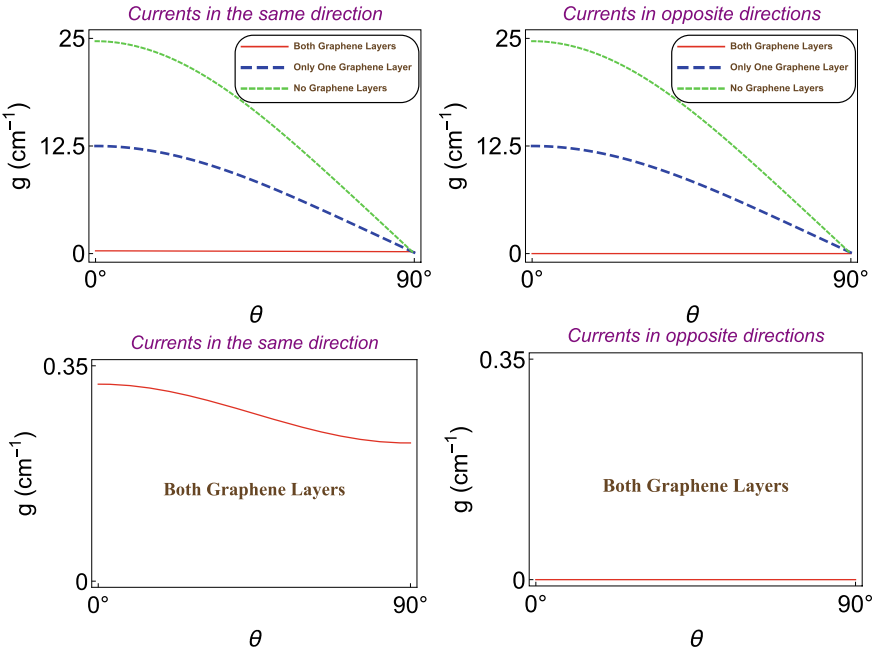

Fig. 4.2 Figure displays the gain coefficient as a function of incident angle θ, corresponding to spectral singularities given by Eq. 4.25. Figures on the left panel shows the case of current flows in the same direction whereas ones on the right panel correspond to the case of opposite flowing currents. Notice that no lasing condition arises when both graphene layers are conceived in the second case

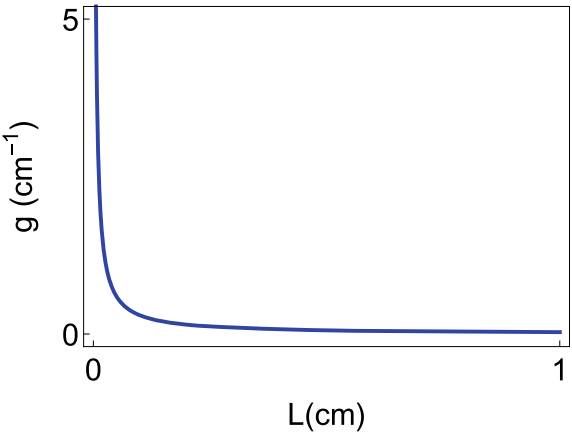

Fig. 4.3 Plot of gain value corresponding to slab thickness L for the system characteristics given by (4.26). Notice that smaller slab thickness results in increasing the gain value whereas higher thickness is more favorable for a much smaller gain amounts

parity conservation [108]. Also, notice the effect of only one graphene sheet placed in the system and gain value falls in half.

Since opposite current flow does not allow lasing condition, we proceed our analysis by employing only the case of same-direction current flow. Figure 4.3 displays how the gain value depends on the slab thickness. We attain the result that higher thickness values are more desirable in obtaining the lasing condition.

Figure 4.4 reveals the effect of graphene sheets on the lasing condition of Nd:YAG slab. Notice that rise of temperature has rather restricted impact on gain value while adjustment of chemical potential is quite significant. Chemical potentials around $\mu \approx 0.92$ eV yields a peak on the gain value, which is not desired for our purpose. Once it is increased considerably, gain amount decreases to much lower values. Also, lower chemical potentials give rather well gain values.

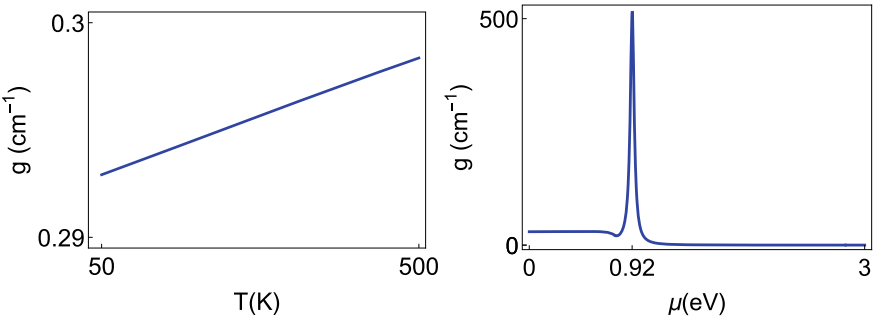

Fig. 4.4 Plots of gain value corresponding to changes of temperature T (left panel) and chemical potential μ (right panel) of graphene sheets, whereas temperature rise slightly increases gain value and chemical potential leads to a peak of gain value around $\mu \approx 0.92$ eV. Thus, chemical potentials around 0.92 eV are not desired for the emergence of a lasing condition

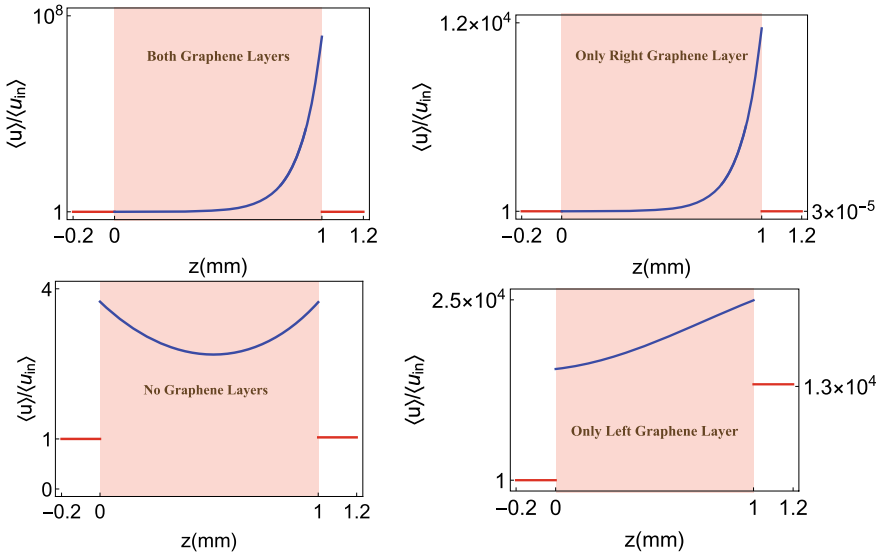

Fig. 4.5 Figure depicts the energy configurations inside and outside the gain slab confined between graphene layers for different situations shown on the panels. Notice that maximum energy density inside the slab is obtained when graphene layers are placed at both ends, whereas minimum energy configuration is attained by the removal of both graphene layers

Once we extract the effect of parameters on the spectral singularities, we can organize the optimal parameters leading to the lasing threshold condition. We can obtain the corresponding energy configurations by means of these optimal parameters. As an illustration, we employ the following parameters to reveal the spectral singularity points so that Fig. 4.5 displays the energy densities for different situations in all regions of space corresponding to spectral singularities. It turns out that maximum energy configuration occurs when both graphene layers are situated around the slab. If both graphene layers are removed, then energy density inside the slab is symmetric and is lowered considerably. Moreover, If only one graphene layer is placed, energy configuration depends on which side graphene sheet is located. Graphene sheet on the left results in high energy density inside the slab. In addition, higher energy is leaving out the system as seen in Fig. 4.5. On the other hand, if the graphene sheet is placed on the right surface, then energy exit would be considerably small compared to all other situations.

One can also consider the presence of dispersion effects within the slab if the refractive index $\mathfrak{n}$ is influenced by the wavenumber k. In this case, we assume that active part of the optical system forming the gain ingredient is formed by doping a host medium of refractive index n_0, and its refractive index satisfies the dispersion relation

$$\mathfrak{n}^2 = n_0^2 - \frac{\hat{\omega}_p^2}{\hat{\omega}^2 - 1 + i\hat{\gamma}\,\hat{\omega}}, \tag{4.28}$$

where $\hat{\omega} := \omega/\omega_0$, $\hat{\gamma} := \gamma/\omega_0$, $\hat{\omega}_p := \omega_p/\omega_0$, ω_0 is the resonance frequency, γ is the damping coefficient, and ω_p is the plasma frequency. The $\hat{\omega}_p^2$ can be expressed in leading order of the imaginary part κ_0 of $\mathfrak{n}$ at the resonance wavelength $\lambda_0 := 2\pi c/\omega_0$ by the expression $\hat{\omega}_p^2 = 2n_0\hat{\gamma}\kappa_0$, where quadratic and higher-order terms in κ_0 are ignored [109]. We replace this equation in (4.28) and employ the first expression of (4.23), and neglecting quadratic and higher-order terms in κ_0, we obtain the real and imaginary parts of refractive index as follows [57–59, 109]

$$\eta \approx n_0 + \frac{\kappa_0\hat{\gamma}(1-\hat{\omega}^2)}{(1-\hat{\omega}^2)^2 + \hat{\gamma}^2\hat{\omega}^2}, \qquad \kappa \approx \frac{\kappa_0\hat{\gamma}^2\hat{\omega}}{(1-\hat{\omega}^2)^2 + \hat{\gamma}^2\hat{\omega}^2}. \tag{4.29}$$

κ_0 can be written as $\kappa_0 = -\lambda_0 g_0/4\pi$ at resonance wavelength λ_0, see (4.24). Substituting this relation in (4.29) and making use of (4.23) and (4.19), we can determine λ and g_0 values for the spectral singularities corresponding to the lasing threshold condition. These are explicitly calculated for various parameters in Table 4.2 for our setup of the Nd:YAG slab covered by graphene sheets. Furthermore, Nd:YAG crystals forming the slab material hold the following $\hat{\gamma}$ value corresponding to the related refractive index and resonance wavelength [107]:

$$n_0 = 1.8217, \qquad \lambda_0 = 808\,\text{nm}, \qquad \hat{\gamma} = 0.003094. \tag{4.30}$$

Notice that resonance wavelength of Nd:YAG is at 808 nm. Table 4.2 reveals that graphene sheets must be used in order to lower the threshold gain value. Also, increasing incidence angle θ to steeper degrees leads to decrease the gain value significantly. This is quite sensible and consistent because the optical path between graphene sheets is enhanced eminently. Gain values demonstrated in Fig. 4.6 support our argument.

Table 4.2 Spectral singularity points corresponding to a Nd:YAG slab situations with two graphenes, single graphene, and no graphene sheets. Other relevant parameters in table are chosen to be $L = 1$ cm, $T = 300\ K$ and $\mu = 0.005$ eV

κ	g_0 (cm^{-1})	λ (nm)	θ	Number of graphene sheets
-2.056×10^{-6}	0.3198	808.028	0°	Double graphene
-1.802×10^{-6}	0.2803	808.025	40°	Double graphene
-1.460×10^{-6}	0.2289	807.887	80°	Double graphene
-8.035×10^{-5}	12.5253	807.940	0°	Single graphene
-5.913×10^{-5}	9.2253	807.931	40°	Single graphene
-1.304×10^{-5}	2.0283	807.993	80°	Single graphene
-1.586×10^{-4}	24.6858	808.027	0°	No graphene
-1.165×10^{-4}	18.1200	808.023	40°	No graphene
-2.462×10^{-5}	3.8599	807.888	80°	No graphene

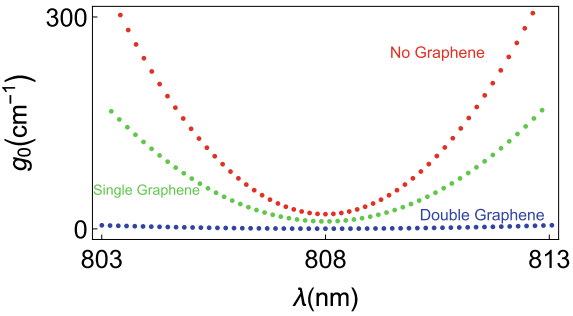

Fig. 4.6 Spectral singularity points in λ-g_0 plane in the presence of dispersion. Notice that existence of graphene sheets reduces the gain values dramatically

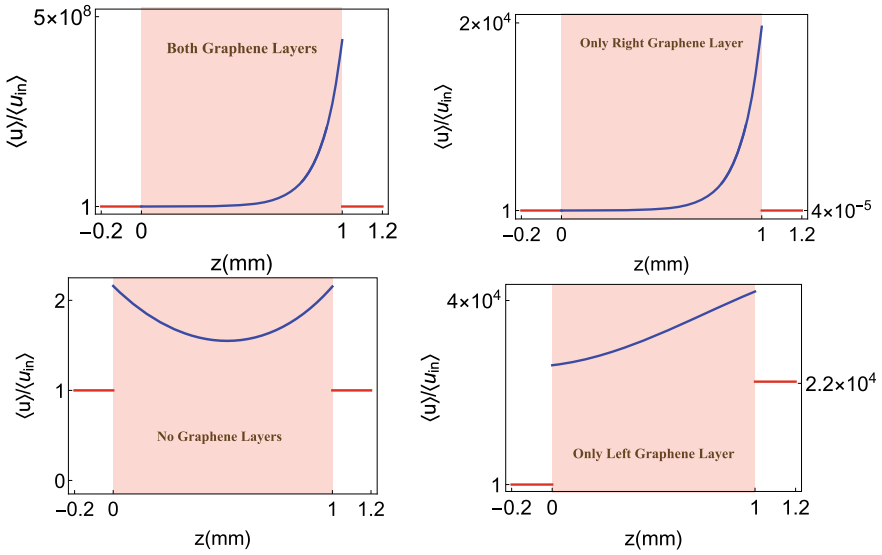

Fig. 4.7 Energy configurations inside and outside the gain slab covered by the graphene sheets in the presence of dispersion. Notice the effect of dispersion on the enhancement of energy storage inside the slab

Figure 4.7 unveils that dispersion effect helps energy storage inside between graphene layers enhance substantially. This is the impact of wavenumber around the spectral singularities and resonance values. Again similar behaviors are observed as in the case of non-dispersive medium.

To understand usage of graphene sheets in other cases like transparency, right and left reflectionlessness, one pursues similar steps performed in spectral singulary phenomenon. Transparency is obtained by the condition $T = 1$ using (4.16). Thus, it is attained that transparency is fulfilled by

$$\zeta(\mathfrak{u}_{-}^{(1)};\mathfrak{u}_{+}^{(2)}) = -2\gamma\, \mathrm{e}^{-ik_z L}, \tag{4.31}$$

together with $A_{\pm} = 0$ for left/right one. Once we employ (4.31) in the corresponding boundary conditions and also in (4.17), it is easy to obtain the energy configurations inside and outside the graphene sheets. Likewise, left and right reflectionlessness conditions are satisfied by imposing $R^l = 0$ and $R^r = 0$, respectively, which lead to

$$\zeta(\mathfrak{u}_{\pm}^{(1)};\mathfrak{u}_{\pm}^{(2)}) = 0, \tag{4.32}$$

where $+/-$ corresponds to left/right reflectionlessness situations. One imposes the requirement (4.32) in standard boundary conditions and thus obtains the relevant energy configurations inside and outside regions around the graphene sheets. Another interesting point to be considered is the invisibility phenomenon since it is of wonder how the energy configuration is settled inside the graphene sheets in such a case. But, it is known that a system with just a single gain or lost component cannot be invisible, we have no chance to investigate energy configurations of invisible patterns. To do that, one needs to construct a pair of gain and loss structure covered by graphene sheets so that $\mathcal{PT}$-symmetry is provided and thus obtain the invisible patterns by employing the combined transfer matrix of the whole system. In our study, since a general framework was drawn on how to obtain the most general energy forms by following the steps we performed, we are contented with showing the basic formulations of these distinct phenomena and leave the rest of calculations for the reader.

4.5 Concluding Remarks

In this study, we use graphene/graphene oxide as the efficient energy storage material surrounding a complex optically active slab material. Recently numerous graphene studies enable various applications of these distinctive 2D materials especially on energy-related activities. In view of our findings, one can use graphene sheets respecting parity invariance in achieving optimal energy configurations. If the formalism we developed in this study is employed, one can satisfy the necessary parameter adjustments of the graphene and slab material to acquire the maximum energy storage. In light of our method, we derived all possible solutions of the s-polarized configurations and found the most general energy density expressions in between and outside the graphene sheets. We showed that this is realized in case of spectral singularities which lead to the lasing threshold condition by producing the purely outgoing waves.

Our treatment is based on basic principles satisfying Maxwell's equations such that one can shape reliable energy storage devices provided that parameters specifying the graphene and complex slab system are well-adjusted. We point out that the effect of graphene sheets appears with the presence of function $\mathfrak{u}_{\pm}^{(1,2)}$, which is characterized by the scalar conductivity $\sigma^{(1,2)}$, in the components of transfer matrix, see Eq. 4.13. In view of reflection and transmission amplitudes, we obtained the relations

for the energy configurations in (4.17), which relate the necessary parameters of the optical slab system covered by the graphene sheets. We demonstrated the optimal conditions of the parameters contributing to the screening of energy configurations. Typically, one desires improving amplification (or absorption in case of loss) inside a gain medium in order to increase the energy density. This is achieved by augmenting the optical path inside the gain medium. But, in our case, graphene helps the energy density increase enormously because of its distinctive features. We explored that this is achieved especially at parity conservation situation which occurs when currents flowing on the surfaces of graphene sheets are in the same direction. Furthermore, it is observed that graphene sheets cause the necessary gain amount to be smaller. We demonstrate this on a toy model using spectral singularities. It is observed that when parity invariance is broken, no gain values can give rise to spectral singularities and optimal energy conditions cannot be reached [61]. We explicitly demonstrated these findings on appropriate figures. We also presented in Table 4.2 some spectral singularity points which gave rise to maximum energy configurations. We indicated these configurations in Fig. 4.7. The results of this study guide attempts for realization of energy storage devices using graphene.

References

1. J.J. Sakurai, *Modern Quantum Mechanics*, rev edn. (Addison-Wesley, 1994)
2. R. Shankar, *Principles of Quantum Mechanics* (Springer, US, 1984)
3. P.A.M. Dirac, *The Principles of Quantum Mechanics* (Clarendon Press, 1992)
4. C.M. Bender, S. Boettcher, Phys. Rev. Lett. **80**, 5243 (1998)
5. K.G. Makris, R. El-Ganainy, D.N. Christodoulides, Z.H. Musslimani, Phys. Rev. Lett. **100**, 103904 (2008)
6. A. Regensburger, C. Bersch, M.A. Miri, G. Onishchukov, D.N. Christodoulides, U. Peschel1, Nature **488**, 167 (2012)
7. A. Mostafazadeh, Int. J. Geom. Meth. Mod. Phys. **7**, 1191 (2010)
8. C.M. Bender, D.C. Brody, H.F. Jones, Am. J. Phys. **71**, 1095 (2003)
9. M. Znojil, SIGMA **5**, 001 (2009)
10. N. Moiseyev, *Non-Hermitian Quantum Mechanics* (Cambridge University Press, 2011)
11. M. Hasan, B.P. Mandal, arXiv:1901.02357 (2019)
12. M. Hasan, B.P. Mandal, Ann. Phys. (NY) **396**, 371–385 (2018)
13. B. Bagchi, C. Quesne, Phys. Lett. A **273**, 285 (2000)
14. A. Guo, G.J. Salamo, D. Duchesne, R. Morandotti, M. Volatier-Ravat, V. Aimez, G.A. Siviloglou, D.N. Christodoulides, Phys. Rev. Lett. **103**, 093902 (2009)
15. B. Christian, E. Rüter, K.G. Makris, R. El-Ganainy, D.N. Christodoulides, M. Segev, D. Kip, Nat. Phys. **6**, 192–195 (2010)
16. L. Feng, M. Ayache, J. Huang, Y. Xu, M. Lu, Y. Chen, Y. Fainman, A. Scherer, Science **333**, 729 (2011)
17. L. Chen, R. Li, N. Yang, D. Chen, L. Li, Proc. Rom. Acad., Ser. A: Math. Phys. Tech. Sci. Inf. Sci. **13**, 46–54 (2012)
18. R. Li, P. Li, L. Li, Proc. RomanianAcad. A **14**, 121 (2013)
19. L. Feng, Y.L. Xu, W.S. Fegadolli, M.H. Lu, J.E. Oliveira, V.R. Almeida, Y.F. Chen, A. Scherer, Nat. Mater. **12**, 108–113 (2013)

20. Y. Shen, X. Hua Deng, L. Chen, Opt. Express **22**, 19440–19447 (2014)
21. A.A. Zyablovsky, A.P. Vinogradov, A.A. Pukhov, A.V. Dorofeenko, A.A. Lisyansky, Phys Uspekhi **57**, 1063 (2014)
22. W.-X. Yang, A.-X. Chen, X.-T. Xie, L. Ni, Phys. Rev. A **96**, 013802 (2017)
23. J.P. Deka, A.K. Sarma, Appl. Opt. **57**, 1119–1126 (2018)
24. F. Loran, A. Mostafazadeh, Opt. Lett. **42**, 5250–5253 (2017)
25. Y.D. Chong, L. Ge, H. Cao, A.D. Stone, Phys. Rev. Lett. **105**, 053901 (2010)
26. S. Longhi, Physics **3**, 61 (2010)
27. S. Longhi, Phys. Rev. A **82**, 031801 (2010)
28. S. Longhi, Phys. Rev. A **83**, 055804 (2011)
29. S. Longhi, Phys. Rev. Lett. **107**, 033901 (2011)
30. W. Wan, Y. Chong, L. Ge, H. Noh, A.D. Stone, H. Cao, Science **331**, 889 (2011)
31. L. Ge, Y.D. Chong, S. Rotter, H.E. Türeci, A.D. Stone, Phys. Rev. A **84**, 023820 (2011)
32. D.G. Baranov, A.E. Krasnok, T. Shegai, A. Alù, Y.D. Chong, Nat. Rev. Mater. **2**, 17064 (2017)
33. C. Yan, M. Pu, J. Luo, Y. Huang, X. Li, X. Ma, X. Luo, Opt. Laser Technol. **101**, 499–506 (2018)
34. M.A. Naimark, Trudy Moscov. Mat. Obsc. **3**, 181 (1954) in Russian, English translation: Amer. Math. Soc. Transl. (2), **16**, 103 (1960)
35. GSh Guseinov, Pramana. J. Phys. **73**, 587 (2009)
36. A. Mostafazadeh, Geometric methods in physics, in Trends in Mathematics, ed. by P. Kielanowski, P. Bieliavsky, A. Odzijewicz, M. Schlichenmaier, T. Voronov (Springer, Cham, 2015), pp. 145–165; arXiv: 1412.0454
37. A. Mostafazadeh, Phys. Rev. A **87**, 012103 (2012)
38. S. Longhi, Phys. Rev. A **82**, 032111 (2010)
39. S. Longhi, J. Phys. A **44**, 485302 (2011)
40. M. Sarısaman, Phys. Rev. A **95**, 013806 (2017)
41. P.A. Kalozoumis, C.V. Morfonios, G. Kodaxis, F.K. Diakonos, P. Schmelcher, Appl. Phys. Lett. **110**, 121106 (2017)
42. S. Longhi, Phys. Rev. A **96**, 042106 (2017); Y. Huang, Y. Shen, C. Min, S. Fan, G. Veronis, Nanophotonics **6(5)**, 977–996 (2017)
43. A. Mostafazadeh, N. Oflaz, Phys. Lett. A **381**, 3548–3552 (2017)
44. O.V. Shramkova, K.G. Makris, D.N. Christodoulides, G.P. Tsironis, Photon. Res. **6**, A1–A5 (2018)
45. S.S. Deka, S.H. Pan, Q. Gu, Y. Fainman, A. El Amili, Opt. Lett. **42**, 4760–4763 (2017)
46. X. Wu, C. Jin, C. Fu, Opt. Commun. **402**, 507–510 (2017)
47. S. Longhi, J. Phys. A **47**, 485302 (2014)
48. A. Mostafazadeh, Phys. Rev. A **89**, 012709 (2013)
49. A. Mostafazadeh, Phys. Rev. A **90**, 023833 (2014)
50. B. Midya, Phys. Rev. A **89**, 032116 (2014)
51. L.L. Sanchez-Soto, J.J. Monzon, Symmetry **6**(2), 396 (2014)
52. Z. Lin, H. Ramezani, T. Eichelkraut, T. Kottos, H. Cao, D.N. Christodoulides, Phys. Rev. Lett. **106**, 213901 (2011)
53. A. Mostafazadeh, Phys. Rev. A **92**, 023831 (2015)
54. A. Mostafazadeh, Phys. Rev. A **91**, 063812 (2015)
55. J.P. Deka, M. Kulkarni, A.K.Sarma (2018). arXiv:1812.10126
56. D. Novitsky, A. Shalin, A. Novitsky (2018) arXiv:1811.03928
57. A. Mostafazadeh, M. Sarisaman, Phys. Lett. A **375**, 3387 (2011)
58. A. Mostafazadeh, M. Sarisaman, Proc. R. Soc. Lond. Ser. A Math. Phys. Eng. Sci. **468**, 3224 (2012)
59. A. Mostafazadeh, M. Sarisaman, Phys. Rev. A **87**, 063834 (2013)
60. A. Mostafazadeh, M. Sarisaman, Phys. Rev. A **88**, 033810 (2013)
61. A. Mostafazadeh, M. Sarisaman, Phys. Rev. A **91**, 043804 (2015)
62. A. Mostafazadeh, M. Sarısaman, Ann. Phys. (NY) **375**, 265–287 (2016)
63. H. Ghaemi-Dizicheh, A. Mostafazadeh, M. Sarısaman, J. Opt. **19**, 105601 (2017)

64. K. Doğan, A. Mostafazadeh, M. Sarısaman, Ann. Phys. (NY) **392**, 165–178 (2018)
65. M. Sarısaman, M. Tas, Phys. Rev. B **97**, 045409 (2018)
66. M. Sarısaman, M. Tas, J. Opt. Soc. Am. B **35**, 2423 (2018)
67. M. Sarısaman, M. Tas, Ann. Phys. (NY) **401**, 139–148 (2019)
68. M. Sarısaman, M. Tas, J. Appl. Phys. **126**, 163102 (2019)
69. F. Schedin, A.K. Geim, S.V. Morozov, E.W. Hill, P. Blake, M.I. Katsnelson, K.S. Novoselov, Nat. Mater. **6**, 652 (2007)
70. R. Stine, J.T. Robinson, P.E. Sheehan, Cy.R. Tamanaha, Adv. Mater. **22**, 5297 (2010)
71. G. Lu, L.E. Ocola, J. Chen, Appl. Phys. Lett. **94**, 083111 (2009)
72. J.T. Robinson, F.K. Perkins, E.S. Snow, Z. Wei, P.E. Sheehan, Nano Lett. **8**, 3137 (2008)
73. Y. Shao, J. Wang, H. Wu, J. Liu, I.A. Aksay, Y. Lin, Electroanalysis **22**, 1027–1036 (2010)
74. Q. He, S. Wu, Z. Yin, H. Zhang, Chem. Sci. **3**, 1764 (2012)
75. S. Wu, Q. He, C. Tan, Y. Wang, H. Zhang, Small **9**, 1160 (2013)
76. J. Duffy, J. Lawlor, C. Lewenkopf, M.S. Ferreira, Phys. Rev. B **94**, 045417 (2016)
77. S. Chen, Z. Han, M.M. Elahi, K.M.M. Habib, L. Wang, B. Wen, Y. Gao, T. Taniguchi, K. Watanabe, J. Hone, A.W. Ghosh, C.R. Dean, Science **353**, 1522 (2016)
78. P.-Y. Chen, A. Alu, ACS Nano **5**, 5855 (2011)
79. M. Danaeifar, N. Granpayeh, J. Opt. Soc. Am. B **33**, 1764 (2016)
80. M. Naserpour, C.J. Zapata-Rodríguez, S.M. Vuković, H. Pashaeiadl, M.R. Belić, Sci. Rep. **7**, 12186 (2017)
81. A.K. Geim, K.S. Novoselov, Nat. Mater. **6**, 183 (2007)
82. A.K. Geim, Science **324**, 1530 (2009)
83. A.H. Castro Neto, F. Guinea, N.M.R. Peres, K.S. Novoselov, A.K. Geim, Rev. Mod. Phys. **81**, 109 (2009)
84. O.V. Yazyev, Rep. Progr. Phys. **73**, 056501 (2010)
85. T. Smolenski, T. Kazimierczuk, M. Goryca, M.R. Molas, K. Nogajewski, C. Faugeras, M. Potemski P. Kossacki, 2D Mater. **5**, 015023 (2018)
86. D. Jariwala, T. Marks, M. Hersam, Nat. Mater. **16**, 155 (2017)
87. A. Gupta, T. Sakthivel, S. Seal, Prog. Mater. Sci. **73**, 44–126 (2015)
88. A. Molle, J. Goldberger, M. Houssa, Y. Xu, S.C. Zhang, D. Akinwande, Nat. Mater. **16**, 163–169 (2017)
89. W.K. Chee, H.N. Lim, Z. Zainal, N.M. Huang, I. Harrison, Y. Andou, J. Phys. Chem. C **120**, 4153–4172 (2016)
90. S. Ye, J. Feng, P. Wu, A.C.S. Appl, Mater. Interfaces **5**(15), 7122–7129 (2013)
91. J. Song, Z. Yu, M.L. Gordin, D. Wang, Nano Lett. **16**(2), 864–870 (2016)
92. B. He, Q. Tang, M. Wang, H. Chen, S. Yuan, A.C.S. Appl, Mater. Interfaces **6**(11), 8230–8236 (2014)
93. X. Zhou, J. Bao, Z. Dai, Y. Guo, J. Phys. Chem. C **117**(48), 25367–25373 (2013)
94. S.P. Gumfekar, *Graphene-Based Materials for Clean Energy Applications* (Elsevier, Nanomaterials for Green Energy, 2018)
95. S. Zanotto, F. Bianco, V. Miseikis, D. Convertino, C. Coletti, A. Tredicucci, APL Photon. **2**, 016101 (2017)
96. F. Liu, Y.D. Chong, S. Adam, M. Polini, 2D Mater. **1**, 031001 (2014)
97. Y. Fan, F. Zhang, Q. Zhao, Z. Wei, H. Li, Opt. Lett. **38**, 6269 (2014)
98. S.M. Rao, J.J.F. Heitz, T. Roger, N. Westerberg, D. Faccio, Opt. Lett. **39**, 5345 (2014)
99. Y. Fan, Z. Liu, F. Zhang, Q. Zhao, Q. Fu, J. Li, C. Gu, H. Li, Sci. Rep. **5**, 13956 (2015)
100. A. Mostafazadeh, Phys. Rev. Lett. **102**, 220402 (2009)
101. G. Oktay, M. Sarisaman, M. Tas, Sci. Rep. **10**, 3127 (2020)
102. B. Wunsch, T. Stauber, F. Sols, F. Guinea, New J. Phys. **8**, 318 (2006)
103. E.H. Hwang, S. Das Sarma, Phys. Rev. B **75**, 205418 (2007)
104. L.A. Falkovsky, Phys.-Uspekhi **51**, 887 (2008)
105. L. Rayleigh, Phil. Mag. Series 6, 20:120, 1001 (1910)
106. L. Rayleigh, Phil. Mag. Ser. **6**27, 157, 100 (1914)
107. W.T. Silfvast, *Laser Fundamentals* (Cambridge University Press, Cambridge, 1996)
108. A. Mostafazadeh, J. Phys. A **47**, 505303 (2014)
109. A. Mostafazadeh, Phys. Rev. A **83**, 045801 (2011)

Chapter 5
Electrical Biosensor Using Graphene Field-Effect Transistor and Small Receptor Molecules

Takao Ono, Yasushi Kanai, Yasuhide Ohno, Kenzo Maehashi, Koichi Inoue, and Kazuhiko Matsumoto

5.1 Introduction

Graphene is a two-dimensional carbon material (Fig. 5.1) and attracting much attention in variety of fields from its discovery in 2004 [1], due to its unique physical properties [2, 3]. We have investigated a biosensing application of graphene field-effect transistor (FET) [4–7]. Graphene FET has a strong potential for ideal electrical biosensor, owing to the following characteristics of graphene: (1) Graphene exposes its two-dimensional electron gas and has ideally high surface-to-volume ratio. Also, it is stable in water owing to its wide potential window [8]. Therefore, detection target in aqueous solution directly attaches to graphene channel and modulates carrier density of graphene. (2) Graphene has the highest mobility in known materials [9, 10]. Therefore, graphene FET transduces the carrier modulation to large drain current change, that is, graphene FET has high sensitivity in electrical detection. We named the biosensing platform using graphene FET as "lab-on-a-graphene-FET" after lab-on-a-chip [11]. Figure 5.2 shows a typical configuration of lab-on-a-graphene-FET. Graphene channel of graphene FET is immersed in sample solution, and top-gate voltage is applied using Ag/AgCl reference electrode.

T. Ono (✉) · Y. Kanai · Y. Ohno · K. Maehashi · K. Inoue · K. Matsumoto (✉)
The Institute of Scientific and Industrial Research, Osaka University, 8-1 Mihogaoka, Ibaraki-shi, Osaka 567-0047, Japan
e-mail: t-ono@sanken.osaka-u.ac.jp

K. Matsumoto
e-mail: k-matsumoto@sanken.osaka-u.ac.jp

Y. Ohno
Institute of Post-LED Photonics, Tokushima University, 2-1 Minamijosanjima, Tokushima-shi, Tokushima 770-8506, Japan

K. Maehashi
Institute of Engineering, Tokyo University of Agriculture and Technology, 2-24-16 Nakacho, Koganei-shi, Tokyo 184-8588, Japan

S. Kaneko et al. (eds.), *Carbon Related Materials*,
https://doi.org/10.1007/978-981-15-7610-2_5

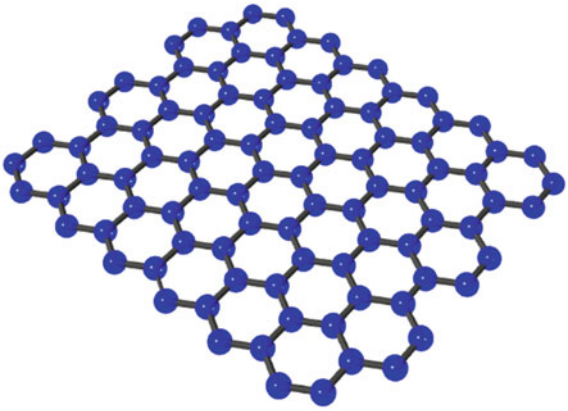

Fig. 5.1 Graphene structure

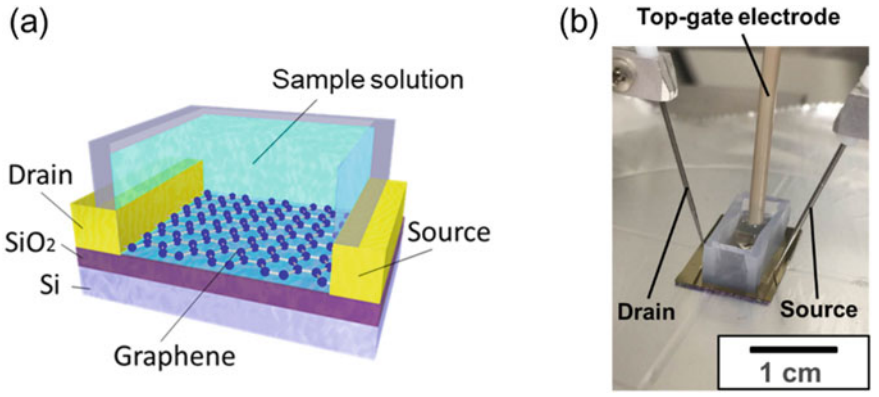

Fig. 5.2 Device and measurement setup. **a** Schematics of the device. Graphene channel is immersed in the sample solution. **b** Photograph of the device in measurement. Cited from [21]. Copyright 2018 The Japan Society of Applied Physics

Lab-on-a-graphene-FET detects protons (pH) in a wide range of pH at least between pH 2 and 12 [12]. In the sensing of such small molecules, lab-on-a-graphene-FET finely shows reversible response to the molecular concentration [13–15]. The detection mechanism is still under discussion, but one prevailing theory is based on site-binding model: Target molecules in the solution associate with and dissociate from hydroxyl groups of graphene defects and modify carrier density of the graphene. In the sensing of polymer molecules such as proteins, non-specific adsorption degrades the reversibility. Once proteins and other polymers adhere on the graphene surface, it is hard to remove them and to bring the graphene surface back to the initial state. The adsorbed protein can be identified by their charge state (Fig. 5.3). However, this method is not sufficient for selective detection of wide

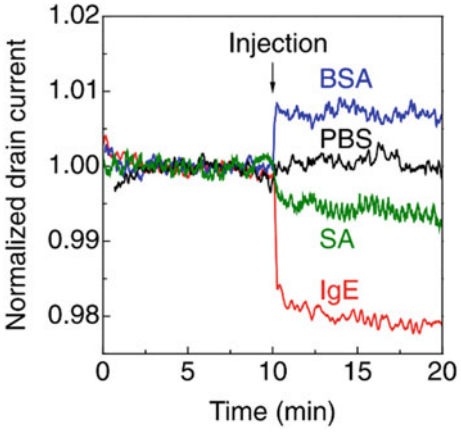

Fig. 5.3 Drain-currents time course of graphene FETs with injection of various proteins in phosphate-buffered saline (PBS, pH 6.8). Positively charged IgE and SA decreased the hole current, whereas negatively charged BSA increased the current. Cited from [6]. Copyright 2011 The Japan Society of Applied Physics

range of targets. For this purpose, graphene channel surface needs to be immobilized with receptor molecules which specifically bind to the detection targets. In this case, Debye screening of target's surface charges causes a serious problem. The surface charges of targets are neutralized by aqueous ions, and electrical potential around the targets rapidly attenuates from the target surface with the characteristic length, Debye screening length λ_D, given by:

$$\lambda_D = \sqrt{\frac{\varepsilon RT}{2F^2 I}} \tag{5.1}$$

where ε, R, T, F and I are permittivity, gas constant, temperature, Faraday constant, and ionic strength. Debye screening length is less than 1 nm in physiological ionic strength [16], which is smaller than the size of almost all receptors. Therefore, it is difficult to detect electrical charges of the detection targets captured by receptor molecules. To solve this problem, it is useful to elongate Debye screening length by decreasing ionic strength. However, if the concentration of the ionic content of buffer solution is too low, buffering ability of the solution is lost, and a binding affinity of the receptors to the targets is deteriorated. To detect targets in relatively high ion concentration such as in ten or a hundred times dilution of a conventional buffer solution, small receptor molecule is necessary. In this article, we report some results using such small receptor molecules immobilized on lab-on-a-graphene-FET. Also, we report some related researches about controlling graphene surface.

5.2 Lab-On-A-Graphene-FET Using DNA Aptamer [5]

Antibody such as immunoglobulin G is the most common category of the target-specific receptor molecule, but its size (approximately 15 nm [17]) is too large to be

used as a receptor for graphene FET biosensing. Aptamer is one alternative. Aptamer is a small artificial oligonucleotide. It makes specific structure using complemental parts in its own strand and shows specific binding ability to the target. The size of the aptamer was approximately 3 nm in this experiment. Therefore, target-receptor interaction was occurred inside the electrical double layer, and surface charge of the target, immunoglobulin E (IgE) in this study, was able to be detected even when the target was separated from graphene surface by the receptor. To immobilize aptamer on graphene channel surface, we used 1-pyrenebutanoic acid succinimidyl ester (PBASE, Fig. 5.4) as a linker molecule. PBASE has succinimide group which forms covalent bond with amino group at aptamer terminus and has pyrenyl group which forms π-π stacking with π-conjugated system at graphene surface. Immobilization of the aptamer was confirmed by atomic force microscopy (AFM). After immobilization, thickness of graphene channel was increased from its original value (0.3 nm) to around 3 nm (Fig. 5.5). This value is comparable to the size of the aptamer.

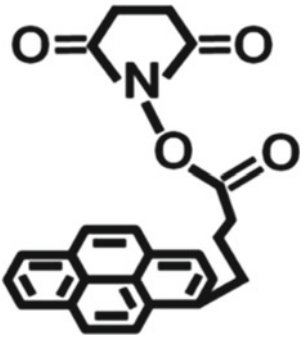

Fig. 5.4 Structure of PBASE

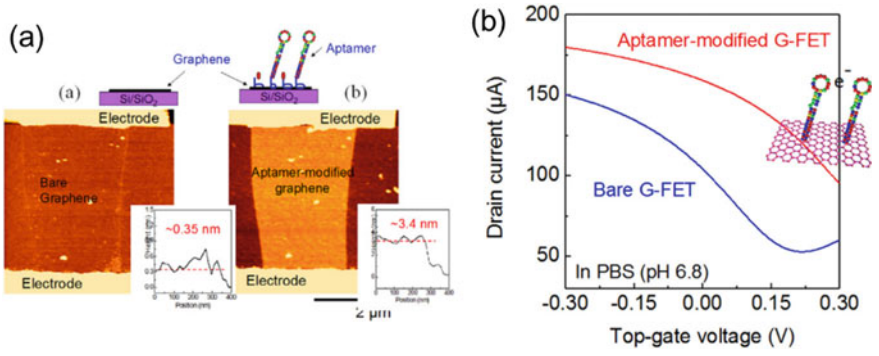

Fig. 5.5 Aptamer-immobilized graphene biosensor. **a** AFM images of graphene FET before and after aptamer immobilization. Inset shows cross-sectional profile at the edge of graphene channel. **b** Transfer characteristics of graphene FET before and after aptamer immobilization. Cited from [5, 7]. Copyright 2010 American Chemical Society and 2014 IOP Publishing

Also, the immobilization was confirmed by electrical measurement of graphene FET. DNA molecule has negative charges which induces hole carrier in graphene. After immobilization, transfer characteristics shows increase in hole current of graphene FET (Fig. 5.5).

We introduced three proteins, bovine serum albumin (BSA), streptavidin (SA), and IgE, monitoring drain current of graphene FET under fixed gate voltage. The value of the gate voltage was chosen to monitor hole current in the whole measurement. Only after IgE introduction, hole current rapidly decreased owing to positive charges of IgE (Fig. 5.6). In comparison with the result in Fig. 5.3, IgE-specific graphene FET biosensor was successfully constructed by aptamer immobilization. Sub-nanomolar sensitivity was obtained with this method. In this method, the amount of current changes corresponds to the amount of carriers induced in graphene, i.e., the amount of IgE (its surface charges) captured on graphene surface. Also, aptamer molecules bind to IgE molecules one by one. Therefore, the amount of current changes under increasing IgE concentration was able to be fitted by Langmuir adsorption isotherm as follows:

$$\Delta I = \frac{\Delta I_{\max} C_{\mathrm{IgE}}}{(K_{\mathrm{D}} + C_{\mathrm{IgE}})} \tag{5.2}$$

where ΔI, $\Delta I_{\max}$, C_{IgE} and K_{D} were the drain current change of the graphene FET, the maximum drain current change, IgE concentration, and dissociation constant of IgE from aptamer, respectively. The experimental result was well fitted by this equation, and it indicated that the electrical response of the lab-on-a-graphene-FET was caused by specific binding of IgE molecules to aptamer molecules modified on graphene surface. These experiments demonstrated a proof-of-concept that graphene FET modified with small receptor molecules is able to be applied to electrical biosensor which does not require additional reagent such as fluorescent labels used in conventional optical biosensors.

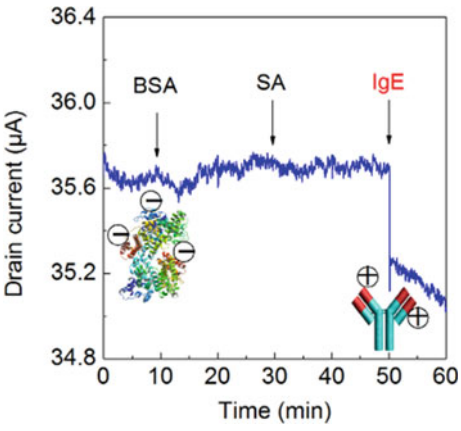

Fig. 5.6 Selective detection of IgE using aptamer-immobilized graphene FET. The graphene FET did not respond to BSA and SA. In contrast, the hole current rapidly decreased after the introduction of IgE. Cited from [5, 7]. Copyright 2010 American Chemical Society and 2014 IOP Publishing

5.3 Detection of Pseudo-influenza Virus Using Sialoglycan-Functionalized Graphene FET [11]

Influenza virus infection starts from its binding to sialoglycan molecules on the cell surface. At this early stage, influenza virus recognizes the terminal structure of the sialoglycan, which is different between human and avian species. Therefore, avian influenza virus does not affect to human species. However, in 1918, Spanish flu was caused by avian influenza virus naturally-mutated and achieving human infectivity. This kind of mutant influenza virus have emerged on several-tens of years and have caused severe global infection, pandemic [18]. To take measures against oncoming pandemic caused by new mutant influenza virus, it is necessary to monitor binding affinities of influenza viruses to human-type sialoglycan. For this purpose, we developed sialoglycan-immobilized graphene FET. In this study, glycan-binding proteins, lectins, was used instead of influenza virus. Lectins derived from *Sambucus sieboldiana* (SSA) and *Maackia amurensis* (MAM) have specific binding affinities to human-type sialoglycan (α2.6 sialoglycan) and avian-type sialoglycan (α2.3 sialoglycan), and used as alternatives to human-infectious and avian-infections influenza virus, respectively (Fig. 5.7a).

After immobilization of sialoglycan, thickness of the graphene increased as in aptamer immobilization and showed successful immobilization of the sialoglycan. The size of the sialoglycan is enough small (approximately 2 nm, Fig. 5.7b), and lectins were captured inside the electrical double layer. Also, sialic acid at the sialoglycan terminus has negative charge. Sialoglycan modification was confirmed by the changes in transfer characteristics of graphene FET (increment in hole current, Fig. 5.7c).

We introduced two lectins and BSA as a control to sialoglycan-immobilized graphene FET. Graphene FET immobilized by human-type, α2.6 sialoglycan responded only to pseudo-human infectious influenza virus, SSA (Fig. 5.7d), while graphene FET immobilized by avian-type, α2.3 sialoglycan responded only to pseudo-avian infectious influenza virus, MAM (Fig. 5.7e). Although the experimental data cannot be fitted by Langmuir adsorption isotherm, because dissociation constant between sialoglycan and lectin is as high as micromolar or millimolar range, which is too high to be achieved, sub-nanomolar sensitivity to pseudo-influenza virus was successfully demonstrated based on species-specific infection mechanism. Lab-on-a-graphene-FET has a potential to be high-sensitive influenza virus sensor against oncoming mutant virus pandemic. Now, we are considering the next experiment using real influenza virus.

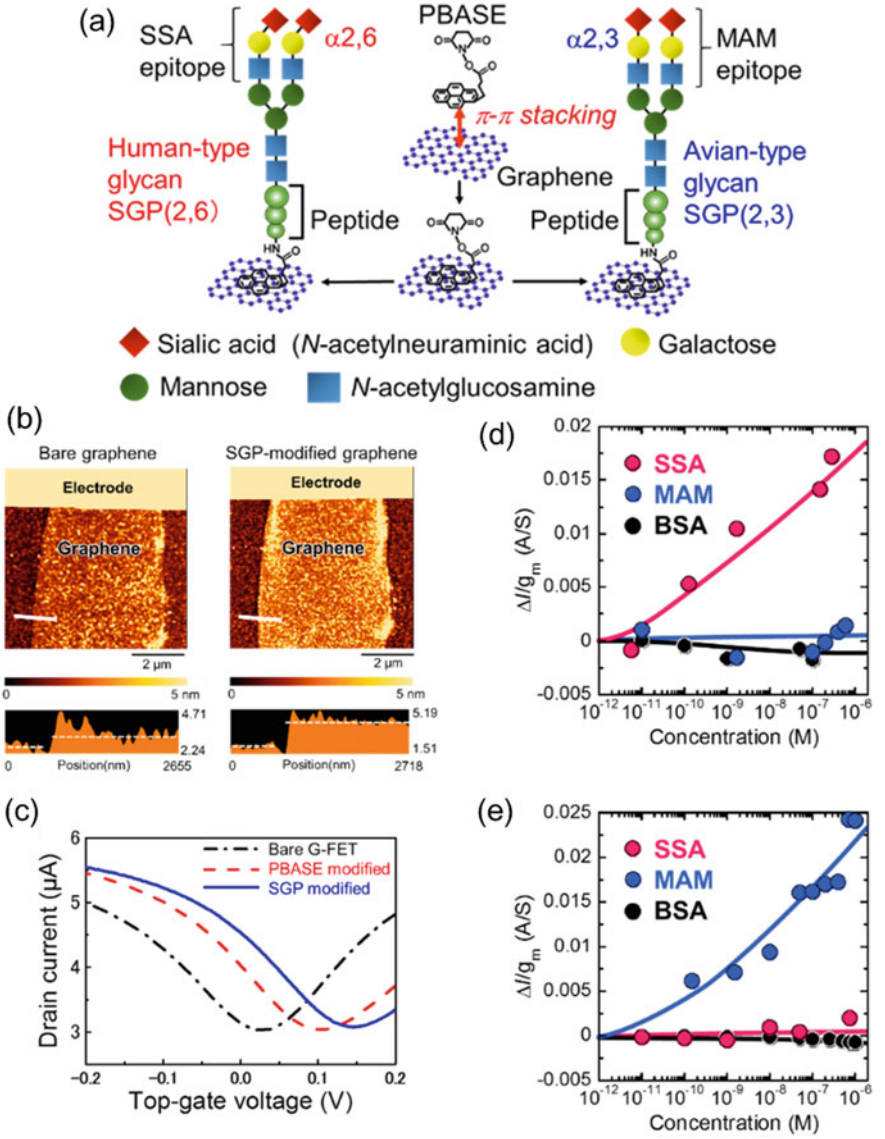

Fig. 5.7 Sialoglycan-functionalized graphene FET and detection of pseudo-influenza virus. **a** Schematics of the immobilization of sialoglycan. Both human-type sialoglycan (SGP(2,6)) and avian-type sialoglycan (SGP(2,3)) have two binding sites for corresponding lectins at their sialic acid terminus. **b** AFM images of bare graphene channel and sialoglycan-modified channel, and their height profiles at the edge of the channels (white lines). **c** Transfer characteristics of graphene FET with bare graphene (black line), PBASE-modified graphene (red line), and sialoglycan-modified graphene (blue line). **d**,**e** Drain current changes (ΔI) of graphene FET modified with human-type glycan **d** and avian-type glycan **e** under increasing concentration of SSA lectin (pseudo human-infectious virus), MAM lectin (pseudo avian-infectious virus), and BSA. ΔI values were normalized by the transconductance g_m. Cited from [11]. Copyright 2018 The Japan Society of Applied Physics

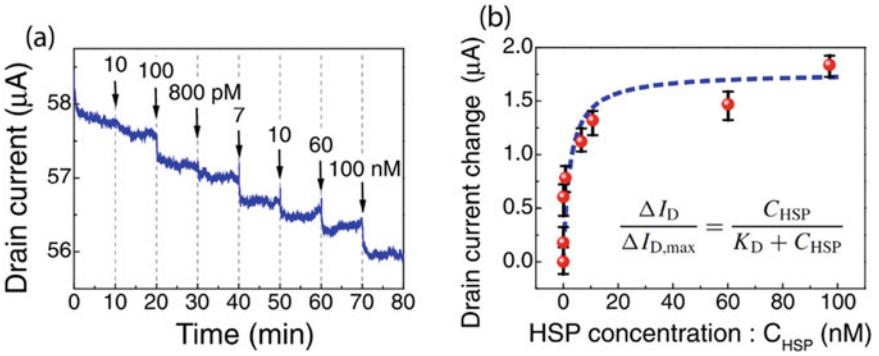

Fig. 5.8 Electrical response of Fab-immobilized graphene FET to HSP. **a** Drain-current time course under increasing concentration of HSP. **b** Drain current changes under various concentrations of HSP, fitted by the Langmuir adsorption isotherm (dotted line). Cited from [19]. Copyright 2012 The Japan Society of Applied Physics

5.4 Other Small Receptor Molecules

There are many types of receptors other than that described above, and we have applied these receptors to lab-on-a-graphene-FET. For example, although antibody is too large to be applied as it is, its fragment with epitope is a useful small receptor. This fragmented antibody, Fab, was applied to detection of heat shock protein (HSP). The experimental results in Fig. 5.8 show successful detection of the protein binding to Fab. The electrical response was well fitted by Langmuir adsorption isotherm with appropriate value of dissociation constant (2.3 nM), and detection sensitivity at picomolar level was achieved [19].

Single DNA strand is a sensitive receptor for complementary strand, even if it does not act as the aptamer. We have developed graphene FET sensor for the detection of DNA hybridization (Fig. 5.9). In this case, the amount of electrical charges of single DNA molecule (17e C) was calculated from number of bases. Since these charges capacitively induced hole carrier to graphene, surface density of receptor molecules was estimated from changes in transfer characteristics before and after receptor immobilization. The surface density was as high as 1 molecule/10 nm square. The surface density of captured complementary DNA was also estimated as 30% of receptor DNA [20].

5.5 Other Methods for Controlling Graphene Surface

The surface control of lab-on-a-graphene-FET is not limited in the selection of receptor molecules. For example, it is control of the surface density of receptor

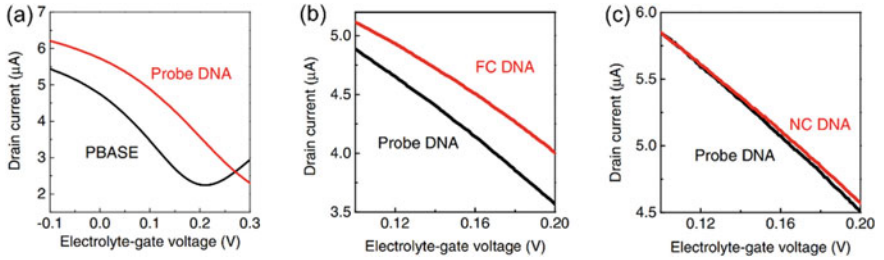

Fig. 5.9 Electrical detection of complementary strand of DNA. **a** Transfer characteristics before (PBASE) and after (Probe DNA) immobilization with receptor DNA. **b**, **c** Transfer characteristics before (Probe DNA) and after introduction of the complementary DNA strand (FC DNA, **b**) or the non-complementary DNA strand (NC DNA, **c**). Cited from [20]. Copyright 2013 The Japan Society of Applied Physics

molecules. Inclement of the density of binding site enhances the detection sensitivity, because it increases $\Delta I_{\max}$ in Eq. (5.2). For this purpose, we adopted new linker molecule tetrakis(4-carboxyphenyl)porphyrin (TCPP) instead of PBASE. In comparison with PBASE, TCPP has larger π-conjugated system and four carboxyl groups as binding sites to receptors (Fig. 5.10a). From the changes in transfer characteristics of graphene FET after aptamer immobilization and IgE introduction, it was found that TCPP immobilized 4.6 times denser aptamer molecules and increased maximum IgE binding amount 1.7 times compared to PBASE (Fig. 5.10b). The difference in these two numbers was attributed to steric hindrance of IgE which is much larger than the linker and the aptamer. TCPP linker increased detection sensitivity in single digit (Fig. 5.10c) [21].

Controlling backside of the graphene, i.e., device substrate surface, is also important for the surface control. For optical observation of graphene, we have used Si substrate with 280-nm thick SiO_2 layer as the device substrate. Sensor performance of graphene FET on the substrate with additional Al_2O_3 layer at the top was compared that on the substrate treated with hydrogen annealing. In this study, to simplify the device structure, graphene surface was not immobilized and exposed to vacuum circumstance. The oxygen gas adsorption on graphene was measured with back-gating. On Al_2O_3 layer, graphene FET showed lower sensitivity in around one digit to oxygen gas adsorption (Fig. 5.11). The reason of this lowering sensitivity is still unclear, but surface potential of Al_2O_3 may affect to adsorption of oxygen in vacuum through graphene. Precise control of the device performance by substrates will be realized in future [22].

5.6 Conclusion

In this article, we reviewed our achievements in application of graphene FET to high-sensitive biosensor by using small receptor molecules. Although large receptor

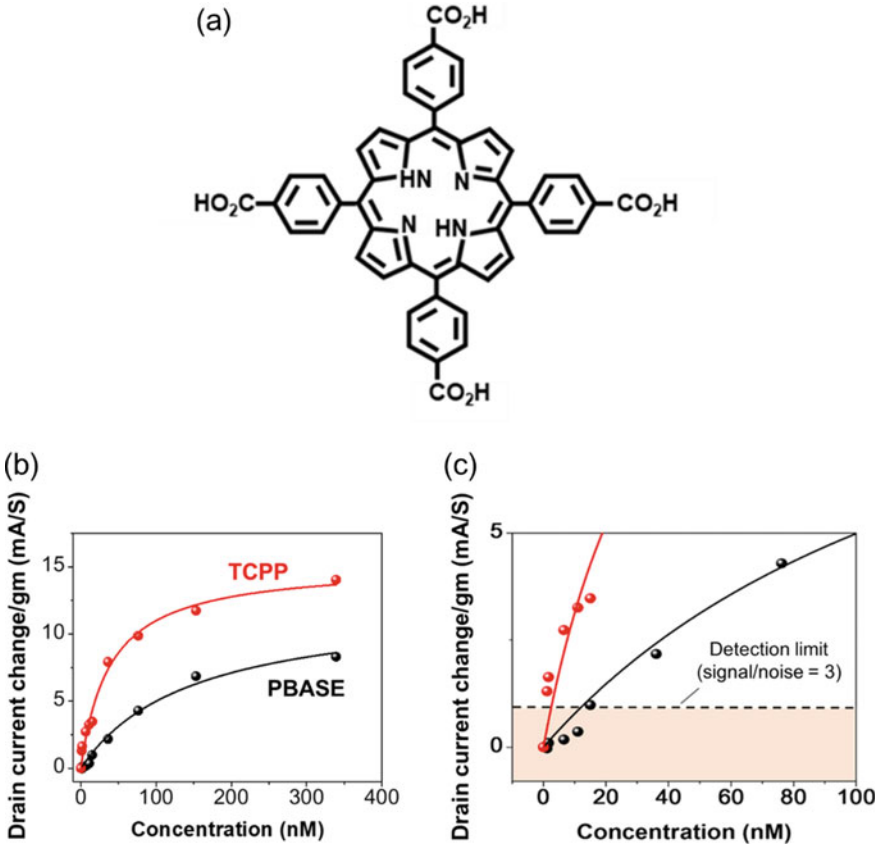

Fig. 5.10 Performance of graphene FET sensor with different types of linker molecules. **a** Structure of TCPP. **b** Drain current changes of the graphene FET (standardized by the transconductance g_m) under various IgE concentrations, fitted by the Langmuir adsorption isotherm (solid lines). **c** Enlargement of the low concentration region in **b**. The dashed line shows the detection limit, i.e., three standard deviations of the current noise. Cited from [21]. Copyright 2018 The Japan Society of Applied Physics

molecules such as antibody cannot be applied to graphene FET biosensor due to Debye screening, there are various types of small receptors such as aptamer, sialoglycan, and others. Graphene FET immobilized with these small receptors electrically monitored specific binding of the detection targets to receptors and showed detection limit as low as sub-nanomolar range. The biosensing platform using graphene FET, lab-on-a-graphene-FET, is expected to be a killer application of graphene and to be applied in real world in future.

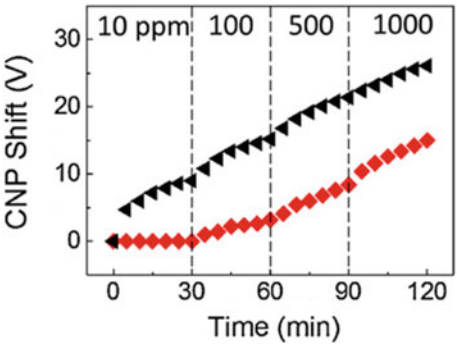

Fig. 5.11 Electrical response of graphene FET gas sensor on Si substrates with H_2 annealing (black dots) and Al_2O_3 coating (red dots) under increasing concentration of oxygen gas. The response is shown as charge neutrality point (CNP) shift in transfer characteristics of graphene FET. Cited from [22]. Copyright 2015 The Japan Society of Applied Physics

Acknowledgements This study was partially supported by JST CREST (JPMJCR15F4) from Japan Science and Technology agency. This study was also supported by JSPS KAKENHI (16K13638 and 18K14107) from the Ministry of Education, Culture, Sports, Science, and Technology of Japan (MEXT).

References

1. K.S. Novoselov et al., Science **306**, 666 (2004)
2. K.S. Novoselov et al., Nature **490**, 192 (2012)
3. A.C. Ferrari et al., Nanoscale **7**, 4598 (2015)
4. Y. Ohno et al., Nano Lett. **9**, 3318 (2009)
5. Y. Ohno et al., J. Am. Chem. Soc. **132**, 18012 (2010)
6. Y. Ohno et al., Jpn. J. Appl. Phys. **50**, 070120 (2011)
7. K. Matsumoto et al., J. Phys. D **47**, 094005 (2014)
8. M. Zhou et al., Anal. Chem. **81**, 5603 (2009)
9. E.H. Hwang et al., Phys. Rev. Lett. **98**, 186806 (2007)
10. K.I. Bolotin et al., Solid State Commun. **146**, 351 (2008)
11. T. Ono et al., Jpn. J. Appl. Phys. **56**, 030302 (2017)
12. P.K. Ang et al., J. Am. Chem. Soc. **130**, 14392 (2008)
13. B. M. Giacchetti et al. J. Appl. Phys. **114**, 084505 (2013)
14. X. Tan et al., J. Phys. Chem. C **117**, 27155 (2013)
15. T. Ono et al., Nano Lett. **19**, 4004 (2019)
16. N. Nakatsuka et al., Science **362**, 319 (2018)
17. L.J. Harris et al., J. Mol. Biol. **275**, 861 (1998)
18. J.A. Belser et al., Science **359**, 255 (2018)
19. S. Okamoto et al., Jpn. J. Appl. Phys. **51**, 06FD08 (2012)
20. Y. Ohno et al., Jpn. J. Appl. Phys. **52**, 110107 (2013)
21. T. Kawata et al., Jpn. J. Appl. Phys. **57**, 065103 (2018)
22. M. Nakamura et al., Jpn. J. Appl. Phys. **54**, 06FF11 (2015)

Chapter 6
Hydrogen Storage Performance of Metal Nanoparticle Decorated Multi-walled Carbon Nanotubes

Saratchandra Babu Mukkamala

6.1 Introduction

The progress of a nation is directly related to various developmental activities, i.e., agriculture, industry, transport, and industrialization through consumption of energy. The world is facing the over-consumption of energy due to overwhelming growth of population and changing standard of living [1]. So, the current energy resources are not sufficient to meet the present energy demand. There is a vast difference between advanced countries and under-developed countries in the usage of energy [2]. Rapid development of cities due to industrialization and migration of people from rural to urban areas for employment is the major cause for energy demand. Due to urbanization, majority of the world's population is likely to migrate to the urban areas by 2050 according to UN assessment [3].

In addition to the challenges of meeting the increasing energy demand, there is a severe problem with the emission of hazardous pollutants [4]. CO_2 is the major air pollutant in the environment destroying the livelihood of mankind through greenhouse gas effect [5]. Burning of fossil fuels is the major source of CO_2 emissions and reason for climate change [6]. To tackle the challenges of the future energy demand and environmental pollution, particularly CO_2 emissions, progress in the alternative sources of energy such as ethanol, biodiesel, methanol, and hydrogen is inevitable [7].

Among the renewable energy sources, hydrogen is an ideal energy carrier which is considered for future automotive applications. Hydrogen has high energy density (120 MJ/kg) than petroleum fuels [8, 9]. Water moisture is the end product when hydrogen reacts with oxygen. Economic use, suitable storage medium, and infrastructure are some of the key factors considered for promoting the hydrogen as a fuel

S. B. Mukkamala (✉)
Department of Chemistry, Institute of Science, GITAM (Deemed to be University), Visakhapatnam, A.P. 530045, India
e-mail: smukkama@gitam.edu

S. Kaneko et al. (eds.), *Carbon Related Materials*,
https://doi.org/10.1007/978-981-15-7610-2_6

for substitution to existing fossil fuels. Many investigators reported the significance of hydrogen and its obstacles in commercial applications [10, 11]. Hydrogen is a feasible energy source to fill the gap and perfectly replace the existing fossil fuels. In spite of added advantage, hydrogen fuel has some challenges in onboard vehicle applications such as 300 miles travel range, life time of 1500 cycles, and cost of fuel storage system. The production, storage, and delivery of hydrogen are shown in Fig. 6.1.

Many automobile manufacturers are developing fuel cell vehicles for hydrogen-driven hybrid cars. Reaching the set specific goals of the Department of Energy (DOE) is an uphill task. The 2015 target of the light-duty vehicles with a mileage range of 300 miles is yet to be achieved. Production, storage, and transportation continue to be the major challenge for realization of commercial applications.

The development of an effective and safe hydrogen storage system is a key enabling technology for onboard vehicle applications. The US Department of Energy (DOE) established specific technical targets (6.0 wt% capacity at non-cryogenic conditions) for onboard hydrogen storage systems for hydrogen storage. Storage of hydrogen in stationary power, portable power, and transportation is a crucial technique for the progress of hydrogen-powered fuel cell technologies. Hydrogen storage is widely classified on the basis of physical and chemical processes (Fig. 6.2).

Hydrogen can be stored physically either in gas (high pressure tank, 350–700 bar) or liquid form (cryogenic tank, 77 K). Adsorption on a solid is the key process for the storage of hydrogen at non-cryogenic conditions and moderate pressures. Different sorbents, metal hydrides, metal–organic frameworks (MOFs), porous carbons, nanocones, etc., with necessary modifications could meet the DOE targets [12–14]. The Department of Energy (DOE) has set the targets for hydrogen storage

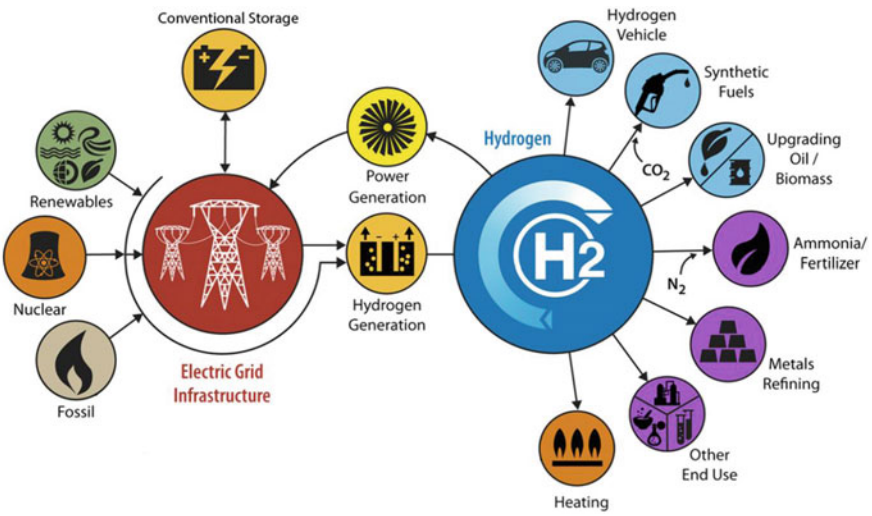

Fig. 6.1 Hydrogen production and applications. *Source* Energy.gov

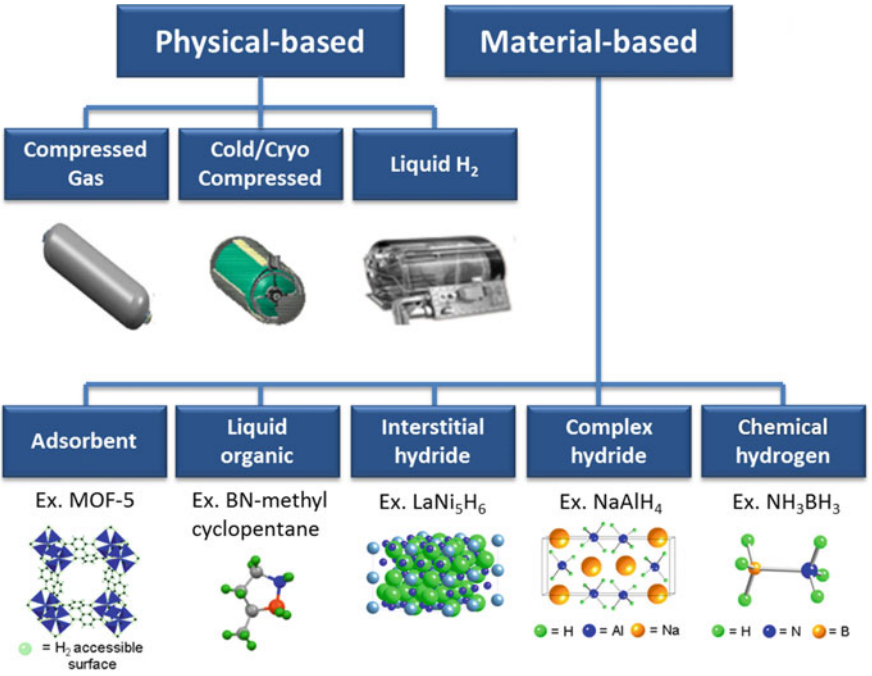

Fig. 6.2 Diverse hydrogen storage methods. *Source* Energy.gov

capacities in terms of volumetric (40 g/L) and gravimetric (5.5 wt%) by 2020 for onboard applications in automobile industry [15]. Carbonaceous materials such as carbon nanotubes (CNTs), graphene, and fullerenes are some of the most promising physical adsorbents for storing hydrogen at non-cryogenic temperatures especially at room temperature [16]. Large surface area, superior chemical and physical properties like hollowness prompt the CNTs as elite entities for promoting hydrogen storage [17–20]. One of the drawbacks of bare CNTs is that the interaction with molecular hydrogen (H_2) is very weak and consequently the uptake of H_2 is not in the appreciable amount. In order to get the high volumetric and gravimetric densities as well as improved binding of CNTs with H_2, numerous studies have been conducted toward enhancement of porosity, surface area, and number of defects by surface functionalization of CNTs [21, 22]. One of the approaches for improving the hydrogen storage efficacy of CNTs is decoration with metal nanoparticles which strengthens the hydrogen–substrate interaction and facilitates the H_2 spillover to CNTs [23–25].

Many studies revealed that the hydrogen storage capacity could be significantly enhanced by incorporating different metals such as Pd, Co, Cu, Fe, Ni, and Ti on MWCNTs at ambient conditions [26, 27]. The hydrogen storage capacity of metal-MWCNTs has been investigated by using an electrochemical hydrogen storage technique. So, after doping the Fe nanoparticles, the hydrogen storage capacity was

enhanced to 0.75 wt% from pristine 0.3 wt% at ambient conditions. Nanocomposites of metal oxides and hydrides also examined for hydrogen uptake. Nanocomposites, MgH_2 and Cr_2O_3, adsorbed 5.2 wt% of hydrogen at 598 K, $LiAlH_4$ and Cr_2O_3 adsorbed 1.9 wt% hydrogen at 448 K [28, 29]. Nickel (Ni) nanoparticles decorated on MWCNTs through functionalization adsorbed 0.87 wt% of hydrogen at 298 K and 100 bar [30]. The hydrogen uptake of MWCNTs had increased 25-folds at 298 K and 16 bar after decorating titanium (Ti) nanoparticles on surface and reached about 2.0 wt% [31]. The spillover effect of Ti increased the H_2 storage ability of MWCNTs. Rather and Hwang have prepared the composite by two different methods, namely ball milling and sputtering, and compared the H_2 storage in the composites prepared from both methods. The H_2 storage was 0.43 and 2.0 wt% for the composites prepared by ball milling and sputtering, respectively, at 298 K and 16 bar. The enhancement of H_2 storage for the composite prepared by the sputtering method is possibly due to the smoother decoration of Ti on the outer surface of the MWCNTs than for that prepared by the ball milling method. The study describes the importance of preparation method in the storage of H_2. Recent reports show that hydrogen storage capacity of MWCNTs had enhanced tenfold at 298 K and ~23 bar after adding cobalt oxide and copper oxide catalyst [32]. The deposition of ultra-fine Co and Cu oxide particles on the outer surfaces of the MWCNTs improved the storage abilities compared to that of pristine MWCNTs. The H_2 storage capacities were 0.8 wt% and 0.9 wt% for Co oxide/MWCNTs and Cu oxide/MWCNTs, respectively, at 298 K and ~23 atm. The spillover mechanism due to embedded Co oxide and Cu oxide on the MWCNTs resulted in the enhancement of storage capacities tenfold for pristine MWCNTs (0.09 wt%) under the same experimental conditions. Studies from the literature showed that experimental conditions such as solvent and metal concentration could play an important role in decorating metal or metal oxide nanoparticles on MWCNTs for uptake of hydrogen [33–36].

6.2 Methods

6.2.1 Functionalization and Synthesis of Metal Decorated MWCNTs

The decoration of multi-walled carbon nanotubes (MWCNTs) with metal/metal oxide nanoparticles is done either by physical mixing through ball milling [37] or chemical process [38]. In contrast to physical method, the chemical method gives reproducible results. Surface modification of carbon nanotube by functionalizing with carboxylic and hydroxyl groups is one of the reported strategies to enhance doping with metal/metal oxide nanoparticles [39–41]. The schematic diagram shows the mechanism for the formation of metal decorated MWCNTs (M@f-MWCNTs) (Fig. 6.3).

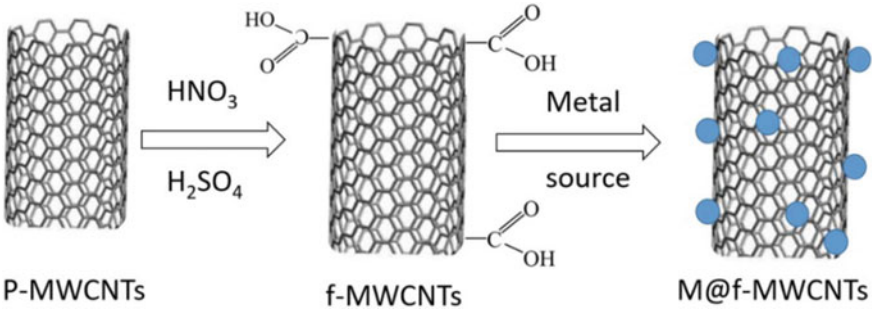

Fig. 6.3 Schematic diagram shows the metal decoration on f-MWCNTs

The raw MWCNTs were placed in a silica crucible and calcined in the furnace at 773–793 K for 2 h followed by treatment with 6.0 M HCl at 368 K for 6 h. Finally, the MWCNTs were washed several times with deionized water until the pH value of the solution became neutral followed by drying overnight at 313 K to get the pristine MWCNT (p-MWCNT). For functionalization of MWCNTs, 0.3 g of the p-MWCNTs and 150 mL of nitration mixture (1:3 HNO_3 and H_2SO_4) were refluxed under magnetic stirring for 48 h. The resulting solid was filtered and washed up to neutral pH, and the sample was dried overnight in vacuum at 313 K. For synthesis of metal oxide nanoparticle decorated f-MWCNTs, 200 mg of carboxylate functionalized MWCNTs (f-MWCNTs) and 0.02 mol [7.36 g of $Ti(NO_3)_4{\cdot}4H_2O$/8.00 g of $Cr(NO_3)_3{\cdot}9H_2O$/8.08 g of $Fe(NO_3)_3$/4.83 g of $Cu(NO_3)_2$/5.94 g of $Zn(NO_3)_2{\cdot}6H_2O$, high metal concentration (HMC)] or 0.01 mol [3.67 g of $Ti(NO_3)_4{\cdot}4H_2O$/4.00 g of $Cr(NO_3)_3{\cdot}9H_2O$/4.04 g $Fe(NO_3)_3$/2.42 g of $Cu(NO_3)_2$/2.97 g of $Zn(NO_3)_2{\cdot}6H_2O$, low metal concentrations (LMC)], were taken in a 500 mL round-bottomed flask. To this, 150 mL distilled water/150 mL distilled water containing 0.5 mL triethyl amine (TEA)/150 mL dimethyl formamide (DMF) was mixed thoroughly and heated at 353 K for 6 h (solution pH of aqueous medium was ~7.0 and TEA medium was ~10.0). The resulting solid was washed till the pH was neutral. The sample was dried overnight in vacuum at 313 K.

The morphology/texture of the obtained compounds p-MWCNTs, f-MWCNT, and M@f-MWCNTs was examined using FEI Quanta 200 FEG scanning electron microscope (SEM) and Philips CM200 transmission electron microscope (TEM). Diffraction patterns were recorded by using PANalytical X'Pert PRO powder X-ray diffractometer with graphite monochromatic CuKα ($\lambda = 1.5406$ Å) radiation at room temperature. The specific surface area was determined according to the Brunauer–Emmett–Teller (BET) method using Quantachrome NOVA 1200e.

The high-pressure hydrogen adsorption measurements for the synthesized materials were conducted on BELSORP-HP (BEL, Japan). Initially, the material was heated thoroughly under dynamic vacuum at different temperatures for long time until the outgas rate was stable in the instrument. After activating the material for long time, the weight of the sample was calculated again and the difference between the two weights could give an idea for the assessment of evacuation of solvent

guest molecules from the pores. Then, the material's hydrogen storage capacity was measured at different temperatures (253 and 298 K) and pressures up to 70 bar. An ultra-pure (99.9999%) helium and hydrogen gases were used for the measurements to get accurate results.

6.2.2 Morphology and Texture

The morphology of the p-MWCNTs, f-MWCNTs, and metal oxide (TiO_2, Cr_2O_3, Fe_2O_3, CuO, and ZnO) decorated MWCNTs (M@f-MWCNTs) has been examined through scanning electron microscopy (SEM) and transmission electron microscopy (TEM). The morphology of p-MWCNTs was examined by SEM is shown in Fig. 6.4a. Tangled tubes with diameters of 20–40 nm of p-MWCNTs were observed. Furthermore, the morphology of MWCNTs before and after carboxylate functionalization was also examined through TEM. The TEM image of p-MWCNTs is shown in Fig. 6.4b. The average diameter of carbon nanotube is 30 nm. Usually, a significant decrease in tube length, change in texture, and/or an opened end-cap structure is observed in functionalized CNT synthesized by chemical oxidation methods. Careful examination of TEM images revealed that both morphology and end-cap structure of carbon nanotubes with the average diameter of CNTs about 30 nm were well-reserved in f-MWCNTs after functionalization (Fig. 6.5). As shown in Fig. 6.5, the inner and outer diameters of MWCNTs were found to be around 7 and 19 nm, respectively.

To identify the optimum conditions required for designing the materials with efficient hydrogen storage properties, a number of chemical reactions were conducted by changing the reaction media (water/amine/DMF) and metal concentration for decorating the carboxylate functionalized MWCNTs with TiO_2 nanoparticles. As shown in SEM and TEM images (Fig. 6.6a, b), TiO_2 nanoparticles of various sizes, about

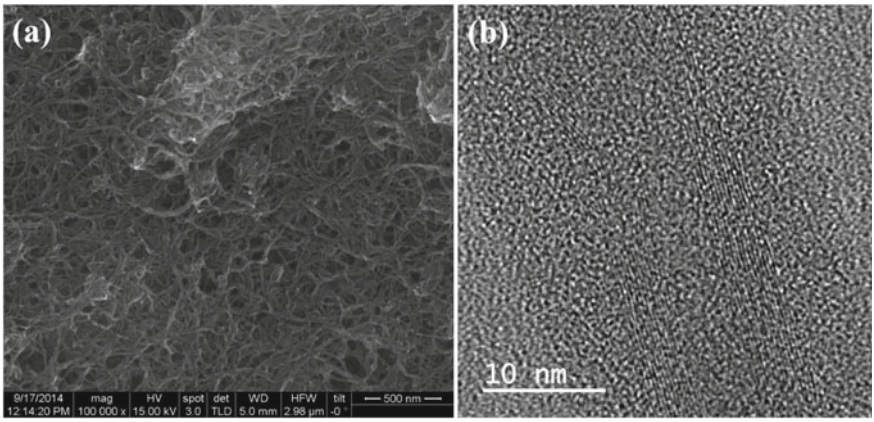

Fig. 6.4 **a** SEM image and **b** TEM images of p-MWCNTs

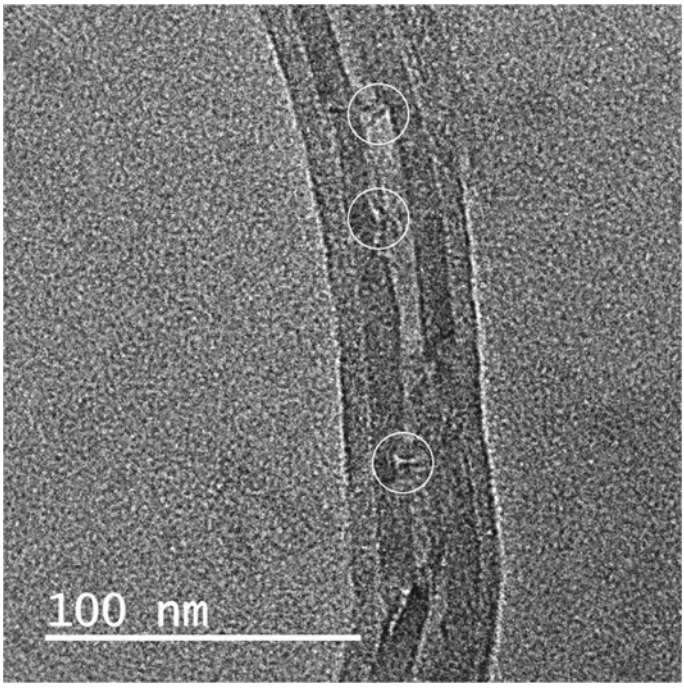

Fig. 6.5 TEM image of f-MWCNTs (encircled: attachment of functional groups on CNT)

50–60 and 10–15 nm, are attached to the outer surface of f-MWCNTs. Elemental composition of TiO_2@f-MWCNTs sample was analyzed through SEM–EDX. As shown in Fig. 6.6c, the presence of C, O, and Ti elements from EDX analysis confirms the presence of the dopant, titanium oxide nanoparticles (16.0 wt%).

Similarly, the carboxylate functionalized MWCNTs were decorated with nanoparticles of Cr_2O_3 through the soft chemical approach. To identify the optimum conditions required for designing the materials with efficient hydrogen storage properties, a number of chemical reactions were conducted by changing the reacting media and the metal concentration for decorating the carboxylate functionalized MWCNTs. As shown in TEM and SEM images (Fig. 6.7a, b), nanoparticles of Cr_2O_3 about 5–10 nm in size are decorated on the surface of f-MWCNTs. Recently, Chen group [42] reported that Cr_2O_3 nanoparticles with size range from 5 to 10 nm are evenly decorated on the surface of the MWCNTs when synthesized though hydrothermal/annealed at 180 and 500 °C. EDX analysis of Cr_2O_3@f-MWCNTs was shown in Fig. 6.7c. These results showed that the presence of Cr, C, and O content confirms the formation of Cr_2O_3 on f-MWCNTs.

For metal decoration on f-MWCNT to produce Fe_2O_3@f-MWCNTs as well as to identify the optimum conditions for efficient hydrogen sorption properties, a number of chemical reactions were conducted like mentioned above. Figure 6.8a, b depicts

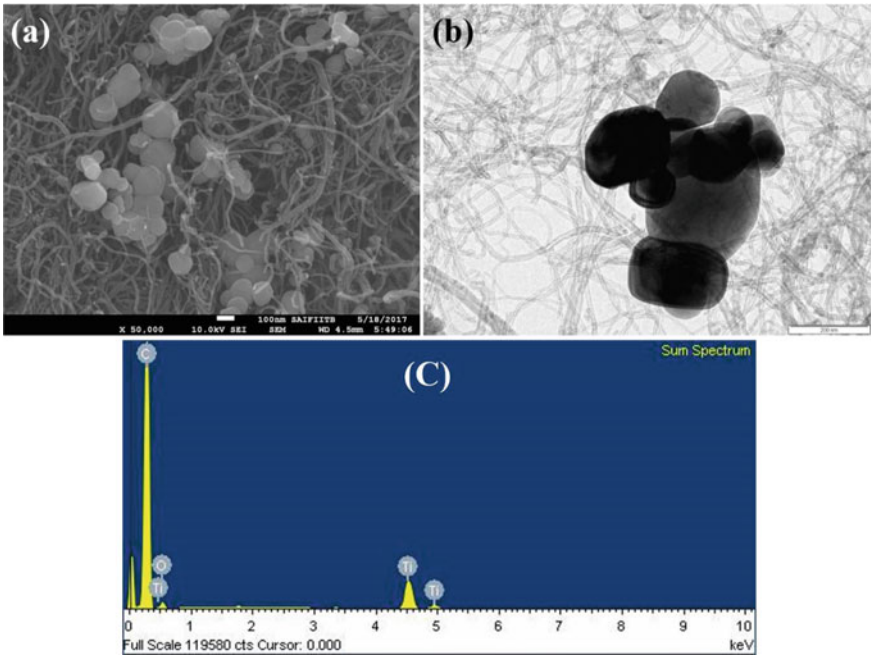

Fig. 6.6 **a** SEM image, **b** TEM image, **c** EDX analysis of TiO_2@f-MWCNTs

the SEM and TEM images of Fe_2O_3@f-MWCNTs. As shown in Fig. 6.8b, 10–20 nm sized nanoparticles of Fe_2O_3 are attached on surface of f-MWCNTs. EDX analysis was also employed to determine the metal content in the synthesized sample (Fig. 6.8c). Our results showed that the amount of Fe_2O_3 doped into the MWCNTs in DMF medium is about 26.83 wt% at higher metal concentration (HMC).

Figure 6.9 depicts the SEM and TEM images of CuO nanoparticle decorated f-MWCNTs. As shown in Fig. 6.9a, b, CuO nanoparticles were attached on the outer walls of the MWCNTs. EDX analysis showed that the amount of CuO doped into the MWCNTs in DMF medium is about 53.95 wt% at HMC (Fig. 6.9c).

Similarly, to identify the optimum conditions required for designing the materials with efficient hydrogen storage properties, a number of chemical reactions were conducted by changing the reaction media and the metal concentration for decorating the carboxylate functionalized MWCNTs with ZnO nanoparticles. Figure 6.10a, b shows SEM and TEM images of ZnO@f-MWCNTs. As shown in Fig. 6.10b, 20–40 nm sized nanoparticles of ZnO are attached on surface of f-MWCNTs. EDX analysis shows the elemental composition of C, O, and Zn which confirmed the presence of the dopant of Zinc oxide nanoparticles (Fig. 6.10c). The present study reveals that the quantity of Zn doped on MWCNTs at MHC was about 0.74 wt% and at MLC was about 0.62 wt%.

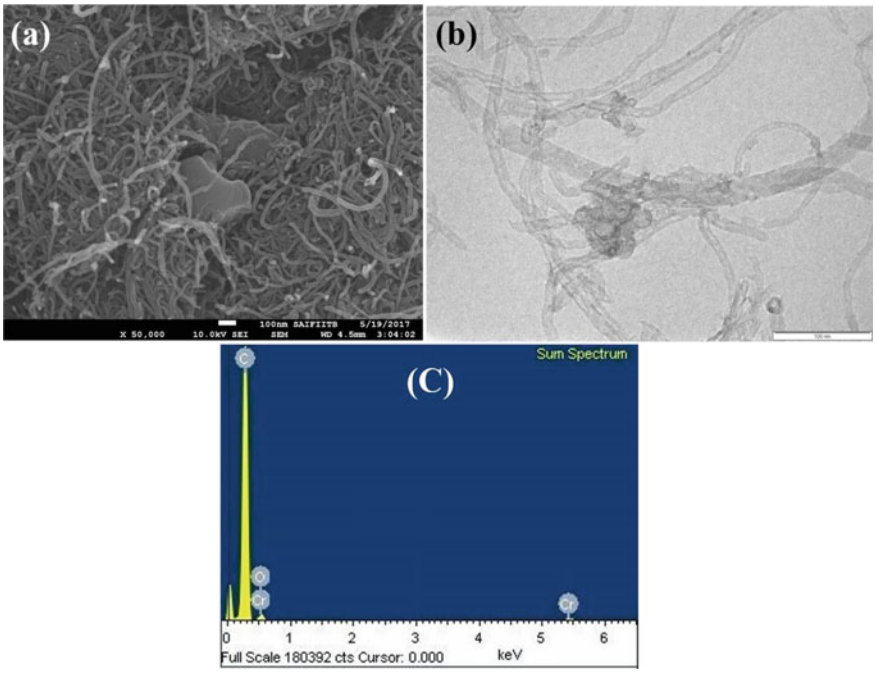

Fig. 6.7 **a** SEM image, **b** TEM image, **c** EDX analysis of Cr_2O_3@f-MWCNTs

6.2.3 Powder XRD Analysis

Powder X-ray diffraction patterns of p-MWCNTs, TiO_2@f-MWCNTs, Cr_2O_3@f-MWCNTs, Fe_2O_3@f-MWCNTs, CuO@f-MWCNTs, and ZnO@f-MWCNTs are shown in Fig. 6.11. The diffraction peaks at 25.4 and 42.9° correspond to (101) and (100) planes of graphite (JCPDS No. 01-0646) (Fig. 6.11a). For TiO_2 decorated MWCNTs (Fig. 6.11b), TiO_2 exists in two phases namely anatase and rutile. The peaks at 24.9, 37.5, 47.7, 53.5, 54.9, and 62.5° correspond to (101), (103), (200), (105), (211), and (204) planes of anatase phase of TiO_2 (major) (JCPDS No. 71-1166). Similarly, the peaks at 27.2 and 35.7 correspond to (110) and (101) planes of rutile phase of TiO_2 (minor) (JCPDS No. 73-1763). The powder XRD pattern of Cr_2O_3@f-MWCNTs is shown in Fig. 6.11c. The diffraction peaks at 18.13°, 27.6°, and 34.2° correspond to (110), (012), and (104) planes of Cr_2O_3 nanoparticles. The peaks at 13.3, 21.8, 36.5, 58.3, 60.9, 62.6° correspond to (111), (220), (311), (511), and (440) planes of iron oxide nanoparticles (Fig. 6.11d). Diffraction peaks at 34.8, 38.1, and 42.6° correspond to (111), (138), and (131) planes of CuO nanoparticles (Fig. 6.11e). The diffraction peaks at 32.0, 34.7, 36.5, 47.7, 56.8, 63.1, 68.1, and 69.2° correspond to (100), (002), (101), (102), (110), (103), (112), and (201) planes of ZnO nanoparticles (JCPDS No. 36-1451) (Fig. 6.11f).

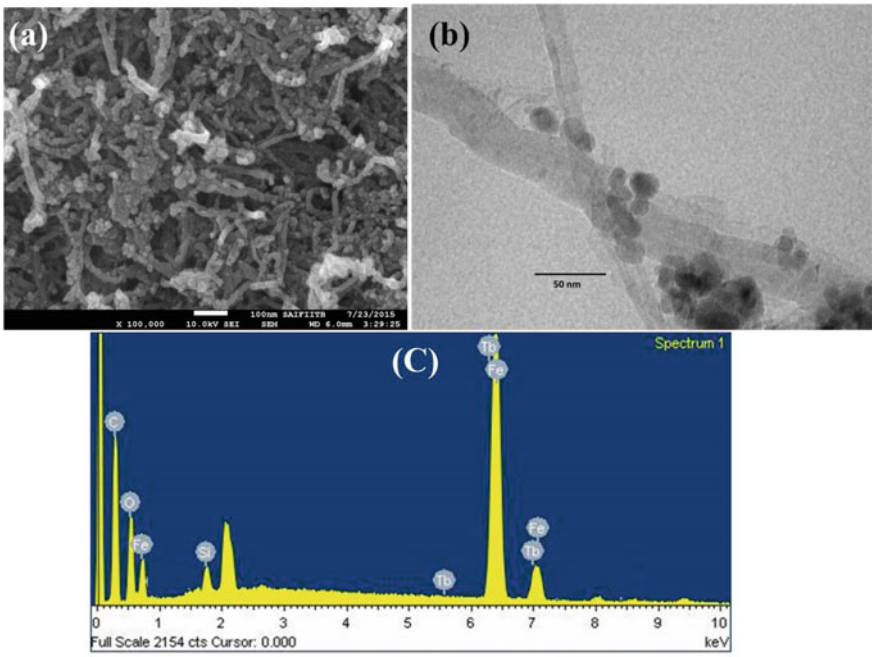

Fig. 6.8 **a** SEM image, **b** TEM image, **c** EDX analysis of Fe_2O_3@f-MWCNTs

6.2.4 Surface Area

The BET specific surface area of p-MWCNTs, f-MWCNTs, and metal decorated MWCNTs was determined by N_2 absorption measurements at 77 K. The surface area of MWCNTs may be influenced by various factors such as tube size, impurities, and surface functionalization (Fig. 6.12). The surface area of p-MWCNTs and f-MWCNTs were 360 and 236 m^2/g. This decrease in surface area is due to blocking of pores by COOH functional groups after surface functionalization of p-MWCNTs. The surface area was further reduced to 229, 212, and 14 m^2/g for TiO_2@f-MWCNTs prepared in water, amine, and DMF, respectively, after metal decoration on f-MWCNTs. Due to the blocking of pores by metal nanoparticles, the surface area is further decreased. The surface area of Cr_2O_3@f-MWCNTs prepared in water, amine, and DMF is 213, 196, 12 m^2/g, respectively. The surface area of Fe_2O_3@f-MWCNTs prepared in water, amine and DMF is 201, 206, and 18 m^2/g, respectively. The surface area of CuO@f-MWCNTs prepared in water, amine, and DMF is 226, 160, and 6 m^2/g, respectively. The surface area of ZnO@f-MWCNTs prepared in water, amine, and DMF is 218, 210, and 17 m^2/g, respectively. A low surface area observed in all cases of metal decorated MWCNTs prepared in DMF media is due to restriction of N_2 access by solvent molecules in the pores of CNTs.

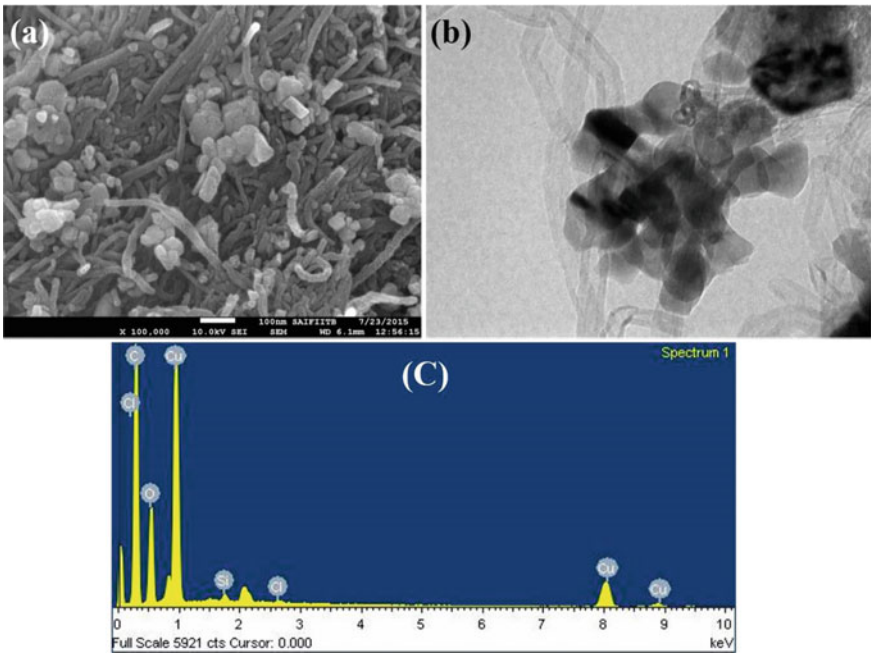

Fig. 6.9 **a** SEM image, **b** TEM image, **c** EDX analysis of CuO@f-MWCNTs

6.3 Hydrogen Storage Property

The hydrogen sorption/uptake capacity of as synthesized compounds were examined volumetrically using high-pressure sorption analyzer BELSORP-HP at non-cryogenic temperatures, i.e., 253 and 298 K. Hydrogen storage capacity of the p-MWCNTs, f-MWCNTs, and M@f-MWCNTs is presented in Table 6.1.

The hydrogen adsorption capacities of TiO_2 decorated MWCNTs along with pristine and functionalized ones were measured volumetrically at 253 and 298 K at moderate pressures of 70 bar. As hydrogen adsorption was reversible in all the samples, the desorption curves have not been shown in Fig. 6.13. The excess sorption isotherms of all the samples display a linear trend typical for monolayer adsorption on porous materials. It was observed that the hydrogen adsorption capacities of pristine and carboxylate functionalized MWCNTs at 253 K and 70 bar pressure are 0.3 and 0.09 wt%, respectively. At 298 K, the hydrogen adsorption capacities of pristine and COOH-MWCNTs are 0.12 and 0.06 wt%, respectively. TiO_2@f-MWCNTs prepared at LMC in water, triethylamine, and DMF adsorbed 0.20, 0.31, and 0.42 wt% of hydrogen (Fig. 6.13a), whereas TiO_2@f-MWCNTs prepared at HMC adsorb 0.67, 0.87, and 1.35 wt% (Fig. 6.13b), respectively, at 253 K. This result indicates that the hydrogen sorption properties drastically increase on increasing the TiO_2 nanoparticle content on the surface of f-MWCNTs. Under the LMC, a linear trend was observed in all the samples. Type III isotherm was observed for the TiO_2@f-MWCNTs prepared

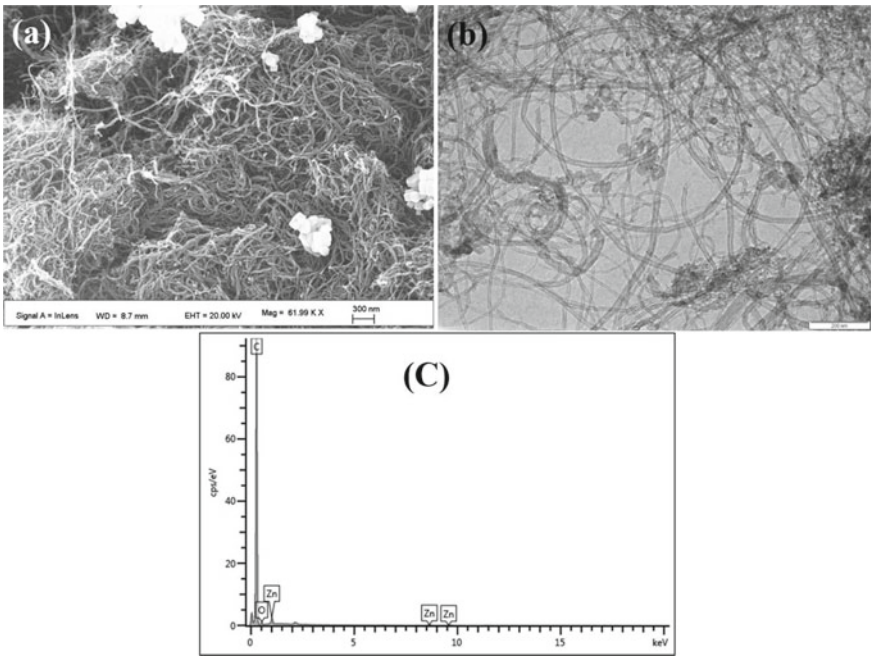

Fig. 6.10 **a** SEM image, **b** TEM image, **c** EDX analysis of ZnO@f-MWCNTs

at LMC in water and DMF due to multilayer formation. Figure 6.13c shows that the hydrogen adsorption isotherms recorded at 298 K for TiO_2@f-MWCNTs prepared at LMC in water, triethylamine, and DMF indicated 0.13, 0.17, 0.22 wt% adsorption. Similarly, TiO_2@f-MWCNTs prepared at HMC under the aforementioned reaction conditions adsorbed 0.31, 0.46, and 0.50 wt% of hydrogen (Fig. 6.13d).

The hydrogen adsorption capacities of Cr_2O_3@f-MWCNTs along with pristine and functionalized ones (p-MWCNTs, f-MWCNTs) were measured volumetrically at 253 and 298 K at moderate pressures of 70 bar. Hydrogen excess sorption isotherms for Cr_2O_3@f-MWCNTs prepared at different metal concentrations (high metal concentration (HMC) and low metal concentration (LMC)) in three different solvents, i.e., water, triethyl amine (TEA), and DMF. Cr_2O_3@f-MWCNTs prepared at (LMC) in water, triethyl amine, and DMF at 253 K adsorbs 0.18, 0.20, and 0.31 wt% of hydrogen (Fig. 6.14a) whereas Cr_2O_3@f-MWCNTs prepared at (HMC) adsorb 0.31, 0.46, and 0.52 wt% (Fig. 6.14b) of hydrogen, respectively. Figure 6.14c shows that the hydrogen adsorption isotherms recorded for Cr_2O_3@f-MWCNTs prepared at (LMC) in water, triethyl amine, and DMF at 298 K indicated 0.13, 0.16, and 0.17 wt% adsorption. Similarly, Cr_2O_3@f-MWCNTs prepared at (HMC) in the above-mentioned reaction conditions adsorbed 0.22, 0.31, and 0.45 wt% of hydrogen (Fig. 6.14d).

The hydrogen storage capacity of Fe_2O_3@f-MWCNTs prepared in water, triethyl amine (TEA), and DMF, at low metal concentration (LMC) was 0.14, 0.18, and

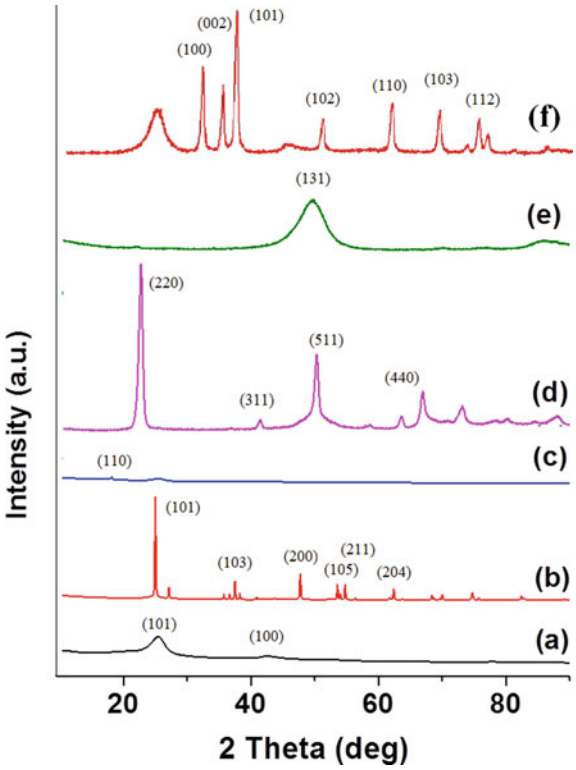

Fig. 6.11 Powder XRD patterns of **a** f-MWCNTs, **b** TiO_2@f-MWCNTs, **c** Cr_2O_3@f-MWCNTs, **d** Fe_2O_3@f-MWCNTs, **e** CuO@f-MWCNTs, **f** ZnO@f-MWCNTs

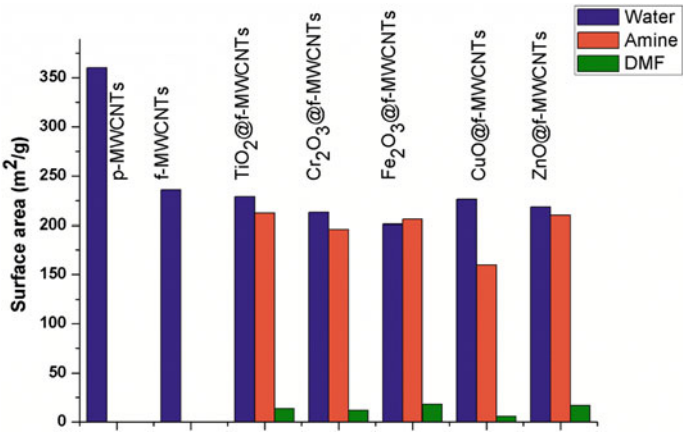

Fig. 6.12 Surface area of p-MWCNTs, f-MWCNTs, and M@f-MWCNTs

Table 6.1 Hydrogen storage capacity of metal decorated MWCNTs

Sample	H_2 storage at 253 K and 70 bar (wt%)			H_2 storage at 253 K and 70 bar (wt%)		
	Medium of sample prepared			Medium of sample prepared		
	Water	Amine	DMF	Water	Amine	DMF
Mg@f-MWCNTs	0.14[a] 0.3[b]	0.25[a] 0.55[b]	0.5[a] 0.67[b]	0.12[a] 0.18[b]	0.17[a] 0.3[b]	0.2[a] 0.45[b]
TiO_2@f-MWCNTs	0.20[a] 0.67[b]	0.31[a] 0.87[b]	0.42[a] 1.35[b]	0.13[a] 0.31[b]	0.17[a] 0.46[b]	0.22[a] 0.50[b]
Cr_2O_3@f-MWCNTs	0.18[a] 0.31[b]	0.20[a] 0.46[b]	0.31[a] 0.52[b]	0.13[a] 0.22[b]	0.16[a] 0.31[b]	0.17[a] 0.45[b]
Fe_2O_3@f-MWCNTs	0.14[a] 0.31[b]	0.18[a] 0.50[b]	0.21[a] 0.55[b]	0.13[a] 0.25[b]	0.14[a] 0.31[b]	0.18[a] 0.39[b]
CuO@f-MWCNTs	0.17[a] 0.39[b]	0.21[a] 0.50[b]	0.39[a] 0.68[b]	0.13[a] 0.31[b]	0.18[a] 0.46[b]	0.31[a] 0.50[b]
ZnO@f-MWCNTs	0.17[a] 0.47[b]	0.19[a] 0.51[b]	0.31[a] 0.87[b]	0.12[a] 0.31[b]	0.17[a] 0.50[b]	0.22[a] 0.67[b]

[a]LMC—Low metal concentration
[b]HMC—High metal concentration

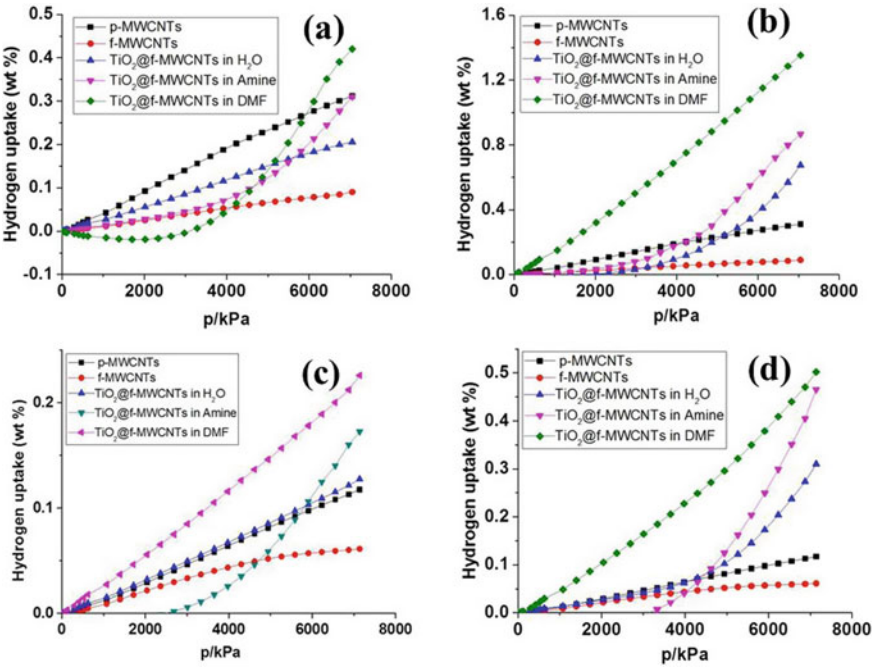

Fig. 6.13 Hydrogen uptake capacities of p-MWCNTs, f-MWCNTs, TiO_2@f-MWCNTs (**a**) at 253 K and LMC (**b**) at 253 K and HMC (**c**) at 298 K and LMC (**d**) at 298 K and HMC

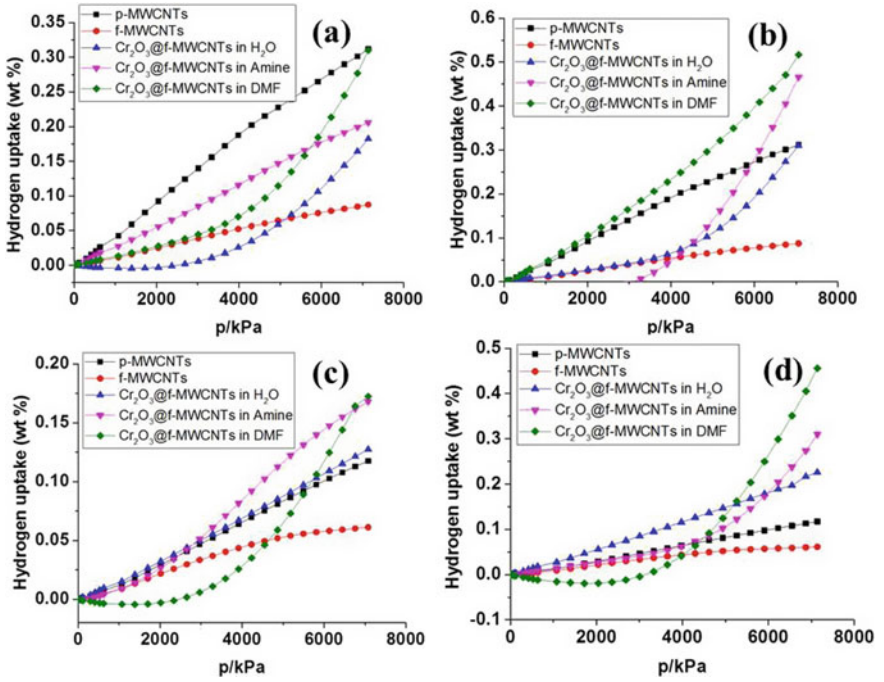

Fig. 6.14 Hydrogen uptake capacities of p-MWCNTs, f-MWCNTs, Cr_2O_3@f-MWCNTs (**a**) at 253 K and LMC (**b**) at 253 K and HMC (**c**) at 298 K and LMC (**d**) at 298 K and HMC (Reproduced with permission from Indian Chemical Society)

0.21 wt%, respectively, at 253 K (Fig. 6.15a), whereas that of prepared at higher metal concentration (HMC) as shown in Fig. 6.15b was 0.31, 0.50, and 0.55 wt%, respectively, at the same temperature, i.e., at 253 K. It was observed that the storage capacity doubled on decorating the surface of CNTs with more iron oxide nanomaterial. The hydrogen storage capacity of Fe_2O_3@f-MWCNTs prepared in water, triethyl amine (TEA), and DMF at low metal concentration (LMC) were 0.13, 0.14, and 0.18 wt%, respectively, at 298 K (Fig. 6.15c). The three materials prepared at high metal concentration (HMC) adsorbed 0.25, 0.31, and 0.39 wt%, respectively, at similar temperature (Fig. 6.15d).

The hydrogen adsorption isotherms of CuO@f-MWCNTs, prepared in water, triethylamine, and DMF, recorded at 253 and 298 K at different metal concentrations (LMC and HMC) are examined. The p-MWCNTs, f-MWCNTs, and CuO@f-MWCNTs prepared water, triethyl amine, and DMF media at LMC adsorbed 0.17, 0.21, and 0.39 wt% of hydrogen (Fig. 6.16a) whereas that prepared at HMC adsorbed 0.39, 0.5, and 0.68 wt% of hydrogen, respectively, at 253 K (Fig. 6.16b). The hydrogen adsorption isotherms of CuO@f-MWCNTs, prepared in the above-mentioned three media, i.e., water, triethyl amine, and DMF, recorded at 298 K are shown in Fig. 6.16c, d. CuO@f-MWCNTs prepared at MLC showed 0.13, 0.18,

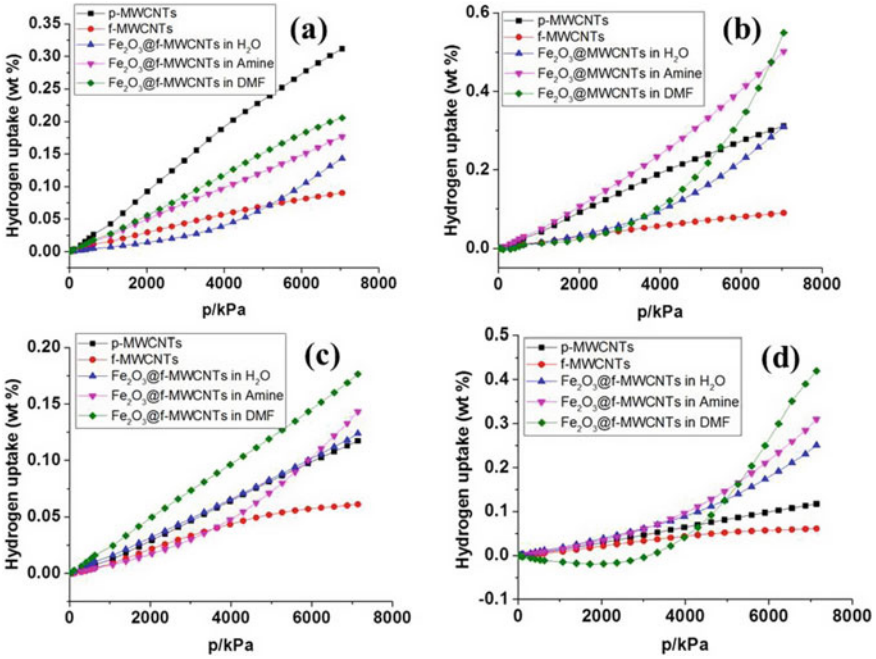

Fig. 6.15 Hydrogen uptake capacities of p-MWCNTs, f-MWCNTs, Fe_2O_3@f-MWCNTs (**a**) at 253 K and LMC (**b**) at 253 K and HMC (**c**) at 298 K and LMC (**d**) at 298 K and HMC (Reproduced with permission from Elsevier)

and 0.31 wt% of hydrogen adsorption, respectively, whereas that prepared at HMC exhibited 0.31, 0.46, and 0.50 wt% of hydrogen adsorption, respectively, at 298 K. The linear isotherm in most of the reactions confirms the monolayer adsorption.

ZnO@f-MWCNTs prepared at LMC in water, triethylamine, and DMF adsorb 0.17, 0.19, and 0.31 wt% of hydrogen (Fig. 6.17a), whereas ZnO@f-MWCNTs prepared at HMC adsorb 0.47, 0.51, and 0.87 wt% (Fig. 6.17b), respectively, at 253 K. This result indicates that the hydrogen sorption properties drastically increase on increasing the ZnO nanoparticle content on the surface of f-MWCNTs. Under the LMC, a linear trend was observed in all the samples. Type III isotherm was observed for the ZnO@f-MWCNTs prepared at LMC in water and DMF due to multilayer formation. Figure 6.17c shows that the hydrogen adsorption isotherms recorded at 298 K for ZnO@f-MWCNTs prepared at LMC in water, triethylamine, and DMF indicated 0.12, 0.17, 0.22 wt% adsorption. Similarly, ZnO@f-MWCNTs prepared at HMC under the aforementioned reaction conditions adsorbed 0.31, 0.50, and 0.67 wt% of hydrogen (Fig. 6.17d). One of the reaction media, DMF, a polar aprotic solvent plays an important role in uniform loading and decoration of ZnO nanoparticles on the surface of MWCNTs. Due to this reason, high storage of hydrogen was observed in the case of ZnO@f-MWCNTs prepared in DMF solvent. Also, the

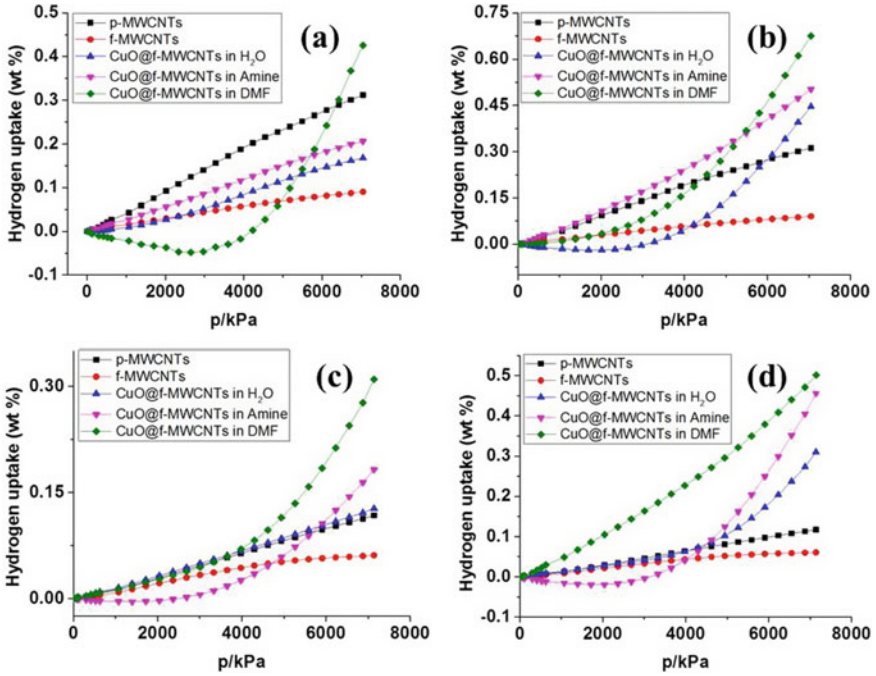

Fig. 6.16 Hydrogen uptake capacities of p-MWCNTs, f-MWCNTs, CuO@f-MWCNTs (**a**) at 253 K and LMC (**b**) at 253 K and HMC (**c**) at 298 K and LMC (**d**) at 298 K and HMC (Reproduced with permission from Elsevier)

adsorption capacity significantly increased at 253 K as compared to that observed at 298 K.

6.3.1 Hydrogen Storage Via Spillover Mechanism

Spillover is an important mechanism to identify the hydrogen adsorption on surface of adsorbents (Fig. 6.18). According to this mechanism, molecular hydrogen adsorbs initially on metal and dissociates later as atomic hydrogen which subsequently migrates to spillover receptor, CNT and enhances the hydrogen storage. The binding energy is the key parameter for ideal adsorption of hydrogen. The essential binding energy for effective hydrogen storage lies between 0.2 and 0.4 eV. In this study, the binding energy calculated for the release of hydrogen was between 0.42 and 0.56 eV. Thus, the hydrogen is attached to the adsorbent by in weak chemical binding rather than chemisorption binding, which requires a larger binding energy (1–10 eV) [43, 44].

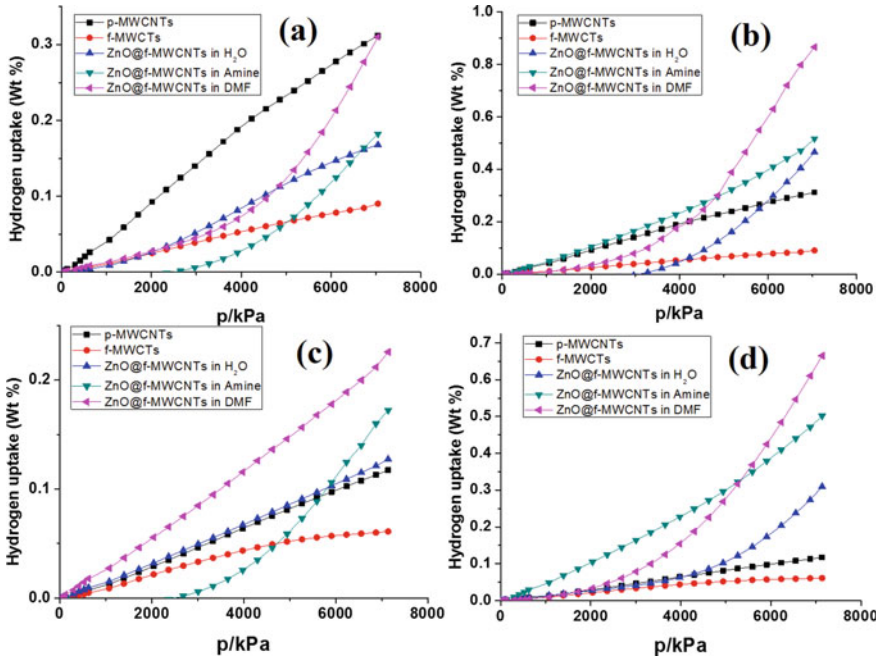

Fig. 6.17 Hydrogen uptake capacities of p-MWCNTs, f-MWCNTs, and ZnO@f-MWCNTs (**a**) at 253 K and LMC (**b**) at 253 K and HMC (**c**) at 298 K and LMC (**d**) at 298 K and HMC (Reproduced with permission from Royal Society of Chemistry)

6.3.2 Cyclic Performance of Adsorption/Desorption of Hydrogen

Cyclic adsorption/desorption performance of hydrogen is the key to evaluate the stability and reusability of material for onboard vehicle applications [26, 45, 46]. So, the selected materials have been examined for multi-cycle test to study the stability and reusability. Every cycle starts with the full evacuation of the chamber to remove the remaining hydrogen. Multi-cycles of adsorption/desorption of hydrogen on the surface of the copper nanoparticle decorated MWCNTs (CuO@f-MWCNTs) which are prepared in DMF media have been examined at 298 K. The adsorption/desorption isotherm is stabilized after 5 cycle measurements and loss in hydrogen storage capacity of about 2.0% was noticed (Fig. 6.19).

Similarly, multi-cycles of adsorption/desorption of hydrogen on the surface of the ZnO nanoparticle decorated MWCNTs (ZnO@f-MWCNTs) which are prepared in triethyl amine media were also examined at 298 K. As shown in Fig. 6.20, the adsorption and desorption isotherm is stabilized after 5 cycle measurements and loss in hydrogen storage capacity of about 6.0% was noticed [36]. So, CuO@f-MWCNTs and ZnO@f-MWCNTs display stable adsorption/desorption of hydrogen.

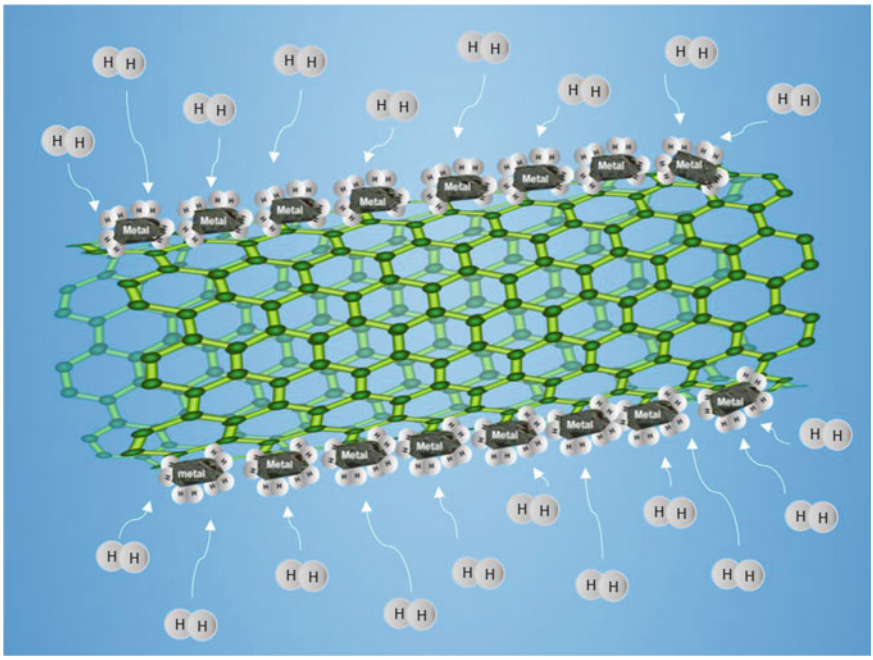

Fig. 6.18 Spillover mechanism of hydrogen storage

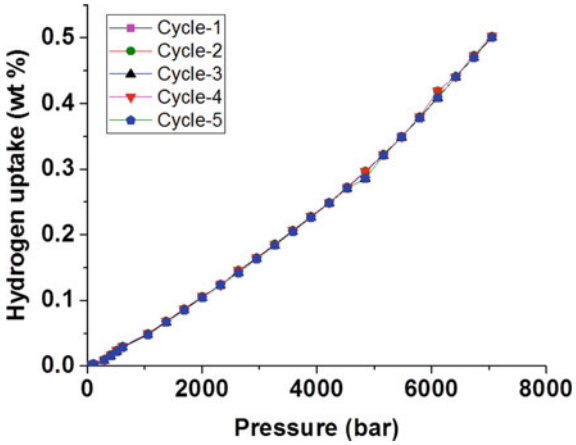

Fig. 6.19 Cyclic life performance of CuO@f-MWCNTs at 298 K

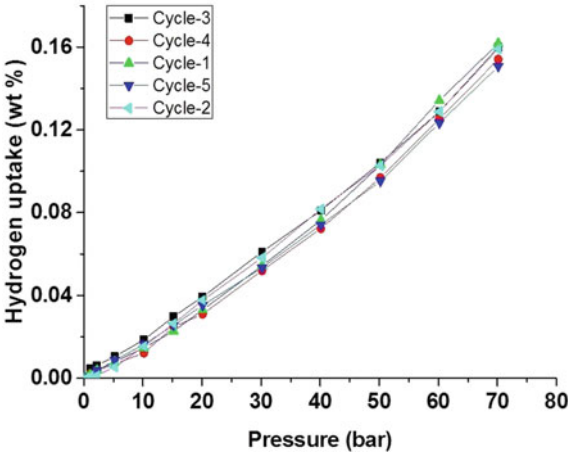

Fig. 6.20 Cyclic life performance of ZnO@f-MWCNTs at 298 K. (Reproduced with permission from Royal Society of Chemistry)

6.4 Conclusions

In conclusion, a substance-based hydrogen storage system using MWCNTs has been investigated. Among carbon materials, carbon nanotubes (SWCNTs and MWCNTs) are actually one of the most promising components for hydrogen storage because of their cage-like structure, high surface area, substantial pore volume, chemical steadiness, and ease of synthesis. The morphology of the synthesized samples was examined using scanning electron microscopy (SEM) and transmission electron microscopy (TEM). One of the biggest issues is usually to fill the cylindrical structure of CNTs with metals and gases. To acquire the substantial volumetric and gravimetric densities as well as better binding of H_2 to CNTs, many studies had been conducted to design effective methods for surface functionalization of CNTs using organic functional groups like carboxyl or hydroxyl to augment porosity and volume of defect. Among the strategies for bettering, the hydrogen storage usefulness of CNTs is decoration with metal nanoparticles, which will strengthen the hydrogen–base interaction and facilitates the H_2 spill to CNTs. The hydrogen storage measurements were conducted at different temperatures and pressures. The decorated metal/metal oxide decoration of nanoparticles is said to raise hydrogen storage capacity through spillover mechanism. Metal nanoparticles on CNTs dissociate the molecular hydrogen and spill it over to CNTs. In this direction, the hydrogen storage capacity of TiO_2, Cr_2O_3, Fe_2O_3, CuO, and ZnO decorated MWCNTs was examined under different experimental conditions such as variable metal concentrations (low metal concentration and high metal concentration) and solvents (water, triethylamine, and DMF) at non-cryogenic temperatures and moderate pressures.

References

1. P. Kennedy, *Preparing for the Twenty-First Century* (Vintage Publications, 2011)
2. J. Rifkin, *The Hydrogen Economy: The Creation of the Worldwide Energy Web and the Redistribution of Power on Earth*, 1st edn. (TarcherPerigee Publications, 2003)
3. E.S. Cassedy, P.Z. Grossman, *Introduction to Energy: Resources, Technology, and Society*, 2nd edn. (Cambridge University Press, Cambridge, 2017)
4. P.J. Crutzen, The "anthropocene", in *Earth System Science in the Anthropocene* (Springer, Berlin, Heidelberg, 2006)
5. R. Gelbspan, *The End of Nature and Beyond. Global Warming and Political Power* (Sage, 2005)
6. A. Demirbas, Potential applications of renewable energy sources, biomass combustion problems in boiler power systems and combustion related environmental issues. Prog. Energy Combust. Sci. **31**, 171–192 (2005)
7. A.K. Mohanty, M. Misra, L.T. Drzal, Sustainable bio-composites from renewable resources: opportunities and challenges in the green materials world. J. Polym. Environ. **10**, 19–26 (2002)
8. K. Mazloomi, C. Gomes, Hydrogen as an energy carrier: prospects and challenges. Renew. Sustain. Energy Rev. **16**, 3024–3033 (2012)
9. R.A. Patricio, A.D. Sales, E.M. Sacramento, L.C. de Lima, T.N. Veziroglu, Wind hydrogen energy system and the gradual replacement of natural gas in the State of Ceará—Brazil. Int. J. Hydrogen Energy **37**, 7355–7364 (2012)
10. S. Chaudhuri, J.T. Muckerman, First-principles study of Ti-catalyzed hydrogen chemisorption on an Al surface: a critical first step for reversible hydrogen storage in $NaAlH_4$. J. Phys. Chem. B **109**, 6952–6957 (2005)
11. C.K. Ngaw, C.E. Zhao, V.B. Wang, S. Kjelleberg, T.T.Y. Tan, Q. Zhang, S.C.J. Loo, A graphene/carbon nanotube biofilm based solar-microbial fuel device for enhanced hydrogen generation. Sustain. Energy Fuels **1**, 191–198 (2017)
12. J.O. Abe, A.P.I. Popoola, E. Ajenifuja, O.M. Popoola, Hydrogen energy, economy and storage: review and recommendation. Int. J. Hydrogen Energy **44**, 15072–15086 (2019)
13. A.A. EL Barbary, Hydrogen storage on cross stacking nanocones. Int. J. Hydrogen Energy **44**, 20099–20109 (2019)
14. A. Joakim, G. Stefan, Large-scale storage of hydrogen. Int. J. Hydrogen Energy **44**, 11901–11919 (2019)
15. DOE, *U.S. Department of Energy—Hydrogen Storage* (2018). https://energy.gov/eere/fuelcells/hydrogen-storage
16. G.E. Froudakis, Nanotubes & nanostructures. Mater. Today **14**, 7–8 (2011)
17. M. Baro, P. Nayak, T.T. Baby, S. Ramaprabhu, Green approach for the large-scale synthesis of metal/metal oxide nanoparticle decorated multiwalled carbon nanotubes. J. Mater. Chem. A **1**, 482–486 (2013)
18. Z. Lei, Z. Yinan, L. Dongfang, L. Heng, Z. Jianxun, C. Peng, L. Wanqiang, Enhanced electrochemical hydrogen storage performance of $Ti_{49}Zr_{26}Ni_{25}$ alloy by doping with Pd nanoparticles deposited MWCNTs. Solid State Sci. **94**, 138–144 (2019)
19. X.L. Ling, Y.Z. Wei, L.M. Zou, S. Xu, Preparation and characterization of hydroxylated multi-walled carbon nanotubes. Colloid Surf. A **421**, 9–15 (2013)
20. S.Z. Mortazavi, P. Parvin, A. Reyhani, R. Malekfarc, S. Mirershadi, Hydrogen storage property of laser induced Pd nanoparticle decorated multi-walled carbon nanotubes. Int. J. Hydrogen Energy **34**, 4243–4255 (2009)
21. W. Song, C. Jeon, M. Kim, Y.T. Kwon, D.S. Jung, S.Y. Kim, The decoration of multi-walled carbon nanotubes with metal nanoparticles of uniform size using MeV electron beam irradiation. Carbon **49**, 1692–1698 (2011)
22. H. Xiao, S.H. Li, J.X. Cao, First-principles study of Pd-decorated carbon nanotube for hydrogen storage. Chem. Phys. Lett. **483**, 111–114 (2009)

23. S.W. Hwang, S. Rather, M. Naik, C.S. Soo, K.S. Nahm, Hydrogen uptake of multiwalled carbon nanotubes decorated with Pt–Pd alloy using thermal vapour deposition method. J. Alloy Compd. **480**, L20–L24 (2009)
24. M.R. Naresh, S. Rajashabala, R. Kannan, Hexagonal boron nitride (h-BN) nanoparticles decorated multi-walled carbon nanotubes (MWCNT) for hydrogen storage. Renew. Energy **85**, 387–394 (2016)
25. A. Reyhani, S.Z. Mortazavi, S. Mirershadi, A.N. Golikand, A.Z. Moshfegh, H_2 adsorption mechanism in Mg modified multi-walled carbon nanotubes for hydrogen storage. Int. J. Hydrogen Energy **37**, 1919–1926 (2012)
26. A. Reyhani, S.Z. Mortazavi, S. Mirershadi, A.Z. Moshfegh, P. Parvin, A.N. Golikand, Hydrogen storage in decorated multiwalled carbon nanotubes by Ca Co, Fe, Ni, and Pd nanoparticles under ambient conditions. J. Phys. Chem. C **115**, 6994–7001 (2011)
27. Z. Xiaojie, L. Zhe, Z. Xiangjun, L. Heng, S. Jing, S. Zhongmin, L. Wanqiang, Z. Jianxun, Improved electrochemical hydrogen storage properties of $Ti_{49}Zr_{26}Ni_{25}$ quasicrystal alloy by doping with Pd and MWCNTs. Int. J. Hydrogen Energy (2019). https://doi.org/10.1016/j.ijhydene.2019.01.103
28. M. Polanski, J. Bystrzycki, R.A. Varin, T. Plocinski, M. Pisarek, The effect of chromium (III) oxide (Cr_2O_3) nanopowder on the microstructure and cyclic hydrogen storage behavior of magnesium hydride (MgH_2). J. Alloys Compd. **509**, 2386–2391 (2011)
29. R. Ud-din, Q. Xuanhui, L. Ping, L. Zhang, M. Ahmad, Hydrogen sorption improvement of $LiAlH_4$ catalyzed by Nb_2O_5 and Cr_2O_3 nanoparticles. J. Phys. Chem. C **115**, 13088–13099 (2011)
30. Y.J. Han, S.J. Park, Influence of nickel nanoparticles on hydrogen storage behaviors of MWCNTs. Appl. Surf. Sci. **415**, 85–89 (2017)
31. S.U. Rather, S.W. Hwang, Comparative hydrogen storage study on titanium-MWCNTs composite prepared by two different methods. Int. J. Hydrogen Energy **41**, 18114–18120 (2016)
32. S.U. Rather, Hydrogen uptake of cobalt and copper oxide-multiwalled carbon nanotube composites. Int. J. Hydrogen Energy **42**, 11553–11559 (2017)
33. M. Konni, S.B. Mukkamala, Hydrogen uptake behavior of Cr_2O_3 nanoparticle decorated f-MWCNTs at non-cryogenic temperatures. J. Ind. Chem. Soc. **95**, 393–397 (2018)
34. M. Konni, N. Narayanam, A.S. Dadhich, S.B. Mukkamala, Effect of reaction media on hydrogen sorption properties of Mg decorated MWCNTs. Fuller. Nanotub. Carbon Nanostruct. **23**, 782–787 (2015)
35. M. Konni, A.S. Dadhich, S.B. Mukkamala, Impact of surface modifications on hydrogen uptake by Fe@f-MWCNTs and Cu@f-MWCNTs at non-cryogenic temperatures. Int. J. Hydrogen Energy **42**, 953–959 (2017)
36. M. Konni, A.S. Dadhich, S.B. Mukkamala, Solvent induced surface modifications on hydrogen storage performance of ZnO nanoparticle decorated MWCNTs. Sustain. Energy Fuels **2**, 466–471 (2018)
37. S.U. Rather, K.S. Nahm, Hydrogen uptake of high energy ball milled nickel-multiwalled carbon nanotube composites. Mater. Res. Bull. **49**, 525–530 (2014)
38. R. Yu, L. Chen, Q. Liu, J. Lin, K. Tan, S. Choon Ng, H.S.O. Chan, G.Q. Xu, T.S. Andy Hor, Platinum deposition on carbon nanotubes via chemical modification. Chem. Mater. **10**(3), 718–722 (1998)
39. J. Aziziani, D.C. Khoei, H. Tahermansour, K. Yadollahzadeh, V. Georgakilas, Functionalization of carboxylated multi-walled carbon nanotubes with 1, 4-phenylendiamine phenylisocynate. Fuller. Nanotub. Carbon Nanostruct. **19**, 753–760 (2011)
40. B. Fernandez-d'Arlas, A. Eceiza, Functionalization of multi-walled carbon nanotubes with urethane segments and their interaction with solvents and a polyurethane elastomer. J. Nanopart. Res. **16**, 2166–2175 (2013)
41. V. Georgakilas, A. Bourlinos, D. Gournis, T. Tsoufis, C. Trapalis, A. Mateo-Alonso, M. Prato, Multipurpose organically modified carbon nanotubes: from functionalization to nanotube composites. J. Am. Chem. Soc. **130**(27), 8733–8740 (2008)

42. B. Chen, Y. Wang, C. Li, L. Fu, X. Liu, Y. Zhu, L. Zhang, Y. Wu, A Cr_2O_3/MWCNTs composite as a superior electrode material for supercapacitor. RSC Adv. **7**, 25019–25024 (2017)
43. K.K. Gangu, S. Maddila, S.B. Mukkamala, S.B. Jonnalagadda, Characteristics of MOFs MWCNTs and graphene mediated materials for hydrogen storage: a review. J. Energy Chem. **30**, 132–144 (2019)
44. D. Silambarasan, M. Kanmani, M. Jeyanthinath, T.R. Ravindran, V. Vasu, Investigation of hydrogen storage in MWCNT–TiO_2 composite. Phys. E Low Dimens. Syst. Nanostruct. **80**, 207–211 (2016)
45. S.S. Kaye, A. Dailly, O.M. Yaghi, J.R. Long, Impact of preparation and handling on the hydrogen storage properties of Zn_4O (1,4-benzenedicarboxylate)$_3$ (MOF-5). J. Am. Chem. Soc. **129**, 14176–14177 (2007)
46. Z. Zhang, S. Xian, Q. Xia, H. Wang, Z. Li, J. Li, Enhancement of CO_2 adsorption and CO_2/N_2 selectivity on ZIF-8 via post synthetic modification. AIChE J. **59**, 2195–2206 (2013)

Chapter 7
On-Chip Carbon Nanotube Interconnects: Adaptation to Multi-gate Transistors

Subindu Kumar and Tarun Kumar Sharma

7.1 Introduction

In the last few decades, scaling or continuous miniaturization of silicon-based electronic devices have resulted in more power-efficient, faster and denser circuits. This has led to dramatic advances in electronic computation, automation, communications and various types of other applications which have affected every aspect of our lives. However, the performance evolution through scaling cannot continue forever; the ultimate silicon device size and performance have been limited by a number of technological and fundamental scientific limitations. New device technologies along with alternate materials have been suggested by the techno-scientific community round the globe to overcome this bottleneck. Carbon nanomaterials in the form of one- and two-dimension (1-D and 2-D) have emerged as a powerful and exciting material for building blocks in future integrated circuits (ICs). Carbon can be found in carbon fibers, graphite, diamond, fullerenes, carbon nanotubes and so on. The analog of CNTs are carbon fibers. In nineteenth century and after the World War II, there was a need for improvised materials possessing special properties. Thomas Alva Edison prepared the first carbon fiber which was utilized for an early model of an electric field bulb [1]. A coiled carbon resistor was prepared with the help of specially selected Japanese Kyoto bamboo filaments which could be heated for a satisfactory filament for candescent bulb. Eventually, it was later replaced by Tungsten. From 1890, research in carbon fibers continued steadily [2, 3] which became application driven in 1950s when there was a need for stiff, strong and lightweight materials with superior mechanical properties for use in aircraft. Late 1950s and 1960s, carbon whiskers were developed due to intensive activity of Aerospace Corporation, Union Carbide and other laboratories [4]. The discovery of fullerenes (C_{60}) in 1985 [5] by Harry Kroto, Jim Heath, Sean O'Brien, Robert Curl and Rick Smalley was one of

S. Kumar (✉) · T. K. Sharma
Indian Institute of Technology (ISM), Dhanbad, Jharkhand, India
e-mail: subindu@iitism.ac.in; subindu.kumar.1976@ieee.org

S. Kaneko et al. (eds.), *Carbon Related Materials*,
https://doi.org/10.1007/978-981-15-7610-2_7

the significant contributions in the subject. Curl, Kroto and Smalley were awarded the 1996 Nobel Prize in chemistry. Major breakthrough in the research of CNT is attributed to Sumio Iijima for experimentally observing CNT using transmission electron microscopy (TEM) [6]. This bridged the gap between theoretical framework of CNT and experimental observations.

The distinct types of valence bonds in a carbon atom [7, 8] are responsible for forming various types of allotropes (Fig. 7.1). While diamond and graphite are well-known 3-D structures of carbon, low-dimensional allotropes such as 2-D graphene, 1-D carbon nanotube (CNT) and 0-D fullerenes are also possible. The extraordinary physical properties of carbon nanomaterials make them exciting candidates for a variety of applications in nanoelectronics [9, 10], optics [11], spintronics [12], biological and mechanical fields [13, 14], material science [15], condense matter physics and so on. CNTs and graphene nanoribbons (GNRs) have initiated tremendous interest particularly in applications in the field of nanoelectronics, such as energy conversion devices (photovoltaic and thermoelectric devices) [16], supercapacitors [17], semiconductor nanotransistors, displays and radiation sources, electrostatic discharge (ESD) protection, nanoelectromechanical systems (NEMS), as well as interconnects [8, 18, 19].

As the most indispensable components, interconnects are used to connect various components in an IC. Running through the entire chip, interconnects are responsible for supplying clock and power supply to all on-chip individual components and functional blocks as well as transmitting data. Figure 7.2 shows the schematic representation of driver-interconnect system, where the interconnections may be copper or carbon-based graphene, single or multi-walled CNT. For the last few decades, copper has been serving as the mainstream material for on-chip interconnects. However, due to scaling, there has been an increase in the surface scattering which has resulted in an increase in the resistivity of copper, and hence latency (product of resistance and capacitance) which is a measure of delay incorporated in interconnects. The

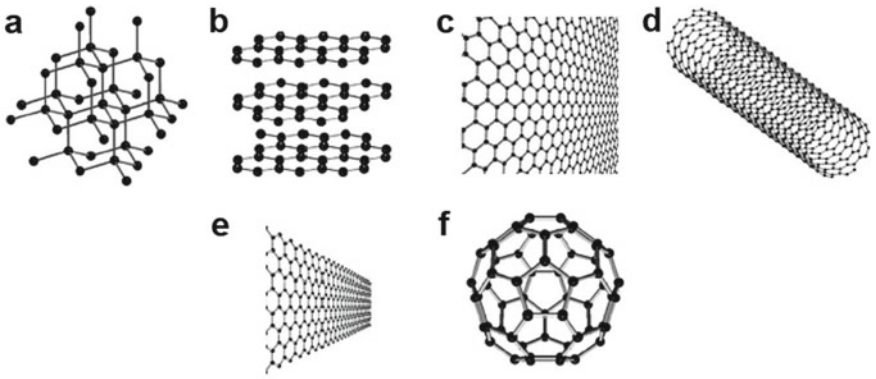

Fig. 7.1 Few allotropes of carbon. **a** 3-D diamond, **b** 3-D graphite, **c** 2-D graphene, **d** 1-D nanotube, **e** 1-D nanoribbon and **f** 0-D fullerenes

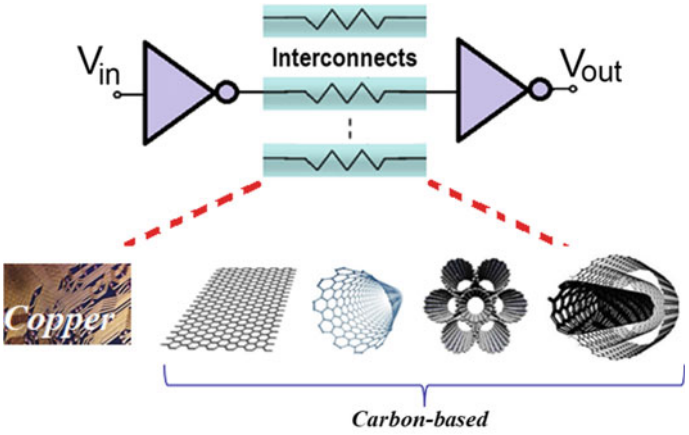

Fig. 7.2 Schematic representation of driver-interconnect system

increase in the current density due to miniaturization has also led copper to suffer from hillock formation and increased electromigration. On the other hand, the 1-D nature of CNTs offers excellent electrical properties such as large momentum relaxation time or mean free path, almost equal charge carrier densities for electrons and holes ($n_e \approx n_h \approx 7 \times 10^{18}$ atoms/cm^3), high mobilities (in the order of 10^4 cm^2/V-s @ room temperature and 10^6 cm^2/V-s @ 4.2 k), high current carrying capacity as compared to copper and so on. These unique properties make CNT a promising post-copper material for on-chip interconnects. On the other hand, multi-gate transistors (MGTs) [20] have helped the semiconductor industry to realize circuits with enhanced performance. Gate-all-around (GAA) field-effect transistors (FETs) have been considered to be the most effective architecture among all MGTs. Driver circuits (Fig. 7.2) utilizing such devices are expected to enhance the electrical performance of on-chip interconnects to a large extend [21]. This demands for an exploration of the adaptability of MGTs with CNT interconnects.

In this chapter, initially, we have focused on the structural and some essential electronic properties of single-walled CNT (SWCNT) which may be helpful for the readers to understand the various parasitic components offered by the nanotube during transmission of signal. A physics-based analysis has been carried out for GAA FETs, highlighting some important electrical aspects which make them most suitable for circuits driving CNT interconnects. Finally, we have presented few results of our computations involving device-circuit co-simulation to explore the possibilities of enhancing the performance of SWCNT interconnects. Effects of GAA device variability on interconnect delay have also been discussed.

7.2 Electronic Properties of CNT

Listed at the top of IVth column of periodic table, each carbon atom has six electrons with orbitals $1s^2$, $2s^2$ and $2p^2$. $1s^2$ forms the two strongly bounded core electrons, while $2s^2$ and $2p^2$ are weakly bounded valence electrons [7]. Valence electrons in the crystalline phase give rise to $2s$, $2p_x$, $2p_y$ and $2p_z$ orbitals. This is important in forming covalent bonds in carbon materials. The binding energy of chemical bonds is larger than the energy difference between $2p$ and lower $2s$ level. The binding energy of carbon atom with its neighboring atoms gets enhanced since the occupation of $2s$ and $2p$ gets changed due to readily mixing of the electronic wave functions of four electrons. This mixing of $2s$ and $2p$ orbitals results in sp^n hybridizations. sp (acetylene), sp^2 (polyacetylene) and sp^3 (methane) are some commonly known hybridizations. Various isomers of carbon include 0-D (C_{60}: sp^2), 1-D (nanotube: sp^2 (sp)), 2-D (sp^2: graphene) and 3-D (sp^3: diamond), the electronic properties of which are semiconducting, metal or semiconducting, semiconducting and insulating, respectively.

Packed into a 2-D honeycomb lattice structure, a graphene sheet serves as the building block of CNT. A convenient way to visualize a SWCNT is by folding or wrapping a graphene sheet. To form a seamless tube in reality and in physical sense, the growth of CNT does not involve any folding phenomena; instead, it grows naturally as cylindrical structures, often with the aid of a catalyst. SWCNTs may have diameters less than 2 nm. A CNT can be considered as 1-D nanostructure if we neglect the two ends and focus on the large aspect ratio which is defined as length to diameter ratio. The small diameter of CNT confines electrons to move in one direction along the CNT length. Various types of SWCNT structure may be formed depends on the six-membered carbon hexagon ring in the honeycomb lattice relative the axis of CNT. Except for the distortion due to the curvature of CNT, the direction of hexagon can be taken almost arbitrarily without any distortion of hexagon. Even though the basic shape of CNT wall is a cylinder, the above fact provides many possible structures for CNTs such as armchair (AC), zigzag (ZZ) and chiral. Termination of each nanotubes is called 'end caps' or 'caps' which are hemispheres of fullerenes.

Figure 7.3 depicts an unrolled honeycomb of a CNT (reproduced from 7). The equator ($\overrightarrow{\mathbf{OA}}$) is perpendicular to CNT axis ($\overrightarrow{\mathbf{OB}}$). Rolling involves coinciding O with A and B with B'. $\overrightarrow{\mathbf{OA}}$ and $\overrightarrow{\mathbf{OB}}$ are called chiral vector ($\vec{\mathbf{C}}_n$) and translational vector ($\vec{\mathbf{T}}$), respectively. $\vec{\mathbf{C}}_n$ is also called the circumferential vector denoted by $\vec{\mathbf{C}}_n = n\mathbf{a_1} + m\mathbf{a_2}$, where $\mathbf{a_1}$ and $\mathbf{a_2}$ represent the unit vectors of hexagonal lattice. n and m are integers ($0 \leq |m| \leq n$) and are given by $\mathbf{a_1} = (\sqrt{3}a/2, a/2)$ and $\mathbf{a_2} = (\sqrt{3}a/2, -a/2)$. The lattice constant of 2-D graphite (graphene), $\mathbf{a}$, can be expressed as $a = |\mathbf{a_1}| = |\mathbf{a_2}| = 1.42 \times \sqrt{3} = 2.46$ Å. An armchair CNT is formed when $n = m$ with $\vec{\mathbf{C}}_n = (n, n)$. When $m = 0$, $\vec{\mathbf{C}}_n = (n, 0)$ which rise to ZZ CNT. For instance, the chiral vector for (5, 0) ZZ CNT takes the form $\vec{\mathbf{C}}_n = 5\mathbf{a_1} + 0\mathbf{a_2}$. Chiral CNT structures are characterized by $\vec{\mathbf{C}}_n = (n, m)$ with $0 < |m| < n$ due to the hexagonal structure. AC CNTs with (n, n) are always metallic while ZZ CNTs with (n, 0) are metallic when n is a multiple of 3, otherwise, semiconducting. Statistically, one-third of CNT are metallic and the

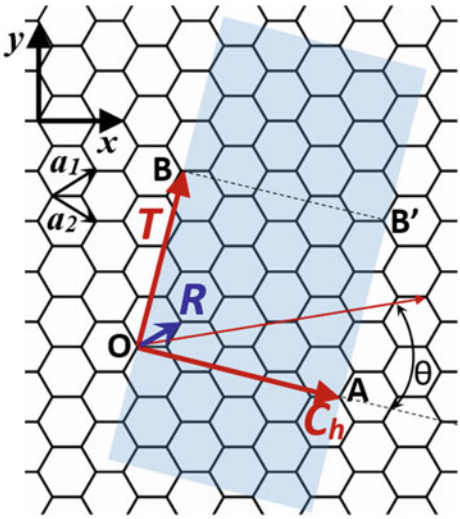

Fig. 7.3 Unrolled honeycomb lattice of a nanotube

other two-third are semiconducting for natural mixing of nanotubes. The diameter of a SWCNT can be expressed as $d_{\mathrm{CNT}} = L/\pi$; where L is the circumferential length represented as [7]

$$L = \left|\overrightarrow{C}_n\right| = \sqrt{\overrightarrow{C}_n \cdot \overrightarrow{C}_n} = a\sqrt{n^2 + m^2 + nm} \tag{7.1}$$

The unit vectors $\mathbf{a_1}$ and $\mathbf{a_2}$ are orthogonal to each other and $\mathbf{a_1} \cdot \mathbf{a_1} = \mathbf{a_2} \cdot \mathbf{a_2} = a^2$ and $\mathbf{a_1} \cdot \mathbf{a_2} = a/2$. This allows us to express d_{CNT} as

$$d_{\mathrm{CNT}} = \frac{a}{\pi}\sqrt{n^2 + m^2 + nm} \tag{7.2}$$

As shown in Fig. 7.3, and following [7], the chiral angle 'θ' is the angle between $\vec{\mathbf{C}}_n$ and $\mathbf{a_1}$ representing the tilt angle of the hexagon with respect to the direction of nanotube axis. Due to the hexagonal symmetry of the lattice, $0 \leq |\theta| \leq 30°$. In term of n and m, θ can be expressed as

$$\cos\theta = \frac{\vec{C}_n \cdot a_1}{\left|\vec{C}_n\right| \cdot |a_1|} = \frac{2n + m}{2\sqrt{n^2 + m^2 + nm}} \tag{7.3}$$

The value of θ is equal to 0° and 30° for ZZ and AC CNT, respectively, which can also be expressed in other forms as

$$\sin\theta = \frac{\sqrt{3}m}{2\sqrt{n^2 + m^2 + mn}} \tag{7.4}$$

$$\tan\theta = \frac{\sqrt{3}m}{2n+m} \tag{7.5}$$

The translational vector ($\vec{\mathbf{T}}$) is considered to be the unit vector for 1-D CNT. $\vec{\mathbf{T}}$ is normal to $\vec{\mathbf{C}}_{\mathbf{n}}$ and parallel to nanotube axis in an unrolled honeycomb lattice. $\vec{T}$ can be represented as $\vec{T} = p\mathbf{a_1} + q\mathbf{a_2}$, where p and q are integers expressed as $p = (2m+n)/d_{\text{gcd}}$ and $q = -(2n+m)/d_{\text{gcd}}$ using $\vec{C}_n \cdot \vec{T} = 0$. d_{gcd} is the greatest common divisor (GCD) of $(2n+m)$ and $(2m+n)$. Considering d as the GCD of m and n, d_{gcd} is equal to d and $3d$ if $(n-m)$ is not a multiple of $3d$ and $(n-m)$ is a multiple of $3d$, respectively. The length of $\vec{T} = \sqrt{3}L/d_{\text{gcd}}$. When $(n-m)$ is a multiple of $3d$ or (n, m) have a common divisor, the length of $\vec{T}$ gets greatly reduced. The rectangle $OAB'B$ defined by $\vec{C}_n$ and $\vec{\mathbf{T}}$ represents the unit cell of CNT. The number of hexagons (N) per unit cell is equal to $2L^2/a^2 d_{\text{gcd}}$. Each unit cell of CNT contains $2N$ number of carbon atoms, since two carbon atoms are present in each hexagon.

One of the biggest challenges in ultra giga-scale integration (UGSI) and nanoscaled circuits is on-chip interconnects because of their electromigration affects, mutual interaction resulting in cross-talk, power consumption and, most significantly, the delay. If optimally utilized, CNTs can address these challenges. This demands for major breakthrough in the techniques to form low-resistance contacts to CNTs and growing high-yield CNT arrays at preselected sites. Using pre-patterned catalyst islands on wafers and using chemical vapor deposition (CVD), significant progress has been made in growing self-assembled aligned CNT. This promising 'top-down' and 'bottom-up' approach are a challenge for UGSI. By taking advantage of the gas flow [22, 23] or by applying an electric field during CVD [24], directed growth of sparse SWCNTs has been demonstrated. Promising reports on low-resistance contacts to vertical bundles of multi-walled CNTs (MWCNTs) or isolated SWCNTs can also be found in the literature. As the growth temperature of CNTs is about 600 °C, compatibility with CMOS process is also one of the major challenges. However, there are reports of growing CNTs at 400–450 °C [25]. Despite these critical challenges, there have always been worldwide efforts to realize on-chip interconnects with sustainable CNTs.

Physical modeling of CNTs for equivalent circuit(s) has been one of the important aspects of research for almost two decades. Realizing equivalent circuits of on-chip interconnects through computer-aided design tools help the designers to predict the performance prior to fabrication. Such predictions are essential as they can help reducing almost 30% of the fabrication cost. This section is devoted to the quantitative and qualitative analysis of parasitic components associated with SWCNTs [8, 25–29], as is necessary for the development of its equivalent circuit models.

7.2.1 Resistance

The conductance of a 2-D Ohmic conductor having conductivity (σ), width (W) and length (L) can be expressed as

$$G_{2D} = \sigma \frac{W}{L} \tag{7.6}$$

CNTs can be treated as mesoscopic systems [30] possessing dimensions which are larger than microscopic objects, such as atoms, but not enough to be Ohmic. According to Landauer approach of mesoscopic transport, the probability that an electron can transmit through a conductor is a measure of the current flowing through it. Following the linear response Landauer formula [30], the conductance of CNT can be expressed as

$$G_n = \frac{2e^2}{h} \int_{x_1}^{x_2} C_n(E) \left(-\frac{\partial f_0}{\partial E} \right) dE \tag{7.7}$$

where

$$f_0(E) = \frac{1}{1 + e^{\frac{(E-E_F)}{k_B T}}} \tag{7.8}$$

is the Fermi–Dirac distribution function. E_F, k_B, T, e and h are the Fermi level, Boltzmann's constant, temperature, elementary charge and Plank's constant, respectively. x_1 (x_2) is equal to $|E_n|(+\infty)$ and $-\infty$ ($-|E_n|$) for electrons and holes, respectively. e^2/h is the fundamental quantum conductance and the factor 2 accounts for spin degeneracy. $\tau_n(E)$ is the transmission coefficient which can be influenced by defects and interactions with other phonons and electrons. The sum of the conductance of all valence and conduction bands represents the total CNT conductance which can take the form

$$G_T = \frac{2e^2}{h} M \tau_e \tag{7.9}$$

where M and τ_e represent the effective number of allowed transport channels and effective transmission coefficient, respectively. Under the assumption that two bands cross at the Fermi level in the band structure of a metallic (7, 7) SWCNT (armchair), M takes the value of 2. For a perfect metal-CNT contact, $\tau_e = 1$. This allows us to express the fundamental quantum of resistance associated with SWCNT as

$$R_Q = \frac{h}{4e^2} = 6.45\,\text{k}\Omega \tag{7.10}$$

for $L_{CNT} < \lambda_{CNT}$, where λ_{CNT} denotes the mean free path (MFP). For such lengths, the transport can be considered to be ballistic and the resistance is independent of CNT length. For the purpose of modeling, R_Q is equally divided between the two metal contacts. The nanotube is non-ballistic if $L_{CNT} > \lambda_{CNT}$ (in presence of scattering). The scattering induced imperfect transmission coefficient can be expressed as

$$\tau_e(E) = \frac{1}{1 + \frac{L_{CNT}}{\lambda_{CNT}}} \neq 1 \tag{7.11}$$

Thus, the total resistance of a SWCNT can be expressed as

$$R_{CNT} = R_C + R_Q\left(1 + \frac{L_{CNT}}{\lambda_{CNT}}\right) \tag{7.12}$$

where R_C denotes the contact resistance which arises due to the dissimilar materials present at the interface between the CNT and contact pad. Current is carried in the contact through many transverse modes, but it is limited to only few modes in CNT. This demands for current redistribution through these unequal number of modes, leading to interface (or contact) resistance which is also divided equally between the contacts, similar to R_Q. The electric field, which varies across the CNT, is larger near the contacts. As such, Eq. (7.12) can also be expressed as [26]

$$\begin{aligned} R_{CNT} &= R_C + R_Q + R_Q \int_0^{L_{CNT}} \frac{dx}{\lambda_{CNT}(x)} \\ &= R_C + R_Q + \left[R_Q \frac{L_{CNT}}{\lambda_{lb}} + \int_0^{L_{CNT}} \frac{\mathrm{d}x}{\left(\frac{I_0}{E(x)} + \frac{l_0}{R_Q}\right)} \right] \end{aligned} \tag{7.13}$$

where I_0 ($\equiv h/(4e(\hbar\Omega)) = 25\ \mu A$) is the saturation current with $\hbar\Omega \approx 0.16$ eV. l_0 can be considered to be 30 nm and λ_{lb} is the low-bias mean free path. In Eq. (7.13), the first two terms in R.H.S., $(R_C + R_Q)$, represent lumped parameters which is split off at two ends. The other term(s) in third bracket represents the distributed nature of SWCNT. Equation (7.13) can also be expressed as

$$R_{CNT} = R_C + R_{lb} + \frac{V_b}{I_0} \tag{7.14}$$

where V_b is the bias voltage and the low-bias resistance (R_{lb}) and scattering resistance (R_S) can be written as

$$R_{lb} = R_Q + R_S L_{CNT} \tag{7.15}$$

and

$$R_{\mathrm{S}}\,(\mathrm{p.u.l}) = \frac{h}{4e^2}\cdot\frac{1}{\lambda_{\mathrm{CNT}}} \tag{7.16}$$

respectively, and (p.u.l) stands for per unit length. The total SWCNT resistance for ballistic and non-ballistic transport can thus be summarized as

$$\begin{aligned} R_{\mathrm{CNT}} &= R_{\mathrm{C}} + R_{\mathrm{Q}} \quad \text{if } L_{\mathrm{CNT}} < \lambda_{\mathrm{CNT}} \\ &= R_{\mathrm{C}} + R_{\mathrm{Q}} + L_{\mathrm{CNT}} R_{\mathrm{S}} \quad \text{if } L_{\mathrm{CNT}} > \lambda_{\mathrm{CNT}} \end{aligned} \tag{7.17}$$

Due to the presence of imperfect metal-CNT contact, the resistance of an individual CNT can be high, which can be reduced by using a bundle structure consisting of current carrying parallel CNTs [27]. The Van der Waals intertube binding characterizes the minimum intertube spacing, which varies from 0.32 to 0.34 nm for SWCNT bundles.

CNT bundles may be broadly classified into two types: (1) dense and (2) sparse. For densely packed CNT, the fraction of metallic coefficient ($\mathrm{P_m}$) is considered to be unity, indicating that all CNTs in the bundle are metallic conductors. Not all nanotubes in a CNT bundle are metallic in practical reality. The presence of non-metallic CNTs in a bundle which do not take part in conduction is modeled by sparsely populated bundles where $P_{\mathrm{m}} = 1/3$ [7].

The number of CNTs in a bundle of width 'w' and height 't' along x and y directions can be represented as

$$n_x = \left\lfloor \frac{w - d_{\mathrm{CNT}}}{x_d} \right\rfloor; \quad n_y = \left\lfloor \frac{2(t - d_{\mathrm{CNT}})}{\sqrt{3}x_d} \right\rfloor + 1 \tag{7.18}$$

where x_d is the inner CNT distance which is equal to $d_{\mathrm{CNT}} + \delta$ and $\sqrt{3}d_{\mathrm{CNT}}$ for dense and sparse packing, respectively [27]. The symbol $\boldsymbol{n_{x(y)}}$ refers to the largest integer less than or equal to $n_{x(y)}$. Alternatively, Eq. (7.18) can also be written as

$$n_x = \frac{w + \delta}{d_{\mathrm{CNT}} + \delta}; \quad n_y = \frac{t + \delta}{d_{\mathrm{CNT}} + \delta} \tag{7.19}$$

The total number of CNTs in a bundle can thus be written as

$$\begin{aligned} N_{\mathrm{CNT}} &= \left[n_x n_y - \frac{n_y}{2} \right] P_m \quad \text{if } n_y \text{ is even} \\ &= \left[n_x n_y - \frac{(n_y - 1)}{2} \right] P_m \quad \text{if } n_y \text{ is odd} \end{aligned} \tag{7.20}$$

Since all CNTs in a bundle are parallel, the total resistance of a CNT bundle takes the form

$$R_{\mathrm{CNT,B}} = \frac{R_{\mathrm{CNT}}}{N_{\mathrm{CNT}}} \tag{7.21}$$

7.2.2 Capacitance

The electrochemical potential energy of a 1-D conductor, on addition of an external voltage, gets affected in two way: (1) when a charge δQ is added, the change in the electrostatic potential is given by $(\delta Q)^2/2C_E$, where C_E is the electrostatic capacitance representing the conventional macroscopic capacitance action; (2) the quantum energy states above Fermi level needs to be occupied by the charge δQ due to the low density of states (DOS). $(\delta Q)^2/2C_Q$ represents this additional quantum energy, where C_Q is the quantum capacitance. Quantitatively, these two effects can be combined together to represent the overall change in electrochemical potential as [8, 25]

$$\partial E = \frac{(\partial Q)^2}{2C_E} + \frac{(\partial Q)^2}{2C_Q} \tag{7.22}$$

The effective capacitance of 1-D conductor is the series combination of C_E and C_Q, as shown in Fig. 7.4a. Considering single spin for electrons, for 1-D conductor, the DOS at the Fermi level can be expressed as $D = 1/(\pi\hbar v_F)$, where v_F ($\approx 8 \times 10^5$ m/s) is the Fermi velocity and h ($=2\pi\hbar$) is the Plank's constant. Thus, C_Q takes the form

$$C_Q\,(\text{p.u.l}) = e^2 D = \frac{2e^2}{h v_F} = 100\,\text{aF}/\mu\text{m} \tag{7.23}$$

For 3-D conductors having large DOS, the effect of C_Q on the overall capacitance is small. Now considering two spin directions, an isolated SWCNT having two conducting sub-bands at the Fermi level with overall four conducting channels will have an effective quantum capacitance of

$$C_{Q,CNT}\,(\text{p.u.l}) = 4C_Q\,(\text{p.u.l}) = 400\,\text{aF}/\mu\text{m} \tag{7.24}$$

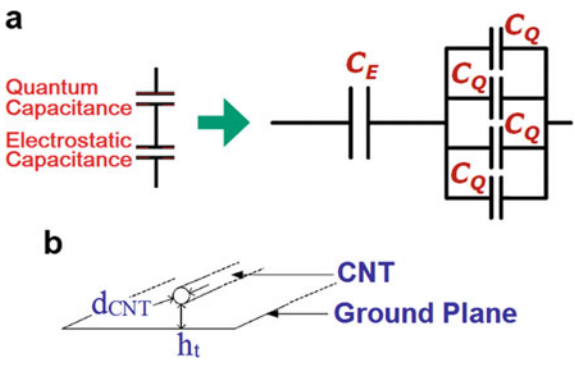

Fig. 7.4 **a** Schematic representation of parasitic capacitances (electrostatic and quantum) of an isolated SWCNT. **b** Geometry of CNT in presence of ground plane

This is pictorially represented in Fig. 7.4a. The electrostatic capacitance of a conductor having circular cross-section located at a distance of h_t above the ground (Fig. 7.4b) can be expressed as

$$C_{\mathrm{E}}\ (\mathrm{p.u.l}) = \frac{2\pi\varepsilon}{\cosh^{-1}\left(\frac{2h_t}{d_{\mathrm{CNT}}}\right)} \tag{7.25}$$

$$\approx \frac{2\pi\varepsilon}{\ln\left(\frac{h_t}{d_{\mathrm{CNT}}}\right)} \tag{7.26}$$

where $\varepsilon = \varepsilon_0\varepsilon_{\mathrm{r}}$ with ε_{r} being the relative permittivity of the material separating the nanotube from the ground plane and $\varepsilon_0 = 8.854 \times 10^{-12}$ F/m. For $h_{\mathrm{t}} > 2 - d_{\mathrm{CNT}}$, Eq. (7.25) gives fairly good approximation. Equation (7.26) should be used in such cases where $h_t > L_{\mathrm{CNT}}$. Thus, the capacitance (p.u.l) of an isolated SWCNT can be represented as

$$\frac{1}{C_{\mathrm{CNT}}} = \frac{1}{C_{\mathrm{Q}}} + \frac{1}{C_{\mathrm{E}}} \tag{7.27}$$

Taking into account the quantum capacitance of SWCNT bundle, $C_{\mathrm{Q,B}}$ ($= N_{\mathrm{CNT}}C_{\mathrm{Q}}$) and the electrostatic capacitance, $C_{\mathrm{E,B}}$, the effective bundle capacitance (p.u.l) ca be expressed as

$$\frac{1}{C_{\mathrm{CNT,B}}} = \frac{1}{C_{\mathrm{Q,B}}} + \frac{1}{C_{\mathrm{E,B}}} \tag{7.28}$$

7.2.3 Inductance

The flow of current (I) through 1-D conductor causes a net charge of energy

$$\partial E = \frac{1}{2}L_{\mathrm{K}}(\partial I)^2 + \frac{1}{2}L_{\mathrm{M}}(\partial I)^2 \tag{7.29}$$

where L_{K} and L_{M} are the kinetic and magnetic inductance, respectively (Fig. 7.5). The first term in R.H.S. of Eq. (7.29) represents the kinetic component due to low DOS in the nanotube. The second term corresponds to the conventional magnetic component which is also present in 3-D conductors. The kinetic inductance of a 1-D nanotube can be expressed as

$$L_{\mathrm{K}}\ (\mathrm{p.u.l}) = \frac{h}{2\mathrm{e}^2\nu_{\mathrm{F}}} \tag{7.30}$$

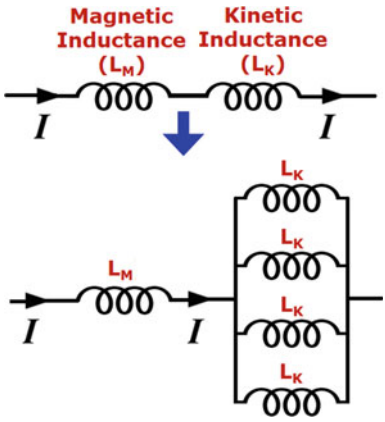

Fig. 7.5 Schematic representation of intrinsic parasitic inductances (magnetic and kinetic) of an isolated SWCNT

At high bias voltages or for $L_{CNT} \gg \lambda_{CNT}$, the kinetic energy decreases and thus L_K can be neglected. As shown in Fig. 7.5, considering four non-interacting parallel conducting channels in an isolated SWCNT, L_K and L_M can be written as

$$L_{K,CNT}\,(\text{p.u.l}) = \frac{L_K}{4} = 4\,\text{nH}/\mu\text{m} \tag{7.31}$$

and

$$L_{M,CNT}\,(\text{p.u.l}) = \frac{\mu}{2\pi}\cosh^{-1}\left(\frac{2h_t}{d_{CNT}}\right) \tag{7.32}$$

$$\approx \frac{\mu}{2\pi}\ln\left(\frac{h_t}{d_{CNT}}\right) \tag{7.33}$$

respectively. μ is the permeability of the medium separating the nanotube from the ground plane. For $h > 2d_{CNT}$, Eq. (7.33) serves as a fairly good approximation. The net inductance of SWCNT can be expressed as the summation of $L_{K,CNT}$ and $L_{M,CNT}$. Assuming that there is no mutual inductance among the nanotube and they are magnetically isolated, the overall inductance of a CNT bundle can be represented as

$$L_B\,(\text{p.u.l}) = \frac{L_{K,CNT} + L_{M,CNT}}{N_{CNT}} \tag{7.34}$$

7.3 Equivalent Circuit Model for SWCNT Bundle and Delay

Figure 7.6 represents two equivalent circuit models for SWCNT bundle which are widely used for the purpose of simulation studies. Figure 7.6a corresponds to ballistic model ($L_{CNT} < \lambda_{CNT}$) while Fig. 7.6b depicts the non-ballistic ($L_{CNT} > \lambda_{CNT}$) behavior. The total contact and quantum resistances are split in two equal halves and appear at both ends of the bundle forming the lumped elements. The resistance R_S is present in the non-ballistic model in order to account for various scattering events. R_S along with capacitance (series combination of quantum and electrostatic) and inductance (series combination of magnetic and kinetic) of the bundle forms the distributed elements. The MG FET driver circuit is characterized by the output on-resistance (R_{dr}) and output capacitance (C_p), the inclusion of which is necessary to consider the overall electrical characteristics of the system. The far end of the CNT is connected to another FET circuit whose input capacitance serves as the load for the CNT. Although we have shown only one load circuit, more than one circuit may also be connected as fan-outs and in such a situation, the total load capacitance will be the parallel combination of the input capacitances of all such fan-out MGT circuits.

The total delay associated in a logic circuit needs to take into account (1) the driver on-resistance and output capacitance, (2) intrinsic resistance and capacitance of CNT and (3) input capacitance of the FET circuit forming the load. The presence of inductance in the equivalent circuit model of SWCNT demands for an analysis considering the transmission line characteristics of the nanotube. However, it has already been established that for delay analysis, the R–C model, without inclusion of inductance can ease our computation, yet giving faithful results [27]. Nevertheless, the equivalent circuit of a SWCNT contains lumped and distributed elements. Flushing a step voltage at the input will excite the system and the time required by the output to

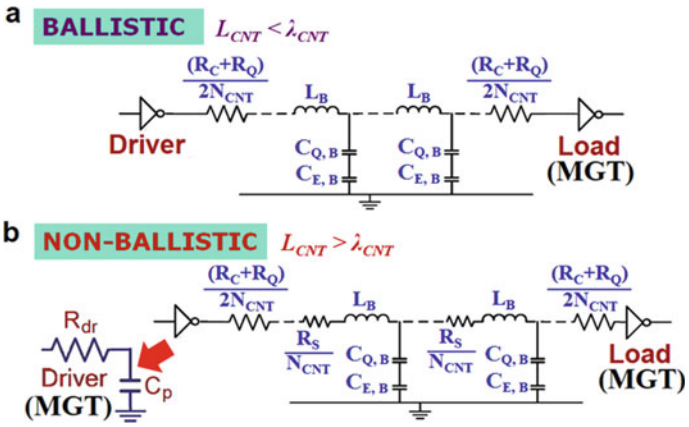

Fig. 7.6 Equivalent circuit models for SWCNT bundle in presence of MGT-based drivers and loads. **a** Ballistic and **b** non-ballistic model showing the parasitic elements of driver

reach from 0 to 50% of the final value may be treated as $T_{50\%}$ delay. As proposed in [31], a good approximation of the delay can be achieved by combining the resistive and capacitive terms and weighing them by the lumped coefficient if they are lumped and by the distributed coefficient if they are distributed. Under such approximation and using Elmore's delay, $T_{50\%}$ of SWCNT bundle with load capacitor, C_{L}, can be evaluated as

$$T_{50\%} = 0.69R_{\mathrm{dr}}(C_{\mathrm{p}} + C_{\mathrm{L}}) + 0.69\left(R_{\mathrm{dr}} + \frac{R_{\mathrm{C}} + R_{\mathrm{Q}}}{2N_{\mathrm{CNT}}}\right)C_{\mathrm{CNT,B}}L_{\mathrm{CNT}} + 0.38\frac{R_{\mathrm{S}}}{N_{\mathrm{CNT}}}C_{\mathrm{CNT,B}}L_{\mathrm{CNT}}^2 + 0.69\left(\frac{R_{\mathrm{S}}}{N_{\mathrm{CNT}}}L_{\mathrm{CNT}} + \frac{R_{\mathrm{C}} + R_{\mathrm{Q}}}{N_{\mathrm{CNT}}}\right)C_{\mathrm{L}} \quad (7.35)$$

7.4 MGT-Based Drivers for CNT Interconnects

As stated in the last section and is also amply clear from Eq. (7.35), the electrical performance of CNT depends on the driver resistance and output capacitance. A classical field-effect device (Fig. 7.7a) has four terminals: source (*S*), gate (*G*), drain (*D*) and substrate/body (*B*). Application of an appropriate voltage at the gate induces opposite polarity charges beneath the silicon-insulator interface through field-effect action, thus, creating a channel from the source to drain region. If the '*S*' and '*D*'

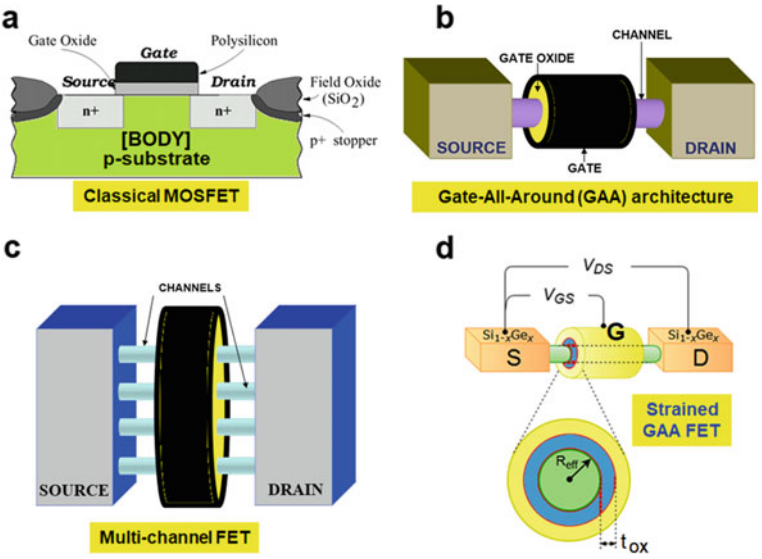

Fig. 7.7 Structure of classical and MG architecture. **a** Planar MOSFET, **b** GAA FET, **c** MC GAA FET and **d** strained GAA device

potentials are unequal, a current will flow through the channel to compensate this difference in potential. The strength of the drain current flowing through the FET depends on the electrostatic coupling between gate and channel region.

It is evident that instead of one gate, if two gates are provided back-to-back, the coupling will increase. Such a structure is the basis of double-gate device. Increasing the number of gates to enhance the device performance leads to the formation of MG architecture [20], which is one of the categories of non-classical FETs. Gate-all-around (GAA) architecture (Fig. 7.7b) provides the highest electrostatic coupling among all MG structures and is high priority research of the present day [32–35]. The GAA FET not only furnishes the highest on-current but also minimizes short-channel effects which are inevitable in low-dimensional devices. The performance of GAA devices can further be enhanced by using multi-channel (MC) configuration (Fig. 7.7c) [34]. Using such a configuration increases the current driving capability of the device to several folds. The on-resistance decreases accordingly. The drastic reduction in the device on-resistance makes GAA FETs to be utilized in driver circuits in interconnect technology.

Strain has been serving as one of the technological boosters since 90 nm technology node. Introducing such boosters in MC GAA devices (Fig. 7.7d) along with MC configuration [35] can further reduce the on-resistance, making it most suitable for driver circuits. The cross-section of GAA devices may not be circular. Due to imperfections in the fabrication processes, the ideal circular nature of cross-section may be lost and the frozen dimension may be elliptical [36] in nature with 'a' and 'b' as major and minor axes, respectively (Fig. 7.8a). Such an elliptical cross-section is characterized by aspect ratio ($AR_{GAA} = a/b$). The AR_{GAA} can lie between 0.5 and 2.0, as reported in the literature [34]. The effective diameter, d_{eff}, of such a cross-section having gate oxide thickness, t_{ox}, can be expressed as [37]

$$\frac{16\varepsilon_{ox}}{4\varepsilon_{Si}d_{eff}t_{ox} + \varepsilon_{ox}d_{eff}^2} = \frac{2\varepsilon_{ox}}{2a\varepsilon_{Si}t_{ox} + \varepsilon_{ox}a^2} + \frac{2\varepsilon_{ox}}{2b\varepsilon_{Si}t_{ox} + \varepsilon_{ox}b^2} \tag{7.36}$$

where ε_{Si} and ε_{ox} are the dielectric constants of silicon and gate oxide, respectively. Variations in AR_{GAA} change the effective diameter of the device, which is shown in Fig. 7.8b. Computations were carried out for International Technology Roadmap for Semiconductors (ITRS) 7 nm technology node [38] and using a simulator which was developed in our laboratory for strained and unstrained GAA devices [35]. The simulator takes into account the finite source and drain series resistance which cannot be neglected in nanoscaled devices. It may be worth noting that computations neglecting such series resistances result in overestimating the drain current [39]. Our simulator has been validated with experimental results as well, which justifies its use for evaluating the performance of GAA devices. The variations in the elliptical cross-section of GAA FETs introduce variability [34] in the devices, which in turn, affects the on-resistance. Computations were carried out to plot the variation of on-resistance with various aspect ratios corresponding to different GAA diameters (Fig. 7.8c) and channel lengths (Fig. 7.8d). The induced changes in on-resistance of

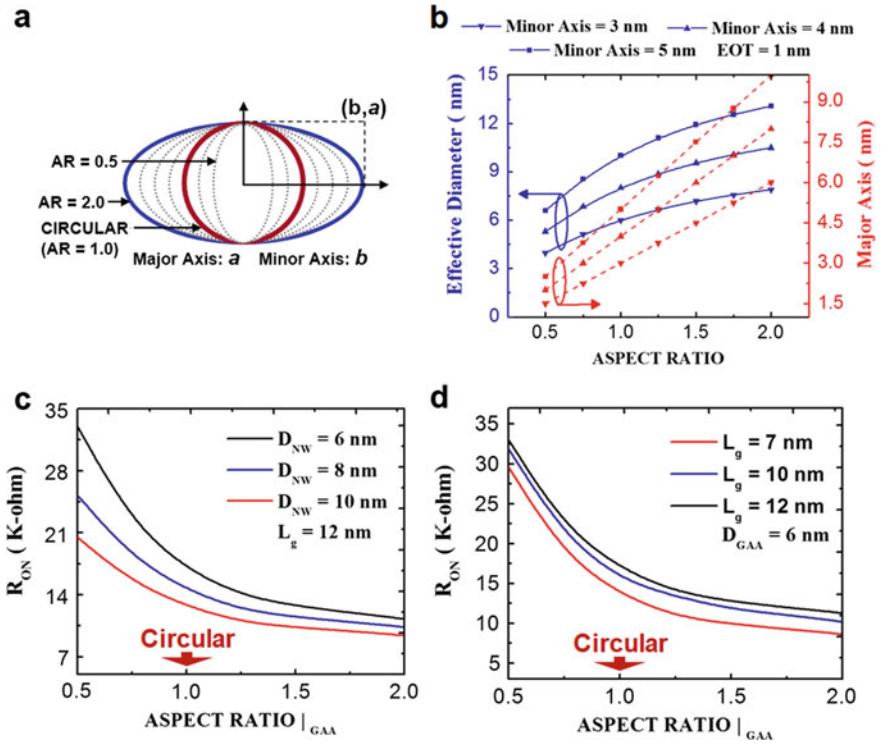

Fig. 7.8 **a** Elliptical cross-section of GAA device showing the major and minor axes. **b** Plot of effective diameter of GAA FET with device aspect ratio for different values of minor axes. Changes in major axis with AR_{GAA} are also shown in the same plot. Variation of on-resistance of GAA device with AR_{GAA} for **c** different device diameters with fixed channel length (L_g) and **d** different L_g for fixed diameter

GAA FET-based driver is bound to affect the signal delay propagating through CNT interconnects, as governed by Eq. (7.35).

7.5 Performance Enhancement of SWCNT Interconnects Using GAA Drivers

In this section, we focus on delay ($T_{50\%}$) enhancement of SWCNT interconnects driven by GAA FET-based drivers. In Fig. 7.9, we have plotted the variation of $T_{50\%}$ delay with interconnect length for ballistic transport corresponding to 14 nm technology node [8]. Three pairs of computations were carried out to explore the advantages of using GAA drivers having twin channels with $R_C = 10$ KΩ, $C_L = 0.065$ fF and $C_p = 0.03$ fF. In the first set, we have used $R_{dr} = 18.33$ KΩ which has been prescribed by ITRS. Results of our computations corresponding to dense

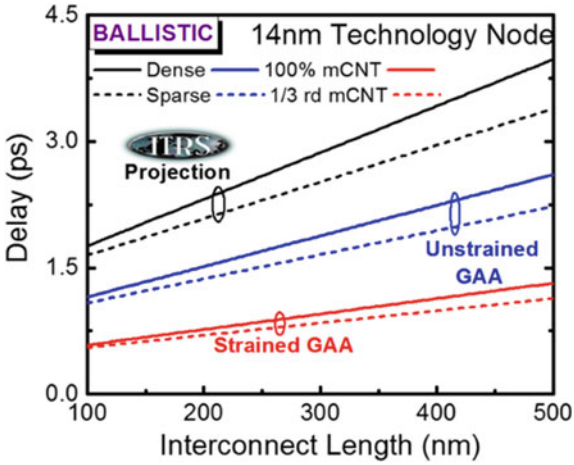

Fig. 7.9 SWCNT bundle delay ($T_{50\%}$) plotted against interconnect length for data corresponding to ITRS prescribed data, unstrained and strained GAA device data of 14 nm technology node. Results are shown for both dense (whole line) and sparse (dotted line) bundle

(whole line) and sparse (dotted line) SWCNT bundle are shown. In the second set, transistors used in the driver circuit were considered to be unstrained GAA devices, while the last set corresponds to strained GAA FETs. N_{CNT} for dense and sparse bundle has been computed to be 204 and 68, respectively. In all three pairs of data, the delay increases almost linearly with interconnect length for ballistic transport. Furthermore, due to the lowest on-resistance offered by strained GAA devices, we obtain the lowest delay. Using MGT through GAA architecture, the performance of CNT interconnects can thus be improved. The gate length, channel doping, GAA device circular diameter and series resistance have been considered to be 14 nm, 4×10^{17} cm^{-3}, 8 nm and 6.95 KΩ, respectively, in accordance with the specifications of 14 nm technology node. R_{dr} for unstrained and strained devices was estimated to be 12 KΩ and 6.05 KΩ, respectively. Regardless of the fact that dense SWCNT bundles offer less resistance path due to the presence of more number of parallel conducting channels than its sparse counterpart, the delay corresponding to dense bundle is more. Our computations reveal that although the resistance is lowered in dense bundles, the bundle capacitance increases to a large extend, thus, incorporating more delay.

Figure 7.10 shows the variation of SWCNT bundle delay ($T_{50\%}$) with the aspect ratio of unstrained GAA device corresponding to 2024 Interconnect Technology Node, 7.5 nm ASIC Macrocell [40]. Computations were carried out for GAA FETs having 2 and 20 number of channels (N_{GAA}) with $R_C = 10$ KΩ, $C_L = 0.014$ fF, $C_p = 3.5 \times 10^{-3}$ fF, $R_S = 5.079$ KΩ (for non-ballistic), $N_{CNTldense} = 63$ and $N_{CNTlsparse} = 21$. Increasing the number of channels in GAA device, decreases delay to several folds, highlighting the significance of MGT in on-chip interconnect applications. There is a monotonic decrease in delay with increasing AR_{GAA} due subsequent decrease in on-resistance of GAA transistor, as shown in the earlier section. We also observe that within the range of AR_{GAA} under consideration, the curves corresponding to dense and sparse bundles for lesser number of device channels (2 in this case), is

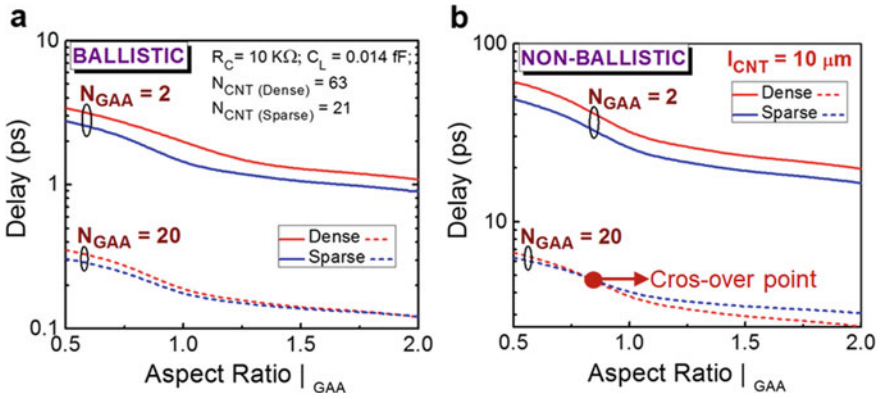

Fig. 7.10 Variation of SWCNT bundle delay ($T_{50\%}$) with AR_{GAA} for 2 and 20 number of GAA channels, corresponding to **a** ballistic and **b** non-ballistic transport. Results are shown for both dense (whole line) and sparse (dotted line) bundle. Computations are shown for 2024 Interconnect Technology Node, 7.5 nm ASIC Macrocell

well separated. However, when N_{GAA} is increased to 20, a converging nature of the curves is observed. This is more pronounced for the non-ballistic computations for the same N_{GAA}, and after a crossover point, the delay corresponding to dense bundle becomes lower than the sparse one. This could be explained as follows. There are two contesting phenomena which happen simultaneously. The resistance of the bundle decreases with increase in the device aspect ratio and number of CNTs present in the bundle. On the other hand, if the conducting CNTs in the bundle are sparsely distributed, the bundle capacitance decreases. For smaller values of AR_{GAA}, the latter dominates which lowers the delay for sparse bundle. As AR_{GAA} increases, the former becomes a dominating factor and lowers the delay for dense bundle.

Figure 7.11 illustrates the combined effects of CNT length and AR_{GAA}, for N_{GAA} = 20 corresponding to a non-ballistic condition. Such a situation can arise if the CNTs are used for local, global or semi-global interconnects. We observe that the crossover point increases with interconnect length as AR_{GAA} decreases. The crossover point determines the critical interconnect length which depends on the interconnect dimensions (technology node), AR_{GAA} and N_{GAA}. For shorter length (local interconnects), R_{dr} dominates over bundle resistance, which is reversed as the length increases.

7.6 Summary

To summarize, we have presented a detailed discussion on the structural and some electronic properties of SWCNT and its bundles which may be helpful for justifying their use as post-copper on-chip interconnects. The mesoscopic behavior of CNTs has been highlighted along with analytical expressions for determining the intrinsic

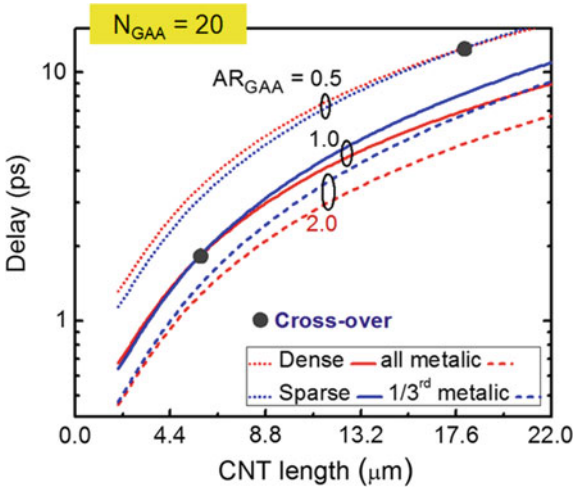

Fig. 7.11 Variation of SWCNT bundle delay ($T_{50\%}$) with interconnect length for $N_{GAA} = 20$, corresponding to $AR_{GAA} = 0.5$, 1.0 and 2.0 for 2024 Interconnect Technology Node, 7.5 nm ASIC Macrocell

parasitic elements, which serves as building blocks for the equivalent circuit models of SWCNT bundles used as interconnects. The combined performance of interconnect and driver circuit is an important issue in integrated circuits. The evolution of MGTs has improved the device performance to a large extend. GAA architecture is considered to be the most efficient structure among all MGTs. Adaptation of CNT interconnects with such devices is an active research field and also a need of the present era. In this chapter, we have tried to address this issue. We have shown that the performance of SWCNT interconnects can be enhanced to several folds using GAA devices. Using some inherent properties of GAA devices, such as, more than one channel, the device on-resistance can be reduced significantly. This, in turn, plays an important role in lowering the overall delay of the system. Deviations from the ideal circular cross-section introduce variability in GAA devices. The effects of this deviation on the delay of driver-interconnect co-system have also been presented. The optimization remains an open problem for the current scientific era.

References

1. T.A. Edison, US Patent 470 (1892), p. 925
2. P. Schützenberger, L. Schützenberger, Compt. Rend. **111**, 774 (1890)
3. C.H. Pelabon, Compt. Rend. **137**, 706 (1905)
4. R. Bacon, J. Appl. Phys. Rev. **85**, 1060 (1952)
5. H.W. Kroto et al., C_{60}: Buckminsterfullerene. Nature **318**, 162–163 (1985)
6. S. Iijima, Helical microtubules of graphitic carbon. Nature **354**(56), 6348 (1991)
7. R. Saito, G. Dresselhaus, S. Dresselhaus, *Physical Properties of Carbon Nanotubes* (Imperial College Press, London, UK, 1998)
8. H. Li et al., Carbon nanomaterials for next-generation interconnects and passives: physics, status, and prospects. IEEE Trans. Electron Devices **56**(9), 1799–1821 (2009)

9. P. Avouris, Z. Chen, V. Perebeinos, Carbon-based electronics. Nat. Nanotechnol. **2**(10), 605–613 (2007)
10. Q. Cao, J.A. Rogers, Ultrathin films of single-walled carbon nanotubes for electronics and sensors: a review of fundamental and applied aspects. Adv. Mater. **21**(1), 29–53 (2009)
11. J.A. Misewich, Electrically induced optical emission from a carbon nanotube FET. Science **300**(5620), 783–786 (2003)
12. K. Tsukagoshi, B.W. Alphenaar, H. Ago, Coherent transport of electron spin in a ferromagnetically contacted carbon nanotube. Nature **401**(6753), 572–574 (1999)
13. F. Lu et al., Advances in bioapplications of carbon nanotubes. Adv. Mater. **21**(2), 139–152 (2009)
14. M.-F. Yu et al., Strength and breaking mechanism of multiwalled carbon nanotubes under tensile load. Science **287**(5453), 637–640 (2000)
15. N. Wang et al., Materials science: single-walled 4 Å carbon nanotube arrays. Nature **408**(6808), 50–51 (2000)
16. H. Ago et al., Composites of carbon nanotubes and conjugated polymers for photovoltaic devices. Adv. Mater. **11**(15), 1281–1285 (1999)
17. C. Du, J. Yeh, N. Pan, High power density supercapacitors using locally aligned carbon nanotube electrodes. Nanotechnology **16**(4), 350–353 (2005)
18. F. Kreupl et al., Carbon nanotubes in interconnect applications. Microelectron. Eng. **64**(1–4), 399–408 (2002)
19. A. Alizadeh, R. Sarvari, Temperature-dependent comparison between delay of CNT and copper interconnects. IEEE Trans. VLSI Syst. **24**(2), 803–807 (2016)
20. J.T. Park, J.P. Colinge, Multiple-gate SOI MOSFETs: device design guidelines. IEEE Trans. Electron Devices **49**(12), 2222–2229 (2002)
21. D. Prasad et al., Adapting interconnect technology to multigate transistors for optimum performance. IEEE Trans. Electron Devices **62**(12), 3938–3944 (2015)
22. S. Huang et al., Growth mechanism of oriented long single walled carbon nanotubes using 'fast-heating' chemical vapor deposition process. Nano Lett. **4**(6), 1025–1028 (2004)
23. L. Huang et al., Long and oriented single-walled carbon nanotubes grown by ethanol chemical vapor deposition. J. Phys. Chem. B **108**(42), 16451–16456 (2004)
24. A. Ural, Y. Li, H. Dai, Electric-field-aligned growth of single-walled carbon nanotubes on surfaces. Appl. Phys. Lett. **81**(18), 3464–3466 (2002)
25. M. Nihei, et al., Low-resistance multi-walled carbon nanotube vias with parallel channel conduction of inner shells, in *Proceedings of the IEEE 2005 International Interconnect Technology Conference* (2005), pp. 234–236
26. A. Naeemi, J.D. Meindl, Design and performance modeling for single-walled carbon nanotubes as local, semiglobal, and global interconnects in gigascale integrated systems. IEEE Trans. Electron Devices **54**(1), 26–37 (2007)
27. N. Srivastava et al., On the applicability of single-walled carbon nanotubes as VLSI interconnects. IEEE Trans. Nanotechnol. **8**(4), 542–559 (2009)
28. A. Naeemi, J.D. Meindl, Physical modeling of temperature coefficient of resistance for single- and multi-wall carbon nanotube interconnects. IEEE Electron Device Lett. **28**(2), 135–138 (2007)
29. N. Srivastava, K. Banerjee, Performance analysis of carbon nanotube interconnects for VLSI applications, in *Proceedings of the IEEE/ACM International Conference on ICCAD* (2005), pp. 383–390
30. S. Datta, *Electronic Transport in Mesoscopic Systems* (Cambridge University Press, Cambridge, UK, 1995)
31. H.B. Bakoglu, *Circuits, Interconnections, and Packaging for VLSI* (Addision-Wesley, Reading, MA, 1990)
32. A. Kumar, P.K. Tiwari, An explicit unified drain current model for silicon-nanotube-based ultrathin double gate-all-around MOSFETs. IEEE Trans. Nanotechnol. **17**(6), 1224–1234 (2018)

33. A. Dasgupta et al., Compact modeling of cross-sectional scaling in gate-all-around FETs: 3-D to 1-D transition. IEEE Trans. Electron Devices **65**(3), 1094–1100 (2018)
34. S. Kumar, S. Jha, Impact of elliptical cross-section on the propagation delay of multi-channel gate-all-around MOSFET based inverters. Microelectron. J. **44**, 844–851 (2013)
35. S. Kumar, A. Kumari, M.K. Das, Modeling gate-all-around Si/SiGe MOSFETs and circuits for digital applications. J. Comput. Electron. **16**, 47–60 (2017)
36. S. Bangsaruntip, et al., High performance and highly uniform gate-all-around silicon nanowire MOSFETs with wire size dependent scaling. IEDM Tech. Dig., 297–300 (2009)
37. L. Zhang et al., Modelling short-channel effect of elliptical gate-all-around MOSFET by effective radius. IEEE Electron Device Lett. **32**(9), 1188–1190 (2011)
38. ITRS, International Technology Roadmap for Semiconductor (2015), http://www.itrs2.net. Accessed 16 Nov 2018
39. S. Kumar, A. Kumari, M.K. Das, Development of a simulator for analyzing some performance parameters of nanoscale strained silicon MOSFET-based CMOS inverters. Microelectron. J. **55**, 8–18 (2016)
40. E.K. Farahani, R. Sarvari, Design of *n*-tier multilevel interconnect architectures by using carbon nanotube interconnects. IEEE Trans. VLSI Syst. **23**(10), 2128–2134 (2014)

Chapter 8
Carbon Materials as Electrodes of Electrochemical Double-Layer Capacitors: Textural and Electrochemical Characterization

Belén Lobato

8.1 Introduction

The rapid growth of the population of contemporary society and the modernization of its infrastructure has led to an increase in the demand for energy worldwide. This situation has caused a depletion of fossil fuel resources and has had a heavy environmental impact [1].

Renewable energy resources are clean, abundant and inexhaustible. New technologies based on solar, wind, marine and biomass sources have emerged, and they will form the backbone of the future economic cycle. Based on a life cycle assessment (LCA) study [2], electrical energy generated from these sources has an impact (in terms of g_{CO2eq}/kWh) around ten times lower than that obtained from coal. Given adequate support, renewable energy technologies can meet most of the growing demand at a lower price than that envisaged for conventional energy. However, these sources are handicapped by a serious disadvantage in that they are subject to fluctuation which is independent of the existing demand. The discontinuous supply disrupts the electric grid, resulting in blackouts and damage to installations.

For this reason, the development of electrical energy storage technologies (EES) is essential for the optimal operation of these systems. There are numerous systems which are usually classified according to the mechanism via which the storage process takes place (Fig. 8.1).

Such EES systems are (i) mechanical, (ii) thermal, (iii) chemical, (iv) electrochemical or (v) electrical. Among the latter are to be found supercapacitors (SCs).

These devices are capable of both high electrical energy densities (5–10 Wh kg^{-1}) and high power densities (>10 kW kg^{-1}). Additionally, they provide a lifetime over

B. Lobato (✉)
Instituto de Ciencia y Tecnología del Carbono (INCAR)—Consejo Superior de Investigaciones Científicas (CSIC), Francisco Pintado Fe, 26, 33011 Oviedo, Spain
e-mail: belen@incar.csic.es

S. Kaneko et al. (eds.), *Carbon Related Materials*,
https://doi.org/10.1007/978-981-15-7610-2_8

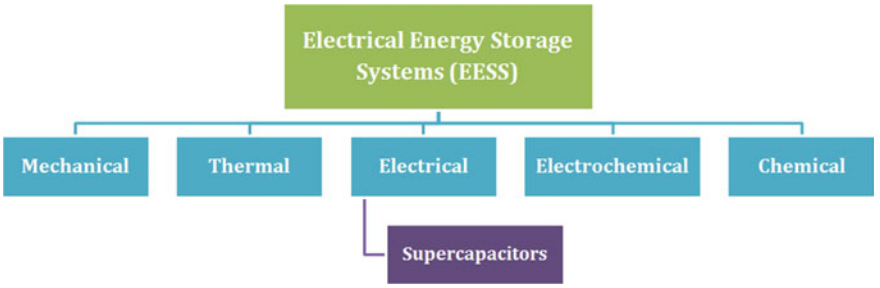

Fig. 8.1 Classification of EES technologies based on the process mechanism

one million charge–discharge cycling operations and an excellent performance over a wide range of temperatures. They also require little maintenance and are environmentally friendly. As can be seen in Fig. 8.2, supercapacitors fill the gap between dielectric capacitors and batteries and fuel cells.

Electrochemical capacitors offer a higher energy density than capacitors, albeit with slightly lower values of power density. On the other hand, compared to batteries, supercapacitors of equal size store significantly less energy although this limitation is compensated for by their ability to supply power pulses.

Despite the fact that the first patent was registered as early as 1957 [3], supercapacitors only began to be commercialized in the seventies [4] experiencing a very strong growth in the last two to three decades. According to market research studies [5, 6], the experts estimate that this technology will exhibit a compound annual growth rate (CAGR) of between 19.9 and 21.1% during the period 2016–2023 (Fig. 8.3).

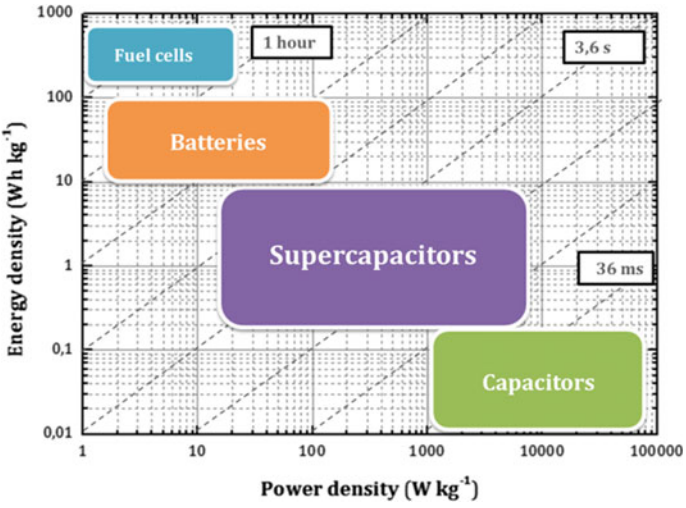

Fig. 8.2 Comparison of energy-power densities of different systems for electrical energy storage

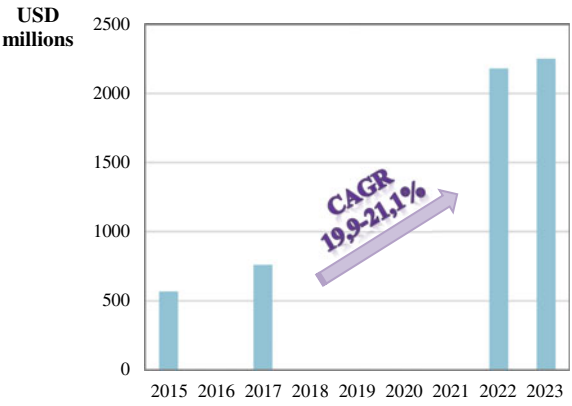

Fig. 8.3 Global supercapacitor market

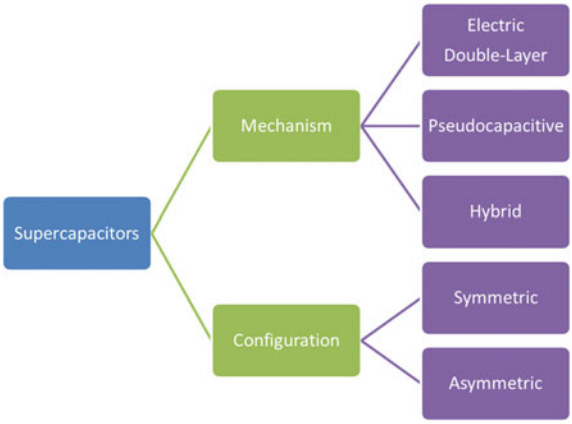

Fig. 8.4 Classification of electrochemical capacitors

Currently, supercapacitors are used in a wide variety of fields, including energy, industry, etc. Consumer electronics and transport are the most important sectors for these devices. They are essential components of uninterruptible power sources (UPS), phones, computers, solid-state drives, toys, flashlights, emergency lighting, watches, cordless screwdrivers, traffic signs, etc. However, transport is currently the most attractive segment market for SC manufacturers because of the strict regulations on fuel consumption and pollutant emissions [7]. This sector is extremely demanding in performance, reliability and safety. In stationary standby applications, electrochemical capacitors are better than alternative devices due to their outstanding power release. This segment will be the backbone of the next economic cycle. Other important niches for SC include the aerospace, military and medical industries.

- Types of supercapacitors

Supercapacitors are usually classified according to two criteria: (i) the mechanism by means of the energy is stored and (ii) their configuration, as exhibited in Fig. 8.4.

On the basis of their operational mechanism, three types can be distinguished: (i) electrochemical double-layer capacitors, (ii) pseudocapacitors and (iii) hybrid capacitors.

Electrochemical double layer capacitors (EDLC) are based on the separation of negative and positive charges generated at the electrode–electrolyte interface when a potential difference is applied to the electrodes. The electrostatic interaction between the charged electrode surface and the electrolyte ions (no faradaic reactions) leads to very fast charge–discharge processes without any serious degradation of the electrodes or electrolytes.

This chapter focuses on these devices since the majority of commercial supercapacitors employ one of these systems in which the electrodes are all made of porous carbons. These materials exhibit a high porosity and electrical conductivity, a strong resistance to corrosion and stability over a wide temperature range. Because of their low cost, activated carbons are the most competitive candidates for use in SC [8]. Depending on their porous structure and chemical features, activated carbons exhibit specific capacitances ranging from 50 to 300 F g^{-1} [9–11].

Pseudocapacitors store electrical energy through electrosorption and redox reactions or intercalation between the electrode and the electrolyte at certain potentials. The most common electrode materials in these devices are based on transition metal oxides and conducting polymers. Of the metal oxides, ruthenium oxide (RuO_2) displays the best performance with a high specific capacitance (720 F g^{-1}) and an excellent electrical conductivity (300 S cm^{-1}) [12]. However, its high price prevents its large-scale implementation. More economic alternatives are MnO_2, TiO_2, Cr_2O_3, Co_2O_3, V_2O_5, NiO, SnO_2, etc., and mixed oxides with a perovskite structure ($SrRuO_3$) or nitrides (VN) [13–18]. In parallel, research is also being carried out on the deposition of metal oxide nanoparticles upon the surface of porous materials in order to reduce the amount of oxides [19, 20].

Electroactive polymers in supercapacitors include derivatives of polypyrrole (PPy), poly (3-methylthiophene) (PT), polyethylenedioxythiophene (PEDOT) and polyaniline (PANI), which can attain capacitances of over 300 F g^{-1} [21–23].They acquire electrical conductivity of up to 500 S cm^{-1} [24]. Nevertheless, the polymers suffer from swelling and contraction during the charge and discharge which result in low cyclability. Composites of polymer-carbon with high capacitance are currently being investigated to overcome this drawback [23, 25–27].

Hybrid capacitors operate with a combination of EDL and pseudocapacitive mechanisms. This setup provides the possibility of operating at higher voltages and of achieving higher capacitances although the cycle lifespan is somewhat reduced. Supercapattery is a recent term used to describe a wide range of devices in which the charge storage mechanisms of both the supercapacitor and battery are combined into one device in order to attain a high power density in the former and a high energy density in the latter [28–30]. Sodium ion capacitors (NICs) and lithium ion capacitors (LICs) belong to this group [31, 32]. An example of the latter is the system based on $Li_4Ti_5O_{12}$/carbon composite which combines the intercalation–deintercalation of lithium ions at the anode and the adsorption–desorption of ions at the carbon cathode [33, 34].

The composition of the electrodes, in symmetric systems, is identical, whereas in asymmetric devices, the electrodes are composed of different active materials, regardless of the operating mechanism.

- EDLC: general characteristics

Schematically, an electrochemical double-layer capacitor consists of two electrodes separated by an ion-permeable membrane impregnated with an electrolyte solution which acts as an ion-conducting medium (Fig. 8.5).

This configuration shows that the system performs with each electrode acting as a capacitor, both of which are connected in series. Therefore, the overall capacitance, C_{SC}, is given by the equation:

$$\frac{1}{C_{SC}} = \frac{1}{C_{1+}} + \frac{1}{C_{2-}} \tag{8.1}$$

where C_{1+} and C_{2-} are the capacitances of the positively and negatively charged electrodes, respectively.

By analogy with a conventional capacitor, capacitance (C) in Farads (F) is defined as:

$$C = \frac{\varepsilon A}{d} \tag{8.2}$$

where ε is the dielectric constant, A is the extent of the electrolyte–electrode interface, and d is the effective thickness of the double layer (Fig. 8.5). The value of the latter parameter depends on the concentration of the electrolyte and size of the ions. In the case of concentrated solutions, d is ~5–10 Å.

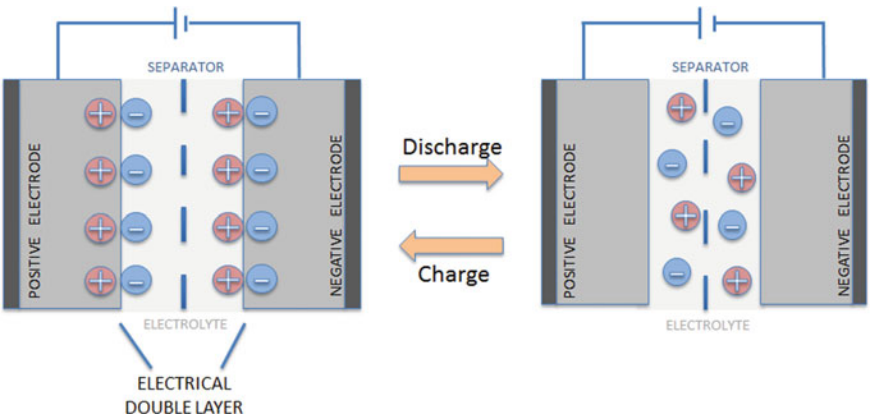

Fig. 8.5 Scheme of an electrochemical double-layer capacitor

The most important parameters that characterize the behaviour of a supercapacitor are the maximum amount of energy that it is capable of being stored E (J), and the maximum power P (W) that can be produced.

The energy (E) of a supercapacitor is expressed by the equation:

$$E = \frac{1}{2} C_{SC} V^2 \tag{8.3}$$

where C_{SC} (F) is the electrical capacitance of the device and V (V) is the operating voltage.

Power is another important parameter that determines how quickly the supercapacitor accumulates and supplies the energy. It is given by the formula:

$$P = \frac{V^2}{4R_{ESR}} \tag{8.4}$$

where R_{ESR} is the equivalent series resistance (ESR).

As the energy storage in EDLCs is based on electrostatic interactions at the electrode–electrolyte interface, the characteristics of both components affect this interface greatly. Materials with a large specific surface area and a suitable porous network as well as an affinity for the electrolyte are required for the electrodes (Eq. 8.2) (see Sect. 8.4). It should be noted, however, that the operation voltage and the internal resistance of SCs are constrained mainly by the properties of the electrolytes (Eq. 8.4).

- Electrolytes for EDLC

Slesinski et al. [35] report that the main features of a good electrolyte are (i) a high concentration, (ii) wettability, (iii) viscosity and (iv) thermal capacity. Their impact on electrochemical behaviour is shown in Fig. 8.6.

The wide variety of electrolytes is generally broken down into three main categories: liquid electrolytes, solid-state or quasi-solid-state electrolytes and redox-active electrolytes. To date, the SC manufacturers have used liquid electrolytes, mainly of an organic type.

Aqueous electrolytes are usually concentrated solutions of H_2SO_4 or KOH, although pH neutral solutions, such as Na_2SO_4, Li_2SO_4, etc., have also been used to reduce corrosion and widen the range of operational voltage [37]. The small size of the ions of aqueous electrolytes facilitates the participation of the entire electrode surface in the formation of the double layer, but the narrow potential window available for operation due to the decomposition of water voltage limits the amount of energy that can be stored (Table 8.1). On the positive side, the high conductivity (up to 1 S cm^{-1}) of aqueous media reduces the resistance of the cell, which favours relatively high powers.

Quaternary ammonium salts dissolved in acetonitrile or polypropylene carbonate are the most commonly used in commercial SCs. Their main advantage is their ability to operate up to 2.8 V, which results in high energy densities. On the other hand, their ionic conductivity is lower than that of aqueous electrolytes, and their bulky

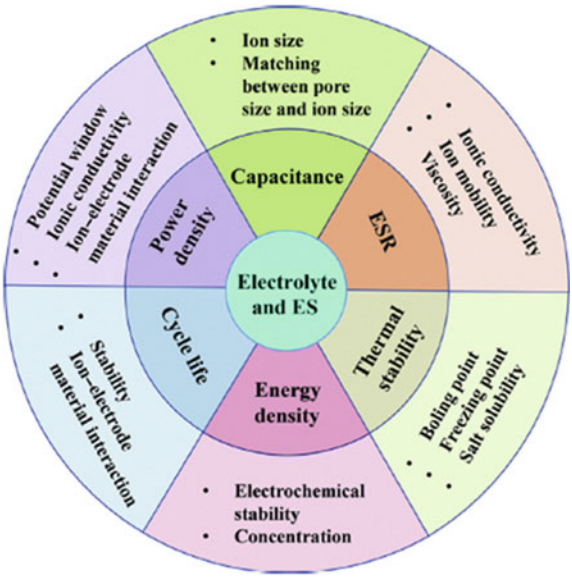

Fig. 8.6 Relationship between the electrolyte and electrochemical capacitor performance. Reproduced with permission from [36]

Table 8.1 Comparison of standard features of liquid electrolytes

Electrolyte	Aqueous	Organic	Ionic liquid
Operation voltage (V)	0.8–1	2.5–2.8	Up to 3.5
Conductivity	High	Low	Often low
Safety	Safe	Non-safe	Safe
Cost	Low	High	High
Environment	Friendly	Unfriendly	Friendly
Manipulation	Air	Inert	Inert

ions may not gain access to the all of the electrode's surface. In addition, the total absence of moisture is a requisite for the device to function properly, so the assembly is highly complex (Table 8.1).

Other electrolytes are currently under investigation, one of which is ionic liquid (IL) [38]. ILs are molten salts composed of bulky, asymmetric organic cations and weakly coordinating inorganic/organic anions [39]. They exhibit a very low vapour pressure which is why there is very little risk of explosion or environmental damage. Their stability makes it possible to operate at high voltages and temperatures of over 80 °C (Table 8.1). Numerous ionic liquids are currently being investigated, and those based on pyrrolidinium and imidazolium have offered promising results in the case of EDLCs [37].

In order to avoid the high viscosity and low conductivity associated with most ILs, mixtures of ionic liquids with organic solvents, such acetonitrile or propylene carbonate, are being investigated [38, 40, 41].

8.2 Textural Characterization: Gas Adsorption

The study of porosity in carbon materials involves the use of a wide variety of techniques, including gas adsorption, electron microscopy, mercury porosimetry, small-angle X-ray and neutron scattering (SAXS and SANS), immersion calorimetry, etc.

Gas adsorption is a well-established tool for the characterization of the texture of porous solids and fine powders [42]. In the case of supercapacitors, this is the main and most commonly used technique, since it provides quantitative information about porosity (over a pore sizes range of 0.35 to >100 nm).

After this brief introduction, the following section now discusses the different recommended methods employed to interpret isotherms, an analysis of which provides reliable information about pore structure and key parameters such as surface area, pore volume and pore size distribution.

Adsorption, in a gas/solid system, is defined as the enrichment of molecules, atoms or ions in the vicinity of an interface which corresponds to the solid surface and the exterior of the solid structure. Material in the adsorbed state is known as the adsorbate, while the adsorptive is the same component in fluid phase [43].

According to a IUPAC technical report, pores are classified according to their size as follows:

1. pores with widths exceeding 50 nm are called macropores
2. pores with widths between 2 and 50 nm are referred to as mesopores
3. pores with widths not exceeding 2 nm are called micropores.

It is important to remember that the term nanopore embraces all three categories of pores (upper limit ~100 nm). It is also useful to distinguish between narrow micropores (also called ultramicropores) of approximate width <0.7 nm and wide micropores (also called supermicropores).

The determination of pore structure in carbons is mainly carried out by means of adsorption/desorption isotherms of nitrogen at 77 K and of carbon dioxide at 273 K.

Sample preparation plays an important role in obtaining reliable and accurate information, as well as, reproducible results. Therefore, before beginning the analysis, all of the physisorbed species need to be removed from the surface of the adsorbent. For this purpose, drying and outgassing under a high vacuum are recommended. The pre-treatment conditions must be adapted to the nature of the sample so that the material does not undergo any transformation.

In accordance with the most up-to-date classification [43], the physisorption isotherms (Fig. 8.7) are classified as follows:

Type I isotherms are obtained from microporous solids with relatively small external surfaces, such as activated carbons. For nitrogen and argon adsorption at 77 and 87 K, Type I(a) isotherms are produced by microporous materials with mainly narrow micropores, while Type I(b) isotherms correspond to materials with pore size distributions over a broader range, including wider micropores and possibly narrow mesopores (<~2.5 nm).

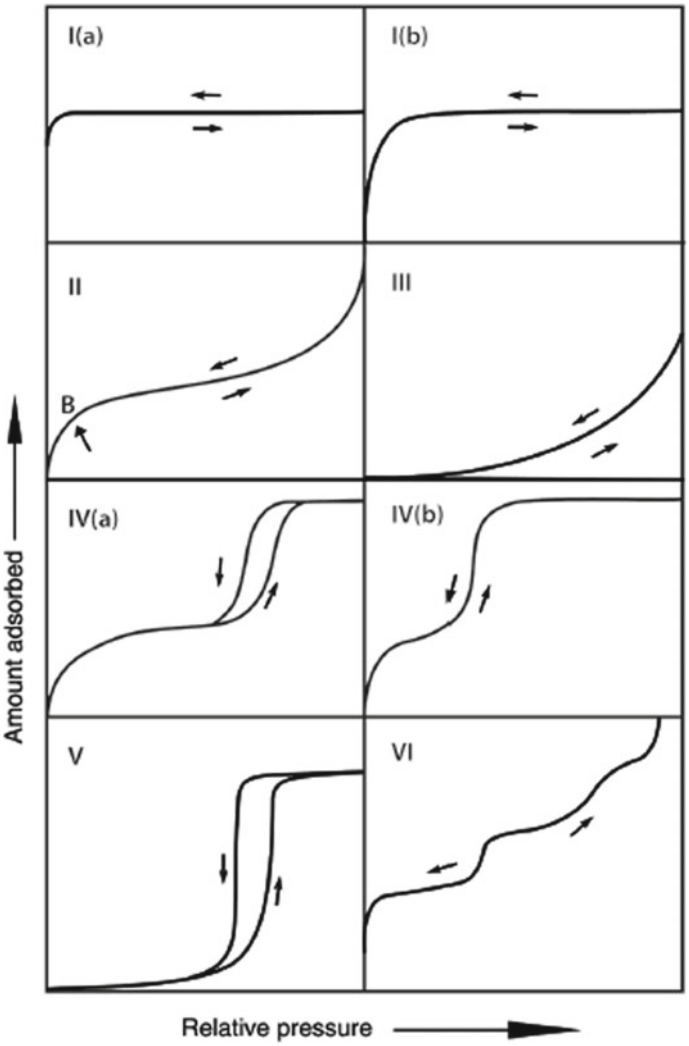

Fig. 8.7 Types of physisorption isotherms. Reproduced with permission from [43]

Type II isotherms are produced by the physisorption of most gases on nonporous or macroporous adsorbents. Their shape is the result of unrestricted monolayer–multilayer adsorption up to a high p/p_0. If the knee is sharp, it corresponds to the completion of monolayer coverage. A more gradual curvature is an indication of a significant amount of overlap of monolayer coverage and the onset of multilayer adsorption.

In the case of the Type III isotherm, the adsorbent–adsorbate interactions are relatively weak, and the adsorbed molecules are clustered around the most favourable sites on the surface of a nonporous or macroporous solid.

Type IV isotherms are produced by mesoporous adsorbents. The adsorption behaviour in mesopores is determined by adsorbent–adsorptive interactions and also by the interactions between molecules in a condensed state. In this case, the initial monolayer–multilayer adsorption on the mesopore walls is followed by pore condensation. A typical feature of type IV isotherms is a final saturation plateau (sometimes reduced to a mere point of inflexion).

In the case of the Type IV(a) isotherm, capillary condensation is accompanied by hysteresis. This occurs when the pore width exceeds a certain critical width, which is dependent on the adsorption system and temperature. For adsorbents with mesopores of smaller width, completely reversible, Type IV(b) isotherms are also observed.

The shape of Type V isotherm can be attributed to relatively weak adsorbent–adsorbate interactions. At a higher p/p_0 ratio, molecular clustering is followed by pore filling. For instance, Type V isotherms are produced when water is adsorbed on hydrophobic microporous and mesoporous adsorbents.

The Type VI isotherm is representative of layer-by-layer adsorption on a highly uniform nonporous surface. The step-height represents the capacity of each adsorbed layer, while the sharpness of the step is dependent on the system and temperature.

8.2.1 The Physical Adsorption of N_2

In order to obtain reliable information, N_2 isotherms are analysed by different methods. It is important to note that each method has been developed on the basis of its own assumptions.

- The BET equation

The most widely used method to estimate the specific surface area of a material was originally proposed by Brunauer, Emmet and Teller (BET method) [44]. The linearization of the N_2 isotherm by means of the BET equation provides the monolayer capacity n_m^a, and, subsequently, the specific area of the solids is estimated by applying the following Eq. (8.5):

$$S = n_m^a \sigma N_A \tag{8.5}$$

taking into account the area occupied by a molecule of N_2 at 77 K ($\sigma = 0.162\ \text{nm}^2$) and Avogadro's number (N_A).

S_{BET} is obtained by selecting in each case the best linear fit of the corresponding plot following the criteria listed by Rouquerol et al. [45]. They found that the linear range for BET analysis in the case of microporous carbons is below the classical p/p_0 domain of 0.05 and 0.3.

A systematic study by Centeno et al. [46] has shown that the BET-surface area is closely related to the micropore volume and suggests an area of approximately 2200–2300 $m^2\ cm^{-3}$, whatever the micropore width. It follows that S_{BET} can be representative only of carbons with pore widths of around 0.9 nm. Therefore, other

methods must be employed to obtain a reliable assessment of the total surface area (see Sect. 8.5).

- The Dubinin–Radushkevich equation

Physical adsorption of gases and vapours in microporous carbons is described by the Dubinin–Radushkevich (D-R) [47] Eq. (8.6). It relates the thermodynamic potential $A = \mathrm{RTln}(p_0/p)$ to the volume W of condensed vapour filling the total micropore volume W_o,

$$W = W_0 \exp\left[-\left(\frac{A}{\beta E_0}\right)\right] \tag{8.6}$$

where $\beta = 0.33$ for N_2.

The characteristic energy E_0 is related to the average width L_0 of slit-shaped micropores by Eq. (8.7):

$$L_0 = \frac{10.8}{(E_0 - 11.4)} \tag{8.7}$$

The surface area of slit-shaped micropores is close to the simple geometrical relation (8.8):

$$S_{\mathrm{mic}} = 2000\left(\frac{W_0}{L_0}\right) \tag{8.8}$$

It follows that for microporous carbons, the total surface area is

$$S_{\mathrm{tot}}(D - R) = S_{\mathrm{mi}} + S_{\mathrm{e}} \tag{8.9}$$

where S_e (external surface) is the area in the larger pores and on the outside of the sample. The external surface can be obtained by various techniques, one of which is the comparison plot.

- The α_s-plot

This method was developed by Gregg and Sing [48] and, subsequently, refined by Kaneko et al. [49] and Setoyama et al. [50]. It consists in comparing the isotherm of the sample under study with that of a standard nonporous carbon material used as reference.

The α_s plot is constructed by plotting the adsorbed amount of the sample at p/p_0 versus the parameter α_s. This parameter is obtained by means of the normalization at $p/p_0 = 0.4$ of the adsorbed amount of the reference material ($n/n_{0.4}$). This pre-selected relative pressure is justified since micropores are filled and capillary condensation has not yet begun. With this method, it is important to choose an appropriate reference material since it is heavily dependent on. Typically, carbon blacks are used.

The absence of any deviation of the linearity means that the sample has the same porous structure as reference material.

The deviations for below $\alpha_s = 1$, which provides essential information related to the microporosity, were termed as [33]:

- the filling swing (FS) ascribed to the presence of micropores with a width less than 1 nm and associated with primary micropore filling
- cooperative adsorption (CS) attributed to the presence of micropores with a width larger than 1 nm.

As shown in Fig. 8.8, the α_s plot method provides micropore volume (W_o) and external surface area (S_e) which are calculated from the intercept and slope of the blue line, respectively. On the other hand, the slope of the line passing through the origin represents the total surface area (S_{comp}).

- Density Functional Theory (DFT)

The density functional theory is based on the simulation of adsorption isotherms by means of theoretical calculations, which implies that the results are heavily dependent on the calculation parameters. This method provides the pore size distributions (PSD). DFT-software is included with most commercial instruments.

The inherent complexity and heterogeneity of pore structures in carbons has led to efforts to improve the models. The non-local density functional theory (NLDFT) has proved to be a reliable method for characterization of ordered silica materials, though the pore size analysis of carbons remains problematic due to the treatment of the pore walls as if they were homogeneous graphite-like plane surfaces [52]. Gor et al. [53] have proposed a new Quenched solid density functional theory (QSDFT) method for the characterization of micro-mesoporous carbons using N_2 adsorption at 77 K.

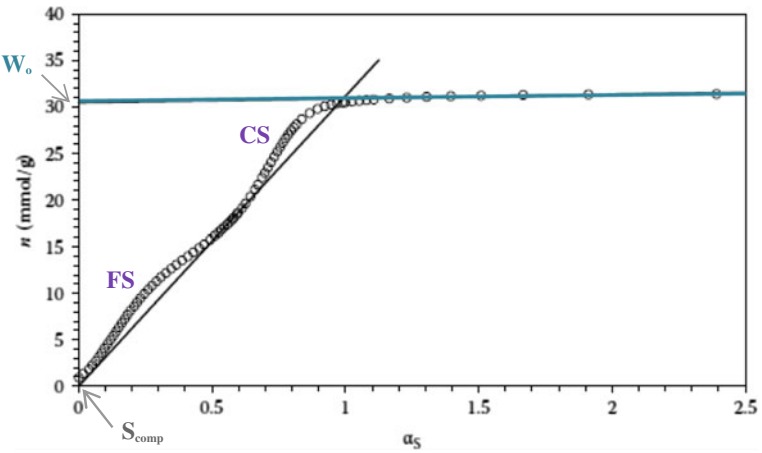

Fig. 8.8 α_s plot of activated carbon fibres with was Spheron 6 carbon used as reference material. Adapted from Ref. [51]

This model takes into account the geometries of the pores, solid–fluid interactions and surface roughness that is specific to carbons so that the isotherms do not reflect the artificial layering steps in the regions of ~1 and ~2 nm that are characteristic of NLDFT calculations.

- The KJS Method

This method, which was originally proposed by Kruk, Jaroniec and Sayari [54], estimates mesopore size distributions. The maximum distribution as revealed by N_2 isotherm analysis is taken as the pore size (D_p).

8.2.2 The Physical Adsorption of CO_2

The characterization of samples by CO_2 adsorption at 273 K provides complementary information to that derived with N_2 as adsorbate at 77 K. As previously reported [55], a low N_2 adsorption capacity may not indicate the absence of porosity but rather hindered access. Due to the low adsorption temperature (77 K), the filling of narrow cavities is a very slow process, and equilibrium is not achieved in the standard operation times. In contrast, CO_2 is adsorbed more quickly as the higher adsorption temperature (273 K) avoids diffusional problems. Moreover, as a consequence of the relatively high saturation pressure (~26,000 Torr), the standard CO_2 isotherm at 273 K is typically obtained up to a relative pressure p/p_o of 0.03 and provides exclusive information about ultramicroporosity (<0.8 nm). Information about the textural parameters is obtained from an analysis of the isotherm by applying the Dubinin–Radushkevich Eq. (8.6).

8.3 Electrochemical Characterization

The carbon electrodes of EDLCs are usually composites made up of porous carbon as active material (activated carbon, carbon fibres, carbon nanotubes, graphene, etc.), binder (polytetrafluoroethylene, polyvinylidene fluoride, carboxymethyl cellulose, etc.) and a conductive material (carbon black, graphite flakes, carbon nanotubes, graphene, etc.). The ratio of each component depends on the nature of the active material. It is highly recommended to use electrodes with the same thickness and carbon load as that of their commercial counterparts (100–200 μm and ~10 mg cm^{-2}) rather than extremely thin electrodes with a low content of active material which might lead to overestimate a material's performance [56]. Two-electrode cells mimic packed devices, so these systems generally provide an accurate picture of an electrode material's behaviour [57]. It is important to emphasize that the electrochemical measurements of active materials should be tested under the same experimental conditions in the same cell in order to obtain reliable and comparative information

put special emphasis on working with electrodes matching the thickness and carbon loading of commercial electrodes.

As mentioned in the introduction, the configuration of the cell corresponds to each electrode acting as a capacitor with both of them connected in series. The total capacitance of the supercapacitor is described by Eq. (8.1) and, therefore, for a symmetrical system with equal electrodes, this implies that:

$$C_{\text{electrode}} = 2C_{\text{SC}} \tag{8.10}$$

8.3.1 Galvanostatic Charge–Discharge Cycles

In galvanostatic cycling, the system is subjected to a constant current density, while the potential versus time is recorded between 0 and 0.8–1 V for the aqueous media (Fig. 8.9), 0–2.5 V for organic electrolytes and 0–3.5 V for the ILs.

The cell capacitance is calculated from the slope of the discharge section by applying the following equation:

$$C_{\text{SC}} = \frac{2i\,\Delta t_{\text{d}}}{m_{\text{c}}\,\Delta V_{\text{d}}} \tag{8.11}$$

where i is the current intensity, Δt_{d} is the discharge time, ΔV_{d} is the discharge potential and m_{c} the mass of active material.

From the galvanostatic measurements, the resistance of the cell (R_{ESR}) is also determined by means of the following equation:

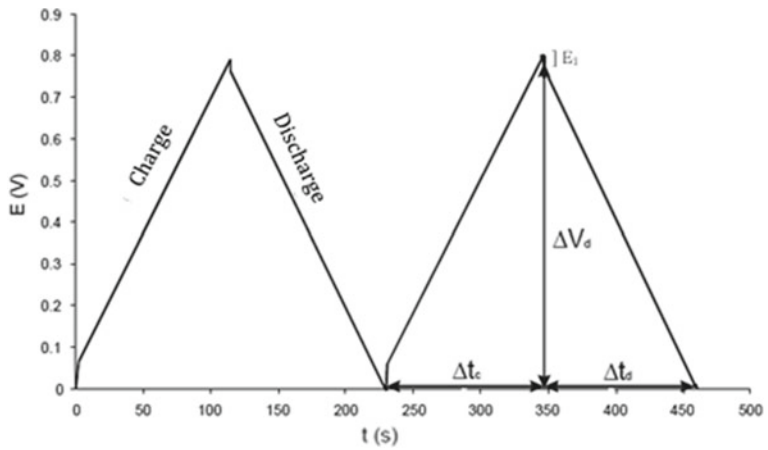

Fig. 8.9 Galvanostatic charge–discharge cycles of activated carbon in 2M H_2SO_4

$$E_1 = 2i\,R_{\mathrm{ESR}} \tag{8.12}$$

where E_1 is the potential drop due to this resistance and i is the applied current.

This parameter displays the non-ideal behaviour of the system and corresponds to various ohmic contributions associated to the cell configuration (electrolyte resistance, electrode resistance, electrode-collector resistance, etc.) [51].

As noted in the introduction, an overall assessment of the EDLC potential is provided by its capacity to store energy and is calculated as follows:

$$E = \frac{1}{2} C_{\mathrm{SC}}(\Delta V_{\mathrm{d}}) \tag{8.13}$$

whereas its ability to deliver power is determined by applying the equation:

$$P = \frac{E}{\Delta t_{\mathrm{d}}} \tag{8.14}$$

Frequently, in order to facilitate comparison of the materials under study, performance is associated to the specific energy density and specific power density:

$$E_{\mathrm{sp}} = \frac{E}{m_{\mathrm{c}}} \tag{8.15}$$

$$P_{\mathrm{sp}} = \frac{E_{\mathrm{sp}}}{\Delta t_{\mathrm{d}}} \tag{8.16}$$

where m_{c} corresponds to the mass (kg) of active material in both electrodes.

8.3.2 Cyclic Voltammetry

Cyclic voltammetry consists in a linear potential sweep at a constant scan rate between 0 and 0.8 V in the case of aqueous electrolyte (Fig. 8.10) and up to 2.5–3.5 V in an organic medium and ILs, respectively. The sweep is reversed after reaching maximum potential.

Specific capacitance (F g^{-1}) is calculated by the equation:

$$C_{\mathrm{SC}} = \frac{(q_{\mathrm{a}} + |q_{\mathrm{c}}|)}{m_{\mathrm{c}} \Delta V} \tag{8.17}$$

where q_{a} and q_{c} the anodic and cathodic charge, respectively, correspond to the positive and negative sweep; $\mathrm{m_c}$ is the mass of active material in the cell, and ΔV is the potential window.

The slope $\Delta i / \Delta v$ is related to the equivalent series resistance ($\mathrm{R_{ESR}}$) of the device.

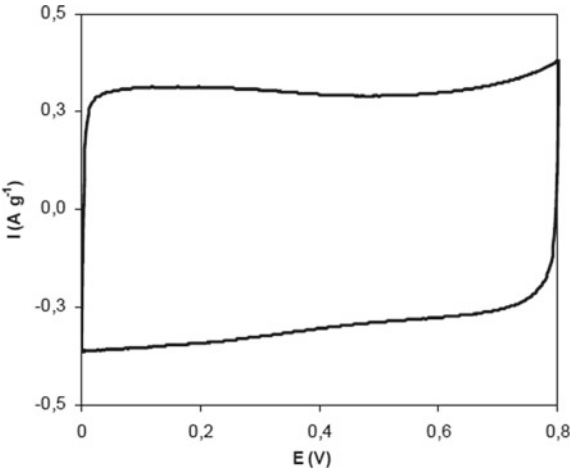

Fig. 8.10 Voltammogram of a EDLC in aqueous electrolyte

8.3.3 Electrochemical Impedance Spectroscopy (EIS)

Electrochemical impedance spectroscopy is a powerful technique for characterizing supercapacitors and provides reliable information on the dependence of their behaviour on frequency.

If it is considered the supercapacitor as a whole by simply using the impedance data [58, 59], then:

$$Z(\omega) = \frac{1}{j\omega \times C(\omega)} \tag{8.18}$$

The impedance $Z(\omega)$ can be written in its complex form, as follows:

$$Z(\omega) = Z'(\omega) + jZ''(\omega) \tag{8.19}$$

Equations (8.18) and (8.19) lead to Eq. (8.20):

$$C(\omega) = \frac{-\left(Z'(\omega) + jZ'(\omega)\right)}{\omega|Z(\omega)|^2} \tag{8.20}$$

Hence, it is possible to define:

$$C(\omega) = C'(\omega) + jZC''(\omega) \tag{8.21}$$

$$C'(\omega) = \frac{-Z''(\omega)}{\left[\omega Z(\omega)^2\right]} \tag{8.22}$$

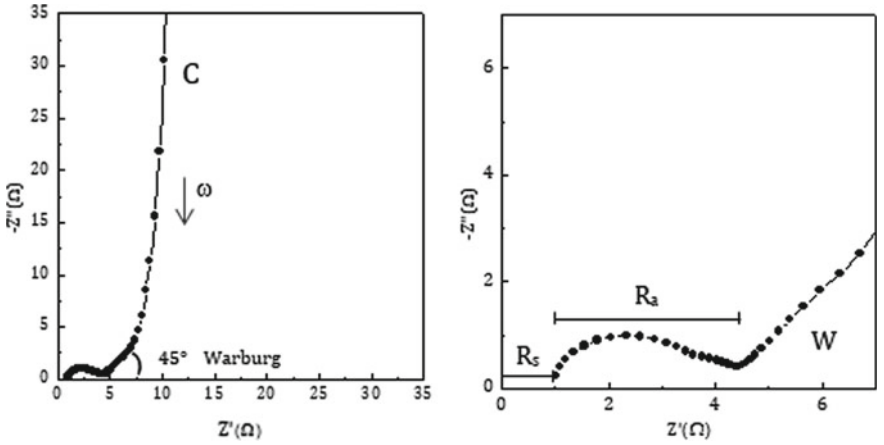

Fig. 8.11 Nyquist plot

$$C''(\omega) = \frac{Z'(\omega)}{\left[\omega Z(\omega)^2\right]} \tag{8.23}$$

where $C'(\omega)$ is the real part of the capacitance $C(\omega)$. $C''(\omega)$ is the imaginary part of the capacitance $C(\omega)$, and $|Z(\omega)|$ is the impedance modulus.

Nyquist plot (Fig. 8.11) depicts the real part of the impedance versus the imaginary part. Each point is the impedance at one frequency. Three responses, which provide different information, can be distinguished [59–63]:

- at low frequencies, a vertical line parallel to y-axis, which reflects a capacitive behaviour, is characteristic
- at high frequencies, the contribution of the resistance is observed for ESR. R_s is usually ascribed to the ionic resistance of the bulk electrolyte. R_a is associated to resistance at the electrode and the electrode/collector contact.
- the middle range of frequencies is known as the Warburg response, which is a line at an angle of 45° to the real axis. This section reflects intraparticle ion-transport resistance.

Figure 8.12 represents the change of the real part of capacitance versus frequency. The capacitance increases when the frequency decreases and is constant at low frequencies.

The characteristic curve obtained by plotting the change of the imaginary part of capacitance versus frequency (Fig. 8.13) exhibits a maximum at a given frequency which is defined as a time constant τ_0:

$$\tau_0 = \frac{1}{\omega_0} \tag{8.24}$$

where ω_0 is the angular frequency at the maximum of the C'' peak.

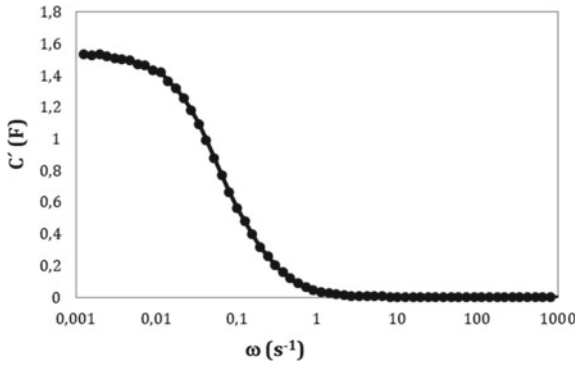

Fig. 8.12 Variation of the real part of the capacitance (C') versus frequency (ω)

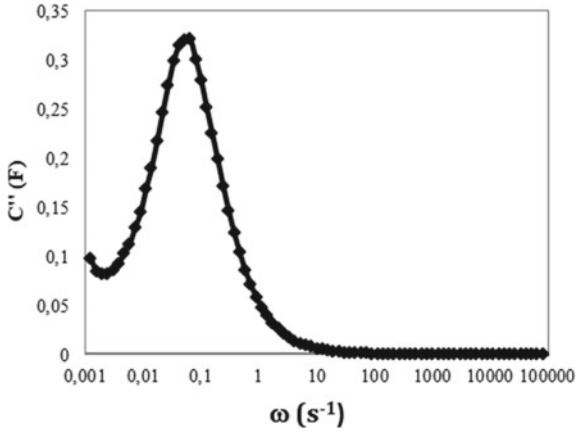

Fig. 8.13 Evolution of the imaginary part of the capacitance (C'') versus frequency (ω)

8.4 Carbon Materials for EDLC Electrodes

The technological implementation of nanoporous carbons in supercapacitors is possible due to their high porosity and electric conductivity, mechanical and thermal stability, resistance to corrosion, high purity, ease of processing and low cost.

- Activated carbons (ACs)

Activated carbons are the most commonly used active materials in commercial SCs due to their ready availability in different forms (granular, fibres, fabrics, etc.) and their competitive performance/cost ratio. Traditionally, they are produced by charring carbon-rich compounds followed by physical activation using steam, air, carbon dioxide, etc., or by a chemical process employing $ZnCl_2$, H_3PO_4, NaOH, KOH, K_2CO_3, etc., to create porosity. There are a wide variety of materials that can be used as precursors such as coal [64, 65], coke [66–68], pitch [69, 70], but at present, biomass wastes (wood, shells, pits, leaves, etc.) [71–80] are the most frequently

used. Nowadays, activated carbons from coconut shell excel as electrode materials in commercial supercapacitors [8].

Activated carbon in fibrous form (with a length/diameter greater than 10/1 ratio and a diameter of less than 250 μm [81]) is of great use for SC application. Activated carbon fibres are very strong, flexible and light and may be used directly without binders. They also have higher conductivities (between 200 and 1000 S cm^{-1}) than conventional activated carbons. However, their high production cost limits their use to very specific applications.

Activated carbons have BET-surface areas in the range of 500–2500 m^2 g^{-1} and achieve specific capacitances between 150 and 300 F g^{-1} in aqueous electrolytes, whereas these values are generally limited to 75–150 F g^{-1} in organic media and to 35–120 F g^{-1} in ionic liquids [40, 64–80, 82, 83].

Various studies have pointed out the limitations of activated carbons for high-power applications. Although they may have wide pore size distributions in the 0.4–50 nm range, in the majority of activated carbons, more than 90% of the total surface corresponds to micropores (<2 nm). It has been suggested, therefore, that some of the porosity may be inaccessible to an electrolyte. In addition, micropores significantly hinder the movement of ions, and as a result, a high rate capability, which is one of the advantages of EDLCs, may not be achieved. These limitations are more pronounced in the case of organic electrolytes and ionic liquids due to their larger ions [84–86].

- Mesoporous carbons

It has been suggested that high surface area carbons with a porosity formed essentially by micropores and with mesopores (2–50 nm) acting as transport channels or almost exclusively by mesopores with sizes in a narrow range would be more suitable for EDLC electrode application. The preparation of carbon materials with these porous features is not easy by conventional methods of activation [87], and diverse techniques [88] have been developed to obtain carbons with pore volumes >1 cm^3 g^{-1}, BET-surface areas of around 1500–2000 m^2 g^{-1} and narrow pore size distributions in the range of 2–50 nm. Such materials may achieve a specific capacitance of 150–225 and 100–180 F g^{-1} in aqueous and organic electrolytes, respectively [89–93]. More recently, advanced carbons with a hierarchical porosity have been prepared from different precursors and following diverse procedures. Their specific capacitance is in the range of 120–300 F g^{-1}, 120–180 F g^{-1} and 150–200 F g^{-1}, in aqueous, organic and ionic liquid electrolytes, respectively [94–96]. It has been reported that nitrogen and/or oxygen-enriched materials of this type achieve 300–640 F g^{-1} [97–102]. Such high values are claimed to be a result of their porous structure being specially adapted to achieve a quick charge/discharge response.

- Carbon gels

In recent years, carbon gels have attracted a great deal of interest for use in SC. They correspond to agglomerates or colloidal-type chains of polymeric nanoparticles (obtained from a sol–gel reaction) which retain their polymer structure after the

carbonization process. Organic gels are mainly prepared from phenol, furfural, resorcinol or formaldehyde, and depending on the process of solvent removal, they are classified into xerogel, aerogel and cryogels [103, 104]. Cryogels are not as attractive for use in SC because of their high cost.

Carbon gels have a porosity that occupies more than 80% of the total volume, with a high proportion of mesopores and a BET surface between 400 and 900 m^2 g^{-1}. These properties can be modulated by controlling the variables in the preparation process. Some studies have shown that the activation of aerogels and xerogels generates microporosity [105–107], making it possible to duplicate the capacitance by as much as 250 F g^{-1} in an aqueous electrolyte and 150 F g^{-1} in an organic medium [108–114]. Their capacitances are not significantly reduced with an increase in current density indicating that carbon gels would be very useful for high-power applications.

- Carbide-derived carbons (CDCs)

Carbide-derived carbons have been promoted as excellent materials for SC electrodes. They are synthesized by extracting the metal from carbide powders (SiC, TiC, ZrC, HFCs, NbC, Cr_2C_3, WC, etc.) in a chlorine flow at high temperatures (700–1000 °C) [115, 116]. They correspond to nanostructured materials whose structural properties (particle size and morphology) and textural properties (pore volume, pore size distribution, specific surface area) can be tailored by controlling the synthesis variables [115, 117, 118]. Such advanced carbons display a high microporosity formed by extremely narrow pore size distributions and a BET-surface area of more than 2000 m^2 g^{-1}. It has been reported that CDCs with a porosity suitable for desolvated ions can reach capacitances of up to 170 F g^{-1} in organic electrolyte [119–121], whereas capacitances as high as 250 F g^{-1} and 185 F g^{-1} have been reported, respectively, in aqueous [119, 122–124] and ionic liquid electrolytes [122, 124–127]. It should also be noted that, as a result of their high density, their volumetric capacitance (in F cm^{-3}) is much higher than that of most porous carbons.

- Carbon nanotubes (CNTs)

Carbon nanotubes are cylindrical carbon structures, with diameters of nanometre scale. They can be considered as rolled up graphite sheets that appear as monolayers (single-wall carbon nanotubes, SWCNT) or concentric tubes (multi-wall carbon nanotubes, MWCNT). Carbon nanotubes are generally prepared by chemical vapour deposition (CVD), the arc-discharge method and laser ablation [128, 129].

The porosity of carbon nanotubes consists essentially of mesopores of low specific surface area ranging between 100 and 400 m^2 g^{-1}. This mesoporous structure is easily accessible to electrolyte ions, and a high electrical conductivity makes them very good materials for high-power supercapacitors. However, their limited capacitance, 5–80 F g^{-1} [130, 131] and their much higher cost compared to conventional porous carbons are an obstacle to their implementation on a large scale [132]. Although specific post-treatments (activation, oxidation, etc.) and advanced electrode configurations [133–138] can increase their performance significantly (their capacitance in aqueous and organic media can attain 300 and 100 F g^{-1}) [139–141], they are still

less competitive than other carbons. Currently, the main application of CNTs is an additive because their presence, even in small quantities, notably increases electrode conductivity and improves the overall operation of the devices [132, 142].

- Carbon nano-onions (CNOs)

Carbon nano-onions are concentric shells of graphitic carbon, ca. 5–10 nm in diameter. They are synthesized by vacuum annealing 5 nm nano-diamond powders at 1200–2000 °C [143]. As with carbon nanotubes, their mesoporous surface is fully accessible to electrolyte ions, but it is limited to 500 $m^2\ g^{-1}$ [144]. They were observed that CNOs perform better after being decorated with metal oxides, conducting polymers, redox species and surface functional groups [145, 146].

- Graphene

According to IUPAC, a graphene layer is described as: "a single carbon layer of graphite structure, describing its nature by analogy to a polycyclic aromatic hydrocarbon of quasi infinite size" [147]. Nevertheless, under the term "graphene" is often included a variety of related carbon materials of few or several multilayer stacks. An editorial communication in Carbon [148] has pointed out the need for a clear nomenclature. "Graphene materials" or "graphene-based materials" are recommended as terms to describe these emerging 2D materials accompanied by precise descriptions of them. The other members of the graphene family exhibit significantly different properties (apart from their cost) as a result of the synthetic route used in their preparation.

Because of its exceptional properties [149], graphene is a potential material for a wide range of applications, but a recent report [150] has highlighted that the market is pivoting towards energy storage applications, which it is estimated will account for more than a third of the applications in 2026, even though the current use of graphene in commercial SCs still faces many challenges, such as the need for a high quality material at low cost that can easily be reproduced.

Graphene suffers from agglomeration and the need for re-stacking, and this undesirable effect increases during the processing of graphene-based electrodes, leading to a loss of surface area and electrical conductivity. The different shapes of the N_2 adsorption isotherms show that the materials have different porosities. Importantly, the total area of the graphene-related materials estimated by this technique does usually not exceed 500 $m^2\ g^{-1}$ [151]. This value is significantly lower than the theoretical 2600 $m^2\ g^{-1}$ of graphene and 1000 $m^2\ g^{-1}$ of standard activated carbons. Moreover, some authors have suggested that the results obtained at laboratory scale may not give a realistic picture of its performance in real supercapacitors because the electrochemical measurements are carried out on electrodes that lack essential characteristics, such as the carbon weight, like the ones used in commercial SC.

Despite these drawbacks, the potential of graphene materials (as main active material and in composite electrodes) for use in supercapacitors has been emphasized in numerous scientific studies [82, 152–158].

8.5 Relationship Between Capacitance and Surface of Carbons in EDLC

In accordance with Eq. (8.2), capacitance is expected to be proportional to the specific surface area of the carbon used in the electrode. The lack of a clear linear relationship which is the missing link between C and S_{BET} or S_{DFT} has given rise to numerous studies on the specific role of carbon porosity in the formation of the double layer, and a variety of interpretations has been proposed. Of these, the following deserve to be mentioned:

- Some materials have a significant proportion of narrow micropores that are inaccessible to ions of the electrolyte, and therefore, the entire surface cannot be used for charge accumulation [10, 159]. This hypothesis seems reasonable, but it is puzzling that capacitance tends to level off in microporous materials with pores mostly above 1.2–1.5 nm in width and with negligible ultramicroporosity (<0.7 nm). Because of this, the limitation of capacitance in highly porous carbons has been attributed to the space constriction for the accommodation of the charge in their very thin pore walls [160, 161].
- Capacitance corresponds to separate contributions from the surface of the micropore walls (C_{mi}) and the external surface (C_{ext}) [162, 163]. The fact that the sets of C_{mi} and C_{ext} values differ from one type of carbon to another reveals that this interpretation is not generally applicable [162–167].
- The finding that the double-layer capacitance of the edge orientation of graphite was one order of magnitude higher than that of the basal layer [168] suggests that carbons with a similar specific surface area but higher ratio of edge/basal orientations may achieve a higher capacitance [169–171].
- Pores with sizes matching those of the ions are more effective for storing charge and maximize the capacitance normalized by the surface area (in F m^{-2}) [172–174].
- The puzzling interfacial capacitance found in certain highly porous carbon electrode materials may be caused by the quantum capacitance of the graphene layers, in addition to their surface area [175].

In order to address these matters, Lobato et al. [151] have presented a comprehensive study of the correlations between surface and electrochemical capacitance based on the behaviour of a large variety of carbon materials in EDLC systems which has been analysed in depth and tested under the same conditions.

Different studies have illustrated that the specific surface areas of carbons based on the standard analysis of the N_2 adsorption isotherm at 77 K using the BET equation are not reliable for determining the porosity involved in charge storage. IUPAC systematically draws attention to the specific limitations of each of the methods available for the interpretation of physisorption isotherms [43, 176]. The BET equation was developed to explain the adsorption of multilayers on open surfaces. In the case of microporous carbons, this model is misleading the fact that the BET-surface area is equivalent to the total volume adsorbed [46, 177]. On the other hand, minor

discrepancies have been found between the areas derived using other approaches such as the comparison plot (S_{comp}), the Dubinin equation (S_{DR}) and the adsorption of phenol from aqueous solutions (S_{phenol}), whereas the specific surface area based on the density functional theory (S_{DFT}) shows some scatter with respect to the other determinations [46] due to the complexity of this modelling approach with its strict requirements [43, 177].

Consequently, the simultaneous use of several independent techniques is recommended in order to cross-check the results and eliminate possible contradictions. It has previously been reported [46, 178] that the average value of S_{DR}, S_{comp}, S_{DFT}, S_{phenol} leads to reasonably accurate evaluation of the specific surface area (S_{total}) of carbons. Centeno et al. [179] conducted a systematic study of a large variety of microporous carbons, in which they found a quantitative correlation between S_{BET} and S_{total} given by the following equation:

$$S_{total} = \frac{S_{BET}}{1.19\, L_0} \tag{8.25}$$

where L_o is the average micropore width.

Equation (8.25) clearly shows that S_{BET} underestimates the total surface area of carbons with a high proportion of pores below 0.8 nm and overestimates it with micropores above 1.1 nm [46].

Figure 8.14c, d shows a totally different pattern for the dependence of C and S_{total} than that achieved by the standard S_{BET} (Fig. 8.14a, b). An increase in capacitance with the more reliable S_{total} is suggested, although, in view of the scatter, this would only be suggestive for the whole spectrum of porous carbons. Different studies have noted that the absence of a proportionality in Fig. 8.14c with values ranging between 0.1 and 0.3 F m^{-2} (dashed lines) simply reflects the fact that in classical aqueous electrolytes such as H_2SO_4 and KOH, the energy storage mechanism involves certain surface functionalities through Faradaic pseudocapacitive reactions [180–188]. Additionally, surface chemistry may also influence the hydrophobic/hydrophilic character of carbon and consequently the interaction between the electrolyte and electrode.

Numerous investigations have revealed a marked capacitance improvement through reversible oxidation/reduction of hydroquinone/quinone O-groups and pseudocapacitive interactions on negatively charged pyrrolic- and pyridinic-N functionalities [180, 181, 183–185]. An enhancement of electron transfer through the carbon appears to derive from the positive charges on quaternary-N and pyridinic-N-oxide [185].

Studies of activated carbons in 2M aqueous H_2SO_4 have reported that the fraction of the surface functionalities desorbed as CO in TPD experiments contributes as much as 50–60 F $mmol^{-1}$ [186–188]. The correction of the experimental capacitances by subtracting the corresponding pseudocapacitance led to 0.105 F m^{-2} which virtually corresponds to the contribution from the double layer in this electrolyte [187]. This matches the lower boundary displayed in Fig. 8.14c for carbons with low oxygen content.

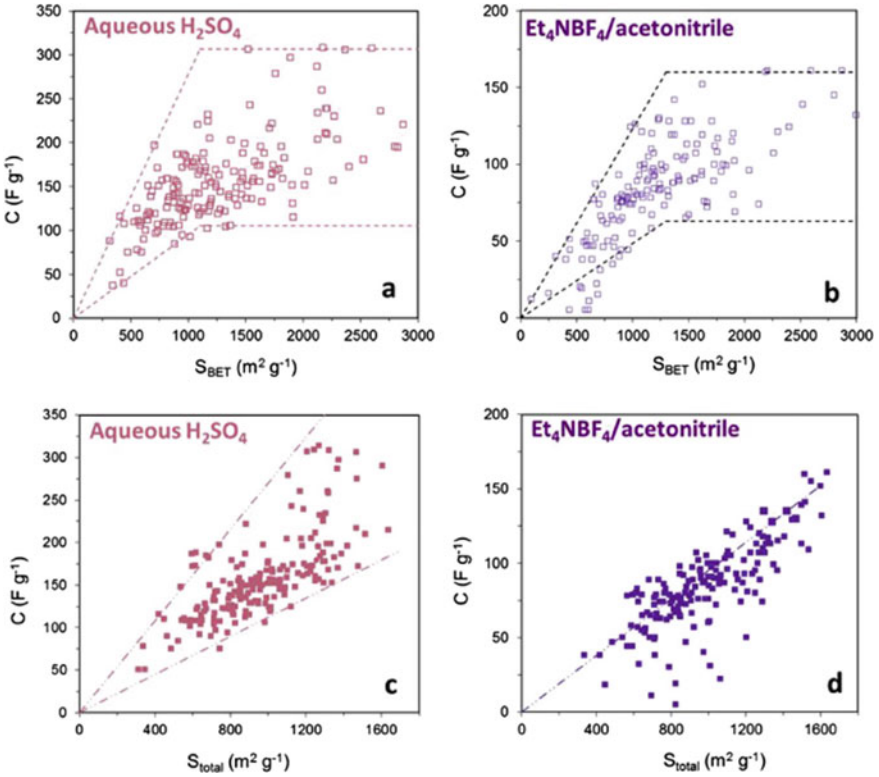

Fig. 8.14 Variation of the gravimetric capacitance of carbons in aqueous (2M H_2SO_4) and organic (1M Et_4NBF_4/ACN) electrolytes with the specific surface area estimated by BET equation, S_{BET} (**a**, **b**) and by a combination of different methods, S_{total} (**c**, **d**). Reproduced with permission from [151]

The good agreement observed between the experimental capacitances in H_2SO_4 and those calculated from the enthalpies of immersion of carbons in benzene and water confirms the participation of oxygen functionalities [187]. Whereas the enthalpy of immersion in benzene is related to the porous structure, the enthalpy of immersion in H_2O also reflects the oxygen content of the surface.

The possibility of increasing the energy density of aqueous supercapacitors by pseudocapacitance has encouraged the development of carbon materials with a tailored surface. It has been claimed that outstanding capacitance can be achieved by functionalized carbons with extremely low specific surface areas determined by N_2 adsorption at 77 K.

Materials derived from biomass wastes [189, 190], melamine [191–193], polyaniline [194–196], polypyrrol [197] and sodium alginate [198] are able to reach surface-capacitance values ranging from 0.8 to 33 F m^{-2} which are largely beyond the upper limit of around 0.25–0.3 F m^{-2} for typical porous carbons [186, 187, 199–201]. Such an enhancement is usually attributed to the huge pseudocapacitance afforded

by certain surface groups acting as extraordinary redox-active sites. Nevertheless, recent studies [202, 203] have challenged this interpretation by illustrating that the pseudocapacitance of functionalized carbons may be largely overestimated due to an inadequate characterization of the porous structure. As previously reported [55], a low N_2 adsorption capacity in carbons is not always indicative of the absence of pores. Thus, in one study, textural characterization by CO_2 adsorption at 273 K revealed that the specific surface area of a laver-based carbon was as high as 410 m^2 g^{-1} instead of <2 m^2 g^{-1} indicated by N_2 at 77 K [202]. Further systematic studies carried out by Wu et al. [203] on a variety N-doped carbons confirmed that pores below 0.7 nm participate actively in the formation of the double layer in aqueous electrolyte and the initial values of 0.31–2.52 F m^{-2} based on S_{N2} (22–312 m^2 g^{-1}) actually range from 0.16 to 0.28 F m^{-2} when the more reliable S_{CO2} (383–587 m^2 g^{-1}) is used.

Although the surface area of most carbons is almost totally accessible to the ions of aqueous electrolyte, as Fig. 8.14d shows, the relation C/S_{total} fails for a large number of materials in organic electrolyte. It should be pointed out that the specific surface areas determined by physical adsorption with standard molecular probes (N_2, Ar, CO_2) involve micropores with widths as low as 0.3–0.4 nm, which are not accessible to the large ions of organic electrolytes [172] and ionic liquids [82]. Therefore, it follows that predictions based on the classical probes (N_2, Ar, CO_2, etc.) no longer apply and the technique must be adapted in order to provide an accurate assessment of the surface area available to larger ions.

Advanced analyses of isotherms based on DFT methods have been carried out to evaluate nanoporous carbon porosity taking into account the dimensions of ions. For this purpose, the pore size distribution is estimated, and the surface area involved in charge storage is calculated by subtracting the surface are with pores smaller than the sizes of the ions. Nevertheless, numerous studies have reported uncertainty in the textural characterization of these materials using DFT models. As mentioned in Sect. 8.2, DFT is heavily dependent on the accuracy of the isotherms.

In addition to the pore size distribution, unexpected reductions in capacitances are also caused by the so-called bottleneck pores. The presence of constrictions at the entrance of the pores, which hinder the access of ions of suitable pore size, cannot be detected by the standard method of physisorption of small molecules [204]. In these cases, immersion calorimetry is a powerful tool as the enthalpies of immersion of the carbon in liquids with different molecular dimensions (0.33–1.5 nm) reveal the volume accessible to the different probes. This technique yields the "effective pore-size distribution" (and implicitly the effective surface area), unlike adsorption which yields the "absolute PSD" [205]. Recent results based on a combination of N_2-physisorption and immersion calorimetry in CH_2Cl_2 (0.33 nm), C_6H_6 (0.41 nm) and CCl_4 (0.63 nm) showed that the surface accessible to the cation Et_4N^+ of the organic electrolyte Et_4NBF_4 in acetonitrile was reduced by 20–27% with respect to the total surface area of carbon monolith electrodes [206]. The extent of the surface involved in the energy storage is limited by that accessible to Et_4N^+ as the anion BF_4^- has a smaller size. Carbon tetrachloride (0.63 nm) and norbornadiene (0.65 nm) due

to their critical dimensions are convenient probes for the reliable assessment of the surface area accessible to the cation Et_4N^+ (0.68 nm) [179, 207].

Figure 8.15 shows that the total surface area of a variety of activated carbons is not perceptible to the organic electrolyte, though such a deviation from the general pattern for a carbon with narrow porosity disappears when a surface area with pores above 0.63 nm is used. The figure also shows the excellent linear correlation between C and S obtained for different carbon materials with average pore sizes of between 0.66 and 15 nm [179, 208]. This linear relationship (dotted line) provides useful insights into the operation of carbons in SCs. In the case of this electrolyte, their performance depends essentially on a double-layer mechanism with a constant contribution of the surface area of around 0.094 F m^{-2} (dotted line), in contrast with their behaviour in aqueous media.

A recent study [206] carried out using binder-free electrodes of carbon monoliths with a narrow micropore size distribution fits into the 0.094 ± 0.011 F m^{-2} range obtained by Stoeckli et al. and refutes the possibility that the presence of binder or wide PSD might conceal variations in surface-capacitance with pore size [209]. This constant pattern agrees with modelling studies [187, 210–214] and is consistent with a decrease in the relative permittivity (ε_r) in narrow micropores [208, 215].

The finding of a constant contribution from the carbon surface area of around 0.1 F m^{-2} in both electrolytes is of great importance in the field of carbon EDLCs, as it suggests the existence of limits for these systems. A constant surface-capacitance indicates that the upper bound for specific capacitance (and consequently, the energy storage capacity of the resulting SC) is determined by the specific surface area that can be generated in carbons. Although great progress has been made in engineering

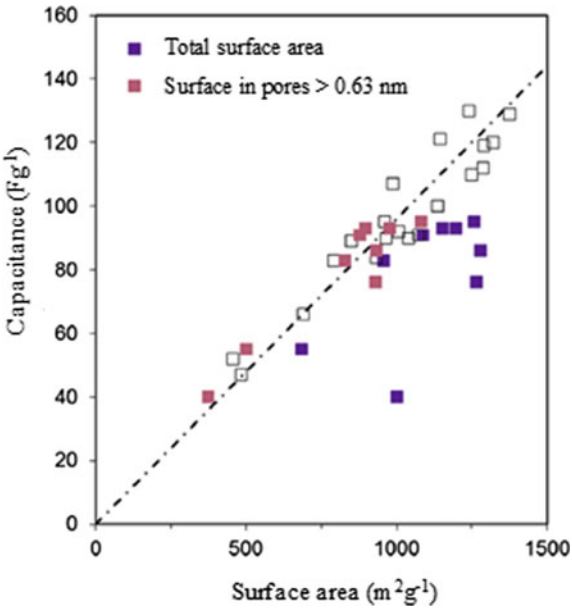

Fig. 8.15 Variation of the specific capacitance of activated carbons in organic electrolyte with the total surface area (■) and the surface area with pores larger than 0.63 nm (■). Data for activated carbons with no ultramicropores (□). Reproduced with permission from [151]

appropriate porous structures, an overall assessment based on the results obtained and data quoted in the literature suggests that a realistic maximum for the total surface area of carbons is currently at around 1700–1800 $m^2\ g^{-1}$ [119, 173, 178, 216, 217, 218]. The preparation of carbons with a much larger surface area and, hence, higher energy storage density is one of the greatest challenges facing EDLCs.

Graphene (2630 $m^2\ g^{-1}$) has emerged as a promising candidate for SC electrodes, although it is subject to certain limitations, as noted in Sect. 8.4. It should be noted, however, that based on the finding of recent studies [155, 156], the approaches described above are not necessarily applicable to all some graphene-related materials. The possibility of obtaining an outstanding surface-capacitance relationship is not excluded, but it may be hindered by it being difficult to estimate accurately the surface area actually involved in the storage of energy.

References

1. L. Pérez-Lombard, J. Ortiz, C. Pout, A review on buildings energy consumption information. Energy Build. **40**, 394–398 (2008)
2. S. Abate, G. Centi, P. Lanzafame, S. Perathoner, The energy-chemistry nexus: A vision of the future from sustainability perspective. J. Energy Chem. **24**, 535–547 (2015)
3. H.I. Becker, Low voltage electrolytic capacitor (1957)
4. J.R. Miller, A. Burke, Electrochemical capacitors: challenges and opportunities for real-world applications. Electrochem. Soc. **17**, 53–57 (2008)
5. Super Capacitor Market Size, Share—Segmented by type of capacitor (double layer, pseudo, hybrid), End-user Industry (aerospace & defense, utilities, industrial), and Region—Growth, Trends and Forecasts (2018–2023). https://www.mordorintelligence.com/industry-reports/supercapacitor-market
6. Supercapacitor Market worth 2.18 Billion USD by 2022, https://www.marketsandmarkets.com/PressReleases/supercapacitor.asp
7. International Council on Clean Transportation, https://www.theicct.org/
8. L. Weinstein, R. Dash, Supercapacitor carbons: Have exotic carbons failed? Mater. Today **16**, 356–357 (2013)
9. E. Frackowiak, F. Béguin, Carbon materials for the electrochemical storage of energy in capacitors. Carbon **39**, 937–950 (2001)
10. A.G. Pandolfo, A.F. Hollenkamp, Carbon properties and their role in supercapacitors. J. Power Sourc. **157**, 11–27 (2006)
11. P. Simon, A. Burke, Nanostructured carbons: double-layer capacitance and more. Electrochem. Soc. **17**, 38–43 (2008)
12. J.P. Zheng, Hydrous ruthenium oxide as an electrode material for electrochemical capacitors. J. Electrochem. Soc. **142**, 2699 (1995)
13. M. Huang, F. Li, F. Dong, Y.X. Zhang, L.L. Zhang, MnO_2 -based nanostructures for high-performance supercapacitors. J. Mater. Chem. A. **3**, 21380–21423 (2015)
14. Y. Wang, J. Guo, T. Wang, J. Shao, D. Wang, Y.-W. Yang, Mesoporous transition metal oxides for supercapacitors. Nanomaterials. **5**, 1667–1689 (2015)
15. M. Fukuhara, T. Kuroda, F. Hasegawa, Amorphous titanium-oxide supercapacitors. Sci. Rep. **6**, 35870 (2016)
16. W. Wei, X. Cui, W. Chen, D.G. Ivey, Manganese oxide-based materials as electrochemical supercapacitor electrodes. Chem. Soc. Rev. **40**, 1697–1721 (2011)
17. L. Feng, Y. Zhu, H. Ding, C. Ni, Recent progress in nickel based materials for high performance pseudocapacitor electrodes. J. Power Sourc. **267**, 430–444 (2014)

18. G. Zhang, X. Xiao, B. Li, P. Gu, H. Xue, H. Pang, Transition metal oxides with one-dimensional/one-dimensional-analogue nanostructures for advanced supercapacitors. J. Mater. Chem. A. **5**, 8155–8186 (2017)
19. F. Liu, H. Su, L. Jin, H. Zhang, X. Chu, W. Yang, Facile synthesis of ultrafine cobalt oxide nanoparticles for high-performance supercapacitors. J. Colloid Interface Sci. **505**, 796–804 (2017)
20. Y. Hu, *Carbon and Metal Oxides Based Nanomaterials for Flexible High Performance Asymmetric Supercapacitors* (Springer Singapore, 2018)
21. K. Naoi, M. Morita, Advanced polymers as active materials and electrolytes for electrochemical capacitors and hybrid capacitor systems. Electrochem. Soc. Interface. **17**, 44–48 (2008)
22. G.A. Snook, P. Kao, A.S. Best, Conducting-polymer-based supercapacitor devices and electrodes. J. Power Sourc. **196**, 1–12 (2011)
23. Q. Meng, K. Cai, Y. Chen, L. Chen, Research progress on conducting polymer based supercapacitor electrode materials. Nano Energy. **36**, 268–285 (2017)
24. K. Lota, V. Khomenko, E. Frackowiak, Capacitance properties of poly(3,4-ethylenedioxythiophene)/carbon nanotubes composites. J. Phys. Chem. Solids. **65**, 295–301 (2004)
25. V. Kumar, S. Kalia, H.C. Swart (eds.), *Conducting Polymer Hybrids* (Springer International Publishing, Cham, 2017)
26. S. Kondawar, *Conducting Polymer Nanocomposites for Supercapacitors* (Smithers Rapra, Shrewsbury, 2015)
27. I. Shown, A. Ganguly, L.-C. Chen, K.-H. Chen, Conducting polymer-based flexible supercapacitor. Energy Sci. Eng. **3**, 2–26 (2015)
28. L. Yu, G.Z. Chen, Redox electrode materials for supercapatteries. J. Power Sourc. **326**, 604–612 (2016)
29. B. Akinwolemiwa, G. Chen, B. Akinwolemiwa, G.Z. Chen, Fundamental consideration for electrochemical engineering of supercapattery. J. Braz. Chem. Soc. **29**, 960–972 (2018)
30. J. Ding, W. Hu, E. Paek, D. Mitlin, Review of hybrid ion capacitors: from aqueous to lithium to sodium. Chem. Rev. **118**, 6457–6498 (2018)
31. P. Han, G. Xu, X. Han, J. Zhao, X. Zhou, G. Cui, Lithium ion capacitors in organic electrolyte system: scientific problems, material development, and key technologies. Adv. Energy Mater. **8**, 1801243 (2018)
32. V. Aravindan, M. Ulaganathan, S. Madhavi, Research progress in Na-ion capacitors. J. Mater. Chem. A. **4**, 7538–7548 (2016)
33. L. Ye, Q. Liang, Y. Lei, X. Yu, C. Han, W. Shen, Z.-H. Huang, F. Kang, Q.-H. Yang, A high performance Li-ion capacitor constructed with $Li_4Ti_5O_{12}$/C hybrid and porous graphene macroform. J. Power Sourc. **282**, 174–178 (2015)
34. T. Rauhala, J. Leis, T. Kallio, K. Vuorilehto, Lithium-ion capacitors using carbide-derived carbon as the positive electrode—a comparison of cells with graphite and $Li_4Ti_5O_{12}$ as the negative electrode. J. Power Sourc. **331**, 156–166 (2016)
35. A. Slesinski, K. Fic, E. Frackowiak, New trends in electrochemical capacitors. Adv. Inorg. Chem. **72**, 247–286 (2018)
36. C. Zhong, Y. Deng, W. Hu, J. Qiao, L. Zhang, J. Zhang, A review of electrolyte materials and compositions for electrochemical supercapacitors. Chem. Soc. Rev. **44**, 7484–7539 (2015)
37. F. Béguin, V. Presser, A. Balducci, E. Frackowiak, Carbons and electrolytes for advanced supercapacitors. Adv. Mater. **26**, 2219–2251 (2014)
38. M. Salanne, Ionic liquids for supercapacitor applications. Top. Curr. Chem. **375**, 63 (2017)
39. A. Brandt, S. Pohlmann, A. Varzi, A. Balducci, S. Passerini, Ionic liquids in supercapacitors. MRS Bull. **38**, 554–559 (2013)
40. A. Brandt, C. Ramirez-Castro, M. Anouti, A. Balducci, An investigation about the use of mixtures of sulfonium-based ionic liquids and propylene carbonate as electrolytes for supercapacitors. J. Mater. Chem. A. **1**, 12669 (2013)

41. S. Lall-Ramnarine, S. Suarez, N. Zmich, D. Ewko, S. Ramati, D. Cuffari, M. Sahin, Y. Adam, E. Rosario, D. Paterno, J. Wishart, Binary ionic liquid mixtures for supercapacitor applications. ECS Trans. **64**, 57–69 (2014)
42. F. Rouquerol, J. Rouquerol, K.S.W. Sing, P. Llewellyn, G. Maurin, *Adsorption by Powders and Porous Solids: Principles, Methodology and Applications* (Academic Press, Amsterdam, Elsevier, 2014)
43. M. Thommes, K. Kaneko, A.V. Neimark, J.P. Olivier, F. Rodriguez-Reinoso, J. Rouquerol, K.S.W. Sing, Physisorption of gases, with special reference to the evaluation of surface area and pore size distribution (IUPAC Technical Report). Pure Appl. Chem. **87**, 1051–1069 (2015)
44. S. Brunauer, P.H. Emmett, E. Teller, Adsorption of Gases in Multimolecular Layers. J. Am. Chem. Soc. **60**, 309–319 (1938)
45. J. Rouquerol, P. Llewellyn, F. Rouquerol, Is the bet equation applicable to microporous adsorbents? in *Characterization of Porous Solids VII Proceedings of the 7th International Symposium on the Characterization of Porous Solids (COPS-VII)* ed. by Elsevier. (Amsterdam, 2007), pp. 49–56
46. T.A. Centeno, F. Stoeckli, The assessment of surface areas in porous carbons by two model-independent techniques, the DR equation and DFT. Carbon **48**, 2478–2486 (2010)
47. M.M. Dubinin, L.V. Radushkevich, Equation of the characteristic curve of activated charcoal. Proc. Acad. Sci. Phys. Chem. Sect. USSR. **55**, 331–333 (1947)
48. K.S.W. Sing, F. Rouquerol, J. Rouquerol, *Adsorption by Powders and Porous Solids Methodology, and Applications* (Academic Press, London Principles, 1999)
49. K. Kaneko, C. Ishii, M. Ruike, H. Kuwabara, Origin of superhigh surface area and microcrystalline graphitic structures of activated carbons. Carbon **30**, 1075–1088 (1992)
50. N. Setoyama, T. Suzuki, K. Kaneko, Simulation study on the relationship between a high resolution αs-plot and the pore size distribution for activated carbon. Carbon **36**, 1459–1467 (1998)
51. F. Béguin, E. Frackowiak, *Carbons for Electrochemical Energy Storage and Conversion Systems* (CRC Press, Boca Raton, FL, 2010)
52. A.V. Neimark, Y. Lin, P.I. Ravikovitch, M. Thommes, Quenched solid density functional theory and pore size analysis of micro-mesoporous carbons. Carbon **47**, 1617–1628 (2009)
53. G.Y. Gor, M. Thommes, K.A. Cychosz, A.V. Neimark, Quenched solid density functional theory method for characterization of mesoporous carbons by nitrogen adsorption. Carbon **50**, 1583–1590 (2012)
54. M. Kruk, M. Jaroniec, A. Sayari, Application of large pore MCM-41 molecular sieves to improve pore size analysis using nitrogen adsorption measurements. Langmuir **13**, 6267–6273 (1997)
55. D. Lozano-Castelló, D. Cazorla-Amorós, A. Linares-Solano, Usefulness of CO_2 adsorption at 273 K for the characterization of porous carbons. Carbon **42**, 1231–1236 (2004)
56. Y. Gogotsi, P. Simon, True performance metrics in electrochemical energy storage. Science **334**, 917–918 (2011)
57. M.D. Stoller, R.S. Ruoff, Best practice methods for determining an electrode material's performance for ultra capacitors. Energy Environ. Sci. **3**, 1294–1301 (2010)
58. P.L. Taberna, P. Simon, J.F. Fauvarque, Electrochemical characteristics and impedance spectroscopy studies of carbon-carbon supercapacitors. J. Electrochem. Soc. **150**, A292 (2003)
59. F. Pico, C. Pecharroman, A. Ansón, M.T. Martínez, J.M. Rojo, Understanding carbon–carbon composites as electrodes of supercapacitors. J. Electrochem. Soc. **154**, 579–586 (2007)
60. C. Emmenegger, P. Mauron, P. Wenger, V. Hermann, R. Gallay, A. Züttel, Investigation of electrochemical double-layer (ECDL) capacitors electrodes based on carbon nanotubes and activated carbon materials. J. Power Sourc. **124**, 321–329 (2003)
61. A. Garcia-Gomez, P. Miles, T.A. Centeno, J.M. Rojo, Uniaxially oriented carbon monoliths as supercapacitor electrodes. Electrochim. Acta. **55**, 8539–8544 (2010)
62. C. Portet, P.L. Taberna, P. Simon, C. Laberty-Robert, Modification of Al current collector surface by sol-gel deposit for carbon-carbon supercapacitor applications. Electrochim. Acta. **49**, 905–912 (2004)

63. S.R.S. Prabaharan, R. Vimala, Z. Zainal, Nanostructured mesoporous carbon as electrodes for supercapacitors. J. Power Sourc. **161**, 730–736 (2006)
64. L. Wang, R. Wang, H. Zhao, L. Liu, D. Jia, High rate performance porous carbon prepared from coal for supercapacitors. Mater. Lett. **149**, 85–88 (2015)
65. K. Kierzek, E. Frackowiak, G. Lota, G. Gryglewicz, J. Machnikowski, Electrochemical capacitors based on highly porous carbons prepared by KOH activation. Electrochim. Acta. **49**, 515–523 (2004)
66. M.H. Tan, P. Li, J.T. Zheng, T. Noritatsu, M.B. Wu, Preparation and modification of high performance porous carbons from petroleum coke for use as supercapacitor electrodes. New Carbon Mater. **31**, 343–351 (2016)
67. Y. Zhang, T. Cai, J. Huang, W. Xing, Z. Yan, Functionalized activated carbon prepared form petroleum coke with high-rate supercapacitive performance. J. Mater. Res. **31**, 3723–3730 (2016)
68. Y. Zhang, Y. Zhang, J. Huang, D. Du, W. Xing, Z. Yan, Enhanced capacitive performance of N-doped activated carbon from petroleum coke by combining ammoxidation with KOH activation. Nanoscale Res. Lett. **11**, 0–6 (2016)
69. X. Meng, Q. Cao, L. Jin, X. Zhang, S. Gong, P. Li, Carbon electrode materials for supercapacitors obtained by co-carbonization of coal-tar pitch and sawdust. J. Mater. Sci. **52**, 760–769 (2017)
70. C.-W. Huang, C.-T. Hsieh, P.-L. Kuo, H. Teng, Electric double layer capacitors based on a composite electrode of activated mesophase pitch and carbon nanotubes. J. Mater. Chem. **22**, 7314 (2012)
71. M. Olivares-Marín, J.A. Fernández, M.J. Lázaro, C. Fernández-González, A. Macías-García, V. Gómez-Serrano, F. Stoeckli, T.A. Centeno, Cherry stones as precursor of activated carbons for supercapacitors. Mater. Chem. Phys. **114**, 323–327 (2009)
72. G. Zhang, Y. Chen, Y. Chen, H. Guo, Activated biomass carbon made from bamboo as electrode material for supercapacitors. Mater. Res. Bull. **102**, 391–398 (2018)
73. F.O. Ochai-Ejeh, A. Bello, J. Dangbegnon, A.A. Khaleed, M.J. Madito, F. Bazegar, N. Manyala, High electrochemical performance of hierarchical porous activated carbon derived from lightweight cork (Quercus suber). J. Mater. Sci. **52**, 10600–10613 (2017)
74. X.L. Su, J.R. Chen, G.P. Zheng, J.H. Yang, X.X. Guan, P. Liu, X.C. Zheng, Three-dimensional porous activated carbon derived from loofah sponge biomass for supercapacitor applications. Appl. Surf. Sci. **436**, 327–336 (2018)
75. N. Querejeta, C. Pevida, T.A. Centeno, L. Guardia, L. Su, Winery wastes as precursors of sustainable porous carbons for environmental applications **193** 614–624 (2018)
76. X. Zhu, S. Yu, K. Xu, Y. Zhang, L. Zhang, G. Lou, Y. Wu, E. Zhu, H. Chen, Z. Shen, B. Bao, S. Fu, Sustainable activated carbons from dead ginkgo leaves for supercapacitor electrode active materials. Chem. Eng. Sci. **181**, 36–45 (2018)
77. H. Xuan, G. Lin, F. Wang, J. Liu, X. Dong, F. Xi, Preparation of biomass-activated porous carbons derived from torreya grandis shell for high-performance supercapacitor. J. Solid State Electrochem. **21**, 2241–2249 (2017)
78. H. Yang, Y. Tang, X. Huang, L. Wang, Q. Zhang, Activated porous carbon derived from walnut shells with promising material properties for supercapacitors. J. Mater. Sci. Mater. Electron. **28**, 18637–18645 (2017)
79. A. Jain, S.K. Tripathi, Nano-porous activated carbon from sugarcane waste for supercapacitor application. J. Energy Storage. **4**, 121–127 (2015)
80. M. Karnan, K. Subramani, P.K. Srividhya, M. Sathish, Electrochemical studies on corncob derived activated porous carbon for supercapacitors application in aqueous and non-aqueous electrolytes. Electrochim. Acta. **228**, 586–596 (2017)
81. N.D. Nogués, Preparación y activación de fibras a partir de breas de aceite de antraceno (2013)
82. S. Pohlmann, B. Lobato, T.A. Centeno, A. Balducci, The influence of pore size and surface area of activated carbons on the performance of ionic liquid based supercapacitors. Phys. Chem. Chem. Phys. **15**, 17287–17294 (2013)

83. S. Leyva-García, D. Lozano-Castelló, E. Morallón, T. Vogl, C. Schütter, S. Passerini, A. Balducci, D. Cazorla-Amorós, Electrochemical performance of a superporous activated carbon in ionic liquid-based electrolytes. J. Power Sourc. **336**, 419–426 (2016)
84. C. Zhong, Y. Deng, W. Hu, D. Sun, X. Han, J. Qiao, J. Zhang (eds.), *Electrolytes for Electrochemical Supercapacitors* (CRC Press/Taylor & Francis Group, Boca Raton, 2016)
85. F. Béguin, E. Frąckowiak (eds.), *Supercapacitors: Materials, Systems, and Applications* (Wiley-VCH, Weinheim, 2013)
86. M.F. Dupont, S.W. Donne, Charge storage mechanisms in electrochemical capacitors: Effects of electrode properties on performance. J. Power Sourc. **326**, 613–623 (2016)
87. T. Kyotani, Control of pore structure in carbon. Carbon **38**, 269–286 (2000)
88. W. Li, J. Liu, D. Zhao, Mesoporous materials for energy conversion and storage devices. Nat. Rev. Mater. **1** (2016)
89. H. Zhang, X. Zhang, Y. Ma, Enhanced capacitance supercapacitor electrodes from porous carbons with high mesoporous volume. Electrochim. Acta. **184**, 347–355 (2015)
90. M.-B. Wu, L.-Y. Li, J. Liu, Y. Li, P.-P. Ai, W.-T. Wu, J.-T. Zheng, Template-free preparation of mesoporous carbon from rice husks for use in supercapacitors. New Carbon Mater. **30**, 471–475 (2015)
91. A.B. Fuertes, G. Lota, T.A. Centeno, E. Frackowiak, Templated mesoporous carbons for supercapacitor application. Electrochim. Acta. **50**, 2799–2805 (2005)
92. K. Wilgosz, X. Chen, K. Kierzek, J. Machnikowski, R.J. Kalenczuk, E. Mijowska, Template method synthesis of mesoporous carbon spheres and its applications as supercapacitors. Nanoscale Res. Lett. **7**, 1–5 (2012)
93. Y. Fu, N. Zhang, Y. Shen, X. Ge, M. Chen, Micro-mesoporous carbons from original and pelletized rice husk via one- step catalytic pyrolysis. Bioresour. Technol. **269**, 67–73 (2018)
94. Y.S. Yun, M.H. Park, S.J. Hong, M.E. Lee, Y.W. Park, H.J. Jin, Hierarchically porous carbon nanosheets from waste coffee grounds for supercapacitors. ACS Appl. Mater. Interfaces. **7**, 3684–3690 (2015)
95. M.H. Kim, K.B. Kim, S.M. Park, K.C. Roh, Hierarchically structured activated carbon for ultracapacitors. Sci. Rep. **6**, 2–7 (2016)
96. L. Fang, Y. Xie, Y. Wang, Z. Zhang, P. Liu, N. Cheng, Facile synthesis of hierarchical porous carbon nanorods for supercapacitors application. Appl. Surf. Sci. **464**, 479–487 (2019)
97. D. Ma, G. Wu, J. Wan, F. Ma, W. Geng, S. Song, Oxygen-enriched hierarchical porous carbon derived from biowaste sunflower heads for high-performance supercapacitors. RSC Adv. **5**, 107785–107792 (2015)
98. Z. Zhang, Z. Zhou, H. Peng, Y. Qin, G. Li, Nitrogen- and oxygen-containing hierarchical porous carbon frameworks for high-performance supercapacitors. Electrochim. Acta. **134**, 471–477 (2014)
99. M. Demir, A.A. Farghaly, M.J. Decuir, M.M. Collinson, R.B. Gupta, Supercapacitance and oxygen reduction characteristics of sulfur self-doped micro/mesoporous bio-carbon derived from lignin. Mater. Chem. Phys. **216**, 508–516 (2018)
100. Y. Zhou, J. Ren, Y. Yang, Q. Zheng, J. Liao, F. Xie, W. Jie, D. Lin, Biomass-derived nitrogen and oxygen co-doped hierarchical porous carbon for high performance symmetric supercapacitor. J. Solid State Chem. **268**, 149–158 (2018)
101. Z. Liu, Z. Zhu, J. Dai, Y. Yan, Waste biomass based-activated carbons derived from soybean pods as electrode materials for high-performance supercapacitors. Chem. Sel. **3**, 5726–5732 (2018)
102. B. Wang, Y. Wang, Y. Peng, X. Wang, N. Wang, J. Wang, Nitrogen-doped biomass-based hierarchical porous carbon with large mesoporous volume for application in energy storage. Chem. Eng. J. **348**, 850–859 (2018)
103. H.S. Nalwa, *Encyclopedia of Nanoscience and Nanotechnology*, vol. 4 (American Scientific Publishers, Stevenson Ranch Calif, 2004)
104. A.C. Pierre, M. Pajonk, Chemistry of aerogels and their applications. Chem. Rev. **102**, 4243–4265 (2002)

105. A. Halama, B. Szubzda, G. Pasciak, Carbon aerogels as electrode material for electrical double layer super capacitors—synthesis and properties. Electrochim. Acta. **55**, 7501–7505 (2010)
106. G. Rasines, C. Macías, M. Haro, J. Jagiello, C.O. Ania, Effects of CO_2 activation of carbon aerogels leading to ultrahigh micro-meso porosity. Microporous Mesoporous Mater. **209**, 18–22 (2015)
107. M.S. Contreras, C.A. Páez, L. Zubizarreta, A. Léonard, S. Blacher, C.G. Olivera-Fuentes, A. Arenillas, J.-P. Pirard, N. Job, A comparison of physical activation of carbon xerogels with carbon dioxide with chemical activation using hydroxides. Carbon **48**, 3157–3168 (2010)
108. B. Fang, L. Binder, A modified activated carbon aerogel for high-energy storage in electric double layer capacitors. J. Power Sourc. **163**, 616–622 (2006)
109. D. Liu, J. Shen, N. Liu, H. Yang, A. Du, Preparation of activated carbon aerogels with hierarchically porous structures for electrical double layer capacitors. Electrochim. Acta. **89**, 571–576 (2013)
110. M. Enterría, F.J. Martín-Jimeno, F. Suárez-García, J.I. Paredes, M.F.R. Pereira, J.I. Martins, A. Martínez-Alonso, J.M.D. Tascón, J.L. Figueiredo, Effect of nanostructure on the supercapacitor performance of activated carbon xerogels obtained from hydrothermally carbonized glucose-graphene oxide hybrids. Carbon **105**, 474–483 (2016)
111. E.J. Lee, Y.J. Lee, J.K. Kim, M. Lee, J. Yi, J.R. Yoon, J.C. Song, I.K. Song, Oxygen group-containing activated carbon aerogel as an electrode material for supercapacitor. Mater. Res. Bull. **70**, 209–214 (2015)
112. F. Li, L. Xie, G. Sun, F. Su, Q. Kong, Y. Cao, X. Guo, C. Chen, Structural evolution of carbon aerogel microspheres by thermal treatment for high–power supercapacitors. J. Energy Chem. **27**, 439–446 (2018)
113. G. Diossa, C.D. Castro, Z. Zapata-Benabithe, G. Quintana, G. Diossa, C.D. Castro, Zapata-Benabithe, Z., Quintana, G.: Evaluación de la capacidad de almacenamiento de energía en xerogeles de carbono activados obtenidos a partir lignina. Rev. Ion, Investig. Optim. y nuevos procesos en Ing. **30**, 17–30 (2018)
114. E.G. Calvo, F. Lufrano, P. Staiti, A. Brigandì, A. Arenillas, J.A. Menéndez, Optimizing the electrochemical performance of aqueous symmetric supercapacitors based on an activated carbon xerogel. J. Power Sourc. **241**, 776–782 (2013)
115. Y. Gogotsi, V. Presser, *Carbon Nanomaterials* (CRC Press, Taylor & Francis Group, 2014)
116. K. Ozoemena, S. Chen, *Nanomaterials in Advanced Batteries and Supercapacitors* (Springer International Publishing, 2018)
117. J. Eskusson, A. Jänes, A. Kikas, L. Matisen, E. Lust, Physical and electrochemical characteristics of supercapacitors based on carbide derived carbon electrodes in aqueous electrolytes. J. Power Sourc. **196**, 4109–4116 (2011)
118. L. Zheng, Y. Wang, X. Wang, X. Wang, H. An, L. Yi, The effects of surface modification on the supercapacitive behaviors of carbon derived from calcium carbide. J. Mater. Sci. **45**, 6030–6037 (2010)
119. J.A. Fernández, M. Arulepp, J. Leis, F. Stoeckli, T.A. Centeno, EDLC performance of carbide-derived carbons in aprotic and acidic electrolytes. Electrochim. Acta. **53**, 7111–7116 (2008)
120. Y. Korenblit, M. Rose, E. Kockrick, L. Borchardt, A. Kvit, S. Kaskel, G. Yushin, High-rate electrochemical capacitors based on ordered mesoporous silicon carbide-derived carbon. ACS Nano **4**, 1337–1344 (2010)
121. E. Tee, I. Tallo, H. Kurig, T. Thomberg, A. Jänes, E. Lust, Huge enhancement of energy storage capacity and power density of supercapacitors based on the carbon dioxide activated microporous SiC-CDC. Electrochim. Acta. **161**, 364–370 (2015)
122. M. Rose, Y. Korenblit, E. Kockrick, L. Borchardt, M. Oschatz, S. Kaskel, G. Yushin, Hierarchical micro- and mesoporous carbide-derived carbon as a high-performance electrode material in supercapacitors. Small **7**, 1108–1117 (2011)
123. H. Wang, Q. Gao, Synthesis, characterization and energy-related applications of carbide-derived carbons obtained by the chlorination of boron carbide. Carbon **47**, 820–828 (2009)
124. K. Brousse, P. Huang, S. Pinaud, M. Respaud, B. Chaudret, C. Lethien, P.-L. Taberna, P. Simon, P, On-chip carbide derived carbon films for high performance micro-supercapacitors,

in *2016 IEEE Nanotechnology Materials and Devices Conference (NMDC)* (IEEE, 2016), pp. 1–3
125. E. Tee, I. Tallo, T. Thomberg, A. Jänes, E. Lust, Supercapacitors based on activated silicon carbide-derived carbon materials and ionic liquid. J. Electrochem. Soc. **163**, A1317–A1325 (2016)
126. A. Jänes, J. Eskusson, T. Thomberg, T. Romann, E. Lust, Ionic liquid-1,2-dimethoxyethane mixture as electrolyte for high power density supercapacitors. J. Energy Chem. **25**, 609–614 (2016)
127. J.-K. Ewert, D. Weingarth, C. Denner, M. Friedrich, M. Zeiger, A. Schreiber, N. Jäckel, V. Presser, R. Kempe, Enhanced capacitance of nitrogen-doped hierarchically porous carbide-derived carbon in matched ionic liquids. J. Mater. Chem. A. **3**, 18906–18912 (2015)
128. A. Jorio, G. Dresselhaus, M.S. Dresselhaus, *Carbon Nanotubes: Advanced Topics in the Synthesis, Structure, Properties, and Applications* (Springer, Berlin Heidelberg, 2008)
129. J. Prasek, J. Drbohlavova, J. Chomoucka, J. Hubalek, O. Jasek, V. Adam, R. Kizek, Methods for carbon nanotubes synthesis—review. J. Mater. Chem. **21**, 15872 (2011)
130. E. Frackowiak, K. Jurewicz, K. Szostak, S. Delpeux, F. Béguin, Nanotubular materials as electrodes for supercapacitors **77–78**, 213–219 (2002)
131. L.M. Liz-Marzán, M. Giersig, *Low-Dimensional Systems: Theory, Preparation, and Some Applications* (Kluwer Academic Publishers, Dordrecht, 2003)
132. Y. Zhang, H. Wu, L. Cheng, L. Zheng, W. Yuan, Carbon nanotubes for electrochemical capacitors, in *Industrial Applications of Carbon Nanotubes*, ed. by H. Peng, Q. Li, T. Chen (Elsevier, 2016), pp. 277–321
133. E. Frackowiak, K. Metenier, V. Bertagna, F. Beguin, Supercapacitor electrodes from multiwalled carbon nanotubes. Appl. Phys. Lett. **77**, 2421–2423 (2000)
134. Q. Jiang, M.Z. Qu, G.M. Zhou, B.L. Zhang, Z.L. Yu, A study of activated carbon nanotubes as electrochemical super capacitors electrode materials. Mater. Lett. **57**, 988–991 (2002)
135. E. Frackowiak, S. Delpeux, K. Jurewicz, K. Szostak, D. Cazorla-Amoros, F. Béguin, Enhanced capacitance of carbon nanotubes through chemical activation. Chem. Phys. Lett. **361**, 35–41 (2002)
136. J.Y. Lee, K.H. An, J.K. Heo, Y.H. Lee, Fabrication of supercapacitor electrodes using fluorinated single-walled carbon nanotubes. J. Phys. Chem. B. **107**, 8812–8815 (2003)
137. C.G. Liu, H.T. Fang, F. Li, M. Liu, H.M. Cheng, Single-walled carbon nanotubes modified by electrochemical treatment for application in electrochemical capacitors. J. Power Sourc. **160**, 758–761 (2006)
138. I.B. Dogru, M.B. Durukan, O. Turel, H.E. Unalan, Flexible supercapacitor electrodes with vertically aligned carbon nanotubes grown on aluminum foils. Prog. Nat. Sci. Mater. Int. **26**, 232–236 (2016)
139. C. Niu, E.K. Sichel, R. Hoch, D. Moy, H. Tennent, High power electrochemical capacitors based on carbon nanotube electrodes. Appl. Phys. Lett. **70**, 1480–1482 (1997)
140. Q.L. Chen, K.H. Xue, W. Shen, F.F. Tao, S.Y. Yin, W. Xu, Fabrication and electrochemical properties of carbon nanotube array electrode for supercapacitors. Electrochim. Acta **49**, 4157–4161 (2004)
141. B. Kim, H. Chung, W. Kim, High-performance supercapacitors based on vertically aligned carbon nanotubes and nonaqueous electrolytes. Nanotechnology **23**, 155401 (2012)
142. Y.J. Kim, Y.A. Kim, T. Chino, H. Suezaki, M. Endo, M.S. Dresselhaus, Chemically modified multiwalled carbon nanotubes as an additive for supercapacitors. Small **2**, 339–345 (2006)
143. C. Portet, G. Yushin, Y. Gogotsi, Electrochemical performance of carbon onions, nanodiamonds, carbon black and multiwalled nanotubes in electrical double layer capacitors. Carbon **45**, 2511–2518 (2007)
144. K.L. Van Aken, K. Maleski, T.S. Mathis, J.P. Breslin, Y. Gogotsi, Processing of onion-like carbon for electrochemical capacitors. ECS J. Solid State Sci. Technol. **6**, M3103–M3108 (2017)
145. M.E. Plonska-Brzezinska, D.M. Brus, A. Molina-Ontoria, L. Echegoyen, Synthesis of carbon nano-onion and nickel hydroxide/oxide composites as supercapacitor electrodes. RSC Adv. **3**, 25891–25901 (2013)

146. M. Zeiger, N. Jäckel, V.N. Mochalin, V. Presser, Review: carbon onions for electrochemical energy storage. J. Mater. Chem. A. **4**, 3172–3196 (2016)
147. A.D. McNaught, A. Wilkinson, Graphene layer, in *IUPAC Compendium of Chemical Terminology* (Blackwell Scientific Publications, Oxford, 1997)
148. A. Bianco, H.-M. Cheng, T. Enoki, Y. Gogotsi, R.H. Hurt, N. Koratkar, T. Kyotani, M. Monthioux, C.R. Park, J.M.D. Tascon, J. Zhang, All in the graphene family – A recommended nomenclature for two-dimensional carbon materials. Carbon **65**, 1–6 (2013)
149. C. Soldano, A. Mahmood, E. Dujardin, Production, properties and potential of graphene. Carbon **48**, 2127–2150 (2010)
150. Market View: Graphene—Energy Storage Journal https://www.energystoragejournal.com/2016/06/09/market-view-graphene/
151. B. Lobato, L. Suárez, L. Guardia, T.A. Centeno, Capacitance and surface of carbons in supercapacitors. Carbon **122**, 434–445 (2017)
152. W. Yang, M. Ni, X. Ren, Y. Tian, N. Li, Y. Su, X. Zhang, Graphene in supercapacitor applications. Curr. Opin. Colloid Interface Sci. **20**, 416–428 (2015)
153. Q. Ke, J. Wang, Graphene-based materials for supercapacitor electrodes—a review. J. Mater. **2**, 37–54 (2016)
154. S.K. Kandasamy, K. Kandasamy, Recent advances in electrochemical performances of graphene composite (Graphene-Polyaniline/Polypyrrole/Activated Carbon/Carbon Nanotube) electrode materials for supercapacitor: a review. J. Inorg. Organomet. Polym. Mater. **28**, 559–584 (2018)
155. B. Lobato, V. Vretenár, P. Kotrusz, M. Hulman, T.A. Centeno, Reduced graphite oxide in supercapacitor electrodes. J. Colloid Interface Sci. **446**, 203–207 (2015)
156. B. Lobato, R. Wendelbo, V. Barranco, T.A. Centeno, Graphite oxide: an interesting candidate for aqueous supercapacitors. Electrochim. Acta. **149**, 245–251 (2014)
157. J. Bae, O.S. Kwon, C.-S. Lee, Energy efficient graphene based high performance capacitors. Recent Pat. Nanotechnol. **11**, 93–100 (2017)
158. J.R. Miller, R.A. Outlaw, B.C. Holloway, Graphene electric double layer capacitor with ultra-high-power performance. Electrochim. Acta **56**, 10443–10449 (2011)
159. J. Yan, Q. Wang, T. Wei, Z. Fan, Recent advances in design and fabrication of electrochemical supercapacitors with high energy densities. Adv. Energy Mater. **4**, 1300816 (2014)
160. O. Barbieri, M. Hahn, A. Herzog, R. Kötz, Capacitance limits of high surface area activated carbons for double layer capacitors. Carbon **43**, 1303–1310 (2005)
161. M. Lazzari, F. Soavi, M. Mastragostino, Mesoporous carbon design for ionic liquid-based double-layer supercapacitors. Fuel Cells. **10**, 840–847 (2010)
162. D. Qu, H. Shi, Studies of activated carbons used in double-layer capacitors. J. Power Sourc. **74**, 99–107 (1998)
163. H. Shi, Activated carbons and double layer capacitance. Electrochim. Acta **41**, 1633–1639 (1996)
164. L.-H. Wang, M. Toyoda, M. Inagaki, Dependence of electric double layer capacitance of activated carbons on the types of pores and their surface areas. New Carbon Mater. **23**, 111–115 (2008)
165. L. Wang, M. Fujita, M. Inagaki, Relationship between pore surface areas and electric double layer capacitance in non-aqueous electrolytes for air-oxidized carbon spheres. Electrochim. Acta. **51**, 4096–4102 (2006)
166. G. Gryglewicz, J. Machnikowski, E. Lorenc-Grabowska, G. Lota, E. Frackowiak, Effect of pore size distribution of coal-based activated carbons on double layer capacitance. Electrochim. Acta. **50**, 1197–1206 (2005)
167. F. Stoeckli, T.A. Centeno, Structural and chemical characterization of carbons used as supercapacitors, in *Recent Advances in Supercapacitors, 2006*. ed. by V. Gupta, B.E. Conway (Transworld Research Network, Kerala India, 2006), pp. 57–77
168. J.-P. Randin, E. Yeager, Differential capacitance study on the basal plane of stress-annealed pyrolytic graphite. J. Electroanal. Chem. Interfacial Electrochem. **36**, 257–276 (1972)

169. J.-P. Randin, E. Yeager, Differential capacitance study on the edge orientation of pyrolytic graphite and glassy carbon electrodes. J. Electroanal. Chem. Interfacial Electrochem. **58**, 313–322 (1975)
170. D. Qu, Studies of the activated carbons used in double-layer supercapacitors. J. Power Sourc. **109**, 403–411 (2002)
171. T. Kim, S. Lim, K. Kwon, S.-H. Hong, W. Qiao, C.K. Rhee, S.-H. Yoon, I. Mochida, Electrochemical Capacitances of Well-Defined Carbon Surfaces. Langmuir **22**, 9086–9088 (2006)
172. J. Chmiola, G. Yushin, Y. Gogotsi, C. Portet, P. Simon, P.L. Taberna, Anomalous increase in carbon capacitance at pore sizes less than 1 nanometer. Science **313**, 1760–1763 (2006)
173. E. Raymundo-Piñero, K. Kierzek, J. Machnikowski, F. Béguin, Relationship between the nanoporous texture of activated carbons and their capacitance properties in different electrolytes. Carbon **44**, 2498–2507 (2006)
174. C. Largeot, C. Portet, J. Chmiola, P.-L. Taberna, Y. Gogotsi, P. Simon, Relation between the ion size and pore size for an electric double-layer capacitor. J. Am. Chem. Soc. **130**, 2730–2731 (2008)
175. H. Ji, X. Zhao, Z. Qiao, J. Jung, Y. Zhu, Y. Lu, L.L. Zhang, A.H. MacDonald, R.S. Ruoff, Capacitance of carbon-based electrical double-layer capacitors. Nat. Commun. **5**, 3317 (2014)
176. J. Rouquerol, D. Avnir, C.W. Fairbridge, D.H. Everett, J.M. Haynes, N. Pernicone, J.D.F. Ramsay, K.S.W. Sing, K.K. Unger, Recommendations for the characterization of porous solids (Technical Report). Pure Appl. Chem. **66**, 1739–1758 (1994)
177. D. Lozano-Castelló, F. Suárez-García, D. Cazorla-Amorós, Á Linares-Solano, Porous texture of carbons, in *Carbons for Electrochemical Energy Storage and Conversion Systems*. ed. by F. Béguin, E. Frackowiak (CRC Press, Boca Ratón, 2010), pp. 115–162
178. M. Sevilla, S. Álvarez, T.A. Centeno, A.B. Fuertes, F. Stoeckli, Performance of templated mesoporous carbons in supercapacitors. Electrochim. Acta. **52**, 3207–3215 (2007)
179. T.A. Centeno, O. Sereda, F. Stoeckli, Capacitance in carbon pores of 0.7 to 15 nm: a regular pattern. Phys. Chem. Chem. Phys. **13**, 12403 (2011)
180. H.A. Andreas, B.E. Conway, Examination of the double-layer capacitance of an high specific-area C-cloth electrode as titrated from acidic to alkaline pHs. Electrochim. Acta. **51**, 6510–6520 (2006)
181. K. Okajima, K. Ohta, M. Sudoh, Capacitance behavior of activated carbon fibers with oxygen-plasma treatment. Electrochim. Acta. **50**, 2227–2231 (2005)
182. M.J. Bleda-Martínez, J.A. Maciá-Agulló, D. Lozano-Castelló, E. Morallón, D. Cazorla-Amorós, A. Linares-Solano, Role of surface chemistry on electric double layer capacitance of carbon materials. Carbon **43**, 2677–2684 (2005)
183. E. Raymundo-Piñero, F. Leroux, F. Béguin, A high-performance carbon for supercapacitors obtained by carbonization of a seaweed biopolymer. Adv. Mater. **18**, 1877–1882 (2006)
184. M. Seredych, D. Hulicova-Jurcakova, G.Q. Lu, T.J. Bandosz, Surface functional groups of carbons and the effects of their chemical character, density and accessibility to ions on electrochemical performance. Carbon **46**, 1475–1488 (2008)
185. D. Hulicova-Jurcakova, M. Seredych, G.Q. Lu, T.J. Bandosz, Combined effect of nitrogen- and oxygen-containing functional groups of microporous activated carbon on its electrochemical performance in supercapacitors. Adv. Funct. Mater. **19**, 438–447 (2009)
186. T.A. Centeno, F. Stoeckli, The role of textural characteristics and oxygen-containing surface groups in the supercapacitor performances of activated carbons. Electrochim. Acta **52**, 560–566 (2006)
187. T.A. Centeno, F. Stoeckli, Surface-related capacitance of microporous carbons in aqueous and organic electrolytes. Electrochim. Acta **56**, 7334–7339 (2011)
188. V. Barranco, M.A. Lillo-Rodenas, A. Linares-Solano, A. Oya, F. Pico, J. Ibañez, F. Agullo-Rueda, J.M. Amarilla, J.M. Rojo, Amorphous carbon nanofibers and their activated carbon nanofibers as supercapacitor electrodes. J. Phys. Chem. C. **114**, 10302–10307 (2010)
189. S.T. Senthilkumar, B. Senthilkumar, S. Balaji, C. Sanjeeviraja, R. Kalai Selvan, Preparation of activated carbon from sorghum pith and its structural and electrochemical properties. Mater. Res. Bull. **46**, 413–419 (2011)

190. Z. Li, L. Zhang, B.S. Amirkhiz, X. Tan, Z. Xu, H. Wang, B.C. Olsen, C.M.B. Holt, D. Mitlin, Carbonized chicken eggshell membranes with 3D architectures as high-performance electrode materials for supercapacitors. Adv. Energy Mater. **2**, 431–437 (2012)
191. D. Hulicova, J. Yamashita, Y. Soneda, H. Hatori, M. Kodama, Supercapacitors prepared from melamine-based carbon **17**, 1241–1247 (2005)
192. X. Xiang, E. Liu, H. Xie, Y. Tian, Y. Wu, Z. Wu, Y. Zhu, Highly stable performance of supercapacitors using microporous carbon derived from phenol–melamine–formaldehyde resin. J. Solid State Electrochem. **16**, 2661–2666 (2012)
193. C. Ma, Y. Song, J. Shi, D. Zhang, Q. Guo, L. Liu, Preparation and electrochemical performance of heteroatom-enriched electrospun carbon nanofibers from melamine formaldehyde resin. J. Colloid Interface Sci. **395**, 217–223 (2013)
194. J. Yan, T. Wei, W. Qiao, Z. Fan, L. Zhang, T. Li, Q. Zhao, A high-performance carbon derived from polyaniline for supercapacitors. Electrochem. Commun. **12**, 1279–1282 (2010)
195. J. Han, G. Xu, B. Ding, J. Pan, H. Dou, D.R. MacFarlane, Porous nitrogen-doped hollow carbon spheres derived from polyaniline for high performance supercapacitors. J. Mater. Chem. A. **2**, 5352–5357 (2014)
196. Y. Song, Z. Qin, Z. Huang, T. Liu, Y. Li, X.-X. Liu, Nitrogen-doped carbon "spider webs" derived from pyrolysis of polyaniline nanofibers in ammonia for capacitive energy storage. J. Mater. Res. **33**, 1109–1119 (2018)
197. F. Su, C.K. Poh, J.S. Chen, G. Xu, D. Wang, Q. Li, J. Lin, X.W. Lou, Nitrogen-containing microporous carbon nanospheres with improved capacitive properties. Energy Environ. Sci. **4**, 717–724 (2011)
198. E. Raymundo-Piñero, M. Cadek, F. Béguin, Tuning carbon materials for supercapacitors by direct pyrolysis of seaweeds. Adv. Funct. Mater. **19**, 1032–1039 (2009)
199. B.E. Conway, Electrochemical Supercapacitors: Scientific Fundamentals and s(Plenum Press, 1999)
200. G. Lota, T.A. Centeno, E. Frackowiak, F. Stoeckli, Improvement of the structural and chemical properties of a commercial activated carbon for its application in electrochemical capacitors. Electrochim. Acta. **53**, 2210–2216 (2008)
201. T.A. Centeno, M. Hahn, J.A. Fernández, R. Kötz, F. Stoeckli, Correlation between capacitances of porous carbons in acidic and aprotic EDLC electrolytes. Electrochem. Commun. **9**, 1242–1246 (2007)
202. X. Wu, W. Xing, J. Florek, J. Zhou, G. Wang, S. Zhuo, Q. Xue, Z. Yan, F. Kleitz, On the origin of the high capacitance of carbon derived from seaweed with an apparently low surface area. J. Mater. Chem. A. **2**, 18998–19004 (2014)
203. X. Wu, J. Zhou, W. Xing, Y. Zhang, P. Bai, B. Xu, S. Zhuo, Q. Xue, Z. Yan, Insight into high areal capacitances of low apparent surface area carbons derived from nitrogen-rich polymers. Carbon **94**, 560–567 (2015)
204. S. Pohlmann, B. Lobato, T.A. Centeno, A. Balducci, The influence of pore size and surface area of activated carbons on the performance of ionic liquid based supercapacitors. Phys. Chem. Chem. Phys. **15**, 17287 (2013)
205. F. Stoeckli, A. Slasli, D. Hugi-Cleary, A. Guillot, The characterization of microporosity in carbons with molecular sieve effects. Microporous Mesoporous Mater. **51**, 197–202 (2002)
206. F. Stoeckli, T.A. Centeno, On the characterization of microporous carbons by immersion calorimetry alone. Carbon **35**, 1097–1100 (1997)
207. A. García-Gómez, G. Moreno-Fernández, B. Lobato, T.A. Centeno, Constant capacitance in nanopores of carbon monoliths. Phys. Chem. Chem. Phys. **17**, 15687–15690 (2015)
208. T.A. Centeno, J.A. Fernandez, F. Stoeckli, Correlation between heats of immersion and limiting capacitances in porous carbons. Carbon **46**, 1025–1030 (2008)
209. F. Stoeckli, T.A. Centeno, Optimization of the characterization of porous carbons for supercapacitors. J. Mater. Chem. A. **1**, 6865 (2013)
210. W. Gu, G. Yushin, Review of nanostructured carbon materials for electrochemical capacitor applications: advantages and limitations of activated carbon, carbide-derived carbon, zeolite-templated carbon, carbon aerogels, carbon nanotubes, onion-like carbon, and graphene. Wiley Interdiscip. Rev. Energy Environ. **3**, 424–473 (2014)

211. F. Stoeckli, T.A. Centeno, Pore size distribution and capacitance in microporous carbons. Phys. Chem. Chem. Phys. **14**, 11589 (2012)
212. T.A. Centeno, F. Stoeckli, The volumetric capacitance of microporous carbons in organic electrolyte. Electrochem. commun. **16**, 34–36 (2012)
213. D. Jiang, Z. Jin, D. Henderson, J. Wu, Solvent effect on the pore-size dependence of an organic electrolyte supercapacitor. J. Phys. Chem. Lett. **3**, 1727–1731 (2012)
214. D. Jiang, J. Wu, Unusual effects of solvent polarity on capacitance for organic electrolytes in a nanoporous electrode. Nanoscale. **6**, 5545–5550 (2014)
215. W. Hsieh, T.-L.A. Horng, H.-C. Huang, H. Teng, Facile simulation of carbon with wide pore size distribution for electric double-layer capacitance based on Helmholtz models. J. Mater. Chem. A. **3**, 16535–16543 (2015)
216. A. Garcia-Gomez, V. Barranco, G. Moreno-Fernandez, J. Ibañez, T.A. Centeno, J.M. Rojo, Correlation between capacitance and porosity in microporous carbon monoliths. J. Phys. Chem. C. **118**, 5134–5141 (2014)
217. T.A. Centeno, M. Sevilla, A.B. Fuertes, F. Stoeckli, On the electrical double-layer capacitance of mesoporous templated carbons. Carbon **43**, 3012–3015 (2005)
218. J.A. Fernández, T. Morishita, M. Toyoda, M. Inagaki, F. Stoeckli, T.A. Centeno, Performance of mesoporous carbons derived from poly(vinyl alcohol) in electrochemical capacitors. J. Power Sourc. **175**, 675–679 (2008)

Chapter 9
Carbon Nanomaterial-Based Photovoltaic Solar Cells

N. Ma. Rosas-Laverde and A. Pruna

9.1 Introduction into Photovoltaics

Renewable energy is one of the most important fields of research. It attracted increased interest worldwide as a solution for environmental pollution [1] as it allows the reduction in global warming, air pollution, and acid rain [2, 3]. Moreover, it allows the reduction in generation of greenhouse gases such as CO_2 [4]. Renewable energy could also replace the use of fossil fuels, e.g., petroleum or others such as natural gas and coal [4]. Nowadays, the demand for energy is estimated to increase exponentially worldwide and so it will double by 2050 and triple by 2100 [5].

Despite the environmental issues caused by the use of fossil fuels, it was not until after the oil crisis in 1973, when some countries decided to start researching other kind sources of energy alternatives. At the beginning of 1990, some researches focused on the generation of energy by using solar cells [6].

In order to reduce and control the environmental problems, alternatives to produce cleaner and more renewable energies such as hydro, wind, thermal, geothermal, biomass, and solar energy were sought. Furthermore, other kinds of fuels such as biofuels and fuel cells were proposed [5].

Considering this field, the photovoltaic (PV) solar energy is one of the most growing industries [2]. Photovoltaics represent a clean energy and the most popular option. In addition, this kind of renewable energy is low cost and easily fabricated [2] as it uses solar energy radiation.

N. Ma. Rosas-Laverde
Department of Materials and Mechanical Engineering, Universitat Politècnica de València, Valencia, Spain

Department of Materials, Escuela Politécnica Nacional, Quito, Ecuador

A. Pruna (✉)
Center for Surface Science and Nanotechnology, Polytechnic University of Bucharest, Bucharest, Romania
e-mail: apruna@itm.upv.es

S. Kaneko et al. (eds.), *Carbon Related Materials*,
https://doi.org/10.1007/978-981-15-7610-2_9

Solar energy is the most abundant, safe, clean, cheap, and renewable energy source on Earth [7–9] given that the sun is the largest source of energy in our solar system [4]. The solar power reaching the Earth equals 170,000,000 GW [3], and it could produce electric energy without pollution or environmental problems through photovoltaic effect [7].

Therefore, the challenge nowadays is to convert the solar energy into electricity by considering combined low-cost and highly efficient materials [10]. In this respect, it is important to develop new architectures that allow the manufacture of devices with photovoltaic applications [8]. Solar cells are devices which transform sunlight into electricity through photoelectric effect [7, 9, 11]. It is considered that this kind of energy would cover 20% of primary energy demands by 2050 [12]. Therefore, the development of new architectures and technologies to obtain improved yields is of paramount importance.

The first photovoltaic device fabricated by Chapin in 1954 achieved an efficiency of 6% with a silicon p–n junction solar cell [4, 5]. One of the alternatives to improve the performance of photovoltaic devices considered the manufacture of structures at nanometric scale because these materials present significant improvements and/or provide with novel unique synergetic properties [13] that allow the expanding of their field of application [14]. Furthermore, structures at nanoscale can be fabricated with specific properties, their sizes, structures, and morphologies can be tailored so as to meet the given requirements of manufacturing a device for photovoltaic applications [14].

The research in solar cells field has grown exponentially since the beginning, when French physicist Antoine-Cesar Edmond Becquerel observed the photovoltaic effect for the first time in 1839 [6]. There are about 125,436 research articles, reviews, and book chapters among others that cover this topic. However, it is only in the last 10 years that the largest scientific production has been produced, generating more than 80% of the total publications in this area. Figure 9.1 shows (a) the number of published articles in the field of solar cells from 1994 until now and (b) countries with publications greater than 4000. Some countries such as USA, Japan and others from Europe Union keep working in solar cells field since 1990 [6].

Photovoltaic energy presents some advantages over other conventional energy sources. By comparison with fossil fuels, this technology does not produce serious environmental problems during its production and does not need to be extracted, refined, or transported [2]. Furthermore, with respect to other renewable sources, it has a low cost of operating, it can be installed in the urban places and does not need a large area to be installed [2].

Nevertheless, the photovoltaic energy has some disadvantage, as well, e.g., it needs more material and human resources than other energy sources and its efficiency is related to the incidence of sunlight, area and it supposes a high investment cost [2].

Generally speaking, PV solar cells are semiconductor diodes [6]. They convert solar energy into electrical energy in the following stages: (a) light radiation (photon absorption) emission by the sun that gets absorbed and electron–hole pairs generation, (b) the electron–hole pair diffusion, (c) charge separation within the structure of the cell by the electric field of the junction, and (d) carrier transport and collection of

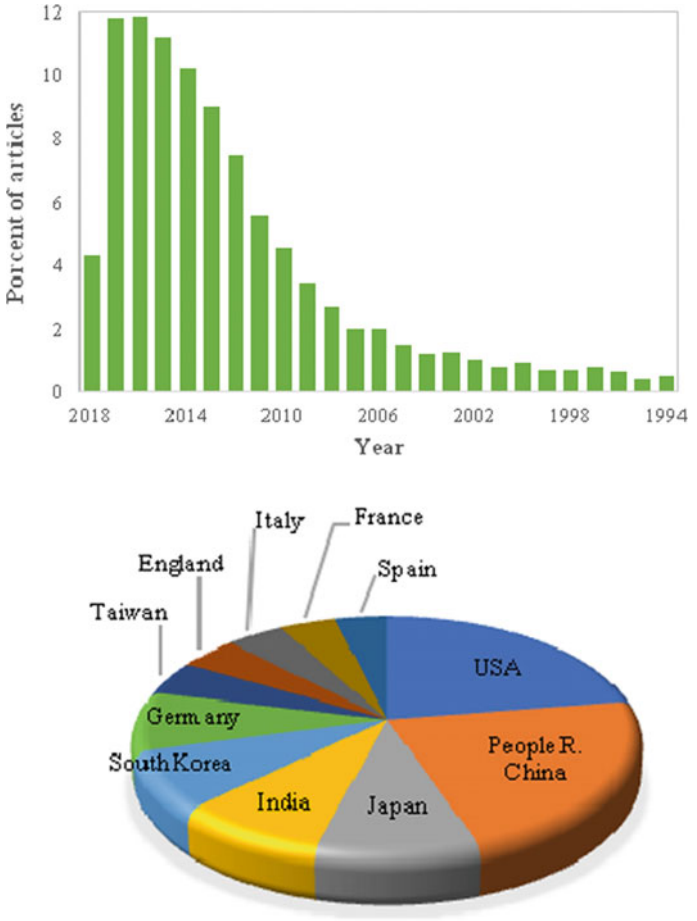

Fig. 9.1 Number of publications per year since 1994 (upper figure) and number of countries exceeding 4000 publications on solar cells until now (lower figure). The counts were obtained using the keywords "solar cell" or "photovoltaic cell" or "solar photovoltaic" or "photovoltaic solar energy" or "photovoltaic" in the ISI Web of Science portal data accessed on June 22, 2018

the electrons in n–type semiconductor and the holes in p–type semiconductor. The electrical energy is produced through the flow of electrons from the n–zone to the p–zone [5, 15, 16].

Photovoltaic solar cells are organized into three global groups according to their generation [2, 5, 17, 18]. The power conversion efficiency (*PCE*) of a solar cell, regardless of the type of generation, depends on the architecture of the structure, the forms and the methods of deposition/fabrication, the compatibility and interaction between the components, as well as the crystalline features [19] as shown in Table 9.1.

Table 9.1 Solar cells classification by type of generation

Generation	Type of solar cell—power conversion efficiency (*PCE*, %)	Advantages and disadvantages	References
First	Crystalline silicon, 25.6 • Simple crystalline, 28 • Multicrystalline, 15	• The highest efficiency • 90% commercial production • High manufacturing, installation, and material cost	[5, 19–21]
Second	Thin film technology • Amorphous silicon, 16.55 • Chalcogenide, 22.6 • Heterojunction	• Low cost of components and production process • Lower performance • Cd is heavily toxic	[5, 19, 21–24]
Third	• Organic solar cells, 11.7 • Dye-sensitized solar cells, 14 • Quantum dot solar cells, 9 • Perovskite solar cells, 22	• Lightweight, flexibility, high transparency • Lower-cost fabrication • Eco-friendliness, low toxicity • Working under reduced radiation and in the range of 25–65 °C • Lower *PCE*	[1, 3–5, 20, 25]

9.1.1 Silicon Solar Cells

Silicon solar cells are the most important and popular photovoltaic devices worldwide [20] due to the highest efficiency exhibited. At present, they represent 90–93% of the photovoltaic cell market [2, 26], where the simple crystalline silicon solar cells represent a 24% whereas that multicrystalline silicon solar cells correspond to 69% [26]. Their base material is silicon and this element was the main material available to produce PV diodes since late 1950s [6]. This element is an abundant material on Earth, and it exhibits stability, non-toxicity, and a bandgap of 1.2 eV, ideally adapted to the terrestrial solar spectrum [2, 26] and to sunlight absorption [12]. The silicon is an indirect bandgap semiconductor [26].

Nevertheless, these kinds of cells show some disadvantages including their stability and service life [27]. One of the most important drawbacks of such solar cells is given by the manufacturing process as it could be complicated or carry a high price [5]. It was indicated that around 20–25% of the cost of crystalline panels is represented only by the base material, the pure Si [26].

These solar cells have had an important development given that their *PCE* has grown from 6%, when Chapin and co-workers developed a p–n silicon solar in 1954 [5], to 28% [21] nowadays. It is important to note that such solar cells have a thickness around 180 μm. Nevertheless, because of the high price of silicon, it is necessary to reduce the thickness to 100 μm [26].

These solar cells can be classified according to their silicon structure such as monocrystalline (m-Si) and polycrystalline (p-Si) cells. The m-Si cells are developed using by the Czochralski process. These cells show an excellent conversion efficiency, but they have high manufacturing costs and require the use of very pure materials

[2, 27]. In order to obtain n–type or p–type silicon semiconductor, phosphorous and boron can be added as dopants during fabrication process [21]. In order to reduce the cost and the requirements, the p-Si cells represent a better alternative. Such cells have low production costs, less energy consumed, lower greenhouse effect, and its crystalline structure is no perfect [2]. There are other forms to use silicon in solar cells such as silicon nanowire cells (SiNWs) [2]. These cells using crystalline Si convert 11–25% solar radiation into electricity [2, 4] in comparison to theoretical 30% [28].

9.1.2 Thin Film Solar Cells

Thin-film-based cells represent the second generation of solar cells, and they have emerged as a response to reducing raw material and production cost in silicon solar cells. Moreover, thin-film cells require less semiconductor material with respect to crystalline silicon solar cells in order to absorb the same amount of sunlight [2]. The thickness is generally between 35 and 260 nm [21].

This type of solar cells is manufactured in two stages: (a) nucleation and (b) film growth. Some properties of the film are directly dependent on parameters such as growth and thickness [28].

Some of the advantages of these solar cells include their device design, fabrication [28], high flexibility, easy installation, low cost, ability to diffuse light efficiency of approximately 12%, and a service life of 25 years [2].

This group includes amorphous silicon cells, chalcogenide thin-film solar cells, others like ZnO/Cu_2O heterojunction solar cells [2, 5, 21, 24], and so on. Normally, CdTe and Cu(In,Ga)(S,$Se)_2$ (CIGS) solar cells are more commercialized than the others due to their low cost [26]. Nonetheless, they have several drawbacks, including high cost, lower concentration in the nature, and toxicity of some elements like Cd, In, and Te [2, 4, 5].

The manufacturing process of thin-film solar cells is based on the deposition of a photoactive film on a transparent substrate [2]. These cells convert 5–15% solar radiation into electricity [2, 21] less than crystalline silicon solar cells. However, there are multijunction solar cells exhibiting around 46% efficiency [29] but their cost production is too expensive and therefore they only are used in space applications.

9.1.2.1 Amorphous Silicon Solar Cells

Amorphous silicon (a-Si:H) layers were first synthesized time by Chittick et al. in 1969 by radio-frequency glow discharge deposition at 200 °C [30]. It was not until 1982 that a-Si:H solar cells with 10% efficiency were fabricated [31]. a-Si:H solar cells represent a good alternative to replacing crystalline silicon solar cells thanks to some advantages including lower deposition temperatures (200–300 °C) [6] which allow the use of cheaper substrates [6, 28], bandgap of 1.7 eV [21], and higher

absorption coefficient than silicon crystalline [28]. Amorphous silicon solar cells can be fabricated by plasma-enhanced chemical vapor deposition (PECVD) method [28, 32]. Nevertheless, their efficiency decreases due to light-induced degradation effect [31].

Microcrystalline silicon (mc-Si:H) layers were first obtained by Veprek and Marecek in 1968 at 600 °C [33] but this structure showed high density defects, making it impossible to be used as a solar cell [31]. However, Meier et al. synthesized p–n–type fully microcrystalline thin film with 7.7% efficiency in 1996 [31].

Nowadays, some researchers have succeeded in obtaining *PCE* of 26.7% with amorphous silicon/crystalline silicon heterojunction; however, there is a one drawback associated with the high-temperature annealing to passivate the surface of the Si wafer [34].

9.1.2.2 Chalcogenide Thin Film Solar Cells

Chalcogenide thin-film solar cells have attracted worldwide interest in recent years given that their raw materials are abundant and some have low prices. These solar cells are based on chalcogenide absorbers such as CdTe, $CuInSe_2$, $Cu(In,Ga)(S,Se)_2$, and $Cu_2ZnSn(S,Se)_4$ [24, 35, 36]. Heterostructure metal oxides such as ZnO/Cu_2O [37–39], ZnO/SnO_2 [40–42], or $SnO_2/ZnO/Cu_2O$ [43] can be included within this group as it has been shown that they are a good alternative to fabricate solar cells. All of these solar cells have a p–n junction structure. This structure is generally formed by an absorber layer, which is p–type and n–type window, that can be a transparent conductive oxide (TCO) or other buffer layers [44].

CdTe, cadmium telluride, is an ideal semiconductor with a direct bandgap [31] of 1.45 eV [45] and ~10^5 cm as absorption coefficient in the visible region [28], which makes it perfect for solar energy conversion [46] and high light absorption [15]. CdTe-based solar cells can be made with high quality by different methods such as close-spaced sublimation, chemical spraying [15], or by electrodeposition and screen printing methods that allow scalable production [28, 46] with low-cost production [15].

CdTe solar cells have improved their *PCE* from the beginning until now. One of the first solar cells was made by alloying indium with n–type CdTe and formed a heterojunction solar cell with a *PCE* of 2.1%. Other cells such as n-CdS/p-CdTe heterojunction showed a *PCE* over 10% [46] that reached until 15% [21] and finally, CdTe solar modules which reached 22.1% in 2016 [24]. Nevertheless, the main problem with CdTe-based solar cells is that Cd is a heavy metal [5] toxic and carcinogenic [15] that results in environmental issues [2].

In order to overcome the associated drawbacks, $Cu(In,Ga)(S,Se)_2$ (CIGS) or $Cu_2(Zn,Sn)(S,Se)_2$ (CZTS) solar cells emerged. CIGS-based solar cells have experimented a rapid growth and have reached a *PCE* around 20.9%. Sputtering or thermal evaporation has been employed for the fabrication of such cells [47]. On the other hand, CZTS-based solar cells have been recently used as absorber layer in solar cells thanks to its ideal bandgap [35], from 1.0 to 1.6 eV [48]. In addition, the cost of those

solar cells is lower as In and Ga in the solar cell structure are replaced with Zn and Sn, respectively [36]. Hence, these solar cells combine, two main important aspects, low cost and friendly environmental routes of production [35]. The corresponding raw materials are non-toxic, earth-abundant and have excellent optoelectronic properties [49].

Different methods such as solution routes, electrodeposition, or high vacuum deposition techniques have been applied for fabricating such cells [35]. Some of these methods employ toxic compounds or require sophisticated equipment that limits their applications. Homogeneous precipitation reaction has been applied to synthetize nanocrystals of CZTS but this method does not allow the complete decomposition of nanocrystals during the synthesis process.

CZTSSe-based solar cells obtained by using water as the only solvent had 5.14% of *PCE* [35, 49] while others using hydrazine showed up to 12.6% of *PCE* [18].

9.1.3 Third-Generation Solar Cells

Third-generation solar cells emerge as an economical and environmental alternative for replacing silicon cells [18]. Such cells show an architecture and technology more mature and developed as compared to the other solar cells. They have some advantages in terms of flexibility, and they are semitransparent and can work even in lower light conditions [5]. Nevertheless, these cells present some drawbacks associated with their degradation and have low *PCE* with respect to silicon cells [1] if it is considered that their lifespan is approximately three years [18].

9.1.3.1 Organic Solar Cells (OSCs)

Organic solar cells (OSCs) have been developed from early 1950s [50] for the purpose of overcoming some drawbacks related to high manufacturing cost, low-flexibility, and sensibility to impurities [51] of the other solar cells, including silicon solar cells.

Advantages such as flexibility, semitransparency, low-cost fabrication, low temperature, and easy and simple method are observed for this group [2, 15, 25]. Moreover, these solar cells could be fabricated on a variety of substrates [15]. Nevertheless, limited durability, low stability, poor absorption, lower conversion, and high oxygen sensibility have been reported [1, 2].

The structure of such cells is flat and includes two different electrodes: one of them has to be (semi)-transparent like the indium tin oxide (ITO) and the other organic semiconductors, as a polymer, which is composed of an organic pigment and carbon-based nanostructures (fullerenes, nanotubes, graphene) [2].

The most popular fullerenes used in OSCs include [6,6]-phenyl-C61 butyric acid methyl ester ([60]PCBM) and [70]PCBM [4, 20]. In order to control the open-circuit voltage (V_{oc}), LUMO values in fullerene need to be changed. Therefore, some other structures were synthesized with different values of LUMO such as

diphenylmethanofullerenes (DPMs), which increased V_{oc} value at 100 mV with 11% *PCE* [4].

9.1.3.2 Dye-Sensitized Solar Cells (DSSCs)

These category is considered as the most developed one within the group of solar cells, third-generation solar cells [1], due to their simple, environment-friendly and low-cost production, stability over time and relatively high efficiency [2, 13, 52]. They can convert 7–12% solar radiation into electricity [2, 4].

Grätzel and Brian O'Regan obtained the first dye-sensitized solar cell (DSSC) in 1991. For this reason, it is also known as Grätzel cell [9]. In these cells, the dye is the light absorber and it is not involved in the separation of charges [2, 3].

The basic structure consists of a layer of transparent conductive oxides (TCOs), photoanode (mesoporous metal oxide films as TiO_2 or ZnO), photosensitive dye (inorganic or organic photosensitizer), cathode (normally platinum is used as catalytic layer), and electrolyte solution (iodide/triiodide redox system) [1, 3, 4, 9, 13, 20]. Despite the high catalytic activity, there is research on replacing platinum as counter electrode in DSSCs as it has a high cost, and possible corrosion through electrolyte solution and shortage in resources can appear as well [1, 3]. Carbon, conductive plastics, CoS, WO_2, Mo_2C and WC, TiN are some materials which can be used instead of platinum [3].

DSSCs show some drawbacks related with the stability to light and high temperatures for long duration. In addition, there are some recombination processes, and the platinized cathode can be oxidized by the electrolyte [1].

In order to overcome those problems, a block layer between TCO and the electrolyte can be placed, or carbon structures such as graphene can be incorporated thanks to their high electrical conductivity [1].

Quantum dye-sensitized solar cells (QDSSCs) work the same as DSSCs, but they use nanocrystals known as quantum dots to absorb the light. These solar cells show some advantages in comparison with other solar cells given the tunneling characteristics that allow them to have a wider absorption range (from UV–vis to IR); the *PCE* value is about 9.2% and they have a greater stability in air [1].

9.1.3.3 Perovskites Solar Cells (PSCs)

Perovskites are chemical compound whose formula is ABX_3 and their basic structure is similar to $CaTiO_3$ mineral [19, 53]. Gustav Rose discovered them in 1839 in Ural Mountains [54] and named in honor of Count Lev Alekseevich Perovski [19]. In 1978, Weber reported for the first time the structure of hybrid halides perovskites [55]. They have a sandwich-type structure: one inorganic layer between two hydrocarbon layers [19].

The rapid development of PSCs has allowed increasing the initial efficiency of 2.19% with $CH_3NH_3PbBr_3$ with I^-/I_3^- electrolyte in 2006 [19], to 22% in a few years

[4, 20, 22, 56]. PSCs are shown as novel and promise replacement for silicon solar cells as they have low-cost production and relative high performance. In addition, they have a good long-term stability and excellent optoelectronic properties [53]. However, PSCs present some drawbacks related with the environment and time stability [4, 19].

The PSC structure consists of a sandwich-type structure where a layer of perovskite is placed in between the electron transport layer (ETL) and a hole transport layer (HTL). In order to seal the structure, a transparent conductive oxide (TCO) below ETL and, finally, a metallic contact over HTL can be applied [18, 53, 57]. There are some methods to fabricate PSCs such as thermal evaporation technique which allows to obtain a *PCE* of 4.7% or spray-assisted and gas-assisted solution processed deposition that obtain a *PCE* of 6.3% and 6.07%, respectively [58].

9.2 Carbon Nanomaterials for Photovoltaics

Carbon nanomaterials generally exhibit both sp^2 and sp^3 hybridization. Such hybridization allows them to produce some different allotropic forms such as carbon dots, fullerenes, single and multicarbon nanotubes, or graphene [4]. The specific properties of these structures induced by their atomic structure and surface chemistry [13] allow them to be used in different applications like photovoltaic, sensors, and storage energy applications [4, 59].

In most cases, carbon nanomaterials are used to overcome some drawbacks of some solar cells that are usually associated with the lower performance with respect to silicon solar cells, as seen in Table 9.1. These materials are used as an alternative in solar cells as they improve the performance of the solar cells.

The carbon nanostructures including nanodots, fullerenes, nanotubes, graphene, and carbon nanotubes show innovative and excellent optoelectronic, physical, thermal, and mechanical properties, high surface area, thermal conductivity, electron mobility, and mechanical strength which make them favorable for use in solar cells structures [1, 2, 10, 13, 60]. In this respect, Fig. 9.2 shows the number of publications on solar cells based on carbon materials.

Carbon nanomaterials have been indicated as a promising alternative to be used in the structure of solar cells thanks to their electronic, optical, thermal, and mechanical properties. Many reports showed they can significantly improve the solar cells performance.

In the next section, some characteristics of carbon nanomaterials are briefly introduced along with their implementation within the structure of solar cells. The description below is given in accordance to the chronological discovery.

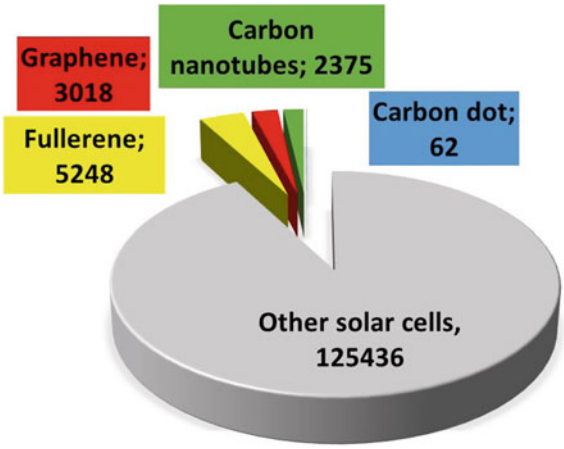

Fig. 9.2 Number of publications on solar cells based on carbon materials. The counts were obtained using the keywords "fullerene"; "graphene" or "graphene oxide" or "reduced graphene oxide" or "graphene quantum dots"; "carbon nanotube*" or "CNT" or "single-walled" or "multiwalled"; "carbon dots" with "solar cell" or "photovoltaic cell" or "solar photovoltaic" or "photovoltaic solar energy" or "photovoltaic" in the ISI Web of Science portal accessed on June 22, 2018

9.2.1 Fullerene-Based Photovoltaics

Fullerene (C_{60}) is a n–type [25] semiconductor [27] with structure characterized by a cylindrical zero-dimensional geometry (0D) [13, 59] that was discovered by Kroto, Smalley, and Curl in 1985 [4]. Fullerene shows face-centered-cubic (fcc) crystal structure with $sp^2 + sp^3$ carbon bonds hybridization and a bandgap of 1.8 eV [27].

Within organic solar cells, the fullerene is part of the active layer in which structure is compounded by an electron donor semiconductor (polymer) and an electron acceptor (fullerene and its derivates) [61, 62]. These materials show high electron affinity in polymer/fullerene bulk heterojunction solar cells [4, 61]. The most popular derivatives of fullerene are C_{60} and C_{70} with 60 and 70 π-electrons, respectively. C_{60} exhibits high electron affinity and good electron-transporting properties. On the other hand, C_{70}exhibits a wider absorption spectrum in comparison with C_{60} [63].

Compounds with fullerenes such as phenyl-C_{61}-butyric acid methyl ester ($PC_{61}BM$) and phenyl-C_{71}-butyric acid methyl ester ($PC_{71}BM$) have been used in the OSCs [62]. A dependence on the open-circuit voltage (V_{oc}) with the fullerene content was observed to exist in the OSCs. This configuration reached a *PCE* of 8.3% [15].

9.2.2 Carbon Nanotubes-Based Photovoltaics

Carbon nanotubes (CNTs) were discovered in 1991 [64] and are characterized by a cylindrical one-dimensional (1D) geometry [13, 59] and exhibit different lengths, widths, and structures [4]. The length-to-diameter ratio can be of up to 28,000,000:1, reaching lengths of several millimeters [4]. CNTs can be classified in different groups depending on their structural arrangement or diameter, and they can be (a) metallic or semiconducting, (b) armchair, zigzag, and chiral nanotubes depending on the indices of the chiral vector, and (c) single-walled (SWCNTs) or multiwalled (MWCNTs), with scroll-like or seamless cylinder structures [4, 13]. For exemplification, Fig. 9.3 shows a variety of CNTs.

CNTs have earth-abundant source materials, scalable fabrication, purification methods, and solution processability. Their one-dimensional properties allow to be highly thermally conductive and mechanical, chemical, and radiation resistant [10]. These nanomaterials can conduct electricity [3] due to the fact that they are metallic/semiconducting materials with $sp^2 + sp^3$ hybridization and have bandgap of 0.3–2.0 eV [27].

Methods such as arc discharge, chemical vapor deposition (CVD), laser ablation, electrolysis, pyrolysis, flame synthesis, electron or ion beam irradiation, and solar approaches were applied to synthesize CNTs [13]. Many of these methods are expensive or require sophisticated equipment which increases their production cost. However, CNTs with desirable properties including size, diameter, and possibility to control the wall number of CNTs can be obtained by processes such as CVD [13]. Increased research is focused on producing CNTs at large scale by considering a balance in the cost-effective relationship and a reduction of contaminants [13].

The use in solar cells for CNTs is limited with respect to the other carbon nanomaterials due to their purification issues [4, 13]. In addition, it is difficult to control their size and chirality [4]. Moreover, SWCNTs have high cost, they are difficult to synthesize and their solubility is poorer than C–dots [60]. However, CNTs may be employed in solar cells as TCO (to replace FTO or ITO) thanks to their flexibility,

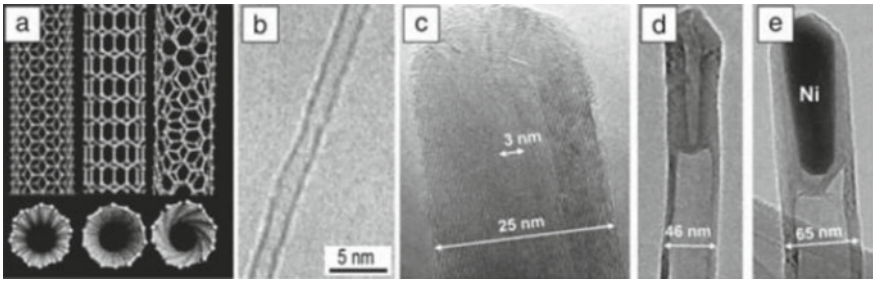

Fig. 9.3 Different types of CNTs **a** schematics of armchair, zigzag, and chiral SWCNTs (from left to right); **b** SWCNT; **c–d** MWCNT. Reprinted by permission from Springer-Verlag [65], copyright (2003)

very good optoelectronic properties, conductivity, or high optical transmittance in the UV to mid-IR spectral region (i.e., 90%) [13]. It is important to note that CNTs require the combination with other materials like conjugated polymers in order to act as the active layer or they can be hybridized with structures like fullerenes in order to reach higher values of full factor (FF) and short-circuit current (J_{sc}) as well as photovoltaic performance [4].

CNTs could be added to the silicon solar cells in order to impede charge recombination, for transferring charge carriers and as photoactive material [5]. In the De Nicola et al. study, single-walled carbon nanotubes (SWCNTs) with n–type crystalline silicon (n-Si) (32 nm/200 μm) formed heterojunction solar cells which showed improved optoelectronic properties and exhibited a *PCE* of 8 ± 1%, a short-circuit current (J_{sc}) of 34.4 ± 0.1 mA/cm^2, open-circuit voltage (V_{oc}) of 0.52 ± 0.01 V, and a full factor (FF) of 42 ± 7%, under AM 1.5 G. In addition, it was indicated that the *PCE* can increase with 50% if doping with HNO_3 vapors for 10 s is applied [10].

Meanwhile in CdTe-based solar cells, the hybridization of CNTs with CdTe quantum dots [66] resulted in photoresponse in the UV–vis range [14].

In DSSCs, CNTs can be used in different ways, e.g., as working electrode thanks to the improvement in the charge transport properties; as part of the electrolyte thanks to their excellent electrochemical catalytic activity for electrolyte reduction; as counter electrode in order to replace platinum thanks to their excellent electrical and thermal properties, stability and specially due to their low cost, and so on [5, 13]. Furthermore, CNTs can be considered as a replacement for TCOs such as FTO or ITO because they are almost transparent, flexible, and strong, and they exhibit a low resistivity and high electronic mobility which is ideal as the hole-extraction or hole-transporting layer in photovoltaic cells [3, 5]. However, the recombination of dye ions due to photogenerated charge carriers in the CNTs may reduce the *PCE* of solar cell [3].

In the case of PSCs, MWCNTs aerogel was employed so as to replace Au or Al on the top of the structure (or as anode inverted solar cell) as it is an excellent charge collector and it can increase their conductivity as well as transmittance [19].

9.2.3 Carbon Dot-Based Photovoltaics

Carbon dots (C–dots) also known as carbon quantum dots (CQDs) are characterized by 0D geometry (zero-dimensional) [59] and were first discovered by Xu et al. in 2004 while purifying single-walled carbon nanotubes by arc discharge method [67]. C–dots dimensions are lower than 10 nm, their behavior is similar to quasi-spherical nanoparticles, and they are decorated by some surface functional groups like –OH, C–H, –COOH, C–O–C, C–O, C=C and –C=O [59, 60].

Their properties are better than other semiconductor-based inorganic quantum dots like low toxicity, easy production, good aqueous dispersability [59, 60]. C–dots can be used in photochemical and electrochemical applications such as solar cells, sensors, energy storage (batteries and supercapacitors), and photocatalysis

thanks to their excellent photoluminescence properties [59] which result in improved performance of related devices [60].

C–dots could be prepared by top-down and bottom-up approaches. Top-down routes include arc discharge, laser ablation, acidic exfoliation, electrochemical oxidation, physical cleavage, and microwave-assisted hydrothermal synthesis [59, 60]. This approach is simple, easy, and cheap that allows large-scale production [60, 68]. Nevertheless, there are some drawbacks that involve fluorescence properties and use of strong acid or electrolytes [59]. Depending on the type of process, the raw material to produce C–dots can consist of different types of crude soot, graphite powder, and so on [59].

On the other hand, bottom-up approaches could overcome the drawbacks of top-down approach [59] and allow a uniform size control [68], shape of the C–dots, and the possibility of tuning their properties [60]. Within these approaches, hydrothermal, microwave-assisted pyrolysis, ultrasonic, pyrolysis, dehydration/direct heating methods, and solution chemistry reactions [20, 59] are included. The raw carbon material in these methods can consider organic molecules with carbon in their structure, e.g., glucose, fructose, sucrose, ascorbic acid, chitosan, glycerol, etc. [59]. However, such methods need complex synthetic procedures while the special organic precursors may be difficult to obtain [60]. In addition, extra purification process and superficial modification are needed in order to improve their behavior [20]. Figure 9.4 shows the different approaches employed to synthetize C–dots.

Some of their properties may vary according to the synthesis methods. C–dots show a strong optical absorption in the UV region but their spectrums and their peaks positions could be different depending on the synthesis methods, e.g., different photoluminescence (PL) mechanisms and emitting PL with different colors, including UV, blue, green, yellow, and red and in the near-infrared region [60].

C–dots can be classified in two groups: (a) quasi-spherical nanoparticles, which form amorphous aggregates with diameters less than 10 nm and (b) graphene quantum dots which are crystalline structures [20].

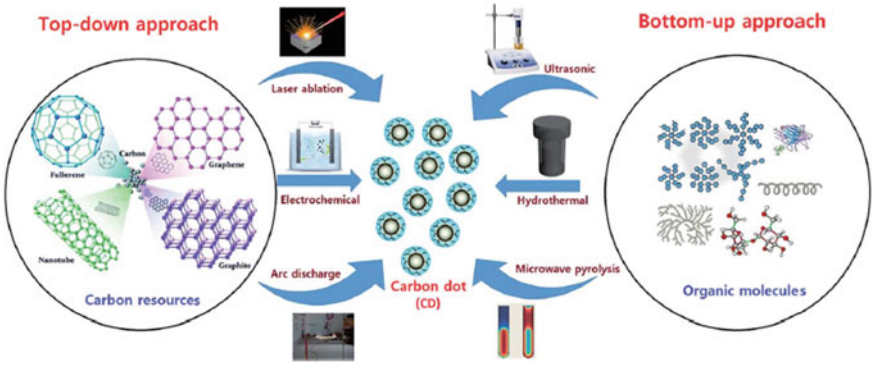

Fig. 9.4 Schematic representations of the top-down and bottom-up routes to synthetized C–dots. Reproduced from Ref. [59] with permission from the Royal Society of Chemistry

Thanks to excellent photoabsorption capacity, electron acceptance, and transport properties, and C–dots can be used in photoenergy conversion application. They are employed as photosensitizers in solar cells. Due to their important role like photoabsorption agents, sensitizers, and transporting layers, the photoelectric conversion efficiency can be enhanced [60].

C–dots can be used as a photosensitizer in DSSCs, e.g., for TiO_2-based DSSCs. For this end, C–dots can or not be doped with nitrogen in order to obtain more efficient transfer of photoinduced electrons to the conductance band of TiO_2 [59]. The resulting *PCE* reaches 0.79% for nitrogen-doped C–dots solar cell [69] under AM 1.5 G.

The C–dots size represents another important parameter. The open-circuit voltage (V_{oc}) of the device was observed to increase while the short-circuit current (J_{sc}) decreases with the decrease in size [60]. Despite this outcome, their efficiency is still low in comparison to conventional organic solar cells [60]. The conversion efficiency could reach 6.1% when C–dots and dyes are combined and 28.2% when these materials are introduced into the active layer of polymer solar cells [60].

Furthermore, C–dots can be employed as photoanode and counter electrode in QDSSCs. In order to improve the C–dots performance as counter electrode, some nanostructures like gold nanoparticles may be added [59]. As such, a remarkable improvement in solar cell performance is noted. C–dots may act as hole transport material in PSCs, as well [59].

9.2.4 Graphene-Based Photovoltaics

Graphene (G) is an atomically thin mesh, which has ~0.34 nm thickness [7, 70], of carbon atoms covalent bonded and arranged in a hexagonal structure like a honeycomb pattern [4, 22]. G is characterized by a 2D geometry [7, 13, 59] that can have two arrangements: zigzag and armchair [7]. G exhibits high optical transparency, carrier mobility, mechanical strength [7], and a surface area as large as 2600 m^2/g [4]. G could be considered as semimetallic/semiconducting material [27]. In this, groups are included: graphene (G), graphene oxide (GO), reduced graphene oxide (rGO) [59], and graphene quantum dots (GCDs). G has a sp^2–carbon structure hybridization [68] and a zero bandgap [4, 23] which can be changed as a function of oxidation methods or by induction of other heteroatoms and defects into the graphene moiety [4, 68].

G material can be obtained by different approaches like epitaxial graphene, mechanical exfoliation, chemical vapor deposition (CVD), reduction of silicon carbide, supersonic spray, laser, and exfoliation of graphite by solvents (Coleman's method) among others [4, 22]. One of the most popular method to synthesize G is the traditional Hummer's method, which allows to obtain first GO [22] and then rGO by chemical, electrochemical, photo, or thermal reduction methods [1]. rGO shows

more similar physical properties and structure as G [7] while GO shows insulating properties that can be changed by reduction process [34]. Depending on the type of arrangement, graphene can form different structures such as CNTs, fullerene, and graphite, as shown in Fig. 9.5 [8, 70]. G structure shows less defects with reference to C–dots [60].

G is indicated as a future material due to its unique and versatile properties. In addition, upon addition of another material such as a metal or a metal oxide semiconductor to graphene, novel materials with high potential are obtained. In order to improve its photovoltaic applications, G can be modified with different functional groups [4].

Thanks to its excellent mechanical, thermal, and electrical properties, especially its high conductivity [68], G can be used in solar cell devices such as transparent electrode, hole/electron transport material, and interfacial buffer layer [7]. One approach to use G in OSCs is as TCO due to its properties including lower air diffusion and transparency $T \approx 91$, better than ITO, which can be obtained with few layers of graphene [7]. Furthermore, G can form Schottky junction with a semiconductor which allows it to be employed as active layer for solar cells [4].

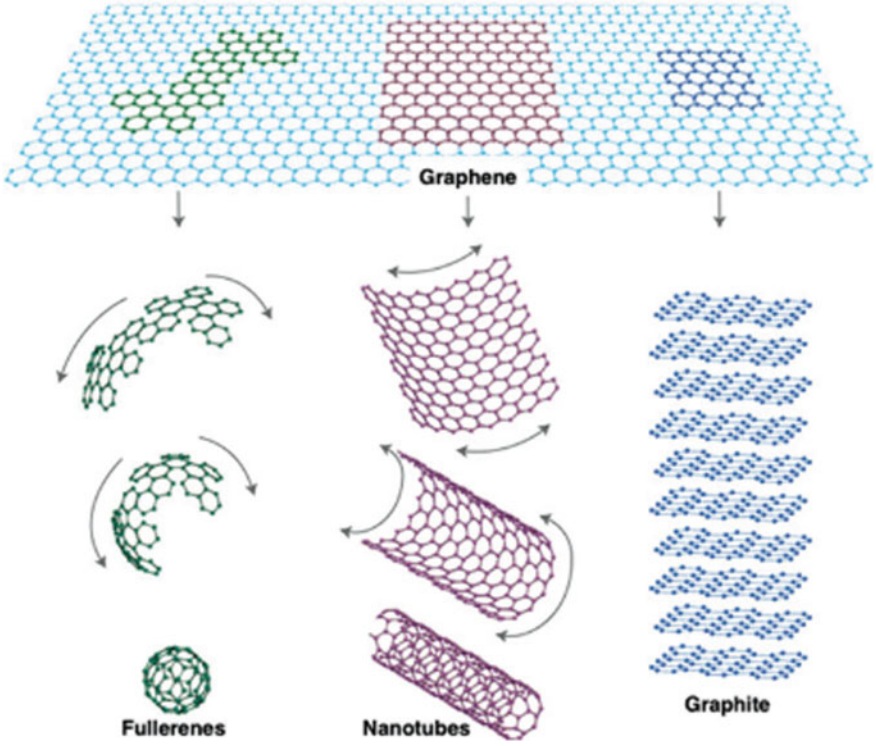

Fig. 9.5 Fullerene, carbon nanotubes, and graphite obtained from graphene. Reprinted by permission from Nature Publishing Group [71], copyright (2007)

G can be used in different ways in CdTe-based photovoltaic devices. Since G layer fabricated by CVD shows high transparency, carrier mobility, flexibility, and increased stability for photovoltaic devices, one alternative considers it as contact material instead of ITO or FTO [22, 72]. For exemplification, CdTe-based thin-film solar cell with a final structure such as glass/graphene/ZnO/CdS/CdTe/(graphite paste) show a *PCE* of 4.17% [72]. By replacing CdS with G, a *PCE* of 2.08% is obtained [22]. On the other hand, with the graphene/CdTe quantum dots heterojunction solar cells, it is possible to obtain an improvement in *PCE* from 2.1 to 3.1% [73]. Finally, another application of G considers the back contact in CdTe-based solar cells, e.g., glass/FTO/Cds/CdTe/graphene solar cell which exhibits a *PCE* of 9.1% with the fill factor (FF) of 0.58, a short-circuit current (J_{sc}) of 20.10 mA/cm^2, and open-circuit voltage (V_{oc}) of 0.78 V [22].

Moreover, given the increase in absorption of dye molecules in photoanode in DSSCs and improvement of charge transport/extraction layers for high performance [1], G can be used in DSSCs, as well [29]. G can form a block layer between TCO and mesoporous TiO_2 layer, as well [74] or it can replace Pt with Pt-graphene due to its high conductivity and catalytic properties [7].

On the other hand, rGO nanomaterials exhibit some defects in its structure as function of oxidation process, that further confer it with excellent electrocatalytic activity [9].

GQDs are graphene particles with varying size from ~1.5 to ~60 nm and lateral dimensions of 2–20 nm [23] with sp^2–sp^2 hybridization [68]. GQDs bandgap is ~3 eV depending on their size [23]. They show higher conductivity than GO and good hole-transporting ability, high transparency, and surface area [68]. Furthermore, they have biocompatibility, low toxicity, and water solubility [23, 75]. GQDs can be produced by bottom-up and top-down approaches, but it is necessary to control the base material [68]. They can be used in DSSCs to produce highly porous structure [20]. The photo-optical properties, such as J_{sc} and FF, can be controlled by the GQDs concentration [20].

In ZnO-Cu_2O heterojunction solar cells, the performance can be increased by adding GO within the structure of one of the semiconductors and then reducing it by thermal process, such as the one indicated by Rosas et al. which results in increasing the J_{sc} of the solar cell from 39.3 μA/cm^2 to ZnO-Cu_2O to 242.5 μA/cm^2 to GO-modified solar cell. Nevertheless, it was noted that V_{oc} decreases from 100.7 to 53.2 mV [76].

In DSSCs, Siddick et al. demonstrated that by using rGO with TiO_2 as photoanode, it allowed the improvement in the photoelectrical properties due to increasing of the photocatalytic activity during the irradiation. The photoelectrical properties for TiO_2-rGO were J_{sc} of 10.91 mA/cm^2, V_{oc} of 0.67 V and *PCE* of 4.18% with FF 0.48 [77]. Meanwhile, in the case of ZnO modified with graphene and employed as photoanode, Effendi et al. determined that the performance of DSSCs was of 10.89 mA/cm^2, 0.91 V, 7.01% and 0.66, respectively [78].

In the PSCs, the *PCE* can be increased with ~15% by using GQDs layer between perovskite and TiO_2 layer just as Zhu et al. [79] due to the fact that GQDs serve as a transporter channel for the injected electrons from the halide perovskite into

TiO_2. The configuration of corresponding solar cells was $CH_3NH_3PbI_3$/GQDs/TiO_2 and $CH_3NH_3PbI_3$/TiO_2 and they exhibited J_{sc} values of 17.06 and 15.43 (mA/cm^2), V_{oc} of 0.937 and 0.939 (V), and *PCE* of 10.15 and 8.81% with FF 0.635 and 0.612, respectively.

9.3 Conclusions and Perspectives

In this chapter, the recent progress of carbon-based nanomaterials for different photovoltaic applications has been presented. It has been shown that carbon-based nanomaterials show potential as material in the development and manufacturing of varying solar cells.

It has been shown that perovskite layers, hole transport layers, and replacement of metal electrodes can be achieved using CNTs. The modification of hole transport layers in photovoltaics with CNTs while a CNT-based composite is used as counter electrodes has been indicated as an alternative for improving photovoltaics efficiency. While the CNTs are still pricey, they could be employed as a stable material in solar cells by increasing production and lowering the cost. Thus, the addition of CNTs to photovoltaics is expected to lead to high efficient and more environmentally stable photovoltaics.

On the other hand, the potential of graphene-based nanomaterials for transparent electrode, active layer or interfacial one in photovoltaics devices, has been demonstrated thanks to their unique properties and versatility of graphene thus graphene-based solar cells emerged having additional advantages favorable for flexible and lightweight devices. Nevertheless, the research in this field is still at its beginnings. Many challenges involve the use of graphene nanomaterials as component in photovoltaics. The most important one refers to the synthesis protocol so that the procedure features include simplicity, scalability, and cost efficiency. One of the goals in this field is to obtain graphene-based materials for hole transport layer easily deposited from neutral aqueous suspensions and highly conductive by functionalization with various agents. On the other hand, better control of the structure–property relationship in graphene-based nanomaterials for solar cells, e.g., to increase the transparency and decreasing the sheet resistance since an increased number of graphene layers leads to improved conductivity but at the cost of reduced transparency.

While further increase in power conversion efficiency is needed for commercialization of solar cells, it is believed the continuous efforts into development of materials and fabrication techniques would make the carbon nanomaterials promising for photovoltaic applications.

Acknowledgements Financial support from Escuela Politécnica Nacional (project number PIMI 15–09) and Secretaria de Educación Superior, Ciencia, Tecnología e Innovación (SENESCYT) of Ecuador and Romanian National Authority for Scientific Research and Innovation CNCS—UEFISCDI (project number PN-III-P1-1.1-TE-2016-1544) are gratefully acknowledged.

References

1. N. Balis, E. Stratakis, E. Kymakis, Graphene and transition metal dichalcogenide nanosheets as charge transport layers for solution processed solar cells. Mater. Today **19**, 580–594 (2016). https://doi.org/10.1016/j.mattod.2016.03.018
2. P.G.V. Sampaio, M.O.A. González, Photovoltaic solar energy: conceptual framework. Renew. Sustain. Energy Rev. **74**, 590–601 (2017). https://doi.org/10.1016/j.rser.2017.02.081
3. L.A. Dobrzański, A. Mucha, M. Prokopiuk vel Prokopowicz et al., Characteristics of dye-sensitized solar cells with carbon nanomaterials. Mater. Tehnol. **50**, 649–654 (2016). https://doi.org/10.17222/mit.2014.134
4. N. Martín, Carbon nanoforms for photovoltaics: myth or reality? Adv. Energy Mater. **7**, 1601102 (2017). https://doi.org/10.1002/aenm.201601102
5. T. Grace, C. Shearer, D. Tune et al., Use of carbon nanotubes in third-generation solar cells, in *Industrial Applications of Carbon Nanotubes* (Elsevier, 2017), pp. 201–249
6. A. Shah, P. Torres, R. Tscharner et al., Photovaltaic technology: the case for thin-film solar cells. Science (80-) **285**, 692–698 (1999)
7. T. Mahmoudi, Y. Wang, Y.-B. Hahn, Graphene and its derivatives for solar cells application. Nano Energy **47**, 51–65 (2018). https://doi.org/10.1016/j.nanoen.2018.02.047
8. M. Kawamoto, P. He, Y. Ito, Green processing of carbon nanomaterials. Adv. Mater. **29**, 1602423 (2017). https://doi.org/10.1002/adma.201602423
9. L.A. Dobrzański, M. Prokopiuk vel Prokopowicz, A. Drygała et al., Carbon nanomaterials application as a counter electrode for dye-sensitized solar cells. Arch. Metall. Mater. **62**, 27–32 (2017). https://doi.org/10.1515/amm-2017-0004
10. F. De Nicola, M. Salvato, C. Cirillo et al., 100% internal quantum efficiency in polychiral single-walled carbon nanotube bulk heterojunction/silicon solar cells. Carbon N Y **114**, 402–410 (2017). https://doi.org/10.1016/j.carbon.2016.12.050
11. I. Jeon, Y. Matsuo, S. Maruyama, Single-walled carbon nanotubes in solar cells. Top. Curr. Chem. **376**, 4 (2018). https://doi.org/10.1007/s41061-017-0181-0
12. K. Yoshikawa, H. Kawasaki, W. Yoshida et al., Silicon heterojunction solar cell with interdigitated back contacts for a photoconversion efficiency over 26%. Nat. Energy **2**, 17032 (2017). https://doi.org/10.1038/nenergy.2017.32
13. S. Kumar, M. Nehra, D. Kedia et al., Carbon nanotubes: a potential material for energy conversion and storage. Prog. Energy Combust. Sci. **64**, 219–253 (2018). https://doi.org/10.1016/j.pecs.2017.10.005
14. Z. Xu, Y. Liu, F. Ren et al., Development of functional nanostructures and their applications in catalysis and solar cells. Coord. Chem. Rev. **320–321**, 153–180 (2016). https://doi.org/10.1016/j.ccr.2016.03.002
15. T. Markvart, L. Castan, *Principles of Solar Cell Operation*, 2nd edn. (Elsevier, 2013)
16. M. Ibánez Plana, J.R. Rosell Polo, J.I. Rossell Urrutia, Células y Módulos Fotovoltaicos, in *Energías Renovables Tecnología Solar* (Ediciones Mundi-Prensa, Lleida, 2004), p. 544
17. S. Kumar, M. Nehra, A. Deep et al., Quantum-sized nanomaterials for solar cell applications. Renew. Sustain. Energy Rev. **73**, 821–839 (2017). https://doi.org/10.1016/j.rser.2017.01.172
18. T. Ibn-Mohammed, S.C.L. Koh, I.M. Reaney et al., Perovskite solar cells: an integrated hybrid lifecycle assessment and review in comparison with other photovoltaic technologies. Renew. Sustain. Energy Rev. **80**, 1321–1344 (2017). https://doi.org/10.1016/j.rser.2017.05.095
19. N. Ashurov, B.L. Oksengendler, S. Maksimov et al., Current state and perspectives for organo-halide perovskite solar cells. Part 1. Crystal structures and thin film formation, morphology, processing, degradation, stability improvement by carbon nanotubes. A review. Mod. Electron. Mater. **3**, 1–25 (2017). https://doi.org/10.1016/j.moem.2017.05.001
20. S. Paulo, E. Palomares, E. Martinez-Ferrero, Graphene and carbon quantum dot-based materials in photovoltaic devices: from synthesis to applications. Nanomaterials **6**, 157 (2016). https://doi.org/10.3390/nano6090157

21. V.V. Tyagi, N.A.A. Rahim, N.A. Rahim, J.A.L. Selvaraj, Progress in solar PV technology: research and achievement. Renew. Sustain. Energy Rev. **20**, 443–461 (2013). https://doi.org/10.1016/j.rser.2012.09.028
22. Z. Shi, A.H. Jayatissa, The impact of graphene on the fabrication of thin film solar cells: current status and future prospects. Materials (Basel) **11**, 36 (2017). https://doi.org/10.3390/ma11010036
23. S.-H. Choi, Unique properties of graphene quantum dots and their applications in photonic/electronic devices. J. Phys. D Appl. Phys. **50**, 103002 (2017). https://doi.org/10.1088/1361-6463/aa5244
24. A. Reinders, P. Verlinden, A.F. Wilfried van Sark, *Photovoltaic Solar Energy* (Wiley, Chichester, 2016)
25. E.A. Katz, Fullerene thin films as photovoltaic material, in *Nanostructured Materials for Solar Energy Conversion* (Elsevier, 2006), pp. 361–443
26. E. Płaczek-Popko, Top PV market solar cells 2016. Opto-Electron. Rev. **25**, 55–64 (2017). https://doi.org/10.1016/j.opelre.2017.03.002
27. H. Zhu, J. Wei, K. Wang, D. Wu, Applications of carbon materials in photovoltaic solar cells. Sol. Energy Mater. Sol. Cells **93**, 1461–1470 (2009). https://doi.org/10.1016/j.solmat.2009.04.006
28. K.L. Chopra, P.D. Paulson, V. Dutta, Thin-film solar cells: an overview. Prog. Photovolt. Res. Appl. **12**, 69–92 (2004). https://doi.org/10.1002/pip.541
29. M.A. Green, Y. Hishikawa, W. Warta et al., Solar cell efficiency tables (version 50). Prog. Photovolt. Res. Appl. **25**, 668–676 (2017). https://doi.org/10.1002/pip.2909
30. R.C. Chittick, J.H. Alexander, H.F. Sterling, The preparation and properties of amorphous silicon. J. Electrochem. Soc. **116**, 77 (1969)
31. A.V. Shah, H. Schade, M. Vanecek et al., Thin-film silicon solar cell technology. Prog. Photovolt. Res. Appl. **12**, 113–142 (2004). https://doi.org/10.1002/pip.533
32. M. Crose, W. Zhang, A. Tran, P.D. Christofides, Multiscale three-dimensional CFD modeling for PECVD of amorphous silicon thin films. Comput. Chem. Eng. **113**, 184–195 (2018). https://doi.org/10.1016/j.compchemeng.2018.03.011
33. A. Shah, E. Vallat-Sauvain, P. Torres et al., Intrinsic microcrystalline silicon (μc-Si:H) deposited by VHF-GD (very high frequency-glow discharge): a new material for photovoltaics and optoelectronics. Mater. Sci. Eng. B **69–70**, 219–226 (2000). https://doi.org/10.1016/S0921-5107(99)00299-8
34. M. Lozac'h, S. Nunomura, H. Sai, K. Matsubara, Passivation property of ultrathin SiOx: H/a-Si: H stack layers for solar cell applications. Sol. Energy Mater. Sol. Cells **185**, 8–15 (2018). https://doi.org/10.1016/j.solmat.2018.05.004
35. V. Foncrose, J. Persello, P. Puech et al., Chemical insights into the formation of Cu_2ZnSnS_4 films from all-aqueous dispersions for low-cost solar cells. Nanotechnology **28**, 445709 (2017). https://doi.org/10.1088/1361-6528/aa873a
36. G. Han, S. Zhang, P.P. Boix et al., Towards high efficiency thin film solar cells. Prog. Mater. Sci. **87**, 246–291 (2017). https://doi.org/10.1016/j.pmatsci.2017.02.003
37. N.H. Ke, L.T.T. Trinh, P.K. Phung et al., Changing the thickness of two layers: i-ZnO nanorods, p-Cu_2O and its influence on the carriers transport mechanism of the p-Cu_2O/i-ZnO nanorods/n-IGZO heterojunction. SpringerPlus **5**, 710 (2016). https://doi.org/10.1186/s40064-016-2468-y
38. Y. Ievskaya, R.L.Z. Hoye, A. Sadhanala et al., Fabrication of ZnO/Cu_2O heterojunctions in atmospheric conditions: improved interface quality and solar cell performance. Sol. Energy Mater. Sol. Cells **135**, 43–48 (2015). https://doi.org/10.1016/j.solmat.2014.09.018
39. K. Cheng, Q. Li, J. Meng et al., Interface engineering for efficient charge collection in Cu_2O/ZnO heterojunction solar cells with ordered ZnO cavity-like nanopatterns. Sol. Energy Mater. Sol. Cells **116**, 120–125 (2013). https://doi.org/10.1016/j.solmat.2013.04.021
40. A.S. Ismail, M.H. Mamat, M.F. Malek et al., Heterogeneous SnO_2/ZnO nanoparticulate film: facile synthesis and humidity sensing capability. Mater. Sci. Semicond. Process. **81**, 127–138 (2018). https://doi.org/10.1016/j.mssp.2018.03.022

41. Z. Chen, S. Li, W. Zhang, Pulse electrodeposition of ZnO/SnO_2 composite films: growth mechanism, structural and optical studies. J. Alloys Compd. **557**, 274–278 (2013). https://doi.org/10.1016/j.jallcom.2012.11.177
42. L.F. Da Silva, O.F. Lopes, A.C. Catto et al., Hierarchical growth of ZnO nanorods over SnO_2 seed layer: insights into electronic properties from photocatalytic activity. RSC Adv. **6**, 2112–2118 (2016). https://doi.org/10.1039/C5RA23824B
43. S. Chatterjee, S.K. Saha, A.J. Pal, Formation of all-oxide solar cells in atmospheric condition based on Cu_2O thin-films grown through SILAR technique. Sol. Energy Mater. Sol. Cells **147**, 17–26 (2016). https://doi.org/10.1016/j.solmat.2015.11.045
44. S. Siebentritt, Basics of chalcogenide thin film solar cells, in *Photovoltaic Solar Energy* (Wiley, Chichester, 2017), pp. 167–178
45. S.J. Fonash, Introduction, in *Solar Cell Device Physics*, 2nd edn. (Elsevier, 2010), pp. 1–8
46. A. Goetzberger, C. Hebling, H.-W. Schock, Photovoltaic materials, history, status and outlook. Mater. Sci. Eng. R Rep. **40**, 1–46 (2003). https://doi.org/10.1016/S0927-796X(02)00092-X
47. S. Spiering, S. Paetel, F. Kessler et al., Copper variation in Cu(In,Ga)Se_2 solar cells with indium sulphide buffer layer. Thin Solid Films **582**, 328–331 (2015). https://doi.org/10.1016/j.tsf.2014.11.027
48. T.D. Lee, A.U. Ebong, A review of thin film solar cell technologies and challenges. Renew. Sustain. Energy Rev. **70**, 1286–1297 (2017). https://doi.org/10.1016/j.rser.2016.12.028
49. J. Zhong, Z. Xia, C. Zhang et al., One-pot synthesis of self-stabilized aqueous nanoinks for $Cu_2ZnSn(S,Se)_4$ solar cells. Chem. Mater. **26**, 3573–3578 (2014). https://doi.org/10.1021/cm501270j
50. N. Yeh, P. Yeh, Organic solar cells: their developments and potentials. Renew. Sustain. Energy Rev. **21**, 421–431 (2013). https://doi.org/10.1016/j.rser.2012.12.046
51. R. Ilmi, A. Haque, M.S. Khan, High efficiency small molecule-based donor materials for organic solar cells. Org. Electron. **58**, 53–62 (2018). https://doi.org/10.1016/j.orgel.2018.03.048
52. B. Paulchamy, G. Arthi, B.D. Lignesh, A simple approach to stepwise synthesis of graphene oxide nanomaterial. J. Nanomed. Nanotechnol. **06**, 2–5 (2015). https://doi.org/10.4172/2157-7439.1000253
53. J.-P. Correa-Baena, A. Abate, M. Saliba et al., The rapid evolution of highly efficient perovskite solar cells. Energy Environ. Sci. **10**, 710–727 (2017). https://doi.org/10.1039/C6EE03397K
54. J.P. Attfield, P. Lightfoot, R.E. Morris, Perovskites. Dalton Trans. **44**, 10541–10542 (2015). https://doi.org/10.1039/C5DT90083B
55. A. Walsh, Principles of chemical bonding and band gap engineering in hybrid organic-inorganic halide perovskites. J. Phys. Chem. C **119**, 5755–5760 (2015). https://doi.org/10.1021/jp512420b
56. J. Bouclé, N. Herlin-Boime, The benefits of graphene for hybrid perovskite solar cells. Synth. Met. **222**, 3–16 (2016). https://doi.org/10.1016/j.synthmet.2016.03.030
57. F. Cataño, L. Allende, H. Gómez, Electrodeposition of ZnO nanorod arrays for application in perovskite based solar cells. J. Chil. Chem. Soc. **60**, 2940–2943 (2015). https://doi.org/10.4067/S0717-97072015000200017
58. M. Aamir, T. Adhikari, M. Sher et al., Fabrication of planar heterojunction $CsPbBr_2I$ perovskite solar cells using ZnO as an electron transport layer and improved solar energy conversion efficiency. New J. Chem. **42**, 14104–14110 (2018). https://doi.org/10.1039/C8NJ02238K
59. B. De, N. Karak, Recent progress in carbon dot–metal based nanohybrids for photochemical and electrochemical applications. J. Mater. Chem. A **5**, 1826–1859 (2017). https://doi.org/10.1039/C6TA10220D
60. J. Gao, M. Zhu, H. Huang et al., Advances, challenges and promises of carbon dots. Inorg. Chem. Front. **4**, 1963–1986 (2017). https://doi.org/10.1039/C7QI00614D
61. H. Hoppe, N.S. Sariciftci, Organic solar cells: an overview. J. Mater. Res. **19**, 1924–1945 (2004). https://doi.org/10.1557/JMR.2004.0252
62. C.B. Nielsen, S. Holliday, H.-Y. Chen et al., Non-fullerene electron acceptors for use in organic solar cells. Acc. Chem. Res. **48**, 2803–2812 (2015). https://doi.org/10.1021/acs.accounts.5b00199

63. X. Liu, H. Chen, S. Tan, Overview of high-efficiency organic photovoltaic materials and devices. Renew. Sustain. Energy Rev. **52**, 1527–1538 (2015). https://doi.org/10.1016/j.rser.2015.08.032
64. V.L. Davis, S. Quaranta, C. Cavallo et al., Effect of single-chirality single-walled carbon nanotubes in dye sensitized solar cells photoanodes. Sol. Energy Mater. Sol. Cells **167**, 162–172 (2017). https://doi.org/10.1016/j.solmat.2017.03.007
65. Y. Gogotsi, How safe are nanotubes and other nanofilaments? Mater. Res. Innov. **7**, 192–194 (2003). https://doi.org/10.1007/s10019-003-0257-z
66. Z. Zhang, L. Wei, X. Qin, Y. Li, Carbon nanomaterials for photovoltaic process. Nano Energy **15**, 490–522 (2015). https://doi.org/10.1016/j.nanoen.2015.04.003
67. X. Xu, R. Ray, Y. Gu et al., Electrophoretic analysis and purification of fluorescent single-walled carbon nanotube fragments. J. Am. Chem. Soc. **126**, 12736–12737 (2004). https://doi.org/10.1021/ja040082h
68. S. Bak, D. Kim, H. Lee, Graphene quantum dots and their possible energy applications: a review. Curr. Appl. Phys. **16**, 1192–1201 (2016). https://doi.org/10.1016/j.cap.2016.03.026
69. H. Wang, P. Sun, S. Cong et al., Nitrogen-doped carbon dots for "green" quantum dot solar cells. Nanoscale Res. Lett. **11**, 27 (2016). https://doi.org/10.1186/s11671-016-1231-1
70. A. Ali, J. Jo, Y.J. Yang, K.H. Choi, Direct fabrication of graphene/zinc oxide composite film and its characterizations. Appl. Phys. A **114**, 323–330 (2014). https://doi.org/10.1007/s00339-013-8136-y
71. A.K. Geim, K.S. Novoselov, The rise of graphene. Nat. Mater. **6**, 183–191 (2007). https://doi.org/10.1038/nmat1849
72. M.Z. Iqbal, A.-U. Rehman, Recent progress in graphene incorporated solar cell devices. Sol. Energy **169**, 634–647 (2018). https://doi.org/10.1016/j.solener.2018.04.041
73. S. Lin, Y. Lu, J. Xu et al., High performance graphene/semiconductor van der Waals heterostructure optoelectronic devices. Nano Energy **40**, 122–148 (2017). https://doi.org/10.1016/j.nanoen.2017.07.036
74. S.R. Kim, M.K. Parvez, M. Chhowalla, UV-reduction of graphene oxide and its application as an interfacial layer to reduce the back-transport reactions in dye-sensitized solar cells. Chem. Phys. Lett. **483**, 124–127 (2009). https://doi.org/10.1016/j.cplett.2009.10.066
75. S. Paulo, G. Stoica, W. Cambarau et al., Carbon quantum dots as new hole transport material for perovskite solar cells. Synth. Met. **222**, 17–22 (2016). https://doi.org/10.1016/j.synthmet.2016.04.025
76. N.M. Rosas-Laverde, A. Pruna, D. Busquets-Mataix et al., Improving the properties of Cu_2O/ZnO heterojunction for photovoltaic application by graphene oxide. Ceram. Int. **44**, 23045–23051 (2018). https://doi.org/10.1016/j.ceramint.2018.09.107
77. S.Z. Siddick, C.W. Lai, J.C. Juan, S.B. Hamid, Reduced graphene oxide–titania nanocomposite film for improving dye-sensitized solar cell (DSSCs) performance. Curr. Nanosci. **13**, 494–500 (2017). https://doi.org/10.2174/1573413713666170519123159
78. N.A.S. Effendi, N.S. Samsi, S.A. Zawawi et al., Studies on graphene zinc-oxide nanocomposites photoanodes for high-efficient dye-sensitized solar cells, in *AIP Conference Proceedings* (2017), p. 090005
79. Z. Zhu, J. Ma, Z. Wang et al., Efficiency enhancement of perovskite solar cells through fast electron extraction: the role of graphene quantum dots. J. Am. Chem. Soc. **136**, 3760–3763 (2014). https://doi.org/10.1021/ja4132246

Chapter 10
Electrochemical DNA Biosensors Based on Carbon Nanomaterials

Luisa Pilan and Matei Raicopol

10.1 Introduction

The field of DNA biosensors is an active research area and many designs and detection mechanisms have been tested in order to achieve superior detection features in clinical diagnostics or genetic screening [1]. Detection of specific DNA sequences at ultralow concentration proved to be of great importance for other applications including drug screening [2, 3], food analysis [4, 5] or environmental monitoring [4, 6]. DNA biosensors have the potential to overcome the limitations of traditional hybridization assays by offering faster, cheaper, and highly sensitive analytical tools for obtaining specific DNA sequence information [7]. Although the latest advances are exciting and encouraging, the manufacturing of highly sensitive and selective DNA biosensing systems is still an important challenge. With the DNA hybridization as the main concept of DNA biosensors, increasing the sensitivity and specificity of the biorecognition process emerges as the most important topics in their design [8].

Electrochemistry-based sensing represents nowadays one of the most attractive routes due to well-known advantages such as high sensitivity, fast response, simple design, low cost, easy miniaturization, low power requirements, and ability to perform detection at decentralized settings [9]. Also, the association of electrochemical transduction with amplified and specific DNA hybridization sensing represents

L. Pilan (✉)
Department of Inorganic Chemistry, Physical Chemistry and Electrochemistry, University "Politehnica" of Bucharest, 1-7 Polizu St, 011061 Bucharest, Romania
e-mail: luisa.pilan@upb.ro

M. Raicopol (✉)
"Costin Nenitzescu" Department of Organic Chemistry, University "Politehnica" of Bucharest, 1-7 Polizu St, 011061 Bucharest, Romania
e-mail: m_raicopol@chim.upb.ro

S. Kaneko et al. (eds.), *Carbon Related Materials*,
https://doi.org/10.1007/978-981-15-7610-2_10

a forward step towards the development of point-of-care (POC) devices. An electrochemical DNA-based biosensor can be characterized as a device that integrates DNA as a biological recognition element and an electrode as a physicochemical transducer [10]. While the selection of an appropriate immobilization strategy for the biorecognition element and the detection mechanism for the hybridization event are important issues in the construction of electrochemical DNA biosensors [8], the choice of transducer material is essential in determining the overall performance [11]. The detection of specific DNA sequences in a complex environment requires a powerful transduction of the biorecognition event. In the same time, the performance of DNA biosensors is highly dependent on the immobilization of the DNA capture probes (cpDNAs) and require a favourable distribution for optimum target hybridization [12].

Carbon nanomaterials (CNs) offered some of the most promising results in enhancing the sensor performance due to their excellent electric and mechanical properties, high specific surface area, and biocompatibility [13]. Their superior surface area to volume ratio confers an increased catalytic response as well as better optical, magnetic, and electrical properties and also facilitates the immobilization of cpDNAs in high amounts, which translates into improved sensitivities [12–14]. Recent advances in CNs design and synthesis enabled powerful electrochemical DNA detection platforms by tuning the performance of each component:

- The recognition element of the sensor, where CNs provide binding sites for target DNA (tDNA) sequence or molecules capturing tDNA,
- The transducer component, where the molecular interaction at the CNs-based electrode is converted into a measurable signal, or
- In signal amplification, because CNs can function as labels for tDNA [13].

The family of CNs includes the two-dimensional graphene, one-dimensional CNTs, and zero-dimensional graphene or carbon quantum dots (GQDs or CQDs), all being successfully applied in many other active research fields, such as electronics, energy or gene, and drug delivery [15]. Figure 10.1 shows the schematic representation of some of the most important CNs employed for construction of DNA electrochemical biosensors.

CNTs and graphene are the most representative in the big family of CNs and have received a lot of attention for electrochemical biosensing applications due to unique advantages like high surface area to volume ratio, excellent conductivity, chemical stability, and mechanical strength [17]. Although zero-dimensional fullerenes and GQDs have been employed as building blocks in such applications, they are not as widely applied as the 1D and 2D CNs [18]. In addition, the use of graphene and CNTs has been greatly widened by tuning their physicochemical properties through chemical modification of their surface. Pristine graphene and CNTs have similar carbon structure arrangements. Graphene is basically an one-atom-thick planar sheet of sp^2-bonded carbon atoms with delocalized π electrons across the plane that provides excellent electrical conductivity [19]. Materials included in the graphene family comprise single and multilayer graphene, graphene oxide (GO), reduced graphene

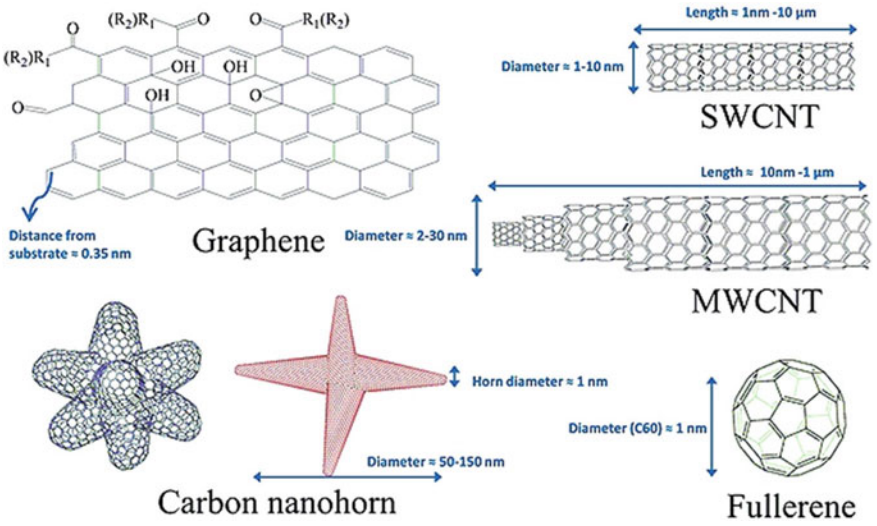

Fig. 10.1 Some of the most important CNs employed in electrochemical DNA biosensors. Reprinted from [16], Copyright 2018, with permission from Elsevier

oxide (RGO), and GQDs, each exhibiting different defect density and different physical, chemical, electrical, and mechanical properties. CNTs possess a cylindrical structure resembling single-rolled graphene sheets with nanometre diameters and lengths in the micron range [20]. CNTs can be classified in two structural groups, i.e. single (SWCNTs) and multi-wall carbon nanotubes (MWCNTs) and, depending on their helicity and diameter, they act in a fashion similar to that of a semiconductor or metal [20, 21]. However, graphene possesses several advantages over CNTs, like higher surface area, abundant surface functional groups, easier dispersibility, and lack of catalytic metallic impurities when prepared by exfoliation. In addition, graphene materials are easily transferable to various substrates due to their planar structure [22].

Carbon nanodots (CDs) represent a new class of CNs that has gradually attracted enormous interest mainly due to their strong fluorescence, for which they are referred to as fluorescent carbon [23]. Depending on their structure, CDs can be classified as carbon quantum dots (CQDs), representing quasi-spherical carbon nanoparticles with size less than 10 nm, and graphene quantum dots (GQDs) formed by small pieces of graphene with lateral size less than 10 nm [24]. Due to their fascinating characteristics such as large surface area, facile functionalization, excellent biocompatibility, and intrinsic electrical conductivity (for GQDs), their performances in electrochemical biosensors have been extensively investigated in the last years [25, 26].

Fullerenes are also promising members of CNs family. The closed cage, nearly-spherical C_{60}, and related analogues possess notable physical, chemical, and electrical properties such as stability in many redox forms, easy functionalization, signal

mediation, and light-induced switching [27]. Tuning the physical and chemical properties of fullerenes by covalent or noncovalent functionalization enabled their wide application in the design of novel biosensor systems [25]. The role of fullerene derivatives as electron transfer mediators in detecting different types of biomolecules has been reported in numerous studies [27–29].

Carbon nanohorns (CNHs), one of the newly discovered forms of CNs, have attracted increasing attentions due to their unique morphology and structure [30]. They consist of horn-shaped graphene sheets and, due to a similar atomic arrangement, are structural analogues of CNTs [31]. Nonetheless, unlike CNTs, single-walled carbon nanohorns (SWCNHs) assemble during synthesis to form spherical aggregates with high surface area and excellent porosity. The high porosity and adsorption potential endow them applicability as nanocarriers or substrates for biosensing devices [32]. As well, their mass production at room temperature without using any metal catalysts [33] confers several advantages over CNTs in practical use: low toxicity, no interference from residual metal impurities and the direct use in applications without any post-treatment [32]. Similar to CNTs and graphene, CNHs can be partially oxidized and carry oxygen-containing groups on their surface [25].

This chapter aims to provide an overview of the recent advances and methodologies in the construction of different electrochemical DNA biosensors based on the previously introduced types of CNs, particularly, with regards to probe immobilization chemistry, transduction principles, and amplification strategies applied in different DNA-sensing schemes.

Besides the survey and comparison of different methodologies reported in recent papers, the purpose of this chapter is to highlight the importance of CNs in addressing some of the issues required for an extensive implementation of DNA biosensors in POC technology.

10.2 Chemistry of Probes Immobilization onto CNs

The basic design of an electrochemical DNA biosensor usually involves the immobilization of specifically designed single-stranded (ss) nucleic acids (capture probe) on the electrode surface for complementary DNA or RNA (target) recognition via a highly efficient and highly specific hybridization process. In general, synthetic oligodeoxyribonucleotides (ssDNA) are used as capture probes in the DNA hybridization sensors, as the RNA oligonucleotides are more expensive. End-labels like thiol and amine groups or biotin are introduced in order to facilitate the immobilization of capture probes onto the transducer surface [10].

Other molecules that can be used as capture probes in addition to conventional ssDNA are peptide nucleic acids (PNAs) and nucleic acid aptamers. PNAs are synthetic DNA analogues, with a pseudopeptide backbone that enables high sensitivity due to its neutral character which eliminates electrostatic repulsion between the two hybridized strands [34]. Nucleic acid aptamers are short single-stranded oligonucleotides optimized for high-affinity binding to a given target and are selected through

systematic evolution of ligands by exponential enrichment technique (SELEX) from random sequence libraries [35]. Furthermore, hairpin DNA (hpDNA) structures proved to exhibit higher selectivity as capture probes compared to linear cpDNAs [36]. HpDNAs possess two regions in the same strand with complementary sequences that pair each other to form a double-helix structure ending in an unpaired loop [37]. Among these hpDNA probes, electrochemical molecular beacons (EMB) have attracted great interest due to their remarkable molecular recognition specificity. EMBs involve an oligonucleotide immobilized at the electrode by one end and a reversible redox marker label at the other, such as the label is positioned in close proximity to the electrode surface [10].

The immobilization step is essential in developing a robust biosensing interface, and therefore a judicious control at this level is important for ensuring proper orientation, accessibility, and stability of the capture probe on the sensor surface [11]. In some cases, blocking the remained unoccupied sites on the surface proved to be necessary in order to prevent nonspecific binding [13]. In this context, the CNs functionalization is of great importance for adjusting the interface properties in order to facilitate probe attachment and subsequent target recognition [38]. Commonly, this adjustment of surface properties is attained by covalent and noncovalent modifications. The combination of CNs with polymers or inorganic composites may offer, as well, more reproducible, stable, sensitive, and selective structures [39]. In many cases, functional composites such as CNs—metallic nanoparticles (NPs) hybrids can act synergistically to offer favourable properties for sensing applications [40].

In the following, a brief overview of various immobilization strategies of the biorecognition element that have been successfully employed in DNA biosensors based on different types of CNs is presented.

10.2.1 Noncovalent Immobilization

The noncovalent functionalization of CNs provides a means for immobilization of biorecognition elements while maintaining the integrity of the sp^2-hybridized carbon network. The main advantages of noncovalent functionalization are its simplicity, flexibility, minimal steric interference, and the preservation of the original physicochemical properties of immobilized biomolecules [41]. Nonetheless, some disadvantages can be mentioned: the relatively weak bonds involved that can induce detaching of biomolecules from the surface, and random attachment that can determine inaccessibility of parts involved in target recognition, both affecting the hybridization efficiency [38].

For the CNs-based DNA sensors, physical adsorption is the simplest immobilization method, driven by π–π stacking interactions between the aromatic ring of the cpDNAs nucleobases and the hexagonal lattice of graphene and CNTs [42]. The strength of these interactions depends on the number of aromatic rings of the adsorbed molecules and on the curvature at the contact between the aromatic part of the molecule and the CNs surface [43]. A wide variety of aromatic molecules can be

noncovalently attached by π–π interactions to the plane of pristine graphene [44] or to the sidewalls of CNTs [45].

CNs with oxygen-containing groups such as GO, RGO, and acid-treated CNTs exhibit very different interactions with DNA than their pristine analogues, because of the interruption of electron delocalization and sp^3 defects. For instance, pristine graphene possesses an almost planar extended aromatic system that interacts strongly with aromatic molecules. A different behaviour is expected in case of RGO and GO, considering that RGO has a decreased aromatic character, while GO can be viewed as a nonaromatic surface with small isolated aromatic areas and extended deviations from planarity [46]. However, the sp^3 defects of GO proved to be very beneficial for DNA biosensing and it was successfully employed as platform to differentiate DNA sequences [47]. GO adsorbs easily linear ssDNA structures, but the interaction with the rigid structure of double-stranded DNA (dsDNA) is very loose due to the bases shielding within the densely negatively charged phosphate backbone [48]. The ability of GO to discriminate between different types of DNA structures combined with its fluorescence quenching properties have been especially exploited for developing fluorescence resonance energy transfer (FRET) biosensors [49]. Nevertheless, an electrochemistry-based detection would be the best choice for POC devices, given its high speed, low cost, simple instrumentation, and ease of miniaturization of the biosensing components. Such an approach was developed by Bonanni and Pumera [36], who applied a noncovalent immobilization of hpDNA probes on electrochemically reduced GO (ERGO) modified electrodes for the detection of DNA sequences correlated with Alzheimer's disease. The sensing mechanism consisted on the partial release of hpDNA probes from ERGO surface after the hybridization with the complementary target, the event being translated by a decrease of the charge-transfer resistance in EIS measurements. However, the interaction between DNA and GO is quite complex, the adsorption properties being affected by the type and length of DNA sequence, and its concentration and the adsorption site on the GO surface [48]. Wu et al. [50] studied the adsorption and desorption of DNA oligonucleotides onto GO as a function of salt concentration and DNA length. They found that shorter DNAs are adsorbed more rapidly and bind more tightly to graphene, and the adsorption is favoured at lower pH and higher ionic strength. Moreover, Yang and co-workers investigated the binding ability and stability of ssDNA and ssRNA on GO, finding that GO provides the additional advantage of protecting DNA and RNA from enzymatic digestion [51].

On the other hand, the binding between C_{60} and DNA molecules can be mainly attributed to the hydrophobic interaction between the fullerene surface and hydrophobic sites on the DNA [27]. C_{60} fullerene has been widely utilized for improving the sensitivity of DNA electrochemical biosensors by providing either a suitable immobilization platform for DNA or by inducing a proper orientation of redox-active proteins, thus, enhancing the electron transfer properties [27]. For instance, Zhang et al. designed a highly sensitive biosensing platform based on fullerene C_{60} nanotubes (FNTs) that subsequently formed hybrids with ssDNA. The authors showed that the strong physisorption of DNA onto the FNTs with the formation of FNT/DNA hybrids was determined by π–π stacking and hydrophobic

interactions [52]. Several other methods of DNA noncovalent immobilization at C_{60} modified electrodes have been tested. Gholivand et al. studied electrochemically the mechanism of Parkinson's disease prevention with the drug Carbidopa, by exploiting the immobilization of a dsDNA at fullerene-modified GC electrodes [53]. The fullerene-modified GC electrode was prepared by drop-casting a suspension of C_{60} in CH_2Cl_2 and then dsDNA was simply adsorbed at the electrode surface from an aqueous solution. A similar approach was proposed by Shiraishi et al. who immobilized DNA onto a screen-printed electrode prepared with a paste containing fullerene. The DNA modified electrode was applied for the electrochemical detection of 16S rDNA extracted from *Escherichia coli* [54].

Surface blocking is also common practice in DNA biosensors based on physical adsorption of capture probes [55], as it improves specificity by reducing nonspecific adsorption [56]. Many types of molecules (e.g. polymers, surfactants, and homopolymer DNAs) can be adsorbed onto CNs, serving as blocking agents and potentially removing weakly adsorbed cpDNAs [57]. Moreover, when blocking the heterogeneous GO surface, a methodical investigation of potential blocking agents is needed in order to maximize the performance of DNA sensors.

10.2.2 Covalent Immobilization

The covalent attachment of biomolecules to CNs is the preferred approach in sensor applications due to a more stable and robust substrate modification with oriented biomolecules [58]. Compared to sensors based on physisorbed probes, covalent immobilization leads to regenerable sensors less prone to nonspecific probe displacement. However, the covalent strategies can determine the alteration of the CNs electronic structure, so there is always a trade-off between the functionalization degree and the preservation of electrical properties [59]. In covalent modification, either the surface defects or the oxygen functionalities present on the CNs could be utilized for functionalization. For example, carboxylic groups presented at the edges or basal plane of CNs can form covalent bonds with primary amine-containing molecules [19]. The coupling of amino groups in biomolecules with the carboxyl functionalities using the well-known carbodiimide protocol is one of the most common procedures for DNA covalent immobilization. Usually, single-stranded amino-labelled DNA (NH_2-DNA) or label-free short DNA sequences are bound to these groups by their amino tags [34] and deoxyguanosine residues, respectively [60]. This protocol has been recently applied for assembling GQDs on a double-stranded DNA structure [61]. The carboxyl groups of GQDs were activated with *N*-(3-(dimethylaminopropyl)-*N*′-ethyl-carbodiimide hydrochloride (EDC) and *N*-hydroxysuccinimide (NHS) and then coupled with NH_2-DNA through amide bonds. GQDs functioned as platform for immobilization of HRP protein for an amplified detection of miRNA-155 (detection limit of 0.14 fM) [61]. Using a similar procedure, Li et al. [62] constructed a sensitive miRNA-24 sensor by drop-casting MWCNTs on a GCE followed by the immobilization of aminated ssDNA capture probes on the electrode surface. Usually,

CNTs are pre-treated in strong acids before further functionalization is attempted, which results in the formation of oxygenated functional groups at the more reactive open ends or defect sites on the side walls. Other approaches that were used for the more difficult sidewall functionalization involved highly reactive species (e.g. fluorine) or reduction of aromatic diazonium salts, which generates aryl radicals [11]. Despite some disadvantages such as defect formation, the electrochemical reduction of aryldiazonium salts has been successfully applied in recent studies since it leads to the formation of covalent bonds in a controllable fashion and assures a reproducible functionalization degree [63–68].

The covalent functionalization of graphene can be performed at the sp^2 carbon atoms, the oxygen-containing groups of GO and by heteroatom doping [69]. Nitrogen and boron are commonly used as dopants in heteroatom-doped graphene due to their similarity with carbon [69]. Some reports demonstrated that nitrogen doping can significantly increase the electron conductivity and also enhance the biocompatibility and sensitivity of graphene in biosensing applications [70]. Chen et al. constructed a label-free electrochemical DNA biosensor using a hybrid nanomaterial based on N-doped graphene and Au NPs-modified GC electrode for ultrasensitive and highly selective detection of the human multidrug resistance gene 1 (MDR1 gene). It was shown that the use of N-doped graphene greatly increased the electrode surface area and electrical conductivity, while the AuNPs further enhanced the immobilization of the cpDNA and hybridization ability [71].

The decoration of CNs with inorganic materials (metallic nanoparticles (NPs), metal, or semimetal oxides) represents another strategy in biosensors design that can provide unique properties for sensing applications. The obtained hybrid structures exhibit both the advantages of the individual nanoparticles and CNs, as well as synergistic properties. In this regard, Zhang et al. reported a simple and efficient fabrication method for label-free impedimetric DNA sensors using CNTs functionalized with Fe_3O_4 NPs as substrate for the capture probe [72].

10.2.3 Affinity Binding

The immobilization of biomolecules via supramolecular or coordinative interactions have also been widely applied for the surface binding of biomolecules [73]. The typical example encountered in the field of biosensor design is the biotin/avidin (or streptavidin) system [18]. The avidin–biotin bond is the strongest noncovalent interaction, its stability being comparable with that of covalent bonds. Typically, avidin (or streptavidin) is first immobilized on the transducer surface followed by binding of the biotinylated oligonucleotides [19]. Erdem et al. [74] has successfully demonstrated the immobilization of biotinylated cpDNAs to a streptavidin-modified CNTs electrode. The biosensor demonstrated excellent selectivity, because of the high specific affinity of the streptavidin/biotin system. A very important advantage of streptavidin-modified surfaces is that non-complementary DNAs can easily be removed by a brief washing step, thus, improving the biosensor selectivity and reproducibility [74].

10.3 Detection Strategies for CNs-Based Electrochemical DNA Biosensors

10.3.1 Methods for Transducing the Hybridization Signals in Electrochemical DNA Biosensors

An electrochemical biosensor is a device that consists of a biorecognition element integrated with an electrochemical signal transducer such as electrode or a field effect transistor (FET) [75]. Generally, the detection mechanism of electrochemical biosensors is based on the change of current or voltage when the analyte is recognized by the biorecognition element. Depending on the mode of signal transduction, electrochemical biosensors can be classified into amperometric, voltammetric, impedimetric, and FET biosensors [25]. Amperometric and voltammetric sensors are the most common approaches for DNA electrochemical sensing and involve monitoring of a current related to the concentration of analyte under controlled potential conditions. The potential applied at the electrode is set at a desired constant value (amperometric) or is scanned in a chosen range during the test (voltammetric). The most frequently used voltammetric methods for DNA electroanalysis include cyclic voltammetry (CV), differential pulse voltammetry (DPV), and square-wave voltammetry (SWV).

The electrochemical impedance spectroscopy (EIS) technique measures the response of an electrochemical system by monitoring the current upon a voltage perturbation with small amplitude [38]. The EIS frequency-domain response can give useful information about the physical and chemical changes that occur when an analyte binds to a biomolecule immobilized on an electrode, making it particularly appropriate for the detection of DNA hybridization [76, 77]. EIS measurements can be performed in either faradic or non-faradic modes [78]. In the faradaic EIS detection, the analytical signal is the charge-transfer resistance (R_{ct}) between the solution and the electrode surface when affinity binding occurs and this requires the addition of redox-active species, such as $[Fe(CN)_6]^{3-/4-}$ or $[Ru(NH_3)_6]^{2+/3+}$ [79, 80]. In the non-faradaic EIS detection no additional reagent is needed, as the analytical signal is the electrical double layer capacitance [25]. For a successful detection of the formation of dsDNA, a careful design of the probe layer depending on the desired operating mode is required. A compact or insulating layer free of leakage current is needed for non-faradaic approach while less-packed or conductive layers that permit the access of redox species are desirable for the faradaic biosensor [81].

FET-based biosensors use an electric field to control the conductivity of a semiconducting channel between two electrodes, source, and drain. This can be attained by varying the electric field potential, relative to the source and drain electrodes, of a third electrode known as gate [82]. In this case, the analytical signal is the source-drain current which is proportional to the analyte concentration when the semiconductor channel incorporating the biorecognition element is brought into contact with the analyte environment [25]. Due to the semiconductors' sensitivity to changes induced by hybridization of surface-immobilized cpDNAs, this label-free approach

is one of the most effective for DNA detection [79]. CNs, especially CNTs and graphene, are key materials for FET sensors due to their excellent electric properties, ultrahigh sensitivity, and potential for miniaturization. The semi-metallic behaviour of graphene enabled the development of graphene FETs for quantitative detection of DNA attachment by a shift in the Dirac point with the change in the surface charge [83]. However, for CNTs, a major drawback is the difficulty in the separation of metallic nanotubes from semiconducting ones [84].

10.3.2 Detection Mechanisms for CNs-Based DNA Electrochemical Biosensors

The working principle of DNA biosensors is based on the affinity of two complementary ssDNA strands, one with known nucleotide sequence (cpDNA) and its investigated counterpart (tDNA). The hybridization of the two strands occurs through the pairing of purine bases (adenine and guanine) with pyrimidine complementary ones (cytosine and thymine) [85]. Several approaches have been considered for the recognition of DNA hybridization, which can be classified as label-based and label-free detection. Label-based methods involve the use of some signal reporter species such as redox-active molecules or enzymes that bind to DNA, while the label-free methods are based on changes in the electroactivity of DNA due to hybridization. According to a IUPAC report, a clear distinction is needed regarding label-free and reagentless DNA electrochemical biosensors. Label-free techniques use no chemical modification of DNA probes, DNA targets, or other analytes, while reagentless techniques use no additional chemical reagents (indicators, redox mediators, and enzyme substrates) to generate the analytical signal [10].

10.3.2.1 Label-Free DNA Hybridization Detection Method

Detection of DNA Through Intrinsic Electroactivity of DNA Bases

Most of the label-free electrochemical methods for DNA detection rely on the intrinsic electroactivity of DNA purine bases [8]. The first assay of label-free DNA electrochemical detection, developed by Paleček 60 years ago, discriminated ssDNA versus dsDNA through direct reduction of DNA bases at a mercury electrode [86]. Among the four nucleobases, guanine and adenine were found to be the most easily oxidized at carbon electrodes [87]. Thereupon, the approach based on the change of reduction/oxidation current signal of guanine and adenine after hybridization has been extensively exploited in the development of label-free electrochemical DNA sensors [8]. The interaction of free bases in a DNA probe with the complementary ones in tDNA during hybridization leads to less accessible guanine/adenine bases and their redox activity decreases. Electrochemical signals generated from oxidation or

reduction of DNA nucleobases can be investigated by voltammetry-based techniques. Their direct detection at conventional carbon materials has a low sensitivity [88], but Zhou et al. demonstrated that the chemically reduced GO provides far better electrochemical activity for all four A, G, C, T bases [89]. Moreover, direct voltammetric studies performed on DNA by Lim et al. at anodized epitaxial graphene demonstrated that all four DNA bases in dsDNA could be simultaneously detected and ssDNA can be differentiated from dsDNA [90]. Compared to pristine graphene, which shows disadvantages such as slow electron transfer kinetics or high background current, electrochemically oxidized graphene, or graphene containing a large number of defects were found to significantly enhance the nucleobases' response. Furthermore, the basal planes of graphene are substantially less electrochemically active than the edge sites of graphene sheets [90, 91]. Considering these aspects, Ambrosi and Pumera applied structured graphene electrodes based on nanofiber-stacked graphene whose edge planes have been preferentially exposed, for studying a ssDNA oligonucleotide specific of the human influenza A (H1N1) virus. The authors demonstrated an enhanced electrochemical response compared with other carbon materials such as GC, MWCNTs, edge plane pyrolytic graphite, and graphite microparticles [91]. Still, numerous studies evidenced that CNTs show a catalytic effect on electrooxidation of nucleic acids and their bases, enhancing the signal considerably [92–96]. Amplification of the guanine response has been reported at MWCNTs-modified carbon paste electrodes [97], SWCNTs or MWCNTs-modified GC electrodes [92, 96], and at graphite pencil electrodes modified with MWCNTs [93]. MWCNTs have also been used to develop a simple, label-free, and sensitive electrochemical biosensor for detection of miRNA by monitoring the oxidation signal of guanine by DPV. MicroRNAs (miRNAs) are single-stranded small non-coding RNAs that play important roles as endogenous gene regulators [98]. Synthetic ssDNAs complementary with miRNA-24 were covalently immobilized as capture probes onto the surface of MWCNTs-modified GC electrodes. For optimized conditions, the proposed miRNA-24 biosensor proved a good sensitivity, a limit of detection (LOD) of 1 pM, good specificity and acceptable recovery and reproducibility [62].

The label-free approach provides reduced analysis time and is free from other unfavourable effects that labels have, such as instability and steric hindrance [55, 99]. There are however limitations such as high background signals due to nonspecific adsorption of DNAs containing guanine bases and high oxidation potentials required to detect the nucleobases. The latter can be surmounted by using redox mediators with reversible electrochemical responses at lower potentials [10]. Other limitations may arise from the fact that only bases in the close vicinity of the electrode can undergo direct electrooxidation. Again, redox mediators such as rhodium or ruthenium complexes that can shuttle electrons from guanine residues in inaccessible parts of the DNA sequence to the electrode could overcome this disadvantage [100]. Still, the major drawback of this strategy remains the irreversibility of electrochemical reduction and oxidation of DNA bases and, thus, the limited reusability of the sensor due to the denaturation of nucleic acids [75].

Detection of DNA Through Impedance Changes Induced by Hybridization

EIS provides another label-free approach for DNA hybridization detection [93]. Impedimetric biosensing relies on changes in the electrical properties of the surface (resistance and capacitance), resulting solely from capturing the target molecule by the DNA probe.

For impedance measurements, it is beneficial to have a large surface area for biomolecules immobilization and highly conductive transducing materials. Graphene is an ideal surface for impedimetric biosensing as it exhibits metallic conductivity, high heterogeneous electron transfer rates and, as already mentioned, a very large surface area [101]. Recently, Kilic et al. developed a sensitive and selective method to detect miR-122 in cell lysates by measuring the R_{ct} of a redox probe at graphene-modified pencil graphite electrodes [102]. The biosensor exhibited a LOD of 1 pmol with a good selectivity and could be applied for detecting several miRNA sequences in real samples. A sensitive impedimetric DNA biosensor for HIV-1 gene detection was developed by Gong et al. The authors showed that the use of ERGO as immobilization platform for cpDNA enhances the EIS response and a LOD down to 0.3 pM can be attained [103]. Zhang et al. proposed an effective label-free EIS biosensor for the detection of a 21-mer oligonucleotide sequence from the hepatitis B virus by employing RGO as detection platform [104]. In their study, RGO was functionalized with tryptamine (TRA), which is irreversibly anchored via its indole ring to the large hydrophobic surface of graphene by π-stacking interactions. The amino-substituted oligonucleotide probe was conjugated to TRA by cross-linking with glutaraldehyde. Under optimal conditions, the proposed biosensor proved a high sensitivity for complementary DNA and a LOD as low as 5.2×10^{-13} M. The reported results based on EIS approaches proved that this technique can serve as a low-cost procedure for genetic studies.

Detection of DNA by Altering the Accessibility of Redox Probes Induced by Hybridization

The limitations of methods that rely on the intrinsic electroactivity of DNA bases motivated the development of other label-free detection strategies that exploit the signal changes of electrochemically active species (indicators) due to different interactions (electrostatic, intercalation, etc.) with ssDNA and dsDNA or as a result of changes in the indicator accessibility at the electrode driven by analyte binding or alteration of a biorecognition element's conformation [79]. These species can be either freely diffusing or attached to the DNA double helix [10].

(a) The simplest approach involves a charged (electrostatic) redox indicator that responds to differences in negative charge density between ssDNA and dsDNA. The mostly widely used is the negatively charged $[Fe(CN)_6]^{3-/4-}$ and, commonly, the voltammetric redox signal of $[Fe(CN)_6]^{3-/4-}$ decreases after the hybridization of a ssDNA probe with tDNA [79]. The use of uncharged

PNA as probe proved to offer a better discrimination between the probe and the negatively charged PNA-DNA hybrid [10]. However, when cpDNA is noncovalently adsorbed at CN-based electrodes a different behaviour can be expected. For example, hybridization-induced desorption of the hpDNA probes from graphene surfaces favours the redox reaction of $[Fe(CN)_6]^{3-/4-}$ [36]. This approach served as a sensitive method for the detection of DNA sequences and single nucleotide polymorphism (SNP) correlated to Alzheimer's disease. The same strategy proved that a GO platform allows a more accurate discrimination among three different ssDNA targets than ERGO and TRGO (thermally-reduced graphene oxide) [37]. Zhao et al. [105] proposed a simple and efficient electrochemical platform for detecting specific ssDNA sequences employing GQD-modified electrodes and $[Fe(CN)_6]^{3-/4-}$ as redox indicator. The ssDNA probes adhered strongly to the modified electrode surface via their interaction with GQDs, thus, inhibiting $[Fe(CN)_6]^{3-/4-}$ electron transfer, while in the presence of target molecules signal currents increased significantly.

Another redox indicator frequently used to monitor changes in negative charge density through impedimetric or voltammetric techniques is the cationic complex $[Ru(NH_3)_6]^{3+/2+}$, which is attracted to the negatively charged backbone of DNA. Ruthenium complexes are "cleaner" species that do not adsorb on carbon electrodes the way $[Fe(CN)_6]^{3-/4-}$ or other species employed as intercalators do, a drawback which can influence the DNA interaction signal [106]. Du et al. employed ERGO films deposited on polyaniline modified GC electrodes to noncovalently bind the ssDNA probes and then redox $[Ru(NH_3)_6]^{3+}$ cations were attached via electrostatic interaction with the negatively charged phosphate backbone of DNA [107]. For recognizing the hybridization event, the change in the voltammetric response of surface-bound $[Ru(NH_3)_6]^{3+}$ before and after hybridization of the ssDNA probe with tDNA was monitored. The authors reported that the biosensor could detect the sequence-specific DNA of a cauliflower mosaic virus gene with a LOD of 3.2×10^{-14} mol L^{-1} [107].

(b) A different label-free strategy for electrochemical DNA detection has been developed by Teymourian et al. using as a detection platform an electrode modified with Fe_3O_4/RGO nanocomposite [108]. In this strategy, a voltammetric signal is produced by the underlying Fe(II)/Fe(III) redox system attached to the transducing interface, as the electron transfer reaction is influenced by subtle surface changes induced by DNA binding or hybridization. A remarkable attomolar sensitivity and high specificity for tDNA have been reported for this approach.

A similar label-free strategy was adopted by Ye et al. [109], who selected thionine (Thi), a cationic phenothiazine dye, as an electrochemical active species for DNA detection. In this case, the electrochemical transducing interface consisted of AuNPs and a thionine-functionalized reduced graphene oxide (Thi-RGO) modified GC electrode. Thiolated cpDNA sequences were immobilized onto the transducing platform through S–Au bonds (Fig. 10.2) and the detection of specific DNA sequences was based on the decrease of thionine's DPV response induced by hybridization. The proposed DNA biosensor exhibited excellent

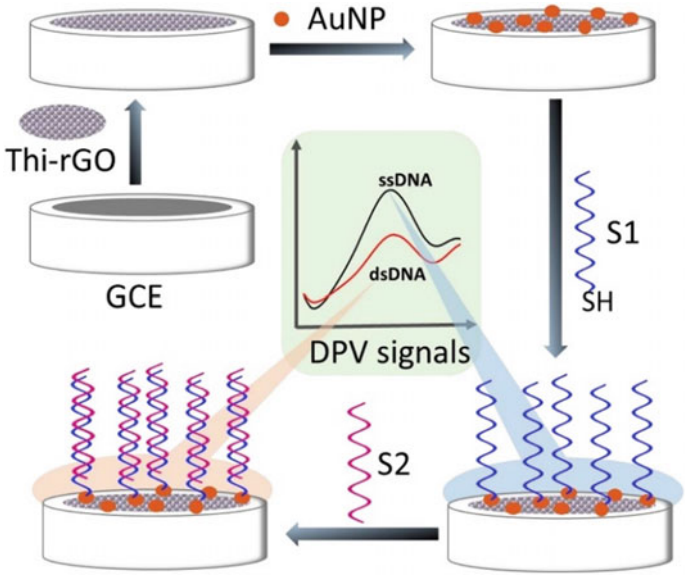

Fig. 10.2 Schematic illustration of the fabrication and DNA detection procedure with a biosensor based on AuNPs and Thi-RGO-modified GC electrode. Reprinted from [109], Copyright 2018, with permission from Elsevier

analytical performance in terms of detection limit, linear range, stability, and sensitivity [109].

(c) The use of intercalator molecules that bind with high affinity to the dsDNA duplex conformation leads to a selective accumulation of these species on the electrode surface when the analyte is also present, so the voltammetric signal increases accordingly [110]. Intercalators are planar organic molecules with several condensed aromatic rings and typical examples include daunomycin, ethidium bromide, osmium bipyridine, ruthenium(II) polypyridyl complexes, phenoxazines, etc. [111]. Some of these redox intercalators that contain osmium and ruthenium ions are rather toxic and expensive, therefore, newer, cost-effective, and benign intercalators with excellent redox reversibility have been synthesized [8]. For example, Wang et al. [112] used an original polypyridyl copper complex as intercalator and a chitosan–MWCNTs nanocomposite film (Fig. 10.3) as immobilization platform for cpDNA. The hybridization of cpDNA with a target 20-mer oligonucleotide fragment related to the phosphinothricin acetyltransferase gene could subsequently be monitored due to the ability of the copper complex to discriminate between hybridized and unhybridized DNA [112].

(d) Other electroactive species that can function as redox indicators for hybridization events are substances that associate preferentially with ssDNA, a common example being methylene blue (MB), which interacts with unpaired guanine residues [10]. Such an approach was developed using flexible

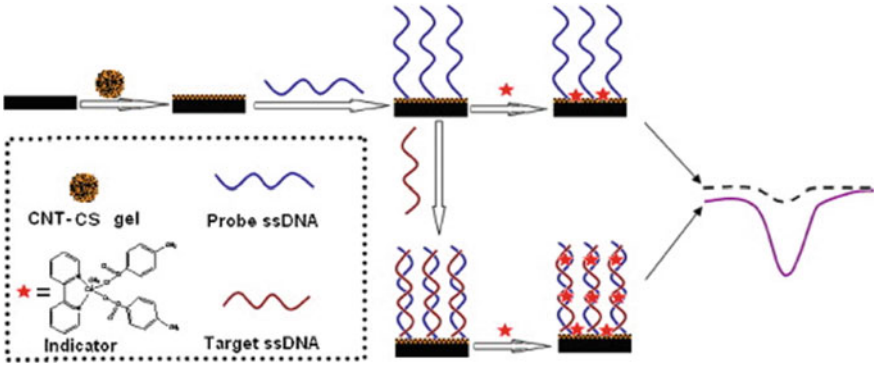

Fig. 10.3 Schematic diagram for the fabrication of a DNA biosensor having a polypyridyl copper complex as intercalator and a chitosan–MWCNTs nanocomposite film as immobilization platform for cpDNA. Reprinted from [112], Copyright 2011, with permission from Elsevier

MWCNTs/polydimethylsiloxane electrodes for the immobilization of ssDNA capture probes through π–π interactions with MWCNTs [113]. The mechanism of detection using MB as redox indicator is presented in Fig. 10.4. The MB indicator can be both adsorbed onto the electrode surface, while the positively charged MB binds to negatively charged phosphate in the ssDNA capture probes (P1) and non-complementary sequences (T3), leading to an increase of the concentration of MB near the electrode surface. In the presence of a complementary DNA sequence (T1), the π–π interactions between the nucleobases of dsDNA and the MWCNTs are significantly reduced and a decrease in the concentration of MB near the electrode can be monitored by the diminishing peak currents in CV and DPV [113]. Since the probe was attached through π–π interactions between ssDNA and MWCNTs, the sensor could be easily regenerated by simply washing the electrodes with water.

However, several other studies revealed that MB can function only as intercalator for the dsDNA double helix and accordingly a higher MB reduction current is recorded after hybridization than in the presence of only the ssDNA capture probe [113–115]. The apparent disagreement of these results can be attributed either to variations in the structure of biorecognition molecules or to the different immobilization strategies [115]. Du et al. fabricated a DNA-sensing platform through the immobilization of uncharged PNA probes at ERGO electrodes using 1-pyrenebutyric acid as linker [115]. A DPV method was employed to monitor the hybridization event using MB as electrochemical indicator. The authors reported that MB interacted easily with the guanine residues and intercalated into the PNA–DNA helix structure, leading to an increase in peak current after PNA–DNA hybridization. Both the utilization of PNA probes for tDNA recognition and the ability of ERGO to promote electron transfer reactions determined a high selectivity for DNA, a wide dynamic range and a low LOD (0.5 pM). A similar approach involving the covalent immobilization of

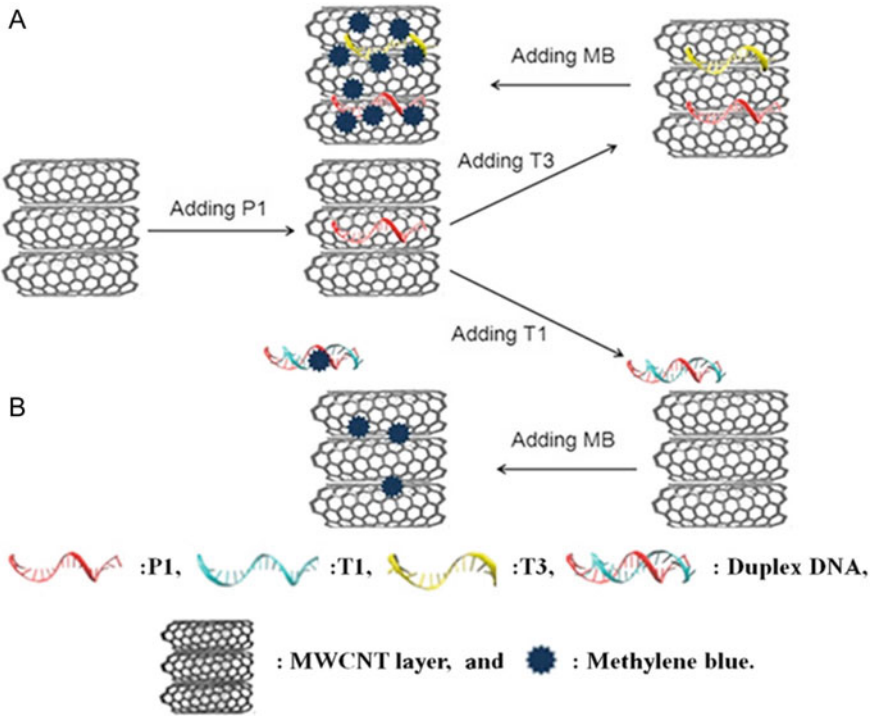

Fig. 10.4 Schematic representation of the DNA-sensing mechanism employing MWCNT-based electrodes and MB as indicator (P1: cpDNA; T1: complementary tDNA; T3: non-complementary tDNA). Some of MB molecules can be intercalated into dsDNA. Reprinted from [113], Copyright 2015, with permission from Elsevier

cpDNA was described by Chen et al. [71], but these authors employed a hybrid nanomaterial composed of N-doped graphene and Au NPs as platform for ultrasensitive DNA detection. The N-doped graphene significantly increased the electrode surface area and electrical conductivity, while the Au NPs allowed the covalent immobilization of a thiolate ssDNA probe. Results of DPV analyses using MB as indicator showed that the biosensor displayed high selectivity, increased sensitivity for a wide linear range, and low detection limit for MDR1 gene [71].

Another DNA-sensing approach employed a RGO-modified GC electrode as detection platform and $[Cu(phen)_2]^{2+}$ as electrochemical indicator and anchor for cpDNA immobilization. RGO benefits were both in increasing the electrode surface area to support high loadings of the indicator and DNA probe, but also in accelerating the electron transfer rate. The planar structure of 1,10-phenanthroline afforded ssDNA immobilization through intercalative interactions between the helix of cpDNA and the aromatic phenanthroline rings. Thus, the detection mechanism relied on the decrease in $[Cu(phen)_2]^{2+}$ electrochemical response when the DNA probe hybridized with its complementary sequence and hindered the charge transfer.

The biosensor displayed a LOD of 1.99 10^{-13} M and a good discrimination ability by effectively detecting one-base mismatch [116].

The concepts presented above are in agreement with the current understanding of the DNA surface conformations, but it should be pointed out that structural changes in immobilized DNA can unpredictably affect the binding properties of redox indicators [79].

Detection of DNA by CN-Based FETs

The ability of CN-based FETs to detect DNA hybridization events in a label-free manner offered a new perspective for developing a new generation of simple and inexpensive DNA chips [117]. By taking advantage of the superior properties of CNs, many strategies have been developed to create SWCNTs or graphene-based FET biosensors for the direct detection of DNA hybridization and even for DNA–protein interactions. An important aspect of using CN-based FETs in biosensing is their capacity to detect biomolecules at the single-molecule or single-cell level because of their size and excellent biocompatibility [118]. For instance, DNA physically adsorbed onto CVD-grown SWCNTs and deposited on SiO_2/Si wafers was used in a FET configuration that specifically recognized in the HFE gene the H63D SNP discrimination, which is responsible for hereditary hemochromatosis [119]. However, some studies reported that nonspecifically adsorbed ssDNA molecules cannot easily bind with their complementary strand and that a more robust immobilization method is needed to bind ssDNA probes onto the surface of CNTs [117]. Goldsmith et al. developed an electrochemical method to create single-point defects in SWCNTs in a controllable manner and then covalently attached biomolecules at the defect sites [120]. It has been demonstrated that a FET device built on this principle exhibits sufficient sensitivity to detect the binding of a single molecule as a result of coulombic interaction with the defect site. This strategy was further exploited by Sorgenfrei et al. These authors coupled an—NH_2 terminated ssDNA probe to a –COOH functionalized point defect in a CNT, thus, obtaining single-molecule label-free biosensors capable of probing molecular kinetics at microsecond timescales, an approach which shows great potential for label-free SNP detection[121].

Graphene is an ideal material for the fabrication of FET biosensors because it is a zero-bandgap semiconductor. Furthermore, its large surface area, biocompatibility, and exceptional electronic properties such as ultrahigh charge mobility, low charge scattering, and ambipolar field effect make it superior to CNTs for such applications [106]. Dong et al. [122] demonstrated that large-size CVD-grown graphene films are highly sensitive to DNA hybridization. Their device was able to detect the hybridization of tDNA at a LOD of 0.01 nM and even distinguished single-base mismatch. Grafting probe molecules on the surface of graphene without affecting its electrical conductivity can be easily achieved through π-π interactions with linker molecules containing pyrene, pyridine, benzene, or quinoline groups [25].

Some disadvantages of CVD-grown graphene are its high cost and, sometimes, reproducibility issues when considered for integrated circuits [123]. Chemically

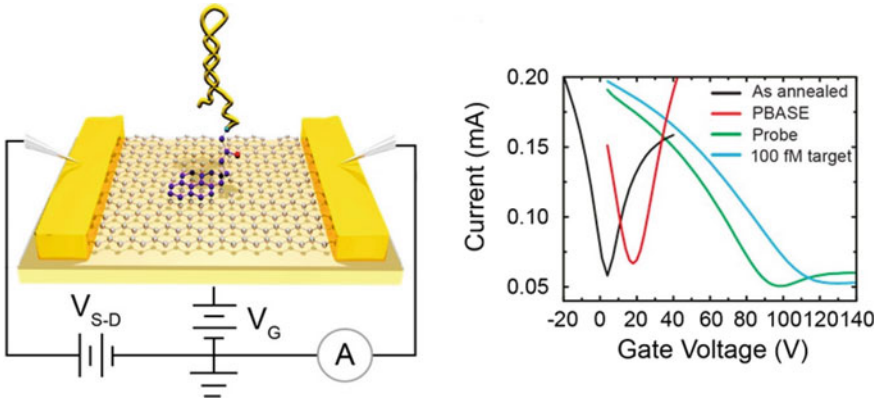

Fig. 10.5 Schematic representation of hpDNA bound to a back-gated G-FET using a pyrene linker (left side) and the current-gate voltage curve evolution of G-FET following different chemical treatment steps (right side). G-FETs were functionalized by π–π stacking interaction with 1-pyrenebutyric acid N-hydroxysuccinimide and incubated in aminated hpDNA solutions that led to an increase in the Dirac potential. Reprinted with permission from https://pubs.acs.org/doi/10.1021/acs.nanolett.8b00572 [125]. Copyright 2018 American Chemical Society

modified graphenes with tunable surface chemistry can become an alternative for CVD-grown, providing comparable results for DNA-sensing FETs. Cai et al. reported a RGO-based FET biosensor for ultrasensitive label-free detection of DNA [124]. A PNA capture probe was immobilized onto the RGO surface using a pyrene molecule as linker. The attained LOD, as low as 100 fM, was mainly attributed to the use of a PNA probe with a higher sequence-specific affinity and stability to tDNA in respect to traditional ssDNA probes. Another strategy developed by Gao et al. exploited a hpDNA probe that allowed for target recycling and hybridization chain reaction to amplify the transduction signal (Fig. 10.5), thus, improving the LOD by a factor of 20,000 [125] and enhancing specificity. By using the graphene-based FET (G-FET), a multiplexed detection principle that overrun the tDNA length limitations and opens the way for high sensitivity nucleic acid testing was demonstrated, with significant benefits for diagnostics in a real-life clinical context [125].

10.3.2.2 Label-Based DNA Hybridization Detection Methods

When label-free approaches are not sensitive enough or not appropriate for a particular transduction principle, a strategy based on labels must be employed in order to provide a relevant electrochemical signal [19]. The attachment of electrochemically detectable DNA labels (either for the DNA target or DNA probe) such as redox species (e.g. ferrocene) or enzymes catalyzing reactions that generate electroactive products (e.g. hydrogen peroxide) usually induce an enhanced sensitivity and selectivity for the detection. Unfortunately, such procedures can also increase the complexity of the device and associated cost [10].

Target Labelling

One of the label-based DNA detection strategies adopted at CN-based platforms relies on chemical labelling of tDNA sequences with redox-active molecules or enzymes as signal reporters [75]. The use of enzymes as reporters serves also as amplification strategy for the hybridization event by catalytic generation of electrochemically active species. For example, alkaline phosphatase (ALP) is able to hydrolyze a large number of phosphoesters and the resulting dephosphorylated products can be detected electrochemically, while for horseradish peroxidase (HRP) and glucose oxidase (GOD), the generated H_2O_2 is monitored amperometrically [10]. For instance, considerable sensitivity and selectivity were achieved for the detection of DNA sequences related to the breast cancer BRCA1 gene with a biosensor based on a MWCNT-modified GC electrode transducer and ALP-labelled tDNA [126]. In this case, the detection principle relied on cpDNA immobilization at the sensor surface and further hybridization with biotinylated tDNA labelled with streptavidin–ALP. The ALP catalyzed the hydrolysis of α-naphthyl phosphate to α-naphthol, an electroactive product which was detected by chronoamperometry [126]. A similar approach using ALP-labelled tDNA was developed by Berti et al. for the DPV detection of the 35S promoter, a common marker for genetically modified organisms (GMOs) [127]. The group tested several MWCNTs thin films prepared by CVD as sensing platforms and then combined an optimized CNs platform with enzyme labelling to achieve LOD in the nanomolar range, sufficient for most applications involving gene expression and sequence analysis. He and Dai described a method for preparing highly sensitive and selective DNA sensors by attaching cpDNAs on both the tip and wall of plasma-activated aligned CNTs combined with tDNA pre-labelled with ferrocenecarboxaldehyde [128]. The redox response of ferrocene moieties could be recorded at the CNT electrode when complementary DNA was present, whereas non-complementary DNA chains showed no redox response [128].

Probe Labelling—Sandwich Affinity Structures

Sandwich hybridization assays employ covalently labelled probes (reporter probes, RP) and consist of two recognition steps (cpDNA–tDNA and tDNA–RP), resulting in a significant improvement in the selectivity. The design of RPs allows the hybridization with tDNA at an adjacent site to the sequence recognized by the cpDNA, thus, contributing to an efficient electron transfer between the label moiety and the electrode [10]. There are two main approaches for integrating CNs with sandwich affinity biosensors: one uses CN-modified electrodes in order to improve the electrochemical response of the label group and the second involves the integration of CNs with the redox species/catalysts employed as RPs [129]. Both procedures have been widely validated in many label-based DNA hybridization studies. Such a sandwich-type DNA detection system where CNTs provide double-step amplification pathways (for both recognition and transduction events) was designed by Wang et al. [130]. The CNTs-based amplified detection protocol involved the sandwich hybridization

of cpDNA immobilized onto streptavidin-modified magnetic beads, the tDNA, and a DNA RP conjugated in a SWCNT/ALP adduct. The chronopotentiometric stripping detection of the enzyme reaction product (α-naphthol) was possible at CNTs/GC electrode by enzymatic amplification. The CNT's dual amplification role, as carriers for enzyme labels and for accumulating the enzyme reaction product, assured an excellent sensitivity for DNA detection, with a LOD of around 54 aM [130]. A somewhat similar sandwich structure for DNA sensing was later reported in a study by Yang et al. These authors employed a ferrocene (Fc)-SWCNTs adduct conjugated with a DNA probe as reporter and exploited the electrocatalytic properties of Fc/SWCNT towards H_2O_2 [131]. The Fc-SWCNTs/DNA adducts hybridized to a tDNA sequence already paired with a second DNA probe immobilized on a gold electrode. In this case, SWCNTs played a double role, both in the recognition/transduction events and for enhancing the electron transfer [131].

A recent study described a sandwich hybridization assay based on gold nanoparticle-modified graphene oxide (AuNPs-GO) as transduction platform for detecting the breast cancer marker ERBB2 (Fig. 10.6). Thiolated cpDNAs (ERBB2-c) immobilized onto AuNPs-GO and a HRP-labelled probe were used to assay tDNA hybridization. Using the amperometric detection principle, a LOD of 1.6×10^{-10} M was achieved for ERBB2, a value lower than the normal physiological level which proves this strategy is suitable for early stage screening of breast cancer [12].

Another approach devised for the integration of CNs with sandwich hybridization assays uses CNs-based reporter labels as enzyme substitutes for signal amplification. For example, Wang et al. described a sensitive DNA biosensor using a HRP mimic as reporter label which was combined with a biotinylated molecular beacon immobilized onto AuNPs–SWCNH modified GC electrodes [132]. Iron porphyrins such as hemin and iron(III)meso-tetrakis(N-methylpyridinum-4-yl)porphyrin (FeTMPyP), attracted considerable interest lately because they can substitute the biological function of HRP [133, 134]. In another study, the reporter label was prepared by assembling the iron(III) porphyrin FeTMPyP onto GO by noncovalent π-π interactions, yielding a high peroxidase activity towards o-phenylenediamine (o–PD) oxidation in the presence of H_2O_2. The use of graphene-based enzyme mimic combined with AuNPs–SWCNH composite as transducer determined an increased detection sensitivity and a LOD down to attomole levels [135].

10.4 Signal Amplification Strategies in CNs-Based Electrochemical DNA Biosensors

As already mentioned in the previous paragraphs, signal amplification is another important feature for DNA biosensors which enables the detection of small analyte quantities in complex matrices, usually, in the presence of excess nonspecific sequences [10]. In the last few years, substantial advances were made in the development of more sensitive transducers and new amplification schemes that generate

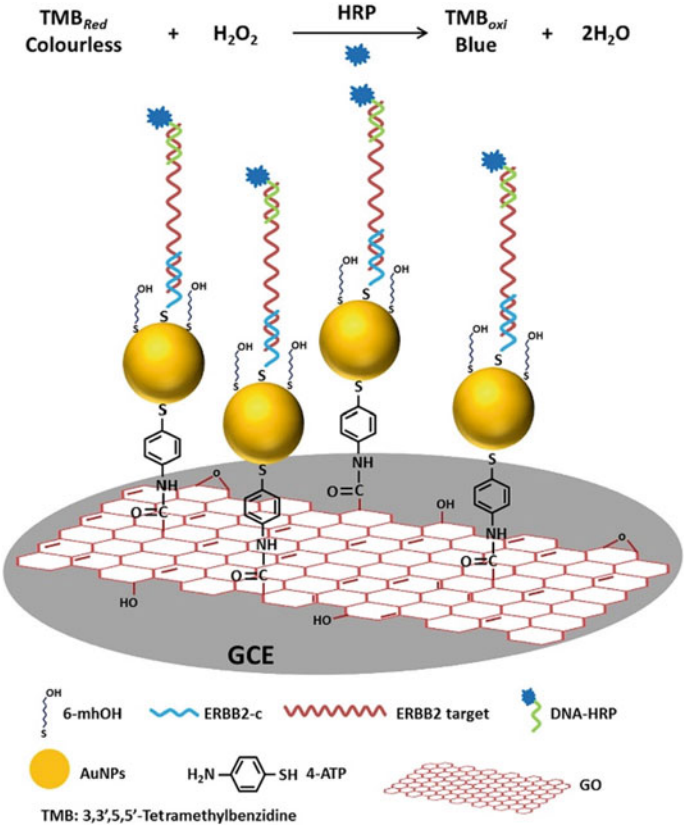

Fig. 10.6 Schematic representation of a sandwich-type DNA sensor for the detection of breast cancer marker ERBB2 showing the prepared AuNPs-GO/GC and the hybridization of tDNA (ERBB2 target) with the specific cpDNA (ERBB2-c) and HRP-labelled RP. Reprinted from [12], Copyright 2017, with permission from Elsevier

enhanced signals from just a few analyte molecules [136]. To address the assay sensitivity issues, researches designed highly functional nanomaterials and, by fine-tuning their structure and functions, were able to amplify detection signals [137]. Because of their interesting properties, the use of CNs dominates in a wide range of biosensing schemes. The high surface-to-volume ratio and the superior conductivity of CNs amplifies surface interactions and provides a high surface density of probe or analyte molecules, hence, increasing the sensitivity and allowing device miniaturization [21]. Despite the unique advantages of CNs, their combination with various functional materials can contribute synergistically to signal amplification [138–143]. IUPAC reviewed several ways to accomplish signal amplification in electrochemical DNA biosensors: using multiple electrochemically active species in tDNA or signalling probes, employing biocatalysts, using NPs-based strategies or multilevel signal amplification through different types of nanomaterials such as CNs, each

loading other amplifying entities (simple redox labels, nanoparticles, or enzymes) [10]. The amplification methods which employ CNs in order to achieve ultrahigh assay sensitivities will be discussed in the following section.

10.4.1 Amplification Methods Based on Redox-Active Species

Several innovative amplification schemes in which mediators are used for the oxidation of nucleobases [143, 144] or employ electrochemically active species (either intrinsic components of nucleic acids or synthetic labels) in tDNA [110] or in signalling probes[145, 146] have been described in the literature. Cai et al. were the first to use CNTs in an electrochemical DNA biosensor fabricated through covalent immobilization of cpDNAs onto a MWCNT-modified GC electrode and performed the tDNA hybridization detection by DPV in the presence of an electroactive intercalator, daunomycin [147]. The MWCNTs platform conferred improved sensitivity during the transduction stage and their device achieved a LOD of 1.0×10^{-10} M for the target sequence [147]. The use of mediators for nucleobase oxidation, such as ruthenium [143] or osmium complexes [144], has been also proposed in order to amplify the sensing signal and, thereby, increase the sensitivity. Moreover, by combining a MWCNTs-modified nanoelectrode array with $[Ru(bpy)_3]^{2+}$ mediated guanine oxidation, ultrasensitive (sub-attomole) detection of DNA hybridization was achieved [143].

As already mentioned in the previous section, all sandwich-type biosensors can be constructed with reporter probes bearing a small quantity of redox species such as ferrocene [145] or methylene blue (MB) [148]. The performance of these devices can be augmented by employing CN-modified electrodes that amplify the electrochemical signal due to their favourable interfacial redox properties [129]. A sensitive sandwich-type DNA sensor based on graphene decorated with Au NPs as sensing platform was reported by Wang et al. [148] (Fig. 10.7). Thiolated cpDNA was covalently attached to AuNPs on the electrode surface and the tDNA hybridized with two different regions of the RP (labelled with MB) and cpDNA, forming sandwich-like aggregates. The Au NPs/RGO film enhanced the accumulation of immobilized cpDNA and the formation of long DNA concatemers, highly improving the sensitivity of the biosensor. This approach allowed the detection of tDNA with a LOD of 0.35 fM and very good selectivity [148].

10.4.2 Enzyme-Assisted Amplification

Enzyme-assisted nucleic acid amplification technology is a very powerful tool for signal amplification, considering that one enzyme molecule used as an nucleic acid tag catalyzes the transformation of a large number of substrate molecules into electroactive products [10]. Recently, Liu et al. devised a label-free electrochemical

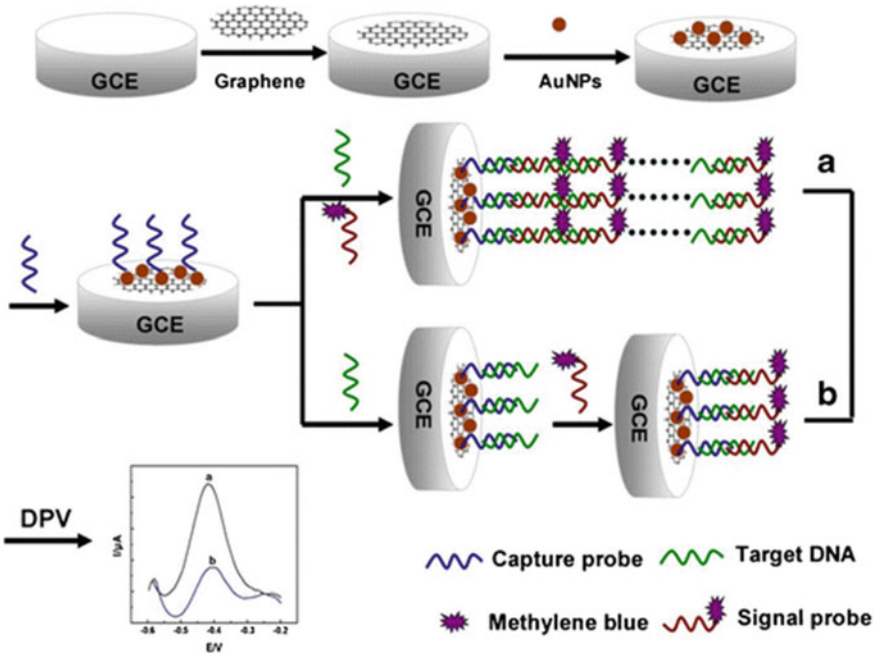

Fig. 10.7 Schematic representation of the fabrication procedure for the DNA biosensor described in Ref.[148] (cpDNA: capture probe, tDNA: target DNA, RP: signal probe). Reprinted by permission from Springer Nature: Springer, Microchimica Acta [148], Copyright 2014

detection strategy for 17β-estradiol (E2) based on graphene and DNase I enzyme-assisted cycling amplification. In the proposed design, graphene had a multiple role, as substrate for the E2 binding aptamer, the recognition element for E2, and as controllably switch on the electron transfer between the substrate electrode and a redox probe in the solution in the presence of the E2 analyte (by assembling on the SAM thiols modified Au electrode). A DPV method was adopted to measure the current response determined by the controllable assembling of the graphene that could be correlated with the E2 concentration. Due to the synergistic effect of DNase I enzyme-assisted cycling amplification (that could successively generate bare graphene, see Fig. 10.8), a high sensitivity and a LOD of 50 fM for E2 could be attained. As well, this detection principle showed enhanced selectivity in complex samples, displaying promising potential for E2 detection in wastewater [149].

Recent studies revealed that the simple rules that govern nucleic acid hybridization of can be tailored for signal amplification [150]. DNA amplification techniques, such as rolling circle amplification (RCA), hybridization chain reaction (HCR) [151], catalyzed hairpin assembly (CHA) [152], have been explored as signal amplification strategies with a synergic role in the design of CNs-based DNA biosensors. Commonly, these techniques are enzyme-free and rely only on hybridization and

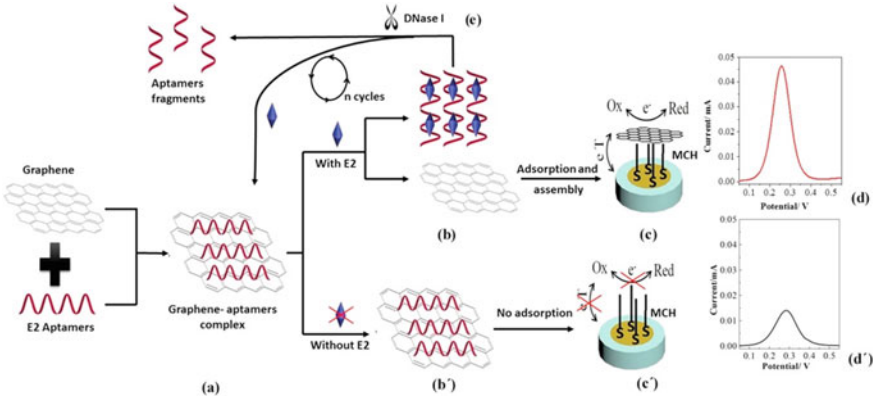

Fig. 10.8 Schematic representation of the principle of an aptasensor for E2 detection: DNase I enzyme splits the aptamer attached to E2 and releases E2. The free E2 reattaches to other aptamers, successively creating bare graphene and, thus, a cycling electrochemical response amplification. Reprinted from [149], Copyright 2018, with permission from Elsevier

strand-exchange reactions, but can be connected favourably with enzyme amplification schemes [150]. For instance, Shuai et al. [153] reported a highly sensitive electrochemical sensor for miRNA detection based on a WO_3-RGO composite platform that coupled enzyme signal amplification with CHA target recycling. Through the synergic combination of large specific surface area WO_3-RGO composites with the high selectivity from CHA target miRNA recycling, and the enzymatic electrochemical-chemical redox cycling reactions, a remarkably low LOD of 0.05 fM was achieved. Later, the same group reported an ultrasensitive electrochemical aptasensor using nitrogen-doped graphene oxide (N-GO) and AuNPs as sensing platform and signal carrier MoS_2 spheres in a sandwich-type configuration [154]. All these features combined with a signal amplification strategy based on HCR and enzymatic redox cycling, led to an ultrahigh sensitivity, a very low LOD (0.027 fM) and a good selectivity for thrombin detection [154].

10.4.3 Nanoparticles as Signal Amplification Elements in CN-Based Electrochemical DNA Biosensors

Another typical strategy to increase the sensitivity of CNs-based DNA biosensors involves the use of functional hybrids comprised of CNs and nanoparticles (NPs) that can act synergistically for the amplification of electrochemical signals. In certain cases, by decorating CNs with NPs, one can efficiently improve the electron transfer occurring between an analyte and the electrode and also increase the amount of immobilized cpDNA. Another approach consists in including NP-bound reporter probe molecules in sandwich-based assays which can lead to considerable signal

enhancement [10]. Recently, various hybrid AuNPs/graphene nanocomposites with application in DNA sensors have been prepared [8, 142]. Wang et al. [155] modified a GC electrode with AuNPs-decorated GO sheets in order to enable the covalent immobilization of cpDNA at the hybrid nanocomposite through Au–S bonds. In a similar approach, a well-dispersed graphene/AuNP nanocomposite suspension was drop-casted on the surface of a GC electrode [156] and then a DNA probe was immobilized through the formation of Au–S bonds, emphasizing the versatility of the chemisorption technique in the fabrication of DNA biosensors. In another example, Huang et al. successfully fabricated ultrasensitive electrochemical DNA sensors by assembling thiolated cpDNA on a MoS_2/MWCNTs-modified electrode functionalized with AuNPs and glucose oxidase [157]. Moreover, AuNPs can be replaced by cheaper AgNPs, as has been illustrated in another study, where a cpDNA labelled at 5′ with a thiolated linker was immobilized at a AgNP/polydopamine–graphene/GC electrode and then DPV was employed to monitor the DNA hybridization event using MB as an electrochemical indicator [158]. Moreover, 6-mercaptohexanol was added after immobilization of the cpDNA in order to induce an orientation which allows better recognition. The multiple amplification methods used in this study determined a LOD of 3.2 fM and a linear sensing range from 0.1 pM to 0.1 nM [158].

An electrochemical biosensor based on PtNPs-decorated MWCNTs in which daunomycin was used as indicator for DNA hybridization was presented by Zhu et al. [111]. The authors demonstrated that due to the large surface area of CNTs and their ability to promote electron transfer reactions combined with the increased electrocatalytic activity of PtNP an exceptional analytical sensitivity can be achieved. As an alternative for chemical reduction methods mentioned above, CNs/NPs composites could also be obtained via electrochemical approaches, which proved to be more advantageous by easily controlling the density and size of the NPs through the characteristic synthesis parameters. For example, Cheng et al. [159] reported an ultrasensitive electrochemical quantification method for microRNA in cell lysates using as detection platform a graphene-functionalized screen-printed Au electrode decorated with bimetallic Pd–Pt NPs.

Dong et al. adopted an amplification strategy for DNA hybridization based on a SWCNTs-FET (SNFET) and introduced reporter DNA probes labelled with AuNPs in the hybridization step, which resulted in a significant improvement of LOD (approx. 100 fM) [160]. Later, the same research team demonstrated that a single large-sized graphene film obtained through CVD can provide a highly sensitive platform for DNA hybridization as the change in gate voltage is large enough to achieve a LOD of 0.01 nM [122]. Moreover, by decorating graphene with AuNPs, a linear response up to a concentration of 500 nM was obtained [122].

10.5 Challenges for Integrating CN-Based Electrochemical DNA Biosensors in POC Devices

Recent advances in CNs-based electrochemical DNA-sensing platforms have already shown tremendous potential for a wide range of applications, including not only clinical diagnostics but also environmental and food safety analysis [161]. Table 10.1 summarizes the methods and analytical characteristics of some selected configurations of CN-based electrochemical DNA biosensors applied in such fields. Despite the fact that many of these CNs-based devices allow sensitive, selective, yet in the same time, simple and inexpensive DNA assays that meet the requirements of point-of-care (POC) clinical diagnostics, still most of them are in the proof of principle stage and only few prototypes have been developed [162]. The many challenges encountered when translating a laboratory prototype to a commercial product need integrated interdisciplinary efforts [163]. For instance, performance validation with established techniques and applicability in real sample analysis are essential for proving that electrochemical biosensors can perform better than standard detection methods [83]. Also, an effective implementation of POC technology for real clinical applications requires the integration of sample preparation and automated detection in one single device, as common POC assays comprise several steps including a PCR amplification before the final detection is performed [164]. Among recently developed technologies, microfluidic lab-on-a-chip (LOC) devices provide new benefits for integrated molecular diagnostics, such as miniaturization, portability, low sample volumes, automation, and higher throughput [165]. Exploiting the advantageous properties of CNs and electrochemical methods in DNA analysis by LOC biosensors is not extensively reported in the literature, still various promising solutions were considered in the past few years [166]. For example, a microfluidic platform that integrates an electrochemical sensor based on MWCNTs and ferrocene as redox indicator was developed by Zribi et al. [164]. This electrochemical microfluidic biosensor was employed for the label-free detection of pathogenic viral DNA from Hepatitis C and genomic DNA from mycobacterium tuberculosis in clinical samples without PCR amplification [164].

Achieving a balance between manufacturing cost and functionality represents another challenge for POC devices. In this context, screen printing emerged as a rapid, simple, and robust technique that facilitates the large-scale manufacturing of miniaturized sensors that can be connected to portable instruments for DNA or other biomarkers detection [167]. Recently, considerable advancement has been made towards the integration of screen-printed electrodes (SPEs) in portable POC devices [168]. Commercial carbon SPEs modified with carboxyl-functionalized SWCNTs were employed for the monitoring of DNA hybridization by DPV and EIS techniques for the detecting the breast cancer early onset gene mutant *BRCA1* [169]. Loo et al. developed a highly sensitive, label-free, disposable aptasensor for thrombin employing as detection platform a SPCEs modified with GO and a specific thrombin DNA aptamer. The impedimetric detection was based on the charge-transfer resistance modification of a redox indicator after the binding event between

Table 10.1 Summary of methods and analytical characteristics of CN-based electrochemical biosensors for different analytes

CN-based detection platorm//label, intercalator	Detection electrochemical method	Analyte	Linear range	Detection limit	Ref.
AuNPs-GO//HRP	CA	Breast cancer biomarker ERBB2	3.7×10^{-10} to 1.0×10^{-8} M	1.6×10^{-10} M	[12]
GQDs//HRP	CA	miRNA-155	1.0×10^{-15} to 1.0×10^{-10} M	1.4×10^{-16} M	[61]
MWCNTs (label free)	DPV	miRNA24	1.0×10^{-12} to 1.0×10^{-9} M	1.0×10^{-12} M	[62]
N-Gr/AuNP//MB	DPV	MDR1 DNA	1.0×10^{-14} to 1.0×10^{-7} M	3.12×10^{-15} M	[71]
Fe_3O_4/CNTs (label free)	EIS	BCR/ABL fusion gene from chronic myelogenous leukaemia	1.0×10^{-15} to 1.0×10^{-9} M	$2.1 \cdot 10^{-16}$ M	[72]
MWCNTs-STR (label free)	DPV	DNA	0–300 mg mL^{-1}	1.45×10^{-7} M	[74]
Gr (label free)	DPV	miRNA-155	–	1.0×10^{-12} M	[102]
ERGO (label free)	EIS	HIV-1 gene	1.0×10^{-12} to 1.0×10^{-9} M	3×10^{-13} M	[103]
TRA–RGO (label free)	EIS	DNA from hepatitis B virus (HBV)	1.0×10^{-12} to 1.0×10^{-7} M	5.2×10^{-13} M	[104]
ERGO/PAN (label free)	DPV	DNA of cauliflower mosaic virus (CaMV35S) gene	1.0×10^{-12} to 1.0×10^{-7} M	3.2×10^{-14} M	[107]
Fe_3O_4/RGO	DPV	DNA	1.0×10^{-17} to 1.0×10^{-9} M	2.0×10^{-18}	[108]

(continued)

Table 10.1 (continued)

CN-based detection platorm//label, intercalator	Detection electrochemical method	Analyte	Linear range	Detection limit	Ref.
AuNPs/Thi-RGO (label free)	DPV	DNA	1.0×10^{-17} to 1.0×10^{-12} M	4.28×10^{-19} M	[109]
PtNPs-MWCNTs//DA	DPV	DNA	2.25×10^{-11} M to 2.25×10^{-7} M	1.0×10^{-11} M	[111]
CS–MWCNTs//Cu(bpy)(MBZ)$_2$(H_2O)	DPV	DNA	5.0×10^{-10} to 1.0×10^{-8} M	5.0×10^{-10} M	[112]
MWCNTs–PDMS//MB	DPV	DNA	1.0×10^{-8} to 1.0×10^{-6} M	1.3×10^{-10} M	[113]
PASE–ERGO//MB	DPV	DNA	1.0×10^{-12} to 1.0×10^{-7} M	5.45×10^{-13} M	[115]
Gr//$[Cu(phen)_2]^{2+}$	SWV	DNA	1.0×10^{-12} to 1.0×10^{-6} M	1.99×10^{-13} M	[116]
SWCNTs (label free)	FET	HFE gene	–	SNP discrimination	[119]
Gr (label free)	FET	DNA	–	1.0×10^{-11} M	[122]
RGO (label free)	FET	DNA	–	1.0×10^{-13} M	[124]
Gr (label free)	FET	DNA	–	5.0×10^{-15} M	[125]
MWCNTs//SA-ALP	DPV	Promoter 35S	5.0×10^{-8} to 2.0×10^{-7} M (5.0×10^{-7} to 1.0×10^{-5} M for label-free sensor)	–	[127]
AuNPs–SWCNH/FeTMPyP/STR–GO//MB	DPV	DNA	1.0×10^{-16} to 1.0×10^{-11} M	2.2×10^{-17} M	[132]

(continued)

Table 10.1 (continued)

CN-based detection platorm//label, intercalator	Detection electrochemical method	Analyte	Linear range	Detection limit	Ref.
MWCNTs–COOH//DA	DPV	DNA	2.0×10^{-10} M to 5.0×10^{-8} M	1×10^{-10} M	[147]
RGO-AuNP//MB	DPV	DNA	1.0×10^{-15} to 1.0×10^{-7} M	3.5×10^{-16} M	[148]
MCH-Au/Gr-ssDNA (label free)	DPV	17β-Estradiol	7.0×10^{-14} M to 1.0×10^{-11}	5.0×10^{-14} M	[149]
AuNPs/WO_3-Gr // SA-ALP	DPV	miRNA	1.0×10^{-16} to 1.0×10^{-10} M	5.0×10^{-17} M	[153]
AuNPs/N-GO–thrombin aptamer/MoS_2–AuNPs // Avidin-HRP	DPV	thrombin	1.0×10^{-14} to 1.0×10^{-10} M	2.7×10^{-17} M	[154]
Gr/AuNR-PThi//$Ru(phen)_3]^{2+}$	DPV	HPV DNA	1.0×10^{-13} M to 1.0×10^{-10} M	4.03×10^{-14} M	[156]
MWCNTs/MoS2/AuNP//GOD	DPV	DNA	1.0×10^{-14} M to 1.0×10^{-8} M	7.9×10^{-16} M	[157]
AgNPs/Pdop/Gr (label free)	DPV	DNA	$1.0 \cdot 10^{-13}$ M to $5.0 \cdot 10^{-8}$ M	3.2×10^{-15} M	[158]
Pt/Pd/RGO//SA-ALP	DPV	miRNA let-7b	1.0×10^{-14} M to 1.0×10^{-10} M	3.55×10^{-15} M	[159]
SWCNTs/DNA–AuNP	FET	DNA	–	1.0×10^{-13} M	[160]

Abbreviations CA (chronoamperometry); CP (chronopotentiometry); DPV (differential pulse voltammetry); SWV (square wave voltammetry); Gr (graphene); GO (graphene oxide); RGO (reduced graphene oxide); GQDs (graphene quantum dots); N-Gr (nitrogen-doped graphene); N-GO (nitrogen-doped GO); SWCNH (single-walled carbon nanohorns); TRA (tryptamine); PAN (polyaniline nanofibers); CS (chitosan); MDR1 (multi- drug resistance gene 1); FeTMPyP (iron(III) meso-tetrakis(N-methylpyridinum-4-yl)porphyrin); bpy (2,2′-bipyridine); MBZ (p-methylbenzoate); STR (streptavidin); (SA-ALP) alkaline phosphatase-labelled streptavidin; GOD (glucose oxidase); PDMS (polydimethylsiloxane); PASE (1-pyrenebutanoic acid succinimidyl ester); PtNPs (platinum nanoparticles); AuNR (Au nanorods); AuNPs (gold nanoparticles); Thi (thionine); PThi (polythionine); Pdop (polydopamine); MB (methylene blue); DA (daunomycin)

thrombin and the aptamer [170]. Shiraishi et al. demonstrated a new procedure for immobilizing DNA onto a fullerene impregnated SPEs for the detection of 16S rDNA extracted from *Escherichia coli* [54]. Another disposable DNA biosensor was reported for the amperometric detection of SNP-containing p53 tumour suppressor (TP53) gene sequences, one of the most popular genes in cancer research [171]. The electrochemical platform consisted of carbon SPEs modified with RGO—carboxymethylcellulose hybrid material and displayed an improved storage stability [171].

The capillary flow platform, also known as lateral flow assay (LFA), is another promising tool for the identification of DNA sequences with POC devices [172]. Recently, by coupling MWCNTs with LFA strips, Qiu et al. developed a rapid, sensitive, and highly reproducible method for DNA detection [173].

FETs are emerging as another detection platform that can be integrated into POC assays, especially due to their portability, label-free operation, and very low detection limits that help in early diagnosis and screening [174]. However, because analytes cannot be efficiently removed after detection, FETs are generally disposable, which may impede their widespread use in low-cost POC devices [175]. In this context, Wang and et al. developed a renewable, label-free, and portable graphene-based FET (G-FET) aptasensor for lead detection in blood [176]. Moreover, Xu et al. described a G-FET platform which could monitor oligonucleotide binding kinetics in real time and, moreover, was capable of distinguishing single-base mutations in real time. The sensor chip could be regenerated at least 50 times showing promise for future use in low-cost quantification of DNA biomarkers [177]. Ordinario et al. developed a microfluidic SWCNTs-FET for the monitoring of protein–DNA interactions which allowed the sequence-specific detection of prototypical DNA-binding proteins (restriction enzymes) at picomolar concentrations [178].

Throughout this chapter, we emphasized some of the issues encountered when integrating electrochemical DNA biosensors with POC devices. However, there are still major challenges that impede the integration of CNs-based platforms in POC devices, such as large-scale manufacturing costs [179], biocompatibility [179, 180], operational stability, and reproducibility [180].

10.6 Conclusions

The growing demand for devices capable of detecting specific DNA sequences motivated the development of new DNA biosensors [11] and throughout this chapter we have summarized the recent advances brought by the integration of CNs with nucleic acids as biorecognition elements and electrochemical analytical methodologies. Although carbon nanotubes and graphene remain the most exploited in the fabrication of DNA electrochemical biosensors, other less common carbon nanoforms like fullerene, carbon nanohorns, or graphene quantum dots have demonstrated their usefulness as innovative transducing materials or nanolabels [171]. We have also provided an overview of the DNA capture probe immobilization methods as

well as the signal amplification strategies and electrochemical detection techniques commonly employed in DNA biosensing. Moreover, we have shown that a synergistic combination of two or more types of nanomaterials and amplification techniques can significantly improve device sensitivity. Therefore, we expect that further development in CNs-based electrodes and the use of improved amplification strategies will lead to a new generation of electrochemical DNA biosensors with exceptional performances [181]. However, despite the important progress made in this field, joint efforts are still needed to meet the ASSURED criteria for wearable POC diagnostics devices: affordable, sensitive, specific, user-friendly, rapid and robust, equipment-free, and deliverable to those who need them [165].

Acknowledgements This work was supported by a grant of Ministry of Research and Innovation, CNCS—UEFISCDI, project number PN-III-P4-ID-PCE-2016-0629, within PNCDI III.

References

1. Q. Feng, X. Zhao, Y. Guo, M. Liu, P. Wang, Stochastic DNA walker for electrochemical biosensing sensitized with gold nanocages@graphene nanoribbons. Biosens. Bioelectron. **108**, 97–102 (2018)
2. R. Shamagsumova, A. Porfireva, V. Stepanova, Y. Osin, G. Evtugyn, T. Hianik, Polyaniline-DNA based sensor for the detection of anthracycline drugs. Sens. Actuat. B Chem. **220**, 573–582 (2015)
3. D. Kahanda, N. Singh, D.A. Boothman, J.D. Slinker, Following anticancer drug activity in cell lysates with DNA devices. Biosens. Bioelectron. **119**(July), 1–9 (2018)
4. F. Long, A. Zhu, H. Shi, H. Wang, J. Liu, Rapid on-site/in-situ detection of heavy metal ions in environmental water using a structure-switching DNA optical biosensor. Sci. Rep. **3**, 1–7 (2013)
5. M. Ligaj, M. Tichoniuk, D. Gwiazdowska, M. Filipiak, Electrochimica Acta Electrochemical DNA biosensor for the detection of pathogenic bacteria *Aeromonas hydrophila*. Electrochim. Acta **128**, 67–74 (2014)
6. R.M. Mazhabi, M. Arvand, Disposable electrochemical DNA biosensor for environmental monitoring of toxicant 2-aminoanthracene in the presence of chlorine in real samples. J. Chem. Sci. **126**, 4, 1031–1037 (2014)
7. M. Debnath, G.B.K.S. Prasad, P.S. Bisen, Molecular diagnostics: promises and possibilities. Mol. Diagnost. Promises Possibilities 1–520 (2005)
8. J.I.A. Rashid, N.A. Yusof, The strategies of DNA immobilization and hybridization detection mechanism in the construction of electrochemical DNA sensor: A review. Sens. Bio-Sensing Res. **16**, 19–31 (2017)
9. M. Freitas, H.P.A. Nouws, C. Delerue-Matos, Electrochemical biosensing in cancer diagnostics and follow-up. Electroanalysis **30**(8), 1584–1603 (2018)
10. G.E. Jan Labuda, A.M. Oliveira Brett, I.P. Miroslav Fojta, M. Mascini, M. Ozsoz, J.W. Emil Paleček, Electrochemical nucleic acid-based biosensors: concepts, terms, and methodology (2010)
11. M. Ozsoz, *Electrochemical DNA Biosensors*. Taylor & Francis Group, LLC (2012)
12. A.A. Saeed, J.L.A. Sánchez, C.K. O'Sullivan, M.N. Abbas, DNA biosensors based on gold nanoparticles-modified graphene oxide for the detection of breast cancer biomarkers for early diagnosis. Bioelectrochemistry **118**, 91–99 (2017)

13. T. Pasinszki, M. Krebsz, T.T. Tung, D. Losic, Carbon nanomaterial based biosensors for non-invasive detection of cancer and disease biomarkers for clinical diagnosis. Sensors (Switzerland) **17**(8), 1–32 (2017)
14. G. Maduraiveeran, M. Sasidharan, V. Ganesan, Electrochemical sensor and biosensor platforms based on advanced nanomaterials for biological and biomedical applications. *Biosens. Bioelectron.* **103**, 113–129 (2018)
15. H. Sun, J. Ren, X. Qu, Carbon nanomaterials and DNA: from molecular recognition to applications. Acc. Chem. Res. **49**(3), 461–470 (2016)
16. M. Rezaee, B. Behnam, M. Banach, A. Sahebkar, The Yin and Yang of carbon nanomaterials in atherosclerosis. Biotechnol. Adv. **36**(8), 2232–2247 (2018)
17. Z. Zhu, An Overview of Carbon Nanotubes and Graphene for Biosensing Applications. Nano-Micro Lett. **9**(3), 1–24 (2017)
18. J.N. Tiwari, V. Vij, K.C. Kemp, K.S. Kim, Engineered carbon-nanomaterial-based electrochemical sensors for biomolecules. ACS Nano **10**(1), 46–80 (2016)
19. N. Wongkaew, M. Simsek, C. Griesche, A. J. Baeumner, Functional nanomaterials and nanostructures enhancing electrochemical biosensors and lab-on-a-chip performances: recent progress, applications, and future perspective. Chem. Rev. (2018)
20. A.C. Power, B. Gorey, S. Chandra, J. Chapman, Carbon nanomaterials and their application to electrochemical sensors: a review. Nanotechnol. Rev. **7**(1), 19–41 (2018)
21. B. Wang, U. Akiba, J. I. Anzai, Recent progress in nanomaterial-based electrochemical biosensors for cancer biomarkers: a review. Molecules **22**(7) (2017)
22. M. Pumera, Graphene-based nanomaterials and their electrochemistry. Chem. Soc. Rev. **39**(11), 4146–4157 (2010)
23. H. Li, Z. Kang, Y. Liu, S.T. Lee, Carbon nanodots: Synthesis, properties and applications. J. Mater. Chem. **22**(46), 24230–24253 (2012)
24. Y. Dong, J. Lin, Y. Chen, F. Fu, Y. Chi, G. Chen, Graphene quantum dots, graphene oxide, carbon quantum dots and graphite nanocrystals in coals. Nanoscale **6**(13), 7410–7415 (2014)
25. Y. Yang, X. Yang, Y. Yang, Q. Yuan, Aptamer-functionalized carbon nanomaterials electrochemical sensors for detecting cancer relevant biomolecules. Carbon N. Y. **129**, 380–395 (2018)
26. M. Tuerhong, Y. Xu, X. B. Yin, Review on carbon dots and their applications. Chin. J. Anal. Chem. **45**(1), 139–150 (2017)
27. S. Pilehvar, K. De Wael, Recent advances in electrochemical biosensors based on fullerene-C60nano-structured platforms. Biosensors **5**(4), 712–735 (2015)
28. C. Ye, X. Zhong, R. Yuan, Y. Chai, Sensors and actuators B : chemical a novel ECL biosensor based on C 60 embedded in tetraoctylammonium bromide for the determination of glucose. Sens. Actuat. B. Chem. **199**, 101–107 (2014)
29. J. Han et al., Multi-labeled functionalized C60 nanohybrid as tracing tag for ultrasensitive electrochemical aptasensing. Biosens. Bioelectron. **46**, 74–79 (2013)
30. S. Iijima et al., Nano-aggregates of single-walled graphitic carbon nano-horns. Chem. Phys. Lett. **309**(August), 165–170 (1999)
31. B. He et al., Single-walled carbon-nanohorns improve biocompatibility over nanotubes by triggering less protein-initiated pyroptosis and apoptosis in macrophages. Nat. Commun. **9**(1) (2018)
32. X. Liu, H. Li, F. Wang, S. Zhu, Y. Wang, G. Xu, Functionalized single-walled carbon nanohorns for electrochemical biosensing. Biosens. Bioelectron. **25**(10), 2194–2199 (2010)
33. P. Yáñez-Sedeño, S. Campuzano, J. Pingarrón, Carbon nanostructures for tagging in electrochemical biosensing: a review. C **3**(1), 3 (2017)
34. M. Yang, M.E. McGovern, M. Thompson, Genosensor technology and the detention of interfacial nucleic acid chemistry. Anal. Chim. Acta **346**(3), 259–275 (1997)
35. S. Eissa, M. Zourob, Selection and characterization of DNA aptamers for electrochemical biosensing of carbensdazim. Anal. Chem. **89**(5), 3138–3145 (2017)
36. A. Bonanni, M. Pumera, Graphene platform for hairpin-DNA-based impedimetric genosensing. ACS Nano **5**(3), 2356–2361 (2011)

37. M. Giovanni, A. Bonanni, M. Pumera, Detection of DNA hybridization on chemically modified graphene platforms. Analyst **137**(3), 580–583 (2012)
38. B. Cardenas-Benitez, I. Djordjevic, S. Hosseini, M.J. Madou, S.O. Martinez-Chapa, Review—covalent functionalization of carbon nanomaterials for biosensor applications: an update. J. Electrochem. Soc. **165**(3), B103–B117 (2018)
39. J. Ping et al., Recent advances in aptasensors based on graphene and graphene-like nanomaterials. Biosens. Bioelectron. **64**, 373–385 (2015)
40. H. Kj, L. Yj, W. Hb, W. Yy, A sensitive electrochemical DNA biosensor based on silver nanoparticles-polydopamine@graphene composite. Electrochim. Acta **118**, 130–137 (2014)
41. S. Gupta, C.N. Murthy, C.R. Prabha, Recent advances in carbon nanotube based electrochemical biosensors. Int. J. Biol. Macromol. **108**, 687–703 (2018)
42. L. Meng, C. Fu, Q. Lu, Advanced technology for functionalization of carbon nanotubes. Prog. Nat. Sci. **19**(7), 801–810 (2009)
43. S. Sabater, J.A. Mata, *Catalytic Applications of Metal Complexes Immobilized by Non-Covalent Interactions onto Chemically Derived Graphenes and Related Materials.* Wiley, New York (2016)
44. A. Hirsch, J.M. Englert, F. Hauke, Wet chemical functionalization of graphene. Acc. Chem. Res. **46**(1), 87–96 (2013)
45. Y. Lee, K.E. Geckeler, Carbon nanotubes in the biological interphase: the relevance of noncovalence. Adv. Mater. **22**(36), 4076–4083 (2010)
46. V. Georgakilas et al., Noncovalent functionalization of graphene and graphene oxide for energy materials, biosensing, catalytic, and biomedical applications. Chem. Rev. **116**(9), 5464–5519 (2016)
47. S. Akca, A. Foroughi, D. Frochtzwajg, H.W.C. Postma, Competing interactions in DNA assembly on graphene. PLoS ONE **6**(4), 4–7 (2011)
48. B. Liu, S. Salgado, V. Maheshwari, J. Liu, DNA adsorbed on graphene and graphene oxide: fundamental interactions, desorption and applications. Curr. Opin. Colloid Interface Sci. **26**, 41–49 (2016)
49. H. Zhang, H. Zhang, A. Aldalbahi, X. Zuo, C. Fan, X. Mi, Fluorescent biosensors enabled by graphene and graphene oxide. Biosens. Bioelectron. **89**, 96–106 (2017)
50. M. Wu, R. Kempaiah, P.-J.J.J.J. Huang, V. Maheshwari, J. Liu, Adsorption and desorption of DNA on graphene oxide studied by fluorescently labeled oligonucleotides. Langmuir **27**(6), 2731–2738 (2011)
51. L. Cui et al., Graphene oxide protected nucleic acid probes for bioanalysis and biomedicine. Chem. A Eur. J., **19**(32), 10442–10451 (2013)
52. X. Zhang, Y. Qu, G. Piao, J. Zhao, K. Jiao, Reduced working electrode based on fullerene C60 nanotubes@DNA: characterization and application. Mater. Sci. Eng. B Solid-State Mater. Adv. Technol. **175**(2), 159–163 (2010)
53. M. Gholivand, A.R. Jalalvand, H. C. Goicoechea, Multivariate analysis for resolving interactions of carbidopa with dsDNA at a fullerene-C60/GCE. Int. J. Biol. Macromol., 1–13 (2014)
54. H. Shiraishi et al., Electrochemical detection of *E. coli* 16S rDNA sequence using air-plasma-activated fullerene-impregnated screen printed electrodes. Bioelectrochemistry **70**(2), 481–487 (2007)
55. V. Kavita, DNA biosensors—a review. J. Bioeng. Biomed. Sci. **07**(02) (2017)
56. T. Terse-Thakoor, S. Badhulika, A. Mulchandani, Graphene based biosensors for healthcare. J. Mater. Res. **32**(15), 2905–2929 (2017)
57. B. Liu, P.J.J. Huang, E.Y. Kelly, J. Liu, Graphene oxide surface blocking agents can increase the DNA biosensor sensitivity. Biotechnol. J. **11**(6), 780–787 (2016)
58. X. Zhang, H. Hu, DNA molecules site-specific immobilization and their applications. Cent. Eur. J. Chem. **12**(10), 977–993 (2014)
59. P. Bollella et al., Beyond graphene: Electrochemical sensors and biosensors for biomarkers detection. Biosens. Bioelectron. **89**, 152–166 (2017)

60. K.M. Millan, S.R. Miskkelsen, Sequence-selective biosensor for DNA based on electroactive hybridization indicators. Anal. Chem. **65**(17), 2317–2323 (1993)
61. T. Hu, L. Zhang, W. Wen, X. Zhang, S. Wang, Enzyme catalytic amplification of miRNA-155 detection with graphene quantum dot-based electrochemical biosensor. Biosens. Bioelectron. **77**, 451–456 (2016)
62. F. Li et al., Carbon nanotube-based label-free electrochemical biosensor for sensitive detection of miRNA-24. Biosens. Bioelectron. **54**, 158–164 (2014)
63. S.Z. Mousavisani, J.B. Raoof, A.P.F. Turner, R. Ojani, W.C. Mak, Label-free DNA sensor based on diazonium immobilisation for detection of DNA damage in breast cancer 1 gene. Sens. Actuat. B Chem. **264**, 59–66 (2018)
64. B.D. Ossonon, D. Bélanger, B. Daniel, D. Bélanger, Functionalization of graphene sheets by the diazonium chemistry during electrochemical exfoliation of graphite. Carbon N. Y. **111**, 83–93 (2017)
65. L. Pilan, M. Raicopol, A. Pruna, V. Branzoi, Polyaniline/carbon nanotube composite films electrosynthesis through diazonium salts electroreduction and electrochemical polymerization. Surf. Interface Anal. **44**(8), 1198–1202 (2012)
66. M. Raicopol, L. Necula, M. Ionita, L. Pilan, Electrochemical reduction of aryl diazonium salts: a versatile way for carbon nanotubes functionalisation. Surf. Interface Anal. **44**(8), 1081–1085 (2012)
67. M.D. Raicopol et al., Organic layers via aryl diazonium electrochemistry: towards modifying platinum electrodes for interference free glucose biosensors. Electrochim. Acta **206**, 226–237 (2016)
68. C. Ott et al., Functionalized polypyrrole/sulfonated graphene nanocomposites: Improved biosensing platforms through aryl diazonium electrochemistry. Synth. Met. **235**, 20–28 (2018)
69. J. Liu, Z. Liu, C.J. Barrow, W. Yang, Molecularly engineered graphene surfaces for sensing applications: A review. Anal. Chim. Acta **859**, 1–19 (2015)
70. G. Yang, L. Li, R.K. Rana, J.J. Zhu, Assembled gold nanoparticles on nitrogen-doped graphene for ultrasensitive electrochemical detection of matrix metalloproteinase-2. Carbon N. Y. **61**, 357–366 (2013)
71. M. Chen, C. Hou, D. Huo, J. Bao, H. Fa, C. Shen, An electrochemical DNA biosensor based on nitrogen-doped graphene/Au nanoparticles for human multidrug resistance gene detection. Biosens. Bioelectron. **85**, 684–691 (2016)
72. W. Zhang, Application of Fe_3O_4 nanoparticles functionalized carbon nanotubes for electrochemical sensing of DNA hybridization. J Appl Electrochem **46**(5):559–566 (2016)
73. S.B. Georgia-Paraskevi Nikoleli, S. Karapetis, V.N.P. Dimitrios, P. Nikolelis, N. Tzamtzis, *Graphene-Based Electrochemical Biosensors: New Trends and Applications*, 2nd edn. Scrivener Publishing LLC (2017)
74. A. Erdem, P. Papakonstantinou, H. Murphy, M. McMullan, H. Karadeniz, S. Sharma, Streptavidin modified carbon nanotube based graphite electrode for label-free sequence specific DNA detection. Electroanalysis **22**(6), 611–617 (2010)
75. S. Cosnier, Electrochem. Biosens. (2013)
76. L. Hu, Y., Li, F., Han, D., Niu, Graphene for DNA biosensing. In: *Biocompatible Graphene for Bioanalytical Applications*, vol. 2. (Springer, 2015), pp. 11–34
77. A. Benvidi, N. Rajabzadeh, H. Molaye Zahedi, M. Mazloum-Ardakani, M.M. Heidari, L. Hosseinzadeh, Simple and label-free detection of DNA hybridization on a modified graphene nanosheets electrode. Talanta **137**, 80–86 (2015)
78. M. Gebala, L. Stoica, S. Neugebauer, W. Schuhmann, Label-free detection of DNA hybridization in presence of intercalators using electrochemical impedance spectroscopy. Electroanalysis **21**(3–5), 325–331 (2009)
79. E.E. Ferapontova, Review—DNA electrochemistry and electrochemical sensors for nucleic acids. Annu. Rev. Anal. Chem. **11**(1), 197–218 (2018)
80. T. Yang, Q. Li, L. Meng, X. Wang, W. Chen, K. Jiao, Synchronous electrosynthesis of poly(xanthurenic acid)-reduced graphene oxide nanocomposite for highly sensitive impedimetric detection of DNA. ACS Appl. Mater. Interfaces **5**(9), 3495–3499 (2013)

81. J. Park, S. Park, DNA hybridization sensors based on electrochemical impedance spectroscopy as a detection tool, pp. 9513–9532 (2009)
82. E.R. Dorothee Grieshaber, R. MacKenzie, J. Voros, Electrochemical biosensors—sensor principles and architectures. Sensors (Switzerland), **8**, 1400–1458 (2008)
83. E. Morales-Narváez, L. Baptista-Pires, A. Zamora-Gálvez, A. Merkoçi, Graphene-based biosensors: going simple. Adv. Mater. **29**(7), 1604905 (2017)
84. S. Sang, Y. Wang, Q. Feng, Y. Wei, J. Ji, W. Zhang, Progress of new label-free techniques for biosensors: a review. Crit. Rev. Biotechnol. **36**(3), 465–481 (2016)
85. A. Umasankar Yogeswaran, S. Kumar and S.-M. Chen, *Nanostructured Materials for Electrochemical Biosensors* (2009)
86. E. Paleček, Oscillographic polarography of highly polymerized deoxyribonucleic acid. Nature **188**, 656 (1960)
87. E. Paleček, From polarography of DNA to microanalysis with nucleic acid-modified electrodes. Electroanalysis **8**(1), 7–14 (2018)
88. K. Ghosal, K. Sarkar, Biomedical applications of graphene nanomaterials and beyond. ACS Biomater. Sci. Eng. **4**(8), 2653–2703 (2018)
89. M. Zhou, Y. Zhai, S. Dong, Electrochemical sensing and biosensing platform based on chemically reduced graphene oxide. Anal. Chem. **81**(14), 5603–5613 (2009)
90. C.X. Lim, H.Y. Hoh, P.K. Ang, K.P. Loh, Direct voltammetric detection of DNA and pH sensing on epitaxial graphene: An insight into the role of oxygenated defects. Anal. Chem. **82**(17), 7387–7393 (2010)
91. A. Brotons, F.J. Vidal-Iglesias, J. Solla-Gullón, J. Iniesta, Carbon materials for the electrooxidation of nucleobases, nucleosides and nucleotides toward cytosine methylation detection: a review. Anal. Methods **8**(4), 702–715 (2016)
92. J. Wang, M. Li, Z. Shi, N. Li, Z. Gu, Electrochemistry of DNA at single-wall carbon nanotubes. Electroanalysis **16**(1–2), 140–144 (2004)
93. A. Erdem, P. Papakonstantinou, H. Murphy, Direct DNA hybridization at disposable graphite electrodes modified with carbon nanotubes. Anal. Chem. **78**(18), 6656–6659 (2006)
94. T. Abdullin, O. Bondar', A. Rizvanov, I. Nikitina, Carbon nanotube-based biosensors for DNA structure characterization. Appl. Biochem. Microbiol. **45**(2), 229–232 (2009)
95. K. Balasubramanian, M. Burghard, Biosensors based on carbon nanotubes. Anal. Bioanal. Chem. **385**(3), 452–468 (2006)
96. X. Zhang, K. Jiao, S. Liu, Y. Hu, Readily reusable electrochemical DNA hybridization biosensor based on the interaction of DNA with single-walled carbon nanotubes. Anal. Chem. **81**(15), 6006–6012 (2009)
97. G.A. Rivas et al., Carbon nanotubes paste electrodes. A new alternative for the development of electrochemical sensors. Electroanalysis **19**(7–8), 823–831 (2007)
98. S.M. Majd, A. Salimi, F. Ghasemi, An ultrasensitive detection of miRNA-155 in breast cancer via direct hybridization assay using two-dimensional molybdenum disulfide field-effect transistor biosensor. Biosens. Bioelectron. **105**, 6–13 (2018)
99. I.O. K'Owino, S.K. Mwilu, O.A. Sadik, Metal-enhanced biosensor for genetic mismatch detection. Anal. Biochem. **369**(1), 8–17 (2007)
100. N.D. Popovich, H.H. Thorp, New strategies for electrochemical nucleic acid detection. Electrochem. Soc. Interface **11**(4), 30–34 (2002)
101. I.P. Melis Asal, Ö. Özen, M. Sahinler, Recent developments in enzyme, DNA and immunobased biosensors. Sensors **18**, 1–16 (2018)
102. T. Kilic, M. Kaplan, S. Demiroglu, A. Erdem, M. Ozsoz, Label-free electrochemical detection of MicroRNA-122 in real samples by graphene modified disposable electrodes. J. Electrochem. Soc. **163**(6), B227–B233 (2016)
103. Q. Gong, H. Yang, Y. Dong, W. Zhang, A sensitive impedimetric DNA biosensor for the determination of the HIV gene based on electrochemically reduced graphene oxide. Anal. Methods **7**(6), 2554–2562 (2015)
104. Z. Zhang, L. Luo, G. Chen, Y. Ding, D. Deng, C. Fan, Tryptamine functionalized reduced graphene oxide for label-free DNA impedimetric biosensing. Biosens. Bioelectron. **60**, 161–166 (2014)

105. J. Zhao, G. Chen, L. Zhu, G. Li, Graphene quantum dots-based platform for the fabrication of electrochemical biosensors. Electrochem. Commun. **13**(1), 31–33 (2011)
106. A. Smerald, *Springer Theses*, vol. 53, no. 9 (2013)
107. M. Du, T. Yang, X. Li, K. Jiao, Fabrication of DNA/graphene/polyaniline nanocomplex for label-free voltammetric detection of DNA hybridization. Talanta **88**, 439–444 (2012)
108. H. Teymourian, A. Salimi, S. Khezrian, Development of a new label-free, indicator-free strategy toward ultrasensitive electrochemical DNA biosensing based on Fe_3O_4 nanoparticles/reduced graphene oxide composite. Electroanalysis **29**(2), 409–414 (2016)
109. Y. Ye et al., A label-free electrochemical DNA biosensor based on thionine functionalized reduced graphene oxide. Carbon N. Y. **129**, 730–737 (2018)
110. S.B. Gayathri, P. Kamaraj, Development of electrochemical DNA biosensors—a review. Chem. Sci. Trans. **4**(2), 303–311 (2015)
111. N. Zhu, Z. Chang, P. He, Y. Fang, Electrochemical DNA biosensors based on platinum nanoparticles combined carbon nanotubes. Anal. Chim. Acta **545**(1), 21–26 (2005)
112. Q. Wang et al., DNA hybridization biosensor using chitosan-carbon nanotubes composite film as an immobilization platform and [Cu(bpy)(MBZ)2(H2O)] (bpy = 2,2′-bipyridine, MBZ = p-methylbenzoate) as a novel redox indicator. Electrochim. Acta **56**(11), 3829–3834 (2011)
113. J. Li, E.C. Lee, Carbon nanotube/polymer composite electrodes for flexible, attachable electrochemical DNA sensors. Biosens. Bioelectron. **71**, 414–419 (2015)
114. L. lan Xu et al., Perylenetetracarboxylic acid and carbon quantum dots assembled synergistic electrochemiluminescence nanomaterial for ultra-sensitive carcinoembryonic antigen detection. *Biosens. Bioelectron.* **103**, 6–11 (2018)
115. D. Du, S. Guo, L. Tang, Y. Ning, Q. Yao, G.-J. Zhang, Graphene-modified electrode for DNA detection via PNA–DNA hybridization. Sens. Actuat. B Chem. **186**, 563–570 (2013)
116. X. Li et al., [Cu(phen)2]2+ acts as electrochemical indicator and anchor to immobilize probe DNA in electrochemical DNA biosensor. Anal. Biochem. **492**, 56–62 (2016)
117. M.T. Martinez, Y.-C. Tseeng, N. Ormategui, I. Loinaz, R. Eritja, J. Bokor, Label-free DNA biosensors based on functionalized carbon nanotube field effect transistors. Nano Lett. **9**(2), 530–536 (2009)
118. S. Liu, X. Guo, Carbon nanomaterials field-effect-transistor-based biosensors. NPG Asia Mater. **4**(8), e23–e10 (2012)
119. A. Star, E. Tu, J. Niemann, J.-C.P. Gabriel, C.S. Joiner, C. Valcke, Label-free detection of DNA hybridization using carbon nanotube network field-effect transistors. Proc. Natl. Acad. Sci. **103**(4), 921–926 (2006)
120. B. R. Goldsmith, Conductance-controlled point. Science **315** 77–81 (2007)
121. S. Sorgenfrei et al., Label-free single-molecule detection of DNA-hybridization kinetics with a carbon nanotube field-effect transistor. Nat. Nanotechnol. **6**, 126 (2011)
122. X. Dong, Y. Shi, W. Huang, P. Chen, L.J. Li, Electrical detection of DNA hybridization with single-base specificity using transistors based on CVD-grown graphene sheets. Adv. Mater. **22**(14), 1649–1653 (2010)
123. Y. Hu, F. Li, D. Han, L. Niu, Biocompatible Graphene for Bioanalytical Applications, vol. 2, pp. 11–34 (2015)
124. B. Cai, S. Wang, L. Huang, Y. Ning, Z. Zhang, G.-J. Zhang, Ultrasensitive label-free detection of PNA–DNA hybridization by reduced graphene oxide field-effect transistor biosensor. ACS Nano **8**(3), 2632–2638 (2014)
125. Z. Gao et al., Detection of sub-fM DNA with target recycling and self-assembly amplification on graphene field-effect biosensors. Nano Lett. **18**(6), 3509–3515 (2018)
126. J. Wang, A.N. Kawde, M.R. Jan, Carbon-nanotube-modified electrodes for amplified enzyme-based electrical detection of DNA hybridization. Biosens. Bioelectron. **20**(5), 995–1000 (2004)
127. F. Berti, L. Lozzi, I. Palchetti, S. Santucci, G. Marrazza, Aligned carbon nanotube thin films for DNA electrochemical sensing. Electrochim. Acta **54**(22), 5035–5041 (2009)
128. P. He, L. Dai, Aligned carbon nanotube–DNA electrochemical sensors. Chem. Commun. **4**(3), 348–349 (2004)

129. J. Filip, P. Kasák, J. Tkac, Graphene as signal amplifier for preparation of ultrasensitive electrochemical biosensors. Chem. Pap. **69**(1), 112–133 (2015)
130. J. Wang, G. Liu, M.R. Jan, Ultrasensitive electrical biosensing of proteins and DNA: carbon-nanotube derived amplification of the recognition and transduction events. J. Am. Chem. Soc. **126**(10), 3010–3011 (2004)
131. X. Yang, Y. Lu, Y. Ma, Z. Liu, F. Du, Y. Chen, DNA electrochemical sensor based on an adduct of single-walled carbon nanotubes and ferrocene. Biotechnol. Lett. **29**(11), 1775–1779 (2007)
132. Q. Wang, J. Lei, S. Deng, L. Zhang, H. Ju, Graphene-supported ferric porphyrin as a peroxidase mimic for electrochemical DNA biosensing. Chem. Commun. **49**(9), 916–918 (2013)
133. T. Xue et al., Graphene-supported hemin as a highly active biomimetic oxidation catalyst. Angew. Chemie Int. Ed. **51**(16), 3822–3825 (2012)
134. H. Yamaguchi, K. Tsubouchi, K. Kawaguchi, E. Horita, A. Harada, Peroxidase Activity of cationic metalloporphyrin-antibody complexes. Chem. A Eur. J. **10**(23), 6179–6186 (2004)
135. Z. Wang et al., A sequence-selective electrochemical dna biosensor based on HRP-labeled probe for colorectal cancer DNA detection. Anal. Lett. **41**(1), 24–35 (2008)
136. Y. Wu, R.D. Tilley, J.J. Gooding, The challenges and solutions in developing ultrasensitive biosensors. J. Am. Chem. Soc. **141**(3), 1162–1170 (2018)
137. J. Jeon, D.K. Lim, J.M. Nam, Functional nanomaterial-based amplified bio-detection strategies. J. Mater. Chem. **19**(15), 2107–2117 (2009)
138. P. Krzyczmonik, E. Socha, S. Skrzypek, Immobilization of glucose oxidase on modified electrodes with composite layers based on poly(3,4-ethylenedioxythiophene). Bioelectrochemistry **101**, 8–13 (2015)
139. M.H. Ghalehno, M. Mirzaei, M. Torkzadeh-Mahani, Double strand DNA-based determination of menadione using a Fe_3O_4 nanoparticle decorated reduced graphene oxide modified carbon paste electrode. Bioelectrochemistry **124**, 165–171 (2018)
140. H.F. Wang et al., A versatile label-free electrochemical biosensor for circulating tumor DNA based on dual enzyme assisted multiple amplification strategy. Biosens. Bioelectron. **122**, 224–230 (2018)
141. L. Tian, L. Liu, Y. Li, Q. Wei, W. Cao, Ultrasensitive sandwich-type electrochemical immunosensor based on trimetallic nanocomposite signal amplification strategy for the ultrasensitive detection of CEA. Sci. Rep. **6**(July), 1–8 (2016)
142. Y. Song, Y. Luo, C. Zhu, H. Li, D. Du, Y. Lin, Biosensors and bioelectronics recent advances in electrochemical biosensors based on graphene two-dimensional nanomaterials. Biosens **76**, 195–212 (2016)
143. J. Li et al., Carbon nanotube nanoelectrode array for ultrasensitive DNA detection. Nano Lett. **3**(5), 597–602 (2003)
144. M. Fojta, P. Kostečka, M. Trefulka, L. Havran, E. Paleček, 'Multicolor' electrochemical labeling of DNA hybridization probes with osmium tetroxide complexes. Anal. Chem. **79**(3), 1022–1029 (2007)
145. J. Jiang, X. Lin, G. Diao, Smart combination of cyclodextrin polymer host-guest recognition and Mg^{2+}-assistant cyclic cleavage reaction for sensitive electrochemical assay of nucleic acids. ACS Appl. Mater. Interfaces **9**(42), 36688–36694 (2017)
146. J.Y. Huang et al., A high-sensitivity electrochemical aptasensor of carcinoembryonic antigen based on graphene quantum dots-ionic liquid-nafion nanomatrix and DNAzyme-assisted signal amplification strategy. Biosens. Bioelectron. **99,** 28–33 (2018)
147. H. Cai, X. Cao, Y. Jiang, P. He, Y. Fang, Carbon nanotube-enhanced electrochemical DNA biosensor for DNA hybridization detection. Anal. Bioanal. Chem. **375**(2), 287–293 (2003)
148. J. Wang, A. Shi, X. Fang, X. Han, Y. Zhang, Ultrasensitive electrochemical supersandwich DNA biosensor using a glassy carbon electrode modified with gold particle-decorated sheets of graphene oxide. Microchim. Acta **181**(9–10), 935–940 (2014)
149. M. Liu, H. Ke, C. Sun, G. Wang, Y. Wang, G. Zhao, A simple, supersensitive and highly selective electrochemical label-free aptasensor of 17β-estradiol based on signal amplification of bi-functional grapheme. Talanta **194**, 266–272 (2018)

150. B. Li, A.D. Ellington, X. Chen, Rational, modular adaptation of enzyme-free DNA circuits to multiple detection methods. Nucl. Acids Res. **39**(16) (2011)
151. X. Miao, X. Ning, Z. Li, Z. Cheng, Sensitive detection of miRNA by using hybridization chain reaction coupled with positively charged gold nanoparticles. Sci. Rep. **6**, 1–9 (2016)
152. X. Wu, Y. Chai, R. Yuan, Y. Zhuo, Y. Chen, Dual signal amplification strategy for enzyme-free electrochemical detection of microRNAs. Sens. Actuat. B Chem. **203**, 296–302 (2014)
153. H.L. Shuai, K.J. Huang, L.L. Xing, Y.X. Chen, Ultrasensitive electrochemical sensing platform for microRNA based on tungsten oxide-graphene composites coupling with catalyzed hairpin assembly target recycling and enzyme signal amplification. Biosens. Bioelectron. **86**, 337–345 (2016)
154. H.L. Shuai, X. Wu, K.J. Huang, Molybdenum disulfide sphere-based electrochemical aptasensors for protein detection. J. Mater. Chem. B **5**(27), 5362–5372 (2017)
155. J. Wang, A. Shi, X. Fang, X. Han, Y. Zhang, An ultrasensitive supersandwich electrochemical DNA biosensor based on gold nanoparticles decorated reduced graphene oxide. Anal. Biochem. **469**, 71–75 (2015)
156. H. Huang, W. Bai, C. Dong, R. Guo, Z. Liu, An ultrasensitive electrochemical DNA biosensor based on graphene/Au nanorod/polythionine for human papillomavirus DNA detection. Biosens. Bioelectron. **68**, 442–446 (2015)
157. K.-J. Huang, Y.-J. Liu, H.-B. Wang, Y.-Y. Wang, Y.-M. Liu, Sub-femtomolar DNA detection based on layered molybdenum disulfide/multi-walled carbon nanotube composites, Au nanoparticle and enzyme multiple signal amplification. Biosens. Bioelectron. **55**, 195–202 (2014)
158. K.-J. Huang, Y.-J. Liu, H.-B. Wang, Y.-Y. Wang, A sensitive electrochemical DNA biosensor based on silver nanoparticles-polydopamine@graphene composite. Electrochim. Acta **118**, 130–137 (2014)
159. F.-F. Cheng, J.-J. Zhang, T.-T. He, J.-J. Shi, E.S. Abdel-Halim, J.-J. Zhu, Bimetallic Pd–Pt supported graphene promoted enzymatic redox cycling for ultrasensitive electrochemical quantification of microRNA from cell lysates. Analyst **139**(16), 3860–3865 (2014)
160. X. Dong et al., Electrical detection of femtomolar DNA via gold-nanoparticle enhancement in carbon-nanotube-network field-effect transistors. Adv. Mater. **20**(12), 2389–2393 (2008)
161. B.C. Janegitz et al., The application of graphene for in vitro and in vivo electrochemical biosensing. Biosens. Bioelectron. **89**, 224–233 (2017)
162. R. Forsyth, A. Devadoss, O.J. Guy, Graphene field effect transistors for biomedical applications: current status and future prospects (2017)
163. R. Laocharoensuk, Development of electrochemical immunosensors towards point-of-care cancer diagnostics: clinically relevant studies. Electroanalysis **28**(8), 1716–1729 (2016)
164. B. Zribi et al., A microfluidic electrochemical biosensor based on multiwall carbon nanotube/ferrocene for genomic DNA detection of mycobacterium tuberculosis in clinical isolates, Biomicrofluidics **10**(1), 014115, 1–12
165. J. Wu, M. Dong, C. Rigatto, Y. Liu, F. Lin, Lab-on-chip technology for chronic disease diagnosis, pp 1–11 (2018)
166. Z. Pu, C. Zou, R. Wang, X. Lai, H. Yu, *In Microfluidic System: A Continuous Glucose Monitoring Device by Graphene Modified Electrochemical Sensor in Microfluidic System*, vol. 011910 (2016)
167. A.J. Killard, *4—Screen Printing and Other Scalable Point of Care (POC) Biosensor Processing Technologies* (Elsevier Ltd. , 2017)
168. L. Syedmoradi, M. Daneshpour, M. Alvandipour, F. A. Gomez, H. Hajghassem, K. Omidfar, Biosensors and bioelectronics point of care testing: the impact of nanotechnology. Biosens. Bioelectron. **87**, 373–387 (2017)
169. C. Li, H. Karadeniz, E. Canavar, A. Erdem, Electrochimica acta electrochemical sensing of label free DNA hybridization related to breast cancer 1 gene at disposable sensor platforms modified with single walled carbon nanotubes. Electrochim. Acta **82**, 137–142 (2012)
170. A.H. Loo, A. Bonanni, M. Pumera, Impedimetric thrombin aptasensor based on chemically modified graphenes. Nanoscale **4**(1), 143–147 (2012)

171. B. Esteban-ferna et al., Dual functional graphene derivative-based electrochemical platforms for detection of the TP53 Gene with Single Nucleotide Polymorphism Selectivity in Biological Samples. Anal. Chem. **87**(4), 2290–2298 (2015)
172. L. Syedmoradi, M. Daneshpour, M. Alvandipour, F.A. Gomez, H. Hajghassem, K. Omidfar, Point of care testing: the impact of nanotechnology. Biosens. Bioelectron. **87**, 373–387 (2017)
173. W. Qiu et al., Carbon nanotube-based lateral flow biosensor for sensitive and rapid detection of DNA sequence. Biosens. Bioelectron. **64**, 367–372 (2015)
174. E.P. Souto, Electrochemical biosensors in point-of-care devices: recent advances and future trends. ChemElectroChem **4**(4), 778–794 (2017)
175. C. Zhang, J. Xu, Y. Li, L. Huang, D. Pang, Photocatalysis-induced renewable field-effect transistor for protein detection photocatalysis-induced renewable field-effect transistor for protein detection. Anal. Chem. **88**(7), 4048–4054 (2016)
176. C. Wang et al., OPEN a label-free and portable graphene FET aptasensor for children blood lead detection. Nat. Publ. Gr., 1–8 (2016)
177. S. Xu et al., Real-time reliable determination of binding kinetics of DNA hybridization using a multi-channel graphene biosensor. Nat. Commun. **8**, 1–10 (2017)
178. D.D. Ordinario et al., Sequence specific detection of restriction enzymes at DNA-modified carbon nanotube field effect transistors. Anal. Chem. **86**(17), 8628–8633 (2014)
179. J.-Y. Choi, G. Ramachandran, M. Kandlikar, The impact of toxicity testing costs on nanomaterial regulation. Environ. Sci. Technol. **43**(9), 3030–3034 (2009)
180. M. Azimzadeh, M. Rahaie, N. Nasirizadeh, M. Daneshpour, H. Naderi-Manesh, E.T. Nanobiosensor ABSTRAC, "electrochemical miRNA biosensors: the benefits of nanotechnology. Nanomed. Res. J. **2**(21), 36–4836 (2017)
181. S. Campuzano, P. Yáñez-Sedeño, J.M. Pingarrón, Tailoring sensitivity in electrochemical nucleic acid hybridization biosensing: role of surface chemistry and labeling strategies. ChemElectroChem (2018)

Chapter 11
Environmental Impacts and Safety Concerns of Carbon Nanomaterials

Matteo Cossutta and Jon McKechnie

11.1 Origin of the Life-Cycle Assessment (LCA)

In the last two centuries, the improvements in comfort, and therefore in the quality of life, had been associated with the economic growth (i.e. GDP). However, in the last decades, it has become more and more clear that this link between material wealth and happiness is not entirely appropriate. This awareness started in the late 50s and early 60s when studies showed the severity of the world pollution (e.g. linked to the extensive use of pesticides) and the high risk of running out of important natural resources (Hubbert Peak Oil theory—1959). In 1972, the famous "The limits of growth", a report of The Club of Rome commissioned to the MIT, was published and its message was: a world with finite resources cannot experience an exponential growth without collapsing [1]. This fostered the discussion on new models of economic development and the origin of the life-cycle assessment (LCA) technique can be set in this period, at the Midwest Research Institute, but it was known as "Resource and Environmental Profile Analysis" or REPA [2]. This technique stemmed from the energy analysis studies, but included environmental and sustainability criteria and considered the whole life cycle of a product in order to organically understand the real impact of a product/system/service on the environment by avoiding to focus only on one stage of its life (e.g.: production, use-phase or disposal).

In the following years, the REPA technique continue to develop and in 1987, another report was issued that helped its mainstream adoption: the final report titled "Our common future" of the United Nation Commission on Environment and Development (known also as the Brundtland Commission). It spelled the definition of sustainable development as "development that meets the needs of the present without compromising the ability of future generations to meet their own needs". Naturally,

M. Cossutta (✉) · J. McKechnie
Bioprocess, Environmental and Chemical Technologies Research Group, Faculty of Engineering, University of Nottingham, Nottingham NG7 2RD, UK
e-mail: matteo.cossutta@nottingham.ac.uk

S. Kaneko et al. (eds.), *Carbon Related Materials*,
https://doi.org/10.1007/978-981-15-7610-2_11

this type of development imposes some limitation to the growth, but those "limitations are those imposed by the present state of technology (…) and the capacity of the biosphere to absorb the effects of human activities. Technology and social organisation can, however, be managed and improved to user in a new era of economic growth" [3]. This cultural change is now in the making since long, and even if the paradigm shift in the development has not happened yet, this report showed how the usual path for economic growth was short-sighted. It established that what was addressed as a general environmental problem is in reality a complex chain of interconnected events that take origin in the overexploitation of natural resources and end with the overburden of the natural system bearing capacity [4]. The soil, air, and water quality, species loss, and resources depletion are in fact related to each other. Therefore, a more holistic approach was (and is) clearly needed to promote a new model of development that was capable of continuing the economic growth but taking into consideration the environment, with a long-term approach on future issues rather than focusing on immediate problems only. It is in this context that the REPA evolved and in 1990, the term "Life Cycle Assessment" (LCA) was created [5]. Throughout the 90s, the International Organisation for Standardisation (ISO) released four documents defining the LCA principles and methodology (ISO 14040, ISO 140141, ISO 14042, ISO 14043) that were condensed and updated in 2006 when the general methodological framework and guidelines were defined in the ISO 14040 and ISO 14044 and in which the LCA is defined as the "compilation and evaluation of the inputs, outputs and the potential environmental impacts of a product system throughout its life cycle" [6, 7].

This holistic approach inclusive of the environmental impacts, however, leads to an important economic challenge that is the main obstacle to overcome. On this purpose, in 2006, the Stern review was released for the British government, examining the economics of climate change. This report contained a warning of the global economic consequences derived from not acting on the climate change. It also promoted the so-called "green economy" where business act adapting itself in order to mitigate the climate change [8]. This review clearly states that continuing business as usual will generate an equivalent loss of around 5% of the world GDP each year from now on—a loss that could reach 20% of the world GDP by taking into account a wider range of risks [9]. To quote the report: "The scientific evidence is now overwhelming, and the benefits of strong and early action far outweigh the economic costs".

In 2010, the JRC of the European Commission defined the Life Cycle Thinking (LCT) as: "identify possible improvements to goods and services in the form of lower environmental impacts and reduced use of resources across all life cycle stages" [10]. The LCA is now becoming a mainstream tool (with many others, e.g. risk assessment), to support decision making by helping in understanding and analysing the sustainability in a structured quantitative manner, while the Life Cycle Thinking is an important and revolutionary way of thinking that can change the way our society designs, produces and dispose/recycle goods and services.

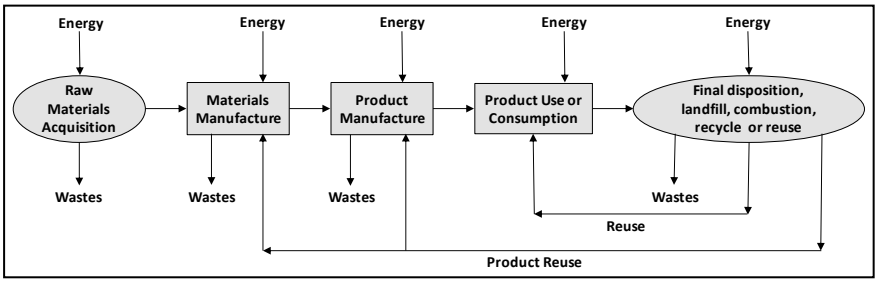

Fig. 11.1 Simplified product/system life cycle [11]

11.2 The Life-Cycle Assessment (LCA)

An LCA is defined in the 14040 ISO standards as a way of addressing "the environmental impacts (e.g. use of resources and the environmental consequences of releases) throughout a product's life cycle from raw material acquisition through production, use, end-of-life treatment, recycling and final disposal (i.e. cradle-to-grave)".

The word "product" is used in this case in its broadest meaning and it embraces physical goods as well as services and processes. It is a systematic and structured technique to measure and quantify all energies and materials inputs and outputs including emissions and wastes. Those quantities are then translated with mathematical models into environmental impacts related to several different impact categories [6]. A simplified cradle-to-grave LCA approach is presented in Fig. 11.1.

An LCA constitutes of four main building blocks (Fig. 11.2):

- Goal definition
- Scope definition
- Inventory analysis (LCI)
- Impact assessment (LCIA)

All blocks are fundamental and must be clearly defined and performed to achieve comprehensive and clear results in the study. It is however essential to understand that the LCA is an iterative process because, as the data are gathered, and more information becomes available and analysed, both goal and scope might vary and, subsequently, might need refining or complete revision. For new and complex products, where little information is available, the first iterations often use averaged and external data sources, especially for the background[1] system. Also in this case, the following iterations will help in refining the study as more information becomes available.

Defining the goal means to identify the purpose of the study and the target audience, hence including the intended application of the LCA and the purpose of the

[1] Background system comprises processes that are part of the system but not under direct control of the producers (e.g. electricity or raw material production).

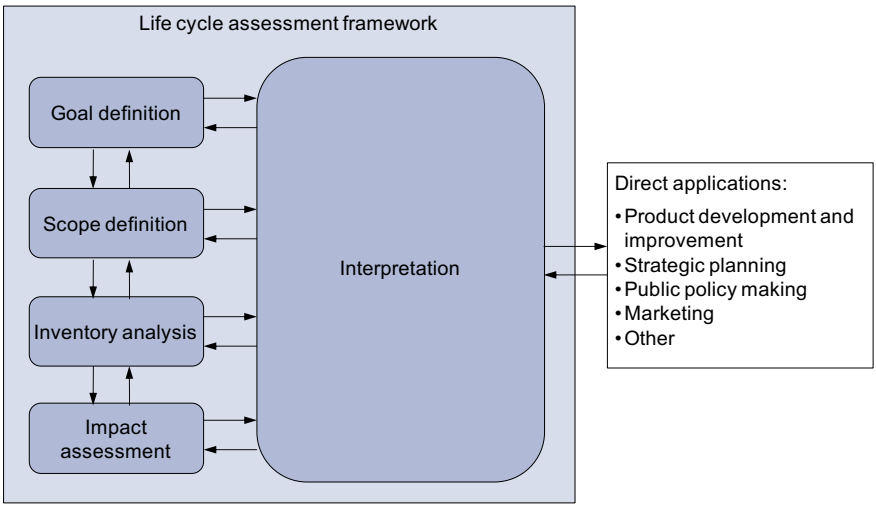

Fig. 11.2 Framework for life-cycle assessment [10]

results. The scope of an LCA can be simply summarised in what to analyse and how. The scope defines in detail the LCA study in line with the goal definition and derives the requirements on methodology, quality, reporting, and review. It aims at clearly identifying and defining in detail the system to be analysed starting from the system(s) function(s)—what is this component supposed to do? Once the function has been identified, the choice of the functional unit(s)—the unit(s) of measure that can quantify its function in terms of what, how much, how well, how long—is key to the LCA outcome. Defining the scope also means to define the system boundaries (i.e. which part of the life cycle and processes belong to the system to be analysed) and the impact categories (an example in Fig. 11.3) that will be assessed. Typical exam-

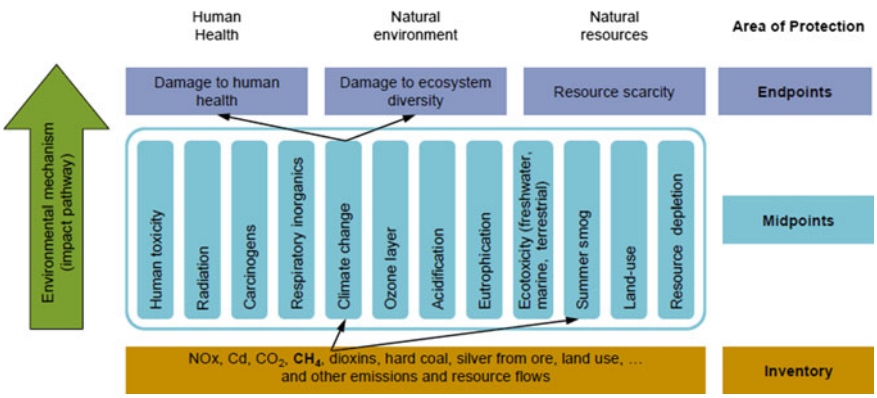

Fig. 11.3 LCIA steps from inventory to category [10]

ples of system boundaries are the so-called "Cradle to Gate" or "Cradle to Grave" approaches, with the first one considering the production of a product until the factory gates while the second one includes also use phase and end-of-life. The cradle-to-grave approach prevents from moving possible problems a step backward or forward in the production/process chain. For example, turning all cars into electric cars will certainly reduce their emissions, as cars will not burn fossil fuels; however, the electricity needed to charge their batteries might be still provided by fossil sources and the additional production and disposal of the batteries would make the overall environmental impact uncertain. Only after performing the LCA analysis, it is possible to indicate which solution, on balance, achieves the lowest environmental impacts [12].

The concept is valid also when the environmental burdens could be shifted from one medium to another, for instance, when a lower rate of emissions in the air corresponds to an increase in solid waste. The scope also sets the quality requirements and level of data completeness, together with the special requirements for comparisons between systems if needed and other LCA parameters.

The life cycle inventory (LCI) is typically the most time-consuming part of an LCA and the one that requires the highest effort to be accomplished. It consists in the actual data collection, system modelling, and results calculation according to the goal and scope definitions. During this phase, all processes that are part of the system under assessment are identified and all data are gathered within the system boundaries with a level of detail defined in the scope definition. All quantities are measured in relation to the functional unit and the sources of data are usually the developers, producers, or operators of the system under analysis for the foreground system[2] (generally the focus of the data collection), while secondary data providers, usually for the background system, are LCI databases, consultancy companies, and research institutes. The final step of the LCI is calculating LCI results: the inventories of all included unit processes (materials and energy inputs/outputs) are scaled in relation to their share in the overall product/system and are aggregated over sub-assemblies, life cycle stages, other. The final LCI results represent exclusively the product prescribed by the functional unit in detail, with all material and energy inputs and outputs including wastes and emissions. Any impact assessment is not included at this stage. Depending on the goal and scope of the LCI/LCA study, scenario analysis and uncertainty calculations should also be performed. This especially applies to product comparisons and more so for future strategy/products comparisons.

The last step of the LCA is called life cycle impact assessment (or LCIA) and is the phase where the inputs and outputs that have been reported in the LCI are translated into impact indicator results related to human health, natural environment, and resource depletion. Based on classification and characterisation of the individual inputs and outputs, the LCIA results are calculated by multiplying the individual

[2]Foreground system is defined in the LCA theory as "the processes which are under the control of the decision-maker for which an LCA is carried out", i.e., the process in place to manufacture/perform the product/service. Together with the Background system (see footnote 1) forms the whole investigated system.

inventory data of the LCI results with the related characterisation factors (which express how much a single unit of mass or energy contributes to an impact category), in order to quantify the impact that of product or service has in each impact category. The interpretation of results is then based on the identification of the main impact contributors (i.e. the most relevant life cycle stages, processes and materials/energies, and the most relevant impact categories) and their sensitivity to key parameters or scenario modelling in order to derive the final conclusions.

As a general rule, the LCA is often a comparative analysis as it is used to assess which, among several options, is the least impacting for the environment and it is frequently used to compare the present system versus a new or alternative one. Therefore, sometimes there is no need to cover the complete cradle-to-grave analysis, but only the significant parts that usually are those where the considered systems differ [13]. Due to its comparative nature, the LCA is often used for decision making and for clarifying environmental disputes [14].

In a broader perspective, the LCA has multiple potential purposes [7] such as:

- a base for environmental strategies,
- environmental product declarations and eco-labelling,
- product improvement (weak point analysis),
- assessment of new and cleaner technologies,
- identification of knowledge gaps,
- policy development and information,
- a systematic organisation of information for environmental impact assessment,

and many others; however, most of the times, this type of analysis is used to [15]:

- decide whether a product, process, or service is reducing the environmental burden or simply transferring it to another part of its life cycle,
- establish where the highest environmental load is in a process,
- make quantitative comparisons between competing alternative technologies concerning their environmental impacts.

It should be noted that LCA only takes into consideration impacts related to normal and abnormal operation of processes and products and not those coming from accidents, spills, and similar [10].

The LCA has several implicit constraints and some of them are defined already by the ISO standard 14040 such as the limit of assessing completely all environmental impacts of a product/system. This happens because of the nature of the LCA itself which focuses only on a particular usage of the system under examination (e.g. a life cycle for a light bulb for home applications might be considerably different from an industrial one). A lack of availability or reliability of data, a required degree of simplification, with all processes is considered as linear (e.g. output of a chemical reaction directly proportional to the inputs when other nonlinear factors like heat or particle distribution, particle orientation, and many others could affect the reaction yield or product quality; emissions to an already polluted or unique environment are not considered more or less problematic; the time of release is not accounted for while some volatile substances are generating more photooxidants during the day

than during night; other), the use of estimations and assumptions that are generally the weakest point of all LCA results [16]. Data could be too expensive to collect or time consuming or upstream in the supply chain and unavailable for commercial reasons. When available, their quality is not always known or verifiable especially when not directly measured. Data could also be taken from similar but not equal processes. Uncertainties lie also in the characterisation factors (the factors used to transform a material or energy input into an environmental impact), as characterisation models can be quite different to the real mechanisms. New materials are always appearing on the market, with limited or no associated dispersion models [17]. Those problems are still affecting this technique and while better models will need to be developed to include the nonlinearity of most processes, for the estimations and assumptions will reduce in time, when more LCAs will be performed and their data available to the public.

The LCA outcomes were often criticized (e.g. [18–21]) for the lack of a standardised approach resulting in different ways of interpreting data and therefore results. For this reason, a lot of work has been carried on in the past years (and still is) to develop and harmonise the LCA methodology such as the PAS 2050 from the ISO standards—a specification addressing only the global warming potential with a simplified approach to assess greenhouse gasses emissions [22]; LCA operational guidelines [23]; the International reference Life Cycle Data system or ILCD handbook [10] from the European Commission Joint Research Centre which provides detailed guide for performing LCA and, quoting from its preface, "… provides governments and businesses with a basis for assuring quality and consistency of life cycle data, methods and assessments". Following the ILCD handbook also ensures compliancy with the ISO standards that are the base on which it is built [10].

The LCA is thus applied at its best potential to mature products, where plenty of data are available to collect and analyse; when used during the development phase of new processes and with scarcity of data, the LCA serves as valuable tool to set environmental targets for the product in an eco-design—and this is the way it is used for carbon nanomaterials.

11.3 A Review of Life-Cycle Assessments on Carbon Nanomaterials

Carbon exists in two forms, amorphous (e.g. coal, soot, charcoal, other) and crystalline. Carbon nanomaterials are part of the second group, together with graphite and diamonds. Carbon atoms can bond forming a hollow cage shape called fullerene, or a tube shape called nanotube, or a flat single-atom-thin surface named graphene. The latter is the most recent discovery in the field of carbon-nanomaterials, and for many years, it was considered a purely theoretical material. Early predictions of two-dimensional materials assessed their instability due to thermal fluctuations, and

this theory was supported by some cases of thin films becoming unstable at reduced thickness [24].

In the early 2000s, however, Geim and Novoselov, managed to show very thin layers of carbon and monolayer graphene simply using scotch tape [25, 26]. Strictly speaking, only a single monoatomic layer of carbon should be called graphene [27] and thus few stacked layers of carbon should be defined as graphene nanoplatelets (GNP). Nevertheless, many papers refer to GNP as graphene, and there is no common agreement on how many layers of carbon can still be called graphene/GNP before it becomes normal graphite. Some papers define graphene/GNPs between few and ten layers of graphene [28] while some other call nanoplatelets also particles made of more than 10 layers [29]. This uncertainty is also linked to the fact that the graphene layers can be stacked in several ways (atom above atom, atom above an empty area but also in a totally asymmetric and random way) and the different stakings exhibit different properties and behaviour [30].

After their discovery, a lot of research focused on exploring the peculiar physical, chemical, electrical, mechanical, magnetic, and thermal properties of these new materials, fostering all types of possible applications like superconductors [31] reinforcement for different materials [32–35], flexible displays [36], membranes [37, 38], transistors [39, 40], sensors [41], solar cells [42–44], electrodes [45–47], and many others. It is forecasted that 3400 products containing nanomaterials will be on the market by 2020 (including non-carbon nanomaterials) [48], and as the manufacture of nanomaterials increases, public concern about their environmental burden, and effect on human health has become a notable issue.

To date, only a limited quantity of life-cycle assessments have been published on carbon nanomaterials but their number is increasing. Some literature reviews about LCA of carbon nanomaterials were published between 2012 and 2014 [48–52] and they include up to 15 studies on carbon nanomaterials excluding graphene, while in 2018, an updated review including 2 studies on graphene was published [53]. To date, 26 studies were found (one of which presenting four different cases on carbon nanotubes (CNT) for a total of 29 cases—see Table 11.1 at the end of the chapter) performing the LCA on carbon nanomaterials. Most of the cases analysed are about carbon nanotubes and, more recently, graphene (Fig. 11.4). Nanotubes are still the most analysed type of material with 14 case studies, but graphene is second with 12 (10 on graphene, 2 on graphene oxide) and rapidly catching up as it is the focus of most of recent studies. In this study, unless differently specified, the term carbon nanomaterial(s) indicates all three types: fullerenes, nanotubes, and graphene.

11.3.1 Data Confidentiality

A common result among the published reviews is that the manufacturing of nanomaterials requires a significantly higher quantity of energy if compared to conventional materials. The different studies analyse several production routes for fullerenes, carbon nanofibres, and multi-/single-walled carbon nanotubes and graphene, and

Table 11.1 Summary of all reviewed studies

Author	Year	Material type	Functional unit	System boundaries	More energy intensive than conventional materials	Lower overall impacts	N. of impact categories	LCI	Commercial scale	Future scenario	NP emissions
Kushnir and Sanden [91]	2008	Fullerenes and CNT	Mass (1 kg)	Prod	Y	n/a	1	Y	Y	N	N
Healy et al. [77]	2008	SWCNT	Mass (1 g)	Prod	Y	n/a	2–5	Y	N	N	N
Bauer et al. [65]	2008	SWCNT	Product/function (field emission display versus CRT and LCD)	Full	N	Y	5–9	N	N	N	N
Khanna et al. [92]	2008	CNF	Mass (1 kg)	Prod	Y	n/a	5–9	Y	N	N	N
Khanna et al. [56]	2009	CNF	Product/function (Equivalent of a steel plate/car lifetime: 150,000 miles)	Prod + use	Y	Y	1	N	N	N	N
Dahlben et al. [93]	2013	CNT	n/a	Full	Y	Y	5–9	N	N	N	N
Griffiths et al. [75]	2013	MWCNT	Mass (300 mg)	Prod	n/a	n/a	10 +	Y	N	N	Y
Arvidsson et al. [70]	2014	Graphene	1 kg	Prod	n/a		2–5	Y	Y	Y	N

(continued)

Table 11.1 (continued)

Author	Year	Material type	Functional unit	System boundaries	More energy intensive than conventional materials	Lower overall impacts	N. of impact categories	LCI	Commercial scale	Future scenario	NP emissions
Pizza et al. [57]	2014	Graphene	Product/function (1 kg epoxy composite (5.8 wt% of filler) assuring: thermal conductivity 1 W/mK and lifetime	Full	n/a	n/a	2–5	Y	N	N	N
Yaseneva et al. [94]	2014	CNF	Product/function (quantity needed to treat 10,000,000 ton. H_20 yr)	prod + use	n/a	Y	10+	N	Y (pilot)	N	N
Notter et al. [58]	2015	MWCNT	Product/function (10 kW HTPEM fuel cell w MWCNTs as carbon substrates for platinum)	Full	n/a	Y	5–9	Y	N	N	N
Hischier [74]	2015	CNT	Product/function (field emission display/1	Full	n/a	Y	10+	Y	N	N	Y
Arvidsson et al. [59]	2016	Graphene	Area (1 cm^2)	Prod + use	N	Y	2–5	Y	Y	Y	N

(continued)

Table 11.1 (continued)

Author	Year	Material type	Functional unit	System boundaries	More energy intensive than conventional materials	Lower overall impacts	N. of impact categories	LCI	Commercial scale	Future scenario	NP emissions
Trompeta et al. [95]	2016	MWCNT	Mass (1 kg)	Prod + use	n/a	n/a	10+	Y	N	N	N
Zhai et al. [60]	2017	MWCNT	Product/Function (1000 kg mass of cement)	Prod + use	n/a	Y/N	1	N	y	Y	N
Zhai et al. [60]	2017	SWCNT	Product/Function (16 Gb capacity of memory)	Prod + use	n/a	Y	1	N	V	Y	N
Zhai et al. [60]	2017	SWCNT	Product/function (16 kWh capacity of battery)	Prod + use	n/a	N	1	N	y	Y	N
Zhai et al. [60]	2017	MWCNT	Product/function (16 kW h capacity of battery)	Prod + use	n/a	Y	1	N	y	Y	N
Pourzahedi et al. [64]	2017	CNT	Product/function (Satellite electromagnetic interference shield)	Prod + use	N	Y	1	Y	Y	N	N

(continued)

Table 11.1 (continued)

Author	Year	Material type	Functional unit	System boundaries	More energy intensive than conventional materials	Lower overall impacts	N. of impact categories	LCI	Commercial scale	Future scenario	NP emissions
Uppahyayula [63]	2017	Graphene	Product/function (2.31 m^2 shielded from corrosion with a coated panel [12 mm (thickness) × 180 mm (width) × 6 m (length)])	Full	N	Y	10+	N	Y	N	N
Celik et al. [76]	2017	SWCNT	Product/function (1 kWh of electricity generated within the lifetime of the PV cell)	Prod + use	n/a	Y/N	10+	Y	Y	N	N
Khanam et al. [96]	2017	Graphene	Mass (1 kg)	Prod	n/a	n/a	10+	Y	N	N	N

(continued)

Table 11.1 (continued)

Author	Year	Material type	Functional unit	System boundaries	More energy intensive than conventional materials	Lower overall impacts	N. of impact categories	LCI	Commercial scale	Future scenario	NP emissions
Chilkoor et al. [62]	2017	Graphene oxide	Product/function (protect 30 m^2 of interior surface (unalloyed steel sheet) of a 10,000 l biodiesel tank against abiotic and biotic	Prod + use	n/a	Y	10+	Y	Y	N	N
Arvidsson and Molander [71]	2017	Graphene	Area (1 cm^2)	Prod	n/a	n/a	2–5	N	Y	Y	N
Lin et al. [97]	2017	Graphene	Product/function (1.2 kg bicycle tyre)	Prod + use	n/a	Y	1	N	N	N	N
Guarino et al. [98]	2017	Graphene	Product/function (Coating of a copper circuit breaker (8 cm, 160 g))	Prod + use	n/a	Y	10+	Y	Y	N	N
Cossutta et al. [55]	2017	Graphene	Mass (1 g) Area (1 cm^2)	Prod	n/a	n/a	10+	Y	Y	Y	N
Long et al. [61]	2018	Graphene oxide	Product/function (cement production	Prod + use	n/a	Y	1	Y	Y	N	N

(continued)

Table 11.1 (continued)

Author	Year	Material type	Functional unit	System boundaries	More energy intensive than conventional materials	Lower overall impacts	N. of impact categories	LCI	Commercial scale	Future scenario	NP emissions
Cossutta et al. [68]	2019	Graphene	Product/function (5 supercapacitors of 5 F each)	Full	Y	Y	10+	Y	Y	Y	Y

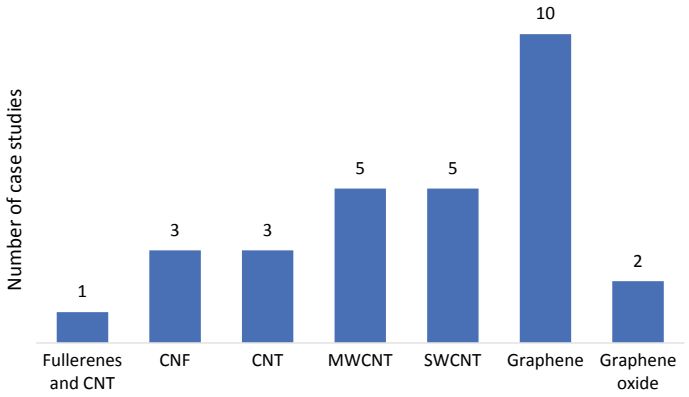

Fig. 11.4 Number of studies per each type of carbon nanomaterials

they present a gap of at least one order of magnitude in their energy use in comparison with conventional materials. This gap is also much larger is several cases, for example, focusing only on CNT production of CNT, according to Upadhyayula et al. [52], the CVD method is the one requiring the least amount of energy (excluding the fixed bed CVD) compared to other routes, like arch discharge, laser ablation, and high pressure carbon monoxide (HiPCO). These show an energy demand at least an order of magnitude higher (but up to 5), making the CVD process appear as the most suitable for commercial-scale production of carbon nanotubes [54]. However, within the CVD method production route, the energy consumption varies by three orders of magnitude.

When comparing similar production routes, the energy input required for their production varies by five orders of magnitude, while the reported material feedstock is more consistent, with some differences in process efficiency. The reason for this gap in energy demand could lie in the data sources, but the limited number of studies and, more important, the lack of input data availability make the results uncertain and this hypothesis difficult to verify [51]. In fact, the real production data are often undisclosed due to commercial sensitiveness; hence, the data gaps are covered with estimations or data from databases or previous studies.

An example is the study on CVD used to synthesising planar graphene by Cossutta et al. [55] that shows energy requirements in line with those from Upadhyayula et al. [52] for the manufacturing of CNT via CVD. This study presents results for batch and continuous production of graphene and the result differs by two orders of magnitude. This shows that not only input data but also operating procedures are key to understand the variation among studies. To have more reliable and definitive results, it is necessary to increase data availability and transparency, especially for commercial-scale carbon nanomaterials production.

11.3.2 The Functional Unit

There are although several limitations to many of the reported studies. The choice "weight" as functional unit, for instance, makes the comparisons not entirely exhaustive, because one kilogram of steel and one kilogram of nanocomposite materials present different properties and are suitable for different applications [50]. Moreover, if this comparison offers a valid indication of the embedded environmental impacts of the two materials, excluding their properties from the analysis penalises those production routes that can synthesise high quality material, as the one showing better properties could be more energy intensive, but less of it might be required to perform a selected function. Comparing the materials not only on the basis of a physical quantity (mass, volume, surface area, other) but also on how well they can perform is a way to include the materials properties in the comparison and thus to allow for proper comparability between LCA studies on material synthesis. This is crucial especially for nanotechnology as a very limited mass or surface area could replace larger quantities of conventional materials.

The presented limitation can be overcome by adding to the analysis the use phase hence extending the system boundaries. The recent years have seen an increase in the number of studies considering not only the production phase but also including either the use phase or at least an analysis of the material properties to be evaluated within the context of a particular application. Roughly, two thirds of the cases presented in this review include either a use phase or some sort of material characterisation that allows to simulate a use phase. The other cases only consider production and their functional unit is weight 8 times out of 9 while the remaining case uses the square centimetre. For the 20 cases, considering a use phase, results show that in general, nanomaterials can be more energy intensive but could have a less impacting use phase and thus a potentially lower overall environmental impact due to their potentially superior properties. For example, the LCA performed by Khanna et al. [56] shows that, due to its lighter weight, carbon nanofibre used as a reinforcement in composite materials has a higher production impact, but saves a lot of fuel when used in a car due to its lighter weight if compared to steel. The same can be said for graphene nanocomposites, for example, in the study of Pizza et al. [57], it is shown that the synthesis of 1 kg GNP is six times more energy consuming and impacts more on the environment than the production of 1 kg of epoxy composite loaded with 0.058 kg of GNP. In the latter, 38% of the total energy consumption is needed to produce the graphene nanoplatelets, but the material is lighter and shows a much higher thermal conductivity suggesting that in some particular applications, the increase in energy consumption might be compensated by the lighter weight (aeronautic, aerospace, transport in general) and the higher thermal conductivity (heat dissipation from electronic components or batteries increasing their lifetime), making the composite material more energy efficient overall.

Another interesting case is provided in the study of Notter et al. [58] in which multi-walled carbon nanotubes (MWCNT) are used as electrode substrate in a PEM fuel cell instead of carbon black. They not only offer a higher corrosion resistance than

carbon black but also thanks to their unique properties they allow for a reduction in the quantity of platinum used as catalyst by 27% without compromising the fuel cell performance. The savings from the platinum reduction were found to outweigh the production impacts of the carbon nanotubes. Other studies show that carbon nanomaterials could replace current technologies and be environmentally better performing, for example, Arvidsson et al. showed that graphene could replace ITO for transparent electrodes [59], Zhai et al. showed that the use of carbon nanotubes can require less energy than current counterparts for flash memories and batteries, and, for particular cases, they can also improve the cements [60]. This last case is supported by the study from Long et al. confirming that cement composites with graphene oxide can be less burdensome for the environment [61]. Other assessments proved carbon nanomaterials having a lower environmental impact than today's solutions when used as coatings: for instance polymer composites with graphene are suitable as anticorrosive layer for biodiesel tanks (improving also the antimicrobial properties) [62] or against harsh atmospheric conditions [63], while carbon nanotubes coatings can be used as shields against electromagnetic interferences for satellites [64]. However, most of the studies do not test the material in a prototype to investigate how well the new material can substitute the current ones. This means that while the production LCA can be considered reliable, the use phase is, for many studies, a theoretical exercise.

11.3.3 Scope of the Study

Extending the system boundaries further to the end of life is also important as the reuse/recycling of the compared materials could displace production of pristine ones generating environmental credits. When the use phase and end of life are considered, even more products including nanomaterials can prove to be less impacting [65]. The end of life is mostly not included in the published studies, in fact only six cases cover it. In those analysis, while the recycling activity is considered for the commonly recycled materials, nanomaterials are either landfilled or incinerated at the end of their life for energy recovery with the non-recyclable parts of the product assessed. The incineration of nanomaterials has also been investigated and some studies suggested that the presence of nanomaterials during combustion could boost the formation of polyaromatic hydrocarbons, chlorinated dioxins, and furans while persisting in the combustion zone and end up in the ashes [66, 67], although these aspects are not included in the LCAs and need further investigation. Bauer et al. [65] were among the first in including the end of life in an LCA on nanomaterials and their study uses a different approach by modelling the recycling of the part of the product containing the CNT using a procedure for a similar product without CNT as proxy.

The only studying reporting the recycling and reuse of carbon nanomaterials is by Cossutta et al. and presents an LCA of graphene in a supercapacitor application. The study compares two racks of five supercapacitors used in a transport application

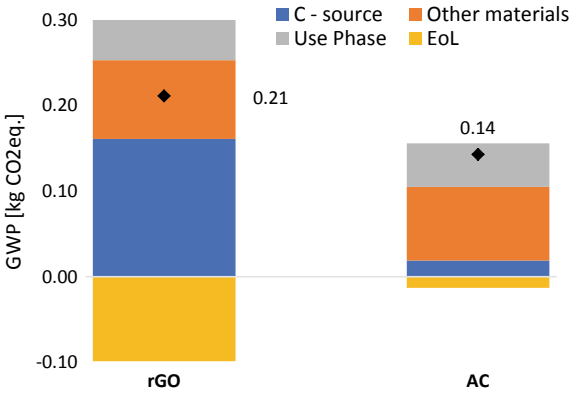

Fig. 11.5 Global warming potential for the compared supercapacitors rack. Modified from Cossutta et al. [68]. Previously published in the Journal of Cleaner production. Copyright Elsevier

with a capacitance of 5 Farads each, one made with prototypes with graphene-based electrodes and the other made with the state-of-the-art commercial supercapacitors using activated carbon-based electrodes. The results show that the graphene prototype has larger environmental impacts than the current technology also when the graphene production is scaled upto commercial scale. The graphene-based supercapacitor shows a much larger production impact that reduces considerably when the recycling is taken into consideration (from 0.31 to 0.21 kg CO_2eq.). This happens because tests have shown that the recovery of graphene is very effective if used as polymer composite (epoxy resin) reinforcement as the moulded material showed enhanced properties that are in line with those shown by epoxy resins reinforced with pristine graphene.

Figure 11.5 shows the global warming potential (GWP) for the two racks of supercapacitors compared, divided into the carbon source (graphene nanoplatelets or activated carbon), the other materials that constitute the supercapacitors (casing, electrolyte, paper separator, other), the use phase (different fuel consumptions over the lifetime of a selected vehicle due to the different weight), and the end of life (a mix of recycling, reusing, and energy recovery).

11.3.4 Scenario Analysis and Scale of the Study

Looking at the studies published so far, one more source of uncertainty lies in comparing current materials available on the market with materials prepared at laboratory scale. Materials prepared in laboratories use often less efficient equipment if compared with an efficient and standardised industrial production process. For example, it has been demonstrated that when producing CNT, the technology readiness has a large impact on the emissions. According to Gavankar et al. [69], the environmental burden for their production can reduce by more than 90% when the large quantities of feedstocks used will make their recycling/reuse economically

viable. Prospective LCA studies that foresee a potential commercial-scale production and, where appropriate, recycling processes are encouraged in order to address this problem. However, this issue is mostly related with the old studies as most of the newer ones consider (or refer to) likely commercial production processes for carbon nanomaterials (18 out of 29).

Of those 18 cases, half present also potential improvements for the graphene technology in terms of improved production efficiency, material properties enhancements or future electricity sector decarbonisation. This is also important as commercial-scale production is often simulated on base of laboratory scenarios or pilot scale that are based on current electricity mixes and material properties. However, those materials will develop further in the years to come, hence, future scenarios should be taken into consideration to reduce uncertainties in the LCA results. Looking at the nine cases presenting future scenarios, four of them are coming from a single publication from Zhai et al. [60] in which the production efficiency is improved, while three are from Arvidsson et al. [59, 70, 71] and two from Cossutta et al. [55, 68] in which possible future scenarios for improved material production, material properties, and future energy mixes are tested.

A couple of other studies also present scenario modelling, but they either test different current electricity mixes or test functionalised graphene instead of normal graphene and while this is interesting research, it is not part of the potential future technology development. Scenario modelling or/and sensitivity analysis are very important because they show not only the current status but also what could be done for future improvements guiding research towards more sustainable solutions. For example, Arvidsson et al. [59] show how the recycling of methane in the CVD process examined can reduce its GHG emissions by two orders of magnitude.

For bulk graphene, instead, according to Cossutta et al. [55], the chemical route (with chemical oxidation and subsequent reduction) seems to be the best candidate for commercial-scale up, at least until the energy sector will be decarbonised. When this will happen, the use of renewable electricity generation will improve the environmental performance of electricity intensive processes (e.g. electrochemical exfoliation of graphite rods).

Cossutta et al. [68] showed that comparing activated carbon with graphene for supercapacitor applications, when both materials reach their highest theoretical specific capacitance (measured in Farads per gram—F/g), the graphene-based supercapacitors will perform better than the activated carbon ones and this is due to two main reasons: the graphene required to perform the same function will be less and, as consequence, the whole supercapacitor will become smaller and lighter resulting in a smaller material input and a reduced fuel consumption for the selected transport application. A further scenario where the electricity used for the foreground system is decarbonised shows enhanced benefits for the graphene-based supercapacitor because the recycling activity brings more credits as its electricity consumption is less impacting than with the current electricity mix (Fig. 11.6).

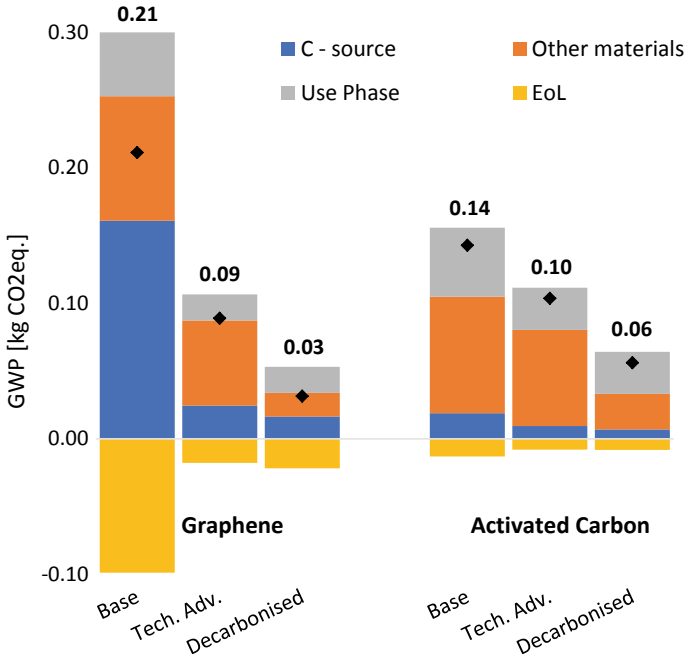

Fig. 11.6 Global warming potential for the compared supercapacitors rack including scenario analysis. Modified from Cossutta et al. [68]. Previously published in the Journal of Cleaner production. Copyright Elsevier

11.3.5 Impact Categories Selection

One additional limiting factor and source of uncertainty of the LCA studies found in literature is that most of them only consider the cumulative energy demand and global warming while other impact categories, especially those regarding the toxicity, are often not taken into consideration. This could also lead to misleading analysis as one product could show low carbon emissions but have a high environmental toxicity.

Like shown in Fig. 11.7, the number of studies reporting only one impact category is high, and for eight cases out of nine, they report only the cumulative energy demand (CED). While CED is the most reported single impact category, the global warming potential (GWP) is the most widely reported. However, most of the cases reported in the studies present 10 impact categories or more, but those reporting only one category are almost in equal number (even though 4 cases are from a single study from Zhai et al. [60]) and some of them are also very recent.

One example of the importance of considering several impact categories is the study from Arvidsson et al. [70] investigating the chemical production of graphene. It shows that using the ultrasonication reduction method can be a less impacting option in terms of energy demand and water footprint if compared to the chemical reduction, but worse for human and eco-toxicity. This shows how misleading some results could

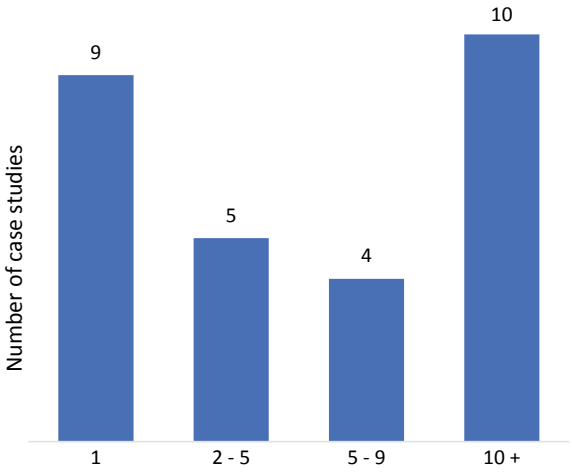

Fig. 11.7 Number of impact categories reported

be when limited to one or two impact categories (especially if they are partially dependent like energy demand and GHG emissions) and how this could increase the risk of promoting one technology for its better environmental performance, while in reality, the environmental burden is only shifted to a different impact category.

11.3.6 General Recommendations

Since performing a life-cycle assessment on a new and fast evolving technology of nanomaterial synthesis can be compared to following a moving target [72], Arvidsson et al. [73] proposed some recommendations on how to perform environmental assessments of emerging technologies. It is suggested that this assessment of technologies that are still at laboratory-scale or at prototype level, and not yet on the market should be called "prospective life cycle assessments". The prospective LCA is the tool to use for nanomaterials, but, compared to standard the standard LCA, it has some additional challenges. For example, comparisons with current materials are more complicated as sometimes it is not clear which materials are direct competitors of the carbon nanomaterials, hence for future studies, it is recommended to increase the number of applications to be compare with carbon nanomaterials in order to use them as building block for additional studies. Moreover, extending the comparison to multiple materials/technologies can increase the chances of not comparing the technology under development with something that could be obsolete by the time the new technology reaches mass adoption.

The recommendations also suggest simulating industrial commercial-scale production when the comparison is against current products, appraising several scenarios, and performing sensitivity analysis on key parameters to assess the effect

of their variation on the environment. The idea is to compare the emerging technology with current materials at the same level of maturity, hence including likely future developments as well as future extreme scenarios. Future developments and scenarios should involve both the foreground system and the background system. In fact, both systems will be affected by future developments: while the technology under examination, and the competitors, could improve in terms of performance, manufacturing efficiency or production yields, also the background system could become different in the years ahead, for example, the share of electricity produced by renewable sources is increasing as well as the share of bio-fuels used in the transport sector.

Arguably, the most important aspect of performing a prospective LCA on an emerging technology like the carbon nanomaterials is the influence it can have on future developments. In fact, improving mature technologies requires more effort since commercial production processes are normally standardised with less room for modifications, especially when the adjustments could involve the whole supply chain. It is then crucial to inform development when the technology is still at an early stage and its industrialisation is not yet started, when its manufacturing process is still flexible. In this view, the LCA becomes an important tool to steer the research and development towards less impacting solutions, before a new technology reaches mass adoption and its full environmental impacts are achieved.

11.4 Nanoparticles Release and Toxicological Impact Characterisation Modelling Difficulties

Besides showing a more impacting production phase than for conventional materials but a less burdensome environmental profile when including the use phase and end of life, almost all the LCA studies on carbon nanomaterials do not consider the release of nanoparticles to the environment. Only two LCA among the 26 studies reported consider the release of nanoparticles, but they do not assess their impacts on the environment due to a lack of characterisation factors for their toxicological effects [74, 75]. A third study, Cossutta et al. [68], shows no nanoparticles release during all phases under assessment, but the measurements are limited to the emissions to air for occupational hazards and they are a separate assessment from the LCA. Only one study attempts at calculating the toxicity impacts related with the release of SWCNT to the environment during the use phase of a PV cell and showing less than 10% toxicity increase in the worst-case scenario. The worst-case estimates are used as characterisation factors due to the lack of agreement on the CNT toxicity [76]. This limitation in the LCA studies holds for all nanomaterials as there is very limited information on the rate of material release during their life cycle, on their environmental fate upon release, and on their impact on ecological and human health upon exposure [48–53]. Several features of nanoparticles contribute to their possible toxicological effects:

- Nanoscale particles have modified properties compared with the basic material increasing the interaction with biological tissue
- Surface area can influence the exposure as the same mass of smaller particles have generally a larger surface area thus possibly reacting at greater rates with the environment
- Shape, aggregation, coating, and solubility could affect psychochemical and transport properties [77]

The application of the LCA methodology on these materials is hence a possible way of determining these aspects; however, the lack of reliable data related to both exposure/toxicology during production/use-phase/end-of-life prevents the LCA it from being an exhaustive tool. As there are no dedicated impact-assessment factors related to the emission of nanoparticles (linked with each specific type of nanomaterial) [52] using the current impact factors will not be sufficient in the future [51] and for this reason several toxicological studies and exposure models are proposed.

The toxicology of carbon nanomaterials has been investigated [78, 79] and showed that nanoparticles can create damages at cellular level generating oxidative stress, tissue inflammation, and they can penetrate the cell membrane and nucleus and in some cases, they can damage the DNA. They can also create oxidative damages to the cells by increasing the number of oxyradicals and can modify the genes involved in cell signalling and the expression of cancer genes. Their level of toxicity is dependent on shape, size, purity, postproduction processing steps, oxidative state, functional groups, dispersion state, synthesis method and route, dose and time of exposure. More complexity is also added when considering the intake of nanoparticles of living organisms in relation to their dose of exposure and the ratio of their uptake (i.e. the portion of the intake that is absorbed into the circulatory system of an organism).

To define a dedicated impact category for (carbon) nanomaterials, though, characterisation factors must be created, but to do so, some issues must be addressed: assess the fate of the nanomaterials released in the environment, the extent of exposure of the environment, and the effects that a certain level of exposure has on living organisms [53]. Several properties affect the interaction of the (carbon) nanomaterials with the environment and especially with living organisms. Their shape, for example, and how they aggregate or coagulate affects their toxicity [49] as biological activity and oxidative stress injury seem to be connected to the particles surface area [80]. Their fate upon release is also unknown as they might degrade when in interacting with plants, animals, water, light, and many other elements and this interaction is connected to their shape, mass, surface area, size, charge, solubility, and other properties and the same can be said about their transport behaviour when released to water, soil, or air.

There are also issues connected with the life cycle of the product. In fact, most of the studies about nanoparticle toxicity investigate the reactions of living organisms to their exposure to pristine nanoparticles generally released during manufacturing or production. During the use phase and end of life, however, the nanoparticles released will most likely not be in pristine form due to wear and aging. Moreover, when the "used" particles are released, they also interact with the environment and could transform and consequently their properties could be altered further. Moreover,

at different stages of the product life cycle, the material released may not only be very different from the material that constituted the original product (e.g. altered while washing textile products), but it might be still in the matrix that contains it, thus the nanoparticles are not released individually [81]. Transformation can occur to the primary particle, to the particle coating or as (de)agglomeration, but one single particle can undergo a sequence of transformations. Understanding the different transformation profiles for different life cycle stages and environments is necessary to comprehend the final fate of nanoparticles as, production phase aside, studying aged nanoparticle can lead to more realistic results about their real environmental impacts [82]. For this reason, it is suggested that the LCI should include all stages of the product lifetime in which nanoparticles could be released, paying also attention to their interactions with the environment and to the type of matrix that constitute the materials in which the nanoparticles might be incorporated [53].

In order to help assessing all those uncertainties, the risk assessment (RA) tool is suggested as complementary tool to the LCA to evaluate the risk that (carbon) nanomaterials pose to the living organisms. RA is different from LCA as it focuses mostly on the toxicity of the material under assessment and even if both adopt the life cycle approach (from their production to their disposal), their point of view is slightly different as the RA focuses on the life of a substance/material within a product rather than on the product itself (made of several materials and energy inputs). Another difference is that while the LCA is very often a comparative exercise, the RA gives absolute results; hence, the two methodologies are difficult to integrate [83]. Moreover, the risk assessment for nanomaterials still suffers of similar problems that are affecting the LCA models. The RA constitutes of generally four phases: hazard identification, dose–response assessment, exposure assessment and risk characterisation and at present, limited data and large uncertainties on the exposure data, exposure estimation models, material characterisation and on toxicological studies make it very difficult to obtain meaningful hazard values for all the four steps of a risk assessment [84]. The combination of the two techniques could achieve important results as the LCA approach would avoid the burden shifting from one phase to the next of the life cycle of a product/process, while the RA approach could provide absolute assessment of the specific risks associated with the exposure to a specific nanomaterial helping in mitigating the risks throughout the product/process lifetime. Results from the RA are also important to define toxicity-related characterisation factor and therefore dedicated impact categories for the LCA studies of (carbon) nanomaterials, while the product life cycle approach of the LCA could also complement the RA analysis [85].

To combine them, though, appropriate metrics need to be developed to assess the fate of nanomaterials upon release, and hazard and exposure models [84] to be used in both. It has been suggested that a better material characterisation is key to identify the hazards and to perform a risk assessment [86]. However, no single physicochemical property has a direct and unique correlation with a particular type of health or environmental hazards; hence, grouping is proposed as a way of identifying families of (carbon) nanomaterials having shared properties affecting human health to facilitate risk and hazard assessments. Group criteria presented are divided

into four: physical and chemical properties, functionality, modes of action, similar biodurability/biokinetics connected to toxicological response and interaction with the endogenous protein lipid component in the body. Genotoxicity is proposed but not always considered as a mechanism linked with the size of the particles [87]. Future studies should verify if the proposed groupings lead to similar effects to human health (and more broadly on the natural environment), evaluate which are the dominant effects of common toxicological and environmental profiles, and generate models that can predict the effects of the exposure to the different groups.

11.5 Conclusions

The life-cycle assessment is a tool that suits the need for a sustainable development of carbon nanomaterials as its holistic and function-based approach is crucial to avoid the shifting of the impacts from one stage of the product/process life cycle to a different one. However, its application to carbon nanomaterials (and nanomaterials in general) is still in its early stages and thus extensive uncertainties are still present in the studies published so far. In order to mitigate the uncertainties presented in this review, several recommendations have been made like including use phase and end of life to the assessment when possible, consider the possible release of nanomaterials during all phases of the product lifecycle, comparisons with current technologies should not only take into account the current state of the technology, but consider also future developments in terms of performance enhancements and production/recovery processes improvements. These suggestions are based on the common findings of previous studies that showed how the synthesis of carbon nanomaterials is more energy intensive than conventional materials, but when the whole lifecycle (i.e. including use phase and end of life) and/or their potential function enhancement are considered, they can be less impacting for the environment. It is also suggested that research should cooperate more with industrial producers to close the data gaps on their real commercial-scale production.

Research should also understand the release of nanomaterials during different lifecycle stages and their behaviour in the receiving environment in order to model their fate, their physicochemical properties and their toxicological effects on living beings. It was noted that to achieve those targets a more detailed characterisation is needed for both pristine and released (carbon) nanomaterials. Especially for the later, future research should focus on understanding the transformation that these materials undergo when interacting with the environment and when aging. Focus should also be on the type of material released from products to understand whether the single nanoparticles are released, or they are still in the matrix containing them.

A deeper knowledge in those areas will help defining dedicated characterisation factors for (carbon) nanomaterials and dedicated impact categories that are missing in today's LCA tools. This issue hampers the exhaustiveness of the LCA applied to nanomaterials as it cannot assess any of their toxicological effects on living beings exposed to their release to the environment (water, air or soil). Nevertheless, the LCA

remains a very important tool capable of assessing the environmental impacts related with the production use and end of life of carbon nanomaterials or of the products containing them.

According to the concept of responsible research and innovation (RRI) [88], the scientists, innovators, business partners, and policy makers should be morally responsible for the risks for the society associated with the emerging technologies [89], however, even if several studies highlighted the risks associated with carbon nanomaterials [78, 79], a survey by Arvidsson et al. [90] found that graphene is considered not a risk for the society among researchers. This survey only involves graphene, but part of the answers could be potentially extended to other carbon nanomaterials. Some of the justification to this claim by the interviewed stakeholders in the research community are: it is not toxic, the potential level of exposure is low, and it is not as dangerous as carbon nanotubes. While this can be partially explained with conceptual difference between risk and hazard, it might also underline either a lack of risk awareness making these scientists irresponsible [90].

On the positive side, the number of LCA studies on carbon nanomaterials has steadily increased over the years and even if uncertainties are still extensive when applied to (carbon) nanomaterials, it is the best tool, especially if combined with the RA, to evaluate the environmental impacts of both products and particles and can support researchers and decision-makers to achieve a desired net benefit for environment and society. Future research should work to cover the highlighted gaps and, through constant model refinement, steer the development of these very promising materials towards the least impacting technological solutions aiming at mitigating their environmental impacts before their deployment.

References

1. U. Colombo, The Club of Rome and sustainable development. Futures **33**(1), 7–11 (2001)
2. R.G. Hunt, J.D. Sellers, W.E. Franklin, Resource and environmental profile analysis: A life cycle environmental assessment for products and procedures. Environ. Impact Assess. Rev. **12**(3), 245–269 (1992)
3. G.H. Brundtland.: *Our common future: report of the World Commission on Environment and Development*. Geneva, UN-Dokument A/42/427 (1987). http://www.un-documents.net/ocf-ov.htm
4. K. Bartels, K.A. Parker, *Teaching Sustainability/Teaching Sustainably* (Stylus Publishing, Sterling, 2011)
5. J. Fava et al., *SETAC Workshop Report: A Technical Framework for Life Cycle Assessments*, 18–23 Aug 1990, Smugglers Notch, Vermont. SETAC, Washington, DC Google Scholar (1991)
6. ISO, *Environmental Management—Life Cycle Assessment—Principles and Framework*. EN ISO 14040:2006, European Standard (2006)
7. ISO, *Environmental Management—Life Cycle Assessment—Principles and framework*. EN ISO 14044:2006, European Standard (2006)
8. A. Camyab et al., Early action on climate change. Power Eng. **20**(6), 20–23 (2006)
9. D. Lewis, Our time is running out. Power Eng. **20**(6), 15–19 (2006)
10. JRC, *ILCD Handbook* (Institute for Environment and Sustainability, European Commission Joint Research Centre, 2010)

11. J.F. Randall, *Designing Indoor Solar Products—Photovoltaic Technologies for AES* (Wiley, New York, 2006)
12. B.G. Hermann, C. Kroeze, W. Jawjit, Assessing environmental performance by combining life cycle assessment, multi-criteria analysis and environmental performance indicators. J. Clean. Prod. **15**(18), 1787–1796 (2007)
13. Waldron, K., *Handbook of Waste Management and Co-Product Recovery in Food Processing*, vol. 2 (Woodhead Publishing, 2009)
14. L.H. Goldberg, W. Middleton, *Green Electronics/Green Bottom Line—Environmentally Responsible Engineering* (Elsevier, Amsterdam, 1999)
15. R.M. Atlas, J. Philp, *Bioremediation—Applied Microbial Solutions for Real-World Environmental Cleanup*. American Society for Microbiology (ASM)
16. G. Finnveden et al., Recent developments in life cycle assessment. J. Environ. Manage. **91**(1), 1–21 (2009)
17. J. Reap et al., A survey of unresolved problems in life cycle assessment. Int. J. Life Cycle Assess. **13**(5), 374 (2008)
18. H.A.U. de Haes, Applications of life cycle assessment: expectations, drawbacks and perspectives. J. Clean. Prod. **1**(3–4), 131–137 (1993)
19. J.R. Ehrenfeld, The importance of LCAs—Warts and all. J. Ind. Ecol. **1**(2), 41–49 (1997)
20. J. Krozer, J.C. Vis, How to get LCA in the right direction? J. Clean. Prod. **6**(1), 53–61 (1998)
21. G. Finnveden, On the limitations of life cycle assessment and environmental systems analysis tools in general. Int. J. Life Cycle Assess. **5**(4), 229–238 (2000)
22. G. Sinden, The contribution of PAS 2050 to the evolution of international greenhouse gas emission standards. Int. J. Life Cycle Assess. **14**(3), 195–203 (2009)
23. J. Guinee, Handbook on life cycle assessment operational guide to the ISO standards. Int. J. Life Cycle Assess. **7**(5), 311–313 (2002)
24. N.D. Mermin, Crystalline order in two dimensions. Phys. Rev. **176**(1), 250–254 (1968)
25. K.S. Novoselov et al., Two-dimensional gas of massless Dirac fermions in graphene. Nature **438**(7065), 197–200 (2005)
26. K.S. Novoselov et al., Electric field effect in atomically thin carbon films. Science **306**(5696), 666–669 (2004)
27. A.K. Geim, Graphene: status and prospects. Science **324**(5934), 1530–1534 (2009)
28. D.A.C. Brownson, D.K. Kampouris, C.E. Banks, An overview of graphene in energy production and storage applications. J. Power Sour. **196**(11), 4873–4885 (2011)
29. Y. Shao et al., Highly durable graphene nanoplatelets supported Pt nanocatalysts for oxygen reduction. J. Power Sour. **195**(15), 4600–4605 (2010)
30. M. Terrones et al., Graphene and graphite nanoribbons: Morphology, properties, synthesis, defects and applications. Nano Today **5**(4), 351–372 (2010)
31. Y. Takabayashi et al., The Disorder-Free Non-BCS Superconductor Cs_3C_{60} Emerges from an Antiferromagnetic Insulator Parent State. Science **323**(5921), 1585–1590 (2009)
32. R.J. Young et al., The mechanics of graphene nanocomposites: A review. Compos. Sci. Technol. **72**(12), 1459–1476 (2012)
33. H. Xia et al., Mechanical and thermal properties of reduced graphene oxide reinforced aluminum nitride ceramic composites. Mater. Sci. Eng., A **639**, 29–36 (2015)
34. J.R. Potts et al., Graphene-based polymer nanocomposites. Polymer **52**(1), 5–25 (2011)
35. D. Sidorenko et al., Carbon nanotube reinforced metal binder for diamond cutting tools. Mater. Des. **83**, 536–544 (2015)
36. C.-M. Gee et al., Flexible transparent electrodes made of electrochemically exfoliated graphene sheets from low-cost graphite pieces. Displays **34**(4), 315–319 (2013)
37. H.M. Hegab, L. Zou, Graphene oxide-assisted membranes: fabrication and potential applications in desalination and water purification. J. Membr. Sci. **484**, 95–106 (2015)
38. Y. Wang et al., A facile nanocomposite strategy to fabricate a rGO–MWCNT photothermal layer for efficient water evaporation. J. Mater. Chem. A **6**(3), 963–971 (2018)
39. P. Li et al., Investigation of the semiconductor/electrode interface in organic thin-film transistor using graphene electrodes. Synth. Met. **202**, 103–109 (2015)

40. C.M. Homenick et al., Fully printed and encapsulated SWCNT-based thin film transistors via a combination of R2R gravure and inkjet printing. ACS Appl. Mater. Interfaces **8**(41), 27900–27910 (2016)
41. Z. Li et al., Decomposable s-Tetrazine copolymer enables single-walled carbon nanotube thin film transistors and sensors with improved sensitivity. Adv. Func. Mater. **28**(13), 1705568 (2018)
42. G.S. Selopal et al., Graphene as transparent front contact for dye sensitized solar cells. Sol. Energy Mater. Sol. Cells **135**, 99–105 (2015)
43. B.C. Thompson, J.M.J. Fréchet, Polymer-fullerene composite solar cells. Angew. Chem. Int. Ed. **47**(1), 58–77 (2008)
44. T.A. Shastry et al., Enhanced uniformity and area scaling in carbon nanotube-fullerene bulk-heterojunction solar cells enabled by solvent additives. Adv. Energy Mater. **6**(2), 1501466 (2016)
45. X. Yu, A. Manthiram, Na2S–carbon nanotube fabric electrodes for room-temperature sodium–sulfur batteries. Chem. A Eur. J. 2015 **21**(11), 4233–4237
46. Y. Xie et al., Stretchable all-solid-state supercapacitor with wavy shaped polyaniline/graphene electrode. J. Mater. Chem. A **2**(24), 9142–9149 (2014)
47. D. Xie et al., Integrated 3D porous C-MoS2/nitrogen-doped graphene electrode for high capacity and prolonged stability lithium storage. J. Power Sour. **296**, 392–399 (2015)
48. S. Gavankar, S. Suh, A.F. Keller, Life cycle assessment at nanoscale: review and recommendations. Int. J. Life Cycle Assess. **17**(3), 295–303 (2012)
49. M. Miseljic, S.I. Olsen, Life-cycle assessment of engineered nanomaterials: a literature review of assessment status. J. Nanopart. Res. **16**(6), 2427 (2014)
50. O. Jolliet, R.K. Rosenbaum, A. Laurent, Life cycle risks and impacts of nanotechnologies. Nanotechnol. Hum. Health **2013**, 213–277
51. R. Hischier, T. Walser, Life cycle assessment of engineered nanomaterials: state of the art and strategies to overcome existing gaps. Sci. Total Environ. **425**, 271–282 (2012)
52. V.K.K. Upadhyayula et al., Life cycle assessment as a tool to enhance the environmental performance of carbon nanotube products: a review. J. Clean. Prod. **26**, 37–47 (2012)
53. B. Salieri et al., Life cycle assessment of manufactured nanomaterials: where are we? NanoImpact **10**, 108–120 (2018)
54. N.M. Mubarak et al., An overview on methods for the production of carbon nanotubes. J. Ind. Eng. Chem. **20**(4), 1186–1197 (2014)
55. M. Cossutta, J. McKechnie, S.J. Pickering, A comparative LCA of different graphene production routes. Green Chem. **19**(24), 5874–5884 (2017)
56. V. Khanna, B.R. Bakshi, Carbon nanofiber polymer composites: evaluation of life cycle energy use. Environ. Sci. Technol. **43**(6), 2078–2084 (2009)
57. A. Pizza et al., Life cycle assessment of nanocomposites made of thermally conductive graphite nanoplatelets. Int. J. Life Cycle Assess. **19**(6), 1226–1237 (2014)
58. D.A. Notter et al., Life cycle assessment of PEM FC applications: electric mobility and μ-CHP. Energy Environ. Sci. **8**(7), 1969–1985 (2015)
59. R. Arvidsson et al., Energy and resource use assessment of graphene as a substitute for indium tin oxide in transparent electrodes. J. Clean. Product. **132**, 289–297 (2016)
60. P. Zhai, J.A. Isaacs, M.J. Eckelman, Net energy benefits of carbon nanotube applications. Appl. Energy **173**, 624–634 (2016)
61. W.-J. Long et al., Performance enhancement and environmental impact of cement composites containing graphene oxide with recycled fine aggregates. J. Clean. Prod. **194**, 193–202 (2018)
62. G. Chilkoor et al., Sustainability of renewable fuel infrastructure: a screening LCA case study of anticorrosive graphene oxide epoxy liners in steel tanks for the storage of biodiesel and its blends. Environ. Sci. Process. Impacts **19**(2), 141–153 (2017)
63. V.K.K. Upadhyayula et al., Screening-level life cycle assessment of graphene-poly(ether imide) coatings protecting unalloyed steel from severe atmospheric corrosion. ACS Sustain. Chem. Eng. **5**(3), 2656–2667 (2017)

64. L. Pourzahedi et al., Life cycle energy benefits of carbon nanotubes for electromagnetic interference (EMI) shielding applications. J. Clean. Prod. **142**, 1971–1978 (2017)
65. C. Bauer et al., Towards a framework for life cycle thinking in the assessment of nanotechnology. J. Clean. Prod.s **16**(8), 910–926 (2008)
66. A.L. Holder et al., Nanomaterial disposal by incineration. Environ. Sci. Process. Impacts **15**(9), 1652–1664 (2013)
67. E.P. Vejerano, A.L. Holder, L.C. Marr, Emissions of polycyclic aromatic hydrocarbons, polychlorinated dibenzo-p-dioxins, and dibenzofurans from incineration of nanomaterials. Environ. Sci. Technol. **47**(9), 4866–4874 (2013)
68. M. Cossutta et al., A comparative life cycle assessment of graphene and activated carbon in a supercapacitor application. J. Clean. Prod. **242**, 118468 (2020)
69. S. Gavankar, S. Suh, A.A. Keller, The role of scale and technology maturity in life cycle assessment of emerging technologies: a case study on carbon nanotubes. J. Ind. Ecol. **19**(1), 51–60 (2015)
70. R. Arvidsson et al., Prospective life cycle assessment of graphene production by ultrasonication and chemical reduction. Environ. Sci. Technol. **48**(8), 4529–4536 (2014)
71. R. Arvidsson, S. Molander, Prospective life cycle assessment of epitaxial graphene production at different manufacturing scales and maturity. J. Ind. Ecol. **21**(5), 1153–1164 (2017)
72. T.G. Gutowski, J.Y.H. Liow, D.P. Sekulic, Minimum exergy requirements for the manufacturing of carbon nanotubes. In: *2010 IEEE International Symposium on Sustainable Systems and Technology (ISSST)* (2010)
73. R. Arvidsson et al., Environmental assessment of emerging technologies: recommendations for prospective LCA. J. Ind. Ecol. **22**(6), 1286–1294 (2018)
74. R. Hischier, Life cycle assessment study of a field emission display television device. Int. J. Life Cycle Assess. **20**(1), 61–73 (2015)
75. O.G. Griffiths et al., Identifying the largest environmental life cycle impacts during carbon nanotube synthesis via chemical vapour deposition. J. Clean. Prod. **42**, 180–189 (2013)
76. I. Celik et al., Environmental impacts from photovoltaic solar cells made with single walled carbon nanotubes. Environ. Sci. Technol. **51**(8), 4722–4732 (2017)
77. M.L. Healy, L.J. Dahlben, J.A. Isaacs, Environmental assessment of single-walled carbon nanotube processes. J. Ind. Ecol. **12**(3), 376–393 (2008)
78. P. Khalid et al., Toxicology of carbon nanotubes-a review. Int. J. Appl. Eng. Res. **11**(1), 148–157 (2016)
79. G. Lalwani et al., Toxicology of graphene-based nanomaterials. Adv. Drug Deliv. Rev. **105**, 109–144 (2016)
80. G. Oberdörster, V. Stone, K. Donaldson, Toxicology of nanoparticles: a historical perspective. Nanotoxicology **1**(1), 2–25 (2007)
81. F. Gottschalk, B. Nowack, The release of engineered nanomaterials to the environment. J. Environ. Monit. **13**(5), 1145–1155 (2011)
82. D.M. Mitrano, B. Nowack, The need for a life-cycle based aging paradigm for nanomaterials: importance of real-world test systems to identify realistic particle transformations. Nanotechnology **28**(7), 072001 (2017)
83. F.M. Christensen, S.I. Olsen, The potential role of life cycle assessment in regulation of chemicals in the European union. Int. J. Life Cycle Assess. **9**(5), 327 (2004)
84. K.D. Grieger et al., Analysis of current research addressing complementary use of life-cycle assessment and risk assessment for engineered nanomaterials: have lessons been learned from previous experience with chemicals? J. Nanopart. Res. **14**(7), 958 (2012)
85. D. Beloin-Saint-Pierre et al., How suitable is LCA for nanotechnology assessment? Overview of current methodological pitfalls and potential solutions: 65th LCA Discussion Forum, Swiss Federal Institute of Technology, Zürich, May 24, 2017. Int. J. Life Cycle Assess. **23**(1), 191–196 (2018)
86. H.F. Krug, Nanosafety research—are we on the right track? Angew. Chem. Int. Ed. **53**(46), 12304–12319 (2014)

87. N.E. Landvik et al., Criteria for grouping of manufactured nanomaterials to facilitate hazard and risk assessment, a systematic review of expert opinions. Regul. Toxicol. Pharmacol. **95**, 270–279 (2018)
88. J. Stilgoe, R. Owen, P. Macnaghten, Developing a framework for responsible innovation. Res. Policy **42**(9), 1568–1580 (2013)
89. R. Owen, P. Macnaghten, J. Stilgoe, Responsible research and innovation: from science in society to science for society, with society. Sci. Publ. Policy **39**(6), 751–760 (2012)
90. Arvidsson, R., et al.: *Just carbon: ideas about graphene risks by graphene researchers and innovation advisors.* NanoEthics (2018)
91. D. Kushnir, B.A. Sandén, Energy requirements of carbon nanoparticle production. J. Ind. Ecol. **12**(3), 360–375 (2008)
92. V. Khanna, B.R. Bakshi, L.J. Lee, Carbon nanofiber production. J. Ind. Ecol. **12**(3), 394–410 (2008)
93. L.J. Dahlben et al., Environmental life cycle assessment of a carbon nanotube-enabled semiconductor device. Environ. Sci. Technol. **47**(15), 8471–8478 (2013)
94. P. Yaseneva et al., Efficient reduction of bromates using carbon nanofibre supported catalysts: Experimental and a comparative life cycle assessment study. Chem. Eng. J. **248**, 230–241 (2014)
95. A.-F. Trompeta et al., Towards a holistic environmental impact assessment of carbon nanotube growth through chemical vapour deposition. J. Clean. Prod. **129**, 384–394 (2016)
96. Khanam, P.N., et al.: Biotechnological production process and life cycle assessment of graphene. J. Nanomater. **2017** (2017)
97. T.-H. Lin, Y.-S. Chien, W.-M. Chiu, Rubber tire life cycle assessment and the effect of reducing carbon footprint by replacing carbon black with graphene. Int. J. Green Energy **14**(1), 97–104 (2017)
98. S. Guarino et al., Life cycle assessment of a new graphene-based electrodeposition process on copper components. J. Clean. Prod. **165**, 520–529 (2017)

Chapter 12
Improvements of Strength of Layered Polypropylene Reinforced by Carbon Fiber by its Sizing Film and Electron Beam Under Protective Nitrogen Gas Atmosphere

Yoshitake Nishi, Shodai Kitagawa, Michael C. Faudree, Helmut Takahiro Uchida, Masae Kanda, Sagiri Takase, Satoru Kaneko, Tamio Endo, Akira Tonegawa, Michelle Salvia, and Hideki Kimura

12.1 Introduction

12.1.1 Background

Climate change has been a serious problem for our Earth. Therefore, lighter and stronger materials contributing to lowering vehicle CO_2 emissions with recyclability are essential. There is vital need for technical innovations such as lighter weight cars and development of electric vehicles (EV) and solar vehicles (SV), along with electric-powered airplanes proposed by JAXA. Demand for carbon fiber reinforced

Y. Nishi (✉) · S. Kitagawa · M. C. Faudree · H. T. Uchida · M. Kanda · S. Takase · A. Tonegawa · H. Kimura
Graduate School of Engineering, Tokai University, Hiratsuka, Kanagawa 259–1292, Japan
e-mail: west@tsc.u-tokai.ac.jp

M. C. Faudree
Faculty of Liberal Arts and Sciences, Tokyo City University, Yokohama 224-8551, Japan

M. Kanda
Center of Applied Superconductivity & Sustainable Energy Research, Chubu University, Kasugai 487-8501, Japan

S. Kaneko
Kanagawa Institute of Industrial Science and Technology, Ebina 243-0435, Japan

T. Endo
Sagamihara Surface Treatment Laboratory, Sagamihara 252-0243, Japan

M. Salvia
École Centrale de Lyon, Ecully Cedex 69134, France

S. Kaneko et al. (eds.), *Carbon Related Materials*,
https://doi.org/10.1007/978-981-15-7610-2_12

plastics (CFRPs) has been expected to increase to replace high-tension steel components along with use for moldable EV car bodies. Carbon fiber reinforced epoxy polymer (CFRP) is one of the typical state-of-the-art light structural materials for dream-worthy ships and automobiles, as well as passenger airplanes to enhance their fuel efficiency, mobility and safety.

However, epoxies are thermosets difficult to recycle due to crosslinking, hence, materials leading to increased environmental sustainability are urgently needed. Thermoplastics, on the other hand, are recyclable since they can be repeatedly remelted and reformed, but have the disadvantage of being lower strength the fiber-matrix interface typically being a weak point. Therefore, we investigate strengthening a thermoplastic polypropylene reinforced by carbon fiber (PP-CFRTP) by applying low voltage electron beam irradiation directly to the CFs prior to lamination assembly and hot-press to increase bending strength.

Since the fiber/matrix interface is one of the keys to strengthening CFRTP composites, we first provide current literature background of enhancing polymer-CF interface to strengthen CFRPs beginning by covering pre-stress of epoxy thermosets. Then to be applied to the difficult to adhere thermoplastic with CF, we review the wide body of research on several CF surface modifications. Finally, we cover high energy irradiation methods, and importantly for our study, low energy irradiation electron beam methods of HLEBI to CFs or specimen surface.

12.1.2 Strengthening Carbon Fiber Reinforced Thermoset Epoxy Polymer (CFRP)

12.1.2.1 Pre-stress

Recently, effects of tensile pre-stress level on impact value of 50 vol% continuous unidirectional zero degree oriented carbon fiber reinforced epoxy polymer (CFRP) have been investigated. Since CFRP, typically epoxies, have long been utilized for light structural materials with high strength for aerospace, automotive and sports equipment [1, 2], the further strengthening with safety enhancement has always been expected for the continuous development of high-speed mover machines with safety and high energy conservation and durable goods. This includes pre-stress layup of continuous unidirectional long fiber composites in which advantages include remarkably increased mechanical properties, and that complex geometries can be accommodated for since fiber pre-stressing and layup are separate operations. Although the concept of pre-stressed concrete is well known [3–6], the method of administering compressive stresses in polymeric matrices by pre-stressing long continuous fibers while curing the resin is relatively recent [7]. In polymer composite beam-shaped structures, pre-stressing the fibers have been reported to increase impact resistance 33% over their non-stressed counterparts [8], while also increasing flexural properties to approximately the same degree [9]. By pre-stressing of fibers in unidirectional

GRE (graphite reinforced epoxy) composite, an increase of about 25% in tensile strength and about 50% increase in tensile modulus were achieved [10]. During pre-stress, the fibers are held for a time to induce creep where a substantial amount of the fiber stressing is viscoelastic; the load then released to impart compressive stress in the resin matrix. This impedes crack formation and propagation in the resin matrix and enhances hardening and elasticity of the part. Recently, in composite of long nylon 6,6 fibers in polyester resin matrix, viscoelastically applied pre-stress has been found to increase impact fracture toughness [7]. In Charpy impact test, viscoelastically pre-stressing samples are also reported to increase impact energy absorption 25–30% over that of unstressed [11]. Data of pre-stressing on mechanical properties has been reported for CFRP with volume fraction (V_f) as small as 3 vol% [12, 13], in which re-stressing from 0.8 to 8.0 MPa remarkably enhanced the a_{uc}, elasticity, tensile strength and its strain, 26, 7, 18 and 13% higher than that the sample with slight pre-stress of 0.8 MPa, respectively. Based on micro-hardness test results, the pre-stressing increased residual compressive stress in the matrix above the unstressed samples [12, 13].

It follows 3 vol% CF is quite small since the maximum possible V_f for unidirectional fibers is 91 vol% calculated for hexagonal closest packing in two-dimensions, isotropy being assumed along the length. However, 91 vol% is impractical due to spare matrix space areas between fibers, therefore, 50–70 vol% is typically used for high load-bearing parts.

Experiments of tensile pre-stress level on Charpy impact value (a_{uc}) of 50 vol% CFRP epoxy whose fibers are continuous unidirectional zero degree oriented [14] has shown success. While the 3 vol% CF-CFRP exhibits large CF inter-distance with small mutual stress fields into the matrix, 50 vol% CF-CFRP exhibits small CF inter-distance with large mutual stress fields into the matrix overlapping on each other. For the 50 vol% CF-CFRP, the literature reports a_{uc} at mid-fracture probability $P_f = 0.50$ induced by a large pre-stress of 17.6 MPa (109 kJ m^{-2}) was increased 30% over that (84 kJ m^{-2}) of slight pre-stress of 0.25 MPa. The statistically lowest impact value a_s at $P_f = 0$ calculated by three-parameter Weibull equation was raised 26% from 73 to 92 kJ m^{-2} showing increased reliability of part strength. Fracture surface observation was reported to show a flat surface extending through the thickness from the impact side generally extending deeper as pre-stress level was raised. This was attributed to the transition depth in the specimen thickness from compression to tension is deeper during impact as pre-stress level was increased acting to raise the impact values [14].

12.1.3 Strengthening Carbon Fiber Reinforced Thermoplastic Polymers (CFRTP)

12.1.3.1 Merits and Problems

It follows thermoset polymers (TPs), widely used for CFRP such as epoxy have higher ultimate strength than thermoplastics. However, disadvantages are long solidification times and difficulty recycling making mass-waste disposal a serious problem for our environment.

On the other hand, thermoplastic polypropylene (PP) is widely used as an eco-friendly commercial polymer that can be recycled and reformed and has shorter solidification cycle times, decent strength and lower cost. Solidification time for PP is only about 10% that of epoxy reducing energy consumption. Other advantages of PP are heat resistance and high chemical resistance: while thermoplastics in general have higher crack resistance than thermosets. PP belongs to the polyolefin group being partially crystalline and non-polar.

However, the typically weak bonding between CF and TP pose serious challenges since CF lattice structure has graphitic basal planes with non-polar surface and is reported [15, 16] to be chemically inert due to manufacturing step of high temperature carbonization and graphitization [17–19]. Moreover, surface smoothness, negligible adsorption characteristics and lipophobicity lead to insufficient bonding with matrix materials [17–19]. CF has drawback of poor adhesion with PP resulting in lower mechanical properties from easy fiber pullout due to low contact area at non-polar CF/PP interface.

12.1.3.2 CF Surface Treatment

Therefore, increasing adhesion of CF to matrix material has been a major goal in composite design. The literature reports several CF surface treatments methods [15, 16] of which we present a brief background.

Acidic modification creates a rougher surface possibly creating higher friction at the interface [20]. However, it can cause surface damage and weight loss [21] decreasing strength [22].

Widely researched is plasma CF surface modifications [23–26] reported to be successful in increasing interlaminar shear strength of CFRP. Plasma oxidation of CF was found to increase interfacial shear stress of CFRP epoxy composites from 6 to 42 MPa [27].

Many methods to increase adhesion create polar functional groups on the CF surface [28–30]. Electro-polymer coating has been carried out depositing polymer coatings on CF surface by chemical grafting reactions introducing functional groups $-OH$, $-NH_2$ and $-COOH$ to increase CF adhesion to epoxy and the strength of CF itself [28]. Rare earth particle attachment method increases functional polar groups on CF surface has improved mechanical properties [29, 30]. It is reported

to increase functional polar groups on CF surface and is usually done by dipping method. For CF/polytetrafluoroethylene, lanthanum (La) chloride coating to CF raises bending and tensile strength 18 and 14%, respectively [31]. In addition, rare earth particle attachment method also increases flexural strength of CF/polyimide composites lightly ~11% along with wear resistance [32].

Multiple treatments have been applied with success. Three treatments to CF: plasma, nitric acid and liquid nitrogen to CF achieved 41 and 106% improvement in tensile and impact strength properties, respectively, of CFRPs [33].

The relatively newer technology of nano-particles: carbon nanotubes, multi-walled carbon nanotubes or graphene have been coated on CFs by electrophoretic deposition, chemical vapor deposition or dip coating, most of which functionalize the highly crystallized inert basal plane sites and increase surface energy [34].

12.1.3.3 Ni Coating

Ni sputtering CF surfaces has been successful. Ni sputtering CF before joining Ti with epoxy-CFRP [35] is reported to increase the impact value, a_{uc} of a Ti/epoxy-CFRP joint with Ni coated CF insert (Ti/NiCF/CFRP) joint to ~3.0 kJ m^{-2}, two times higher than that of either adhesive joint with glue (Ti/glue/epoxy) or without glue (Ti/epoxy) both at a_{uc} ~ 1.5 kJ m [35, 36].

12.1.3.4 High Energy Irradiation Methods

Applying high energy irradiation to CF, for example, ions and γ-rays has been found to enhance fiber/matrix adhesion without use of catalyst [37, 38]. The high energy creates active sites in the crystal lattice while increasing surface roughness.

High energy Ar^+ ion irradiation (0.6–1.4 keV) showed increased carbonyl peak and broadened-OH peak of Fourier-transformation infrared spectroscopy (FTIR) increasing polarity and H-bond formation at CF interface [39]. A 0.30 MGy dose of Co^{60} γ-ray irradiation has been reported to increase surface roughness of CF [40].

12.1.3.5 Low Energy Electron Beam Irradiation (EBI) Method

On the other hand, this study focuses on surface activation by applying a light electron (e^-) charge by homogeneous low potential electron beam irradiation (EBI) to CF surface to increase adhesion with polymer matrix. EBI has a proven track record of improving many materials [23–25, 41, 42] and is relatively easy method that does not use atoms or a catalyst. Moreover, EBI does not require chemical treatment of the CF. Large areas, such as LED TV screens can be treated. When EBI activates the CF surface, it decreases the dangling bond density in the hexagonal graphite structure as evidenced by a decrease in electro spin resonance (ESR) spectroscopy peak intensity [41, 42]. CF is reported to naturally contain dangling bonds [41, 42].

The EBI is reported to enhance crack resistance and increase tensile fracture stress and elasticity, increasing ductility strengthening the CF itself [41, 42].

EBI has been successfully used to increase strength of [metal/CF insert/thermoplastic polymer] joints where CF, acting as the connecting insert between metal and polymer, was directly irradiated with EBI [15, 16]. Activating CF cross-weave inserts with EBI prior to dipping into thermoplastic ABS resin is reported to increase tensile strength (σ_b) in [Ti/EBCF/ABS] joints 2.1 times higher than that of untreated, [Ti/CF/ABS], and 9.1 and 4.2 times higher than that without CFs, mainly of glue [Ti/Glue/ABS] and no glue [Ti/ABS], respectively [15]. Similarly, in [Ti/EBCF/PC] joints, σ_b was raised 3.0 times higher than untreated [Ti/CF/PC] [16]. EBI activation of the CF surface is effective since it generates increased charge site distribution at the CF surface homogeneously the CF being a strong conductor of electricity. The increased charge probably travels over the entire CF surface contributing to successful bonding with polymers. Nucleation sites are enhanced increasing friction force at CF/TP polymer interface, thereby preventing CF pullout, resulting in improved tensile strength. Moreover, in the vacuum during EBI residual trace gasses (O_2, $H_2O_{(g)}$ and N_2) are assumed to act to create weak Van der Walls attractive forces at the polymer/CF interface probably adding to the enhancement

12.1.4 Evaluation of CF/Polymers of Epoxy, as Well as ABS, PC and PP

The conventional carbon fiber reinforced polymer (CFRP) of thermoset epoxy resin matrix with high strength is generally applied to the blades of wind power generators and bodies of airplanes. Strengthening carbon fiber [41, 42] and its reinforced polymers [15, 16, 43–46] has been investigated. However, the long-term solidification of epoxy-CFRP with high strength [43, 44] is a serious problem in preparing them. To shorten the solidification term in production process, thermoplastic polymers [45, 46] are useful, since the solidification term of inexpensive polypropylene (PP) [47] is tremendously shorter (1/10) than that of expensive epoxy.

On the other hand, the adhesive force of sizing film of CFs to epoxy matrix with full entangled contact is extremely larger than that of PP thermoplastic polymers matrix with partial contacts at heterogeneous nucleation sites. In addition, PP is a meandering (branched) polymer with its $-CH_3$ side chains and probably generates spontaneous nano-scale rough interface with CF. Based on the rough interface, partial contact and low adhesive force of PP, the typical decreasing of strength from epoxy to PP mainly corresponds to decreasing the nano-contact area sites from smoother to coarser at CF/polymer interface.

To examine the effect of contact sites of PP with CF, tensile strengthening of CF reinforced thermoplastic PP with sizing film, and with removed sizing film is investigated. We expand on our study from a previous paper [47], where we found that

the sizing film has been effective preventing CF pullout, resulting in strengthening CFRTP [47].

Therefore, our purpose is to: (1) confirm sizing film provided by the factory on CFs improves bending strength σ_b over those with removed sizing film; (2) demonstrate applying EBI treatment to *sized* CF surfaces prior to assembly and hot-press can improve σ_b; and (3) demonstrate the EBI raises the σ_b of *removed sizing film samples*, about as much as improvement by sizing over removed sizing film. This is in a layered carbon fiber reinforced thermoplastic polymer (CFRTP) composite composed of 3 cross-weave CF cloth sheets between 4 polypropylene (PP) mats, $[PP]_4[CF]_3$ (55 vol%-CFs).

12.2 Experimental Procedures

12.2.1 Materials and Removing Sizing Film from CF

Carbon fiber (CF) was TR3110M provided by Mitsubishi Rayon Ltd. Tokyo, and thermoplastic polymer polypropylene was BC06C provided by Novatec, from Nissho Ltd. Tokyo. All provided CF cross-weave cloths contained their initial nano-thick polymer sizing film coating from the factory whose specific chemical name is proprietary. To make the "removed sizing," or "sizing film free" (SFF) samples, CF cloths (6.8 g) were dipped for 20 min (2 dips of 10 min each) in acetone (100 mL, 019–00353: Wako Pure Chemical Industries, Ltd, Osaka) at room temperature, as shown in Fig. 12.1. Since solutes of nano-thickness polymer film coated on CF are eliminated by 20 min-dipping in acetone, the peaks can be detected for acetone solution in proton-NMR (AVANCE500, Neutron Magnetic Resonance, Shimazu, Kyoto).

To confirm removal of polymer sizing film, Fig. 12.2 shows ^{1}H-NMR analysis results of dipping CFs in acetone for 10 min, and an additional 10 min [47]. The 20 min total dipping mostly annihilates all the ^{1}H-NMR δ peaks. These include high intensity peaks at approximately $\delta = 1.6$ and 3.7 ppm, medium intensity peaks at 6.7 and 7.2 ppm, and several low intensity peaks as shown in Fig. 12.5. This data shows 20 min soak in acetone can mostly, if not completely eliminate the sizing film on CF.

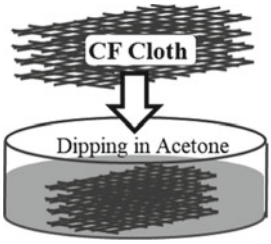

Fig. 12.1 Schematic drawing of dipping sized carbon fiber in acetone at room temperature

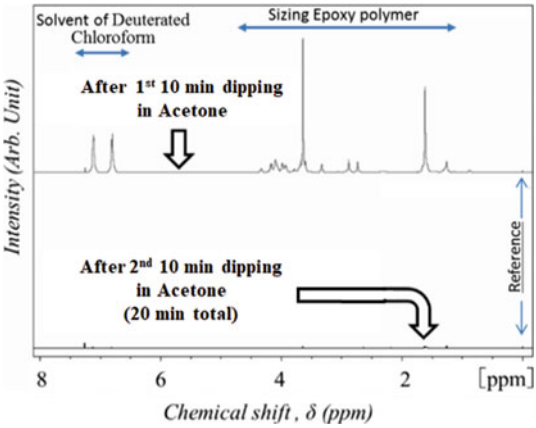

Fig. 12.2 NMR analysis results of sized carbon fibers dipping in acetone for 10 min and additional 10 min to make the "sizing film free" samples

Note we did not add sizing film to the provided CFs. We only removed the present sizing film coated by the factory. A portion of the samples was not dipped in acetone as a control and are referred to here as "sizing film" samples. Those dipped in acetone are referred as "removed sizing film" or "sizing film free" (SFF) samples.

12.2.2 Composite Fabrication

Here, for the "sizing film free carbon fiber" (SFF-CF) samples, fabrication was as follows: ***Step 1***: CF cross-weave was dipped in 100 mL acetone for 20 min total (2 dips of 10 min each) as described above. ***Step 2***: CFs were dried at RT. ***Step 3***: Laminated assembly was carried out 3 CF cross-weave plies were inserted between 4 PP mats to make $[PP]_4[CF]_3$ layup specimens. ***Step 4***: Composite fabrication was performed by hot-press (IMC-185A, Imoto Machinery Co., Ltd) under 4.0 MPa at 473 K for 1 min after pre-heating for 8 min, as shown in Fig. 12.3 [47].

Figure 12.4 illustrates the resulting 55 vol%-carbon fiber reinforced thermoplastic polypropylene (PP-CFRTP) specimens with 3 cross-weave CF cloth sheets between 4 polypropylene (PP) mats, $[PP]_4[CF]_3$ whose dimensions are: 80, 10 and 2 mm.

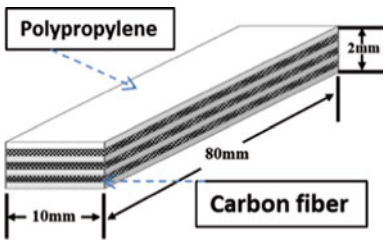

Fig. 12.3 Layered CFRTP specimen geometry

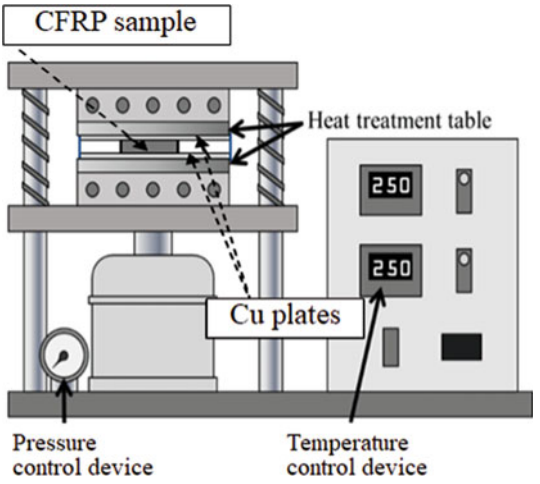

Fig. 12.4 Hot-press and heating machine (Type IMC-185A)

12.2.3 Bending Tests and Sample Characterizations

To test for strength, three-point bending tests were carried out at room temperature with an IMADA Co., Ltd. DPU-50 N/MX-500 N/GA-10 N tester illustrated in Fig. 12.5 [48]. Practical distance between marked points on specimen, chuck length and head speed was 40 mm, 20 mm and 1.0 mm/min, respectively. Bending stress-strain curves of the CFRTP with and without coated sizing polymer film were obtained by using crosshead displacement and confirmed by using a video recording device. Samples were also characterized by nuclear magnetic resonance (NMR) and electron spin resonance (ESR) [47].

Evaluating the accumulative probability of strength (P_f) is a convenient method of quantitative analyzing experimental values and in industry and is often employed in statistical quality control (QC). P_f is expressed by the following equation which is a generalized form of the median-rank method: [49].

$$P_f = (i - 0.3)/(N_s + 0.4) \tag{12.1}$$

Here, N_s and i are total number of samples, and rank order integer of bending strength of each sample, from weakest to strongest. In this case, $N_s = 5$ hence when the i value is 3, its corresponding P_f value is 0.50.

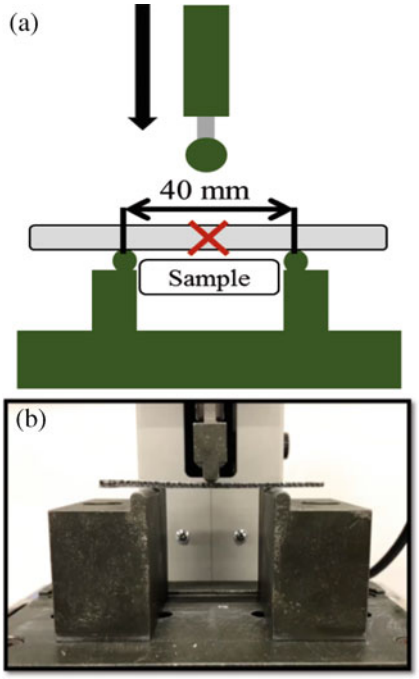

Fig. 12.5 Schematic illustration (**a**) and photograph (**b**) of bending test setup

12.3 Results and Discussion of PP Reinforced by CF with and Without Sizing Film

12.3.1 Improvement Evaluation of Bending Strength from Sizing by Removing Sizing Film from CF

Experimental results in Fig. 12.6 confirm sizing film improvement of bending strength, σ_b 36% from 38 to 52 MPa at median-accumulative probability, $P_f = 0.50$ over those with removed sizing film, in the layered PP $[PP]_4[CF]_3$ samples. Figure 12.7 shows the σ_b improvements (36% from 38 to 52 MPa at median-accumulative probability, $P_f = 0.50$) over the samples with and without sizing film. Moreover, as expected Fig. 12.7 illustrates σ_b is higher for the sized CF than that of the removed sizing film at all P_f. We do not recommend removing epoxy sizing film. This is just to illustrate improvement of sized CF specimens over those with removed sizing film.

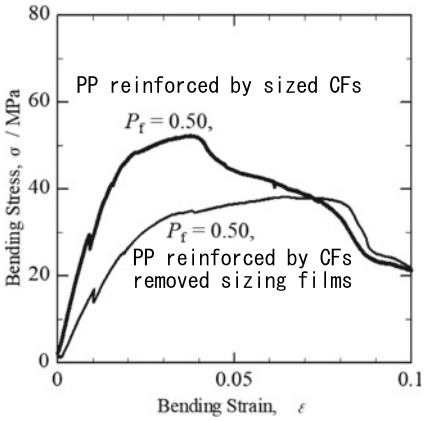

Fig. 12.6 Bending stress-strain curves at medium accumulative probability (P_f) of 0.50 for CFRTP samples constructed with PP matrix and 55 vol% CF with and without sizing film prior to assembly and hot-press

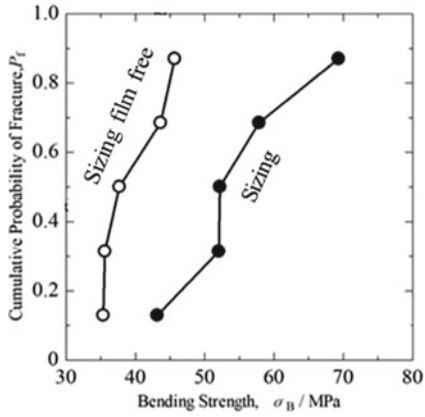

Fig. 12.7 Bending strength (σ_b) at each accumulative probability (P_f) for PP matrix CFRTP with CFs sized (filled circle) and removed sizing film (circle)

12.3.2 Morphological Changes Related to Pullout, Delamination and Thickness Reduction Induced by Sizing Film

Figure 12.8 shows optical photographs and schematic drawings of bending fractured PP-CFRTP samples with (a) and without (removed) sizing film (b). Both sizing and sizing film free samples split into three parts. The later of sizing film free CFs (b) are apt to undergo microdamage as pullout in the form of CF–PP debonding accompanied by larger-scale damage of CF–PP ply delamination and fiber separation extending at least 8 mm from the loading point zone. On the other hand, the former of the presence of sizing film (a) largely prevents fiber pullout with large-scale delamination confined in the loading point zone to 2 or 3 mm.

Unexpectedly, optical observation revealed mean thickness (2.223 mm) of sizing film free CF reinforce PP ($[PP]_4[CF]_3$) samples is 192 μm larger than that (2.031 mm)

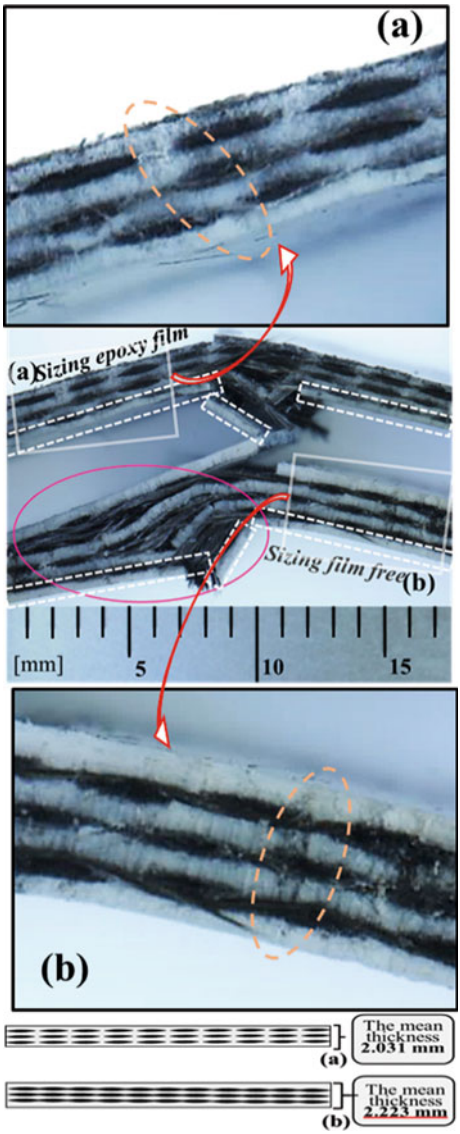

Fig. 12.8 Photograph and schematic drawing of bending fractured CFRTP samples of PP reinforced by CF sized (**a**) and removed sizing film (**b**)

of the sized CFs (see Fig. 12.8). This indicates the sizing film actually reduces the laminate sample thickness.

12.3.3 *Morphological Discussion Related to Delamination, Pullout and Thickness Reduction Induced by Sizing Film*

Figure 12.9 illustrates the adhesive sizing film probably penetrates into the micro-dents of roughness of CFs with high wetting and molecular bonding. Although weak resistance to pullout of laminate assembly of sizing film free (SFF)-CF and PP can be explained by its pint contacts of PP/CF (see Fig. 12.9a), the strong resistance to pullout of laminate assembly of sized CF cross sheets and PP mats is induced by both plain contacts filling into nano-dents on the CF surface with the SF and copolymerization generated by entangling with SF and PP polymers (see Fig. 12.9b).

The removed sizing samples being thicker than the sized can be explained by the PP not impregnating into the CFs without the sizing film. This is probably why considerable CF pullout and delamination occurred easily from PP, as shown in Fig. 12.8b. Namely, the CF with sizing film firmly impregnates with PP due to copolymerization, since mean thickness of CFRTP compressive samples reinforced by commercially used sizing CF is 8% smaller than that by CF removed sizing films. Therefore, the volume reduction (8.6%) of CFRTP (see Fig. 12.8) is direct macroscopic evidence sizing of CFs improves pullout resistance, hence, strengthening the CFRTP (see Figs. 12.6 and 12.7).

PP with low density has the large free volume generated by side chains. When the PP/SF entangling occurs (see Fig. 12.9b), the thickness reduction of laminate assembly of PP mats and CF cross sheets can be explained (see Fig. 12.8a).

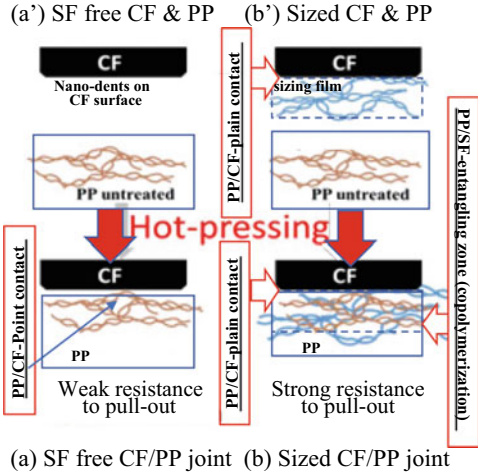

Fig. 12.9 Schematic illustration for **a** SF free and bare CF/PP joints with point contacts and **b** sized CF-SF/PP joint with CF/SF-plain contacts and SF/PP copolymerization before (**a**′, **b**′) and after (**a**, **b**) hot pressing

12.3.4 Nano-scale Discussion Related to Entangling of Sizing Polymer Fiber and Matrix PP Polymers

Since the CF sizing film apparently improves the bending strength, it acts to strengthen the CFRTP. Figure 12.9 illustrates the mechanism in which the sizing typically increases resistance to CF pullout and ply delamination by entangling with the PP by molecular force, along with copolymerization being well adhered to the CF with sizing film.

On the other hand, the density of PP (~0.90 g/cc) is lower than polyethylene (PE) (~0.95 g/cc). The lower density of PP is brought about spontaneous interspaces of polymers induced by the $–CH_3$ side chains as illustrated in Fig. 12.10. Although polyethylene (PE) polymers are constricted by principal chains, PP polymers contain $–CH_3$ side chains along the main chains. With removed sizing film, this probably makes spontaneous larger interspaces in the thermoplastic PP (Fig. 12.10), resulting in easy fiber pullout induced by a relatively small number of point contact sites against the PP/CF interface. Moreover, the PP probably gets twisted and contorted more that of straight polymers of PE resulting in poor adhesion. The C–H atoms of the PP have low wettability with the CFs. Also, compared with epoxy, the thermoplastic PP by itself has no oxygen groups to adhere efficiently to the CF.

Therefore, our data quantitatively shows the degree to which the typically applied sizing film prevents the ply delamination and CF pullout from PP, with its adhesion to CF; and sizing film adhesion to PP occurring by plain contact and entangling with molecular bonding near nano-scale interface enhancing sizing polymer/PP adhesion over that without sizing film.

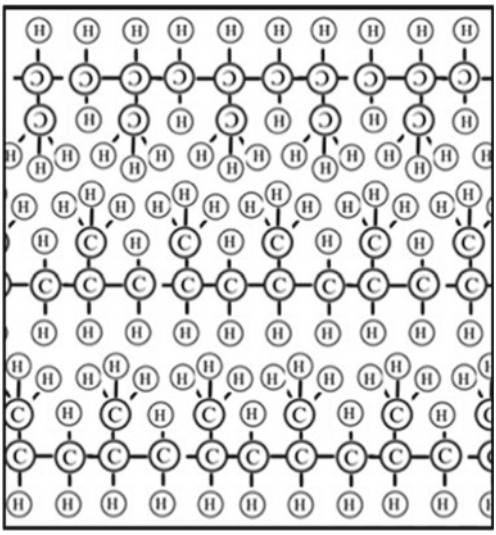

Fig. 12.10 Schematic structure of polypropylene (PP) showing meandering methyl group branches

12.4 Successful Countermeasure of CF Pullout from PP Matrix in CFRTP Strengthened by CF Activated by EB-Irradiation

12.4.1 Principal of CF Activated by EB-Irradiation

We confirmed by quantification decreasing the adhesive strength from sizing polymer to PP against the CF (see Figs. 12.6 and 12.7) results in easy fiber pullout. When one of the authors, Y. Nishi, was an invited Prof. staying in Ecole Central Lyon, Prof. M. Salvia showed that the dendritic crystalline (hard segment) grew on the carbon fiber (CF) in nylon-6, as shown in Fig. 12.11a. Hence, for this study, although the CF is completely wrapped by plain contact with thermoset epoxy polymer, the initial crystalline heterogeneously nucleates at point contacts of CF surface prior to the crystalline growth in thermoplastic PP because of its low wettability to CF. Thus, plies easily delaminate and CF pulls out occurs easily from the PP matrix.

As shown in Fig. 12.12, the activation energy of ideal homogeneous nucleation is the maximum, when the spherical crystalline nucleation before growing the dendrite often occurs at bulk inside with homogeneously distribution in supercooled liquid [50]. At this time, the supercooled liquid with short range order convert to the hard segments with long range order at the solidification interface. As shown in Fig. 12.10b, to improve the delamination and pullout resistivity, the nucleation frequency is improved by activation on CF surface. The surface activation and randomization have been studied for metallic and ceramic glasses by shot peening [51, 52] and EBI (homogeneously low potential electron beam irradiation) [53], respectively.

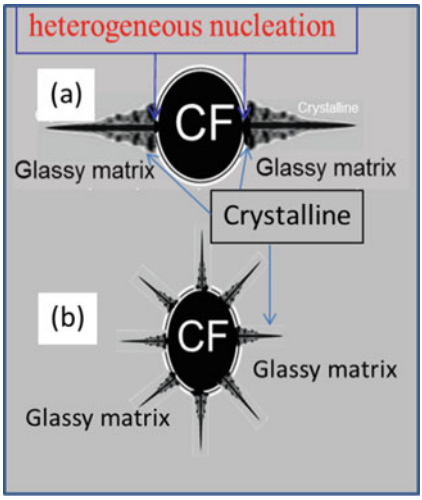

Fig. 12.11 Schematic illustration of crystalline nucleation and growth in polymer on carbon fiber **a** untreated and **b** activated by EB-irradiation

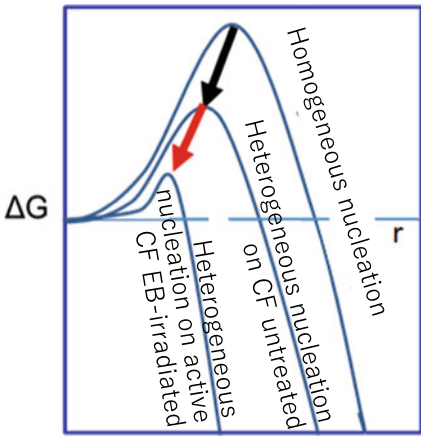

Fig. 12.12 Schematic illustration of changes in Gibb's free energy (ΔG) against crystalline radius (r) with activation energy (ΔG_f) at critical radius (r_c) of heterogeneous nucleation of crystalline, that is, polymer hard segment on CF catalyzer untreated, and lowered ΔG_f activated CF EB-irradiated in polymer matrix, together with ideal homogeneous nucleation curve

The CFs are also strengthened by optimal dose of EB-irradiation [41, 42]. Optimal dose of *EBI* is reported to activate the CF's three sp^3 orbital σ and one π bonds to enhance the resistance to pullout in PEEK matrix of CFRTP [54], as well as even diamond with for four sp^3 orbital σ bonds to improve the wetting and mist-resistance of diamond [55]. Namely, the EB-irradiation often cuts both σ and π bonds and generates the active terminated carbon atoms. When they contact to PP polymers, they decrease both activation energy and critical radius of crystalline nucleation, as shown in Fig. 12.12. As shown in Fig. 12.11b, several crystalline sites should nucleate on the CF surface in the form of point contacts, expecting to strengthen the PP matrix in CFRTP resulting in high resistance to ply delamination and the CF pulls out occurs easily from the PP matrix.

12.4.2 Condition of Electron Beam Irradiation

Figure 12.13 illustrates the schematic drawing of EB-irradiation apparatus. The CFs cloth sheet was homogeneously irradiated by an electron-curtain processor (Type CB175/15/180L, Energy Science Inc., Woburn, MA, Iwasaki Electric Group Co., Ltd., Tokyo) prior to assembly with PP and hot-press [15, 16, 41, 42, 48, 56–59]. This was by linear electron beam gun with low energy through a titanium thin film window attached to a 240 mm diameter vacuum chamber. A tungsten filament in the vacuum was used to generate the electron beam at a low energy condition, with acceleration potential (V_{Acc}: keV) of 170 keV and the irradiating current density (I) of 0.089 A $\times$ m^{-2}.

Although the electron beam is generated in a vacuum, the irradiated sample is kept under protective nitrogen gas N_2(g) at atmospheric pressure. Distance between sample and window was 25 mm. To prevent oxidation, residual concentration of O_2 was kept below 300 ppm in the vacuum chamber. The constant flow rate of N_2(g)

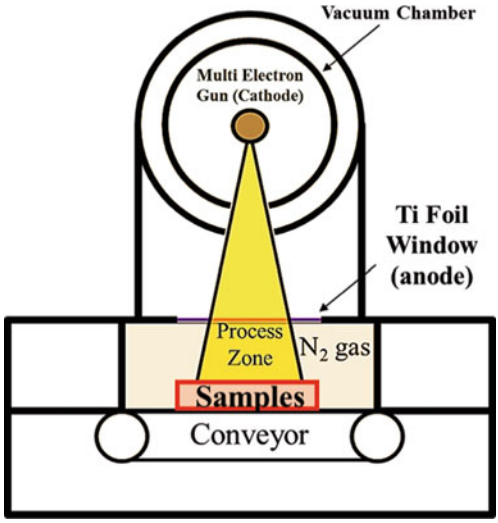

Fig. 12.13 Schematic drawing of EB-irradiation apparatus

was set at 1.5 L/s and 0.1 MPa N_2(g) pressure. Each irradiation dose (0.0432 MGy) was applied for only a short time (0.23 s) to avoid excessive heating of the sample; the temperature of sample surface remained below 323 K just after irradiation. The sample in the aluminum plate holder (0.15 × 0.15 m) was transported on a conveyor at a constant speed of 10 m/min. The sheet EBI was applied intermittently; one sweep going one way is 0.0432 MGy. Repeated irradiations to both side surfaces of the samples were used to increase the total irradiation dose. To keep sample from overheating, the interval condition of 30 s was applied between each sweep. The irradiated dosage was proportional to the irradiation current (I, mA) and number of irradiations (N), whereas it was inversely proportional to the conveyor speed (S, m/min).

Irradiation dose was controlled by integrated irradiation time for each sample. Here, irradiation dose was corrected by using an FWT nylon dosimeter of RCD radiometer film (FWT-60-00: Far West Technology, Inc. 330-D South Kellogg Goleta, California 93117, USA) with an irradiation reader (FWT-92D: Far West Technology, Inc. 330-D South Kellogg Goleta, California 93117, USA). The dose was 0.0432 MGy at each irradiation. Based on the mean density (ρ: kg × m^{-3}) and irradiation potential at the specimen surface (V: keV), the penetration depth (D_{th}: m) of EBI is expressed by the following equation [54, 60].

$$D_{th} = 66.7\,V^{5/3}/\rho \tag{12.2}$$

Using the principal form of Eq. (12.1), specimen surface electrical potential (V) was mainly dropped by the Ti window (ΔV_{Ti}) as well as N_2 gas atmosphere (ΔV_{N_2}).

$$V = 170\,\text{keV} - \Delta V_{Ti} - \Delta V_{N_2} \tag{12.3}$$

The specimen surface electrical potential, V, was estimated to be 129.6 keV from the acceleration potential ($V_{\mathrm{Acc}} = 170\,\mathrm{keV}$), the 10 μm thickness ($T_{\mathrm{Ti}}$) of the titanium window (density: 4540 kg × m^{-3}), and the 25 mm distance between the sample and the window ($T_{\mathrm{N_2}}$) in the N_2 gas atmosphere (density: $\rho_{\mathrm{N_2}} = 1.13\ \mathrm{kg\ m^{-3}}$):

$$\begin{aligned}\Delta V_{\mathrm{Ti}} &= T_{\mathrm{Ti}}/D_{\mathrm{thTi}} \times 170\,\mathrm{keV} = T_{\mathrm{Ti}}\rho_{\mathrm{Ti}}/\left[66.7 \times (170\,\mathrm{keV})^{2/3}\right] \\ &= \left(10^{-5}\,\mathrm{m}\right) \times \left(4540\,\mathrm{kg\,m^{-3}}\right)/\left[66.7 \times (170\,\mathrm{keV})^{2/3}\right] = 22.2\,\mathrm{keV} \end{aligned} \quad (12.4)$$

$$\begin{aligned}\Delta V_{N2} &= T_{N2}/D_{thiN2} \times V_{\mathrm{Ti}} = T_{\mathrm{N_2}}\rho_{\mathrm{N_2}}/\left[66.7 \times (V_{\mathrm{Ti}})^{2/3}\right] \\ &= \left(25 \times 10^{-3}\,\mathrm{m}\right) \times \left(1.13\,\mathrm{kg\,m^{-3}}\right)/\left[66.7 \times (170 - 22.2\,\mathrm{keV})^{2/3}\right] \\ &= 15.2\,\mathrm{keV} \end{aligned} \quad (12.5)$$

Since the dropped potential values were 22.2 keV due to the Ti window and 15.2 keV due to the N_2 gas atmosphere, respectively, the specimen surface electrical potential, V, is obtained to be 132.6 keV using following calculation:

$$V = 170\,\mathrm{keV} - 22.2\,\mathrm{keV} - 15.2\,\mathrm{keV} = 132.6\,\mathrm{keV} \quad (12.6)$$

Based on Eq. (12.3) and density (1760 kg m^{-3}) of CF, the penetration depth, D_{th} of electron beam estimated was 123 μm. Since the CF's diameter was 6 μm the electron beam is assumed to activate throughout the entire thickness deceasing dangling bond density [60].

12.4.3 *Results of Effects of EB-Irradiation Directly to Sized and SF Free CFs on Bending Strength of $[PP]_4[CF]_3$ CFRTP Samples*

Figure 12.14 shows applying 0.30 MGy-EBI dose under protective N_2(g) atmosphere directly to sizing film free CF cross sheet prior to laminate assembly with PP mats prior to hot-press increased the bending strength σ_{b} at median-accumulative probability ($P_{\mathrm{f}} = 0.50$) 45% from 38 to 55 MPa of the $[PP]_4[CF]_3$ sample. In addition, Fig. 12.14 shows by applying EBI doses between 0.043 and 0.43 MGy was increased substantially, namely doses of 0.043, 0.13, 0.22, 0.30 and 0.43 MGy increased σ_{b} from 38 to above 50 MPa.

Likewise, applying 0.22 MGy-EBI dose under protective N_2(g) atmosphere directly to sized CF cross sheet prior to laminate assembly with PP mats prior to hot-press increased the bending strength σ_{b} 6% from 52 to 55 MPa at median P_{f} of the $[PP]_4[CF]_3$ sample. Therefore, optimal EBI dose for the SF free (0.30 MGy) and sized (0.22 MGy) CF samples resulted in the same optimum σ_{b} of 55 MPa which may represent a theoretical maximum. Interestingly, with EBI treatment, samples

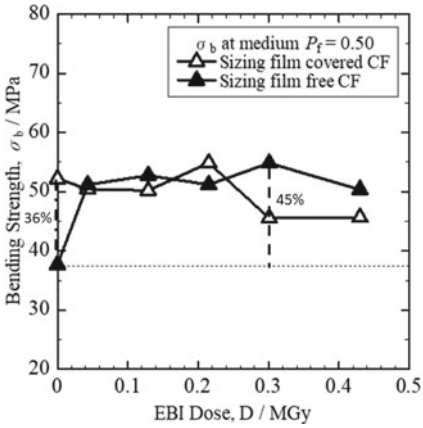

Fig. 12.14 Changes in bending strength (σ_b) at medium accumulative probability (P_f) of 0.50 against irradiation dose of electron beam to commercially used sized (triangle) and sizing film free (filled triangle) CFs reinforced PP

with removed CF sizing can apparently be the same bending strength as that factory sizing.

However, without careful testing for loading composite parts, it is not recommended to remove sizing film from CFs because the composite could be severely weakened. Nevertheless, with optimal EBI condition, strengthening the adhesion force increases interfacial friction force between CF and the difficult to adhere thermoplastic for both sized and SF free CFs to prevent ply delamination and fiber pullout in the CFRTP, resulting in increasing bonding strength σ_b over that of the untreated to become a viable process for practical applications.

12.5 Discussion: EB-Irradiation

The increase in bending strength σ_b of $[PP]_4[CF]_3$ CFRTP samples laminate assembly composed with PP untreated and EBI activated CFs sheets sized and removed SF free CF can be explained by increase in density of chemical bonding points contacts surface area at the fiber/matrix interface, as shown in Fig. 12.11. This is apparently accompanied by increased heterogeneous nucleation sites of dendritic crystal hard segments from the sized and SF free CFs surfaces as found on other thermoplastic polymer nylon-6 by Prof. M. Salvia. The EBI increases resistance to fiber pullout reducing CF/PP delamination between and within plies and confines the damage area along specimen length as shown in Fig. 12.8.

Moreover, dangling bonds spontaneously exist in CF itself [46]. CF is reported to be strengthened by EBI by annihilation of dangling bonds in the graphitic hexagonal structure often enhancing elasticity of CF [46]. The CF strengthening probably also contributes to bending strength increase of the $[PP]_4[CF]_3$ CFRTP samples.

12.5.1 CFRTP Samples with CF Removed Sizing Film

For the $[PP]_4[CF]_3$ CFRTP samples removed sizing film, before EBI, trace gas molecules of nitrogen, oxygen and water (N_2, O_2, H_2O) from the outside atmosphere should co-exist in the CF/PP interfacial spaces in the form of CF–[H_2O, N_2, O_2]–PP weak molecular bonds. However, the resulting slight attractive forces generated are not sufficient to create strong CF/PP adhesive force. Consequently, low interfacial mechanical friction from fewer point contacts results in low resistance to CF pullout and delamination from PP, resulting in the weak $\boldsymbol{\sigma b}$ for CFRTP with untreated CF with SF free. However, by applying the optimal dose of 0.30 MGy-EB-irradiation to the CFs removed SF (see Fig. 12.14), the maximum σ_b (55 MPa) of CFRTP can be obtained and is explained by maximum density of strong covalent bond formation of direct (CF:C:C:PP) and indirect contacts (CF:N:N:PP and CF:C:O:C:PP) at heterogeneous crystal nucleation sites on CF/PP interface induced by EBI-irradiation under protective N_2 atmosphere, together with negligible weak molecular bonding created by impurity gas molecules CF–[H_2O, N_2, O_2]–PP.

12.5.2 CFRTP Samples with Sized CF

For the sized $[PP]_4[CF]_3$ CFRTP samples, the σ_b being raised to the maximum of 55 MPa (see Fig. 12.14) by applying the optimal 0.22 MGy-EBI can be explained by generation of maximum number of the strong covalent bonds of both direct (CF/SF:C:C:PP) and the N_2 and O_2 assisted indirect contacts (CF/SF: N:N:PP and CF/SF: C:O:C;PP) formations at heterogeneous crystal nucleation sites on PP/SF interface induced by EBI-irradiation under protective N_2 atmosphere in addition to the weak molecular bonding created by impurity gas molecules CF/SF–[H_2O, N_2, O_2]–PP.

12.5.3 Comparison of CFRTP Samples Removed SF and Sized CF

Contribution of strength of CFRTP samples with sized CF untreated increase by weak molecular bonding is probably higher than that with SF free CF untreated (see Fig. 12.7). Most importantly, the strong oxygen bonding is enhanced by the EBI mostly creating active dangling bonds with the oxygen groups in the sizing film on the CF surface.

To compare, the CFRP samples with CF removed SF apparently need a higher EBI dosage (0.30 MGy) than that with sized CF (0.22 MGy) to reach the optimum σ_b of 55 MPa, as shown in Fig. 12.14. This is probably due to the higher resistance

to irradiation damages of bare CF removed SF requiring higher activation to reach the optimum than that of SF.

12.5.4 Irradiation Damage Induced by Higher EBI Doses

For the SF free samples, the σ_b decay at higher 0.43 MGy-EBI dose can be explained by excess irradiation damage [14, 16] causing disordering of graphite hexagonal structure in CFs. For the sized CF samples, the σ_b decay from additional EBI dose from 0.30 to 0.43 MGy can be explained by irradiation damage in the form of excess dangling bond formation [14] of sizing film. Therefore, carefulness is highly recommended to adjust for optimal dose of EBI to CFs when using for practical purposes.

Note we did not add sizing film to the provided CFs. We only removed the present sizing film coated by the factory when we received the CFs to investigate its effect. We do not recommend removing sizing film since it will weaken the composite. Nevertheless, with optimal EBI condition, strengthening the adhesion increases the interfacial friction force to prevent fiber pullout and delamination in the CFRTP, resulting in increasing the σ_b over that of the untreated to become a viable process for practical applications.

12.6 Summary

Stronger thermoplastic carbon fiber reinforced thermoplastic polymers (CFRTPs) have always been desired for lightweight and easily formable load-bearing parts due to their recyclability and shorter processing time with high concern for the environment. However, one of the problems has been that they typically have weak adhesion at the fiber/matrix interface. Therefore, we began by giving the reader a thorough literature background on recent state-of-the-art CF surface treatments. Following this, we experimentally quantified increase in bending strength in a thermoplastic polypropylene CFRTP samples with CF sized over removed SF. Next, was employed a novel process of applying low voltage electron beam irradiation (EBI) directly to the CFs sized and removed SF prior to lamination assembly and hot-press. Samples were a layered CFRTP composite composed of 3 cross-wave CF cloth sheets between 4 polypropylene (PP) mats [PP]4[CF]3 (55 vol%-CFs).

1. Experimental results confirmed SF improvement of bending strength, σ_b 36% from 38 to 52 MPa at median-accumulative probability, $P_f = 0.50$ over the SF free in the layered $[PP]_4[CF]_3$ samples. The σ_b was higher for the sized than that of the SF free at all P_f.

2. Fracture analysis showed both sized and SF free samples split into three parts. As expected, the SF was found to reduce delamination, CF separation and pullout considerably from damage area along the specimen length more than 11–4 mm.
3. Unexpectedly, optical observation revealed mean thickness (2.223 mm) of SF free $[PP]_4[CF]_3$ samples were 192 μm larger than that (2.031 mm) of the sized CFs indicating SF actually reduces laminate sample thickness. Strengthening mechanism is probably the result of: Sizing film polymer penetrating into CF surface roughness creating increased wetting and plain contact with molecular bonding (also on smooth CF surfaces) and formation of entanglement and copolymerization of sizing film polymer and PP reducing free volume. Moreover, the sizing film polymers act to replace the inert $–CH_3$ groups of PP at the CF surface with active O groups along with wetting any CF surface roughness increasing bonding sites to increase strength.
4. For sized samples, the novel process of applying EBI (0.22 MGy) to sized CFs under protective N_2 atmosphere prior to lamination assembly and hot-press improved σ_b ($P_f = 0.50$) 6% from 52 to 55 MPa at median P_f of 0.50. The improvements of sized CFs treated by EBI in N_2 were explained by increasing strong chemical bonds (CF–SF:$\boxed{\text{C:C}}$:PP, CF–SF:$\boxed{\text{N:N}}$:PP and CF–SF:$\boxed{\text{C:O:C}}$:PP (from the sizing) at adhesive interface with entangling different polymers of PP and SF, larger than that of untreated with weak molecular bonds (CF–[O_2, N_2, H_2O]–PP) at CF/PP rough interfaces.
5. Likewise, for CFRTP samples with SF free CF, applying 0.30 MGy-EBI to CF surfaces improved σ_b ($P_f = 0.50$) a larger 45% from 38 to 55 MPa. Improvements of CFs with and without SF treated by EBI in N_2 gas can be explained by generation of maximum density of strong covalent bond formation of direct (CF:$\boxed{\text{C:C}}$:PP) and indirect contacts (CF:$\boxed{\text{N:N}}$:PP) at CF/PP interface induced by EBI-irradiation under protective N_2 atmosphere with negligible weak molecular bonding created by impurity gas molecules CF–[H_2O, N_2, O_2]–PP. Moreover, increasing the number of heterogeneous crystal nucleation sites on the CF surface by the EBI can also play a role to prevent CF pullout.
6. Interestingly, the CFRP samples with CF removed SF apparently need a higher EBI dosage (0.30 MGy) than that with sized CF (0.22 MGy) to reach the optimum σ_b of 55 MPa, as shown in Fig. 12.14. This is probably due to the higher resistance to irradiation damages of bare CF removed SF requiring higher activation to reach the optimum than that of SF.
7. In summary, we demonstrated optimal EBI dose can raise bending strength of $[PP]_4[CF]_3$ CFRTP composite samples with removed sizing polymer film to that of the sized. Moreover, optimum EBI dose to carbon fiber with and without sizing film can raise σ_b. However, higher doses damage the composite lowering σ_b so carefulness is always highly recommended to adjust for optimum EBI dose for different conditions.
8. Note, we did not add sizing film to the provided CFs. We only removed the present sizing film coated by the factory when we received the CFs to investigate its effect. We do not recommend removing sizing film since it will weaken the

composite. Nevertheless, with optimal EBI condition, strengthening the adhesion force increases the interfacial friction force to prevent ply delamination and fiber pullout in the CFRTP, resulting in increasing the σ_b over that of the untreated to become a viable process for practical applications.

Acknowledgements The authors wish to gratefully acknowledge Mr. Yasuo Miyamoto for his great assistance with the EPMA and Mr. Yoshiki Oda for his keen help with the NMR. Sincere gratitude also goes to Mr. Naruya Tsuyuki, Mr. Anna Takahashi, Mr. Syo Ishii, Mr. Daisuke Kitahara, Mr. Ryo Nomura, Mr. Hitoki Hasegawa and Prof. Yoshihito Matsumura of Tokai University for their useful help.

References

1. J.D. Brooks, G.H. Taylor, Carbon **3**, 185–193 (1965)
2. T. Chang, A. Okura, Trans. ISIJ **27**, 229–237 (1987)
3. M. Tezuka, R. Sato, K. Yamamoto, S. Tottori, J. Mater. Concr. Struct. Pavem. **613**, 43–57 (1999)
4. S. Shirahana, A. Hattori, T. Miyagawa, J. Mater. Concr. Struct. Pavem. **669**, 85–97 (2001)
5. M. Khin, T. Idemitsu, K. Takewaka, S. Matsumoto, J. Mater. Concr. Struct. Pavem. **526**, 121–131 (1995)
6. H. Sakai, Y. Hamada, M. Hayashida, A. Hattori, T. Miyagawa, J. Mater. Concr. Struct. Pavem. **641**, 1173–1178 (2000)
7. J. Pang, K. Fancey, Compos. Sci. Tech. **68**, 1903–1910 (2008)
8. S. Motahari, J. Cameron, J. Reinf. Plast. Compos. **17**, 123–130 (1998)
9. S. Motahari, J. Cameron, J. Reinf. Plast. Compos. **18**, 279–288 (1999)
10. A.S. Hadi, J.N. Ashton, Compos. Struct. **40**, 305–311 (1997)
11. K. Fancey, Mater. Sci. Eng. A **279**, 36–41 (2000)
12. K. Kutaragi, Y. Harada, K. Tanaka, Y. Nishi, J. Jpn. Inst. Metal. **71**, 598–602 (2007)
13. M. Hirano, A. Matsuo, N. Hironaka, Y. Nishi, J. Jpn. Inst. Metal. **72**, 477–482 (2008)
14. Y. Nishi, T. Okada, S. Okada, M. Hirano, M. Matsuda, A. Matsuo, M.C. Faudree, Maters. Trans. **55**, 318–322 (2014)
15. H. Hasegawa, M.C. Faudree, Y. Matsumuara, I. Jimbo, Y. Nishi, Mater. Trans. **57**, 1202–1208 (2016)
16. H. Hasegawa, M.C. Faudree, Y. Enomoto, S. Takase, H. Kimura, A. Tonegawa, Y. Matsumura, I. Jimbo, M. Salvia, Y. Nishi, Enhanced tensile strength of titanium/polycarbonate joint connected by electron beam activated cross-weave carbon fiber cloth insert. Mater. Trans. **58**, 1606–1615 (2017)
17. Y. Nishi, K. Tanaka, Solid State Phenom. **127** (2006) 185-188. ISSN 1012-0394. Trans Tech Publishing Ltd., http://www.scientific.net
18. N. Harigae, Y. Nishi, J. Jpn. Inst. Metal. **75**, 235–242 (2011)
19. Y. Nishi, K. Tanaka, Mater. Trans. **47**, 1821–1825 (2006)
20. M. Sharma, S. Gao, E. Mader, H. Sharma, L.-Y. Wei, J. Bijwe, Compos. Sci. Tech. **102**, 35–50 (2014)
21. H. Dvir, J. Jopp, M. Gottlieb, J. Colloid Interf. Sci. **304**, 58–64 (2006)
22. M.C. Paiva, C.A. Bernardo, M. Nardin, Carbon **38**, 1323–1327 (2000)
23. K.B. Hung, J. Li, Q. Fan, Z.H. Chen, Compos. A **39**, 1133–1140 (2008)
24. S. Tiwari, M. Sharma, S. Panier, B. Mutel, P. Mitschang, J. Bijwe, J. Mater. Sci. **46**, 964–974 (2011)
25. C.U. Pittman, W. Jiang, G.R. He, S.D. Gardner, Carbon **36**, 25–37 (1998)

26. M.A. Sherwood, Electron Spectrosc. Relat. Phenom. **81**, 319–342 (1996)
27. M.A. Montes-Moran, A. Martinez-Alonso, J.M.D. Tascon, R.J. Young, Compos. A **32**, 361–371 (2001)
28. X.R. Zhang, X.Q. Pei, Q.H. Wang, Ex. Poly. Lett. **1**, 318–325 (2007)
29. J. Jaing, H. Wang, J. Mater. Sci. **35**, 2297–2303 (2000)
30. Z. Xu, L. Chen, Y. Huang, J. Li, X. Wu, X. Li et al., Eur. Polym. J. **444**, 494–503 (2008)
31. D. Bao, X. Cheng, J. Rare Earths **24**, 564–568 (2006)
32. X.R. Zhang, P. Zhao, X.Q. Pei, Q.H. Wang, Q. Jia, Expr. Polym. Lett. **1**, 667–672 (2006)
33. S.Y. Kim, S.J. Baek, J.R. Young, Carbon **49**, 5329–5338 (2011)
34. Z. Xu, Y. Huang, C. Zhang, G. Chen, Mater. Sci. Eng. A **444**, 170–177 (2007)
35. Y. Nishi, S. Ishii, S. Inui, A. Kasai, M.C. Faudree, Mater. Trans. **55**, 323–326 (2014)
36. Y. Nishi, H.T. Uchida, M.C. Faudree, S. Kaneko, H. Kimura, Fracture toughness of CF-plug joints of Ti and thermoplastic polymers, in *Proceeding of the 9th International Conference on Key Engineering Materials* (*ICKEM 2019*), 29 Mar–1 Apr 2019 (in press)
37. L.-G. Tang, J.L. Kardos, Polym. Compos. **18**, 100–113 (1997)
38. Z. Wu, C.U. Pittman, Polym. Compos. **33**, 597–605 (1995)
39. C. Jones, Surf. Interf. Anal. **20**, 357–367 (1993)
40. C.U. Pittman, W. Jiang, Z.R. Yue, S. Gardner, L. Wang, H. Toghiani et al., Carbon **37**, 1797–1807 (1999)
41. Y. Nishi, T. Toriyama, K. Oguri, A. Tonegawa, K. Takayama, J. Mater. Res. **16**(6), 1632–1635 (2001)
42. Y. Nishi, A. Mizutani, A. Kimura, T. Toriyama, K. Oguri, A. Tonegawa, J. Mater. Sci. **38**(1), 89–92 (2003)
43. A. Mizutani, Y. Nishi, Mater. Trans. **44**, 1857–1860 (2003)
44. Y. Nishi, K. Inoue, M. Salvia, Mater. Trans. **47**(11), 2846–2851 (2006)
45. H. Takei, K. Iwata, M. Salvia, A. Vautrin, Y. Nishi, Mater. Trans. **51**(12), 2259–2265 (2010)
46. H. Takei, M. Salvia, A. Vautrin, A. Tonegawa, Y. Nishi, Mater. Trans. **52**, 734–739 (2011)
47. S. Kitagawa, H. Kimura, S. Takase, N. Tsuyuki, D. Kitahara, A. Takahashi, M.C. Faudree, H.T. Uchida, A. Tonegawa, M. Kanda, I. Noriyuki, S. Kaneko, T. Endo, M. Salvia, Y. Nishi, Trans. Mater. Res. Soc. Jpn., 125–128 (2018)
48. A. Kasashima, N. Iwataka, J. Kawano, N. Honda, Y. Nishi, J. Adv. Sci. **9**, 70–71 (1997)
49. T. Nishida, E. Yasuda, *Evaluation of Dynamic Properties of Ceramics* (Ceramics no rikigaku tokusei hyouka in Japanese) (Nikkan Kogyou Shimbun Sha, Tokyo, 1986), pp. 50–51
50. Y. Nishi, K. Mikagi, Phys. Rev. B **34**, 1792–1794 (1986)
51. Y. Nishi, H. Harano, T. Fukunaga, K. Suzuki, Phys. Rev. B. **37**, 28552860 (1988)
52. Y. Nishi, A. Yazawa, C. Seshimo, K. Oguri, J. Mater. Sci. Lett. **15**, 1582–1583 (1996)
53. K. Iwata, Y. Nishi, Mater. Trans. **49**, 2058–2062 (2008)
54. Y. Nishi, R. Ourahmoune, M. Kanda, J. Quan, M.C. Faudree, M. Salvia, Maters. Trans. **55**, 1304–1310 (2014)
55. K. Oguri, N. Iwataka, A. Tonegawa, Y. Hirose, K. Takayama, Y. Nishi, J. Mater. Res. **16**, 553–557 (2001)
56. K. Oguri, K. Fujita, M. Takahashi, Y. Omori, A. Tonegawa, N. Honda, M. Ochi, K. Takayama, Y. Nishi, J. Mater. Res. **13**, 3368–3371 (1998)
57. K. Oguri, Y. Nishi, Mater. Trans. **45**, 1346–1349 (2004)
58. Y. Nishi, S. Iizuka, M.C. Faudree, R. Ohyama, Mater. Trans. **53**, 940–945 (2012)
59. Y. Nishi, A. Mizutani, N. Uchida, J. Thermoplast. Compos. Mater. **17**, 289–302 (2004) (Sage Publishings)
60. R. Christenhusz, L. Reimer, Z. Angew. Phys. **23**, 396–404 (1967)

Chapter 13
Photomechanical Response of Amorphous Carbon Nitride Thin Films and Their Applications in Light-Driven Pumps

Masami Aono and Tomo Harata

13.1 Introduction

Actuators are an important means of transferring energy from one of its many forms into mechanical motion for use in devices, such as pumps and sensors. Therefore, microactuators are the primary drive units in micro-electromechanical systems (MEMS). There are various types of microactuators, including electrostatic [1–3], piezoelectric [4, 5], magnetic [6, 7], and thermal [8, 9].

Light-driven actuators, which can convert light energy into mechanical energy, have attracted considerable attention due to their many advantages, which include the possibility for wireless control and the miniaturization of devices. The use of MEMS with light-driven actuators in medical and space applications is very promising, with high potential for future growth because the MEMS could be controlled remotely without external wires for power supply. Light-driven actuators could also contribute to smaller and lighter MEMS, without the need for a battery. Therefore, exploring new materials with optomechatronic properties is highly desirable for the development of light-driven actuators.

Certain organic materials, such as azobenzenes and spiropyrans, are known to undergo reversible photoinduced deformation. For example, azobenzene-containing materials macroscopically change their shape under UV irradiation because of the isomerization of azobenzene [10–12]. This organic material generally shows a reversible macroscopic deformation originating from the trans–cis photoisomerization of azobenzene moieties [10] induced by light irradiation at two different

M. Aono (✉)
Department of Electrical and Electronics Engineering, Kagoshima University, 1-21-40 Korimoto, Kagoshima 890-0065, Kagoshima, Japan
e-mail: aono@eee.kagoshima-u.ac.jp

T. Harata
Department of Materials Science and Engineering, National Defense Academy, 1-10-20 Hashirimizu, Yokosuka 239-8686, Kanagawa, Japan

S. Kaneko et al. (eds.), *Carbon Related Materials*,
https://doi.org/10.1007/978-981-15-7610-2_13

wavelengths, such as UV and visible light and UV and heat. Cviklinski et al. [13] reported that azobenzene liquid crystal elastomers contract under UV light irradiation, which is accompanied by stress. The response time required for deformation is relatively slow, generally up to several minutes in length. Therefore, rapid response as well as high output power needs to be achieved to realize device applications; however, the stability of the azobenzene liquid crystal elastomers under long-term light irradiation is not yet clear.

The photomechanical response using spiropyrans has reported a combination of photochromism of the spiropyrans and charge transition into hydrogels [14]. The photochromism involves the photoinduced generation of a significant dipole in the merocyanine. Such charge generation in hydrogel matrices will alter their osmotic potential, and hence allow a photomechanical response. Incorporation of spiropyrans into gel structures can be used for the fabrication of photo-controlled liquid flow micro-fluidic manifolds [15] and reversible micro-fluidic valves [16]. Recently, a hydrogel walker based on spiropyran that can reversibly swell and contract when submerged in water or subjected to cycles of white-light irradiation has also been reported [17].

Although the photomechanical properties are less common in inorganic materials, certain piezo-ceramics are well known. $Pb_{(1-x)}La_x(Zr_yTi_{(1-y)})_{(1-x/4)}O_3$ (PLZT) ceramics have high potential as photomechatronic materials due to the emergence of mechanical strain under UV-light irradiation, which is caused by a photostrictive effect arising from the combination of the photovoltaic effect and the piezoelectric effect [18, 19]. Although PLZT exhibits long-term photostability, the output power boost associated with an increase in size is limited. $TlInSe_2$ [20] and As_2S_3 [21] show an irreversible response. Volume expansion of As_2S_3 induced by photon irradiation leads to an increase in the defect density.

For carbon-related materials, carbon nanotubes (CNTs) embedded in polymer films [22] have been reported to undergo considerable photoinduced deformation, originating from the photothermal properties of CNTs. Photoinduced deformation of CNTs on a polymer film has also been reported [23], while the deformation can be attributed to the photothermal effects of CNTs and a difference in the thermal expansion coefficients between CNTs and the polymer film. The time constant of the photomechanical response was reported to be about 0.5 s, which shows a very fast response.

In 2012, we accidentally discovered a photomechanical response in amorphous carbon nitride (a-CN_x) films when we were studying the photoconductivity of a-CN_x films [24]. In the photoconductivity study, delamination of the films by visible-light irradiation was observed. Furthermore, the delamination was prevented by using a thinner substrate and a bending of the sample species was then obtained, as shown in Fig. 13.1. a-CN_x films exhibit a compressive stress nature [25]. For example, a-CN_x bent toward the substrate side under visible-light irradiation when deposited on an ultra-thin SiO_2 substrate or a flexible substrate, such as a polymer film and cellulose nanopapaer [26]. Based on the results of several experiments, the delamination was attributed to photoinduced phenomena. The response is reversible at any wavelength

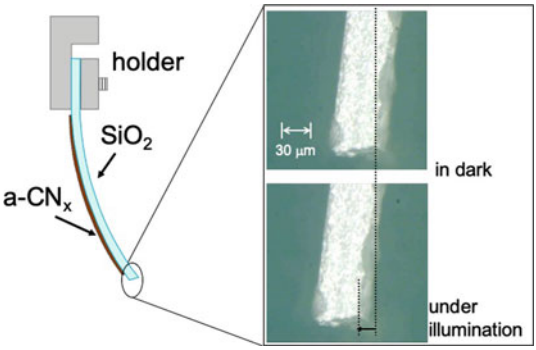

Fig. 13.1 Displacement of the free edge of an a-CN_x/SiO_2 specimen. The a-CN_x film was deposited at 300 °C by reactive radio frequency magnetron sputtering. White excitation light, provided by a Xe lamp, was used

in the visible-light region and thermal effects are relatively insignificant. A detailed analysis of these experiments is presented in this study.

13.2 Methods

13.2.1 Synthesis of Amorphous Carbon Nitride Films

Amorphous carbon nitride thin films are a carbon-related material based on amorphous carbon (a-C) and diamond-like carbon (DLC). A variety of deposition methods have been presented, such as chemical vapor deposition (CVD), sputtering, and laser ablation. The films are categorized into two types, depending on raw materials: hydrogenated and hydrogen-free carbon nitrides.

Hydrogenated amorphous carbon nitride films, a-CN_x:H (also described as a-C:N, DLC:N, and ta-C:N) are synthesized from CH_4, C_2H_6, and/or NH_3 gases [27–29]. On the other hand, hydrogen-free carbon nitride films, a-CN_x, are grown from bulk carbon sources and pure nitrogen gas. These two types of films differ in their maximum nitrogen concentration, chemical bonding states, as well as physical and chemical properties. Thus, amorphous carbon nitrides possess a wide range of characteristics; e.g., the electrical conductivity spans 10 orders of magnitude from 10^3 to 10^{-13} S/cm for amorphous carbon nitrides prepared by various deposition processes [30].

In this study, a-CN_x films were prepared from a graphite target and pure nitrogen using reactive radio frequency (RF) magnetron sputtering. The deposition setup is shown in Fig. 13.2. Standard conditions of a-CN_x deposition were as follows: the nitrogen gas pressure was 0.12 Torr, the RF power (frequency 13.56 MHz) was 85 W, and the substrate temperature was 300 °C. The targeted thickness of the deposited films was about 1 μm. The thickness of the films was determined by field-emission scanning electron microscopy (Hitachi, S-4500).

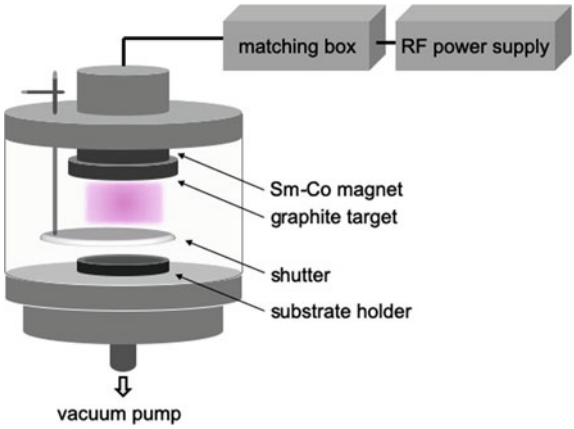

Fig. 13.2 Schematic image of the deposition system (reactive radio frequency magnetron sputtering)

13.2.2 Measurements

Photoinduced deformation was determined by measuring the bending curvature of an a-CN_x film/substrate system under illumination. The specimen was an a-CN_x film on either a Si(100) or a SiO_2 substrate. A standard size of the substrate for photoinduced deformation measurements was 2 mm × 20 mm × 0.05 mm. One end of the specimen was clamped and the displacement of the other free end was measured with an optical-cantilever technique, as shown in Fig. 13.3. The probe beam was a He–Ne laser light ($\lambda = 633$ nm). The photoinduced deformation was estimated by the difference between the positions of laser spots on a bare substrate without a-CN_x films and a sample of a-CN_x films deposited on a substrate. A position-sensitive detector (PSD; Hamamatsu Photonics S3931) was used to detect the displacement. A positive PSD signal indicates displacement toward the film side of the sample. A 150 W Xe lamp was used as the excitation light. A water filter was employed to remove IR irradiation from the Xe lamp. The measurement was performed at room temperature (about 20 °C). The temperature of the samples during illumination was monitored using an IR camera (NEC, TH9100 Pro), with a resolution of 0.02 °C.

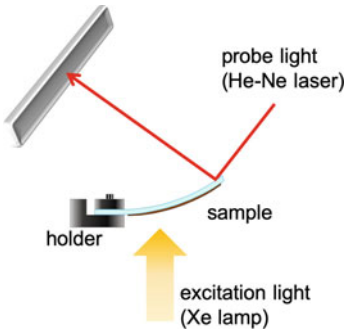

Fig. 13.3 Schematic image of a photoinduced deformation measurement

a-CN_x films in general exhibit a wide variety of bonding configurations through sp^1, sp^2, and sp^3 hybridizations. These various bonding states were determined using X-ray photoelectron spectroscopy (XPS), Fourier transform infrared spectroscopy (FTIR), and Raman spectroscopy.

13.3 Photoinduced Deformation of a-CN_x Films

13.3.1 Effects of Bonding States

The chemical bonding states found in a-CN_x are similar to those in a-C. In the sp^3 configuration, carbon forms four σ ′bonds with other carbon atoms, such as in diamond. The sp^2 configuration of carbon is found in aromatic rings and chain structures, e.g., graphite and polymers. The sp^1 configuration is rare in C–C bonding.

Several research groups have reported the bonding configuration of nitrogen in carbon nitrides [31–33]. Nitrogen forms three σ bonds, with the remaining two electrons in a lone pair. Nitrogen at a four-fold coordinated substitutional site, N_4^+, uses four electrons in σ bonds with the remaining unpaired electron available for doping. A variant of this site is the N_4^+-C_3^- pair [31]. The remaining configurations correspond to π bonds. Nitrogen can substitute carbon in aromatic rings. Thus, nitrogen is bonded to three neighbors in six-fold and a five-fold rings. The other variants of π bonding are double bond units, with nitrogen being two-fold coordinated. The triple bond with an isolated lone pair acts as a termination of the amorphous networks. A wide range of physical properties, including electrical and mechanical properties, determines the bonding configuration. For example, Silva et al.. [33] have shown that nitrogen only acts as a dopant in certain configurations. a-CN_x with high hardness exhibits a large fraction of sp^3 bonding. One of the predicted crystalline structures of carbon nitrides, β-C_3N_4, which is well known as a super hard material, is formed from only sp^3 C–N bonds [34].

The distribution of bonding configurations in a-CN_x films depends on the deposition conditions. Thus, we prepared 13 samples under various deposition conditions: Six samples grown at different temperatures RT to 600 °C, four samples grown at different RF powers from 50 to 170 W, and three samples grown at different gas pressures of 0.12, 0.50, and 0.80 Torr. In the present films, the nitrogen concentration and bonding configurations were estimated from XPS spectra and FTIR spectra, respectively, while the size of graphitic clusters was estimated from Raman spectra. It has been shown that the deposition temperature affects the growth of graphitic networks in carbon nitrides [35].

Due to normalization of the sample size and photon number, photoinduced stress was adopted as a metric in this study. First, the photoinduced stress, σ_p, was calculated from the photoinduced deformation, using the following equation [36]:

$$\sigma_p = \frac{E D^2 \delta_y}{3(1-\nu) L^2 d} \tag{1}$$

where d and D are the thicknesses of the films and the substrate, respectively. E and ν are the Young's modulus and Poisson ratio of the substrate, respectively. L is the distance from the free end of the sample to the PSD. Subsequently, the absorption coefficient of the films was considered in σ_p, because the optical bandgap is different in each film. The normalized photoinduced stress, $\sigma_p{}'$, was given by the following equation:

$$\sigma_p' = \sigma_p \times \int \alpha(\lambda) \mathrm{d}\lambda \tag{2}$$

where α is the absorption coefficient of the films and $h\upsilon$ is photon energy of the incident light.

Figure 13.4 shows normalized photoinduced stress ($\sigma_p{}'$) of all films. The resulting $\sigma_p{}'$ of the samples grown at different temperatures, RF powers, and gas pressures is shown by circles, triangles, and squares, respectively. Figure 13.4a shows $\sigma_p{}'$ depending on the nitrogen concentration (x = N/C) obtained from XPS spectra. $\sigma_p{}'$ increases up to $x = 0.5$, and then decreases. x decreases with increasing deposition

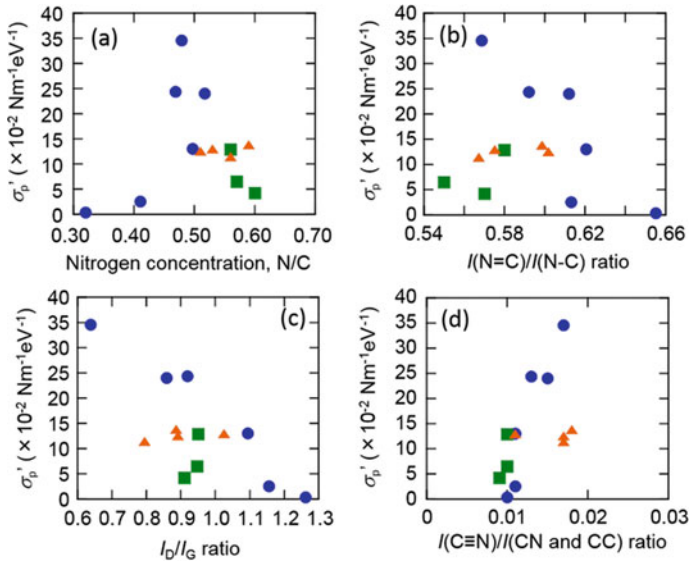

Fig. 13.4 Photoinduced stress ($\sigma_p{}'$) of a-CN_x films prepared under different deposition conditions as a function of **a** nitrogen concentration, **b** C=N/C–N bonding ratio obtained from XPS spectra, **c** intensity ratio of D and G peaks in Raman spectra, and **d** fraction of triple bonds obtained from FTIR spectra. The resulting $\sigma_p{}'$ of the films grown at different temperatures, RF powers, and N_2 gas pressures is shown by circles, triangles, and squares, respectively

temperature, as shown by circles in Fig. 13.4a. On the other hand, x increases and $\sigma_p{}'$ decreases with increasing gas pressure, as shown by squares in Fig. 13.4a.

From FTIR spectra, the intensity ratio between two peaks attributed to isonitrile and nitrile structures, which are centered at 2178 cm^{-1} and 2220 cm^{-1}, respectively, is proportional to the fraction of C≡N triple bonds in the sample [37]. These triple bonds act as a termination bond in amorphous networks. Single bonds (C–C and C–N) and double bonds (C=C and C=N) appear as a broad absorption band, between roughly 1000–1700 cm^{-1}. The intensity ratios of the peaks related to C≡N triple bonds to the broad-band related to single and double bonds for all samples are plotted in Fig. 13.4c. $\sigma_p{}'$ increases with the fraction of triple bonds in the amorphous network.

From Raman spectra, the I_D/I_G ratio, which correlates to the size of graphite clusters in the films, was obtained. The excitation light was an Ar^+ laser (532 nm). The I_D/I_G ratios were calculated from the intensity ratios of the D peak to the G peak in Raman spectra. The G peak is located at around 1584 cm^{-1} and reflects the bond-stretching mode of all pairs of sp^2 bonding including the structures of rings and chains. The D peak is located at around 1360 cm^{-1} and strongly reflects the breathing mode of six-fold rings [38, 39]. The Raman spectra were decomposed into the G and D peaks with a mixture of Gaussian–Lorentzian functions. As a result, the I_D/I_G ratio increases with increasing deposition temperature. This indicates that the size of graphite clusters in the a-CN_x films increases with increasing deposition temperature. On the other hand, the cluster size is less affected by the gas pressure and RF power. Figure 13.4d shows the dependence of $\sigma_p{}'$ on the I_D/I_G ratio; $\sigma_p{}'$ decreases with increasing I_D/I_G ratio. This means that large graphite clusters hinder photoinduced deformation.

With decreasing x and increasing graphitic components, the surface temperature of a-CN_x films under illumination increases. This is due to a decrease in optical bandgaps, i.e., an enhancement of photothermal conversion efficiencies [40]. On the other hand, the photoinduced deformation increases upto $x = 0.5$, then decreases depending on the graphite cluster size. Thus, the photoinduced deformation does not correspond exactly to the rate of increase in surface temperature caused by the irradiation. Consequently, the photoinduced deformation is mainly a direct response to light energy.

Although the mechanism of photoinduced deformation in a-CN_x films has not been elucidated yet, the existence of the C–N triple bonds is necessary for the displacement and small graphite cluster sizes play an important role for the displacement.

13.3.2 Effects of Substrate Materials

The photoinduced deformation is determined by the mechanical properties of substrate materials. In this section, the effects of substrate materials on photoinduced deformation are discussed.

Figure 13.5 shows the photomechanical responses of a-CN_x films deposited on

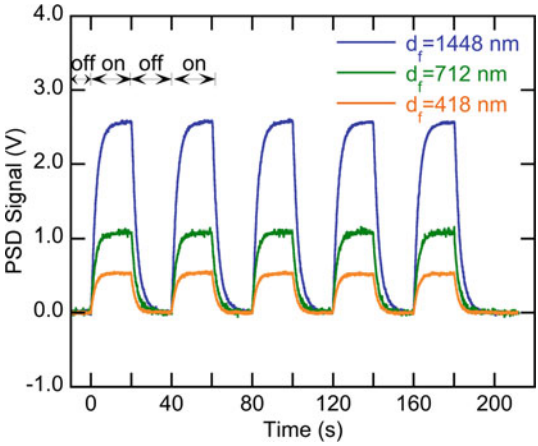

Fig. 13.5 PSD signal intensity variation of a-CN_x films of various thicknesses deposited on 0.05 mm-thick Si substrate. The a-CN_x film thicknesses (d_f) were 418, 712, and 1448 nm

0.05 mm-thick Si substrates. The a-CN_x films were deposited at 300 °C. The thicknesses of the films were 418, 712, and 1448 nm. A displacement of the free edge of the sample corresponds to the PSD signal intensity. The response coincidents with the light irradiation pattern. The maximum PSD signals increases linearly, along with increasing film thickness. If the substrate thickness decreases in an otherwise identical a-CN_x film, the photoinduced deformation drastically increases. In the present case, the limiting substrate thickness below which deformation can be observed is about 0.1 mm for Si. A rapid response can be obtained using thinner substrates [40].

The largest photoinduced deformation was observed in a-CN_x films deposited at 300 °C [41]. The deformation if an a-CN_x/SiO_2 specimen was found to be twice that of an a-CN_x/Si specimen, due to a difference in the mechanical properties of the substrate materials. By considering the mechanical properties of the substrate materials, the photoinduced stress σ_p of a-CN_x/SiO_2 and a-CN_x/Si were calculated from the deformation to be 23.2 MPa and 18.0 MPa, respectively. This difference in σ_p is due to the difference thermal diffusion coefficients of the Si and SiO_2 substrates. The photoinduced deformation increases by about 1.3% per 1 °C due to thermal effects [41].

Understandably, macroscopic response has been observed in a-CN_x films deposited on a flexible substrate, such as a polymer film and cellulose nanopaper [26]. Figure 13.6 shows a ring made from an a-CN_x film deposited at RT on cellulose nanopaper. The a-CN_x film moves to the outside of the ring. Upon irradiation with a He–Ne laser ($\lambda = 633$ nm), the ring opens owing to the photoinduced deformation of the a-CN_x film.

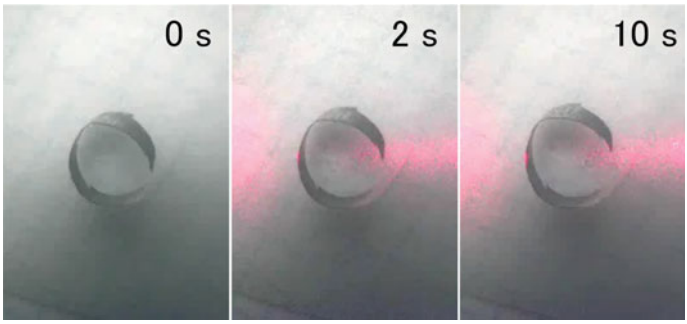

Fig. 13.6 Ring-opening motion of an a-CN_x film deposited on cellulose nanopaper. The film is outside the ring and is illuminated by He–Ne laser light from the left side

13.3.3 Stability of Photoinduced Deformation

As mentioned in the introduction, organic molecules that show photoinduced deformation would be decomposed by long-term light exposure. For inorganic materials such as hydrogenated amorphous silicon (a-Si:H) films and chalcogenide glasses, an increase in the defect density caused by light irradiation has been reported [21, 42, 43]. Therefore, we investigated the photoinduced deformation of a-CN_x films under irradiation.

To investigate the stability of photoinduced deformation, a-CN_x films were deposited at 300 °C, and then irradiated with pulsed excitation light. The pules period (frequency) was 60 s (0.017 Hz), while the total irradiation time was about 60 min. Figure 13.7 [44] shows some of the experimental results for an a-CN_x/SiO_2 specimen under pulsed white-light irradiation. The variability of the bending response was less than 1% and the bending of the a-CN_x/SiO_2 specimen could be repeated at least 120 times. Furthermore, delamination and cracking of the film were not observed. The shapes of N 1 s and C 1 s XPS spectra of a-CN_x films before and after light irradiation seemed to be the same, that is, the bonding states were hardly changed. The N/C

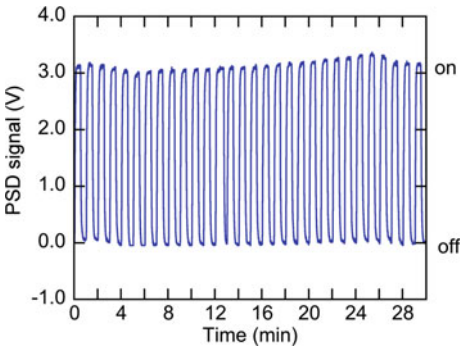

Fig. 13.7 PSD signal intensity variation for an a-CN_x/SiO_2 specimen under pulsed white-light irradiation

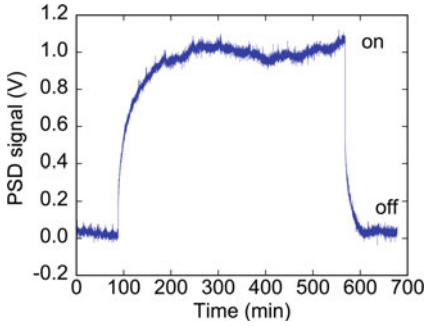

Fig. 13.8 PSD signal intensity variation for an a-CN_x/SiO_2 specimen under continuous white-light irradiation for 500 min

ratios, which were 0.54 and 0.52, respectively, were also almost the same before and after light irradiations.

The reversible response was confirmed in a long-term irradiation test carried out for 500 min, as shown in Fig. 13.8. The effect of thermal drift was removed in this data. The range of PSD signal intensity in the long-term irradiation test (Fig. 13.8) was three times lower than that in the pulsed irradiation test (Fig. 13.7), which is due to a difference in the distance between the PSD and the specimen in both tests. The chemical bonding states were not significantly changed by irradiation. In addition, as evidenced by electron spin resonance (ESR) results, no increase in the defect density of the a-CN_x films was observed after white-light irradiation for long periods of time. This long-term stable performance of a-CN_x films is one of their advantages for application as light-driven microactuators.

13.4 Light-Driven Pump Using a-CN_x Films

A light-driven pump was fabricated by coating a-CN_x on a SiO_2 substrate with a thickness of 10 μm. The diaphragm using a SiO_2 substrate was labeled as device-I. Because a large photoinduced motion is obtained from the pump, poly(ethylenenaphthalate) films (PEN films) were also used as a substrate. PEN films have excellent plasma resistance, thus, the films have been widely used as substrates of transparent conducting thin films deposited by sputtering.[45–47]. The thicknesses of PEN films used here were about 12 and 25 μm. The diaphragms using these two films were labeled as device-II and -III, respectively. The body of the pump, except the diaphragm, was made of quartz glass. The hole was 5 mm in diameter and 50 μm in depth, as shown in Fig. 13.9a. A semiconductor laser was used to provide irradiation at a wavelength of 375 nm. A schematic image of the measurement system is shown in Fig. 13..

A pumping motion was implemented for all of the diaphragms. The films were deposited at RT, which is lower than the glass transition temperature of the PEN films [45]. Figure 13.10 shows the displacement of the center of the diaphragm in device-I

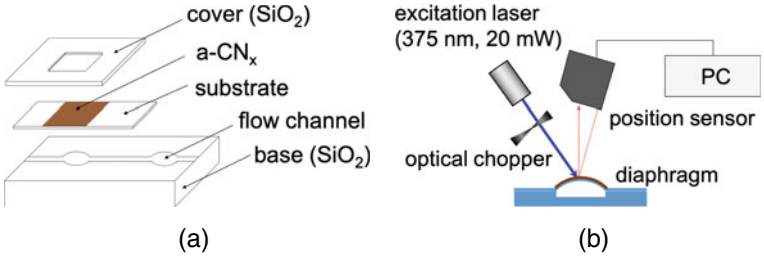

Fig. 13.9 Schematic image of a light-driven pump using an a-CN_x diaphragm (**a**) and the associated measurement apparatus (**b**). The body of the pump, except the diaphragm, was made of quartz glass. The hole was 5 mm in diameter and 50 μm in depth

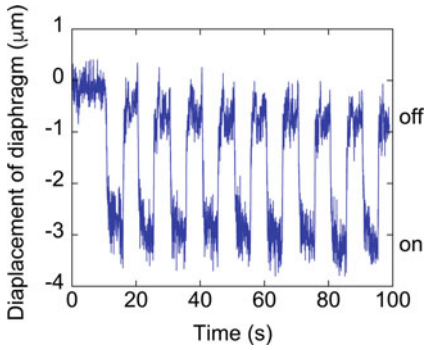

Fig. 13.10 Pumping motion of a-CN_x diaphragms. The films were deposited on a SiO_2 substrate (10 μm) and PEN films (12 and 25 μm) at RT

irradiated with a frequency of 0.1 Hz. The fluctuation of the diaphragm coincides with the light irradiation pattern.

Figure 13.11 shows the dependence of the displacement amplitude on the chopping frequency of the light. The pumping action in all devices was limited to below 10 Hz. This frequency limit is due to the design of the pump, i.e., the diaphragms were probably not fixed well on the body of the pump. The displacement of the diaphragm in device-I was lower than those in device-II and -III for frequencies up

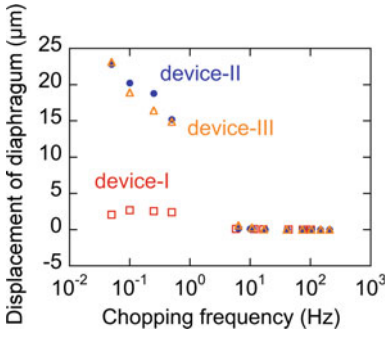

Fig. 13.11 Dependence of the displacement of a-CN_x diaphragms on the chopping frequency of the light

to 1 Hz. Compared with device-I, the displacement of the diaphragm in device-II was 5 times larger at 0.05 Hz.

13.5 Conclusions

Amorphous carbon nitrides are a class of carbon materials with fascinating properties. In this study, we examined the photomechanical response of hydrogen-free amorphous carbon nitride (a-CN_x) films deposited by reactive sputtering.

The maximum deformation was achieved in the films with a relatively high nitrogen concentration and small graphite cluster size. Thus, the existence of C–N bonds is necessary for photoinduced deformation and the graphite cluster size also plays an important role. In addition, the photoinduced deformation is determined by the mechanical properties of the substrate material. Based on the long-term irradiation test results, no photodegradation was observed in a-CN_x films deposited on substrates.

Finally, light-driven pumps were fabricated using a-CN_x deposited on PEN and SiO_2 substrates, while the pumping motion was observed at light chopping frequencies up to 10 Hz.

Acknowledgements This work was supported by JSPS KAKENHI Grant Number 18H01715 and 26790054. A part of this work was performed under the Cooperative Research Program of "Network Joint Research Center for Materials and Devices." The authors would like to thank Dr. Hisashi Miyazaki and Dr. Hiroaki Kishimura in National Defense Academy for fruitful discussions regarding the electrical states in a-CN_x films. PEN films were provided by Teijin DuPont Films Japan Ltd.

References

1. W.S. Chan, M.J. Saarinen, J.J. Talghader, Appl. Phys. Lett. **102**, 243508 (2013)
2. H.-H. Yang, C.-H. Han, J.O. Lee, J.-B. Yoon, J. Micromech. Microeng. **24**, 065012 (2014)
3. W.-M. Zhang, H. Yan, Z.-K. Peng, G. Meng, Sens. Actuators A **214**, 187 (2014)
4. J. Ma, Y. Hu, J. Chen, Y. Cui, X. Xu, J. Chu, Sens. Actuators A **230**, 45 (2015)
5. K.H. Koh, T. Kobayashi, J. Xie, A. Yu, C. Lee, J. Micromech. Microeng. **21**, 075001 (2011)
6. B. Kavčič, D. Babič, N. Osterman, B. Podobnik, I. Poberaj, Appl. Phys. Lett. **95**, 023504 (2009)
7. Y.-P. Hsieh, Z.-H. Wei, M.-C. Yip, Jpn. J. Appl. Phys. **50**, 087202 (2011)
8. R. Cabrera, E. Merced, N. Sepúlveda, J. Microelectromech. Syst. **23**, 243 (2014)
9. X. Wang, D. Xiao, X. Wu, Z. Hou, Z. Chen, Appl. Phys. Lett. **103**, 151902 (2013)
10. M. Yamada, M. Kondo, R. Miyasato, Y. Naka, J. Mamiya, M. Kinoshita, A. Shishido, Y. Yu, C.J. Barrettc, T. Ikeda, J. Mater. Chem. **19**, 60 (2009)
11. K.G. Yager, C.J. Barret, J. Photochem. Photobiol. A **182**, 250 (2006)
12. C.J. Barrett, J. Mamiya, K.G. Yager, T. Ikeda, Soft Matter **3**, 1249 (2007)
13. J. Cviklinski, A.R. Tajbakhsh, E.M. Terentjev, Eur. Phys. J. E **9**, 427 (2002)
14. C.P. McCoy, L. Donnelly, D.S. Jones, S.P. Gorman, Tetrahedron Lett. **48**, 657 (2007)

15. F. Benito-Lopez, R. Byrne, A.M. Răduţă, N.E. Vrana, G. McGuinness, D. Diamond, Lab Chip **10**, 195 (2010)
16. J. ter Schiphorst, S. Coleman, J.E. Stumpel, A. Ben Azouz, D. Diamond, A.P.H.J. Schenning, Chem. Mater. **27**, 5925 (2015)
17. W. Francis, A. Dunne, C. Delaney, L. Florea, D. Diamond, Sens. Actuat. B **250**, 608 (2017)
18. Q. Luo, Z. Luo, L. Tong, Mech. Res. Commun. **38**, 198 (2011)
19. X.J. Wang, J.H. Huang, J. Wang, Smart Mater. Struct. **24**, 075017 (2015)
20. N. Mamedov, K. Wakita, Y. Shim, K. Abe, N. Ogushi, Thin Solid Films **517**, 1434 (2008)
21. K. Tanaka, Phys. Rev. B **57**, 5163 (1998)
22. S.V. Ahir, E.M. Terentjev, Nat. Mater. **4**, 491 (2005)
23. X. Zhang, Z. Yu, C. Wang, D. Zarrouk, J.-W.T. Seo, J.C. Cheng, A.D. Buchan, K. Takei, Y. Zhao, J.W. Ager, J. Zhang, M. Hettick, M.C. Hersam, A.P. Pisano, R.S. Fearing, A. Javey, Nat. Commun. **5**, 2983 (2014)
24. M. Aono, T. Harata, N. Kitazawa, Y. Watanabe, Diamond Relat. Mater. **41**, 20 (2014)
25. M. Aono, S. Nitta, T. Katsuno, T. Iuchi, J. Vac. Sci. Technol. B **18**, 1773 (2000)
26. M. Nogi, S. Iwamoto, A.N. Nakagaito, H. Yano, Adv. Mater. **21**, 1595 (2009)
27. S. Kundoo, K.K. Chattopadhyay, A.N. Banerjee, S.K. Nandy, Vacuum **69**, 495 (2003)
28. M. Othman, R. Ritikos, N.H. Khanis, N.M.A. Rashid, S.M. Ab Gani, S.A. Rahman, Thin Solid Films **529**, 439 (2013) 439
29. D. Dumitriu, P.E. Schmid, R. Sanjinés, A. Karimi, Diamond Relat. Mater. **11**, 1905 (2002)
30. N. Tamura, M. Aono, T. Harata, H. Kishimura, N. Kitazawa, Y. Watanabe, Jpn. J. Appl. Phys. **53**, 02BC03 (2014)
31. S.E. Rodil, Recent Res. Dev. Appl. Phys. **6**, 391 (2003)
32. S. Bhattacharyya, C. Cardinaud, G. Turban, J. Appl. Phys. **83**, 4491 (1998)
33. S.R.P. Silva, J. Robertson, G.A.J. Amaratunga, B. Refferty, L.M. Brown, J. Schwan, D.F. Franceschini, G. Mariotto, J. Appl. Phys. **81**, 2626 (1997)
34. A.Y. Liu, M.L. Cohen, Phys. Rev. B **41**, 10727 (1990)
35. M. Therasse, M. Benlahsen, Solid State Commun. **129**, 139 (2004)
36. D.T. Smith, Thin-Film Deposition (McGraw-Hill, Inc., 1995), pp. 189–193
37. N. Mutsukura, K. Akita, Thin Solid Films **349**, 115 (1999)
38. A.C. Ferrari, J. Robertson, Phys. Rev. B **61**, 14095 (2000)
39. A.C. Ferrari, Diamond Relat. Mater. **11**, 1053 (2002)
40. M. Aono, T. Harata, N. Kitazawa, Y. Watanabe, Jpn. J. Appl. Phys. **55**, 01AA03 (2016)
41. T. Harata, M. Aono, N. Kitazawa, Y. Watanabe, Appl. Phys. Lett. **105**, 051905 (2014)
42. K. Morigaki, Jpn. J. Appl. Phys. **28**, L2128 (1989)
43. T. Gotoh, S. Nonomura, M. Nishio, N. Masui, S. Nitta, M. Kondo, A. Matsuda, J. Non-Cryst, Solids **227–230**, 263 (1998)
44. T. Harata, M. Aono, H. Miyazaki, N. Kitazawa, Y. Watanabe, Diamond Relat. Mater. **63**, 132 (2016)
45. E.L. Bedia, S. Murakami, T. Kitade, S. Kohjuya, Polymer **42**, 7299 (2001)
46. J.-M. Kim, P. Thiyagarajan, S.-W. Rhee, Thin Solid Films **518**, 5860 (2010)
47. H. Shen, H. Zhang, L. Lu, F. Jiang, C. Yang, Prog. Nat. Sci. Mater. Int. **20**, 44 (2010)

Chapter 14
Nanostructured Carbon-Based Electrode Materials for Supercapacitor Applications

Katlego Makgopa, Letlhogonolo F. Mabena, Cheslin G. Brink, Given N. Chauke, Malesela D. Teffu, Kwena D. Modibane, and Mpitloane J. Hato

14.1 Introduction

The environmental concerns accompanied by extreme air pollution and climate change, oil crisis that began as far as 1973, as well as the limited availability of fossil fuels have greatly affected the world's economy and ecology [1, 2]. Recent technological developments and increasing concern over the sustainability and environmental impact of conventional fuel usage have motivated nations, governments, technology providers, and academic societies to strive for the prospect of producing clean, sustainable power in substantial quantities from renewable energy sources [3]. Renewable energy often provides energy in four important areas: electricity generation, air and water heating/cooling, transportation and rural (off-grid) energy services. As much as renewable energy resources (illustrated in Fig. 14.1a) show to be the escalating solution towards the uprising cruelty to the environment, a key obstacle in renewables is the technical difficulties of electricity storage and transmission [4, 5]. It has been projected that with proper intensive research progress and long-term research plan, by the year 2040, there should be a proper infrastructure concerning the use of renewable energy (illustrated in Fig. 14.1b). Hence, the market

K. Makgopa (✉) · L. F. Mabena · C. G. Brink · G. N. Chauke
Department of Chemistry, Faculty of Science, Tshwane University of Technology (Acardia Campus), Pretoria 0001, South Africa
e-mail: makgopak@tut.ac.za

M. D. Teffu · K. D. Modibane (✉) · M. J. Hato (✉)
Department of Chemistry, School of Physical and Mineral Sciences, University of Limpopo (Turfloop), Polokwane, Sovenga 0727, South Africa
e-mail: kwena.modibane@ul.ac.za

M. J. Hato
e-mail: mpitloane.hato@ul.ac

S. Kaneko et al. (eds.), *Carbon Related Materials*,
https://doi.org/10.1007/978-981-15-7610-2_14

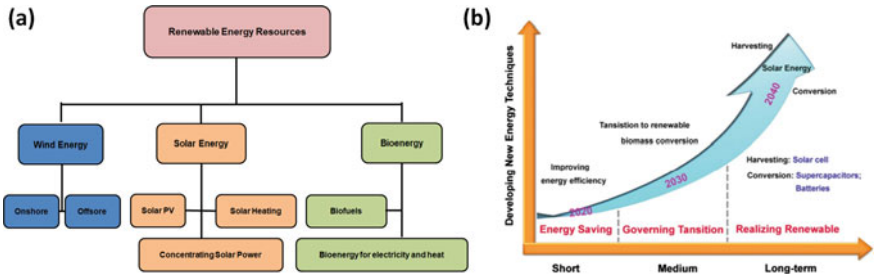

Fig. 14.1 **a** Overview of renewable energy sources and **b** indicative roadmap of future energy scenario [6]

for energy storage applications becomes an integrated critical component in clean energy development and sustainability.

Electrochemical energy storage systems (EES) have gained much attention as a valuable proposition for improving the reliability and overall use of the advantages of renewable energy resources [7]. Thus far, electrochemical energy storages (EES) in the form of batteries and supercapacitors (SCs) are widely used for powering the now-global portable electronics in our society and for the electrification of the transportation sector (i.e. hybrid electric vehicles, HEVs). Therefore, in considering a reliable, stable, and sustainable large-scale use of renewables, supercapacitors (SCs), and batteries have to play a fundamental role in advanced and highly efficient energy storage and management. Lithium-ion batteries (LIBs) are known to store a large amount of energy as high as 150 Wh kg^{-1}, but are confined to their low power density (below 1.0 kW kg^{-1}) and poor cycle life (usually less than 1000 cycles) [7, 8]. As compared to batteries, electrochemical capacitors (ECs) vastly known as supercapacitors (SCs) have demonstrated to be the competing measures with regards to storing energy output that can be delivered at a faster rate without the loss of the device efficiency [9]. SCs have enjoyed the benefits of being utilized as a mediator that bridge the gap between conventional capacitors (that display great power output but limited energy storage output) and batteries (with great energy storage output but limited power deliverance). Due to the abovementioned characteristics, SCs are a preferred electrochemical energy storage device of choice in a range of applications that requires uninterrupted ultra-power output. The advantages of SCs arise from their energy storage mechanism, which involves physical storage of energy through dielectric polarization or electric double layer of ions and electrons as proposed by Helmholtz model and further confirmed by the well-known Stern model (that describes the electrode/electrolyte interface (surface phenomenon)). Fundamentally, there are two types of charge storage mechanisms involved in SCs, viz: (i) "electrochemical double-layer capacitors" (EDLCs) that use carbonaceous materials as the main electrode materials for SCs [7, 10] and (ii) "pseudocapacitors" (PCs) that use metal oxides or conducting polymers as the main electrode materials for SCs [11, 12]. The operation mechanism of the EDLC involves the non-Faradaic separation of charges at the "double-layer" (i.e. electrode/electrolyte interface), best described

by the Helmholtz and Stern models as shown in Fig. 14.2, while PCs involves fast Faradaic, redox reaction of electroactive materials at the electrode/electrolyte interface [7, 13]. As much as the two-mentioned storage mechanisms of SCs have been classically known for this type of EES device, the third storage mechanism known for the "hybrid-supercacitors" (HSCs) has been discovered in order to improve the performance of the SC device. In hybrid-supercacitors (HSCs), the storage mechanisms resulting from the EDLCs and the PCs are combined, where both the non-Faradaic separation of charges and the fast Faradaic, redox reaction of electroactive materials at the electrode/electrolyte interface occurs simultaneously.

The performance comparison of various energy storage devices is known as Ragone plot as shown in Fig. 14.3. The plot shows the power and energy densities comparison of various energy storage and conversion devices. From the Ragone plot, it can be seen that batteries usually exhibit higher energy densities as compared

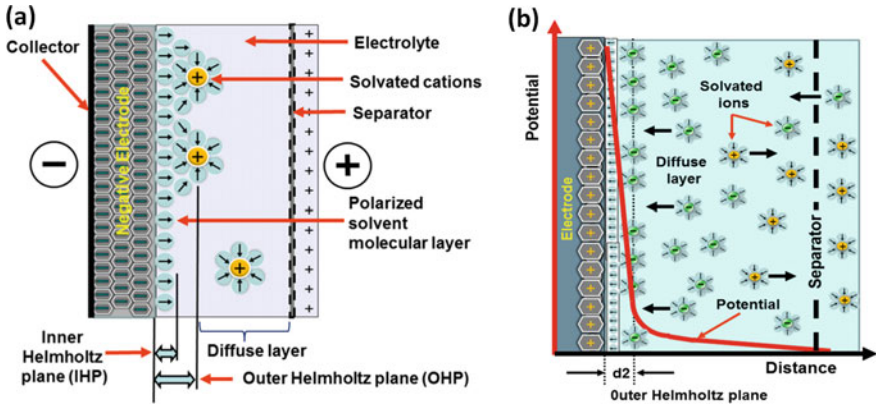

Fig. 14.2 Overview of **a** energy storage mechanism of the SCs electrode/electrolyte interface and **b** the potential distribution in a Helmholtz double-layer

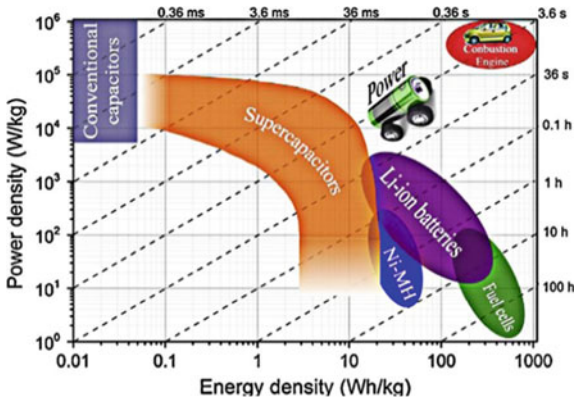

Fig. 14.3 Ragone plots for various electrochemical energy storage systems

to SCs while suffering from low power densities. On the other hand, SCs display greater power densities with lower energy densities as compared to batteries. In most cases, the electrode materials used in EDLCs are carbon materials such as activated carbons, graphene, onion-like carbons, and carbon nanotubes while PCs use redox-active materials such as polymeric complexes such as polyaniline, polypyrrole, and poly(3,4-ethylenedioxythiophene) and metal oxides such as ruthernium oxide, manganese oxide. Hybrid capacitors (HCs) incorporate the EDLC and PC materials that results in the use of the synergy between non-Faradaic and Faradaic storage mechanisms. The hybrid capacitors are thought to give the next generation of high-performance supercapacitor devices due to the enhanced energy storage obtained by these devices [14, 15].

Most packaged SCs devices are two-terminal systems and can be either symmetric or asymmetric depending on the arrangement of the electrodes. The former involves two similar electrodes (i.e. material type, thickness, mass, etc.) sandwich together, whereas the latter is made of two electrodes with different electrode materials and compositions. In most cases, carbon materials such as activated carbon are used as the negative electrode while polymeric complexes and metal oxides or the composites as positive electrode. Under these conditions, of course, an overall evaluation of the *two-electrode* system (without the utilization of a reference electrode) is obtained while providing vital electrochemical information such as energy densities and power densities that are not easily obtainable using data collected at individual electrodes in *three-electrode* cells (reference electrode included). Nevertheless, many researchers still opt for the *three-electrode* system, since its measurements allow one to have fundamental informative on the behaviour of the electrode of an SCs device [16].

14.1.1 Energy Storage Mechanisms in EDLCs

The construction of SCs is similar to that of batteries in the sense that they consist of two electrodes immersed in an electrolyte, with an ion permeable separator located between the electrodes [17]. SCs based on electrochemical double-layer capacitance (EDLC) are electrical energy storage devices that store and release energy by nanoscopic charge separation at the electrochemical interface between an electrode and an electrolyte. The electrostatic charge storing allows reversible ion adsorption from the electrolyte onto active material that is electrochemically stable and has a high surface area [18, 19]. Charge separation occurs upon polarization at the electrode–electrolyte interface producing the double-layer capacitance. Helmholtz first defined this energy storage mechanism in 1879 as shown in Fig. 14.4a. Gouy and Chapman later modified the Helmholtz model upon the extensive consideration of a continuous distribution of cations and anions in the electrolyte solution which is driven by thermal motion referred to as the diffuse layer (see Fig. 14.4b). Later, Stern combined the Helmholtz model with the Gouy–Chapman model that showed two regions of ion distribution: the inner region called the compact layer or Stern layer and the outer region called the diffuse layer (see Fig. 14.4c) [7, 16].

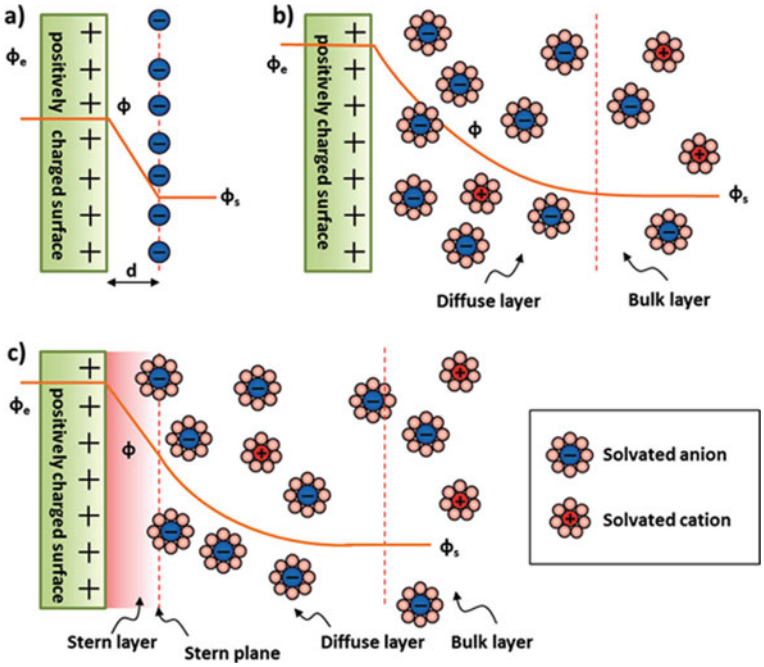

Fig. 14.4 Models of the electrical double layer at a positively charged surface in the aqueous electrolyte: **a** the Helmholtz model, **b** the Gouy–Chapman model, and **c** the Stern model [7]

Several factors that the Helmholtz model (i.e. the diffusion of ions in the solution and the interaction between the dipole moment of the solvent and the electrode) and Gouy–Chapman model (i.e. it is insufficiency for highly charged double layers) could not take into account led to Stern's discovery of his model. The two layers in Stern model are equivalent to two capacitors in series (i.e. C_H (Helmholtz layer) and C_D (diffuse layer)) and from these two layers; the total capacitance of the electrode (C_{DL}) can be calculated using the following equation:

$$\frac{1}{C_{DL}} = \frac{1}{C_H} + \frac{1}{C_D} \tag{14.1}$$

Determination of EDL capacitive performance of the electrode is influenced by the following factors: (i) the electric field across the electrode, (ii) types of the electrolyte ions, (iii) solvent in which the electrolyte are dissolved in, and (iv) the chemical affinity between the adsorbed ions and electrode surface. By applying an electric potential difference between the electrodes in the EDLC, the positive charge carriers, protons, in the positively polarized electrode are balanced by an equal number of negative anions at the electrode/electrolyte interface, while cations electrically balance the holes stored in the negatively polarized electrode. Since there are no redox reactions taking place at the EDLC electrodes due to the electrostatic

charge storage, this mechanism allows very fast energy uptake and delivery interpreted as high power performance. Also, this energy storage mechanism also allows for a large amount of cycling due to the reversibility of the process. However, as a consequence of the electrostatic surface charging the mechanism of the EDLC suffer from a limited energy density [20–23].

14.1.2 Energy Storage in Pseudocapacitors (PCs)

Pseudocapacitors differ from the EDLCs by the means of its energy storage mechanism, where it makes use of some electro-sorption processes, fast redox reactions on the surface of the electrodes with the electrolytes and intercalation of ions through a porous electrode material. In contrast to the double-layer capacitance generated from the potential dependence of surface density and electrostatically (non-Faradaic) storing of charges, pseudo-capacitance arises from thermodynamic conditions and is due to charge acceptance (q) and voltage change (V). The accumulation of electrons on the surface of the electrode is due to the Faradaic process where the electrons produced transferred across the electrode–electrolyte interface [16, 24, 25]. This process is similar to the charging and discharging processes that occur in batteries [26]. Three distinguished Faradaic processes happen in pseudocapacitors, namely reversible adsorption of electrons (adsorption–desorption), redox reactions of transition metal oxides, and reversible electrochemical doping and un-doping of polymer-based electrodes [16, 27]. Electron adsorption–desorption pseudocapacitance results from a reversible process where ions are deposited on the surface of the electrode, creating a monolayer that gives rise to Faradaic charge transfer. Some of the psudocapacitive electrode materials such as manganese-based SCs have been highlighted from the literature [12].

14.1.3 Energy Storage in Hybrid Capacitors (HCs)

The other two relevant parameters of a capacitor apart from the capacitance are its energy and power densities discussed in detail in the coming sections. Since EDLCs gives such a high-power output as compared to the pseudocapacitors while the latter is capable of high energy output, a high energy and high power density at high rates are not simultaneously achievable by either one of the two storage mechanism (i.e. EDLCs or pseudocapacitors). Therefore, to achieve high performance, hybrid capacitors integrate both energy storage mechanisms of the two stated mechanisms in their operation synergistically. Hybrid capacitors utilize both the Faradaic and non-Faradaic processes to store charges [27–29]. Hybrid capacitors are recognizable in three classes, namely composite, asymmetric, and battery-type hybrids [30]. These types of capacitors are tailored to meet the following requirements for a high-performance ECs, namely good electron conductivity, highly accessible specific

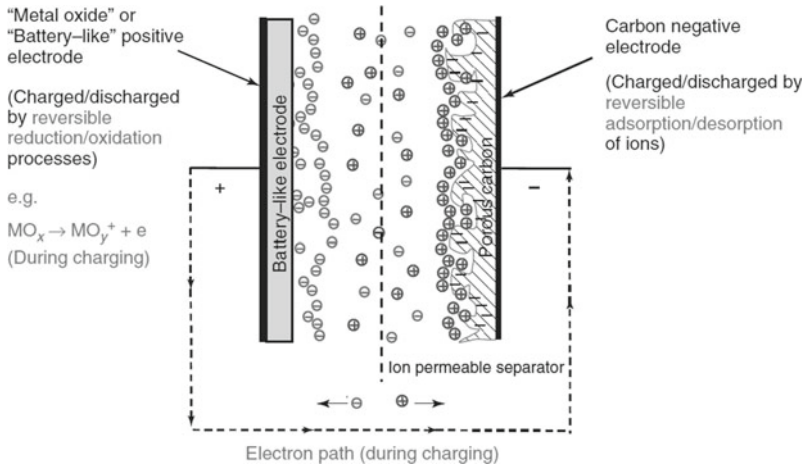

Fig. 14.5 Schematic representation of a charged asymmetric or battery-like electrochemical capacitor [23]

surface area, and efficient mass transport [27]. The most common design of the hybrid capacitor typically consists of a battery-type electrode (e.g. a faradic or intercalating metal oxide) and an EDLC-type electrode (high surface area carbon) as represented schematically in Fig. 14.5.

14.2 Evaluation of Electrochemical Energy Storage Performance in SCs

As explained above, the concepts of an electrochemical capacitor is derived from the EDLCs that consist of two porous electrode materials which are in direct contact with the current collector and separated by a porous separator impregnated with an electrolyte solution. These two porous electrodes of the SCs are equivalent to two capacitors connected in series as illustrated in both Helmholtz and Stern models. The resulting capacitance (C) obtained after polarization of electrodes by applying potential difference (voltage) between them can be expressed according to the following equation:

$$\frac{1}{C_{\text{cell}}} = \frac{1}{C_+} + \frac{1}{C_-} \tag{14.2}$$

where C_{cell}, C_+, and C_- are the capacitance (in Farad = Coulomb/Volt) of the resulting device or cell, of the positive electrode, and of the negative electrode, respectively. The capacitance (C_{cell}) evaluated from the cyclic voltammetry (CV) as well as from the slope of the discharge curve of the galvanostatic charge–discharge

(GCD) profile is obtained by using Eq. (14.3).

$$C_{\text{cell}}\,(\text{F}) = \frac{i}{\Delta V/\Delta t} \tag{14.3}$$

where i (A) is the applied current, $\Delta V/\Delta t$ (V s^{-1}) the slope of the discharge curve after the initial iR drop. In a symmetrical system where the two electrodes (positive and negative electrode) are similar with similar morphological and electronic properties ($C_+ = C_-$), the cell capacitance (C_{cell}), from Eq. (14.2), will therefore be defined according to the following equations:

$$C_{\text{cell}} = \frac{C_{\text{e}}}{2} \tag{14.4}$$

where $C_{\text{e}} = C_+ = C_-$.

From Eq. (14.4), the electrode capacitance is calculated using the following equation:

$$C_{\text{e}} = 2C_{\text{cell}} \tag{14.5}$$

For better comparison between different electrode materials of SCs devices, it is a common practice to provide a specific capacitance, which is related to the capacitance of one single electrode, $C_{\text{e,sp}}$ (F g^{-1}). Hence, dividing Eq. (14.5) by the mass of the single electrode, Eq. (14.6) is used to calculate the specific capacitance:

$$C_{\text{e,sp}}\left(\text{F g}^{-1}\right) = \frac{2C_{\text{cell}}}{m_{\text{e}}} \tag{14.6}$$

where $C_{\text{e,sp}}$ is the measured specific capacitance of each electrode in F g^{-1} (C_{e}/m), and m_{e} (g) is the mass of the single electrode.

The value of a single electrode derived from a *three-electrode* (half-cell) measurement will be higher than the actual cell capacitance obtained from a *two-electrode* (full-cell) measurement.

For a symmetric cell, the specific (gravimetric) capacitance of the two electrodes (C_{sp}) is given by:

$$C_{\text{sp}}\left(\text{F g}^{-1}\right) = \frac{4C_{\text{cell}}}{M} \tag{14.7}$$

where M is the total mass of the active materials of the two electrodes (i.e. $M = 2m_{\text{e}}$ since the weight of each electrode is the same). The multiplier of 4 only adjusts the capacitance of the cell and the combined weight of two electrodes to the capacitance and mass of a single electrode [22, 31].

The other two relevant parameters of a capacitor apart from the C_{sp} are its energy and power density [32]. The energy (E) stored in a capacitor is related to the charge

(Q) at each interface and the potential difference between the two plates. Therefore, energy is directly proportional to the capacitance as shown by the following equation:

$$E_{\mathrm{sp}}\left(\mathrm{Wh\,kg^{-1}}\right) = \frac{C_{\mathrm{cell}}V^2}{2M} \tag{14.8}$$

where M (kg) is the mass of the ECs and V (V) is the maximum voltage of electrochemical stability. The maximum power of the device is calculated using the following equation:

$$P_{\mathrm{max}}\left(\mathrm{W\,kg^{-1}}\right) = \frac{V^2}{4R_{\mathrm{s}}M} \tag{14.9}$$

The internal resistance R_{s} is calculated from the voltage drop at the beginning of a discharge curve and is shown by the following equation:

$$R_{\mathrm{s}}\,(\Omega) = \frac{\Delta V_{\mathrm{IR}}}{2i} \tag{14.10}$$

where ΔV_{IR} is the voltage drop between the first two points from the start of the discharge curve.

For the evaluation of an asymmetric cell, Eqs. (14.2)–(14.10) are used; nonetheless, before they are implemented to the asymmetric cell, the "*mass-balancing*" from the *three-electrode* experiment should be performed by acquiring the electrochemical performance for each electrode. In the symmetric supercapacitor, the applied voltage is split equally between the two electrodes due to the use of the same material having the same composition in each electrode. However, in the asymmetric supercapacitors, the voltage split is dependent on the capacitance of the active material in each electrode of the two electrodes. The capacitance is usually related to the mass and the measured specific capacitance of the active material [33]. Thus, to split voltage equally, the mass balance between the two electrodes must be optimized using the following relationship: $q_+ = q_-$, where q_+ means the charges stored at the positive electrode and q_- means the charges stored at the negative electrode. The following equation is used to express the stored charge:

$$q = C_{\mathrm{sp}} \cdot m \cdot \Delta V \tag{14.11}$$

or:

$$\frac{m_+}{m_-} = \frac{C_{\mathrm{sp}_-}}{C_{\mathrm{sp}_+}} \times \frac{\Delta V_-}{\Delta V_+} \tag{14.12}$$

where m, C_{sp} and ΔV represent the mass, specific capacitance, and potential range obtained from the charging/discharging process of three-electrode configuration of the individual positive and negative electrode, respectively.

14.3 Carbon-Based Electrode Materials for SC Applications

Tremendous progress made in nanoscience and nanotechnology brought inspiration for further development of technologies in electrochemical energy storage, which has made nanostructured materials an increasingly important approach for electrochemical energy storage such as SCs [34, 35]. Due to the intrinsic properties that occur at the electrode/electrolyte interface of a SC device, the understanding of materials used for fabricating the device is of great importance especially for the enhancement of the electrochemical performance of the device. A critical aspect of nanotechnology in SCs, is to reach a compromise between specific surface area (to ensure high capacitance) and pore-size distribution (to permit easy access for the electrolyte) in order to develop a highly effective SC device that can be used in wider applications [36]. Nanomaterials that have the length scale in the order of 2–100 nm have received special interest due to their scientific impact as well as their impending applications that is derived from their intriguing electrical, magnetic and catalytic properties [37, 38]. As compared to the bulk active electrode materials, the nanomaterials display more excellent electrochemical activity, such as greater capacitance, larger surface areas owing to their high surface area to volume ratio and relatively good conductivity. Hence, nanomaterials have vast potential application in the electrochemistry field. The most widely used active electrode materials in SCs are carbon nanomaterials, transition metal oxides and conducting polymers. This chapter is intended to explore the carbon nanomaterials as the main focus for the development of EDLCs.

Carbon is one of the most abundantly available and structurally diverse materials and is the choice material for several industrial applications. Most current commercial EDLCs employ porous carbons as the active electrode material. The intensive use of this material is due to its excellent properties such as its higher specific surface area (~2000 $m^2\ g^{-1}$), non-toxicity, high chemical stability, natural abundance, and its excellent electronic conductivity. Carbon nanomaterials comprise a wide range of allotropic forms and carbon and occur in various micro-textures including more or less ordered structure due to the degree of graphitization and a variety of dimensionality from 0 to 3D. There are also different forms of carbon such as powders, fibres, foams, fabrics.

Various array of carbon allotropes which have been explored and used in electrochemical energy storage systems (SCs) include onions-like carbon (OLC), carbon nanotubes (CNT), activated carbon (AC), carbide-derived carbon (CDC), graphene, graphene oxide, and templated carbons. These carbons are characterized as either porous or nonporous materials. Porous carbons (i.e. AC, CDC, and templated carbon) are characterized by high specific surface area (SSA) and pore volumes. These properties often lead to high gravimetric and volumetric capacitances in electrochemical capacitors. In contrast, nonporous carbons (i.e. carbon nanotubes (CNT), graphene, carbon black (CB), and onions-like carbon (OLC) have displayed limited inner porosities [18, 25, 39–42]. Although nonporous carbons may lack the specific surface area (SSA) compared to their porous counterparts (except single-layer graphene or

SWCNTs), they have shown to possess high conductivities due to high degree of graphitization. This chapter focusses on four types of carbon allotropes (i.e. activated carbon (AC), carbon nanotubes (CNTs), graphene and onion-like carbons (OLCs)), and their application in SCs.

14.3.1 Activated Carbons (ACs)

In supercapacitor, electrodes are typically made of high surface area activated carbons with micropores (<2 nm), mesopores (2–50 nm), and macropores (>50 nm). The process employed to increase carbon surface area and porosity from a carbonized organic precursor is referred to as "activation" . The resulting group of these materials is referred to as activated carbons (AC). Activated carbon can be manufactured from various carbonaceous raw materials such as coal, coconut shell, apricot shell, pines wood through carbonization and activation of organic molecules. Figure 14.6 displays some of the synthetic route used in the synthesis of activated carbon from various precursors. A developed specific surface area of greater than 2000 $m^2\ g^{-1}$, including a controlled distribution of pores during the activation process, can be reached during carbon activation [43]. Activation opens up the pores in carbon precursor, thus creating additional porosity which results in an improved surface area. A control over the resulting porosity together with pore-size distribution is manipulated by varying the carbon precursor and activation conditions (i.e. temperature, gaseous environment, and time). Two well-known general categories of carbon activation include thermal activation (also referred to as physical activation) and chemical activation [44].

Thermal activation of carbon precursor requires controlled gasification, generally at temperatures that are between 700 and 1100 °C in the presence of suitable oxidizing agents that are gases such as carbon dioxide (CO_2), steam, air, or even mixtures of these gases [47]. The oxidizing atmosphere, during gasification process, is the one responsible for an increased pore volume and surface area of the carbon precursor as it creates carbon "burn-off" while also eliminating volatile pyrolysis products. An increased burn-off of the carbon precursor yields a high degree of activation. Nevertheless, the extent of carbon activation can also be achieved by the additional activity resulting from a decrease in carbon strength, reduced yield, lower density, and the widening of pores. The second category, chemical activation, is different from the thermal activation by the fact that it is usually carried out at temperatures that are slightly lower (~400–700 °C) [48]. Chemical activation also involves certain chemical agents such as phosphoric acid (H_2PO_4), zinc chloride ($ZnCl_2$), and potassium hydroxide (KOH) to achieve dehydration. In this type of activation, post-activation washing of the carbon product is usually required to remove residual reactants as well as any inorganic contaminant that originates from the carbon precursor (or the ones introduced during activation). Activated carbons with exceptionally high surface area materials (>2500 $m^2\ g^{-1}$) were prepared and reported in the literature [49]. Figure 14.7 shows the morphological and spectroscopic characterization of the

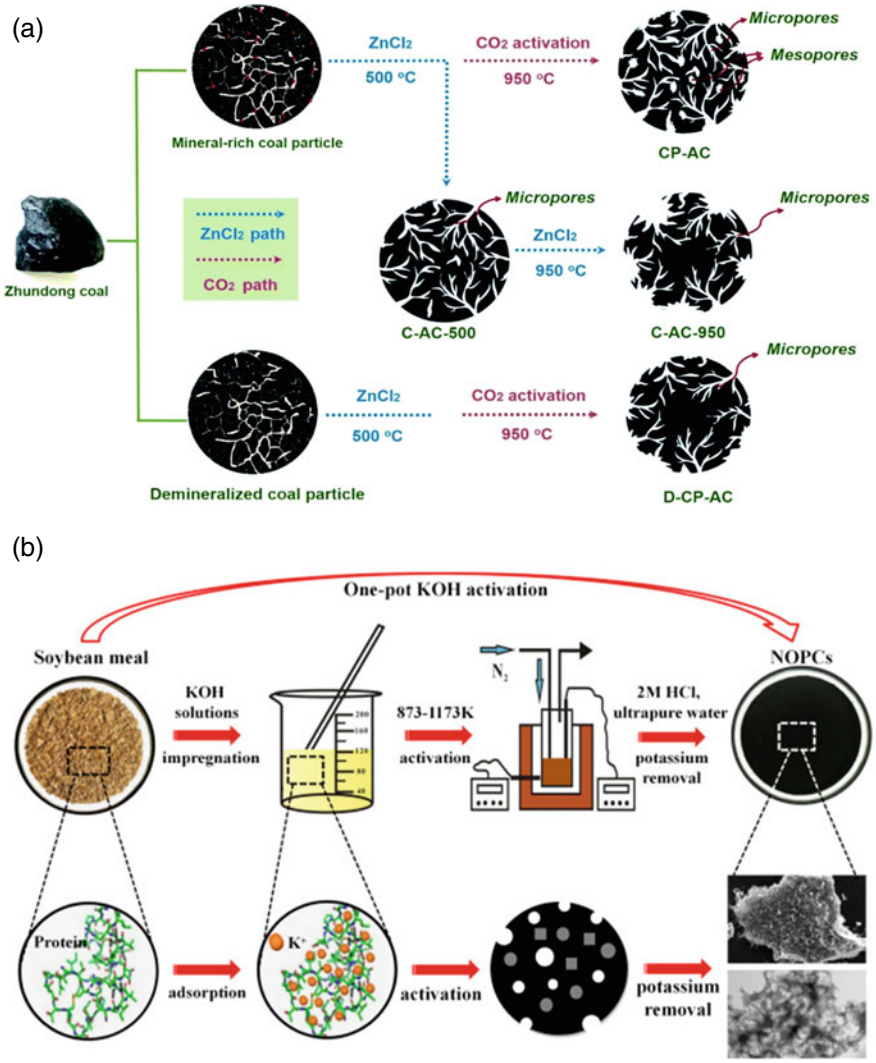

Fig. 14.6 Synthetic route of AC from **a** coal [45] and **b** pine cone [46]

as-prepared NOPC-SD-x.

There are several studies on activated carbons (ACs) as the electrode materials for the EDLCs due to its high surface area. This type of carbon material can be readily obtained commercially or synthesized in the laboratory for various research activities. In 2003, Lozano-Castelló et al. reported a specific capacitance as high as 220 F g^{-1} from a KOH-activated carbon with a large surface area more than 2000 m^2 g^{-1} in a three-electrode system [49]. Yuan et al. at around 2005 successfully incorporated nanometre-scale amorphous particles of NiO on activated carbon to synthesize

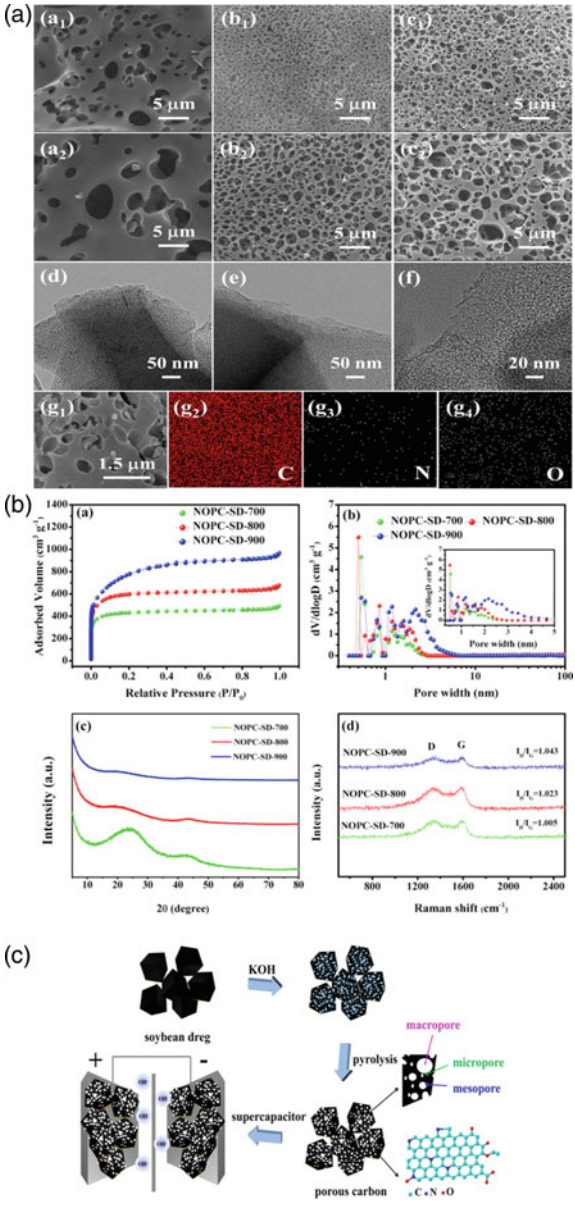

Fig. 14.7 A representation of a **a** SEM images of (a_1, a_2) NOPC-SD-700, (b_1, b_2) NOPC-SD-800, (c_1, c_2) NOPC-SD-900; TEM images of (d, e, f) NOPC-SD-800 at different magnifications; and mapping of (g_1, g_2, g_3, g_4) of NOPC-SD-800, **b** nitrogen adsorption/desorption isotherms, (b) pore-ize distributions, (c) XRD patterns and (d) Raman spectra for NOPC-SD-x, **c** schematic illustration of NOPC-SD-x prepared from soybean dreg [50]

NiO/AC nanohybrid that exhibited specific capacitance value of about 194 F g^{-1} [51]. In 2010, Xu et al. showed that the use of apricot shell as a carbon source can significantly improve supercapacitive performance of EDLCs with maximum specific capacitance of about 339 F g^{-1} [52]. As much as the information arising

from calculating maximum specific capacitance is of great importance, other critical parameters in SC are energy density and power density. In order to improve the energy density of the capacitive electrode materials, one of the factors that needs to be altered is the cell voltage where the electrolyte solution is electrochemically stable. In most cell fabrication of a SC device, mostly organic or ionic liquid is used. Nevertheless, these electrolytes come with the environmental concerns during disposal, thus making an aqueous electrolyte the sole choice when safety is considered. One of the effective ways to increase cell voltage is by developing an asymmetric SCs, which consist of a battery-type Faradic electrode (as energy source) and a capacitor-type electrode (as power source) while not deviating from the use of aqueous electrolyte. In 2010, a high voltage symmetric carbon/carbon SC device was built using a Na_2SO_4 as aqueous electrolyte solution. The device displayed an excellent cycle life during thousands of cycles with maximum voltage value as high as 1.6 V. The desired voltage was due to the fact that the potential of the positive electrode is beyond the oxidation potential of water, thus AC being the one oxidized [53]. In 2015, Rodento et al. prepared activated carbons made by the chemical activation of natural renewable and olive pits from the olive oil displaying an effect if temperature on the supercapacitive performance. The gravimetric capacitance increased from 176 to 218 F g^{-1} when increasing the activation temperature to 800 °C [54]. By the year 2016, nitrogen was used as a dopant to form N-doped AC for supercapacitor application.

The N-AC electrode material exhibited an improved electrochemical performance with maximum specific capacitance of 185 F g^{-1} and the capacitance retention of 86% [55]. Later, Mao et al. demonstrated the effect of co-doping between nitrogen and oxygen on the energy storage capability of AC [56]. The huge-surface area functionalized carbons (HSAFCs) electrode material contained a substantial oxygen and nitrogen content and exhibited specific capacitances of 474 F g^{-1} at 0.5 A g^{-1} and 285 F g^{-1} at 100 A g^{-1} in an aqueous 2 M KOH solution. The electrode also displayed the energy density of 24.4 Wh kg^{-1} at 223 W kg^{-1} and 7.3 Wh kg^{-1} at 9.4 W kg^{-1} and cyclability of 93% capacitance retention after 10,000 cycles [56]. Furthermore, a high-content nitrogen (1.58 at.%) and oxygen (11.41 at.%)-activated carbon electrode material were studied as shown in Fig. 14.8. As a result, the N/O co-doped hierarchical porous carbon derived from waste soybean dregs displays a superior specific capacitance of 321.1 F g^{-1} at the current density of 1 A g^{-1}, high rate capability of 249.7 F g^{-1} at 30 A g^{-1} and excellent cycling durability of 99.5% at 1 A g^{-1} after 10,000 cycles using 6 M KOH electrolyte. An excellent energy density that reach as high as 22.1 Wh kg^{-1} at the power density of 875.0 W kg^{-1} in two-electrode system using $EMIMBF_4$ electrolyte.

14.3.2 Carbon Nanotubes (CNTs)

Carbon nanotubes (CNTs) are one of carbon allotropes made of the cylindrical nanostructure of carbon molecules with novel properties that make them useful in a wide variety of applications in the field of nanotechnology, electronics, optics, and other

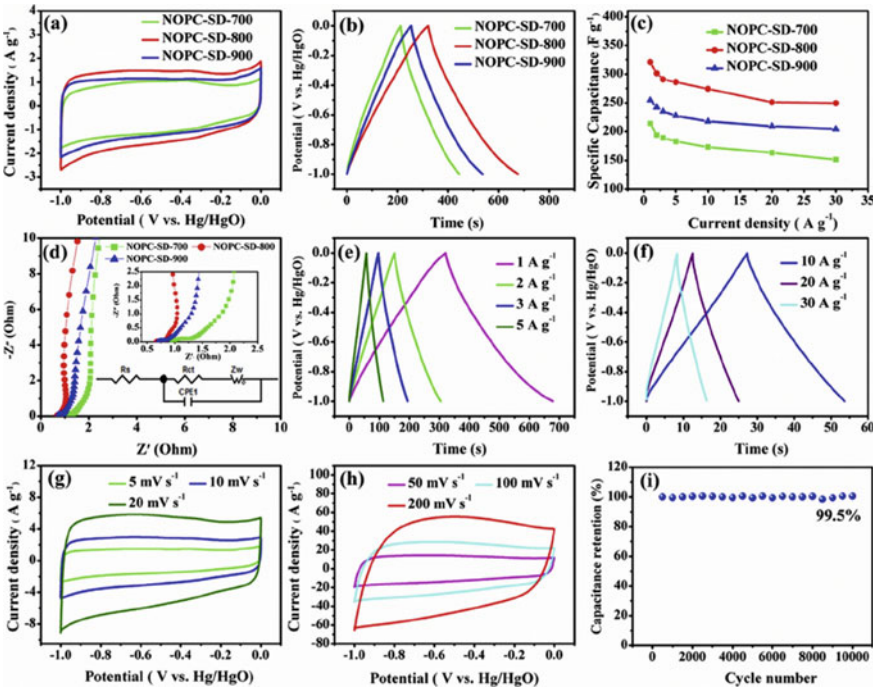

Fig. 14.8 Electrochemical properties of NOPC-SD-x measured in three-electrode system using 6 M KOH solution: **a** CV curves of NOPC-SD-x at a scanning rate of 5 mV s^{-1}; **b** GCD curves of NOPC-SD-x at a current density of 1 A g^{-1}; **c** specific capacitance of NOPC-SD-x at different current densities from 1 to 30 A g^{-1}; **d** Nyquist plots; **e**, **f** GCD curves of NOPC-SD-800 at current density from 1 to 30 A g^{-1}; **g**, **h** CV curves of NOPC-SD-800 at different scan rates from 5 to 200 mV s^{-1}; and **i** cyclic stability of NOPC-SD-800 for 10,000 cycles at current density of 1 A g^{-1} [50]

fields of material science. They are sp^2 hybridized form of carbon atoms made from graphene/graphite sheets that are rolled into cylindrical shaped seamless tubes and capped at the end with fullerene-type hemispheres. There are two main types of CNTs with high structural perfection, namely single-walled carbon nanotubes (SWCNTs) and multi-walled carbon nanotubes (MWCNTs). In essence, SWCNTs are strips of a single-layer graphene sheet that is rolled around a hollow central core forming a tube-like structure with a nanoscale diameter (~1 nm), whereas MWCNTs are made up of two or more layers of graphene sheet rolled up in a similar fashion as SWCNTs. The discovery of carbon nanotubes (CNTs) dates back to 1950s though the theory was not clear at that time. In 1991, Sumio Iijima of NEC reported multi-walled CNTs synthesized from a carbon arc discharge, and two years later at around 1993, Sumio Iijima and Donald Bethume (from IBM) worked independently and found single-walled CNTs [57, 58]. Carbon nanotubes (CNTs) can be classified by the manner in which the graphitic backbone consisting of the sp^2 carbon atoms is

rolled and be described by the two indices (n, m) in a shorthand notation. The properties of the CNTs depend on the atomic arrangement, the diameter and length of the tubes and the morphology. The atomic structure of CNTs is described using the tube chirality (or helicity) and the angle of chirality. The chirality angle measures the extent of the twist within the tube [59]. Various synthetic methods used to synthesize CNTs are illustrated in Fig. 14.9. The chirality angle property results in the single-walled CNT being able to be differentiated into zig-zag and armchair as shown in Fig. 14.9b. Regarding the roll-up vector, the zig-zag carbon nanotube is described as (n, 0) and the armchair carbon nanotube as (n, n). Carbon nanotubes have been widely synthesized using various techniques such as arc discharge [57], laser ablation [60], high-pressure carbon monoxide disproportionation [61] and chemical vapour deposition (CVD) [62]. Carbon nanotubes can be functionalized at the surfaces with functional groups such as carboxylic acid (–COOH) and sulphonic acid (–SO_3H) to give functionalized carbon nanotubes (f-CNTs where f = –COOH or (–SO_3H)) [63].

The tubular structures of CNTs can be clearly seen under both scanning and transmission electron microscope. Figure 14.10A–D shows the morphological and spectroscopic characterization of the synthesized carbon nanotubes with Fig. 14.10D representing (a) FTIR, (b) Raman, (c) optical image indicating the dispersion and (d) XRD, of pristine CNTs and functionalized CNTs. The FTIR spectra of showed a peak at ~1636 cm^{-1} corresponding to the stretching vibrations of the carbon–carbon double bonds (i.e. –C=C– bond stretch). The appearance of an additional peak in functionalised CNTs at ~1742 cm^{-1} (–C=O stretch) and reduction in relative intensity of –C=C– stretch peak differentiate between the pristine CNT to the functionalised CNT and thus confirms the successful oxidation and introduction of carboxylic acid (i.e. –COOH) groups on CNTs backbone. Also, the difference between the pristine CNT can be observed on Raman spectra analysis (Fig. 14.10D (b)), which shows that the I_D/I_G ratio is significantly higher for functionalised CNTs as compared to the pristine CNTs indicating that large number of defects have been introduced upon functionalization. Hence, there is great dispersion of CNTs (Fig. 14.10D (c)) polar solvent such as water. By XRD peak analysis (Fig. 14.10D (d)), the effect of functionalisation can be revealed by observing any peak shift. In this case, the structure remained unaffected by functionalization [66].

Owed to its intrinsic properties fine-tuned, CNT has found its path as the energy storage electrode material in SCs application [67, 68]. By the year 1999, already work was done on CNT, and its electrochemical capacitive performance reported [69]. Frackowiak et al. reported on the pure electrostatic attraction of ions of a pure multi-walled CNT as well as quick pseudo-Faradaic reactions on the functionalized multi-walled CNT, detected upon varying surface functionality of the CNT. The specific capacitance values obtained varied from 4 to 135 F g^{-1} (depending on the type of nanotubes and their post treatments) [70]. In 2005, Du et al. reported a thin film formed using multi-walled CNTs. This electrode material displayed a high packing density and local alignment with an electrical double-layer performance that remained almost rectangular CV at a high scan rate of 1000 mV s^{-1}. This performance led to fast rate capability with a high specific power density of about 30 kW kg^{-1}

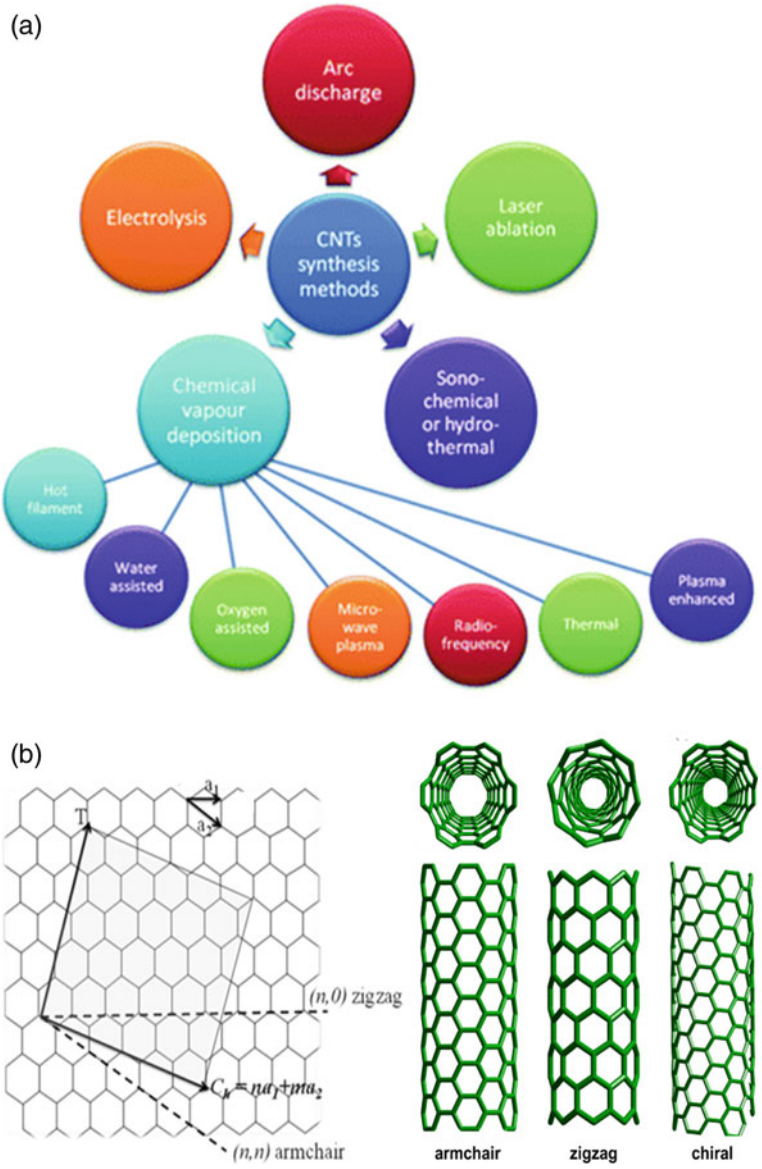

Fig. 14.9 Representation of **a** currently used methods for CNTs synthesis [64], **b** graphene sheet rolled up to show different chirality of the single-walled CNTs, **c** functionalization of CNTs [65]

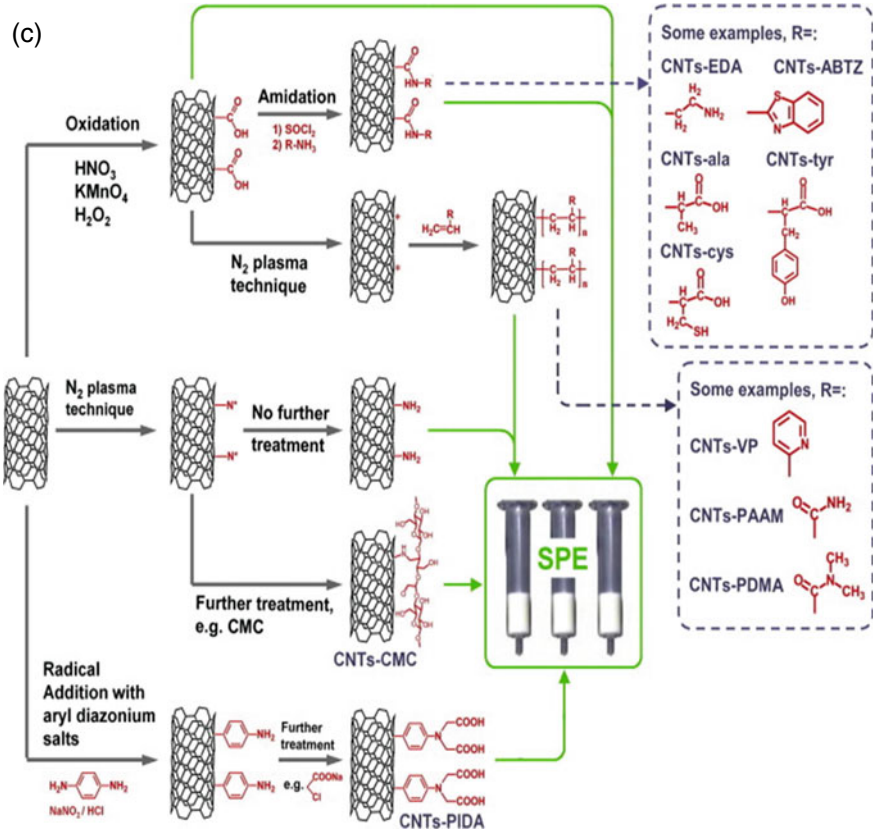

Fig. 14.9 (continued)

[71]. The tremendous performance of CNT as SCs electrode material continued with time without any disappointment, and by the year 2010, Izadi-Najafabadi and co-workers designed a high energy and power performance SCs by operating at the higher voltage range of 4 V in organic electrolyte using single-walled CNT. Their results were a consequence of the combination of high surface area and electrochemical doping that enabled them to achieve an improved specific capacitance around 160 F g^{-1} while simultaneously enhancing the specific energy density to more than 50 Wh kg^{-1} [72]. Due to the good conductivity of CNTs, these nanomaterials have been employed in several fabrications of composites with other potential electrode materials for SCs applications. In 2014, the experimental results by Li et al. indicated that the incorporation of metal oxides with CNTs results in an improved pseudocapacitive performance. The CNT/MnO_2 composite displayed high specific capacitance of 201 F g^{-1}. The assembling of an asymmetric electrochemical capacitor using the CNT/MnO_2 composite as positive electrode and activated carbon (AC) as negative electrode demonstrated that the as-prepared electrode can cycle reversibly in a

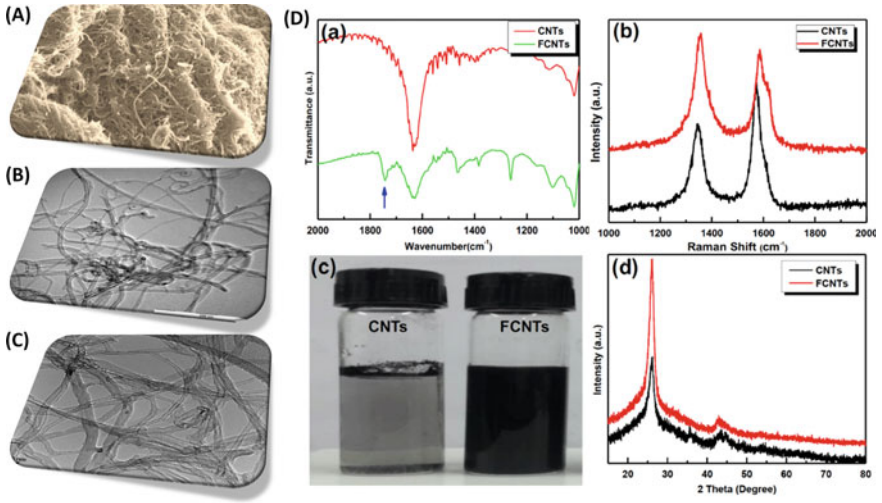

Fig. 14.10 Representation of **A** SEM, **B** low and **C** high magnification TEM, images of CNTs. **D** Representation of (a) FTIR, (b) Raman, (c) optical image indicating the dispersion, and (d) XRD, of pristine CNTs and functionalized CNTs

voltage of 0–1.5 V and give a high energy density of 13.3 Wh kg^{-1} at a power density of 600 W kg^{-1} [73]. To increase the potential use of CNT in SCs, the electrochemical enhancement method followed by annealing at different temperatures in air to add and adjust the redox-active functional groups on freestanding CNT films was explored. The method resulted in functionalized freestanding CNT films, which were used as positive electrodes, and assembled with freestanding CNT/MoO_{3-x} as negative electrodes to fabricate carbon nanotube-based solid-state asymmetric supercapacitors (ASCs) as shown Fig. 14.11. The device displayed excellent electrochemical performance with a high volumetric capacitance of 3.0 F cm^{-3}, energy and power density of 1.5 mWh cm^{-3} and 4.2 W cm^{-3}, respectively [74].

Zhang et al. reported on the development of a high-performance composite electrode material made of hierarchical, porous interlaced ultra-thin Zn and Ni co-substituted Co carbonate hydroxides (ZnNiCo-CHs) nanosheets branched on N-doped CNT arrays (titled: C@ZnNiCo-CHs) grown directly on a nickel foam current collector [75]. The main feature in their work is that the mesoporous and large open spaces of the interlaced ultra-thin ZnNiCo-CHs nanosheets provided a more active sites for redox reactions that facilitated fast mass transport whereas the self-standing N-doped CNT arrays offered a large surface area that also promoted fast electron transport, thus enhancing the stability. The device displayed a high energy density of 70.9 Wh kg^{-1} at a power density of 966 W kg^{-1} while maintaining a capacity retention of 91% after 20,000 cycles at 20 A g^{-1} when fabricated in a two-electrode asymmetric system with C@ZnNiCo-CHs as positive electrode and an N-, S co-doped rGOs as a negative electrode [75]. Recently, Yang et al. demonstrated the effect

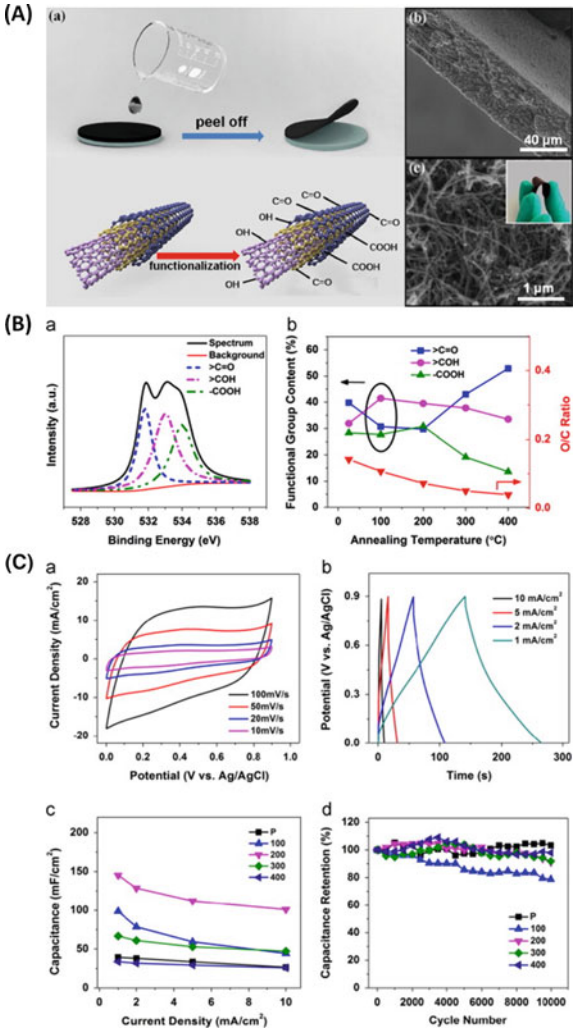

Fig. 14.11 **A** Representation of (a) fabrication procedure, (b) SEM image, (c) enlarged cros section SEM image of the functionalized freestanding CNT films. **B** (a) XPS spectrum of sample 200. (b) O/C ratio and functional groups content for sample with and without annealing. **C** The electrochemical performance of the ASC device. (a) CV scans at rates from 10 to 100 mV/s. (b) Galvanostatic charge/discharge curves. (c) Volumetric capacitance versus current density. (d) Ragone plot of the ASC device compared with other solid-state devices. (e) Nyquist plot and (f) cycle life [74]

of combining the properties of two carbon allotropes to form a freestanding electrode material that exhibits an improved electrochemical performance using CNT and rGO [76]. The freestanding carbon nanotubes/reduced graphene oxides (CNTs/rGO) hybrid films were synthesized via the simple vacuum filtration and thermal reduction methods and its electrochemical properties investigated in KOH and in Et_4NBF_4/AN electrolyte, respectively. The CNTs/rGO hybrid films displayed a maximum specific capacitance of 221 F g^{-1}, a 71% capacitance retention, and an excellent cycle life in 1 M KOH electrolyte and 174 F g^{-1} and good rate capability in Et_4NBF_4/AN

electrolyte, under three-electrode systems. Upon fabricating the freestanding electrode to design a symmetric supercapacitor (CNTs/rGO//CNTs/rGO), the device demonstrated a maximum specific capacitance of 24 F g^{-1} at a high current density of 1 A g^{-1}, also showed a promising energy density of 20.8 Wh kg^{-1} at a power density of 1.27 kW kg^{-1}, and an excellent cycle life of 86.1% capacitance retention after 5000 cycles [76]. All the findings proved that the use of CNT-based materials can generate suitable electrodes for fast energy storage, which may be applicable to creating an efficient and robust electrode materials for other energy-related devices.

14.3.3 Graphene and Graphene Oxide

Graphene is one-atom-thick, two-dimensional (2D), sp^2 hybridized allotrope of carbon with its atoms arranged in a honeycomb crystal lattice that has a hexagonal pattern (see Fig. 14.12a) which possess a broad range of extraordinary properties [77]. There are many theoretical reports on graphene but in 2004 Geim and Novoselov, for the first time isolated a one-atom-thick crystallites from the bulk graphite and this outstanding work saw them winning the prestigious award, Nobel Price, in 2010 [78, 79]. Since then, graphene has emerged as one of the most exciting material for research in the last few years [80]. The extraordinary properties of graphene include a high theoretical specific surface area (2630 m^2 g^{-1}), high Young's modulus (~1 TPa) entailing strong mechanical strength [81]. Several methods have been developed for the synthesis of graphene, such as mechanical exfoliation of graphite, chemical vapour deposition (CVD), unzipping of carbon nanotubes, also through reduction of graphene oxide, etc. (see Fig. 14.12b) [82]. Amongst those various methods, the chemical method via reduction of graphene oxide (see Fig. 14.12c) has been considered since it provides a scalable approach to synthesizing graphene and has been widely utilized to synthesize chemically derived graphene also known as reduced graphene oxide (rGO) [83]. The chemical method involves the oxidation of graphite, to graphene oxide (GO) using the Hummers method [84] or the modified Hummers method [17] then after, the obtained GO is then reduced using reducing agents such as hydrazine solution, sodium borohydride ($NaBH_4$), or any other reducing agents [85, 86].

Kim et al. showed how the porosity and interlayers of graphene can be manipulated to produce a porous functionalised graphene and reduced graphene oxide (rGO). Figure 14.13A shows SEM images of the functionalized graphene and reduced graphene oxide with their respective TEM images. The GO was synthesized chemically via the modified Hummers method and annealed at moderate temperature to produce functionalized graphene, whereas reduced graphene oxide was prepared by annealing GO at high temperature (~800 °C). Both materials displayed similar porous morphology, as indicated by FE-SEM and HRTEM analyses (see Fig. 14.13A). The reduced graphene oxide displayed minimal functional groups as compared to functionalised graphene. A structural elucidation of graphene can be observed and be compared with other carbon allotropes using various spectroscopic techniques as

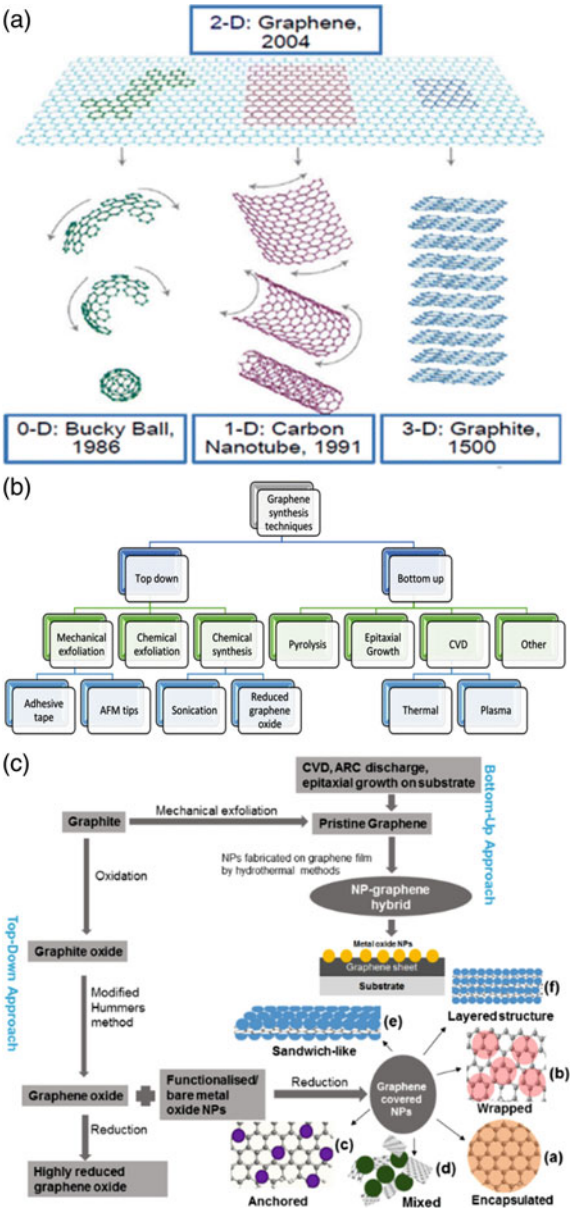

Fig. 14.12 **a** Mother of all graphene forms. Graphene is a 2D building material for carbon material of all other dimensionalities. It can be wrapped up into 0D buckyballs, rolled into 1D nanotubes or stacked into 3D graphite. **b** A process flow chart of Graphene synthesis [87]. **c** Methods used for the formation of graphene–NP hybrids and different structures of (a) graphene-encapsulated NPs, (b) graphene-wrapped NPs, (c) NPs anchored to GSs, (d) mixed graphene–NP structures, (e) graphene–NP sandwich structures, and (f) graphene–NP layered hybrids [88]

shown in Fig. 14.13B–E. Similar to most carbon allotropes, few-layer graphene (estimated number of layers: 2–3), display the D and G bands at 1360 and 1580 cm^{-1}, respectively. To investigate the amount of structural defect and disorder of graphenated materials, the intensity ratio of D band over G band (I_D/I_G) is used. For the

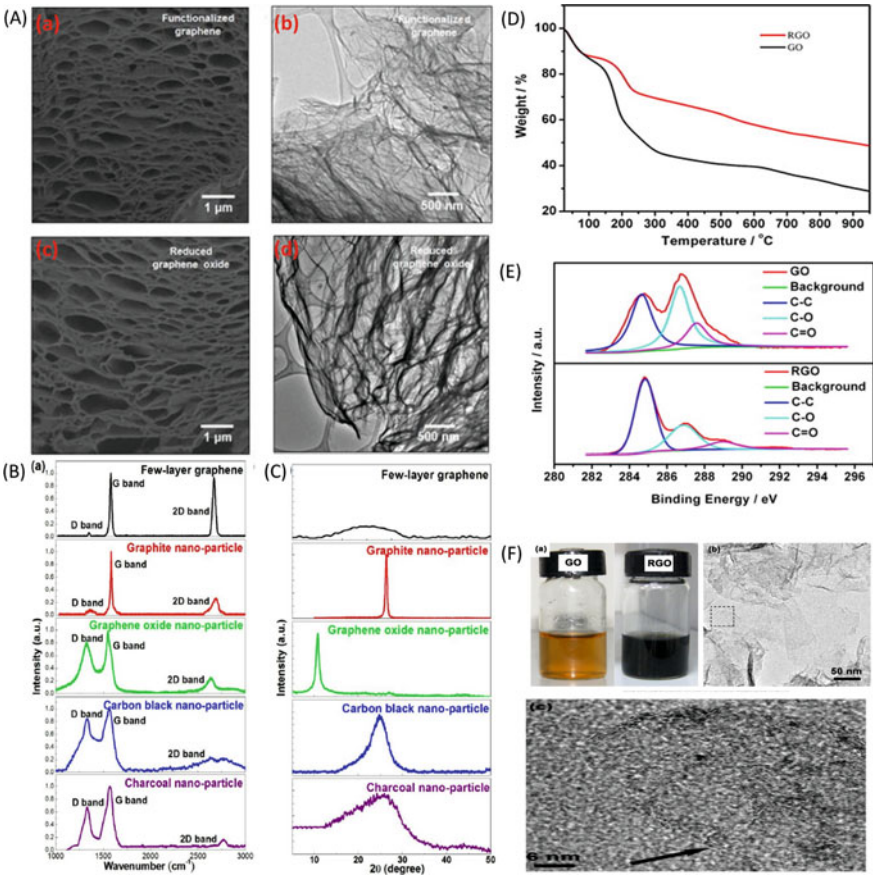

Fig. 14.13 **A** Images (a) and (b) are FE-SEM and HRTEM images of the functionalized graphene, respectively. Images (c) and (d) are FE-SEM and HRTEM images of the reduced graphene oxide, respectively [90]. **B** The Raman scattering spectra and **C** the XRD spectra of few-layer graphene, graphite nano-particle, graphene oxide nano-particle, carbon black nano-particle, and charcoal nano-particle [89]. **D** TGA, **E** XPS of GO and rGO **F** (a) photographs of GO and rGO dispersed in water, (b) TEM and (c) HRTEM image of rGO [33]

few-layer graphene, Kim et al. found the I_D/I_G value of 0.06 and also using the 2D band observed at 2670 cm^{-1} which showed an intensity ratio of I_{2D}/I_G of 0.9.

Those values were compared to the values observed from graphite nano-particles and graphene oxide nano-particles having the I_D/I_G value of 0.08 and 0.8, respective. The Raman spectra of both carbon black and charcoal nano-particles displayed the relatively broad G bands indicating the amorphous graphite phase (see Fig. 14.13B). Kim et al. used XRD in order to show the crystallinity of the carbon-based materials as shown in Fig. 14.13C. The observed results complemented very well with the results from the Raman spectroscopy. They showed expected graphitic peaks observed both in oxidized and non-oxidized carbon backbone [89]. The stability and

the carbon connectivity were well observed from the results obtained in TGA and XPS, respectively, as shown in Fig. 14.13D–E. The design of such porous electrode structures is expected to be advantageous for electrochemical reactions, because they enable greater penetration of the electrolyte into the interior of the electroactive materials [33]. Figure 14.13F shows variations in dispersion of GO and rGO dispersed in water, (b) TEM, and (c) HRTEM image of rGO.

Due to the high theoretical specific surface area, graphene has found attention as a potential electrode material for SCs application [33, 91, 92]. However, graphene sheet has a high tendency of restacking during electrode formation due to strong π−π interactions between neighbouring layers. This interaction leads to a significant decrease in the surface area, consequently resulting in lower specific capacitance values. Several measures such as decoration of graphene sheets with pseudocapacitive materials (i.e. transition metal oxides and conducting polymers) and functionalization of graphene (with chemical moieties such as carbonyl and hydroxyl groups) that ultimately prevents the restacking of graphene has been employed [52, 93]. The advantage of the above approach is that the surface area of graphene can be maximally accessed, thus improving the specific capacitance through the non-Faradaic contribution of graphene and also the Faradaic contribution of the pseudocapacitive materials and chemical moieties [94]. In 2008, Stoller et al. reported a specific capacitance as high as 135 F g^{-1} and 99 F g^{-1} from a graphene in aqueous (KOH) and organic ($TEABF_4$/AN) electrolytes, respectively [17]. Wang et al. in 2009 managed to improve the specific capacitance value of graphene by chemical treatment of GO and obtained the value of about 205 F g^{-1} in aqueous electrolyte [95]. In 2012, El-Kady and his co-workers showed that graphene can be synthesized via an easy method such as burning a disc coated with GO with laser and the obtained graphene (rGO) resulted with an improved specific capacitance of about 276 F g^{-1} in ionic liquid ($EMIMBF_4$) as an electrolyte. The LSG synthesis and their electrochemical performance are shown in Fig. 14.14 [96].

In 2014, Qi et al. reported a remarkable specific capacitance of about 704 μF cm^{-2} for a 3D few-layered graphene (FLG) grown by plasma-enhanced chemical vapour deposition [97]. Later, doping of graphene with nitrogen became of much interest due to the fact that it improves the overall conductivity and SC properties of the device while also enhancing the pseudo–capacitance by the fast and reversible surface redox processes. Sahu et al. developed a cheap and easy process for synthesizing heavily nitrogen-doped graphene (NDG) from non-mulberry silk cocoon membrane (Tassar, Antheraea mylitta) by pyrolyzing the cocoon at 400 °C in argon atmosphere and investigated its performance in a SC device. Our results suggest that NDG obtained from cocoon has improved SC performance [98]. The improved performance is due to the high electronegativity of nitrogen that forms dipoles on the graphene surface. These dipoles consequently enhance the tendency of graphene to attract charged species to its surface. This is a green and clean synthesis approach for developing electronic materials for energy applications. In order to meet the demand of high-performance electrode materials for SCs, scientists continued to strive to design and develop a new class of electrode materials with superior electrochemical performance. In 2018, Yang et al. used a simple hydrothermal method to

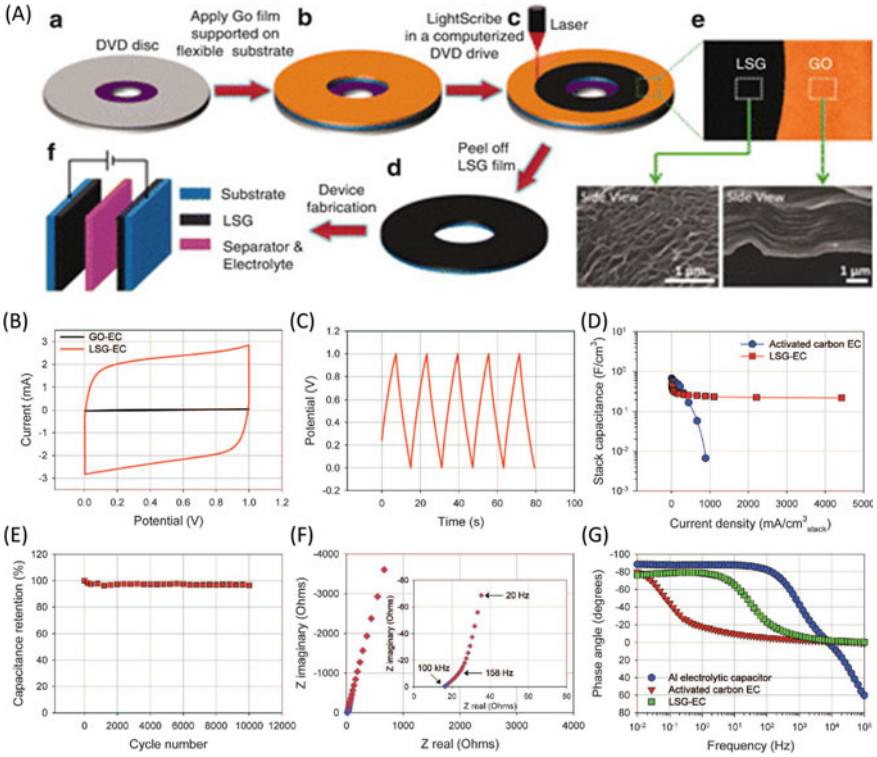

Fig. 14.14 **A** Schematic illustration of the fabrication of laser-scribed graphene-based electrochemical capacitors and **B–G** evaluation of the performance of an LSG electrochemical capacitor

synthesize a composite material made of $NiCo_2S_4$-anchored on graphene nanosheets ($NiCo_2S_4$/GNS). Benefiting from the synergistic effect of graphene and $NiCo_2S_4$, the composite electrode material exhibited an outstanding electrochemical performances, with a high specific capacitance of 1063 F g^{-1} at current density of 2 A g^{-1} and excellent cycling performance that maintained 82% of the initial capacitance value after 10,000 cycles. They further fabricated an asymmetric supercapacitor (ASC) using $NiCo_2S_4$/GNS as positive electrode and nitrogen-doped graphene as negative electrode. The fabricated ASC delivered a remarkable energy density of 54.6 Wh kg^{-1} at a power density of 350.8 W kg^{-1} [99]. Recently, Jadhav et al. designed a SC device made of manganese dioxide/reduced graphene oxide composite for high-performance solid-state SCs [100]. Their cost-effective and simple hydrothermal method successfully formed MnO_2 of nanorods with tunnel structure having a width of 20–40 nm dispersed on the rGO surface. The rGO/MnO_2 nanocomposite electrode exhibited higher specific capacitance of 759 F g^{-1} at the current density of 2 A g^{-1} and demonstrated highly reversible and symmetric capacitive characteristics when operated at a cell potential of 0.9 V in Na_2SO_4 electrolyte.

Furthermore, the SC device fabricated demonstrated a reliable charge storage performance and stored a maximum specific energy density of 64.6 Wh kg^{-1} and high specific power density of 15 kW kg^{-1} when using gel electrolyte in a symmetric configuration [100]. All the observed literature results demonstrated the magnificent electrochemical performance and the promise of the use of graphene, graphene oxide, and their composites materials as a potentials choice in making high-power and high-energy SCs device with promising wide practical applications.

14.3.4 Onion-Like Carbons (OLCs)

Onion-like carbon (a highly disordered and defective with sp^2 hybridization consisting of multiple concentric fullerene-like carbon shells) is an emerging carbon nanomaterial that has begun to attract major research interest in energy storage and conversion. Onion-like carbons (OLCs) were discovered long ago (i.e. before fullerenes and carbon nanotubes) but remained unpopular, and thus, they were poorly investigated. OLCs also known as carbon nano-onions (CNOs) are another type of carbon allotrope that are made up of spherical carbon shells that resemble the concentric-layered structure of onion, hence the origin of their name. OLCs range from the diverse sizes of the concentric shells, from the nested fullerenes to small (<100 nm) polyhedral nanostructures. The knowledge of OLCs dates back to 1980 when Sumio Iijima saw isolated single layers of hexagonal nets of carbon atoms formed inside the shells of the graphitised carbon particles from the carbon black using a transmission electron microscope [101]. At the time, it was rather difficult to synthesize OLCs in a bulk form but instead was mostly observed as a by-product from the synthesis of carbon black. In late 1992, Ugarte and co-workers showed a precise mechanism of producing the spherical graphitic structure by focussing an electron beam on an amorphous carbon sample where OLCs are observed forming in situ. The onion-like rings grew under an electron beam when the amorphous carbon began to curl due to graphitization, and the graphitic structure then closes on itself after being exposed to an electron beam for sufficient time. The curving and closure of the carbon onion structure occur as to minimize the surface energy of the newly formed edge planes of graphite [102]. The method used by Urgate and co-workers to synthesize the OLCs with the diameter of ~45 nm and other synthetic methods explored in previous years was not adequate to produce bulk quantities of OLCs [103–108]. To achieve large-scale production of OLCs, Kuznetsov and co-workers in 1994 proposed and applied the vacuum annealing technique to prepare a large-scale production (gram quantities) of OLCs by graphitization of nanodiamond (ND) precursors at a temperature between 1000 and 1800 °C [109, 110]. This approach became a very useful method to prepare OLCs with a diameter of 6–8 nm. At around 2001, Sano and co-workers used a similar method to vacuum annealing and produced exceptionally large quantities (in tons) of OLCs (with a diameter of 4–36 nm) by annealing in inert gases to transform nanodiamond [111]. The conversion of nanodiamond to OLC can be represented using a molecular dynamics (MD) simulation

(see Fig. 14.15A). Using a representation of the MD simulation, a nanodiamond particle, to cause the outer layers of the nanodiamond to convert to graphitic carbon, an increase in temperature from ~700 to 1700 °C and above is required especially to converts the whole particles to an OLC particles (see Fig. 14.15B, C) [112]. The OLC particles start to polygonize when exposed to the highest annealing temperatures (≥200 °C) due to their structure becoming more ordered [42]. The particles size of the OLC made from the vacuum annealing of nanodiamond precursor adopts more or less similar size of the ND; hence, in general, a 5 nm in diameter ND produces an

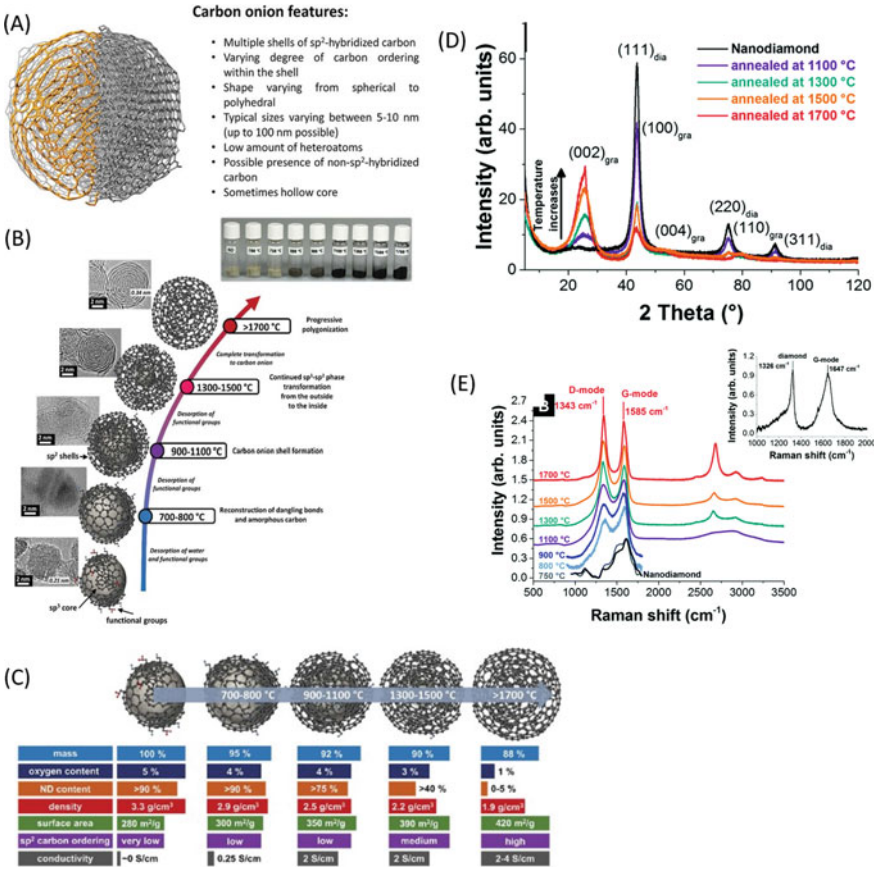

Fig. 14.15 **A** Typical features of carbon onions. **B** Transformation from nanodiamonds to carbon onions by annealing shown using transmission electron micrographs and their optical images. **C** Properties of nanodiamond-derived carbon onions dependent on the synthesis temperature. **D** X-ray diffractograms of nanodiamond and carbon onions synthesized at different temperatures in an argon atmosphere. **E** Raman spectra of nanodiamond-derived carbon onions synthesized in argon measured with a 532 nm laser [114]

OLC particles in the range of 5–10 nm and their structural elucidation can be differentiated using XRD and Raman just like any carbon materials (see Fig. 14.15D, E) [113].

The structural properties of the OLC differ significantly due to the method and conditions of synthesis as well as the nature of the carbon precursor used. In general, the specific surface area (SSA) of the OLC derived from the vacuum annealing of the nanodiamond (in temperatures between 1200 and 1800 °C) ranges between 400 and 600 $m^2\ g^{-1}$. The specific surface area of the OLC entirely depends on the density of the material and the surface of the particles since there is no accessible internal porosity of the material [115].

Onion-like carbon (OLC) in particular show notable performance in high-power applications, due to their external surface which is completely accessible for fast ion adsorption and desorption [115–117]. Due to their small size of typically below 10 nm, the large external surface area, and high conductivity, onion-like carbons (OLCs) are used for electrochemical capacitor applications. OLCs gained interest as energy storage material in EDLCs at around 2006 and 2007 when investigated in both aqueous and organic electrolytes [118, 119]. Due to the inaccessibility of the internal pores of the OLCs, scientist developed a way of penetrating through the rigid structure of the OLC by activating it using chemical activation technique [120]. In 2007, Portet et al. [119] showed that the OLCs are capable of delivering remarkable electrochemical properties. In their work, they showed that a SC device made of OLC can deliver a high power density of about 63 $kW\ kg^{-1}$, the maximum specific capacitance of ~40 $F\ g^{-1}$ at the lower current density and ~30 $F\ g^{-1}$ at higher current density. The stability of the OLCs tested made it clear that these materials can be useful when it come to the overbearing of both high current densities and voltages which is of great deal for industrial applications [121]. Due to the above reason, in 2010, Pech et al. constructed a micro-SCs system using interdigital onion-like carbon electrodes and compared to other SCs system of the same length scale [122]. The micro-SCs system was able to operate efficiently at extremely higher scan rates of ~100 $V\ s^{-1}$ and hence, show much faster performance compared to other pure EDLCs systems that run at the scan rates at around 1 $V\ s^{-1}$ and below. The power performance of the SCs made from the OLC electrodes became 10× greater than that of SCs made from activated carbon (AC) electrodes. But the energy density of the OLC device constantly became lower than that of the activated carbon due to the low specific surface area of the OLCs compared to the activated carbon [42, 122]. The curvature effect of OLCs has been demonstrated to be of positive gain towards energy storage as the particle sizes of the OLCs decreases. Thus, the reason many scientists prefers the nano-onions (with small diameters and particle sizes) derived from the vacuum annealing of the nanodiamond for electrochemical capacitors [115, 123, 124]. In 2013, Gao et al. demonstrated that the increase of the OLC porosity in outer shells through chemical activation results in an improved electrochemical performance of the SCs system. A maximum specific capacitance of 122 $F\ g^{-1}$, the remarkable high power density of 153 $kW\ kg^{-1}$ and excellent energy density of 8.5 $Wh\ kg^{-1}$ was achievable after OLC activation [120]. Due to the relatively high conductivity of the OLC observed from the smooth flow of electrolyte ions

on its surface area and the high rate capability reported in the literature, scientist began to explore this material as conductive additives to replace carbon black [116, 125]. In 2015, Zeiger et al. presented a comprehensive study on the influence of the synthesis atmosphere on the structure and properties of nanodiamond-derived OLCs synthesized at 1300 and 1700 °C in high vacuum or argon flow as shown in Fig. 14.16 [126]. In their work, they showed that the high vacuum annealing yielded OLC with nearly perfect spherical shape (see Fig. 14.16A). They also observed that there is an increase in surface area of the OLCs which was caused by a decrease in particle density when transitioning from sp^3 to sp^2 hybridization. The OLCs from annealing nanodiamonds in flowing argon were highly interconnected by few-layer graphene nanoribbons which helped in improving the electrical conductivity. The OLCs synthesized in argon flow at 1700 °C showed a specific capacitance of 20 F g^{-1} at the extremely high current density of 20 A g^{-1} and 2.7 V cell voltage and which is an improvement of more than 40% compared to the OLC synthesised via vacuum annealing. The OLC synthesised at the temperature of 1300 °C in argon flow displayed similar effect with a 140% higher capacitance at the extremely high

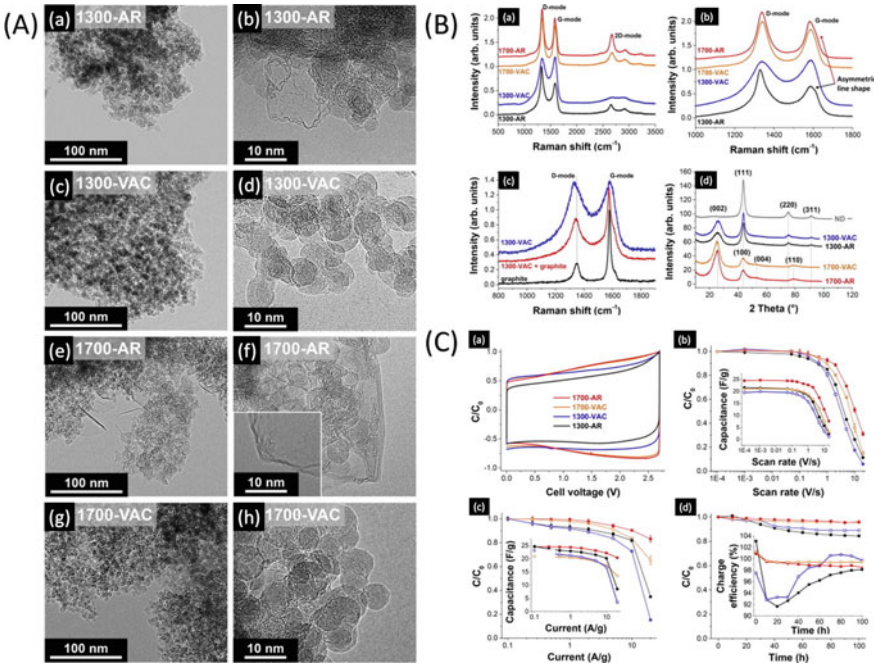

Fig. 14.16 **A** TEM images comparison of OLCs synthesised in argon and in vacuum condition. **B** Raman spectra of the OLC samples (a, b), the combination of carbon onions and graphite flakes (c), and XRD image of OLC (d). **C** Cyclic voltammograms (a), capacitance dependent on the scan rate and capacitance retention for different scan rates (b), galvanostatic cycling using different current densities (c), and long-time voltage floating test with the charge efficiency (charge/discharge capacitance) at a rate of 0.5 A/g (d) [126]

current density of 20 A g^{-1} as compared to the vacuum annealed OLC [126]. The results obtained assured the effects of the synthetic route in designing highly stable OLC electrode materials that can be utilised in high-power output SC device.

In order to improve the energy density of OLC, this material have been used to make composites with other capacitive materials such as conducting polymers and transition metal oxide [32, 127, 128]. The as-synthesized OLC-PANi composites have demonstrated a remarkable specific capacitance of 640 F g^{-1} in symmetric two-electrode system and a stable rate capability even after 10,000 cycles [129]. Makgopa et al. presented a study on the pseudocapacitive properties of birnessite-type MnO_2 grafted on highly graphitized onion-like carbon (OLC/MnO_2) as shown in Fig. 14.17 [40]. The OLC/MnO_2 nanohybrid exhibited a large specific capacitance of 295 and 323 F g^{-1} at high current density of 1 A g^{-1} for the Pt disc and Ni foam, respectively, in a three-electrode configuration. When they fabricated the nanohybrid in a symmetrical two-electrode device, the electrode continued displaying a large specific capaciatance of 254 F g^{-1}, a specific energy density of 5.6 Wh kg^{-1}, and

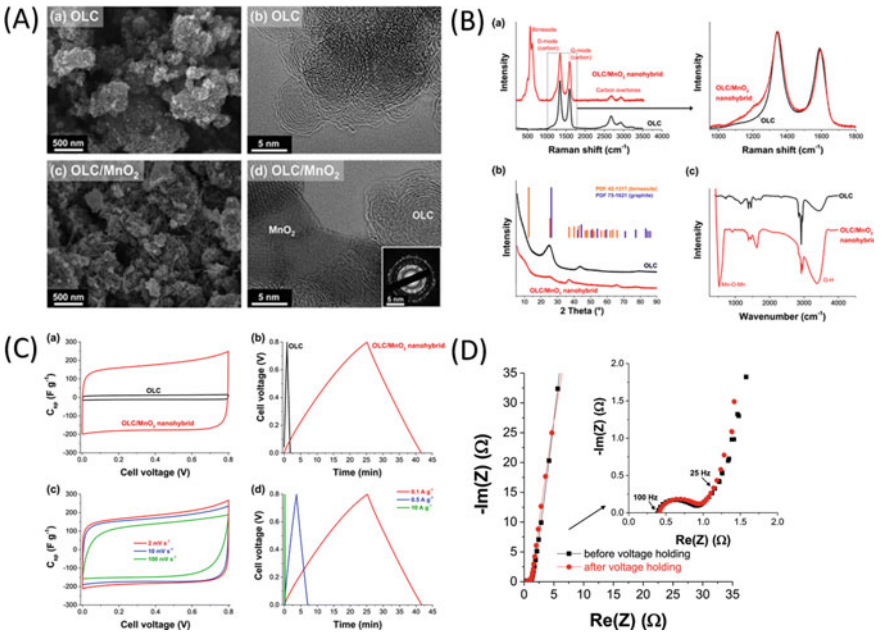

Fig. 14.17 **A** Comparison of SEM images (a, c) and TEM images (b, d) of OLC and OLC/MnO_2 nanohybrid. The inset is the corresponding SAED pattern of (d). **B** Comparison of (a) Raman spectra, (b) X-ray diffraction pattern, and (c) FTIR spectra of OLC and the OLC/MnO_2 nanohybrid. **C** (a) Comparative cyclic voltammograms, (b) comparative galvanostatic charge–discharge curves, for OLC and OLC/MnO_2, (c) CVs at different scan rates for OLC/MnO_2 and (d) comparative galvanostatic charge–discharge curves for OLC and the OLC/MnO_2 nanohybrid at different current densities. **D** Nyquist plot for the OLC/MnO_2 before and after 50 h voltage-holding experiments [130]

an excellent high power density of 74.8 kW kg^{-1}. The device displayed excellent capacity retention when subjected to voltage-holding (floating) experiments for 50 h.

In 2017, Makgopa et al. demonstrated the OLCs have the ability to drastically improve the pseudocapacitive performance of the non-conductive tetragonal hausmannite Mn_3O_4 [28]. The OLC/Mn_3O_4 nanohybrid electrode material demonstrated higher electrochemical performance (in terms of specific capacitance and rate capability as energy storage devices) compared to the pure Mn_3O_4 when fabricated as a symmetric pseudocapacitor device. The nanohybrid exhibited higher specific capacitance of 195 F g^{-1}, specific energy of 4.3 Wh kg^{-1} and power density of 52 kW kg^{-1}, and these results were greatly improved as compared to other carbon nanohybrid materials reported in their studies. The OLC/Mn_3O_4 nanohybrid was further explored as high voltage asymmetric pseudocapacitor, and the electrochemical performance was enhanced with maximum energy densities of 19 Wh kg^{-1} at the current density of 0.1 A g^{-1} and a power density of 45 kW kg^{-1} at the current density of 10 A g^{-1}. These high performance of the OLC-based nanohybrid was ascribed to the combined unique intrinsic properties of the OLC (i.e. high electrical conductivity, highly accessible outer surface, and large interparticle pore volumes) [28].

Recently, Singh et al. fabricated a micro-supercapacitor using nitrogen-doped OLCs using the three-dimensionally interconnected nanoporous gold as a current collector [131]. Their research was aimed in assisting the faster growth of the microelectronics industry and consumer's demand for tiny, portable electronic devices. They used a simple two-step process of thermal evaporation followed by dealloying and electrophoretic deposition for preparing the electrode materials (NP-G/N-OLC). The NP-G/N-OLC micro-supercapacitor device exhibited an areal capacitance of 1.16 mF cm^{-2} (related to the gravimetric capacitance ~259 F g^{-1}), maximum energy density and power density obtained of 0.16 μWh cm^{-2} and 24.87 μW cm^{-2} at the scan rate of 10 mV s^{-1} and 200 mV s^{-1}, respectively. The NP-G/N-OLC micro-supercapacitor also displayed good cyclic stability with nearly 80% capacitance retention up to 10,000 cycles [131]. Their results demonstrated that the use of nitrogen-doped OLC provide a promising future to the development of micro-supercapacitors devices.

14.4 Summary and Future Prospect

Nanostructured carbon materials with their interesting properties such as good stability, good cyclibility, good electrochemical response, excellent conductive, extraordinary surface area have proven themselves as attractive electrode materials for energy storage applications since they can be easily synthesized from various synthetic route even though their synthesis and application is still restricted to the lab-scale production. It is also evident that significant progress has been made in SCs applications, using the carbon nanomaterials (having various micro-textures and wide availability) as electrode materials, which have generated worldwide attention

in these energy storage/conversion devices due to the need to resolve high demands for clean and sustainable energy followed by the fact that fossil fuels have shown potential threat to the environment and thereby deemed unreliable. The advantages of SCs systems account to their high power density, high efficiency, and long life expectancy. The key factors that command the choice of carbon materials for SC electrodes include the controlled pore size, high electrical conductivity, high surface area, interconnected pore structure, good wettability towards the electrolyte and the presence of electrochemically stable surface functionalities. Great progress has been made in the use of carbon nanomaterials where the improved energy storage capability is achieved by designing electrode materials that combines the electric double-layer (EDL) capacitance with the highly reversible pseudo-capacitance, such as metal oxides and conducting polymers. The greatest challenges in the development of SCs technology is still the relatively high cost when compared to other energy devices. Therefore, research should be directed towards the development of carbon materials with high charge capacity while maintaining minimum charge/solution resistance in a cost-effective way. Synthesis that does not involve additional activation process to obtain high density carbon or composite materials would be beneficial while the high rate capability and long cycle life is not sacrificed. As research advances and improvements continue to be made, it is certain that the future held for SCs is an auspicious one especially when carbon nanomaterials are employed in the designing of the device.

Acknowledgements KM, LFM, KDM, and MJH would like to thank the National Research Foundation (NRF-Thuthuka) (Grant Nos. 117984, 118113, and 117727), Tshwane University of Technology, South Africa, Sasol Inzalo Foundation, University of Limpopo (Research Development Grants R202 and R232), South Africa, for financial support. Conflict of Interest: We declare there are no conflict of interest.

References

1. S. Jacobsson, A. Johnson, The diffusion of renewable energy technology: an analytical framework and key issues for research. Energy Policy **28**, 625–640 (2000). https://doi.org/10.1016/S0301-4215(00)00041-0
2. P. Poizot, F. Dolhem, Clean energy new deal for a sustainable world: from non-CO_2 generating energy sources to greener electrochemical storage devices. Energy Environ. Sci. **4**, 2003 (2011). https://doi.org/10.1039/c0ee00731e
3. J. Aghaei, M.I. Alizadeh, Demand response in smart electricity grids equipped with renewable energy sources: a review. Renew. Sustain. Energy Rev. **18**, 64–72 (2013). https://doi.org/10.1016/j.rser.2012.09.019
4. K.B. Hatzell, M. Boota, E.C. Kumbur, Y. Gogotsi, Flowable conducting particle networks in redox-active electrolytes for grid energy storage. J. Electrochem. Soc. **162**, A5007–A5012 (2015). https://doi.org/10.1149/2.0011505jes
5. O. Ellabban, H. Abu-Rub, F. Blaabjerg, Renewable energy resources: current status, future prospects and their enabling technology. Renew. Sustain. Energy Rev. **39**, 748–764 (2014). https://doi.org/10.1016/j.rser.2014.07.113

6. Z. Gao, Y. Zhang, N. Song, X. Li, Biomass-derived renewable carbon materials for electrochemical energy storage. Mater. Res. Lett. **5**, 69–88 (2017). https://doi.org/10.1080/21663831.2016.1250834
7. F. Béguin, V. Presser, A. Balducci, E. Frackowiak, Carbons and electrolytes for advanced supercapacitors. Adv. Mater. **26**, 2219–2251 (2014). https://doi.org/10.1002/adma.201304137
8. M.M. Thackeray, C. Wolverton, E.D. Isaacs, Electrical energy storage for transportation—approaching the limits of, and going beyond, lithium-ion batteries. Energy Environ. Sci. **5**, 7854 (2012). https://doi.org/10.1039/c2ee21892e
9. A. Burke, H. Zhao, Review of the present and future applications of supercapacitors in electric and hybrid vehicles. Inst. Transp. Stud. (2014)
10. A. Ghosh, Y.H. Lee, Carbon-based electrochemical capacitors. ChemSusChem **5**, 480–499 (2012). https://doi.org/10.1002/cssc.201100645
11. G. Wang, L. Zhang, J. Zhang, A review of electrode materials for electrochemical supercapacitors. Chem. Soc. Rev. **41**, 797–828 (2012). https://doi.org/10.1039/c1cs15060j
12. K. Makgopa, P.M. Ejikeme, K.I. Ozoemena, Nanostructured manganese oxides in supercapacitors, in *Nanomaterials in Advanced Batteries and Supercapacitors*. ed. by K.I. Ozoemena, S. Chen (Springer, Cham, 2016), pp. 345–376
13. B.E. Conway, V. Birss, J. Wojtowicz, The role and utilization of pseudocapacitance for energy storage by supercapacitors. J. Power Sources **66**, 1–14 (1997). https://doi.org/10.1016/S0378-7753(96)02474-3
14. A.T. Chidembo, K.I. Ozoemena, B.O. Agboola, V. Gupta, G.G. Wildgoose, R.G. Compton, Nickel(II) tetra-aminophthalocyanine modified MWCNTs as potential nanocomposite materials for the development of supercapacitors. Energy Environ. Sci. **3**, 228 (2010). https://doi.org/10.1039/b915920g
15. M. Toupin, T. Brousse, D. Belanger, Charge storage mechanism of MnO_2 electrode used in aqueous electrochemical capacitor. Chem. Mater. **16**, 3184–3190 (2004)
16. B.E. Conway, *Electrochemical Supercapacitors Scientific Fundamentals and Technological Applications* (1999)
17. M.D. Stoller, S. Park, Y. Zhu, J. An, R.S. Ruoff, Graphene-based ultracapacitors. Nano Lett. **8**, 3498–3502 (2008). https://doi.org/10.1021/nl802558y
18. Y. Zhai, Y. Dou, D. Zhao, P.F. Fulvio, R.T. Mayes, S. Dai, Carbon materials for chemical capacitive energy storage. Adv. Mater. **23**, 4828–4850 (2011). https://doi.org/10.1002/adma.201100984
19. L.L. Zhang, X.S. Zhao, Carbon-based materials as supercapacitor electrodes. Chem. Soc. Rev. **38**, 2520–2531 (2009). https://doi.org/10.1039/b813846j
20. G. Pandolfo, F. Hollenkamp, Carbon properties and their role in supercapacitors. J. Power Sources **157**, 11–27 (2006). https://doi.org/10.1016/j.jpowsour.2006.02.065
21. S. Bose, T. Kuila, A.K. Mishra, R. Rajasekar, N.H. Kim, J.H. Lee, Carbon-based nanostructured materials and their composites as supercapacitor electrodes. J. Mater. Chem. **22**, 767 (2012). https://doi.org/10.1039/c1jm14468e
22. D. Qu, D. Qu, H. Shi, H. Shi, Studies of activated carbons used in double-layer capacitors. J. Power Sources **74**, 99–107 (1998)
23. F. Béguin, E. Frackowiak, *Supercapacitors: Materials, Systems and Applications* (Wiley, Weinheim, 2013)
24. T. Brezesinski, J. Wang, S.H. Tolbert, B. Dunn, Ordered mesoporous alpha-MoO_3 with iso-oriented nanocrystalline walls for thin-film pseudocapacitors. Nat. Mater. **9**, 146–151 (2010). https://doi.org/10.1038/nmat2612
25. L. Bai, D.A. Harrington, B.E. Conway, Behavior of overpotential—deposited species in Faradaic reactions—II. ac impedance measurements on H_2 evolution kinetics at activated and unactivated Pt cathodes. Electrochim. Acta **32**, 1713–1731 (1987). https://doi.org/10.1016/0013-4686(87)80006-3
26. S. Liu, S. Sun, X.-Z. You, Inorganic nanostructured materials for high performance electrochemical supercapacitors. Nanoscale **6**, 2037–2045 (2014). https://doi.org/10.1039/c3nr05403a

27. C.Z. Yuan, B. Gao, L.F. Shen, S.D. Yang, L. Hao, X.J. Lu, F. Zhang, L.J. Zhang, X.G. Zhang, Hierarchically structured carbon-based composites: design, synthesis and their application in electrochemical capacitors. Nanoscale **3**, 529–545 (2011). https://doi.org/10.1039/c0nr00423e
28. K. Makgopa, K. Raju, P.M. Ejikeme, K.I. Ozoemena, High-performance Mn_3O_4/onion-like carbon (OLC) nanohybrid pseudocapacitor: unravelling the intrinsic properties of OLC against other carbon supports. Carbon N. Y. **117**, 20–32 (2017). https://doi.org/10.1016/j.carbon.2017.02.050
29. C. Yu, Y. Wang, J. Cui, D. Yu, X. Zhang, X. Shu, J. Zhang, Y. Zhang, R. Vajtai, P.M. Ajayan, Y. Wu, MOF-74 derived porous hybrid metal oxide hollow nanowires for high-performance electrochemical energy storage. J. Mater. Chem. A **6**, 8396–8404 (2018). https://doi.org/10.1039/c8ta01426d
30. N. Choudhary, C. Li, J. Moore, N. Nagaiah, L. Zhai, Y. Jung, J. Thomas, Asymmetric supercapacitor electrodes and devices. Adv. Mater. **29** (2017). https://doi.org/10.1002/adma.201605336
31. M.D. Stoller, R.S. Ruoff, Review of best practice methods for determining an electrode material's performance for ultracapacitors. Energy Environ. Sci. **3**, 1294–1301 (2010). https://doi.org/10.1039/c0ee00074d
32. M. Zhi, C. Xiang, J. Li, M. Li, N. Wu, Nanostructured carbon-metal oxide composite electrodes for supercapacitors: review. Nanoscale 72–88 (2012). https://doi.org/10.1039/c2nr32040a
33. Y. Chen, X. Zhang, D. Zhang, P. Yu, Y. Ma, High performance supercapacitors based on reduced graphene oxide in aqueous and ionic liquid electrolytes. Carbon N. Y. **49**, 573–580 (2011). https://doi.org/10.1016/j.carbon.2010.09.060
34. P. Simon, Y. Gogotsi, Materials for electrochemical capacitors. Nat. Mater. **7**, 845–854 (2008). https://doi.org/10.1038/nmat2297
35. K. Xie, B. Wei, Nanomaterials for stretchable energy storage and conversion devices. Nanosci. Technol. 159–191 (2016). https://doi.org/10.1007/978-3-319-32023-6_4
36. H. Jiang, T. Zhao, C. Li, J. Ma, Hierarchical self-assembly of ultrathin nickel hydroxide nanoflakes for high-performance supercapacitors. J. Mater. Chem. **21**, 3818–3823 (2011). https://doi.org/10.1039/c0jm03830j
37. C. Burda, X. Chen, R. Narayanan, M.A. El-Sayed, Chemistry and properties of nanocrystals of different shapes. Chem. Rev. **105**, 1025–1102 (2005)
38. Y. Tan, L. Meng, Q. Peng, Y. Li, One-dimensional single-crystalline Mn_3O_4 nanostructures with tunable length and magnetic properties of Mn_3O_4 nanowires. Chem. Commun. (Camb.) **47**, 1172–1174 (2011). https://doi.org/10.1039/c0cc00978d
39. F.W. Richey, B. Dyatkin, Y. Gogotsi, Y.A. Elabd, Ion dynamics in porous carbon electrodes in supercapacitors using in situ infrared spectroelectrochemistry. J. Am. Chem. Soc. **135**, 12818–12826 (2013). https://doi.org/10.1021/ja406120e
40. K. Makgopa, P.M. Ejikeme, C.J. Jafta, K. Raju, M. Zeiger, V. Presser, K.I. Ozoemena, A high-rate aqueous symmetric pseudocapacitor based on highly graphitized onion-like carbon/birnessite-type manganese oxide nanohybrids. J. Mater. Chem. A **3** (2015). https://doi.org/10.1039/c4ta06715k
41. M. Liu, W.W. Tjiu, J. Pan, C. Zhang, W. Gao, T. Liu, One-step synthesis of graphene nanoribbon-MnO_2 hybrids and their all-solid-state asymmetric supercapacitors. Nanoscale **6**, 4233–4242 (2014). https://doi.org/10.1039/c3nr06650a
42. J. McDonough, Y. Gogotsi, Carbon onions: synthesis and electrochemical applications. Electrochem. Soc. Interface **22**, 61–66 (2013)
43. E. Frackowiak, F. Béguin, Carbon materials for the electrochemical storage of energy in capacitors. Carbon N. Y. **39**, 937–950 (2001). https://doi.org/10.1016/S0008-6223(00)00183-4
44. K. Kierzek, E. Frackowiak, G. Lota, G. Gryglewicz, J. Machnikowski, Electrochemical capacitors based on highly porous carbons prepared by KOH activation. Electrochim. Acta **49**, 515–523 (2004). https://doi.org/10.1016/j.electacta.2003.08.026

45. L. Li, F. Sun, J. Gao, L. Wang, X. Pi, G. Zhao, Broadening the pore size of coal-based activated carbon: via a washing-free chem-physical activation method for high-capacity dye adsorption. RSC Adv. **8**, 14488–14499 (2018). https://doi.org/10.1039/c8ra02127a
46. H. Zhao, B. Xinga, C. Zhang, G. Huang, Q. Liu, G. Yi, J. Jia, M. Ma, Z. Chen, C. Zhang, Efficient synthesis of nitrogen and oxygen co-doped hierarchical porous carbons derived from soybean meal for high-performance supercapacitors. J. Alloys Compd. **766**, 705–715 (2018)
47. M.J. Bleda-Martínez, J.A. Maciá-Agulló, D. Lozano-Castelló, E. Morallón, D. Cazorla-Amorós, A. Linares-Solano, Role of surface chemistry on electric double layer capacitance of carbon materials. Carbon N. Y. **43**, 2677–2684 (2005). https://doi.org/10.1016/j.carbon.2005.05.027
48. M.J. Bleda-Martínez, D. Lozano-Castelló, E. Morallón, D. Cazorla-Amorós, A. Linares-Solano, Chemical and electrochemical characterization of porous carbon materials. Carbon N. Y. **44**, 2642–2651 (2006). https://doi.org/10.1016/j.carbon.2006.04.017
49. D. Lozano-Castello, D. Cazorla-Amoros, A. Linares-Solano, S. Shiraishi, H. Kurihara, A. Oya, Influence of pore structure and surface chemistry on electric double layer capacitance in non-aqueous electrolyte. Carbon N. Y. **41**, 1765–1775 (2003). https://doi.org/10.1016/S0008-6223(03)00141-6
50. Y. Zhou, J. Ren, L. Xia, Q. Zheng, J. Liao, E. Long, F. Xie, C. Xu, D. Lin, Waste soybean dreg-derived N/O co-doped hierarchical porous carbon for high performance supercapacitor. Electrochim. Acta **284**, 336–345 (2018). https://doi.org/10.1016/j.electacta.2018.07.134
51. G.H. Yuan, Z.H. Jiang, A. Aramata, Y.Z. Gao, Electrochemical behavior of activated-carbon capacitor material loaded with nickel oxide. Carbon N. Y. **43**, 2913–2917 (2005). https://doi.org/10.1016/j.carbon.2005.06.027
52. B. Xu, Y. Chen, G. Wei, G. Cao, H. Zhang, Y. Yang, Activated carbon with high capacitance prepared by NaOH activation for supercapacitors. Mater. Chem. Phys. **124**, 504–509 (2010). https://doi.org/10.1016/j.matchemphys.2010.07.002
53. L. Demarconnay, E. Raymundo-Piñero, F. Béguin, A symmetric carbon/carbon supercapacitor operating at 1.6 V by using a neutral aqueous solution. Electrochem. Commun. **12**, 1275–1278 (2010). https://doi.org/10.1016/j.elecom.2010.06.036
54. E. Redondo, J. Carretero-González, E. Goikolea, J. Ségalini, R. Mysyk, Effect of pore texture on performance of activated carbon supercapacitor electrodes derived from olive pits. Electrochim. Acta **160**, 178–184 (2015). https://doi.org/10.1016/j.electacta.2015.02.006
55. B. Li, F. Dai, Q. Xiao, L. Yang, J. Shen, C. Zhang, M. Cai, Nitrogen-doped activated carbon for a high energy hybrid supercapacitor. Energy Environ. Sci. **9**, 102–106 (2016). https://doi.org/10.1039/c5ee03149d
56. N. Mao, H. Wang, Y. Sui, Y. Cui, J. Pokrzywinski, J. Shi, W. Liu, S. Chen, X. Wang, D. Mitlin, Extremely high-rate aqueous supercapacitor fabricated using doped carbon nanoflakes with large surface area and mesopores at near-commercial mass loading. Nano Res. **10**, 1767–1783 (2017). https://doi.org/10.1007/s12274-017-1486-6
57. S. Iijima, Helical microtubules of graphitic carbon. Nature **354**, 56–58 (1991). https://doi.org/10.1038/354056a0
58. S. Iijima, T. Ichihashi, Single-shell carbon nanotubes of 1-nm diameter. Nature **363**, 603–604 (1993)
59. E.T. Thostenson, Z. Ren, T.-W. Chou, Advances in the science and technology of carbon nanotubes and their composites: a review. Compos. Sci. Technol. **61**, 1899–1912 (2001). https://doi.org/10.1016/S0266-3538(01)00094-X
60. H. Jiangtao, T.W. Odom, C.M. Lieber, Chemistry and physics in one dimensions: syntesis and properties of nanowires and nanotubes. Acc. Chem. Res. **32**, 435–445 (1999)
61. M.J. Bronikowski, P.A. Willis, D.T. Colbert, K.A. Smith, R.E. Smalley, Gas-phase production of carbon single-walled nanotubes from carbon monoxide via the HiPco process: a parametric study. J. Vac. Sci. Technol. A Vac. Surf. Film **19**, 1800 (2001). https://doi.org/10.1116/1.1380721
62. J. Liu, S. Fan, H. Dai, Recent advances in methods of forming carbon nanotubes. MRS Bull. **29**, 244–250 (2004). https://doi.org/10.1557/mrs2004.75

63. B.O. Agboola, J. Pillay, K. Makgopa, K.I. Ozoemena, Electrochemical characterization of mixed self-assembled films of water-soluble single-walled carbon nanotube-poly(m-aminobenzene sulfonic acid) and iron(II) tetrasulfophthalocyanine. J. Electrochem. Soc. **157**, F159 (2010). https://doi.org/10.1149/1.3481410
64. J. Prasek, J. Drbohlavova, J. Chomoucka, J. Hubalek, O. Jasek, V. Adam, R. Kizek, Methods for carbon nanotubes synthesis—review. J. Mater. Chem. **21**, 15872–15884 (2011). https://doi.org/10.1039/c1jm12254a
65. R. Sitko, B. Zawisza, E. Malicka, Modification of carbon nanotubes for preconcentration, separation and determination of trace-metal ions. TrAC—Trends Anal. Chem. **37**, 22–31 (2012). https://doi.org/10.1016/j.trac.2012.03.016
66. W. Khan, R. Sharma, P. Chaudhury, A. Siddiqui, P. Saini, Synthesis of carboxylic functionalized multi wall carbon nanotubes and their application for static charge dissipative fibers. Int. J. Nanomater. Nanotechnol. Nanomed. **1**, 025–028 (2016)
67. C. Liu, H.-M. Cheng, Carbon nanotubes for clean energy applications. J. Phys. D Appl. Phys. **38**, R231–R252 (2005). https://doi.org/10.1088/0022-3727/38/14/R01
68. M.F.L. De Volder, S.H. Tawfick, R.H. Baughman, A.J. Hart, Carbon nanotubes: present and future commercial applications. Science **339**, 535–539 (2013). https://doi.org/10.1126/science.1222453
69. R. Ma, J. Liang, B. Wei, B. Zhang, C. Xu, D. Wu, Study of electrochemical capacitors utilizing carbon nanotube electrodes. J. Power Sources **84**, 126–129 (1999). https://doi.org/10.1016/S0378-7753(99)00252-9
70. E. Frackowiak, K. Metenier, V. Bertagna, F. Beguin, Supercapacitor electrodes from multiwalled carbon nanotubes. Appl. Phys. Lett. **77**, 2421 (2000). https://doi.org/10.1063/1.1290146
71. C. Du, J. Yeh, N. Pan, High power density supercapacitors using locally aligned carbon nanotube electrodes. Nanotechnology **16**, 350–353 (2005). https://doi.org/10.1088/0957-4484/16/4/003
72. A. Izadi-Najafabadi, S. Yasuda, K. Kobashi, T. Yamada, D.N. Futaba, H. Hatori, M. Yumura, S. Iijima, K. Hata, Extracting the full potential of single-walled carbon nanotubes as durable supercapacitor electrodes operable at 4 V with high power and energy density. Adv. Mater. **22**, 235–241 (2010). https://doi.org/10.1002/adma.200904349
73. L. Li, Z.A. Hu, N. An, Y.Y. Yang, Z.M. Li, H.Y. Wu, Facile synthesis of MnO_2/CNTs composite for supercapacitor electrodes with long cycle stability. J. Phys. Chem. C **118**, 22865–22872 (2014). https://doi.org/10.1021/jp505744p
74. X. Xiao, T. Li, Z. Peng, H. Jin, Q. Zhong, Q. Hu, B. Yao, Q. Luo, C. Zhang, L. Gong, J. Chen, Y. Gogotsi, J. Zhou, Freestanding functionalized carbon nanotube-based electrode for solid-state asymmetric supercapacitors. Nano Energy **6**, 1–9 (2014). https://doi.org/10.1016/j.nanoen.2014.02.014
75. Q. Zhang, Z. Liu, B. Zhao, Y. Cheng, L. Zhang, H.H. Wu, M.S. Wang, S. Dai, K. Zhang, D. Ding, Y. Wu, M. Liu, Design and understanding of dendritic mixed-metal hydroxide nanosheets@N-doped carbon nanotube array electrode for high-performance asymmetric supercapacitors. Energy Storage Mater. **16**, 632–645 (2018). https://doi.org/10.1016/j.ensm.2018.06.026
76. Z. Guang, Y. Ning, N. Liu, S. Dong, F. Shou, T. Yong, P. Gao, Z. Qiang, Supercapacitors based on free-standing reduced graphene oxides/carbon nanotubes hybrid films. SN Appl. Sci. (2019). https://doi.org/10.1007/s42452-018-0059-y
77. A.K. Geim, K.S. Novoselov, The rise of graphene. Nat. Mater. **6**, 183–191 (2007). https://doi.org/10.1038/nmat1849
78. K.S. Novoselov, A.K. Geim, S. Morozov, D. Jiang, Y. Zhang, S. Dubonos, I. Grigorieva, A. Firsov, Electric field effect in atomically thin carbon films. Science **306**, 666–669 (2004). https://doi.org/10.1126/science.1102896
79. The Nobel Price in Physics 2010 (n.d.)
80. Y. Huang, J. Liang, Y. Chen, An overview of the applications of graphene-based materials in supercapacitors. Small **8**, 1805–1834 (2012). https://doi.org/10.1002/smll.201102635

81. T.J. Booth, P. Blake, R.R. Nair, D. Jiang, E.W. Hill, U. Bangert, A. Bleloch, M. Gass, K.S. Novoselov, M.I. Katsnelson, A.K. Geim, Macroscopic graphene membranes and their extraordinary stiffness. Nano Lett. **8**, 2442–2446 (2008). https://doi.org/10.1021/nl801412y
82. S. Russo, M.F. Craciun, T. Khodkov, M. Yamamoto, M. Koshino, S. Tarucha, *Graphene—Synthesis, Characterization, Properties and Applications* (Intech Open Acess, 2011)
83. C. Li, G. Shi, Three-dimensional graphene architectures. Nanoscale **4**, 5549 (2012). https://doi.org/10.1039/c2nr31467c
84. J. William S. Hummers, R.E. Offeman, Preparation of graphitic oxide. J. Am. Chem. Soc. **80**, 1339 (1958). https://doi.org/10.1021/ja01539a017
85. D.R. Dreyer, S. Park, C.W. Bielawski, R.S. Ruoff, The chemistry of graphene oxide. Chem. Soc. Rev. **39**, 228–240 (2010). https://doi.org/10.1039/b920539j
86. C.K. Chua, M. Pumera, Chemical reduction of graphene oxide: a synthetic chemistry viewpoint. Chem. Soc. Rev. **43**, 291–312 (2014). https://doi.org/10.1039/c3cs60303b
87. M.S.A. Bhuyan, M.N. Uddin, M.M. Islam, F.A. Bipasha, S.S. Hossain, Synthesis of graphene. Int. Nano Lett. **6**, 65–83 (2016). https://doi.org/10.1007/s40089-015-0176-1
88. A. Jana, E. Scheer, S. Polarz, Synthesis of graphene-transition metal oxide hybrid nanoparticles and their application in various fields. Beilstein J. Nanotechnol. **8**, 688–714 (2017). https://doi.org/10.3762/bjnano.8.74
89. Y.-H. Lin, C.-Y. Yang, S.-F. Lin, G.-R. Lin, Triturating versatile carbon materials as saturable absorptive nano powders for ultrafast pulsating of erbium-doped fiber lasers. Opt. Mater. Express **5**, 236 (2015). https://doi.org/10.1364/OME.5.000236
90. H. Kim, K.Y. Park, J. Hong, K. Kang, All-graphene-battery: bridging the gap between supercapacitors and lithium ion batteries. Sci. Rep. **4**, 1–8 (2014). https://doi.org/10.1038/srep05278
91. Y. Wang, Y. Wu, Y. Huang, F. Zhang, X. Yang, Y. Ma, Y. Chen, Preventing graphene sheets from restacking for high-capacitance performance. J. Phys. Chem. C **115**, 23192–23197 (2011). https://doi.org/10.1021/jp206444e
92. Z. Bo, X. Shuai, S. Mao, H. Yang, J. Qian, J. Chen, J. Yan, K. Cen, Green preparation of reduced graphene oxide for sensing and energy storage applications. Sci. Rep. **4**, 4684 (2014). https://doi.org/10.1038/srep04684
93. S.D. Perera, M. Rudolph, R. Mariano, N. Nijem, J.P. Ferraris, Y.J. Chabal, K.J. Balkus Jr., Manganese oxide nanorod–graphene/vanadium oxide nanowire–graphene binder-free paper electrodes for metal oxide hybrid supercapacitors. Nano Energy (2013)
94. B. Xu, S. Yue, Z. Sui, X. Zhang, S. Hou, G. Cao, Y. Yang, What is the choice for supercapacitors: graphene or graphene oxide? Energy Environ. Sci. **4**, 2826 (2011). https://doi.org/10.1039/c1ee01198g
95. Y. Wang, Z. Shi, Y. Huang, Y. Ma, C. Wang, M. Chen, Y. Chen, Supercapacitor devices based on graphene materials. J. Phys. Chem. C **113**, 13103–13107 (2009)
96. M.F. El-Kady, V. Strong, S. Dubin, R.B. Kaner, Laser scribing of high-performanceand flexible graphene-based electrochemical capacitors. Science (80-) **335**, 1326–1330 (2012)
97. J.L. Qi, X. Wang, J.H. Lin, F. Zhang, J.C. Feng, W.-D. Fei, A high-performance supercapacitor of vertically-oriented few-layered graphene with high-density defects. Nanoscale **7**, 3675–3682 (2015). https://doi.org/10.1039/C4NR07284G
98. V. Sahu, S. Grover, B. Tulachan, M. Sharma, G. Srivastava, M. Roy, M. Saxena, N. Sethy, K. Bhargava, D. Philip, H. Kim, G. Singh, S. Kumar, M. Das, R. Kishore, Heavily nitrogen doped, graphene supercapacitor from silk cocoon. Electrochim. Acta **160**, 244–253 (2015)
99. X. Yang, H. Niu, H. Jiang, Z. Sun, Q. Wang, F. Qu, One-step synthesis of $NiCo_2S_4$/graphene composite for asymmetric supercapacitors with superior performances. ChemElectroChem **5**, 1576–1585 (2018). https://doi.org/10.1002/celc.201800302
100. S. Jadhav, R.S. Kalubarme, C. Terashima, B.B. Kale, V. Godbole, A. Fujishima, S.W. Gosavi, Manganese dioxide/reduced graphene oxide composite an electrode material for high-performance solid state supercapacitor. Electrochim. Acta **299**, 34–44 (2019). https://doi.org/10.1016/j.electacta.2018.12.182

101. S. Iijima, Direct observation of the tetrahedral bonding in graphitized carbon black by high resolution electron microscopy. J. Cryst. Growth **50**, 675–683 (1980)
102. D. Urgate, Curling and closure of graphitic networks under electron-beam irradiation. Nature **359**, 707–709 (1992)
103. B. Xu, S.-I. Tanaka, Formation of giant onion-like fullerenes under Al nanoparticles by electron irradiation. Acta Mater. **46**, 5249–5257 (1998). https://doi.org/10.1016/S1359-6454(98)00221-3
104. A.G. Nasibulin, A. Moisala, D.P. Brown, E.I. Kauppinen, Carbon nanotubes and onions from carbon monoxide using $Ni(acac)_2$ and $Cu(acac)_2$ as catalyst precursors. Carbon N. Y. **41**, 2711–2724 (2003). https://doi.org/10.1016/S0008-6223(03)00333-6
105. Y. Yang, X. Liu, X. Guo, H. Wen, B. Xu, Synthesis of nano onion-like fullerenes by chemical vapor deposition using an iron catalyst supported on sodium chloride. J. Nanopart. Res. **13**, 1979–1986 (2011). https://doi.org/10.1007/s11051-010-9951-0
106. T. Cabioc'h, M. Jaouen, E. Thune, P. Guérin, C. Fayoux, M. Denanot, Carbon onions formation by high-dose carbon ion implantation into copper and silver. Surf. Coat. Technol. **128–129**, 43–50 (2000). https://doi.org/10.1016/S0257-8972(00)00655-1
107. M. Bystrzejewski, M.H. Rummeli, T. Gemming, H. Lange, A. Huczko, Catalyst-free synthesis of onion-like carbon nanoparticles. New Carbon Mater. **25**, 1–8 (2010). https://doi.org/10.1016/S1872-5805(09)60011-1
108. M. Zhao, H. Song, X. Chen, W. Lian, Large-scale synthesis of onion-like carbon nanoparticles by carbonization of phenolic resin. Acta Mater. **55**, 6144–6150 (2007). https://doi.org/10.1016/j.actamat.2007.07.013
109. V.L. Kuznetsov, A.L. Chuvilin, Y.V. Butenko, I.Y. Mal'kov, V.M. Titov, Onion-like carbon from ultra-disperse diamond. Chem. Phys. Lett. **222**, 343–348 (1994). https://doi.org/10.1016/0009-2614(94)87072-1
110. V.L. Kuznetsov, Y.V. Butenko, V.I. Zaikovskii, A.L. Chuvilin, Carbon redistribution processes in nanocarbons. Carbon N. Y. **42**, 1057–1061 (2004). https://doi.org/10.1016/j.carbon.2003.12.059
111. N. Sano, H. Wang, M. Chhowalla, I. Alexandrou, G.A.J. Amaratunga, Nanotechnology: synthesis of carbon "onions" in water. Nature **414**, 506–507 (2001)
112. L. Hawelek, A. Brodka, S. Tomita, J.C. Dore, V. Honkimäki, A. Burian, Transformation of nano-diamonds to carbon nano-onions studied by X-ray diffraction and molecular dynamics. Diam. Relat. Mater. **20**, 1333–1339 (2011). https://doi.org/10.1016/j.diamond.2011.09.008
113. M.E. Plonska-Brzezinska, L. Echegoyen, Carbon nano-onions for supercapacitor electrodes: recent developments and applications. J. Mater. Chem. A **1**, 13703 (2013). https://doi.org/10.1039/c3ta12628e
114. M. Zeiger, N. Jäckel, V.N. Mochalin, V. Presser, Review: carbon onions for electrochemical energy storage. J. Mater. Chem. A **4**, 3172–3196 (2016). https://doi.org/10.1039/c5ta08295a
115. J.K. McDonough, A.I. Frolov, V. Presser, J. Niu, C.H. Miller, T. Ubieto, M.V. Fedorov, Y. Gogotsi, Influence of the structure of carbon onions on their electrochemical performance in supercapacitor electrodes. Carbon N. Y. **50**, 3298–3309 (2012). https://doi.org/10.1016/j.carbon.2011.12.022
116. D. Weingarth, M. Zeiger, N. Jäckel, M. Aslan, G. Feng, V. Presser, Graphitization as a universal tool to tailor the potential-dependent capacitance of carbon supercapacitors. Adv. Energy Mater. **4**, 1–13 (2014). https://doi.org/10.1002/aenm.201400316
117. Y. Wang, S.F. Yu, C.Y. Sun, T.J. Zhu, H.Y. Yang, MnO_2/onion-like carbon nanocomposites for pseudocapacitors. J. Mater. Chem. **22**, 17584–17588 (2012). https://doi.org/10.1039/c2jm33558a
118. E.G. Bushueva, A.V. Okotrub, P.S. Galkin, V.L. Kuznetsov, S.I. Moseenkov, Electrochemical supercapacitors based on carbon materials, in *Nanocarbon Nanodiamond Conference*, pp. 11–15, St. Petersburg, Russia (2006)
119. C. Portet, G. Yushin, Y. Gogotsi, Electrochemical performance of carbon onions, nanodiamonds, carbon black and multiwalled nanotubes in electrical double layer capacitors. Carbon N. Y. **45**, 2511–2518 (2007). https://doi.org/10.1016/j.carbon.2007.08.024

120. Y. Gao, Y.S. Zhou, M. Qian, X.N. He, J. Redepenning, P. Goodman, H.M. Li, L. Jiang, Y.F. Lu, Chemical activation of carbon nano-onions for high-rate supercapacitor electrodes. Carbon N. Y. **51**, 52–58 (2013). https://doi.org/10.1016/j.carbon.2012.08.009
121. C. Portet, J. Chmiola, Y. Gogotsi, S. Park, K. Lian, Electrochemical characterizations of carbon nanomaterials by the cavity microelectrode technique. Electrochim. Acta **53**, 7675–7680 (2008). https://doi.org/10.1016/j.electacta.2008.05.019
122. D. Pech, M. Brunet, H. Durou, P. Huang, V. Mochalin, Y. Gogotsi, P.-L. Taberna, P. Simon, Ultrahigh-power micrometre-sized supercapacitors based on onion-like carbon. Nat. Nanotechnol. **5**, 651–654 (2010). https://doi.org/10.1038/nnano.2010.162
123. J. Huang, B.G. Sumpter, V. Meunier, G. Yushin, C. Portet, Y. Gogotsi, Curvature effects in carbon nanomaterials: exohedral versus endohedral supercapacitors. J. Mater. Res. **25**, 1525–1531 (2010). https://doi.org/10.1557/JMR.2010.0195
124. G. Feng, D. Jiang, P.T. Cummings, Curvature effect on the capacitance of electric double layers at ionic liquid/onion-like carbon interfaces curvature effect on the capacitance of electric double layers at ionic liquid/onion-like carbon interfaces. J. Chem. Theory Comput. **8**, 1058–1063 (2012). https://doi.org/10.1021/ct200914j
125. N. Jäckel, D. Weingarth, M. Zeiger, M. Aslan, I. Grobelsek, V. Presser, Comparison of carbon onions and carbon blacks as conductive additives for carbon supercapacitors in organic electrolytes. J. Power Sources **272**, 1122–1133 (2014). https://doi.org/10.1016/j.jpowsour.2014.08.090
126. M. Zeiger, N. Jäckel, D. Weingarth, V. Presser, Vacuum or flowing argon: what is the best synthesis atmosphere for nanodiamond-derived carbon onions for supercapacitor electrodes? Carbon N. Y. **94**, 507–517 (2015). https://doi.org/10.1016/j.carbon.2015.07.028
127. L.L. Zhang, S. Zhao, X.N. Tian, X.S. Zhao, Layered graphene oxide nanostructures with sandwiched conducting polymers as supercapacitor electrodes. Langmuir **26**, 17624–17628 (2010). https://doi.org/10.1021/la103413s
128. K. Lota, V. Khomenko, E. Frackowiak, Capacitance properties of poly(3,4-ethylenedioxythiophene)/carbon nanotubes composites. J. Phys. Chem. Solids **65**, 295–301 (2004). https://doi.org/10.1016/j.jpcs.2003.10.051
129. I. Kovalenko, D.G. Bucknall, G. Yushin, Detonation nanodiamond and onion-like-carbon-embedded polyaniline for supercapacitors. Adv. Funct. Mater. **20**, 3979–3986 (2010). https://doi.org/10.1002/adfm.201000906
130. K. Makgopa, P.M. Ejikeme, C.J. Jafta, K. Raju, M. Zeiger, V. Presser, K.I. Ozoemena, A high-rate aqueous symmetric pseudocapacitor based on highly graphitized onion-like carbon/birnessite-type manganese oxide nanohybrids. J. Mater. Chem. A **3**, 3480–3490 (2015). https://doi.org/10.1039/c4ta06715k
131. B.K. Singh, A. Shaikh, R.O. Dusane, S. Parida, Nanoporous gold–nitrogen–doped carbon nano-onions all-solid-state micro-supercapacitor. Nano-Struct. Nano-Obj. **17**, 239–247 (2019). https://doi.org/10.1016/j.nanoso.2019.01.011

Chapter 15
Nanostructured Carbon-Based Materials for Fuel Cell Applications

Letlhogonolo Fortunate Mabena, Katlego Makgopa, Annie Stephanie Tanko-Djoubi, Kwena Desmond Modibane, and Mpitloane Joseph Hato

15.1 Background

15.1.1 Fuel Cells

There is concern regarding the depletion of the fossil-fuel resources and the destruction of the environment accompanied with drastic climate changes, researchers have now derived attention on looking for an alternative clean, sustainable, highly efficient energy conversion and storage technologies/systems [1, 2]. Fuel cell technologies become a tangible and promising path in solving challenges associated with energy conversion until today because of their high power density production of about 2293 mW m^{-2} [3]. It is one of the most promising clean efficient, sustainable energy conversion and to a significant diminution of the environment pollution. It can directly convert fuel into electricity with a high efficiency [4].

Fuel cells (FCs) are electrochemical devices that convert chemical energy stored in fuel molecules (hydrogen, methanol, ethanol, formic acid and many more) into electricity via electrochemical reactions on the interface of electrode and electrolyte. Fuel cells have advantages over other systems because of their high electrical efficiency and fuel flexibility [5]. There are several types of fuel cell that have been developed and categorised according to fuels and nature of their electrolytes. Fuel

L. F. Mabena (✉) · K. Makgopa (✉) · A. S. Tanko-Djoubi
Department of Chemistry, Faculty of Science, Tshwane University of Technology, Arcadia Campus, Pretoria 0001, South Africa
e-mail: mabenalf@tut.ac.za

K. Makgopa
e-mail: makgopak@tut.ac.za

K. D. Modibane · M. J. Hato (✉)
Nanotechnology Research Lab, Department of Chemistry, School of Physical and Mineral Sciences, University of Limpopo (Turfloop), Sovenga, Polokwane 0727, South Africa
e-mail: mpitloane.hato@ul.ac.za

S. Kaneko et al. (eds.), *Carbon Related Materials*,
https://doi.org/10.1007/978-981-15-7610-2_15

cells have been known in sciences field for more than 150 years and brought attention and curiosity in the years of 1800. They had become the subject of many works and development during the years of 1900. Sir William Groves created the first fuel cell in 1839. Groves first experiment was based on decomposition of water into hydrogen and oxygen using electricity and called this process electrolysis. He could then notice after the experiment that by inversing the process, he could generate electricity and water [6]. Therefore, he placed two platinum electrodes in a solution of sulphuric acid, which acted as electrolyte, and the other two ends sealed in two containers fed with hydrogen and oxygen, a current was produced between the electrodes with the presence of water in the containers [7, 8].

15.1.2 Types of Fuel Cells

Different types of fuel cell have been developed after the discovery of the Grove's fuel cell. They are similar in most cases as they generate power through various reagent materials, electrolytes, efficiencies and practical applications, amongst others sources of energy. Classifications of the most common types of fuel cell include alkaline fuel cells (AFCs), proton-exchange membrane fuel cells (PEMFCs), phosphoric acid fuel cells (PAFCs), solid oxide fuel cells (SOFCs), direct methanol fuel cells (DMFC), direct ethanol fuel cells (DEFC) and direct formic acid fuel cell (DFAFC) [9]. However, these fuel cells were very expensive to manufacture. It was not until the 1990s that a commercial fuel cell was launched. Some of the parameters and the reaction mechanisms of the fuel cell systems described are shown in Table 15.1 [8, 10, 11].

15.1.3 Fuel Cell Components and Concepts

Fuel cells are electrochemical conversion devices that produce electrical energy and heat directly by a controlled chemical reaction. They produce energy efficiently and with no handful gases, as compare to conventional sources of energy; fuel cells produce energy as long as the fuel is supplied. The basic elements in the fuel cell are electrolyte and two electrodes anode and cathode as schematically shown in Fig. 15.1. The electrodes are separated from each other by an electrolyte. The temperature allows hydrogen to split into its constituent electrons and protons on electrode (the anode) in a fuel cell. The electrons flow out of the anode, migrate to cathode through an external circuit, while the protons diffuse through an electrolyte to the cathode. Both the electrons and protons react with oxygen on the cathode to produce electricity and the only by-product water [11–14].

Table 15.1 Table of different fuel cells and their reaction mechanism [8, 10, 11]

Fuel cell	Electrolyte	Charge carriers or mobile ions	Operating temperature (°C)	Electrochemical reactions	References
PAFC	H_2PO_4	H^+	150–220	Anode: $H_2 \rightarrow 2H^+ + 2e^-$ Cathode: $1/2O_2 + 2H^+ + 2e^- \rightarrow H_2O$	[8, 11]
AFC	KOH	OH^-	120–250	Anode: $H_2 + 2OH^- \rightarrow 2H_2O + 2e^-$ Cathode: $1/2O_2 + 2e^- + H_2O \rightarrow 2OH$	[8, 11]
SOFC	Yttria stabilized zirconia (YSZ)	O^-	800–1000	Anode: $H_2 + O^{2-} \rightarrow H_2O + 2e^-$ Cathode: $1/2O_2 + 2e^- \rightarrow O^{2-}$	[8, 11]
MCFC	Li_2CO_3, and K_2CO_3 and/or Na_2CO_3	$CO_3{}^{2-}$	600–700	Anode: $H_2 + CO_3{}^{2-} \rightarrow CO_2 + H_2O + 2e^-$ Cathode: $1/2O_2 + CO_2 + 2e^- \rightarrow CO_3{}^{2-}$	[8, 11]
PEMFC	Polymer membrane (Nafion®)	H^+	60–100	Anode: $2H_2 \rightarrow 4H^+ + 4e^-$ Cathode: $2O_2 + 4H^+ + 4e^- \rightarrow 2H_2O$	[10, 11]
DMFC	Polymer membrane (Nafion®)	H^+	64–100	Anode: $CH_3OH + H_2O \rightarrow CO_2 + 6H^+ + 6e^-$ Cathode: $(3/2)O_2 + 6H^+ + 6e^- \rightarrow 3H_2O$	[11]

15.1.3.1 Anode Component

The anode component of the fuel cell is where the catalytic oxidation reaction occurs and the electrons generating power is formed. The rate-determining step of the half-cell reaction at the anode is the adsorption of hydrogen by the catalyst. In principle, the fuel (generally hydrogen) is provided at the anode. The hydrogen fuel releases electrons and creates protons after been catalysed. These electrons are conducted to an external circuit and protons to the cathode. The general half reaction of hydrogen fuel that takes place at the anode is.

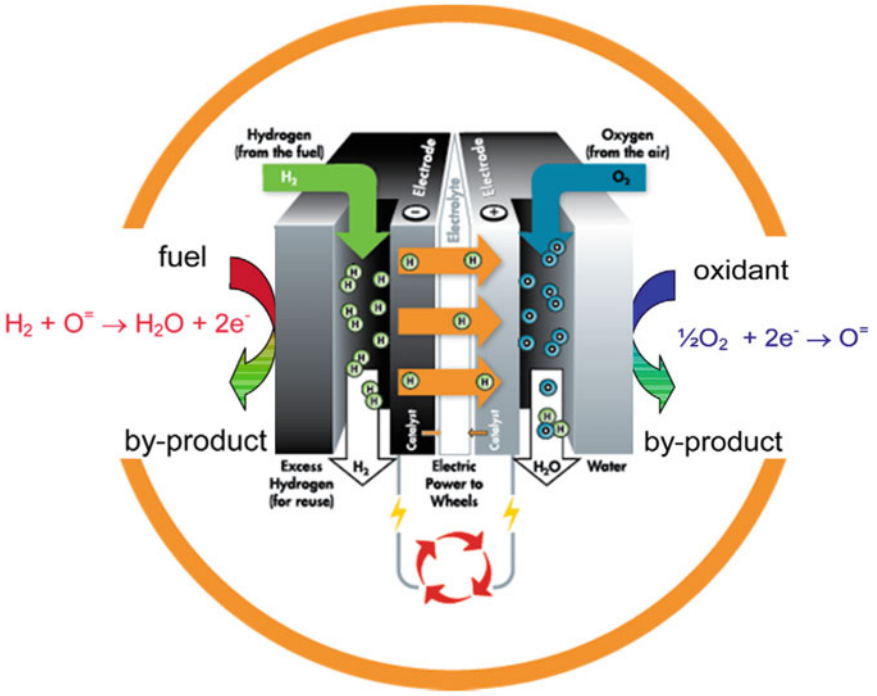

Fig. 15.1 Schematic diagram of fuel cell components, comprised of an electrolyte, an anode and a cathode. The overall chemical reaction is $H_2 + 1/2\ O_2 \rightarrow H_2O$. Anode and cathode reactions given are appropriate only for oxide ion conducting electrolytes. The reactions would be modified for electrolytes with different mobile ions, but the general principle remains unchanged [16]

$$2H_2 \rightarrow 4H^+ + 4e^- \tag{15.1}$$

Desired anode component should be highly conductive, chemically and thermally stable, highly porous structure and highly compatible with other material in order to enhance the fuel cell performance [5, 15]. The anode component is directly connected to the electrolyte.

15.1.3.2 The Electrolyte Component

The electrolytes are ranged from ceramics, polymer to acid salts. The importance thing in an electrolyte solution is the charge carrier that it possesses. The most diverse charge carriers are the O^{2-} and H^+ ions due to their high conductivity. Generally, when hydrogen is used as fuel in the cell, a proton conductor is generated in the electrolyte system. While, when hydrocarbon is the fuel, an oxygen ion serves as conductor. From these conductors, oxide ions conductor is preferable due to direct electro-oxidation of CO to CO_2 which limits the anode catalyst to be affected [17].

Electrolytes must possess a backbone, which provides chemical stability, should be highly conductive and always hydrated in order to function, its most important role is that it should be very thin, dense and work as a barrier to minimise resistance and prevent diffusion and combustion of both gases [5, 15].

15.1.3.3 The Cathode Component

The cathode known as the positive part of the fuel cell is where the oxygen reduction reaction takes place. The cathode is fed of oxygen gas and has a contact layer with electrolyte. The importance of this electrode in the operating cell is to transports both the electrons from the external circuit, which later react with the oxygen present to generate water and transport oxide ions through the electrolyte to the anode in fuel cell. Similar to the anode and electrolyte, cathode electrode catalyst needs certain properties in order to improve the fuel cell performance. Cathode should be able to provide good electrical contact with other components, should have high electrical conductivity, porous structure, thermally stable and most importantly been unreactive with the electrolyte [5, 15]. For a continuous operating system, the electrons and protons produced at the anode react with the present oxygen to form water molecules. The reaction happening at the cathode is shown below [11].

$$O_2 + 4H^+ + 4e^- \rightarrow 2H_2O \tag{15.2}$$

Cathodic oxygen reduction plays an essential role in producing electricity and is a major limit to the cell performance.

15.2 Characteristics of the Fuel Cells

The key performance measure of a fuel cell is the voltage output as a function of electrical current density drawn as shown in Fig. 15.2. In the polarisation curve, high power densities and high efficiencies result when gas diffusion and electron transport through the electrolytes are slow, electrocatalysis at the electrodes is swift, the conductivity of each of the components, particularly, the electrolyte, is high, and mass diffusion through the porous electrodes is narrow. Therefore, the ideal fuel cell electrolyte is not only highly conducting, but also impermeable to gases, electronically resistive and chemically stable under a wide range of conditions. Moreover, the electrolyte must exhibit sufficient mechanical and chemical integrity so as not to develop cracks or pores either during manufacture or in the course of long-term operation [18].

The demands on both fuel cell electrodes are more extreme than those on the electrolyte. The ideal electrode must transport gaseous (or liquid) species, ions and electrons; and, at the points where all three meet, the electrocatalysts must rapidly

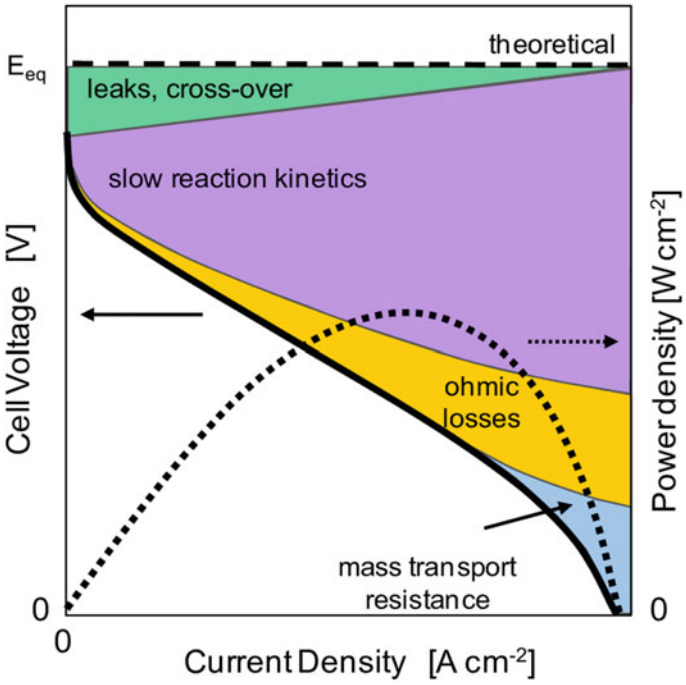

Fig. 15.2 Schematic of a fuel cell polarisation curve, with contributions of various overpotentials as indicated by the shaded regions. The power density (dotted line) is the product of the cell voltage and current density [18]

catalyse electro-oxidation (anode) or electro-reduction (cathode). Hence, the electrodes must be porous, possess high surface area and electronic and ionic conductivity, as well as electrochemical activity. It is rare for a single material to fulfil all of these functions, consequently a composite electrode, of which the electrocatalyst is one component, is often utilised. Thus, the relative contribution of each overpotential and how it varies with current density depend on the fuel cell type and the materials used therein. In order to maintain a sufficiently high power density, or a sufficiently high cell voltage, for a given current density, it is necessary to minimise overpotentials. Crossover effects can be reduced by an appropriate choice of the electrolyte material, specifically one with minimal-to-no electronic conductivity, and by optimising its fabrication so as to obtain high density membranes with low porosity.

15.3 Material in Fuel Cells Applications

The principal reactions in a fuel cell are oxidation of the fuels on anode and the oxygen reduction on cathode. Noble metals and noble metal oxides have been most

commonly used as electrocatalysts for these processes. However, they still suffer from multiple competitive disadvantages, including their low selectivity, poor durability and negative environmental impact [12].

Amongst the noble metal nanocatalysts for anode and cathode reactions, platinum (Pt) exhibits the highest electrocatalytic activities for electro-oxidation of small organic fuels on the anode and the oxygen reduction on the cathode. However, the use of platinum limits the application of fuel cells because of its self-poisoning after the strong CO adsorption on the surface of Pt during oxidation of small organic fuels [19]. On the other hand, platinum electrode, been the most trusted catalyst in fuel cell, is at the origin of the crossover of fuel from anode to cathode. Finally, the high-cost and less abundant Pt hinds the wide commercialisation of fuel cells [20, 21]. Therefore, to obtain ideal electrocatalysts for fuel cells with high and efficient catalytic performance and low price, researchers have turned up to look for a novel structured catalyst.

15.4 Carbon-Based Nanomaterial

Carbon is one of the most abundant elements on earth and is generally used as support material for metal nanoparticles catalysts in low-temperature fuel cells [22]. Carbon nanostructures are versatile carbons, and it has been proved composites derived from carbon can be applied in energy conversion and storage [22, 23]. Carbon with its allotropic characteristics and its unique properties such as physical, chemical, electronic and mechanical can form numerous nanomaterials depending on its atomic arrangement as shown with few examples in Fig. 15.3, [24]. Carbon nanomaterials are ranged from zero to three-dimensional structures. 0D describing quantum dots and spheres, 1D consists of tubes, fibres and wires, 2D corresponds to films, and 3-D are to monolithic carbon systems [13]. Over the past several decades, significant progress has been made in developing carbon materials for catalytic and electrocatalytic applications. The range of these applications of nanostructured carbon material depends on specific properties, morphology, structure and crystallinity which are all determined by the synthesis techniques [13, 25].

Carbon nanomaterials are found to be the best candidates for electrocatalysts and supports not only for the above properties but also for their electrical conductivity to extend the three-phase boundary of the catalyst layer, their ability to support metal catalyst particles and their potential to be modified for specific function [25]. They also exhibits good stability in basic and acidic media as compared to noncarbon materials, such as alumina, metal oxides, electronically conductive polymers, carbides and nitrides [20]. In addition, carbon can be recycled and does not generate huge amounts of solid waste. Catalysts supported on carbon nanomaterial have shown numerous interests because they produce fine distribution and uniform dispersion of catalyst particles. Finally, they also help to hinder the sintering or agglomeration of catalyst particles [8].

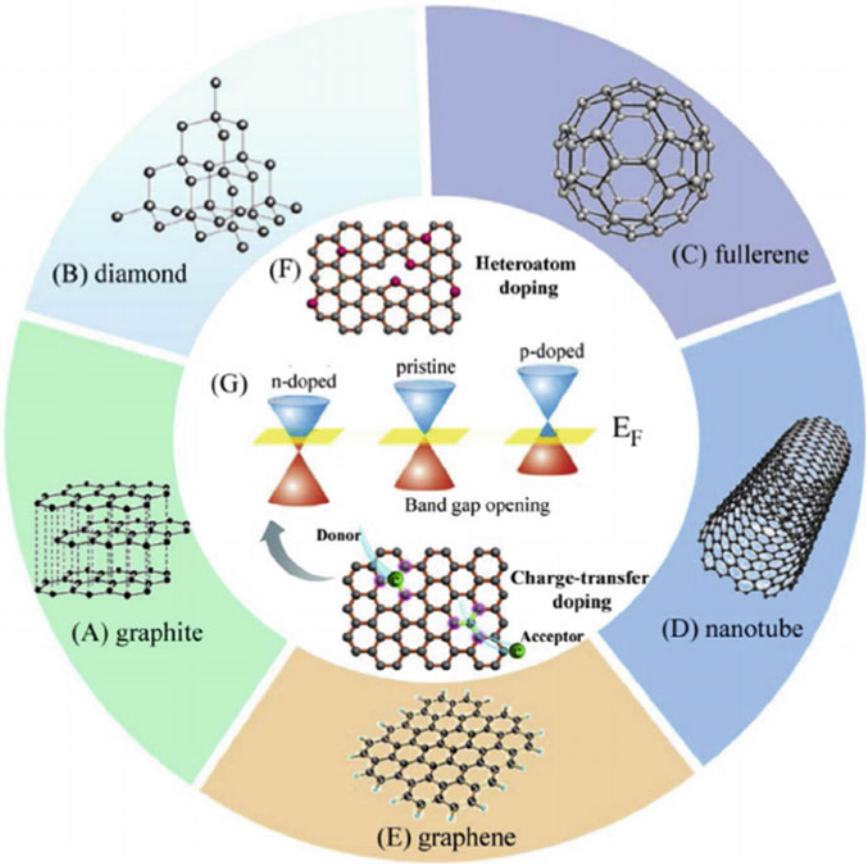

Fig. 15.3 Schematic illustration of the different types of carbon structure [12]

Therefore, the development of carbon nanomaterial in order to meet varieties of applications is imminent. Numerous classes of carbon nanomaterial with different carbon bonding such as sp^1, sp^2 and sp^3 have been tailored and investigated in order to meet the demands of suitable catalyst support for fuel cells.

15.4.1 Carbon Black

Carbon black was among the earliest carbon-based supports used in fuel cell applications. It has been exploited extensively owed to its high availability, low cost and high mesoporous structure and because of its wide range of applications [25–27]. Pt and carbon black are the current popular catalyst and catalyst-support materials in fuel cells due to their high electrocatalytic activities during fuel cell reactions [28]. Since

the 1990s, carbon black materials have been widely used as catalyst supports for Pt and Pt-alloy catalysts in PEMFCs. Presented in Table 15.2 is the characteristics of various carbon types, including a number of carbon blacks reported in the literature [29]. The most commonly used carbon support materials for Pt and Pt-alloy catalysts in PEMFCs are Vulcan XC-72, Black Pearls 2000 and Ketjen all of which have high surface areas (>100 $m^2\ g^{-1}$) and good electrical conductivity (>1 S cm^{-1}).

Similarly, to most carbon material, the carbon black is activated before being used as a catalyst suporpt to increase metal dispersion and its catalytic activity. There are two ways to activate the carbon materials. Chemical activation, also known as oxidative treatment, this method can be achieved using various oxidants such as hydrogen peroxide, nitric acid or ozone gas. The chemical treatment of the carbon surface leads to the loss of basic surface sites and the formation of acidic surface sites. The increasing number of oxygen groups on the carbon support materials enhances the dispersion of the catalyst nanoparticles besides increasing the performance of fuel cells. The second method, the physical activation or a thermal treatment of the carbon is accomplished under inert atmosphere at 800–1100 °C or in air/steam at 400–500 °C, with the aim to remove the impurities present on the carbon surface [22].

Carbon blacks are produced by "furnace black" heating carbon-containing materials, especially hydrocarbons in inert atmosphere, or acetylene process. The former being the mainly used due to costs and availability. Acetylene black has a low surface area over the other types of carbon black, which results in small amount of the catalyst loading and therefore decrease the fuel cell performance. In the "furnace black" process, the heating treatment techniques such as furnace, thermal and channel methods are used [29, 30]. Owing to the nature of the source materials, heat treatment is used (250–500 °C) to remove impurities from the formed carbon. Carbon black consists of spherical particles (diameter less than 50 nm) that may aggregate and form agglomerates (250 nm diameter). The carbonaceous particles have paracrystallite structures comprising of parallel graphitic layers with 0.35–0.38 nm interplanar spacing. The processes produce carbon black with different properties and pores size as illustrated in Fig. 15.4 [31, 32]. Many kind of carbon black, e.g. Vulcan XC-72R, Ketjen carbon black, black pear 2000 and acetylene black are obtained after synthesis [25, 33]. The specific morphology of carbon black depends on the starting material and the heating treatment procedure. For high-performance anode and cathode, carbon black should possess a mesoporous structure surface. Small pores such as micropores do not load high amount of metal catalyst in the carbon black surface.

Additionally, the micropores structures decrease the surface area of the support leading to an increase of the electrical resistance. The catalyst deposits in the primary pores (areas between singular particles) do not participate in the performance of the electrochemical reactions due to the low penetration of the catalysts into these pores. In general, the smaller the pores size distribution, the higher the surface area of the support [25, 34] (Fig. 15.4).

Carmo and co-workers obtained high electrocatalytic performance for both PEMFC and DMFC using PtRu/C–H_2O_2. This performance was achieved because

Table 15.2 Various carbon support materials and their typical characteristics [29]

Carbon support	Supplier	Surface area (m^2 g^{-1})	Particle size (nm)	Conductivity (S cm^{-1})
Carbon black				
Denka black AB	Denkikagaku kogyo	58	40	4
Exp. sample AB	Denkikagaku kogyo	835	30	>1
Shavinigan AB	Gulf oil	70–90	40–50	>1
Conductex 975 FB	Columbian	250	24	>1
Vulcan XC-72R FB	Cabot	254	30	2.77
Black pearls 2000 FB	Cabot	1475	15	>1
3950 FB	Mitsubishi Kasei	1500	16	>1
Ketjen EC 300 J	Ketjen Black International	800	30–40	4
Ketjen EC 600JD	Ketjen Black International	1250	35–40	10–100
Hollow graphite spheres	–	>1000	200	>1
Carbon nanotubes	–	50–1000	1–5 μm	0.3–400
Graphene	–	>2000	10–20 nm	10^3–10^4
Carbon nanofiber	–	50–1000	30–100 μm	200–900
Carbon nanocoils	–	115	50–100 nm	30–180
Ordered mesoporous carbons	–	600–2800	1–20 mm	0.3×10^{-2}–1.37
Carbon aerogels	–	100–1100	0.05–40 μm	25–100
Carbon xerogel	–	460–720	5–46 μm	55 ± 1
Carbon nanocage	–	1276	10–50 nm	813
Carbon nano-onions	–	2–1200	10–45 nm	1–10
Carbon nanohorn	–	300–400	40–50 nm	4.95–7.07

AB acetylene black; *FB* oil-furnace black

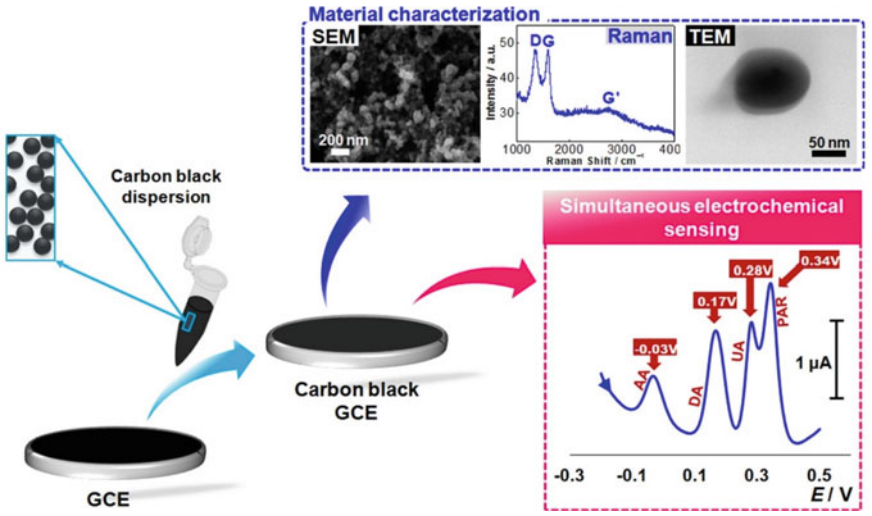

Fig. 15.4 Simulation of the carbon black characterisation [35]

of the good interaction between both the catalyst and the carbon black support that results in good dispersion of the metal catalyst [27]. In 2015, in the same approach, Berber et al. [36] confirmed high performance and durability of the PEMFC. During the experiment, Pt and polybenzimidazole-coated carbon black to form were both used as metal catalyst and support, respectively. The fabricated CB/PyPBI/Pt produced a power density of 375 mW/Cm^2 and a remarkable durability of 500,000 accelerated potentials resulting in a high fuel cell performance.

Xia et al. [37] prepared GO-reflux and Ag/GO composites for comparison. The preparation procedure of Ag/GO was the same as that to prepare the Ag/GO/C except without adding Vulcan XC-72 carbon black. TEM analysis was carried out to characterise the morphology and the dispersion of Ag particle in the Ag/GO colloid and the Ag/GO/C composite as shown in Fig. 15.5. TEM image in Fig. 15.5a, b shows the representative images of the Ag/GO colloid prepared at 100 °C, in which the black spheres are Ag particles and the GO is transparent. It can be seen that the Ag nanoparticles are uniformly dispersed on GO. The histogram for the Ag particle size distribution of the Ag/GO and Ag/GO/C based on statistics on around 200 particles, the average Ag particle size is about 6.9 nm and 12.9 nm, respectively. Compared with the Ag colloid, the Ag particle size in the Ag/GO/C composite is larger. The larger Ag particle size in the presence of Vulcan XC-72 carbon black was possibly caused by electrochemical Ostwald ripening driven by the particle size-dependent work function and standard electrode potential of Ag.

As shown in Fig. 15.5c, compared with the Ag/GO composite, the onset potential and the half-wave potential ($E_{1/2}$) of the ORR over the Ag/GO/C composite shift positively from 0.702 V to 0.826 V and 0.560 V to 0.696 V, respectively. The diffusion-limited ORR current density increases considerably from 1.09 mA cm^{-1}

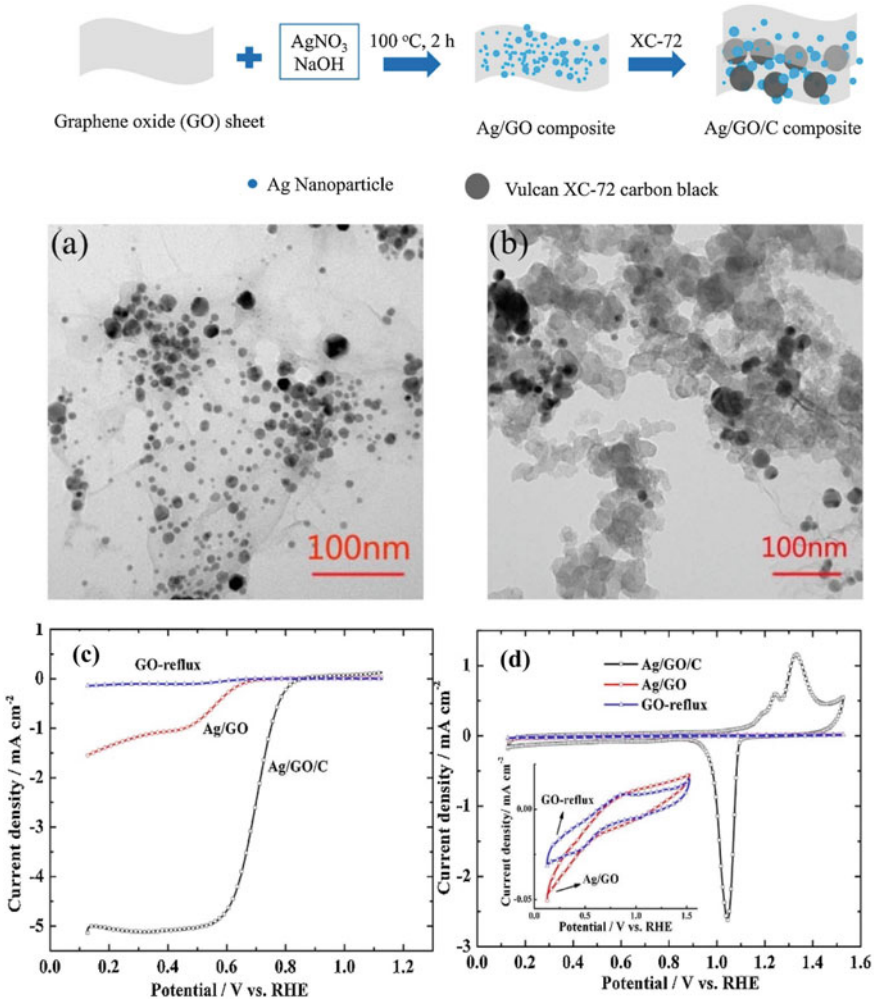

Fig. 15.5 The synthesis procedure for the Ag/GO/C composite. TEM images of **a** Ag/GO colloids and **b** Ag/GO/C, **c** ORR polarisation curves of GO-reflux, Ag/GO and Ag/GO/C composites coated rotating GC electrodes at 1600 rpm in 0.1 M NaOH saturated with O_2. Scanning rate: 10 mV s^{-1}. **d** Background cyclic voltammograms of GO-reflux, Ag/GO and Ag/GO/C composites coated rotating GC electrodes in 0.1 M NaOH saturated with N_2 [37]

over the Ag/GO to 5.10 mA cm^{-1} over the Ag/GO/C. The positive shift of the onset potential and the half-wave potential for the ORR shows the superior activity of the Ag/GO/C.

The electrochemical surface area (ECSA) of Ag for Ag/GO/C is 92.65 m^2/g calculated based on the reduction peak of silver oxide at around 1.04 V during the negative scanning in the background cyclic voltammogram (see Fig. 15.5b), assuming a coulombic charge of 400 μC cm^{-2}. However, ECSA of Ag for the Ag/GO is not

calculated due to the negligible reductive peak. The high ECSA for the Ag/GO/C indicates that the three-dimensional structure constructed by GO and carbon spheres greatly increased the exposed silver active sites. Therefore, the Ag/GO/C composite shows enhanced ORR activity comparing with Ag/GO.

Habibi et al. [38] prepared palladium nanoparticles/nanostructured carbon black composite (PdNPs/NCB) by a chemical reduction method using sodium borohydride as a reducing agent. The composite was supported on the carbon–ceramic electrode (CCE). Figure 15.6a shows the surface morphology of the bare CCE. As seen in this image the surfaces of the bare CCE is dense, scaly and consist of platelets, defined by the layer structure of graphite. Figure 15.6b displays a typical SEM image of NCB, demonstrating that NCB, Fig. 15.6c shows the SEM image of PdNPs/NCB composite. The white visible spots are believed to be PdNPs lying on the NCB surface. In order to obtain the acceptable scientific information about the PdNPs

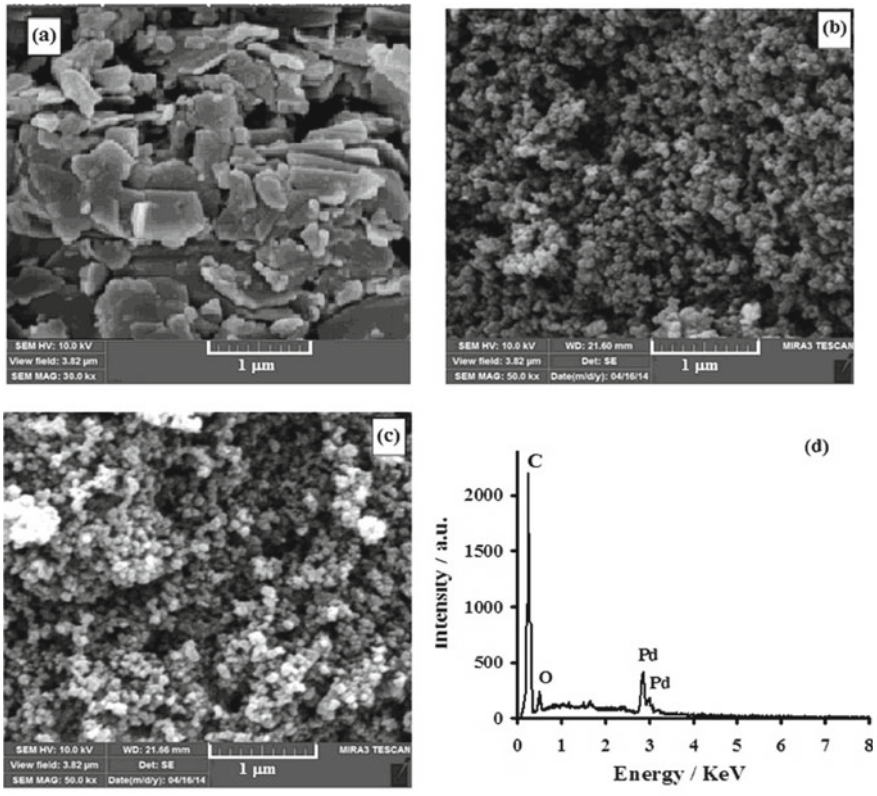

Fig. 15.6 SEM images of **a** CCE, **b** NCB, **c** PdNPs/NCB, **d** EDX analysis of PdNPs/NCB, and **g** cyclic voltammogram of formic acid oxidation on PdNPs/NCB/CCE (curve *a*), PdNPs/CCE (curve *b*) and NCB/CCE (curve *c*) in 0.5 M H_2SO_4 + 1.0 M formic acid solution at room temperature. Inset: cyclic voltammogram of PdNPs/NCB/CCE electrocatalyst in 0.5 M H_2SO_4 (without formic acid) at scan rate of 50 mV/s [38]

on the NCB surface, SEM-energy dispersive X-ray-analysis (SEM/EDX), HRTEM and XRD experiments were carried out as illustrated in Fig. 15.6d–e. The obtained modified electrode, PdNPs/NCB/CCE, was used as an efficient electrocatalyst for the oxidation of formic acid. Electrochemical techniques including cyclic voltammetry and chronoamperometry were applied for electrocatalytic investigations, and it was found that the PdNPs/NCB/CCE was catalytically more active than the Pd nanoparticles supported on the CCE without NCB (PdNPs/CCE) [38].

The effect of some experimental factors was also studied and optimum conditions were suggested. The obtained results show that the PdNPs/NCB/CCE has satisfactory stability and reproducibility for electro-oxidation of formic acid when stored in ambient conditions and improved electrocatalytic activity in continued cycling which make it more attractive for formic acid fuel cell applications.

The other researchers believe that the use of CB-based FC catalyst is a promising way to obtain high energy as compare to traditional CBs because of their large applications in housings and automobiles [36]. Another reasons of the used of carbon black in fuel cell applications are firstly, its low price over CNTs and graphene. Secondly, its agglomerate structure results in uniform dispersion of the metal catalyst particles and high interaction with the catalyst layer and finally even at low electrical conductivity as compare to graphite, carbon blacks are able to keep more electrolytes [39, 40].

Even though carbon blacks possess a number of excellent qualities as an electrocatalyst support, they are still facing some challenges such as poor corrosion resistance. This is due to their highly amorphous structure with is prone to corrosion during oxidation reaction [10]. This issue can be overcome through graphitisation techniques at high temperature and the use of carbon-free electrode [10, 41]. In addition, CB utilisation has tendency for oxidation at the potential of ORR. When used as support, the oxidation of CB can cause agglomeration and loss of metal nanoparticles, resulting in a decrease of the electrochemical surface area and activity of the electrocatalysts [42]. Furthermore, in carbon black, the metal nanoparticles catalyst sometimes stuck in the pore of the carbon black support leading to poor dispersion and distribution of the catalyst and therefore reduce the cell activities [43].

15.4.2 Carbon Nanofibers

Since the discovery of carbon nanofibers (CNFs) by Russian scientists in 1952, the exploration of these carbon nanomaterials has been conducted. This is mainly because of their unique properties including high mechanical strength, electric conductivity, high aspect ratio and surface area which make them suitable in several fields of materials technology, including supported catalysts for energy conversion [19, 44, 45]. CNFs are also produced by various chemical vapour deposition (CVD) techniques. CNFs are synthesised in the same way as CNTs, whereby carbon-containing gases is decomposed, but in this case, carbon is decomposed on transition metal particles surface such as Ni, Co, Fe and many more [44, 46, 47].

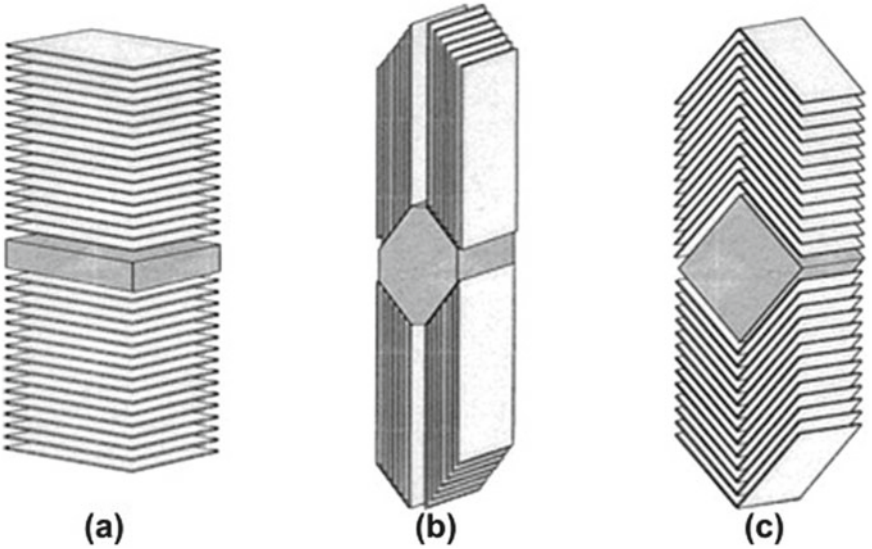

Fig. 15.7 Different types of carbon nanofibers sorted by the orientation of graphite stacks. **a** Platelet; **b** tubular; **c** herringbone [22]

There are three classes of carbon nanofibers as shown in Fig. 15.7; platelet where β, is 90°, Herringbone with β less than 90° and tubular where β is 0°. With β been the angle between the fibre growth axis and the graphene layers. The tubular CNFs (T-CNT) are also known as carbon nanotubes [44, 46, 48]. The additional to the previous types of carbon nanofibers, helical CNFs, twisted and stacked-cup CNFs can also be formed [49]. The type and the pore size of the CNFs after synthesis determine the fuel cell performance. Twisted CNFs in fuel cell, especially in proton exchange membrane (PEM), have proved to be very useful. For instance, Yuan and Ryu [46] in 2004 investigated the fuel cell performance of twisted and straight CNFs against CNTs. The performance showed that twisted CNF have rough, puckered surfaces that can bend easily thus creates more sites and open ends to facilitate incoming particle metal on the CNFs surface.

In summary, carbon nanofiber materials with small diameter and rougher surface have the best fuel cell performance [46]. According to Xi-Zhao and co-workers, the structure of the carbon nanofiber plays also an important role in the performance of the cell. For instance, in 2011, they have successfully deposited Pt on platelet-CNFs for PEMFs. The results showed high performance of the fuel cell [48]. Additionally, Li and others had used stack-cup CNFs supports as a mean to decrease the amount of expensive platinum catalyst in the cell. This reduction of platinum loading was because stack-cup CNFs are able to retain their electrical conductivity [33]. CNFs and other carbon nanomaterials are modified through different processes, which is very crucial during the electrocatalytic reactions. This then incorporate reactive groups, allowing metal deposition onto the substrate without any active reagents needed.

The modified CNF plays various roles in fuel cell applications depending on the quantity; nature of reagent used and processes techniques. High amount of oxygen functional groups loaded can alter the surface of the catalyst supports by decreasing the CNF conductivity leading to low cell performance [50]. Soundararajan et al. [51] deposited on CNF network Pt and Pt–Ni nanoparticles using electrochemical deposition method at various cycle numbers such as 40, 60 and 80. Nanostructured Pt or (Pt–Ni) and its structure were characterised using FE–SEM as shown in Fig. 15.8. The SEM image of bare CNF network shows horizontally aligned nanofibers. The alloy nanoparticles were found to deposit in a well dispersed manner over the CNF network.

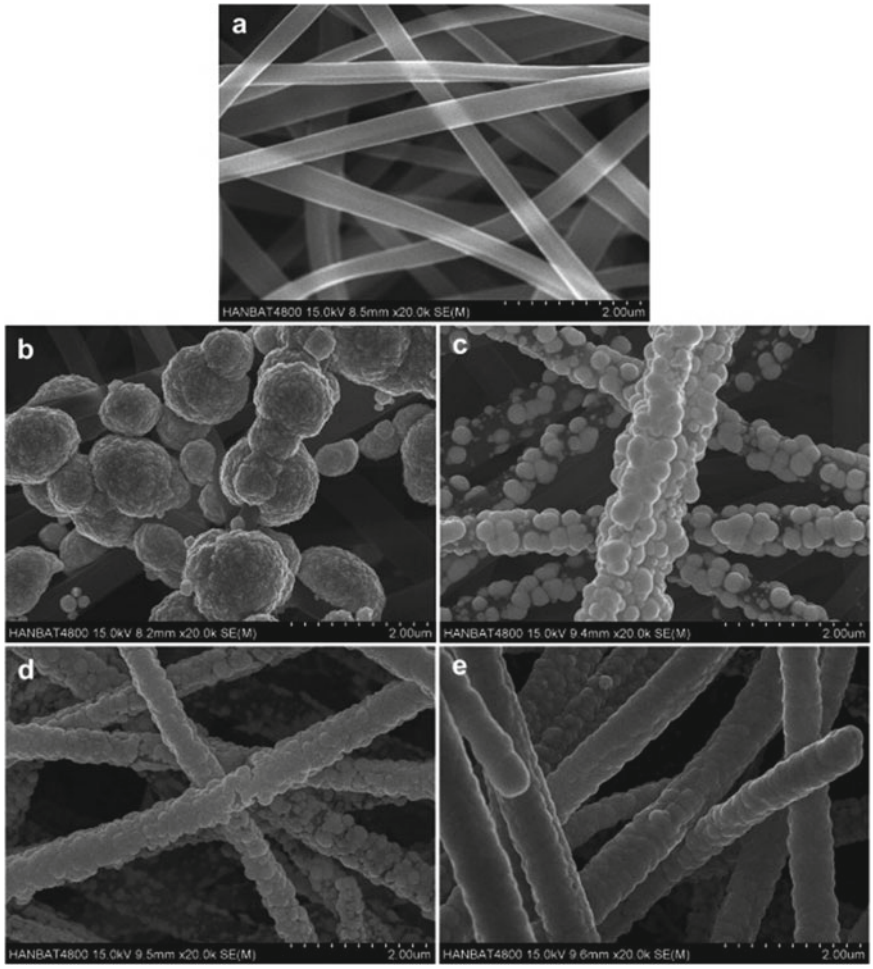

Fig. 15.8 **a**–**e** FE–SEM images of **a** bare CNF. **b** Pt40/CNF. **c** Pt–Ni40/CNF. **d** Pt–Ni60/CNF and **e** Pt–Ni80/CNF [48]

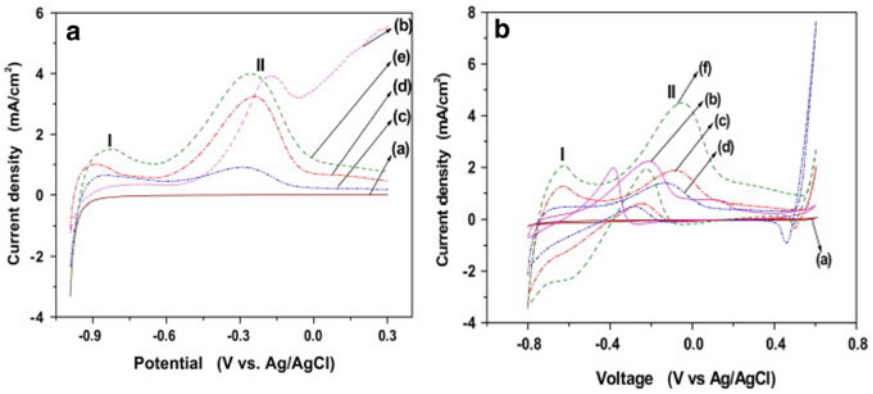

Fig. 15.9 Linear sweep voltammograms (**a**) and cyclic voltammograms (**b**) of charge transfer resistance (% of R_{ct}) of (a) bare CNF (b) Pt40/CNF (c) Pt–Ni40/CNF (d) Pt–Ni60/CNF and (e) PtNi/80/CNF catalyst electrodes [51]

The electroactivity shown in Fig. 15.9, showed a highest performance for the Pt–Ni80/CNF catalyst electrode at a sweep time of 80 with a lower charge transfer resistance of 94 Ω-cm^2. This is because of the increased Ni to Pt atomic ratio and the decrease in particle size with the increase of deposition cycle number. The results reported in this paper indicate that the performance of Pt–Ni80/CNF for the ethanol electro-oxidation is better than that of the pure Pt40/CNF, PtNi40/CNF and PtNi60/CNF in catalytic activity [51].

Highly active and cost-effective FeCo-incorporated CNF electrocatalysts for the ORR in alkaline ethanol fuel cells was studied and characterised using SEM and XRD as shown in Fig. 15.10. It is also clear that the nanoparticle size distribution is not uniform; however, the XRD analysis confirmed the presence of two characteristic diffraction peaks, which can be assigned to conventional graphitic carbon and a mixture of the metallic phases (Fe and Co) in the FeCo-CNF. Most Fe and Co metals embedded in the carbon fibres were then used to stabilize the incorporation of nitrogen and oxygen species more effectively, rather than participating in the ORR [52].

Through a comparison with a commercial Pt/C catalyst, the FeCo-CNF shows potential to replace costly Pt-based catalysts in alkaline ethanol fuel cells, in terms of comparable electrocatalytic activity and high selectivity for the ORR with a remarkably good ability to avoid ethanol crossover problem. Illustration in Fig. 15.11, featureless voltammetric profiles over the potential window for FeCo-CNF and metal-free CNF were observed as compared to commercial Pt/C. However, FeCo-CNF shows a significantly enlarged capacitive current over the entire potential window compared to metal-free CNF and commercial carbon black. CNF electrode and commercial carbon black show a two-step, two-electron process for oxygen reduction

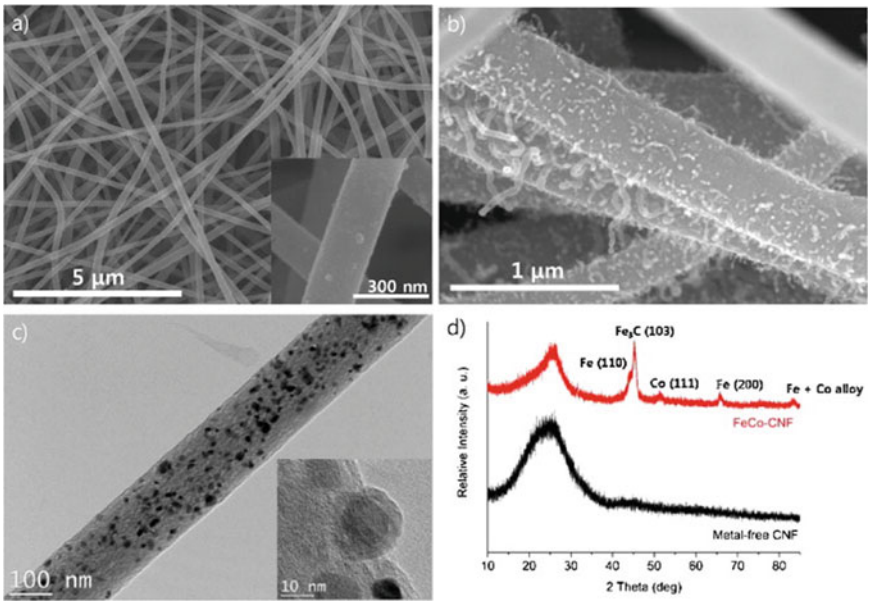

Fig. 15.10 **a** and **b** SEM and **c** TEM images of FeCo-CNF with magnified inset, respectively. **d** XRD patterns of FeCo-CNF and metal-free CNF, respectively [52]

with an onset potential of about −0.3 and −0.2 V, respectively, FeCo-CNF exhibited a very comparable electrocatalytic activity-favoring a one-step, four-electron pathway for the ORR [52].

15.4.3 Carbon Nanotubes

Carbon nanotubes (CNTs) are the one-dimensional manifestation and are constructed from a rolled-up sheet of graphene, have been a great deal of attention since their discovery by Ijima in 1999 [49, 53]. CNTs reportedly have extremely high surface areas, large aspect ratios of greater than 1000 and remarkably high mechanical strength of 400 times greater than steel. The tensile strength of CNTs is 100 times greater than that of steel, and the electrical and thermal conductivities approach those of copper [54].

CNTs as shown in Fig. 15.12 appear in several forms including single-walled carbon nanotubes (SWCNT) and multi-walled carbon nanotubes (MWCNT) depending on the orientation and the number of layers being formed during their synthesis. The SWCNT has a single layer ranged in a random form and MWCNT is consisted of multiple layers (about 250) and are orientated in coaxial stacked graphene sheets [49, 53]. Carbon nanotubes can be rolled in different forms as shown in Fig. 15.12a–c. When rolled in simple layer, it is called single walled, while two or

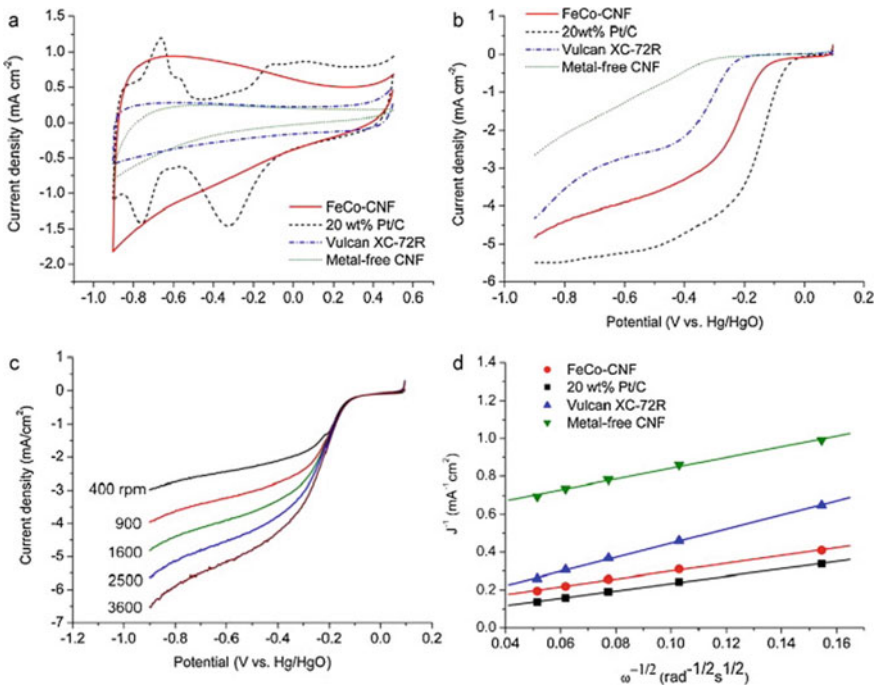

Fig. 15.11 **a** CVs of as-synthesised FeCo-CNF, metal-free CNF, commercial Pt/C and Vulcan carbon black in 0.1 M KOH at a scan rate of 50 mV s^{-1}. **b** LSVs of as-synthesised FeCo-CNF, metal-free CNF, commercial Pt/C, and Vulcan carbon black in O_2 saturated 0.1 M KOH at a rotation rate of 1600 rpm. **c** Rotating disc voltammograms recorded for FeCo-CNF in an O_2 saturated 0.1 M KOH at a scan rate of 5 mV s^{-1}. **d** Koutecky–Levich plot at −0.6 V. The experimental data were obtained from (**c**) and the lines are linear regressions [52]

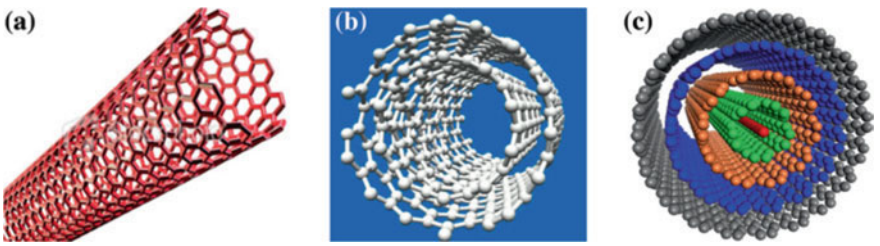

Fig. 15.12 Basic structures of **a** single-walled, **b** double-walled, and **c** multi-walled CNTs [55]

multiple layer, it is called double or multiple walled. Or carbon nanotubes are found in different forms such as single, double and multi-walled [55–57].

The bonding of the graphene sheets ends produces three different types of CNTs helicities, and it determines the electrical properties of the nanotubes as shown in Fig. 15.13. Chirality also describes the angle of the nanotube's hexagonal carbon-

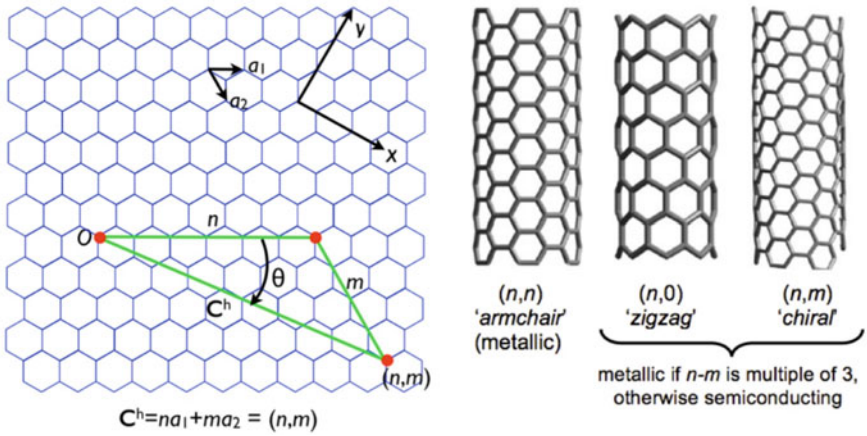

Fig. 15.13 Diagram showing zigzag, armchair and chiral carbon nanotubes [59]

atom lattice. There two main conducting helicities are armchair helicity which exhibit metallic properties and zigzag helicity, which may be semiconducting, and the third one is chiral helicity [49, 58]. Generally, carbon nanotubes have either metallic or semiconductive properties [39]. CNTs with their unique 1D molecular geometry of a large surface area coupled with their excellent electrical properties have become significant materials for the engineering of electrode surfaces where the development of electrochemical devices such as fuel cells with region-specific electron-transfer capabilities is of principal importance.

CNTs are synthesised from the electrocatalytic decomposition of carbon constituted solids or gases molecules. The carbon nanotubes are grown through different methods having chemical vapour deposition (CVD), arc-discharge evaporation and laser ablation as three main techniques (Fig. 15.14) [60]. The first approach is a promising technique, even though it produces a wide range of (MWCNTs), and the later approaches can produce extremely thin SWCNTs [39].

These synthesis techniques also have a great role to play on the CNTs electrocatalytic performance. For instance, bundled CNTs do not improve the activity in the fuel cell applications. Therefore, specific synthesis parameters are to be considered when making carbon nanotubes as catalyst for fuel cell applications. CNTs generally exhibit inner diameters of 3–15 nm, outer diameters of 10–50 nm and lengths of 10–50 μm. These morphologies parameters, the unique surface areas of carbon nanotubes of about 250 $m^2\ g^{-1}$, together with electrical and mechanical properties also make them excellent candidates for fuel cell catalyst supports [2, 58, 62]. CNTs as the supports to anchor well-dispersed particles, it should be modified. The modification of the surface of these supports can be performed through noncovalent or covalent treatment methods. The noncovalent method is based on incorporating surfactants from strong acid. The covalent modification incorporates long alkyl and polymer chains. Noncovalent functionalization is preferable because after modification treatment the CNTs structure and original properties remain unchanged [63]. The

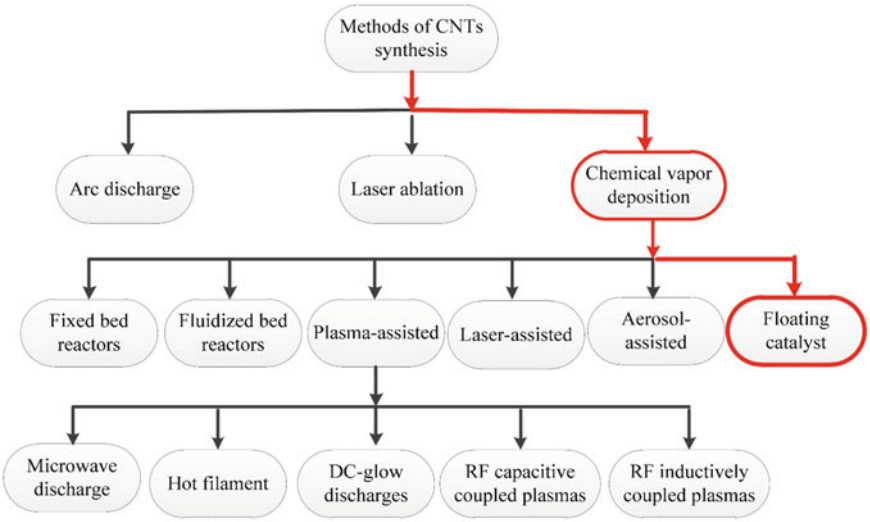

Fig. 15.14 Currently used methods for synthesising carbon nanotubes (CNTs) [61]

technique does not only keep the original properties of CNTs but also fix numerous organic linkers or functional groups (carboxyl, hydroxyls and carbonyls) on the CNTs surfaces, which favour the deposition of incoming metal catalyst leading to fuel cell enhancement [58]. In this same way, Lee and other researchers in 2006 [47] studied the deposition of small platinum size on functionalised CNT. The results showed high ORR activity as compared to electrocatalysed deposition reaction of non-functionalised CNT-supported Pt metal catalyst.

In another study, the nanocomposite of expanded graphite and multi-walled carbon nanotubes (EG-MWCNT) was used as the catalyst supporter owing to its large electrode area. Palladium nanoparticles (Pd NPs) electrodeposited on the EG-MWCNT were employed as the electrocatalysts. As shown in Fig. 15.15, electrochemical activity and double-layer capacitances of the Pd-NP/EG-MWCNT electrocatalysts with different EG-to-MWCNT mass ratios were investigated to optimise their compositions. Electrocatalytic oxidation of alcohols (methanol, ethanol, ethylene glycol), carboxylic acids (formic acid) and aldehydes (formaldehyde) was studied in alkaline media [2]. However, one limitation of CNTs is their poor interaction with other nanomaterials that end up reducing their properties and abilities [53].

15.4.4 Graphene

One of the recent revolutionary carbon materials used in fuel cell is graphene. Since its discovery in 2004, graphene sparked scientific research in the community. This is due to its remarkable features such as electrical conductivity, mechanical strength,

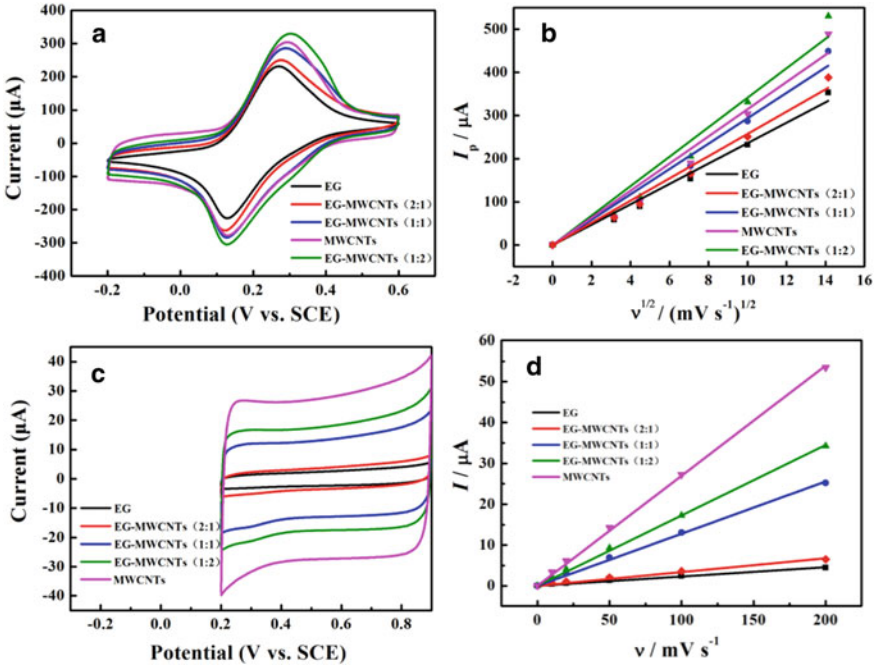

Fig. 15.15 Cyclic voltammograms in 5 mM $[Fe_3(CN)_6]^{3-/4-}$ + 0.1 M KCl solution (**a**) and 0.1 M KCl solution (**c**) at the scan rate of 100 mV s^{-1}. **b** Variation of oxidation peak currents of 5 mM $[Fe_3(CN)_6]^{3-/4-}$ as a function of the square roots of the scan rates. **d** Variation of the capacitive currents in 0.1 M KCl at the potential of 0.6 V as a function of scan rates. The electrodes are EG, EG-MWCNT and MWCNT coated GCEs. The mass ratios of EG to MWCNTs are varied from 2:1, 1:1 to 1:2 [2]

thermal conductivity and super-high specific surface area of about 2600 m^2 g^{-1} [64]. Graphene is a nanomaterial arranged into a two-dimensional (2D) layer of carbon atoms with sp^2 hybridisation that are connected in a hexagonal lattice structure [65]. The production and processing of graphene appears to be more feasible, compared to CNTs and other carbon materials. Graphene has been studies in numerous mechanical experiments and has appeared to be the strongest material on earth [65]. Graphene, also known as the mother of all types of graphite, is considered as the basic block of all king of carbon materials in different dimensions, 0D fullerenes, 1D nanotubes, 2D graphene and 3D graphite and diamond [60].

Graphene is commonly synthesised by two different types of approach, viz. top-down and bottom-up as shown in Fig. 15.16. In top-down approach, the stacked sheets of graphite are broken apart to yield single graphene sheets, whereas bottom-up methods involve synthesising graphene from other carbon containing sources.

For top-down methods separating the stacked sheets, means that the van der Waals forces that hold the layers together must be destroyed. Two main types of graphene

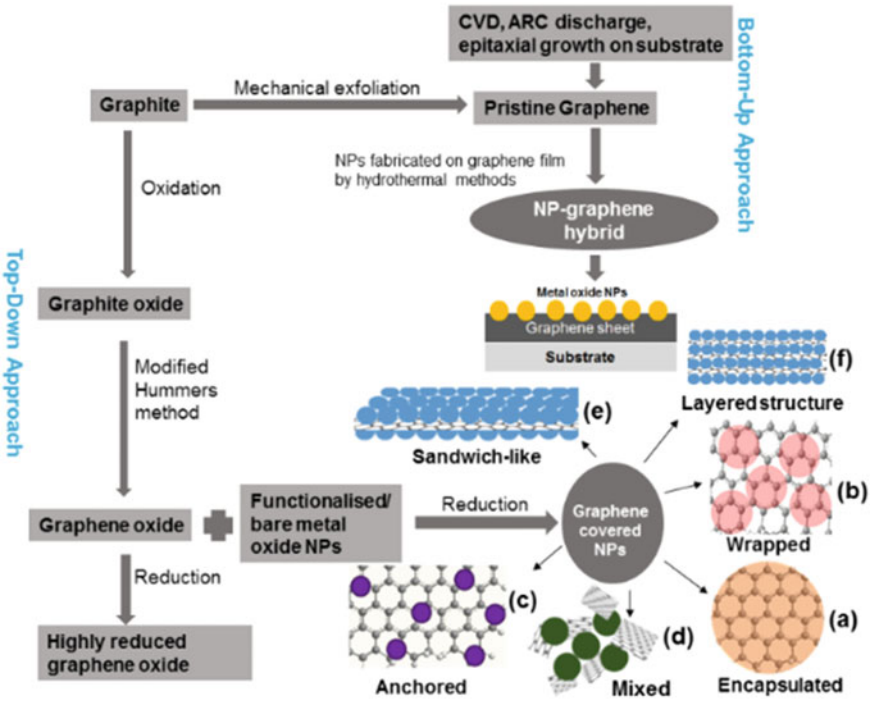

Fig. 15.16 Schematic presentation of top-down and bottom-up methods used for the formation of graphene–NP hybrids and different structures of **a** graphene-encapsulated NPs, **b** graphene-wrapped NPs, **c** NPs anchored to GSs, **d** mixed graphene–NP structures, **e** graphene–NP sandwich structures, and **f** graphene–NP layered hybrids [66]

materials can be obtained from this process. The graphene oxide known as single-layer graphene is decorated with oxygen functional groups which are synthesised via oxidative exfoliation by either the Brodie, Staudenmaier, or Hummers method, or some variation of these methods [67]. The second type is reduced graphene oxide (rGO), obtained through hydrothermal processes or by using reducing agents such as hydrazine, sodium borohydride, aluminium hydride and ammonium hydroxide for the dispersion of the graphene platelets [68, 69] (see Fig. 15.16). Reduction of graphene oxide via thermal treatment has also been reported to be an efficient and low-cost method [67, 68]. Key challenges in this area is effectively separating the layers of graphite without damaging the sheets, and preventing re-agglomeration of the sheets once the layers have been exfoliated. For bottom-up approach such as ark discharge, chemical vapour deposition. high levels of graphitization must be stimulated to produce material of good quality; the processes involved are usually simple and generally require high temperatures. However, the material produced can contain higher levels of defects than observed for top-down methods. In addition to forming graphene nanosheets, bottom-up methods can also be used to form large area graphene films via growth on certain substrates [70]. Of these graphitic groups,

pristine graphene has distinctive properties, large surface area supports that are crucial in enhancing the fuel cells performance [39]. The 3D structure has a cross-linked network, large specific surface area follows by porous nanostructures resulting in high interaction with the metal particle and therefore enhances its electrocatalytic activity, especially in alkaline media of direct methanol fuel cell [64].

As compared to CNTs, graphene synthesis methods are simpler. Another advantage of graphene over CNTs is that graphene surface is free of impurities. The impurities on CNTs decrease their electrochemical properties [71]. Both chemical properties of graphene and the dispersion of the metal nanoparticles catalyst on graphene depend on the layer number of graphene. Lee et al. [72] used Raman spectroscopy techniques to elucidate the issue whereby three samples of single, bi- and tri- layer of graphene were used. This was achieved by looking at the ratio of the D band intensity over the G band intensity (I_D/I_G) values. The ratio values decreased as the number layer of graphene was increasing indicating that single-layer graphene possess numerous oxygen functional groups resulting in high active single-layer graphene as compare to bi- and tri-layer [72]. Another concern of using graphene as support is to see how it could improve the fuel cell performance. In 2015, Liu et al. deposited Pd metal nanocatalyst on 3DGA graphene support. It happened that the electrocatalytic performance was high due the specific surface properties of graphene. Other factors such as small size and well dispersion of Pd nanoparticles on 3DGA are also considered. The facile synthesis of the present Pd/3DGA nanocomposites showed superior electrocatalytic performance towards methanol oxidation reaction [64]. Researchers have been investigated the interaction between the metal and graphene aiming to improve the unique electronic and magnetic properties of graphene through doping in order to meet different fuel cell applications [73].

15.4.5 Doped Carbon Material

In recent years, many researchers have focused on development of heteroatom carbon-based catalyst in order to activate carbon-containing material that will promote the interaction between the metal catalyst, and they are used in fuel cells [74]. Heteroatom doping of carbon nanostructures is one of the approaches that may induce intrinsic catalytic activity in these materials. In addition, such introduction of guest elements into the hexagonal carbon skeleton provides strong nucleation sites, which facilitate the stabilization of nanostructures on their surface [75]. There are many types of heteroatoms nitrogen (N), boron (B), phosphorus (P), sulphur (S) and many more that are used for doping carbon materials. Doping with heteroatoms is changing the physical and chemical behaviour of the carbon material resulting in new state and possibilities material. The doping or functionalising of carbon edges sheets with heteroatoms occurs without damaging the carbon basal plane which can change the carbon work function and impart solubility and catalytic activity [4, 75].

These dopants improve the electrocatalytic activity for oxygen reduction due to the high interaction between the π electrons of carbon and the lone pair electrons

from heteroatom dopants [20, 76]. Of the types of heteroatoms, nitrogen is the most trusted and used because its small atomic size is identical to that of carbon atom [75].

15.4.5.1 Nitrogen-Doped Carbon Materials

Currently, many researchers are looking towards producing better electrocatalysts with various modifications. One such modification involves doping carbon material that is preferable for use as a support for metal catalysts and transition metals due to their low cost, high electrical conductivity stability, long-lifetime and ability to enhance oxygen reduction reaction (ORR) activity [77]. Chemical doping is important factors in tailoring the properties of carbon materials, which has been proved effective nitrogen the doping of CNTs and has greatly broadened their applications [78].

Similar to CNTs when a nitrogen atom is doped into graphene, three common bonding configurations within the carbon lattice, including quaternary-N (or graphitic N), pyridinic-N and pyrrolic-N are observed as shown in Fig. 15.17c [80]. The types of configurations in carbon atoms are generally determine by XPS as shown by example in Fig. 15.17a, b. The different N configurations incorporated in the graphitic structure demonstrates the diverse catalytic activities towards ORR due to their different electronic structures [81]. Nitrogen anchors in carbon material changes the electronic properties of the support by making it denser. The higher density of the catalytic sites on the carbon surface provides better electrochemical performance [81, 82].

The nitrogen atom in the carbon structure brings the lone pair electron. This then interacts strongly with the π-electrons of carbon material and facilitates dispersion process. Moreover, nitrogen doped on carbon also reduces CO_{ads} on Pt by increasing the catalyst poison tolerance [9]. Nitrogen-doped carbon nanomaterials have therefore received increasing attention as effective metal electrocatalysts promising potential catalysts material for ORR because it also offers great electrical conductivity [49]. Graphene is a zero-gap semiconductor; thus, the band structure of graphene consists of two bands as valence and conduction band. Therefore, in graphene nitrogen, doping is one of the effective ways for modification of the electrical structure of graphene and suppressing the density of graphene states near the Fermi energy (F_m) level, end in opening of gap between the valence and conduction band [83].

Numerous experiments regarding nitrogen doping have been done in fuel cells area, Mabena et al. [75] reported the use of the nitrogen-doped carbon nanotubes (N-CNTs) prepared via thermal chemical vapour deposition (CVD), as support for ruthenium (Ru) nanoparticles. The amount of Ru deposited on N-CNTs was varied between 0 and 10 wt%. The activity of the prepared nanocatalysts towards the ORR was characterised using the rotating disk electrode and voltammetry techniques. The ORR activity was higher at low concentrations of Ru on N-CNTs. The four-electron pathway of ORR was more favourable on 2Ru/N-CNTs and 5Ru/N-CNTs than 10Ru/N-CNTs [75].

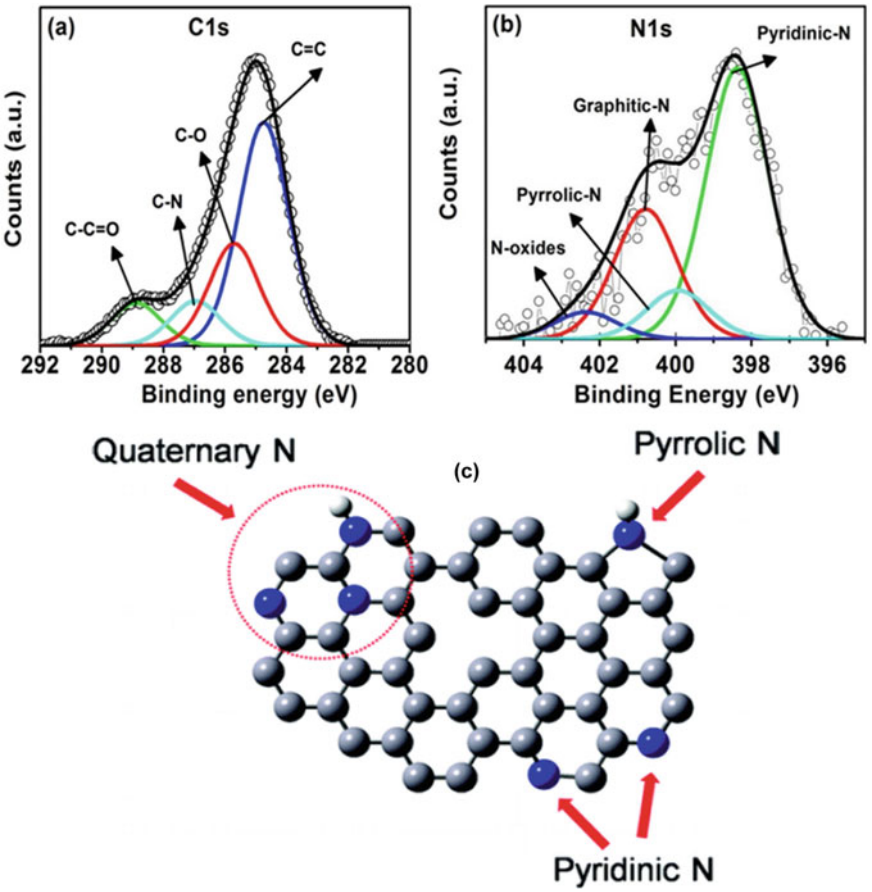

Fig. 15.17 **a** C 1 s spectrum for N-doped graphene. The deconvolution using Doniach–Sunjic line shape analysis shows **b** N 1 s XPS spectrum for N-doped graphene showing three different nitrogen configurations. c. The atomic configuration showing pyridinic-N, pyrrolic-N and graphitic-N (quaternary N) as well as graphene lattice and vacancies. XPS measurements were carried out at an angle of 45° with respect to the sample normal [79, 80]

Wei et al. [83] reported nitrogen-doped and pristine graphene, at the ambient conditions after measuring fifty devices. Amazing and notable features of N-doped graphene were observed in comparison to the pristine graphene. Pristine graphene displays a good conductivity and a linear $I_{ds} - V_{ds}$ behaviour representing good ohmic contacts between the Au/Ti pads and the graphene. V_g decreases as I_{gs} is increased gently and the neutrality point is reached at 15–20 V demonstrating a P-type behaviour and as comparing pristine graphene with the nitrogen-doped graphene, N-graphene also shows relative lower conductivity with greater on/off ratio [83].

15.4.5.2 Other Heteroatom-Doped Carbon Material

Numerous heteroatom-doped graphitic carbons beside N-doped have also been developed as charge extraction materials or metal-free catalysts to replace noble metal catalysts for low-cost renewable generation and storage of clean energy [4]. Recent advances in this exciting field are stated below. Boron has been incorporated into graphite [84] carbon fibre diamond graphene [85] and SWCNHs by various methods including thermal post-treatments with boric acid [86] or boron oxide introduction as a co-dopant after plasma etching, such as in CBN film production or chemical vapour deposition from benzene and boron trichloride mixtures [87]. Figure 15.18 represents the boron atoms successfully doped into the graphene framework. Boron was shown to alter the growth mode of nanocarbons and simultaneously increase their electrochemical stability and oxidation resistance, enabling their use as catalyst supports and electrodes in intermediate temperature fuel cells [87]. Zhen-hua Sheng et al. showed that boron atoms, with strong electron-withdrawing capability, are doped into graphene frameworks forming boron doped graphene (BG) via a catalyst-free thermal annealing approach in the presence of boron oxide. Due to its particular structure and unique electronic properties, the resultant BG exhibits excellent electrocatalytic activity towards ORR in alkaline electrolytes, similar to the performance of Pt catalysts. In addition, the non-metallic BG catalyst shows long-term stability and good CO tolerance superior to that of Pt-based catalysts. These results demonstrate that the BG, as a promising candidate in advanced electrode materials, may substitute Pt-based nanomaterials as a cathode catalyst for ORR in fuel cells [88].

Furthermore, it was found that N-doped nanocarbons co-doped with the secondary heteroatoms such as boron, sulphur or phosphorus (B, S, or P) is able to further enhance their ORR activity [74, 88–94]. Sulphur atoms are of particular interest as they were found to easily replace the C atom when co-doping with N, the S is also interesting due to similar electronegativity and van der Waals radius to carbon and the superior than the N while having two loan pair electrons. For N and P co-doped catalysts, phosphorous exhibits a larger atomic size but a lower electronegativity

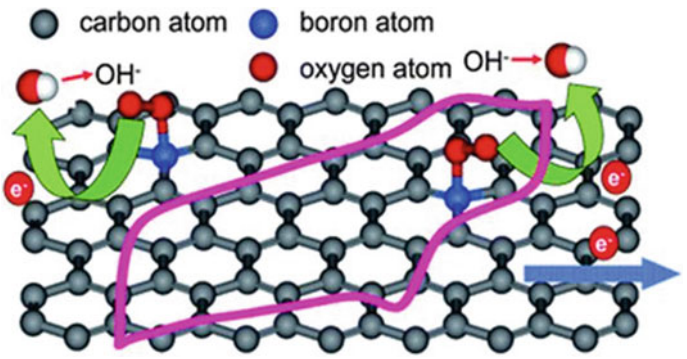

Fig. 15.18 Schematic diagram of Boron hetero-doped graphite [88]

relative to C, which can create defects on the carbon surface-induced active sites for oxygen adsorption during the ORR [95].

Various studies were conducted to gain advantage insight into the synergistic effect of heteroatoms in co-doping as well as the role of each dopant in the enhancement of the electrocatalytic activity. The oxygen reduction reaction (ORR) activity of the doped helical graphene nanoribbons (GNRs) measured in both alkaline and acidic electrolytes, compared with the state-of-the-art platinum/carbon (Pt/C) electrocatalysts have been reported [96]. The nitrogen/sulphur hetero-doped graphene nanoribbons (CN_x/CS_x-GNRs) with helically unzipped structures have shown highly efficient ORR activity that is comparable to Pt/C in onset potential, exchange current density, four-electron pathway selectivity, kinetic current density and methanol tolerance. The nitrogen/sulphur hetero-doped graphene greatly contribute to the development of precious metal-free carbon nanomaterials as electrocatalysts in the cathode of alkaline and proton-exchange membrane fuel cells [96].

In another study, nitrogen and sulphur were co-doped in porous carbon (DPC) as illustrated in Fig. 15.19. Using less hazardous one-step process from a single precursor, DPC was synthesised and investigated as promising cathode electrocatalyst in the half-cell study for ORR in acidic environment. The improved half-cell

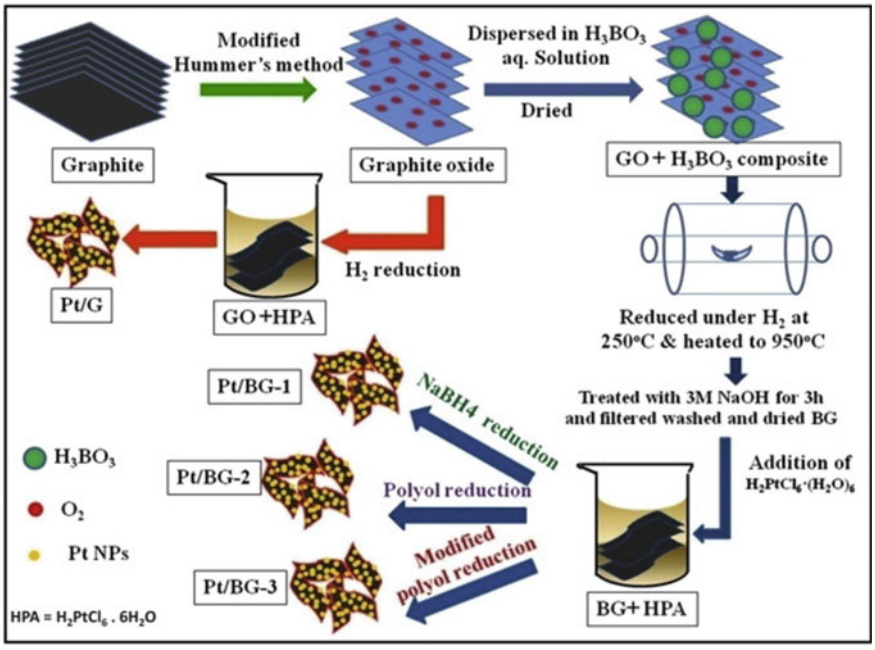

Fig. 15.19 Schematic illustration of the synthesis procedure of Pt/G and Pt/BGs electrocatalysts procedure [87]

performance for DPC comparable to commercial Pt/C were attributed to the synergistic effect of the improved mass transfer, which is owed to porous high surface area carbon and increased active sites attributable to heteroatom doping [87].

J. C. Li et al. developed a low-cost method to synthesise SWCNT@NPC as a bifunctional oxygen reaction catalyst, because of its unique structure and N, P co-doping, the material shows excellent ORR and OER performance (Fig. 15.20a–c). Based on the experimental results and discussion, a possible schematic was put forward as an electrocatalytic model for the reversible oxygen reaction processes on SWCNT@NPC (Fig. 15.20d). SWCNT facilitates electron transfer while porous carbons acted as active materials with N, P co-doping sites for the ORR and N Doping sites for the OER [89].

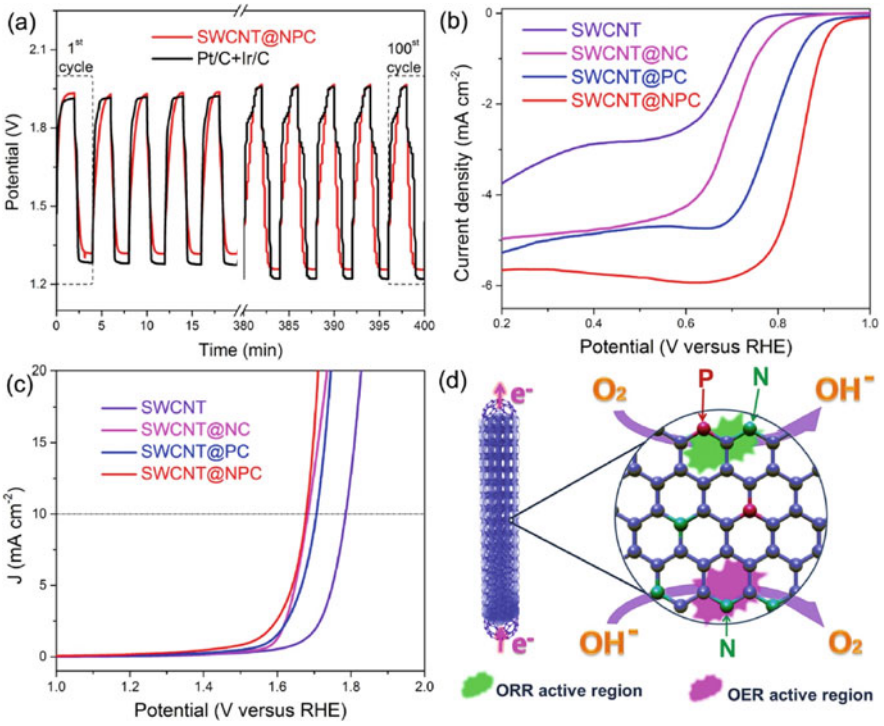

Fig. 15.20 **a** Galvanostatic charge–discharge cycling curves of SWCNT@NPC and Ir/C + Pt/C in the rechargeable Zn-air batteries **b** ORR and **c** OER polarisation curves of SWCNT, SWCNT@NC, SWCNT@PC and SWCNT@NPC **d** schematic for electrocatalytic model for OER and ORR process electron transfer facilitation on NP co-doped carbon nanotubes [89]

15.5 Conclusions

Fuel cells have drawn much attention from scientists because they are both environmentally and highly efficient energy devices. The performance of the fuel cell depends on the reaction rate, which is directly related to the catalyst for the reaction. The ORR of the cathode-side reaction is the primary influencing factor of the performance of the fuel cell. Currently, platinum (Pt) is the most popular catalyst material for ORR. However, the material cost of the Pt catalyst and its susceptibility to poisoning are the main disadvantages. Recent studies indicated that the Pt catalyst contributes around 34% of fuel cell stack costs. It is possible to reduce the manufacture expenses of fuel cell by improving the structural design. The only way to reduce the material cost is to develop high performance and inexpensive ORR catalysts to replace the Pt catalyst. Therefore, this chapter presented the significant influence of different carbon nanomaterials on the fuel cells and their overall performances. The carbon-based electrocatalyst holds a strong potential as high-performance ORR/OER catalyst in fuel cell applications. Carbon is found in dramatically different forms with varying micro-textures. The diverse morphologies make it an attractive material that is widely used in in a large range of electrochemical fuel cell applications. Carbon increases the availability of the electrocatalysts and mass transfer of the reactants. The carbon materials in fuel cells are favoured due to their properties, high volume, surface area ratio, tensile strength and resistance to corrosion. Moreover, carbon is an electron-conducting material with a sufficiently high electrical conductivity to favour the flow of electrons between the electrodes and the catalyst. However, in order to prepare high-performance carbon electrocatalysts, a better understanding of catalytic mechanism is required. A combination of both experimental and theoretical approach would be of high importance in searching the active centres and studying the basic science behind the electrocatalysis. Then, new synthetic and strategies must be developed to precisely control the atomic location, content, and the distribution of the catalytic active centres in carbon-based catalysts.

Acknowledgements The authors immensely appreciate the financial support from the National Research Foundation (NRF) (UID Nos. 113561, 117727 and 117984), Tshwane University of Technology and University of Limpopo, South Africa.

References

1. L. Fan, B. Zhu, P.C. Su, C. He, Nanomaterials and technologies for low temperature solid oxide fuel cells: recent advances, challenges and opportunities. Nano Energy **45**(Dec 2017), 148–176 (2018).
2. H. Li, Y. Zhang, Q. Wan, Y. Li, N. Yang, Expanded graphite and carbon nanotube supported palladium nanoparticles for electrocatalytic oxidation of liquid fuels. Carbon N. Y. **131**, 111–119 (2018)
3. R. Ramachandran, S. Chen, Recent developments in electrode materials for oxygen reduction reaction. Int. J. Electrochem. Sci. **10**, 8581–8606 (2015)

4. C. Hu, D. Liu, Y. Xiao, L. Dai, Functionalization of graphene materials by heteroatom-doping for energy conversion and storage. Prog. Nat. Sci. Mater. Int. **28**(2), 121–132 (2018)
5. A.M. Abdalla, et al., Nanomaterials for solid oxide fuel cells: a review. Renew. Sustain. Energy Rev. **82**(Sept 2016), 353–368 (2018)
6. P.G. Grimes, *Historical Pathways for Fuel Cells the New Electric Century*, Dec 2000
7. E.I. Ortiz-Rivera, A.L. Reyes-Hernandez, R.A. Febo, Understanding the history of fuel cells. **2**(2), 117–122 (2007)
8. A.D. Moore, Synthesis and characterization of carbon catalyst substrates for fuel cell applications school of chemical engineering and analytical science table of contents. The University of Manchester (2011)
9. N. Seselj, C. Engelbrekt, J. Zhang, Graphene-supported platinum catalysts for fuel cells. Sci. Bull. **60**(9), 864–876 (2015)
10. M. Bruno, N. Scientific, F.A. Viva, Carbon materials for fuel cells, in *Carbon Materials for Fuel Cells*, Sept 2014 (Chapter 7)
11. S. Mekhilef, R. Saidur, A. Safari, Comparative study of different fuel cell technologies. Renew. Sustain. Energy Rev. **16**(1), 981–989 (2012)
12. L. Dai, Carbon-based catalysts for metal-free electrocatalysis. Curr. Opin. Electrochem. **4**(1), 18–25 (2017)
13. D. Carolina, G. Nu, Nanostructured carbon materials for applications in polymer electrolyte membrane fuel cells. Catalysts 2–272 (2013)
14. S.P. Jiang, Development of lanthanum strontium manganite perovskite cathode materials of solid oxide fuel cells: a review. J. Mater. Sci. **43**(21), 6799–6833 (2008)
15. F.S. da Silva, T.M. de Souza, Novel materials for solid oxide fuel cell technologies: a literature review. Int. J. Hydrogen Energy **42**(41), 26020–26036 (2017)
16. Hydrogen fuel cell electric bus [Online]. Available: https://www.octa.net/About-OCTA/Environmental-Sustainability/Hydrogen-Fuel-Cell-Electric-Bus/. Accessed: 21 Feb 2019.
17. S.M. Haile, Fuel cell materials and components. Acta Mater **51**, 5981–6000 (2003)
18. L. Ge, R. Ran, R. Cai, Z. Shao, *Solid-Acid Fuel Cells*, Mar 2008, pp. 2–21.
19. Y.I. Kim, D. Soundararajan, C.W. Park, S.H. Kim, J.H. Park, J.M. Ko, Electrocatalytic properties of carbon nanofiber web—supported nanocrystalline Pt catalyst as applied to direct methanol fuel cell. Int. J. Electrochem. Sci. **4**, 1548–1559 (2009)
20. M. Liu, R. Zhang, W. Chen, Graphene-supported nanoelectrocatalysts for fuel cells: synthesis, properties, and applications. Chem. Rev. **114**(10), 5117–5160 (2014)
21. W. Liu, Q. Ru, S. Zuo, S. Yang, J. Han, C. Yao, Controllable synthesis of nitrogen-doped carbon nanotubes derived from halloysite-templated polyaniline towards nonprecious ORR catalysts. Appl. Surf. Sci. **469**(Oct 2018), 269–275 (2019)
22. E. Antolini, Carbon supports for low-temperature fuel cell catalysts. Appl. Catal. B Environ. **88**(1–2), 1–24 (2009)
23. J.R. Siqueira, O.N. Oliveira, Carbon-based nanomaterials. Nanostructures, 233–249 (2017)
24. A. Aqel, K.M.M.A. El-Nour, R.A.A. Ammar, A. Al-Warthan, Carbon nanotubes, science and technology part (I) structure, synthesis and characterisation. Arab. J. Chem. **5**(1), 1–23 (2012)
25. L. Calvillo, V. Celorrio, J.I. Pardo, S. Perathoner, R. Moliner, *Study and Application of Carbon Black Vulcan Xc-72R in Polymeric Electrolyte Fuel Cells*, Jan 2011
26. A. Bayrakçeken, et al., Vulcan-supported Pt electrocatalysts for PEMFCs prepared using supercritical carbon dioxide deposition. Chem. Eng. Commun. **6445**(196:1–2), 194–203 (2008)
27. M. Carmo, M. Linardi, J. Guilherme, R. Poco, H_2O_2 treated carbon black as electrocatalyst support for polymer electrolyte membrane fuel cell applications. Int. J. Hydrogen Energy **33**(21), 6289–6297 (2008)
28. L.T. Soo, K.S. Loh, A.B. Mohamad, W.R.W. Daud, W.Y. Wong, An overview of the electrochemical performance of modified graphene used as an electrocatalyst and as a catalyst support in fuel cells. Appl. Catal. A Gen. **497**, 198–210 (2015)
29. Y.J. Wang, B. Fang, H. Li, X.T. Bi, H. Wang, Progress in modified carbon support materials for Pt and Pt-alloy cathode catalysts in polymer electrolyte membrane fuel cells. Prog. Mater. Sci. **82**, 445–498 (2016)

30. S. Ergun, Structure of carbon. Carbon **6**, 141–159 (1968)
31. P. Trogadas, T.F. Fuller, P. Strasser, Carbon as catalyst and support for electrochemical energy conversion. Carbon N. Y. **75**, 5–42 (2014)
32. J. Liang, S.Z. Qiao, G.Q. Lu, D. Hulicova-Jurcakova, *Carbon-Based Catalyst Support in Fuel Cell Applications* (Elsevier Ltd., 2012)
33. W. Li, M. Waje, Z. Chen, P. Larsen, Y. Yan, Platinum nanopaticles supported on stacked-cup carbon nanofibers as electrocatalysts for proton exchange membrane fuel cell. Carbon N. Y. **48**(4), 995–1003 (2009)
34. E. Mshoperi, R. Fogel, J. Limson, Electrochimica acta application of carbon black and iron phthalocyanine composites in bioelectricity production at a brewery wastewater fed microbial fuel cell. Electrochim. Acta **128**, 311–317 (2014)
35. S.A.S. Machado, O. Fatibello-Filho, P.A. Raymundo-Pereira, B.C. Janegitz, F.C. Vicentini, Nanostructured carbon black for simultaneous sensing in biological fluids. Sens. Actuators B Chem. **227**, 610–618 (2016)
36. M.R. Berber, I.H. Hafez, T. Fujigaya, N. Nakashima, A highly durable fuel cell electrocatalyst based on double-polymer-coated carbon nanotubes. Sci. Rep. **5**, 1–11 (2015)
37. Z. Xia, G. Sun, L. Yuan, J. Liu, S. Wang, L. Jiang, Facile synthesis of silver nanoparticles supported on three dimensional graphene oxide/carbon black composite and its application for oxygen reduction reaction. Electrochim. Acta **135**, 168–174 (2014)
38. B. Habibi, S. Mohammadyari, Palladium nanoparticles/nanostructured carbon black composite on carbon-ceramic electrode as an electrocatalyst for formic acid fuel cells. J. Taiwan Inst. Chem. Eng. **58**, 245–251 (2016)
39. A. Riese, *Nanostructured Carbon Materials for Active and Durable Keywords*, Oct 2015.
40. M. Srivastava, M. Kumar, R. Singh, U.C. Agrawal, M.O. Garg, Energy-related applications of carbon materials—a review. **68**(Feb), 93–96 (2009).
41. T. Tamaki, H. Wang, N. Oka, I. Honma, S.H. Yoon, T. Yamaguchi, Correlation between the carbon structures and their tolerance to carbon corrosion as catalyst supports for polymer electrolyte fuel cells. Int. J. Hydrogen Energy **43**(12), 6406–6412 (2018)
42. A. Bayrakçeken Yurtcan, E. Daş, Chemically synthesized reduced graphene oxide-carbon black based hybrid catalysts for PEM fuel cells. Int. J. Hydrogen Energy, 1–11 (2018)
43. T. Matsumoto, T. Komatsu, K. Arai, T. Yamazaki, M. Kijima, Reduction of Pt usage in fuel cell electrocatalysts with carbon nanotube electrodes. Chem. Commun. **c**, 840–841 (2004)
44. S. Celebi, *Carbon Nanofiber Electrodes for PEM Fuel Cells* (2012)
45. K. Lee, J. Zhang, H. Wang, D.P. Wilkinson, Progress in the synthesis of carbon nanotube- and nanofiber-supported Pt electrocatalysts for PEM fuel cell catalysis. J. Appl. Electrochem. **60**, 507–522 (2006)
46. F. Yuan, H. Ryu, The synthesis, characterization, and performance of carbon nanotubes and carbon nanofibres with controlled size and morphology as a catalyst support material for a polymer electrolyte membrane fuel cell. Nanotechnology **15**(10) (2004)
47. G. Sun, L. Sun, H. Xie, J. Liu, Electrospinning of nanofibers for energy applications. Nanomaterials **6**(7), 129 (2016)
48. W. Xi-Zhao, Platinum nanoparticles supported on carbon nanofibers as anode electrocatalysts for proton exchange membrane fuel cells. Acta Phys. Chim. Sin. **27**(8), 1875–1880 (2011)
49. T. Promanan, T. Sarakonsri, Synthesis and characterization of palladium-based nano-catalyst on N-doped graphene for direct ethanol fuel cells. Rev. Adv. Mater. Sci. **52**, 107–112 (2017)
50. E. Herna, et al., Chemical modification of carbon nanofibers with plasma of acrylic acid. Plasma Process. Polym. **i**, 627–633 (2013)
51. D. Soundararajan, J.H. Park, K.H. Kim, J.M. Ko, Pt–Ni alloy nanoparticles supported on CNF as catalyst for direct ethanol fuel cells. Curr. Appl. Phys. **12**(3), 854–859 (2012)
52. S. Uhm, B. Jeong, J. Lee, A facile route for preparation of non-noble CNF cathode catalysts in alkaline ethanol fuel cells. Electrochim. Acta **56**(25), 9186–9190 (2011)
53. M. Shanbedi, S. Zeinali, A. Amiri, E. Hosseinipour, H. Eshghi, S.N. Kazi, Synthesis of aspartic acid-treated multi-walled carbon nanotubes based water coolant and experimental investigation of thermal and hydrodynamic properties in circular tube. Energy Convers. Manag. **105**, 1366–1376 (2015)

54. K.S. Ibrahim, Carbon nanotubes-properties and applications: a review. Carbon Lett. **14**(3), 131–144 (2013)
55. B.K. Kaushik, M.K. Majumder, Carbon nanotube based VLSI interconnects: analysis and design. SpringerBriefs Appl. Sci. Technol., i–iv (2015). 9788132220466
56. J.M. Herrera-Ramirez, R. Perez-Bustamante, A. Aguilar-Elguezabal, *An Overview of the Synthesis, Characterization, and Applications of Carbon Nanotubes* (Elsevier Inc., 2018)
57. P.S.S.R. Kumar, S.J. Alexis, *Synthesized Carbon Nanotubes and Their Applications* (Elsevier Inc., 2018)
58. S. Buller, M. Heise-Podleska, N. Pfänder, M. Willinger, R. Schlögl, Carbon nanotubes as conducting support for potential Mn-oxide electrocatalysts: influences of pre-treatment procedures. J. Energy Chem. **25**, 265–271 (2016)
59. A.J. Page, F. Ding, S. Irle, K. Morokuma, Insights into carbon nanotube and graphene formation mechanisms from molecular simulations: a review. Rep. Prog. Phys. **78**(3) (2015)
60. S. Ravi, S. Vadukumpully, Sustainable carbon nanomaterials: recent advances and its applications in energy and environmental remediation. J. Environ. Chem. Eng. **4**(1), 835–856 (2016)
61. M.H.-O. Rashid, S.F. Ralph, Carbon nanotube membranes: synthesis, properties, and future filtration applications. Nanomaterials **7**(5), 99 (2017)
62. S.C. Motshekga, S.K. Pillai, S. Sinha Ray, K. Jalama, R.W.M. Krause, Recent trends in the microwave-assisted synthesis of metal oxide nanoparticles supported on carbon nanotubes and their applications. J. Nanomater. **2012** (2012)
63. V.T. Le, C.L. Ngo, Q.T. Le, T.T. Ngo, Surface modification and functionalization of carbon nanotube with some organic compounds. Nanotechnology, 2–7 (2013)
64. M. Liu et al., Pd nanoparticles supported on three-dimensional graphene aerogels as highly efficient catalysts for methanol electrooxidation. Electrochim. Acta **178**, 838–846 (2015)
65. N. Shaari, S.K. Kamarudin, Graphene in electrocatalyst and proton conductiong membrane in fuel cell applications: an overview. Renew. Sustain. Energy Rev. **69**(July 2016), 862–870 (2017)
66. A. Jana, E. Scheer, S. Polarz, Synthesis of graphene-transition metal oxide hybrid nanoparticles and their application in various fields. Beilstein J. Nanotechnol. **8**(1), 688–714 (2017)
67. Y. Zhu et al., Graphene and graphene oxide: synthesis, properties, and applications. Adv. Mater. **22**(35), 3906–3924 (2010)
68. S.K. Bikkarolla, P. Cumpson, P. Joseph, P. Papakonstantinou, Oxygen reduction reaction by electrochemically reduced graphene oxide. Faraday Discuss. **173**, 415–428 (2014)
69. C.P. Deming, R. Mercado, V. Gadiraju, S. W. Sweeney, M. Khan, S. Chen, Graphene quantum dots-supported palladium nanoparticles for efficient electrocatalytic reduction of oxygen in alkaline media. ACS Sustain. Chem. Eng., 1–9 (2015)
70. R.S. Edwards, K.S. Coleman, Graphene synthesis: relationship to applications. Nanoscale **5**(1), 38–51 (2013)
71. K. Jukk, N. Kongi, L. Matisen, T. Kallio, K. Kontturi, K. Tammeveski, Electrochimica acta electroreduction of oxygen on palladium nanoparticles supported on nitrogen-doped graphene nanosheets. Electrochim. Acta **137**, 206–212 (2014)
72. J. Lee, K.S. Novoselov, H.S. Shin, Interaction between metal and graphene: graphene. Am. Chem. Soc. Nano **5**(1), 608–612 (2010)
73. X. Liu, C.-Z. Wang, M. Hupalo, H.-Q. Lin, K.-M. Ho, M. Tringides, Metals on graphene: interactions, growth morphology, and thermal stability. Crystals **3**(1), 79–111 (2013)
74. Z. Yang, H. Nie, X. Chen, S. Huang, Recent progress in doped carbon nanomaterials as effective cathode catalysts for fuel cell oxygen reduction reaction. J. Power Sources **236**, 238–249 (2013)
75. L.F. Mabena, S. Sinha Ray, S.D. Mhlanga, and N. J. Coville, Nitrogen-doped carbon nanotubes as a metal catalyst support. Appl. Nanosci. **1**(2), 67–77 (2011)
76. S. Ren, F. Huang, J. Zheng, S. Chen, H. Zhang, Ruthenium supported on nitrogen-doped ordered mesoporous carbon as highly active catalyst for NH_3 decomposition to H_2. Int. J. Hydrogen Energy **42**(8), 5105–5113 (2017)

77. S. Samad et al., Carbon and non-carbon support materials for platinum-based catalysts in fuel cells. Int. J. Hydrogen Energy **43**(16), 7823–7854 (2018)
78. J.A. Prithi, N. Rajalakshmi, G. Ranga Rao, Nitrogen doped mesoporous carbon supported Pt electrocatalyst for oxygen reduction reaction in proton exchange membrane fuel cells. Int. J. Hydrogen Energy **43**(9), 4716–4725 (2018)
79. D. Puthusseri, S. Ramaprabhu, Oxygen reduction reaction activity of platinum nanoparticles decorated nitrogen doped carbon in proton exchange membrane fuel cell under real operating conditions. Int. J. Hydrogen Energy **41**(30), 13163–13170 (2016)
80. R. Yadav, C.K. Dixit, Synthesis, characterization and prospective applications of nitrogen-doped graphene: a short review. J. Sci. Adv. Mater. Dev. **2**(2), 141–149 (2017)
81. H. Miao et al., Enhancing the pyridinic N content of Nitrogen-doped graphene and improving its catalytic activity for oxygen reduction reaction. Int. J. Hydrogen Energy **42**(47), 28298–28308 (2017)
82. S. Zhuang, B.B. Nunna, D. Mandal, E.S. Lee, A review of nitrogen-doped graphene catalysts for proton exchange membrane fuel cells-synthesis, characterization, and improvement. Nano Struct. Nano Obj. **15**, 140–152 (2018)
83. D. Wei, Y. Liu, Y. Wang, H. Zhang, L. Huang, G. Yu, Synthesis of n-doped graphene by chemical vapor deposition and its electrical properties. Nano Lett. **9**(5), 1752–1758 (2009)
84. B. Li, S.H. Chan, PtFeNi tri-metallic alloy nanoparticles as electrocatalyst for oxygen reduction reaction in proton exchange membrane fuel cells with ultra-low Pt loading. Int. J. Hydrogen Energy **38**(8), 3338–3345 (2013)
85. R.I. Jafri, N. Rajalakshmi, K.S. Dhathathreyan, S. Ramaprabhu, Nitrogen doped graphene prepared by hydrothermal and thermal solid state methods as catalyst supports for fuel cell. Int. J. Hydrogen Energy **40**(12), 4337–4348 (2015)
86. W.Y. Wong, W.R.W. Daud, A.B. Mohamad, A.A.H. Kadhum, K.S. Loh, E.H. Majlan, Influence of nitrogen doping on carbon nanotubes towards the structure, composition and oxygen reduction reaction. Int. J. Hydrogen Energy **38**(22), 9421–9430 (2013)
87. A. Pullamsetty, M. Subbiah, R. Sundara, Platinum on boron doped graphene as cathode electrocatalyst for proton exchange membrane fuel cells. Int. J. Hydrogen Energy **40**(32), 10251–10261 (2015)
88. Z.-H. Sheng, H.-L. Gao, W.-J. Bao, F.-B. Wang, X.-H. Xia, Synthesis of boron doped graphene for oxygen reduction reaction in fuel cells. J. Mater. Chem. **22**(2), 390–395 (2012)
89. J.C. Li, P.X. Hou, M. Cheng, C. Liu, H.M. Cheng, M. Shao, Carbon nanotube encapsulated in nitrogen and phosphorus co-doped carbon as a bifunctional electrocatalyst for oxygen reduction and evolution reactions. Carbon N. Y. **139**, 156–163 (2018)
90. Z. Cui, S. Wang, Y. Zhang, M. Cao, A simple and green pathway toward nitrogen and sulfur dual doped hierarchically porous carbons from ionic liquids for oxygen reduction. J. Power Sources **259**, 138–144 (2014)
91. J. Liu, P. Song, Z. Ning, W. Xu, Recent advances in heteroatom-doped metal-free electrocatalysts for highly efficient oxygen reduction reaction. Electrocatalysis **6**(2), 132–147 (2015)
92. J. Liang, Y. Jiao, M. Jaroniec, S.Z. Qiao, Angewandte sulfur and nitrogen dual-doped mesoporous graphene electrocatalyst for oxygen reduction with synergistically enhanced performance. Angew. Chem. Int. Ed., 11496–11500 (2012)
93. D.C. Higgins, A. Hoque, F. Hassan, J. Choi, B. Kim, Z. Chen, Oxygen reduction on graphene—carbon nanotube composites doped sequentially with nitrogen and sulfur. Acs Catal. (2014)
94. J. Jin, et al., Catalyst-free synthesis of crumpled boron and nitrogen co-doped graphite layers with tunable bond structure for oxygen reduction reaction. ACS Nano **4**, 3313–3321 (2014)
95. P.A. Denis, C.P. Huelmo, F. Iribarne, Theoretical characterization of sulfur and nitrogen dual-doped graphene. Comput. Theor. Chem. **1049**, 13–19 (2014)
96. A. Zehtab Yazdi, E.P.L. Roberts, U. Sundararaj, Nitrogen/sulfur co-doped helical graphene nanoribbons for efficient oxygen reduction in alkaline and acidic electrolytes. Carbon N. Y. **100**, 99–108 (2016)

Editorial Note

Dear Readers,

After almost three years of effort, we publish the special book dedicated to Nobel Laureate Prof. Akira Suzuki. His special lecture was delivered at IUMRS-ICAM 2017 (International Union Materials Research Society—International Conference on Advanced materials) in Kyoto. This book published through contributions from the speakers and attendants of IUMRS-ICAM2017 and other colleagues of the science society.

We would like to warmly thank for their kind help during the revision and editing of the book the colleagues:

Dr. Mpitloane Hato
Univeristy of Limpopo
South Africa
Dr. Bello Abdulhakeem
African University of Science and Technology (AUST)
Abuja Nigeria
Dr. Katlego Makgopa
Tshwane University of Technology
South Africa

We could not deliver the book without their help and contributions.

Here, we would like to express our regret and sorrow over the passing of our friend Ulirich, Prof. Hanns-Ulrich Habermeier. He was an internationally well-known applied physicist, who devoted his career to materials sciences. After he received his PhD at the University of Stuttgart in 1974, he worked at the Max Planck Institute for Metals Research in Stuttgart and became head of Scientific Services Technology at the Max Planck Institute for Solid State Research, Stuttgart.

We spend lots of time at many different conferences over the world and organized many conferences together. He usually showed up at the banquet with his bow tie and black suit and had a list of souvenir his wife gave to him whenever he attended conferences.

His memory and his work will remain alive in scientific world.

S. Kaneko et al. (eds.), *Carbon Related Materials*,
https://doi.org/10.1007/978-981-15-7610-2

Satoru Kaneko at Ebina, Japan
Alina Pruna at Bucharest, Romania
Masami Aono at Kagoshima, Japan
Paolo Mele at Omiya, Japan
Tamio Endo at Mie, Japan

E-MRS, Warshawa, September 2018

IUMRS-ICEM, Daejeon, September 2018

IUMRS-ICAM, Kyoto, August 2017

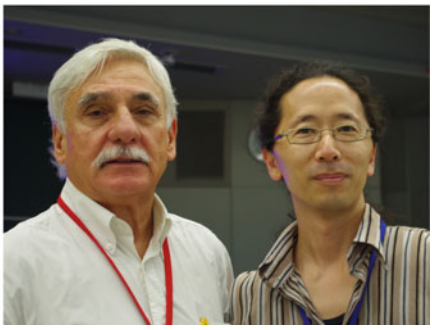

IUMRS-ICA, Fukuoka, August 2014


Memory of IUMRS-ICAM 2017
Step Substrate
ICCE